Ion Beam Science

Solved and Unsolved Problems

Part II

Edited by Peter Sigmund

Matematisk-fysiske Meddelelser 52:2

Det Kongelige Danske Videnskabernes Selskab
The Royal Danish Academy of Sciences and Letters

DET KONGELIGE DANSKE VIDENSKABERNES SELSKAB
udgiver følgende publikationsrækker:

THE ROYAL DANISH ACADEMY OF SCIENCES AND LETTERS
issues the following series of publications:

	Authorized Abbreviations
Historisk-filosofiske Meddelelser, 8°	Hist.Fil.Medd.Dan.Vid.Selsk. (printed area 175 x 104mm, 2700 units)
Historisk-filosofiske Skrifter, 4° (History, Philosophy, Philology, Archaeology, Art History)	Hist.Filos.Skr.Dan.Vid.Selsk. (printed area 2 columns, each 199 x 77 mm, 2100 units)
Matematisk-fysiske Meddelelser, 8° (Mathematics, Physics, Chemistry, Astronomy, Geology)	Mat.Fys.Medd.Dan.Vid.Selsk. (printed area 180 x 126 mm, 3360 units)
Biologiske Skrifter, 4° (Botany, Zoology, Palaeontology, General Biology)	Biol.Skr.Dan.Vid.Selsk. (printed area 2 columns, each 199 x 77 mm, 2100 units)
Oversigt, Annual Report, 8°	Overs.Dan.Vid.Selsk.

General guidelines

The Academy invites original papers that contribute significantly to research carried on in Denmark. Foreign contributions are accepted from temporary residents in Denmark, participants in a joint project involving Danish researchers, or those in discussion with Danish contributors.

Instructions to authors

Manuscripts from contributors who are not members of the Academy will be refereed by two members of the Academy. Authors of papers accepted for publication will receive galley proofs and page proofs; these should be returned promptly to the editor. Corrections other than of printer's errors will be charged to the author(s) insofar as the costs exceed 15% of the cost of typesetting.

Authors receive a total of 50 free copies. An order form, quoting a special price for additional copies, will accompany the page proofs. Authors are invited to provide addresses of up to 20 journals to which review copies could profitably be sent.

Manuscripts can be returned, but only upon request made before publication of the paper. Original photos and artwork are returned upon request.

Ion Beam Science

Solved and Unsolved Problems

Invited lectures presented at a symposium arranged by the Royal Danish Academy of Sciences and Letters Copenhagen, 1-5 May 2006

Part II

Edited by Peter Sigmund

Matematisk-fysiske Meddelelser 52:2

Det Kongelige Danske Videnskabernes Selskab
The Royal Danish Academy of Sciences and Letters

Abstract

This book emerged from a discussion meeting held at the Royal Danish Academy of Sciences and Letters in May 2006. It covers a broad scope of applications and fundamentals in the area of ion beam science. Applications in astrophysics, magnetic and inertial fusion, particle therapy and radiation biology are followed up by topics in materials analysis and modification including radiation damage, particle tracks and phase transitions. Several contributions are devoted to particle-induced emission phenomena. The unusual placement of particle penetration and atomic collisions in the end reflects the structure of the meeting.

The book is neither a comprehensive review nor a tutorial. However, authors were asked to focus on essentials, both on unsolved problems in their general areas and on problems that have been around for a while but have come (close) to a satisfactory solution. The prime purpose of the book is to help those engaged in basic and applied research within ion-beam science to stay or become alert with respect to central problems in and around their area.

Figures were reproduced with the kind permission of the American Nuclear Society, the American Physical Society, Begell House Inc, Elsevier Science, the Institute of Physics, the International Atomic Energy Agency, ITER, the National Institute for Fusion Science, and Springer Verlag.

Prof. P. Sigmund
Department of Physics and Chemistry, University of Southern Denmark
DK-5230 Odense M, Denmark
sigmund@ifk.sdu.dk

Typeset by Karada Publishing Services (KPS), Slovenia. E-mail: kts@siol.net
Printed in Denmark by Special-Trykkeriet Viborg a-s
ISSN 0023-3323 ISBN10 87-7304-330-3 ISBN13 978-87-7304-330-1

Table of Contents

Volume 1

Preface 7

List of Contributors 9

Ion-Solid Interactions in Astrophysics 13
Raúl A. Baragiola

Hadron Therapy: Radiotherapy Using Fast Ion Beams 37
Oliver Jäkel

Spatial Distribution of DNA Double-Strand Breaks from Ion Tracks 59
A. Hauptner, W. Friedland, S. Dietzel, G.A. Drexler, C. Greubel, V. Hable, H. Strickfaden, T. Cremer, A.A. Friedl, R. Krücken, H.G. Paretzke and G. Dollinger

Magnetic Confinement Fusion: Ions in ITER – Beams and Surfaces 87
A.W. Kleyn

High Energy Density Matter Generated by Heavy-Ion Beams, and Application to Fusion Energy 109
A. Blazevic, B. Rethfeld and D.H.H. Hoffmann

Ion Beam Analysis of Lower Dimensional Structures 133
L.C. Feldman

Solved and Unsolved Problems in Ion-Beam Analysis: The Influence of Single Collisions 151
P.L. Grande, A. Hentz, R.P. Pezzi, I.J.R. Baumvol and G. Schiwietz

Nanoscale Morphology Control Using Ion Beams 187
M.J. Aziz

Ion-Induced Surface Evolution in the Linear Instability Regime: Continuum Theory and Kinetic Monte Carlo Simulation 207
Eric Chason and Wai Lun Chan

Some Ion-Beam Modification Issues: Ion-Induced Amorphisation and Crystallisation of Silicon 227
J.S. Williams, G. de M. Azevedo and A. Kinomura

Experimental Phenomena and Thermal Spike Model Description of Ion Tracks in Amorphisable Inorganic Insulators 263
M. Toulemonde, W. Assmann, C. Dufour, A. Meftah, F. Studer and C. Trautmann

Thermal-Spike Models for Ion Track Physics: A Critical Examination 293
S. Klaumünzer

Some Solved and Unsolved Problems in Transmission Electron Microscopy Studies of Radiation Damage in Solids 329
S.E. Donnelly

Radiation Damage in Carbon Nanotubes: What Is the Role of Electronic Effects? 357
K. Nordlund

Index 371

Volume 2

Ion Beam-Induced Amorphization: A Crystal-to-Glass Transition? 383
Harry Bernas

Sputtering: Experiment 405
Andreas Wucher

Sputter Theory 433
Herbert M. Urbassek

A Critical Review of the Electron-Tunnelling Model of Secondary Ion Formation 465
Klaus Wittmaack

Electron Emission from Solids Irradiated with Swift Ion Beams 497
Hermann Rothard and Benoit Gervais

Recent Advances in Slow Heavy Particle Induced Electron Emission 525
HP. Winter, F. Aumayr, H. Winter and S. Lederer

Stopping of Swift Ions: Solved and Unsolved Problems 557
Peter Sigmund

Charge States and Energy Loss of Ions in Solids 595
N.R. Arista

Charge Transfer in Atom-Surface Interactions 625
J.P. Gauyacq

Channeling and Blocking of Energetic Charged Particles in Crystals 655
Jens Ulrik Andersen

Penetration Phenomena at Relativistic Energies 699
U.I. Uggerhøj

Early History of Ion Beam Physics 731
John A. Davies

Index 751

Ion Beam-Induced Amorphization: A Crystal-to-Glass Transition?

Harry Bernas*

CSNSM/CNRS, Université Paris-11
91405 Orsay, France

Abstract

Many static and dynamic properties of amorphous materials are universal, e.g., identical for organic or metallic glasses. This is also true for the liquid-to-glass transformation. This universality is still an open problem. Ion beams bring a novel facet to it, since they may induce the energetically unfavourable crystal-to-glass transformation. We enumerate and discuss the corresponding features in ion beam amorphization, notably those through which the beam-induced crystal-to-glass transformation resembles the Cohen–Grest liquid-to-glass percolation transition, and propose a phase diagram that relates the liquid-to-glass and crystal-to-glass transitions via recent theories of "dynamic jamming". The crystal-to-glass transition's stochastic properties suggest a study of the ion beam-solid interaction's effect on an evolving glass's ergodicity.

Contents

1 Introduction **384**

2 Glasses and the Liquid-to-Glass Transition **385**

3 Mechanisms of Ion-Induced Amorphization **389**
3.1 Ion Beam Amorphization of Semiconductors 390
3.2 Combining Kinetics and Chemistry: Amorphization of Metallic Alloys . . 392
3.3 The Case of Metal-Metalloid Compounds 393

* E-mail: bernas@csnsm.in2p3.fr

4 The Nature of the Amorphization Threshold: A Crystal-to-Glass Transition? 396

5 Ion Beams to Study Glasses? 400

Acknowledgements 401

References 401

1. Introduction

Notwithstanding their considerable differences in electronic properties, a vast compendium of organic or inorganic, insulating, semiconducting or metallic systems display remarkably similar dynamic behaviours when forced into the amorphous ("glassy") state. This has been repeatedly stressed and discussed in excellent reviews and textbooks (e.g., Anderson, 1979; Joffrin, 1979; Zallen, 1983; Jäckle, 1986; Cusack, 1988; Angell, 1995) that provide a basis for the present discussion. The point of view often taken in analyses of ion beam amorphization (e.g., Averback and de la Rubia, 1998, and references therein) stresses the progressive build-up of disorder on a microscopic scale, i.e., the nature and stability of ion-induced damage, the consequences of defect cascade overlap, etc. These important aspects obviously cannot be neglected, but in this paper I attempt to discuss the crystal-to-glass transformation in terms similar to the classical discussion of the liquid-to-glass transition. Such a parallel has its pitfalls – the wealth of data existing on the latter has no equivalent for the former, and suggestive analogies are not proof – but it may suggest new directions for ion beam experiments and simulations.

I summarily recall a few general properties of glasses and of the liquid-to-glass transition, and point out results on ion beam-amorphized systems that may be analyzed in the same perspective, as regards static and dynamic properties. The results suggest the possibility that the ion-induced crystal-to-glass transformation may be analyzed in terms of a percolation transition similar to that proposed by Cohen and Grest (Cohen and Grest, 1979; Grest and Cohen, 1981) for the liquid-to-glass transition. Finally, a most remarkable feature of glass evolution is its relation to ergodicity: the final Section briefly discusses the possible influence of ion irradiation on this basic property. This paper is rather speculative – my excuse is the organizers' request to peer into the highly disordered crystal ball of "open problems".

2. Glasses and the Liquid-to-Glass Transition

How to produce the amorphous, or glassy, state? Starting from the liquid state, slow cooling leads to crystallization via a first-order phase transition at a well-defined temperature T_m. In order to form a glass, the liquid must be supercooled to a temperature below T_g, far below the melting temperature T_m (Figure 1a), at sufficient speed to avoid nucleation of stable crystallites. An amorphous system is thus intrinsically thermodynamically unstable, produced by the slowing-down of relaxation processes that would otherwise return it to the liquid (at high temperature) or some ordered crystalline structure (at low temperature). On a microscopic scale, these processes involve temperature-dependent atomic movements, lattice relaxation and lattice vibrations, which in turn depend on the bonding characteristics of the system (usually ionic for insulating glasses, covalent for amorphous semiconductors, and involving hybridized conduction electrons for amorphous metals). On the macroscopic scale, relaxation processes appear via the temperature evolution of the supercooled liquid's shear viscosity. As the liquid is cooled at a sufficiently fast rate, its viscosity increases; its volume and change of enthalpy decrease until – at a temperature termed the "glass temperature" T_g – both quantities deviate markedly from the extrapolated high-temperature curve, the deviation increasing as the temperature decreases. Just above T_g, the viscosity $\eta(T)$ changes dramatically (typically over more than ten orders of magnitude when the temperature is halved) according to the empirical so-called Fulcher–Vogel law (Cusack, 1988),

$$\eta(T) = \eta(0)\, \mathrm{e}^{A/[k_B(T-T_0)]}, \tag{1}$$

where T_0 is the temperature at which the viscosity diverges – the "free volume" in the glass vanishes. At T_g the viscosity is so high (typically above 10^{13} P) that the material no longer flows: if the liquid is kept at some temperature below – but fairly close to – T_g, the relaxation processes will continue (albeit extremely slowly), and carry the system from the "glass" curve to the extrapolated "supercooled liquid" curve. The crucial point is that the properties of a glass depend on its history, i.e., the initial state (temperature of the melt), cooling rate and quench temperature. As a result, T_g for a given substance is *non-unique* (Figure 1b), as opposed to the melting or freezing temperatures. The glass transition first appears as a kinetic transformation leading to configurational freezing, rather than as a thermodynamic phase transition (there is, in fact, a thermodynamic limitation that we ignore here – see the discussion of the "Kauzmann paradox" by Jäckle, 1986). The relaxation processes involved are sufficiently complex that when a given material becomes glassy, the final structural configuration on any scale is

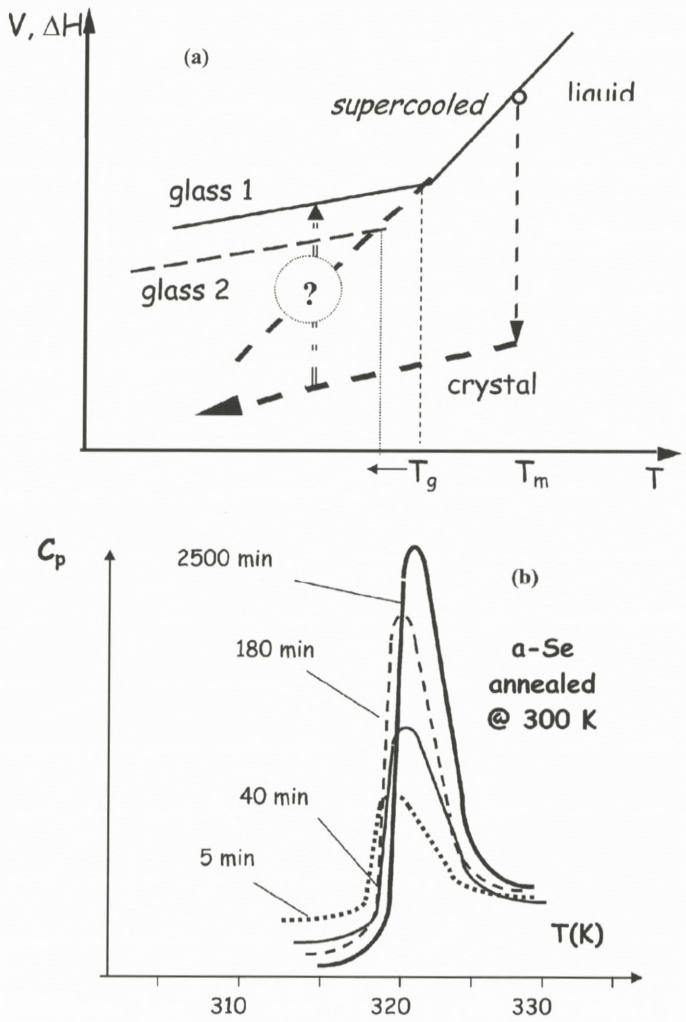

Figure 1. (a) Liquid-to-glass (*versus* liquid-to-crystal) transition as detected from volume or enthalpy change. The glass transition temperature T_g and the glass structure both depend on the cooling speed, leading to different glasses: glass 1, glass 2). The main point of this paper concerns the validity and consequences of the crystal-to-glass transition, denoted by the vertical arrow. (b) The specific heat displays a peak near the glass transition, but this is not a classical second-order phase transition. All curves were obtained after quenching from the same melt temperature, at the same speed and to the same final temperature T_f, well below T_g. After relaxing at T_f for varying times (shown in the figure), samples were annealed at constant speed: the height and position of the specific heat peak both depend on the system's relaxation towards its equilibrium configuration at T_f. Kinetics thus dominate the transition. Adapted from R.B. Stephens, J. Non-Crystalline Solids **20**, 75 (1976).

non-unique. Both the observed glass viscosity change and T_g therefore depend strongly on the ratio of the experimental measuring time to the average structural relaxation time. This also accounts for the specific heat variation shown in Figure 1b, since atomic motion is hindered below T_g, eliminating the relaxation contribution to the free energy. This prevents the viscous liquid from exploring the entire phase space (i.e., all atomic configurations): the system becomes non-ergodic. Glass relaxation, through diffusion or inverse viscosity, then takes place – the system only travels through a part of phase space that depends on the initial and quench conditions, i.e., the glass's past history. Such dynamics are a universal feature of glassy systems (polymers, oxides, metglasses, spin glasses, etc.) and remain a major challenge to theory. We shall return to this in the last section. The "time-window" effect is very relevant to a discussion of ion beam effects, since flux-dependent irradiation-induced (or -enhanced, if thermal effects are present) atomic displacements are the source of structural relaxation in irradiation experiments. The influence of atomic displacements also depends on the size of the structural unit involved in the relaxation process – the microscopic features of defects and defect motion mechanisms in a glass are a continuing subject of debate. In apparent contradiction with the abovementioned dynamics, a wealth of experiments (e.g., Perepezko, 2004) has established that structural stability criteria always play a major role in determining such static properties of glasses as the glass-forming composition range, the chemical short-range order (CSRO) distribution, the relative stabilities, etc., which are practically the same for nominally identical glasses prepared under such very different conditions as melt-cooling, quench-condensation on a cold substrate, solid-state reactions, ion implantation or ion beam mixing. This is a strong indication that the statics of amorphous phases may be related to free energy considerations and thermodynamic phase diagrams. How to reconcile these two aspects?

"Amorphous" does not mean random. On a near-neighbor scale (typically up to 3–5 atomic distances), the atomic arrangement in any amorphous system as determined by the atomic bonds shows that the interatomic distances and bonding angles for a given system display distributions as intuitively expected, but around well-defined average values that are those of some crystalline phase. Short-range order, or more precisely *chemical* short-range order (CSRO), can be defined for an amorphous system in the absence of long-range order. Rather narrow distributions in the number of atoms in a ring and among the bond angles on a short-range scale suffice to produce a solid with no long-range order, as evidenced in X-ray and neutron diffraction experiments, as well as extended X-ray atomic fine structure (EXAFS) experiments performed on all types of glasses. Whatever the nature of the chemical bond, such experiments and corresponding simulations

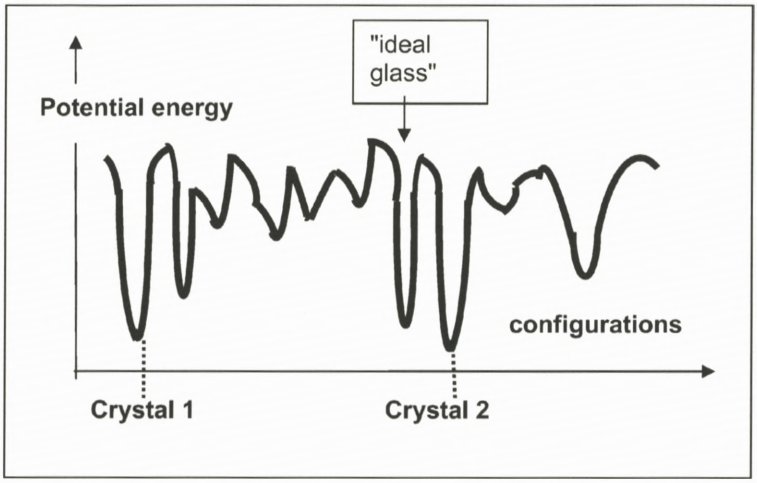

Figure 2. Schematic of potential energy curves corresponding to different possible configurations (i.e., different amorphous phases) of a glass, including the most stable (long-term annealed) glass. Two crystalline phases are also shown. The different configurations are traditionally accessed by different cooling rates. A transition from one configuration to some other is possible via, e.g., annealing or applied pressure, as shown by differential calorimetry, X-ray diffraction or EXAFS experiments.

always confirm the existence of a well- defined CSRO. On the other hand, the existence of *distributions* in the number of neighbors and interatomic distances shows that the free energy of a glass structure is not unique, as opposed to the case of a crystalline structure at the same composition, in which bond lengths and angles are single-valued. The existence and influence of medium-range order, typically beyond the third or fourth nearest neighbor seen in neutron diffraction or EXAFS, is also increasingly recognized and increases the number of possible structural configurations. There are thus (e.g., Laaziri et al., 1999; Sheng et al., 2006) a multiplicity of different amorphous states, corresponding to different minima in configurational space (Figure 2). The effect of irradiation on the short- and medium-range order scale in glasses is likely crucial to ion beam amorphization dynamics, as discussed below.

An analysis of the liquid-to-glass transition was provided by the free-volume theory of Cohen and Grest (1979) and Cohen and Grest (1981). The theory associates a volume v (initially the Voronoi polyhedron) with each molecule (or atom) in a liquid, and when atomic motion leads to v being larger than a critical value v_c, regards the excess volume as free; no local free energy is required for redistribution of free volume v_f among the molecules, and v_f is a fluctuating quantity

(related to fluctuations of the total free volume in the liquid); finally, transport only occurs when a molecule (or atom) acquires enough free volume. Thus the reduction, upon cooling, of molecular (or atomic) mobility – and of structural relaxation – is directly related to the free volume decrease and provides a path to Equation (1). A most important feature is that the above assumptions define two radically different types of cells, "solid-like" ($v < v_c$) and "liquid-like" ($v > v_c$), with free volume exchange only being performed among the latter under conditions (connectivity and a sufficient number of identical neighbouring cells) that are identical to those existing in high-density percolation, favoring dense, well-connected clusters over isolated sites. Denoting $p(T)$ the temperature-dependent fraction of liquid-like cells and p_c the high-density percolation threshold, the glass transition occurs at $p(T) = p_c$, i.e., when $p < p_c$, the system is a solid glass with non-connected finite liquid-like clusters; when $p > p_c$, an infinite liquid-like cluster allows molecular (or atomic) transport throughout the sample. The Cohen-Grest theory relates to thermodynamics by weighting the local free energy functions over the elementary cluster volume size distribution, and introducing an entropy term due to diffusive motion inside the liquid-like clusters.

The following discussion of the crystal-to-glass transition (Section 3) is based on the percolation analysis and on a reinterpretation of the "liquid-like" clusters in terms, not of viscosity or diffusivity, but of "shear transformation" (Falk and Langer, 1998) or "jamming" (Cates et al., 1998) zones. These zones appear in dynamical theories of shear deformation in amorphous solids, colloids or granular material as small (nanometer size) volumes that either block or allow inelastic rearrangements under shear stress, depending on their internal configuration relative to an applied shear stress orientation. Liu and Nagel (1998), Silbert et al. (2002) and Shi and Falk (2005) showed that such strain localization may also occur in the liquid-to-glass transition. In all cases, as the temperature is reduced the system, which at high temperature explored all possible configurations, progressively finds itself limited to the exploration of an increasingly small fraction of phase space – it becomes non-ergodic.

3. Mechanisms of Ion-Induced Amorphization

A thermodynamic crystal-to-glass transition is clearly energetically unfavourable (Figure 1): the transformation only occurs via the forcing due to the ion energy deposition. Irradiation-induced atomic displacements affect not only the phase stability but also the phase transformations, depending both on the temperature at which they occur and on the ion flux. For a discussion of how the combination of both parameters controls ("forces") atomic mobility, see Martin and Bellon

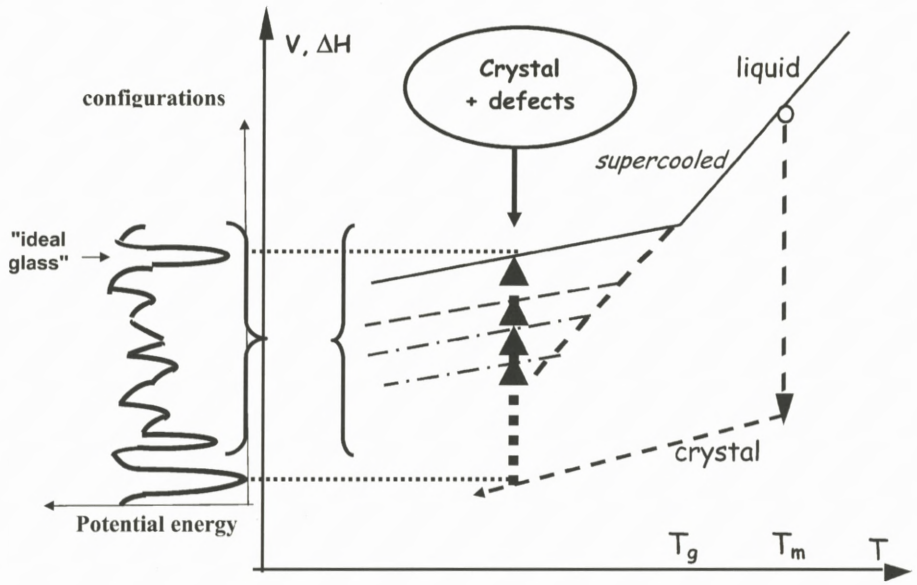

Figure 3. Relating Figure 1a to Figure 2. Different amorphous states (with different CSRO configurations) have different free energies: thermal annealing promotes relaxation from one of these states to a more stable one, while irradiation can allow (full arrows) the system to explore a variety of configurations, independently of their relative stability.

(1997). In this section, the emphasis is on those aspects of ion beam-induced amorphization of diverse materials from which a consistent view of the crystal-to-glass transition may be built. The detailed mechanisms clearly differ according to the nature of the chemical bonds in the irradiated materials, since the latter determine not only the short-range order (Section 1), but also the atomic mobility and the nature of defects.

3.1. Ion Beam Amorphization of Semiconductors

Because of their applications, a wealth of studies exists on semiconductors, and particularly on Si. As regards static properties, the most notable fact is the demonstration (e.g., Laaziri et al., 1999; Glover et al., 2001) via X-ray, neutron, EXAFS, Raman, differential calorimetry, and other experiments that there exist different amorphous states corresponding to different short-range order configurations, that these are accessible by irradiation, and that thermal annealing can promote relaxation from one of these states to a more stable one. This situation is schematized in Figure 3. The results are less clear-cut as regards the dynamical properties. In semiconductors, the dominating directional covalent bonds com-

plicate the amorphization process. The beam-induced crystalline-to-amorphous (c/a) transformation of elemental Si was first observed decades ago. A room-temperature amorphization curve under Si ion irradiation, may be determined via a precise Rutherford Backscattering (RBS) channeling experiment (e.g., Holland and Pennycook, 1989). The observed "damaged fraction" is actually the amorphous fraction α, as verified by transmission electron microscopy (TEM). The experimental curve may be fitted by

$$\alpha(\mathrm{c/a}) = 1 - \mathrm{e}^{-\sigma\phi}, \tag{2}$$

where ϕ is the ion fluence and σ a "damage cross-section" to be determined. Essentially identical curves (with different values of σ, ϕ) are obtained for different irradiating ions in different semiconducting materials. Of course, such a Poisson-type probability distribution does not provide a microscopic description of any specific mechanism. Does amorphization occur inside individual cascades (Morehead and Crowder, 1970), whose ultimate superposition would lead to overall amorphization in the implanted volume? Or is the driving force for transformation the storing of lattice defects, which locally raise the free energy of the sample above that of amorphous Si (Vook and Stein, 1969; Swanson et al., 1971)? The latter was favoured: if defects were only created in the cascade core, amorphization would be far less efficient than experimentally found, and many experiments showed that amorphization became more difficult or impossible just as defects became mobile. In fact, room temperature *in-situ* transmission electron microscopy (TEM) with an ion beam impacting the sample inside the TEM chamber (Ruault et al., 1983) clearly showed (Figure 4) that (for large deposited energy densities at least) both processes coexist, and there is actually a form of nucleation and growth in the amorphization process, mediated by the existence of defected zones outside of the cascade core. Thus, for elemental Si with covalent bonds, the transformation to the amorphous phase is neither unique nor a simple one. Both heterogeneous amorphization and, more frequently, a form of "local" homogeneous nucleation and growth occur in ion-irradiated samples. This rather agrees with the conclusions of Holland and Pennycook (1989). Specifically, the *in-situ* TEM experiments show that many strained-induced contrasts due to dislocations formed in the cascade core survive as amorphization proceeds, so that relatively long-range strain effects – also indicated in early MD simulations (Averback and de la Rubia, 1998) – contribute to lattice destabilization and subsequent amorphization. This feature will reappear when discussing evidence for "jamming" effects. Recent MD simulations (e.g., Pelaz et al., 2004; Lewis and Nieminen, 1996) detailed such structures, and concur with high resolution TEM experiments (Yamasaki 2002) showing that these defects resemble "amorphous nuclei" composed of 5- and 7-member Si rings.

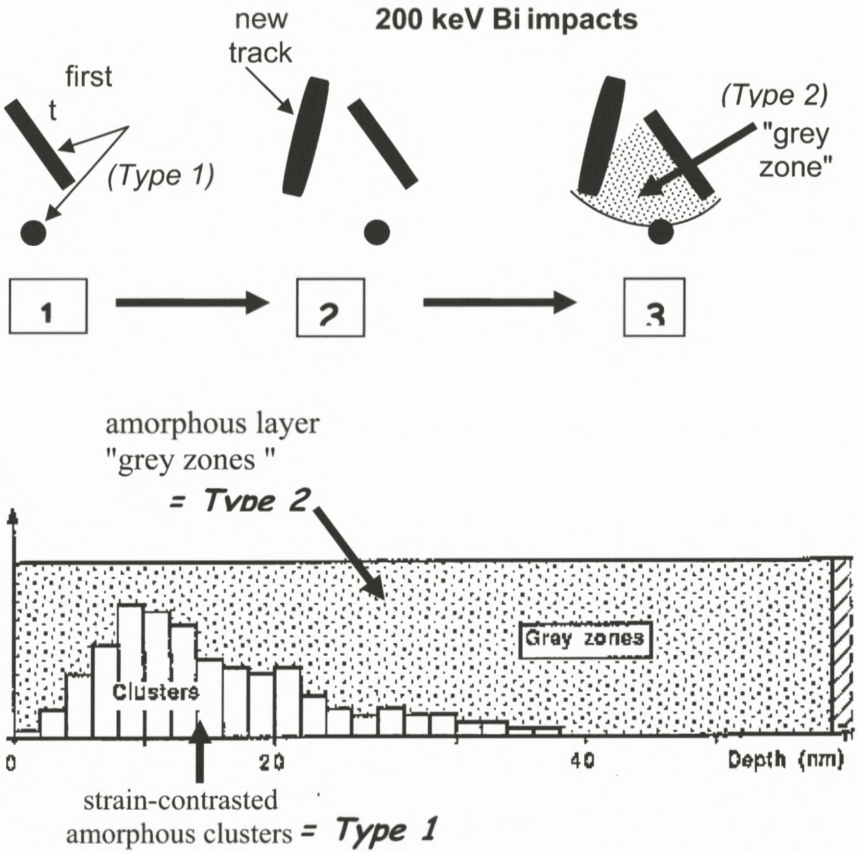

Figure 4. In-situ TEM experiment showing 200 keV Bi^+ ion-induced amorphization process in Si at 300 K. Upper: (1) Two impacts within ca. 60 nm have produced two high-contrast defected areas (dislocations: Type 1 damage); (2) a new impact occurs within ~60 nm, producing another Type 1-contrast area; (3) simultaneously, the entire area within the three impact tracks becomes "grey", identified by selected area diffraction as amorphous (Type 2 damage). Lower: comparing the defect cluster depth histogram as measured via TEM with the amorphous layer thickness as measured by RBS/channeling. The amorphous area extends well beyond the dislocation (Type 1 damage) distribution. Type 1 damage anneals at 500 K; Type 2 damage anneals at 800 K. Figure from Ruault et al. (1983).

3.2. Combining Kinetics and Chemistry: Amorphization of Metallic Alloys

The analysis of crystalline-to-amorphous transformations in metallic alloys containing two or more components with attractive potentials is very informative

because it relates more directly to equilibrium phase diagrams. A simple ordered intermetallic compound (e.g., ABABABA... sequences along one or more low-index directions) may be affected by irradiation via chemical disordering or structural defect accumulation (individual replacements or replacement sequences). The initial crystal lattice structure is preserved if the ordering energy is lower than the energy difference between the amorphous and crystalline states (irradiation-induced ordering may actually occur in this way, see Bernas et al., 2003); the reverse case can lead to amorphization. Experiments and MD simulations indicate that chemical disorder may suffice to amorphize (Massobrio et al., 1990), whereas in other instances (e.g., Sabochik and Nghi, 1990) chemical disordering occurs first, with subsequent amorphization due to defect accumulation in the destabilized lattice. The relative free energies, the initial and final states' stability, interfacial energies and strain all play a role, which we ignore here in searching for general features. We stress, rather, that the progressive amorphization of the $NiZr_2$ system and the correlated change in elastic properties was very well described (Massobrio et al., 1990) by high-density bond percolation of the chemically disordered zones. Crucial information also comes from the amorphizing system's dynamics, since its evolution is driven by a continuous flow of atomic displacements producing first antisite defects, then local order restructuring. Essential results (Watanabe et al., 2003) in this area are discussed in Section 4.

3.3. The Case of Metal-Metalloid Compounds

The transition metal-metalloid compounds around the deep eutectic composition (e.g., Fe_3B, $Ni_{80}P_{20}$, $Pd_{80}Si_{20}$, ...) were the first "metglasses" produced by ultraquenching, due to the presence of covalent metalloid bonds and to the corresponding structural complexity of many of their ordered phases. Starting from the crystalline variety of these compounds, irradiation-induced amorphization occurred at low fluences, in the 0.1 dpa (displacements per atom) range, and the amorphization fluence dependence resembled that of Equation (2).

Alloys of the same nominal composition may be produced by direct implantation of the metalloid into the initially pure crystalline metal, thus providing information on the amorphization dynamics. For example, a combined channeling and *in-situ* TEM study (Cohen et al., 1985; Schack, 1984) of progressive amorphization of P-implanted Ni as a function of the implantation-induced compositional change showed (Figure 5) that at 80 K (precluding defect or atom movement) the amorphous fraction α varies as

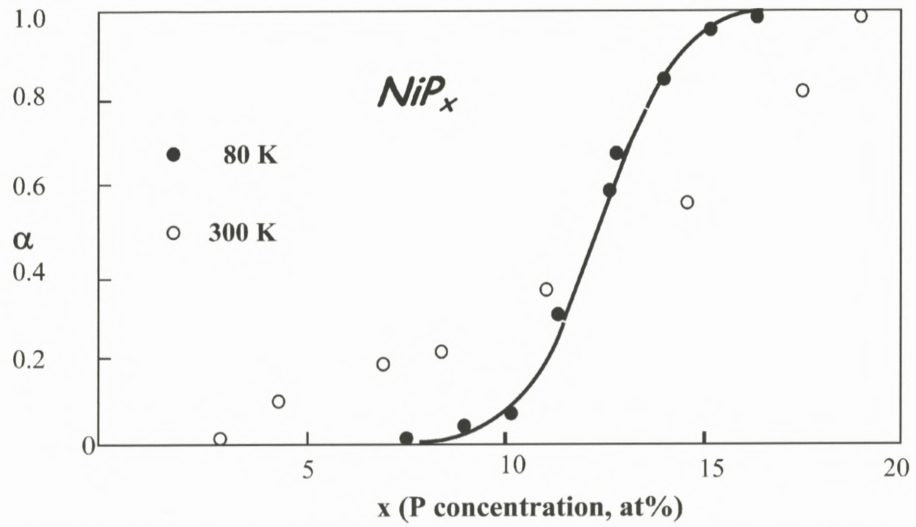

Figure 5. Dependence of amorphous fraction α on concentration x of 100 keV P ions implanted into Ni at 80 K or 300 K. Solid line: best fit to 80 K results with Equation (3) and a critical volume v_c of radius ~1 nm. At 300 K, both collisional defects and P atoms move under implantation; amorphous clusters grow, so that the percolation model is no longer appropriate. Adapted from Cohen et al. (1986).

$$\alpha = \sum_{N=N_C}^{\infty} \frac{(\bar{N})^N}{N!} e^{-\bar{N}}, \tag{3}$$

where it is assumed that amorphization proceeds by a build-up of implantation-induced elementary amorphous clusters of volume v_c, synthesized when $N \geq N_C$, whose size is obtained from a single-parameter fit to Equation (3). The average number $\bar{N}$ of P atoms in a cluster is proportional to the latter's volume and to the mean P concentration c_c in the sample. The "amorphization threshold" corresponds to a critical concentration of $c_c = 12\%$ at 80 K. At these implant concentrations, defect density saturation has long been reached, so amorphization is essentially due to chemical effects, just as it was due to chemical disordering when irradiating intermetallic alloys such as NiTi or the metal-metalloid compounds at the deep eutectic composition.

The radius of the critical volume v_c is found to correspond to the distance over which the CSRO may be defined according to EXAFS, X-ray or neutron diffraction measurements. The same features were found in many similar amorphization experiments, the elementary cluster size remaining the same and the critical concentration depending on the initial lattice structure. The size deduced

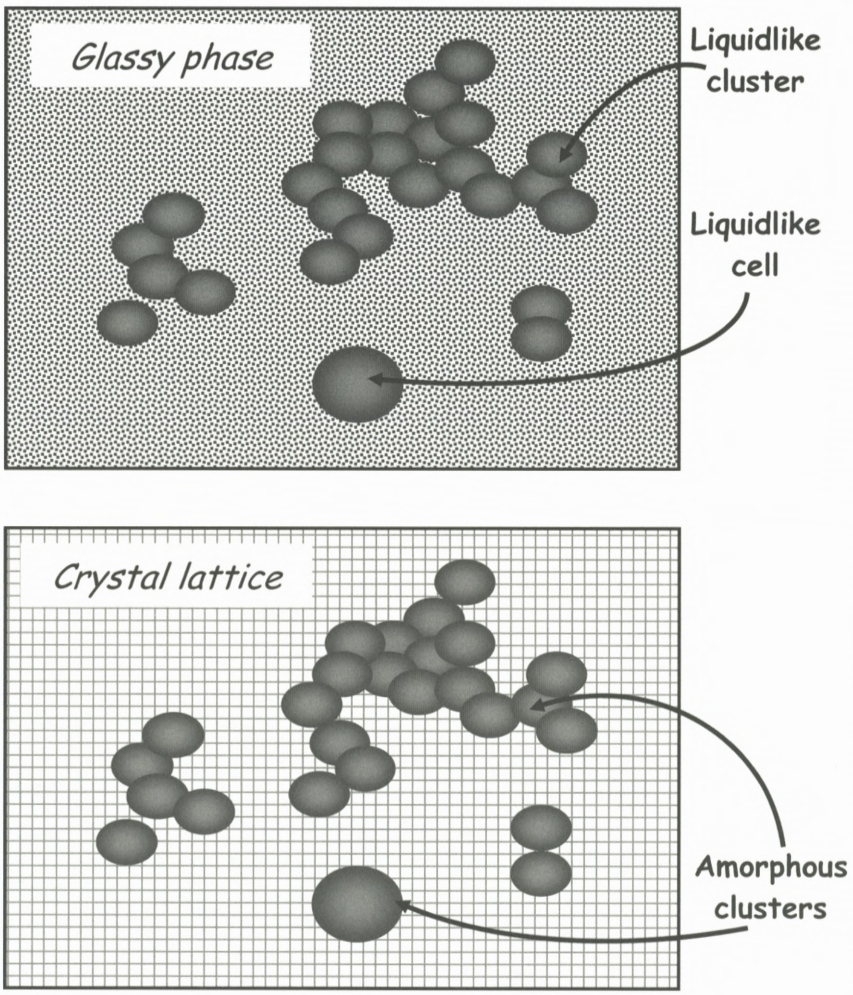

Figure 6. Schematic view of the proposed ion beam-induced amorphization mechanism (lower part), compared to a schematic of the free-volume theory of Cohen and Grest (upper part). Percolation of transformed zones plays the major role in each case.

from the fit to Equation (3) is an indication that, at least for those metglasses whose CSRO is determined by covalent bonds, the amorphous lattice results from a progressive accumulation of nanometer-size elements, whose packing properties are presumably determined both by the CSRO around a solute atom and by the organization of the initially crystalline host. This geometrical aspect suggests the following percolation description.

4. The Nature of the Amorphization Threshold: A Crystal-to-Glass Transition?

The ultimate purpose of this section will be to examine possibly common features of the liquid-to-glass and crystal-to-glass transition, and their differences. First, consider the static properties. As noted above, the "free volume" theory, based on the notion that glasses contain extra volume relative to the crystalline phase with atomic transport being possible only between the corresponding "open cells", projects the glass transition problem onto that of a percolation transition. Percolation theory only requires that the physical structure of the "open cells" be defined by geometry (i.e., whether connections between "lattice points" are determined by sites or by bonds). As a first step, analyzing amorphous materials properties in this way can provide a guide for comparison with MD simulations based on different assumptions regarding the elementary entities that form a glass. Can the implantation-induced amorphization process in NiP_x be analyzed by a percolation model? In writing Equation (3), it was assumed that the initial fcc Ni lattice was progressively filled (Figure 6) by elementary nm-size amorphous volumes. As the concentration of these building-blocks increases, they randomly connect to each other in the fcc lattice and the observed amorphization threshold at 12% is just the three-dimensional bond-percolation threshold of the fcc lattice. (At higher temperatures, the combination of irradiation and thermal activation leads to time fluctuations, diffusion and growth – static percolation no longers holds.) A recent detailed experimental, simulation and modeling study of atomic arrangements in both metal-metal and metalloid-metal (including Ni-P) metglasses (Sheng et al., 2006) has shown that at comparatively low concentrations, solute atoms surround themselves with near-neighbor solvent atoms only, forming different types of icosahedra-like clusters which in turn tend to form "clusters of clusters" via symmetry and connectivity rules. The ion beam amorphization process suggested above is entirely consistent with this picture.

Now consider the dynamic, notably viscoelastic, properties which are a major feature of glasses (Anderson, 1979). Here, we are confronted with the special case of a heterogeneous system, with both a crystalline and an amorphous component. In the case of intermetallics the onset of amorphization is experimentally found to be accompanied (Grimsditch et al., 1987) by a drastic softening of the elastic properties. MD simulations (Massobrio et al., 1990) showed that this effect is directly related to the production of "distorted volumes" by accumulation of antisite defects, and that these volumes percolate with a threshold concentration of 15% (the material is bct), leading to an abrupt increase in the shear modulus. Metal-metalloid systems such as NiP_x or $PdSi_x$ which include both metallic

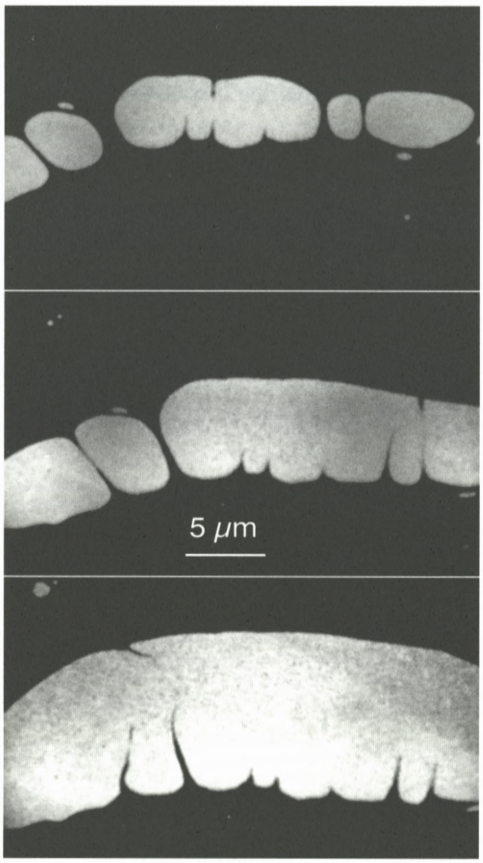

Figure 7. In-situ TEM observation of shear thinning, shear tearing and viscoplastic flow during Si ion implantation into Pd. The figure shows three stages of the same sample area (about 20% increase of the Si concentration between upper and lowest frame) just above the percolation threshold of the amorphous volumes (Schack, 1984).

and covalent bonds are expected to form even more highly distorted volumes leading to larger localized strain, inducing shearing at and above the percolation threshold. This is indeed shown (Figure 7) by *in-situ* TEM experiments (Schack, 1984) on unsupported films. As the implanted metalloid concentration increases in the metal, periodic stress appears in the film (not shown in the figure). When the metalloid concentration reaches the percolation threshold, shear thinning and shear softening abruptly lead to viscous flow and subsequent tearing of the film. The consequences of stress in fully amorphous materials are accounted for (Shi and Falk, 2005; Silbert et al., 2002) by MD simulations assuming the existence of

small volumes (estimated size typically on the nm, CSRO scale) in which stress is localized ("jammed"). Percolation of these "shear transformation zones" corresponds to a threshold for plastic flow, leading to progressive "unjamming" by the creation and disappearance of such trapping volumes. In quenched glasses, the "unjamming" is provided by the strain-rate induced deformation (i.e., changing the quenching speed). My interpretation of the heterogeneous system's behavior in Figure 7 is that the nanometer-sized amorphous volumes inside the residual crystal are also shear transformation zones, the difference being that they are inactive below the percolation threshold. The specific feature of ion beam experiments is that viscous flow sets in quite *suddenly* as soon as the percolation threshold is met. This is ascribed to the constant creation and destruction of "jamming volumes" by successive collisional displacements that accompany metalloid implantation. Above the percolation threshold, even negligible changes in the metalloid concentration correspond to intense structural reorganization via atomic motion on the nm scale. As noted previously, this can correspond to transformations of CSRO among the available local quasicrystalline structures that stabilize the glass configuration (Shi and Falk, 2005), and many tens of such structures have been found (Sheng et al., 2006).

The above picture of the ion-induced crystal-to-glass transition relates it to the liquid-to-glass transition, insofar as the active entities have the same (nanometer) size and the same basic role (shear transformation zones) in both cases. The picture is consistent with available information on the possible variations of CSRO, allowing structural modifications of the shear transformation zones; it is also consistent with the small size scales (due to low energy recoils) and induced stress of defected zones found by MD simulations in ion cascades (Averback and de la Rubia, 1998; Nordlund, 2006). A very interesting indication in the same direction was obtained in a series of *in-situ* high resolution TEM studies (Watanabe et al., 2003) performed during NiTi amorphization (requiring both chemical and defect-induced contributions) by high-energy electron irradiation. These experiments studied the local (nanometer scale) structure under irradiation and found that, while the average number of nanometer-size amorphous zones increased continuously as irradiation proceeded, the amorphous zone formation process was actually *discontinuous and even reversible*: due to atomic displacements, ion flux- and fluence-dependent structural fluctuations occurred under irradiation between the ordered and amorphous phases for a given observed zone. Thus, under irradiation and for this size scale, the free energy difference between one of the possible glass states and some metastable unrelaxed defect state is presumably small and easily modified by the irradiation. Moreover, their power spectrum reveals that the temporal fluctuations of the local order parameter are correlated. These results

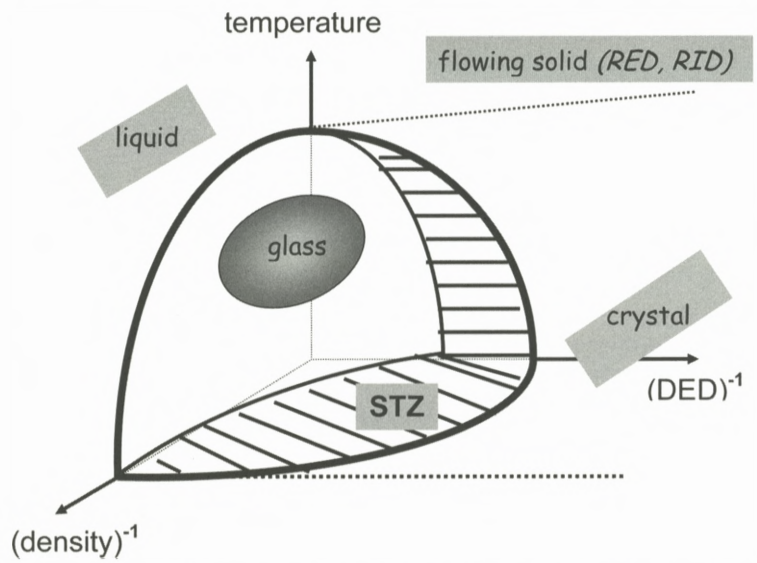

Figure 8. Proposed phase diagram relating both the liquid-to-glass and the (irradiation-induced) crystal-to-glass phase transitions to jamming. Both transitions are assumed to be driven by the formation of shear transformation zones (STZ – hatched volume). The axes are the temperature, the inverse density and the inverse deposited energy density (DED). The outer surface marks the frontier between ergodic and non-ergodic processes. (RED stands for radiation-enhanced diffusion; RID for radiation-induced diffusion).

detail the time-dependence of amorphization, and add confidence to the picture presented above.

We saw that as a system approaches the liquid-to-glass transition (just as for the jamming transition in granular or colloidal materials), it finds itself progressively restricted in its exploration of phase space. If we consider the NiP_x ($PdSi_x$) or NiTi systems as a whole, their evolution under ion-induced amorphization is towards non-ergodicity, and increasingly so as they become totally amorphous. From all the information gathered above, a tentative phase diagram may be drawn where the variables are the temperature, the density and the deposited particle energy density (Figure 8). This figure was suggested by the phase diagram proposed by Liu and Nagel (1998), relating the liquid-to-glass transition to dynamic jamming in granular materials. It is extended to a relation between dynamic jamming and *both* the liquid-to-glass and crystal-to-glass transitions. The drawn outer surface separates ergodic from non-ergodic processes; the hatched volume corresponds to the jamming processes or, more exactly, to the processes where shear transformation zones are active in the crystal-to-glass transition. The diagram suggests

that ion irradiation experiments could be a very adequate means to explore novel aspects of the crystal-to-glass transition, as well as a new tool to explore the liquid-to-glass transition.

5. Ion Beams to Study Glasses?

Consider – in the same samples as above – the subsystem constituted by (i) the nm-sized amorphous clusters inside the crystalline lattice and (ii) for the implanted NiP_x alloy, a time-window and a beam flux such that the displaced atom rate is high, but with no significant concentration change. Because of collision-induced restructuring of the small entities, the evolution of this subsystem is no longer restricted to a limited region of phase space: although the macroscopic system is non-ergodic, *for the nm-scale entities, the evolution tends to become ergodic*, even to the point (Watanabe et al., 2003) where some amorphous clusters revert to the crystalline state while others are subject to the reverse transformation. When the amorphous clusters pervade the whole sample and render it "uniformly amorphous" (thus a non-ergodic metglass), we may still divide up the metglass into nm-sized volumes as before, since this is the scale over which irradiation modifies the local structure and determines the evolution of the jamming site population. If the displacement rate is large enough, the evolution of this sub-population is essentially ergodic under irradiation, and this can affect the overall viscoelastic properties of the glass. The existence in physical systems of components with differing ergodicities (Palmer, 1982) is not exceptional (e.g., in magnetism). But particle irradiation is a physical tool that modifies the statistical, as well as the structural, behavior of the overall system's crucial (CSRO-scale) component. By subjecting a non-ergodic glass to an appropriate combination of ion-induced and thermal atomic mobility, its nanoscale subsystem may become ergodic and might even explore the crystalline phase; this way of looking at the sometimes-observed irradiation- induced amorphous-to-crystalline transformation is akin to a "driven alloy" analysis (Martin and Bellon, 1997).

Another, perhaps even more intriguing possible area for research is that of glasses *per se*, and of the liquid-to-glass transition. To my knowledge, there has been no ion beam work in this field, so the following remarks are speculative. As noted in Section 1, understanding why the dynamic evolution of glass non-equilibrium properties have universal features, as well as the origin of the latter, is a major long-standing problem in condensed matter physics. This is related to the crucial property of "aging" (Cipelletti and Ramos, 2005; Vincent et al., 1997), i.e., the continuous time evolution with sample age (e.g., time elapsed since glass quench) of such characteristic properties as the viscosity, strain relax-

ation, or magnetization in spin glasses. Aging most often involves both reversible quasi-equilibrium "fast" fluctuations and irreversible changes that are increasingly slow as the sample ages. What are the relations between the "slow" and "fast" processes (Sibani and Jensen, 2005; Mazoyer et al., 2006)? Can the corresponding dynamic correlation functions be experimentally identified (Berthier et al., 2005), and possibly acted on? Studies of these processes focus on the temperature range around T_g, largely because there is a reasonable experimental time window (relaxation phenomena are on the 100-second scale when the viscosity is around 10^{13} poise). Irradiation experiments could open new vistas. Under irradiation at low temperature the nanoscale dynamics become ergodic, directly controlled by statistical collisions due to the particle beam rather than to the temperature – the "observational time window" (which is actually an average collision time in a nm-size volume of the sample) depends on the beam intensity, which is also a control parameter of the ergodicity. This opens the possibility of examining directly whether and how acting on the nanoscale configuration and dynamic correlation length affects the slow dynamics' evolution. The results of Figure 7 suggest a significant influence indeed, but of course this requires confirmation in a "homogeneous" glass. More generally, irradiation experiments should also explore conditions where the temperature plays a more significant role, in the range nearer to (but still far below) T_g where thermal relaxation times are considerably shorter and so comparison and overlap with existing glass studies and models can be made.

Acknowledgements

It is a pleasure to acknowledge Peter Sigmund for many thought-provoking discussions during our collaborations and encounters over the years. I am also grateful to the participants of ION'06 for fruitful debate on several problems related (or not) to the topic of this paper. This work owes a major debt to my colleagues at CSNSM – Orsay, especially M.-O. Ruault, and was initially stimulated by an argument with P. Averbuch. I wish to thank S. Lipinska for the gracious hospitality of Moulin d'Andé.

References

Anderson P.W. (1979): Lectures on amorphous systems. In: Balian R., Maynard R. and Toulouse G. (Eds), Ill-Condensed Matter. North Holland, Amsterdam, pp 159–258

Angell C.A. (1995): Formation of glasses from liquids and biopolymers. Science **267**, 1924–1935

Averback R.S. and de la Rubia T.D. (1998): Displacement damage in metals and semiconductors. Solid State Phys. **51**, 281

Bernas H., Attane J.P., Heinig K.H., Halley D., Ravelosona D., Marty A., Auric P., Chappert C. and Samson Y. (2003): Ordering intermetallic alloys by ion irradiation: A way to tailor magnetic media. Phys Rev Lett **91**, 077203

Berthier L., Biroli G., Bouchaud J.P., Cipelletti L., El Masri D., L'Hote D., Ladieu F. and Perino M. (2005): Direct experimental evidence of a growing length scale accompanying the glass transition. Science **310**, 1797–1800

Cates M.E., Wittmer J.P., Bouchaud J.P. and Claudin P. (1998): Jamming, force chains, and fragile matter. Phys Rev Lett **81**, 1841–1844

Cipelletti L. and Ramos L. (2005): Slow dynamics in glassy soft matter. J. Phys. Cond. Matter **17**, R253–R285

Cohen M.L. and Grest G.S. (1979): Liquid-glass transition, a free-volume approach. Phys. Rev. B **20**, 1077–1098

Cohen C., Benyagoub A., Bernas H., Chaumont J., Thome L., Berti M. and Drigo A.V. (1985): Transformation to amorphous state of metals by ion-implantation: P in ni. Phys Rev B **31**, 5–14

Cusack N.E. (1988): The Physics of Structurally Disordered Matter. Adam Hilger, Bristol

Falk M.L. and Langer J.S. (1998): Dynamics of viscoplastic deformation in amorphous solids. Phys Rev E **57**, 7192–7205

Gibbons J.F. (1972): Proc IEEE **60**, 1062

Glover C.J., Ridgway M.C., Yu K.M., Foran G.J., Desnica-Frankovic D., Clerc C., Hansen J.L. and Nylandsted-Larsen A. (2001): Structural-relaxation-induced bond length and bond angle changes in amorphized Ge. Phys Rev B **6307**, 073204

Grest G.S. and Cohen M.L. (1981): Liquids, glasses, and the glass transition: A free-volume approach. Adv Chem **48**, 455

Grimsditch M., Gray K.E., Bhadra R., Kampwirth R.T. and Rehn L.E. (1987): Brillouin-scattering study of lattice-stiffness changes due to ion irradiation – Dramatic softening in Nb_3Ir. Phys Rev B **35**, 883–885

Holland O.W. and Pennycook S.J. (1989): New model for damage accumulation in si during self-ion irradiation. Appl Phys Lett **55**, 2503–2505

Jäckle J. (1986): Models of the glass transition. Rep Progr Phys **49**, 171–231

Joffrin J. (1979): Disordered systems-experimental. In: Balian R., Maynard R. and Toulouse G. (Eds), Ill-Condensed Matter. North Holland, Amsterdam, pp 63–154

Landau L. and Lifshitz I.M. (1958): Statistical Physics, Addison-Wesley

Laaziri K., Kycia S., Roorda S., Chicoine H., Robertson J.L., Wang J. and Moss S.C. (1999): High resolution radial distribution function of pure amorphous silicon. Phys Rev Lett **82**, 3460–3463

Lewis L.J. and Nieminen R.M. (1996): Defect-induced nucleation and growth of amorphous silicon. Phys Rev B **54**, 1459–1462

Liu A.J. and Nagel S.R. (1998): Nonlinear dynamics – Jamming is not just cool any more. Nature **396**, 21–22

Martin G. and Bellon P. (1997): Driven alloys. Solid State Phys Adv Res Appl **50**, 189–331

Massobrio C., Pontikis V. and Martin G. (1990): Molecular-dynamics study of amorphization by introduction of chemical disorder in crystalline $NiZr_2$. Phys Rev B **41**, 10486–10497

Mazoyer S., Cipelletti L. and Ramos L. (2006): ArXiv preprint cond-mat/0603739

Morehead F.F. and Crowder B.L. (1970): A model for the formation of amorphous Si by ion bombardment. Rad Eff Def Sol **6**, 27–32

Nordlund K. (2006): Radiation damage in carbon nanotubes: What is the role of electronic effects? Mat Fys Medd Dan Vid Selsk **52**, 357–370

Palmer R.G. (1982): Broken ergodicity. Adv Phys **31**, 669–735

Pelaz L., Marques L.A., Aboy M. and Barbolla J. (2004): Atomistic modeling of ion beam induced amorphization in silicon. Nucl Instr Meth Phys Res B **216**, 41–45

Perepezko J.H. (2004): Nucleation-controlled reactions and metastable structures. Progr Mater Sci **49**, 263–284

Ruault M.O., Chaumont J. and Bernas H. (1983): Transmission electron microscopy study of ion implantation induced Si amorphization. Nucl Inst Meth **209–210**, 351–356

Sabochick M.J. and Nghi Q.L (1991): Radiation-induced amorphization of ordered intermetallic compounds CuTi, $CuTi_2$, and Cu_4Ti_3: A molecular-dynamics study. Phys Rev B **43**, 5243

Schack M. (1984): PhD Thesis, University of Paris XI

Sheng H.W., Luo W.K., Alamgir F.M., Bai J.M. and Ma E. (2006): Atomic packing and short-to-medium-range order in metallic glasses. Nature **439**, 419–425

Shi Y. and Falk M.L. (2005): Strain localization and percolation of stable structure in amorphous solids. Phys Rev Lett **95**, 095502

Sibani P. and Jensen H.J. (2005): Intermittency, aging and extremal fluctuations. Europhys Lett **69**, 563–569

Silbert L.E., Ertaş D., Grest G.S., Halsey T.C. and Levine D. (2002): Analogies between granular jamming and the liquid-glass transition. Phys Rev E **65**, 051307

Swanson M.L., et al. (1971): Radiat Eff **9**, 249

Vincent E., Hamman J., Ocio M., Bouchaud J.P. and Cugliandolo L.F. (1997): Slow Dynamics and Aging in Spin Glasses, Lecture Notes in Phys. Vol. 492. Springer Verlag, Berlin p 184

Vook F.L. and Stein, H.J. (1969): Radiat Eff **2**, 23

Watanabe S., Hoshino M., Koike T., Suda T., Ohnuki S., Takahashi H., Lam N.Q. (2003): Temporal fluctuation and its power law in the crystalline-to-glass transition during electron irradiation. Phil Mag **83**, 2599–2619

Zallen R. (1983): The Physics of Amorphous Solids. John Wiley, New York

Sputtering: Experiment

Andreas Wucher*

Department of Physics, University of Duisburg-Essen
Lotharstr. 1, D-47048 Duisburg, Germany

Abstract

A few aspects of experiments on particle-induced sputtering of solid surfaces are reviewed. In the *linear cascade* regime, experimental observables like sputter yields, energy and angular distributions of sputtered material are reasonably well understood, but open questions remain as to the physical nature of the surface binding energy, the emission of clusters and the electronic excitation of sputtered particles. In the *spike* regime, the emission mechanisms appear to be less clear. This is illustrated by recollecting some recent experimental data on particle emission under polyatomic projectile ion bombardment. The sputtering of molecular solids, again particularly under polyatomic projectile bombardment, is briefly discussed in terms of surface analytical applications.

Contents

1 Introduction: Experimental Tools **406**

2 The Linear Cascade Regime **408**
2.1 Yields 408
2.2 Energy Distributions 411
2.3 Angular Distributions 413
2.4 Low Energy Bombardment 415
2.5 Cluster Emission 416
2.6 Excitation and Ionization 418

3 The Spike Regime **421**
3.1 Yields 421

* E-mail: andreas.wucher@uni-due.de

3.2 Energy Distributions 422
3.3 Cluster Emission 423
3.4 Ionization and Excitation 424
3.5 Molecular Solids 425

4 Conclusions **427**

References **428**

1. Introduction: Experimental Tools

As a consequence of its widespread application area, the fundamentals of sputtering have been extensively investigated for more than four decades. Important milestones leading to our current understanding of the mechanisms were the early experiments on sputter yields conducted in the sixties and seventies which have been compiled and reviewed by Andersen and Bay (1981). These data were mostly obtained by weight loss measurements employing either electromechanical or quartz crystal microbalances. Due to this experimental technique, most of the available data were taken under so-called *dynamic* conditions, i.e. at large projectile ion fluences, where possible influences of bombardment induced surface modifications like topography evolution, etc., are not always well known.

Additional information on the sputtering process has been obtained from the distributions of the emitted species with respect to their emission energy, angle, excitation and charge state. Particularly the energy distribution of sputtered particles has been investigated extensively, since it provides the ultimate proof of the non-equilibrium character of the emission process. Experimental techniques applied to the determination of emission energy distributions include the time-of-flight analysis of sputtered neutral particles using either mechanical shutters or pulsed projectile beams in connection with time resolved detection of the sputtered particles using either electron impact, resonant or non-resonant laser post-ionization. Usually, post-ionization is followed by mass selection using either electrodynamic mass filters or time-of-flight (ToF) spectrometers. A second class of experiments utilizes the Doppler shift of resonant transitions in the emitted particle using, for instance, laser induced fluorescence for detection. The third tool employed to investigate kinetic energy distributions is electrostatic energy analysis of the emitted particles. With only one recent exception, practically all published energy distribution data of secondary ions have been determined this way, employing various variants of electrostatic energy filters. For neutrals, the method has been combined with post-ionization techniques, mostly by electron impact.

The angular emission distributions of sputtered particles have been investigated by collecting the emitted material on a substrate which is later subjected to surface and thin film analysis. The drawback of this method is that it can only be used in dynamic mode, involving relatively large amounts of sputtered material. Moreover, the mass distribution of sputtered particles is not accessible. For the static analysis of emitted neutrals, a technique has been developed which is based on laser post-ionization in combination with the spatially resolved detection of the generated photoions. In combination with a pulsed projectile ion beam, this allows the angular and energy resolved detection of emitted neutrals (EARN) (Kobrin et al., 1986).

The excitation states of sputtered particles were probed by different methods, depending on the lifetime of the investigated state. Short-lived states, on one hand, are detected by optical spectroscopy of the emitted light (see Yu, 1991, for a review). It has been attempted many times to correlate the distance dependence of the detected photon yield with the emission energy spectrum of the ejected excited particles, but this method is largely disturbed by cascading transitions from higher-lying states and must be regarded unreliable. Doppler broadening of the emitted spectral lines has also been utilized for that purpose (Betz, 1987), but the observed shifts are small and therefore measured line profiles must be fitted by a known functional form of the emission energy distribution. Long-lived metastable states, on the other hand, are probed by the same resonant techniques as ground state particles, just using different resonances specific for the investigated state. Again, detection is made either by laser induced fluorescence or by photoionization and subsequent ToF mass spectrometry.

The purpose of the present paper is not to attempt a comprehensive review of all data and information about sputtering phenomena that have been collected over many years using the above mentioned experimental techniques. In fact, there are a number of extensive reviews the reader is referred to in this respect (see, for instance, "Sputtering by Particle Bombardment", Vols. 1–3 and the upcoming Vol. 4, ed. R. Behrisch et al.). Instead, focus will be given to a few aspects where active research is currently being pursued. In the linear cascade regime, most of the fundamental mechanistic concepts are understood and reasonably good agreement has been achieved between experimental data and theory (Urbassek, 2006). This will be illustrated on a few examples, and a few open questions will be highlighted which still appear to be unsolved after many years of investigation. In the spike regime of collisional sputtering, even the fundamental concepts of bombardment induced particle emission have not been completely understood yet. This will be illustrated in terms of recent data collected for impact of polyatomic or "cluster" projectiles onto either simple elemental or molecular solids. Due to

the fact that (i) neutral particles make up the majority of the sputtered flux and (ii) secondary ion emission may be significantly influenced by ambiguities related to the ionization probability of a sputtered particle, the analysis will be restricted to experimental data obtained for sputtered *neutral* particles. Moreover, the scope of the present paper will be restricted to collisional sputtering phenomena, and electronic sputtering, which occurs at high impact energies or in special target materials like ionic crystals, is therefore not treated here.

2. The Linear Cascade Regime

As outlined in many reviews of sputtering, the concept of linear collision cascades involves a series of binary, mostly elastic collisions to distribute the energy imparted by the projectile among the solid constituents. Linearity is ensured by a low density of moving particles, and therefore each collision can be assumed to occur between a moving particle and a particle at rest. It is important to note that, if more than one of such cascades overlap in space and time, the result will simply be the sum of the effects produced by each cascade (or projectile impact) alone. Every deviation from this expectation will in the following be called a "nonlinear effect". The theory of sputtering in this regime is well developed and found to agree reasonably well with corresponding experimental data (Urbassek, 2006). As a rule of thumb, linear collision cascades are produced if not too heavy projectiles of medium kinetic energies impinge onto surfaces of sufficiently strongly bound solids. A good example of this category is the impact of keV Ar^+ ions onto metallic or semiconductor surfaces.

2.1. Yields

There is an abundant volume of sputtering yield data which has been collected in the linear cascade regime of sputtering, a review of which can be found in the compilation of Andersen and Bay (1981). For elemental target material, the available experimental data have been analyzed in terms of functional forms derived from analytical transport theory, resulting in fit formulae and parameters (Matsunami et al., 1984) which can be used to estimate an unknown yield. For the case of metal targets, these appear to work reasonably well, allowing a prediction within an accuracy of typically a factor of two over a wide range of impact energies. As an example, Figure 1 shows measured data for polycrystalline copper along with the Matsunami fit formula (Matsunami et al., 1984) which can also be found on the web (`http://www.ss.teen.setsunan.ac.jp/e-syb.html`) (solid lines). A similarly good description of the data is provided by analytic sputtering theory

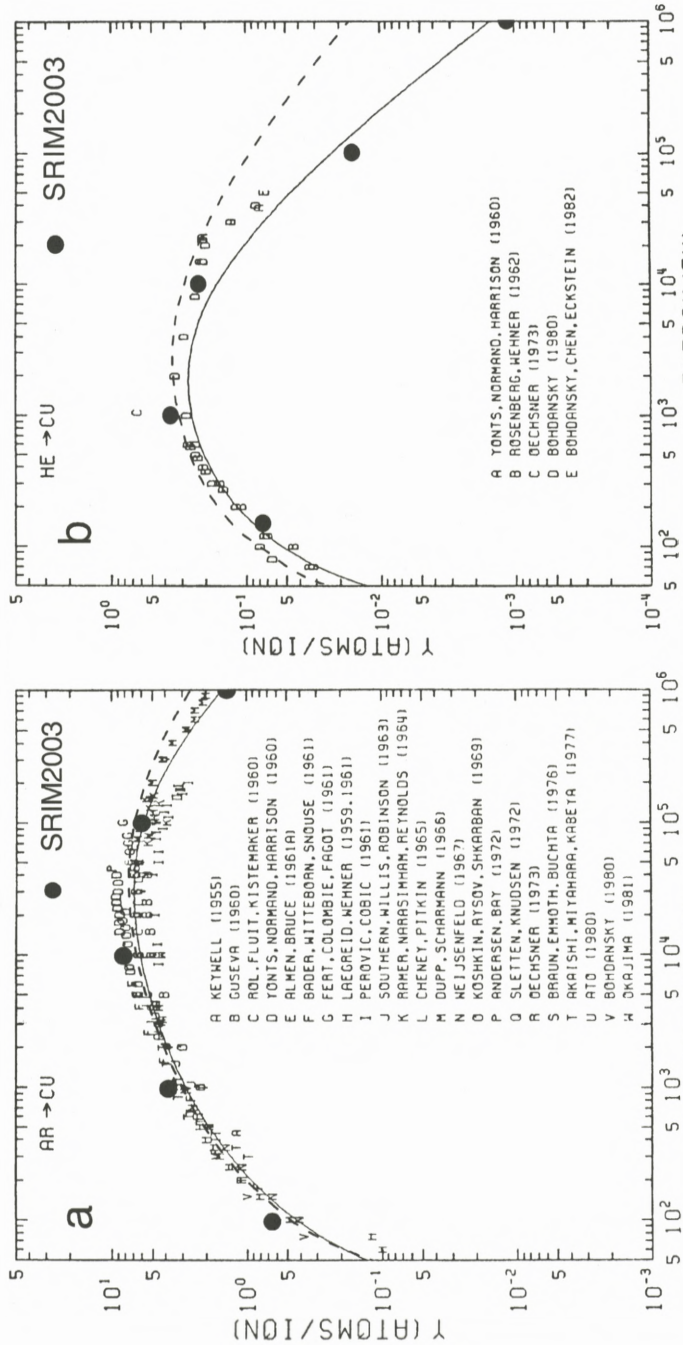

Figure 1. Experimental sputter yield data of polycrystalline Cu bombarded with various projectiles and kinetic energies under normal incidence (reproduced from Matsunami et al., 1984). Solid line: Matsunami fit formula; Dashed line: analytic sputtering theory; Large dots: Calculated values using the Monte Carlo computer simulation code SRIM 2003.

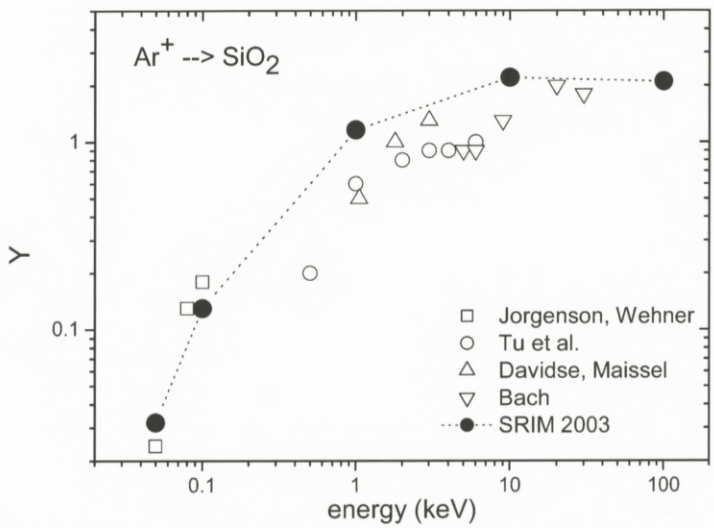

Figure 2. Sputter yield of SiO_2 under Ar^+ bombardment. Open symbols: experimental data taken from Jorgenson et al. (1965) (□), Tu et al. (1980) (○), Davidse and Maisel., 1967) (△) and Bach (1970) and Bach et al. (1974) (▽). Closed symbols: SRIM 2003 calculation.

(Sigmund, 1969) as implemented in Wittmaack (2003) (dashed lines). For comparison, the results of Monte-Carlo (MC) computer simulation using the SRIM 2003 program package (`http://www.srim.org`) are included as large dots.

The situation is not as clear if multicomponent materials are bombarded. Here, the surface composition is often changed due to preferential sputtering, bombardment induced mixing, surface segregation, etc., and the sputter yield will therefore exhibit a strong dependence on ion fluence (for a review, see Betz and Wehner, 1983; Sigmund and Lam, 1993). Moreover, the phase structure of the bombarded material will excert a large influence on the development of ion induced surface topography. As a consequence, the actual system will in general be much different from what is assumed in theoretical approaches (e.g. ideally flat surface, homogenuous spatial distribution of constituents, unchanged surface composition, etc.). Experimentally, much less data exist on sputtering yields of this kind of materials, and no tool has been published which allows an accurate estimate of unknown yield values. One can of course use MC computer simulation (SRIM 2003) to make a prediction. For Ar^+ bombardment of SiO_2, the result is depicted in Figure 2, which shows the so-called total sputter yield, i.e., the number of atoms (regardless of species) emitted per projectile impact. This particular example was chosen here because it represents a case for which a relatively

large set of experimental data exist. The yield calculated with SRIM 2003 appears to be systematically too high, a finding which is understandable since the MC simulation refers to the "static" case, i.e., the limit of negligible projectile fluence, whereas the yields are measured under "dynamic" conditions which result in a modified surface stoichiometry. In fact, the evaluation of total sputter yields from experiments measuring, for instance, the mass loss under ion bombardment is only meaningful under dynamic equilibrium conditions, where the surface composition has adjusted in such a way as to ensure stoichiometric sputtering of all sample constituents. Nevertheless, the data depicted in Figure 2 indicate again that the yield can be predicted within an accuracy of roughly a factor of two. It should be stressed, however, that SiO_2 may represent a very favorable case which certainly cannot be generalized. This is particularly true for multiphase alloys, and therefore great care should be taken in predicting sputter yields of multicomponent targets.

2.2. Energy Distributions

The emission energy distribution of atoms sputtered from elemental targets has been measured many times. In general, the experimental data can be well approximated by the transport theory prediction (Thompson, 1968; Sigmund, 1981)

$$f(E) \propto \frac{E}{(E+U)^{3-2m}}\,, \tag{1}$$

using the surface binding energy U as a fitting parameter. The parameter m in the exponent is either assumed as zero or sometimes also treated as a parameter. Examples of measured energy distributions of neutral atoms sputtered from the respective elemental surfaces are shown in Figure 3. The data have been obtained using three different experimental methods on three different projectile-target combinations. It is seen that the surface binding energy parameter U is of the same order of magnitude as the sublimation energy of the solid. However, the agreement between both quantities is not perfect, a finding which is not surprising in view of the strong non-equilibrium nature of the emission process. In fact, it has been suggested that the acquisition of energy distributions as depicted in Figure 3 should represent an experimental approach to the determination of surface binding energies relevant in sputtering. So far, however, such an assessment does not appear to be unambiguously possible due to the large uncertainty of measured energy distributions particularly in the low energy range. This is illustrated in Figure 4, which shows the fit parameter U extracted from published energy distributions of sputtered neutral atoms as a function of the sublimation energy of the respective

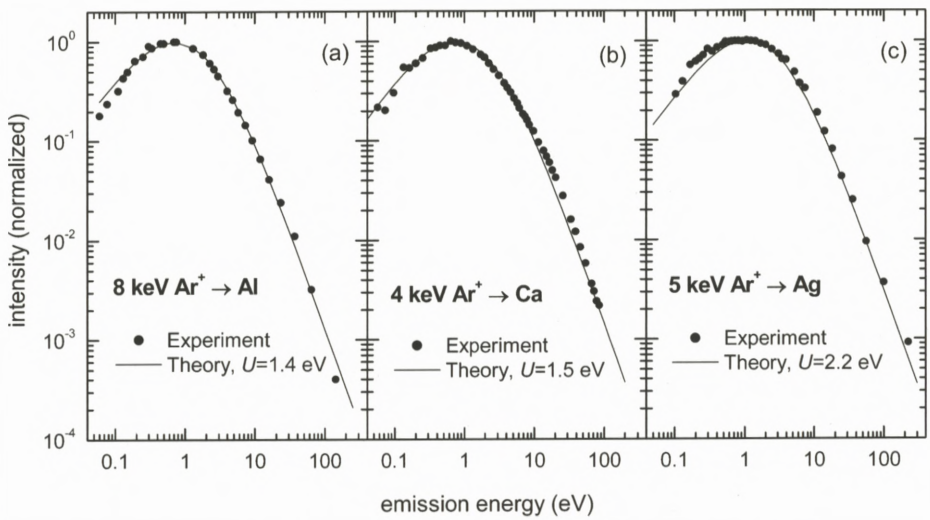

Figure 3. Emission energy distribution of neutral atoms sputtered from the respective elemental surface under bombardment with the indicated projectiles. The data were taken using multiphoton (a) or single photon (c) post-ionization with ToF mass spectrometry or Doppler shift laser fluorescence (b), respectively. The solid lines represent fits of Equation (1) using $m = 0$ and U as indicated. Reproduced from Gnaser (2006), with permission, original data Husinsky et al. (1993), Hansen et al. (1998) and Wahl and Wucher (1994).

elemental solid. It is seen that the measured surface binding energy may fall between 0.3 and 2 times the sublimation energy, depending on the target material and the employed experimental method. Moreover, even the data determined with the same method may exhibit discrepancies as large as a factor or two. The reason is presumably the large difficulty to assess (and eliminate) energy discrimination effects inherent in any of the experimental techniques used to determine the energy distribution. From the experience of the present author, any measured kinetic energy distribution published so far must be assumed to be influenced by such effects to some extent. While there is no debate about the principal shape of the energy distribution of sputtered atoms with a maximum at energies of the order of the sublimation energy and an asymptotic E^{-2} tail in the high energy regime, the actual most probably emission energy is not very accurately known. From an experimental point of view, it must therefore still be regarded as an open question whether the surface binding energy relevant in sputtering physics differs actually from the thermodynamical value of the sublimation energy or not.

For multicomponent targets, energy distributions of the same element sputtered from different compounds are generally found to differ (Gnaser, 2006). This is

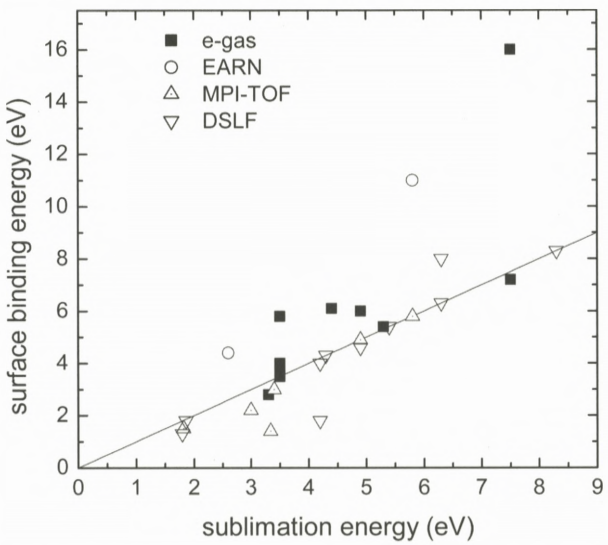

Figure 4. Surface binding energy U (Equation 1) determined for different target materials vs. sublimation energy U_S. The data have been extraxted from experimental kinetic energy distributions of the respective sputtered neutral atoms employing different experimental methods as indicated (see text for meaning of abbreviations). Data taken from the compilation of Betz and Wien (1994) and Gnaser's recent review (2006) plus original data from Wahl and Wucher (1994), Ma et al. (1994) and Staudt et al. (2002) (△) and Baxter et al. (1986) and Garrison (1986) (○).

understandable, since it indicates a variation of the surface binding energy depending on the chemical environment of the ejected atom. In spite of the uncertainty regarding absolute values mentioned above, these effects can unambigously be identified as long as the same method is used to determine all distributions. In this respect, measured energy spectra can provide valuable information about binding conditions at the bombarded surface.

2.3. Angular Distributions

In general, measured angular emission distributions of sputtered material are found to depend on the projectile energy. For amorphous or polycrystalline target materials and normal incidence, a variation from an under-cosine polar angle distribution at low energies to an over-cosine distribution in the limit of high impact energy is often observed. Under oblique incidence, these distributions are superimposed by a preferred off-normal ejection inclined towards the direction of specular projectile reflection. These findings are interpreted in terms of an incomplete randomization of the projectile momentum in the collision cascade.

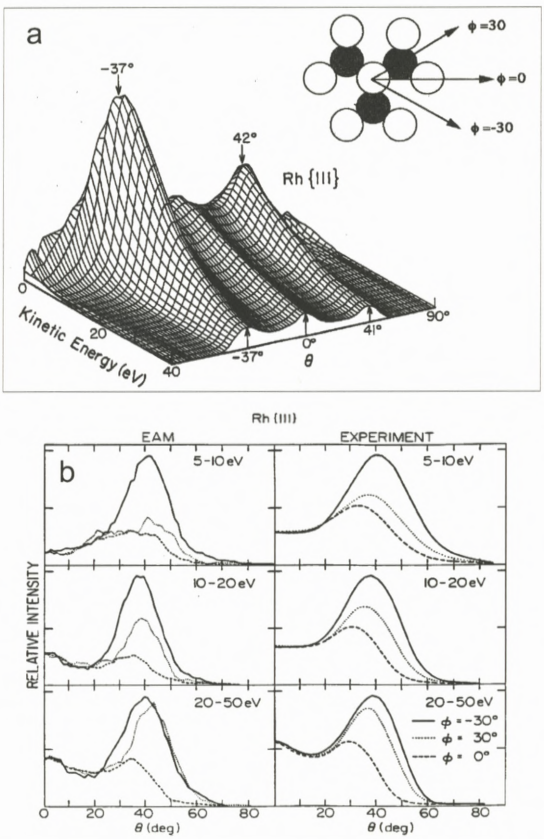

Figure 5. Polar emission angle distribution of neutral Rh atoms sputtered from a Rh(111) single crystal surface measured along two different azimutal directions. For comparison, the same distributions calculated by molecular dynamics are shown (labeled "EAM"). Reproduced from Winograd et al. (1986) (a) and Maboudian et al. (1990) (b) with permission.

For single crystal targets, pronounced structure in the emission angle distributions is observed with preferred ejection along close packed lattice directions. These features are interpreted in terms of focusing collisions in combination with surface scattering of ejected particles. In particular, it has been shown early that the regular structure of only the uppermost two atomic layers may be sufficient to explain the observed distributions (Lehmann and Sigmund, 1966). By comparison with molecular dynamics computer simulations, even subtle details of the measured emission patterns can be reproduced. An example of this is shown in Figure 5, which depicts the energy resolved emission angle distribution of neutral

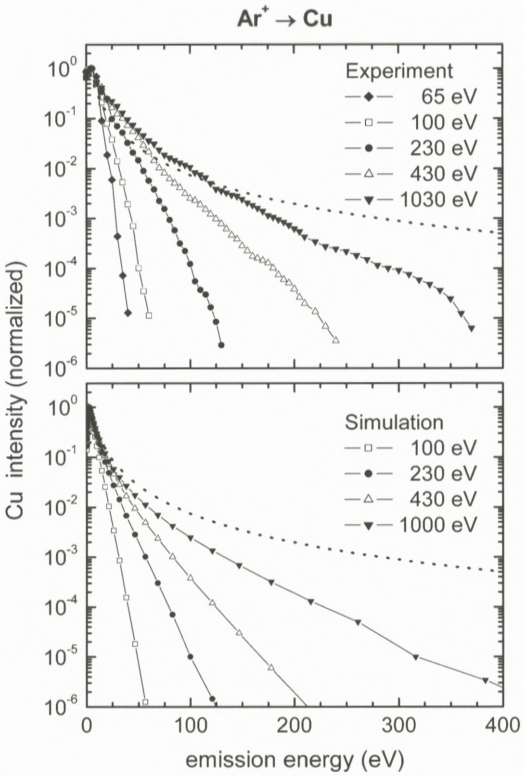

Figure 6. Emission angle integrated energy spectra of Cu atoms sputtered from copper under bombardment with normally incident Ar^+ ions. (a) Experimental data; b) computer simulation. Reproduced from Mousel et al. (1999) with permission.

Rh atoms sputtered along two different azimuth directions from a rhodium(111) surface under bombardment with normally incident 8-keV Ar^+ ions (Winograd et al., 1986). In conclusion, the angular distribution of atomic species ejected under linear cascade conditions appears to be well understood.

2.4. Low Energy Bombardment

At impact energies significantly below 1 keV, deviations from the energy and angle distributions measured at higher energies are found.

First, the measured emission energy distribution appears to be truncated with a steeper than E^{-2} decay at high emission energies, leading to a quasi-exponential decay instead (Mousel et al., 1999). As shown in Figure 6, this experimental finding is reproduced by computer simulation (Mousel et al., 1999) and is, roughly

speaking, understood in terms of a limitation of the maximum energy transferrable to a recoil atom. Note, however, that there is a significant discrepancy between the exact shape of experimental and theoretical energy distributions depicted in Figure 6 particularly in the low emission energy regime. While the computer simulation agrees well with the prediction of linear cascade theory (Equation (1), dotted line), the experimental data do not. A close inspection of the data reveals that, for instance, the measured most probable emission energy is larger than theoretically predicted. This finding is in contrast with other data – taken with a very similar experimental method – which show a pronounced *reduction* of the most probable energy at low impact energies (Brizzolara and Cooper, 1988), again casting doubt about the accuracy of measured energy distributions at very low emission energies.

Second, a pronounced preferred ejection is observed at oblique emission angles, resulting in a heart-shaped polar angle distribution under normal incidence (Wehner and Rosenberg, 1960). This finding is indicative of single knock-on sputtering, i.e., the ejection of surface atoms after short sequences of only a few collisions. At the same time, a threshold behavior of the sputter yield is observed (see Urbassek, 2006, for more details). The angular distributions are of particular interest for multicomponent target materials. Here, the lighter component is often observed to be preferrably ejected along the surface normal, while the heavier component is emitted under more oblique angles (Olson and Wehner, 1977) (see also Betz and Wehner, 1983; Sigmund and Lam, 1993, for a review). These effects, which are also predicted theoretically, are very important for applications of sputtering in thin film deposition and surface analysis. In general, they appear to be the more pronounced the lower the projectile impact energy. They are attributed to different types of collision sequences leading to the emission of different components (Betz and Wehner, 1983).

2.5. Cluster Emission

It is well known that the sputtered flux does not only contain atoms but also molecules and clusters. The formation and emission processes of such polyatomic species are much less completely understood than for sputtered atomic species. Partial sputter yields have been measured mostly for homonuclear clusters emitted from elemental surfaces or for oxide clusters emitted from oxides or oxidized surfaces. In the first case, the relative abundance of clusters vs. size or nuclearity n is generally found to roughly obey a power law (Wucher, 2002) (cf. also figure 11 in Urbassek, 2006)

$$Y(n) \propto n^{-\delta}, \tag{2}$$

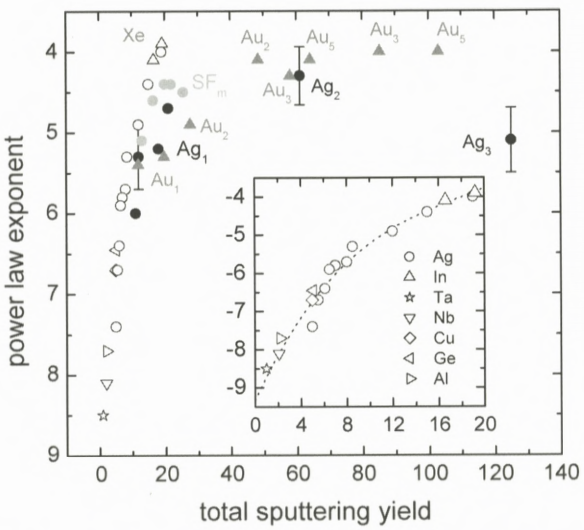

Figure 7. Power law exponent of sputtered cluster size abundance distribution (Equation 2) vs. total sputter yield for different projectiles, impact energies and target materials. The symbol shape codes the target material as indicated in the insert. Open symbols: data taken with rare gas projectile ions. Closed symbols: data taken with metal cluster projectiles as indicated.

with the exponent δ depending on the bombarding conditions and target material. In the linear cascade regime, the slope is found to be strongly correlated with the total sputter yield as illustrated in the insert of Figure 7. The theoretical implication of this observation is discussed in Urbassek (2006). For some favorable cases (e.g. bombardment of silver with 15-keV Xe^+; Staudt and Wucher, 2002a), it has been determined that the *majority* of sputtered atoms leaves the surface in a bound state, i.e., as part of a cluster. The kinetic energy distributions of emitted clusters exhibit similar most probable energies but a steeper asymptotic slope ($\propto E^{-\alpha}$) than the respective atomic species (Brizzolara and Cooper, 1989; Coon et al., 1993; Wahl and Wucher, 1994). Interestingly, the exponent α appears to be largely independent of cluster size. These findings are not yet fully understood and represent an open question in sputtering physics today.

For oxide clusters, a number of studies have been published regarding the relative abundance as a function of chemical composition of both the emitted cluster and the bombarded surface (Plog et al., 1977; Oechsner et al., 1978; Szymczak et al., 2006). Some of the work has been performed for secondary ions and will therefore not be discussed here. For sputtered neutrals, respective data have been accumulated using either electron impact or non-resonant laser post-ionization. Quite consistently, they show a reduction of atom yields and the occurrence of

cluster yields with varying oxygen content if the oxidation state of the surface is increased. Regarding the chemical composition of the sputtered cluster, yields are found to vary roughly according to simple statistical combinatorial models (Plog et al., 1977; Oechsner, 1985) . The quantitative interpretation of these data has, however, been challenged by experiments utilizing resonant photoionization (Homolka et al., 1995; Goehlich, 2001) or laser induced fluorescence (Husinsky et al., 1984; Dullni, 1985) schemes to detect sputtered atoms in their electronic ground state. These experiments reveal an exceedingly low yield of ground state atomic species to be emitted from an oxide target. Similar observations have been made using non-resonant single photon post-ionization (Heinrich, 2002, unpublished), indicating that the low atom yield is not restricted to the electronic ground state alone. In addition, a very different emission energy distribution is measured than under non-resonant post-ionization conditions. These findings suggest that the *large majority* of the particle flux sputtered from an oxide surface may be emitted in form of clusters. This question has not been settled and represents an area of active research.

2.6. Excitation and Ionization

Part of the sputtered material leaves the surface in electronically excited or ionized states. In general, the excitation probability tends to decrease with increasing excitation energy, and sizeable fractions are only found for atoms in low-lying states belonging to the ground state multiplet. The ion fraction is generally small, but may be large in exceptional cases of ionic or quasi-ionic solids (e.g. oxides). It forms the basis of Secondary Ion Mass Spectrometry and is discussed in great detail by Wittmaack (2006). Both excited and ionized fractions have been shown to depend strongly on the chemical environment of the emitted particle.

Excitation of sputtered material can manifest in different ways. For atomic species, *electronic* excitation has been studied extensively for short-lived states, since these are easy to detect by means of the emitted radiation (see Yu, 1991, for a review). However, a straightforward interpretation of the obtained data is not easy due to the interference of cascading transitions from higher-lying states. Metastable states have been investigated using laser spectrometric tools. Figure 8 shows a compilation of measured population partitions as a function of the excitation energy. It is seen that for a specific atom and state multiplet the data can be approximated by a Boltzmann distribution, but the resulting population "temperature" depends strongly on the investigated multiplet and appears to become larger with increasing excitation energy. Hence, the excitation mechanism is certainly not characterized by any sort of thermodynamic equilibrium.

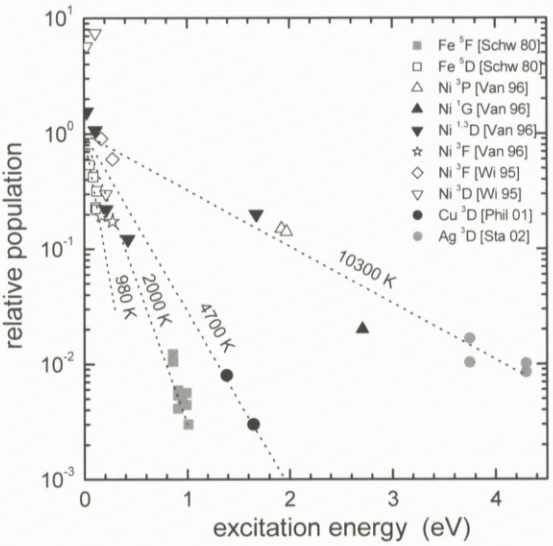

Figure 8. Population partition of metastable states of atoms sputtered from the respective elemental surface under bombardment with keV rare gas projectiles. Data taken from Schweer and Bay (1980), He et al. (1995), Vandeweert et al. (1995, 2001), Philipsen et al. (2000), Philipsen (2001) and Staudt et al. (2002).

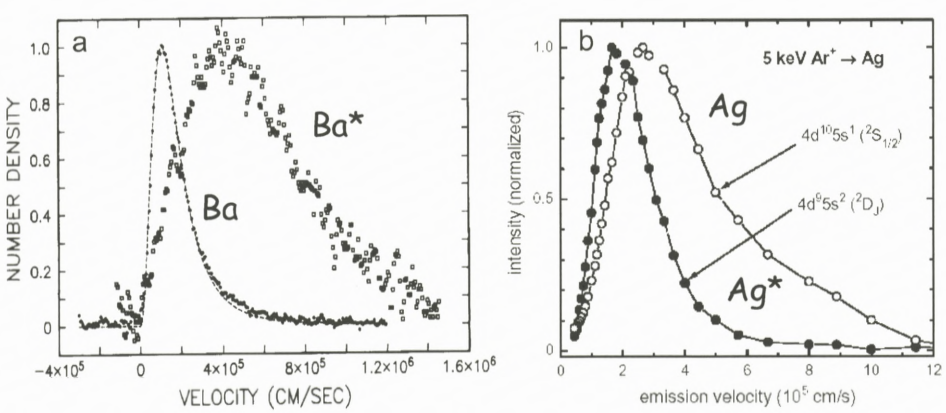

Figure 9. Emission velocity distribution of metastable Ba* (a) and Ag* (b) atoms sputtered from the respective clean elemental surfaces under in comparison with that of ground state Ba and Ag, respectively. Reproduced from Yu et al. (1982) (a) and Staudt et al. (2002) (b) with permission.

The kinetic energy distributions of atoms ejected in excited states are often found to differ from those emitted in the electronic ground state. Examples are depicted in Figure 9, which shows the distributions measured for Ba* (Grischkowsky et al., 1983) and Ag* (Berthold and Wucher, 1997; Staudt et al., 2002) in comparison with those of the respective ground state atoms. The data for barium appear typical for a relatively large set of experiments performed for other metal targets as well (see Garrison et al., 1998, for a review), always revealing a broader distribution for the excited state. This finding has been interpreted in terms of resonant electron transfer between the outgoing atom and the (electronically undisturbed) solid surface (Craig et al., 1986; Vandeweert et al., 2001). Alternatively, it has been suggested that the sputtered atoms carry an excitation signature which "remembers" the electronic band structure in the solid (He et al., 1995). The data depicted for silver, on the other hand, represent an exceptional case where the excited atoms are emitted with *lower* kinetic energy than those in the ground state. Similar findings have been obtained for Cu* as well (Philipsen, 2001). These observations are not understandable by either band structure arguments or resonant electron transfer between single electron states. This is corroborated by the relatively high population of the two Ag* states (Figure 8), since these states are energetically located well above the Fermi level and are therefore outside the excitation window generally thought to be accessible by such processes. A sound interpretation of these observations is still lacking. It has been attempted to interpret the experimental results via a time dependence of the collision induced electronic excitation processes within the solid, leading to different ejection times of excited and ground state atoms (Sroubek et al., 2003). However, the picture is far from being complete and represents an area of active research.

Besides electronic excitation, molecular species emitted from the surface may be *ro-vibrationally* excited. For diatomic molecules, this phenomenon has been investigated by laser spectroscopy (Fayet et al., 1986; De Jonge et al., 1986; Wucher, 1994). In one case, these experiments have been extended to larger clusters as well (Staudt et al., 2001). It was found that sputtered clusters are internally hot, exhibiting vibration temperatures which may be as high as several thousand Kelvin. Molecular dynamics studies have revealed that the clusters initially leave the surface with internal energies of the order of 1 eV per constituent atom (Lindenblatt et al., 2001). These "nascent" clusters are unstable and therefore decompose by unimolecular fragmentation during their flight away from the surface, leading to either stable or metastable "final" fragments which are then detectable by experiment. While MD reveals that this decomposition mainly proceeds on a picosecond time scale, the late stages of such fragmentation chains may be observed on a nano- or microsecond time scale tractable by experiment. Unfortunately, most of

these experiments have been performed for molecular secondary ions (Begemann et al., 1986; Dzhemilev et al., 1991; Delcorte et al., 2005). The available data reveal, however, clear evidence for the occurrence of metastable fragmentation in vacuum.

3. The Spike Regime

A general characteristic of a spike is that the condition of linearity breaks down and collisions between moving particles become important. It is important to note that – due to the statistical nature of the sputtering process – spikes can occur for specific impacts even under conditions where the average event falls well into the linear cascade regime. As outlined in Andersen's review (1993), spikes form if the energy per target atom deposited by the projectile impact becomes comparable with the binding energy in the solid. One possible scenario involves the impact of sufficiently heavy atomic projectiles onto a sufficiently weakly bound target. A second scenario which has been actively studied during the recent years is by impact of cluster projectiles. In the following, particular emphasis will be put on this latter aspect, since it bears great implication for applications of the sputtering process.

3.1. Yields

In many cases, cluster bombardment leads to strong enhancements of the sputter yield which are nonlinear in the sense that the yield observed under cluster impact is larger than that observed for the constituents impinging independently at the same velocity. For di- and triatomic projectiles, examples of this effect have been demonstrated many years ago (Andersen and Bay, 1974). More recently, the spectrum of available projectile size has been dramatically extended, and giant sputter yields of thousands of atoms per projectile impact have been measured, for instance, under bombardment of gold and silver with Au_n^+ cluster ions ($n = 1$–13) (Bouneau et al., 2002). The simple minded picture behind this observation is that the projectile cluster disintegrates upon impact, leaving each constituent with a reduced kinetic energy (corresponding to the same impact velocity as the original cluster) which is then deposited relatively close to the surface. As a consequence, the energy density condition for nonlinearity is easily fulfilled in the near-surface region and spikes develop even for moderate impact energies.

It should be noted at this point that yield enhancements observed under cluster bombardment are not necessarily nonlinear. In fact, one has to be careful with the language in this respect. Analyzing, for instance, data measured under 10-keV impact of SF_6^+ onto metallic surfaces, it was shown that the observed yield increase

with respect to Xe^+ projectiles (of roughly the same mass and *kinetic energy*) can be fully understood by a linear superposition of effects induced individually by the projectile constituents (Ghalab and Wucher, 2004). In this case, the large enhancement observed for corresponding secondary ion yields are largely attributable to an increase of the ion fraction, presumably induced by the incorporation of fluorine into the surface.

In other cases, on the other hand, strong nonlinearity is observed. This is particularly true for heavy projectiles like Au_m (Bouneau et al., 2002), larger clusters like C_{60} (Winograd, 2005), Au_{400} (Tempez et al., 2004), Ar1000 (Matsuo et al., 1997) or even more massive clusters containing about 10^6 glycerol molecules (Mahoney et al., 1991). Particularly the sizeable yields observed in the two latter cases manifest an infinite nonlinear enhancement in the sense defined above, since each Ar or glycerol constituent would impinge with an impact energy of only several eV, i.e., certainly below the threshold for sputtering, and therefore the added yields induced by the cluster constituents impinging independently would be zero. For large projectiles, collective emission processes must therefore prevail.

3.2. Energy Distributions

Models of emission scenarios under spike conditions are summarized in Urbassek (2006). The experimental yield data have mainly been analyzed in terms of thermodynamical models involving either thermal evaporation or hydrodynamic expansion mechanisms. Some of these models make a prediction with respect to the emission energy distribution of the sputtered material. Corresponding reliable experimental data, however, have become available only recently. As an example, the velocity distributions of In atoms and In_2 dimers sputtered from polycrystalline indium under bombardment with Au_m^- projectile ions are depicted in Figure 10 (Samartsev and Wucher, 2006a). Although not shown, the spectra measured under Au_3 bombardment are practically identical to that depicted for Au_2 projectiles (Samartsev and Wucher, 2005). It is seen that cluster bombardment leads to a pronounced contribution of low-energy sputtered material, which is incompatible with the prediction of linear cascade theory (solid line in Figure 10) and represents a clear signature of the spike emission process. Analyzing the exact form of this contribution, one finds reasonable agreement with a gas flow model involving a "phase explosion" of supercritically heated material (cf. Urbassek, 2006), while the measured spectrum cannot be explained by a thermal desorption mechanism (Samartsev and Wucher, 2005). In addition, the velocity distributions of sputtered atoms and dimers are found to be quite similar (see Figure 10). The same observation has been made for other metals under bombardment with C_{60} projectiles (Sun et al., 2005). In contrast, energy spectra of monomers

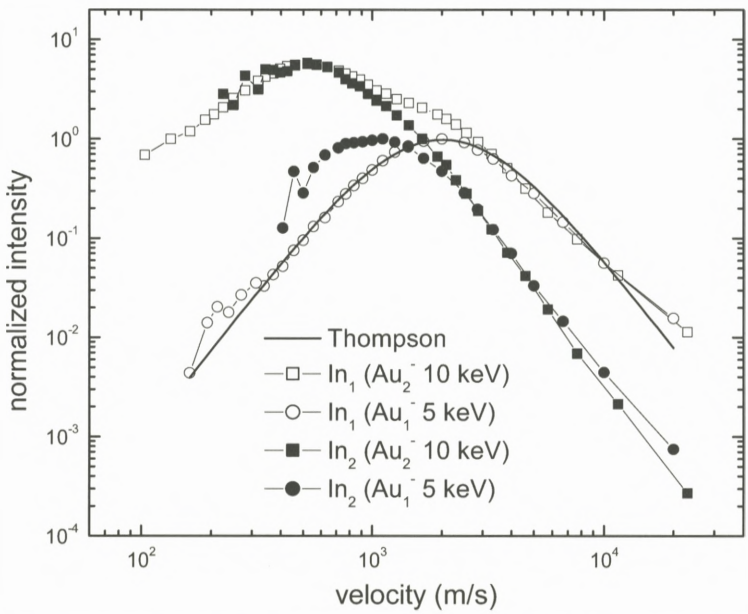

Figure 10. Emission velocity distribution of In atoms and In_2 dimers sputtered from polycrystalline Indium under bombardment with 5-keV/atom Au_m projectiles. Reproduced from Samartsev and Wucher (2006a) with permission.

and dimers are found to be distinctly different under linear cascade sputtering conditions (Brizzolara and Cooper, 1989; Coon et al., 1993). Unfortunately, no experimental data on the velocity distributions of larger neutral clusters produced under polyatomic projectile bombardment are available yet. Measurements of the corresponding secondary ions (Morozov and Rasulev, 2004) suggest that this similarity may continue towards larger sputtered molecular species as well. These findings would be consistent with a hydrodynamical spike emission process.

3.3. Cluster Emission

In view of the large sputter yields from spikes, one may ask about the magnitude of cluster emission in this regime of sputtering. If the scaling of cluster abundance with total sputter yield observed in the linear cascade regime was continued, one would expect the flux of particles sputtered from spikes to be largely dominated by clusters. Experiment, however, shows that this is not the case. As depicted in Figure 7, the power law exponent characterizing the cluster abundance distribution (Equation 2) becomes roughly constant for yields above approximately 20

atoms/projectile. Interestingly, is has been suggested that a yield value of this order should separate the linear cascade from the spike regimes of sputtering (Sigmund and Claussen, 1981; Andersen, 1993). Hence, spikes appear to produce cluster emission at a rate which is largely independent of the total sputter yield. Conversely, one example has been published where *less* cluster emission was observed under bombardment with *larger* clusters of *higher* impact energy, leading to *larger* sputter yield (Heinrich and Wucher, 2003) (cf. the data for 7-keV/atom Ag_n^+ projectiles in Figure 7). This observation has been interpreted in terms of the average energy deposited in the spike volume. As shown by computer simulation (Colla and Urbassek, 1996), optimum conditions for cluster emission prevail if the deposited energy density roughly equals the binding energy per atom. A crude estimate shows that this condition is approximately fulfilled under bombardment of silver with 14-keV Ag_2, while the optimum energy density is exceeded for 21-keV Ag_3 impact, and therefore the abundance of clusters in the sputtered flux is diminished.

In this light, the data set displayed in Figure 7 can be interpreted as follows. In the spike regime, cluster emission appears to be largely governed by the deposited energy density. Optimum conditions are found if the deposited energy equals the binding energy of atoms or molecules within the solid. In contrast, the total sputter yield seems to scale with the total energy of the impinging projectile (Urbassek, 2006), and no apparent correlation is found between cluster abundance and total sputter yield. This is different in the linear cascade regime. All published MD simulations show that (large) cluster emission is always connected to specific events where spikes are formed. This appears to be true even if the average event produced under the prevailing bombardment conditions clearly falls into the linear cascade regime. In this case, the observed scaling with total sputter yield simply reflects the probability for spike events to occur, which of course increases with increasing yield. As a consequence, one may conclude that the emission of clusters larger than dimers in sputtering is largely a spike phenomenon rather than a collision cascade effect.

3.4. Ionization and Excitation

As outlined above, spikes are associated with large deposited energy density, leading to drastic enhancements of sputter yields. A very pronounced effect of electronic excitation in this scenario is that of a sink of kinetic energy, acting to effectively cool the spike in metallic targets (Flynn and Averback, 1988). One may of course ask if the excitation degree within the spike volume, as manifested, for instance, by electron emission yields or excition/ionization probabilities of sputtered particles, is enhanced as well. The available experimental data suggest that

this is not the case. Although several publications have advocated the idea of enhanced secondary ion formation under cluster bombardment (Belykh et al., 2002), recent measurements of ionization probabilities of In atoms sputtered under Au_n cluster impact reveal no change as a function of projectile nuclearity n (Samartsev and Wucher, 2006b). As of today, no data exist regarding excitation probabilities of sputtered material under cluster impact. Experiments on ion induced electron emission even indicate a "sub-linear" effect, i.e., the electron yield per projectile constituent atom observed under Au_n cluster bombardment of insulating target materials is found to decrease with increasing n (Baudin et al., 1998). To the best of our knowledge, corresponding data for metal targets are not yet available, and the question of electronic excitation under cluster bombardment is a topic of active research.

3.5. Molecular Solids

Probably the largest advantage of cluster vs. atomic projectiles is observed for molecular solids. For this class of target material, exceedingly large sputter yields are found quite regularly. As an example, about 2700 H_2O molecule equivalents are sputtered from a water ice surface bombarded with 20-keV C_{60} projectiles (Wucher et al., 2004). In comparison, the largest yield value measured for any atomic projectile amounts to about 100 molecule equivalents per projectile impact (Baragiola et al., 2003). Similar observations are made for organic samples. For instance, a thick overlayer of trehalose ($C_{12}H_{22}O_{11} \times 2H_2O$, a sugar) on, say, a Si substrate, exhibits a yield of about 300 molecule equivalents under the same bombardment conditions (Cheng et al., 2006). These values reveal that about 10^4 atoms are sputtered per cluster projectile impact.

This finding has generated large interest in the use of cluster projectiles in surface analysis. In this field of applications, one central role of the sputtering process is to generate the signal detected in mass spectrometric techniques like SIMS. It is obvious that yield enhancements of an order of magnitude will increase the detection sensitivity accordingly. Moreover, static SIMS spectra of molecular samples often reveal less fragmentation and therefore a more complete preservation of the molecular information for cluster compared to isoenergetic atomic projectiles (see Wucher, 2006, for a review). The largest advantage, however, is found in sputter depth profiling applications, where the sputtering process is utilized as a microsectioning tool eroding the surface. For decades, it has been common wisdom that this method is virtually impossible to apply to molecular solids, since the ion bombardment inevitably leads to the accumulation of chemical damage which ultimately destroys the molecular integrity of the investigated surface. With the advent of ion sources delivering cluster projectile beams of sufficient quality to

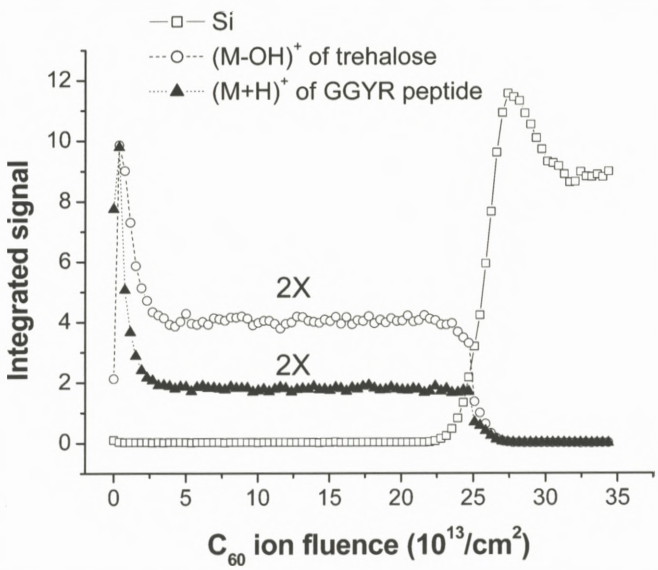

Figure 11. SIMS sputter depth profile of a 300-nm Trehalose overlayer doped with GGYR peptide on a Si substrate. The data were obtained using a 20-keV C_{60}^+ projectile ion beam for sputter erosion and data acquisition. Reproduced from Cheng et al. (2005) with permission.

be employed for surface analysis, however, this notion has changed dramatically. Using cluster ion beams like Au_3^+, Bi_3^+ or C_{60}^+, it was recently demonstrated that sputter depth profiles of organic overlayers may be acquired without accumulation of chemical damage, thereby preserving the molecular information until complete removal of the entire overlayer. An example of such an application is shown in Figure 11, where a 300-nm overlayer of trehalose doped with a GGYR peptide on a Si substrate was subjected to 20-keV C_{60}^+ ion bombardment for sputter erosion and mass spectrometric characterization of the receding surface. The SIMS signals observed for the molecular ions of the trehalose matrix and the peptide dopant, respectively, are preserved throughout the removal of the entire overlayer, until they drop sharply at the interface to the underlying Si substrate. While a similar result is obtained under Au_3^+ bombardment, it is impossible to acquire such a depth profile using atomic projectiles of any mass and impact energy. The reason is seen from a simple model describing the erosion dynamics (Cheng et al., 2006); the large sputter yield obtained under cluster bombardment ensures that most of the debris produced by ion induced chemical damage is removed during the same impact event, exposing intact molecules to analysis at the eroded surface.

4. Conclusions

Many of the experimental observations on sputtering in the linear cascade regime have been properly understood. From the perspective of an experimentalist, the prevailing emission mechanisms are clear, and observables like sputter yields or energy and angular distributions of the sputtered material can be predicted with reasonable accuracy. There are, however, a few open questions which remain to be unsolved even after many years of investigation. These are

- What is the exact nature of the surface binding energy relevant in sputtering?
- Why are the cluster abundance distributions power laws and what determines the power law exponent?
- What are the physical mechanisms behind the electronic excitation of sputtered particles?

In the spike regime, things are less clear. From the presently available data, it is obvious that mesoscale hydrodynamic emission mechanisms must be operative instead of the often assumed "thermal spikes". Material is ejected at very large yields and with lower average kinetic energy than in the linear cascade regime. Moreover, clusters and atoms are emitted with comparable velocity distributions. Ionization of the sputtered material does not seem to be enhanced very much. So far, these observations have not been well understood, and it is certainly not possible for an experimentalist to make a reasonable estimate of quantities like yields, energy or angle distributions or ion fractions on the basis of the published models. According to my understanding, the main open questions in this regime of sputtering are

- How does the sputter yield scale with experimental parameters like energy, mass and nuclearity of the impinging projectiles as well as the binding energy of the bombarded solid?
- Why can measured sputter yields be reasonably well interpreted in terms of thermal spike models, but the resulting spike "temperatures" are (i) much larger than the critical temperature of the solid material and (ii) incompatible with measured energy spectra?
- What is the angular distribution of sputtered material and how is it influenced by experimental conditions?
- Is there a common physical basis behind spike sputtering and laser ablation?
- Is there an enhanced probability of electronic excitation or ionization of sputtered species under spike conditions?

- How does the spike mechanism prevent the accumulation of damage in the limit of large projectile fluence?
- What is the depth of origin of sputtered material and how does it relate to depth resolution achievable in sputter depth profiling applications?

Many of these questions are currently actively investigated. This is particularly true for the spike sputtering regime, since the advent of commercially available cluster ion sources has sparked renewed interest in the application of polyatomic projectiles in thin film technology and surface analysis. Particularly for the latter, cluster bombardment may constitute a major breakthrough with respect to the three-dimensional characterization of organic and biological systems.

References

Andersen H.H. (1993): Nonlinear effects in collisional sputtering under cluster impact. In: Sigmund P. (Ed.), Fundamental Processes in Sputtering of Atoms and Molecules (SPUT 92). Det Kongelige Danske Videnskabernes Selskab, Copenhagen, pp 127–153

Andersen H.H. and Bay H.L. (1974): Nonlinear effects in heavy-ion sputtering. J Appl Phys **45**, 953–954

Andersen H.H. and Bay H.L. (1981): Sputtering yield measurements. In: Behrisch R. (Ed.), Sputtering by Particle Bombardment, Vol. 1. Springer, Berlin, pp 145–218

Bach H. (1970): Determination of bond energy of silica glass by means of ion sputtering investigations. Nucl Instrum Meth **84**, 4–12

Bach H., Kitzmann I. and Schröder H. (1974): Sputtering yields and specific energy losses of Ar(sup +) ions with energies from 5 to 30 KeV at SiO(sub 2). Radiat Eff **21**, 31–36

Baragiola R.A., Vidal R.A., Svendsen W., Schou J., Shi M., Bahr D.A. and Atteberry C.L. (2003): Sputtering of water ice. Nucl Instrum Meth B **209**, 294–303

Baudin K., Parilis E.S., Blankenship J.F., van Stipdonk M.J. and Schweikert E.A. (1998): Sublinear effect in light emission from cesium iodide bombarded by keV polyatomic projectiles. Nucl Instrum Meth B **134**, 352–359

Baxter J.P., Singh J., Schick G.A., Kobrin P.H. and Winograd N. (1986): Energy and angle-resolved studies of neutrals desorbed from ion bombarded polycrystalline metal surfaces. Nucl Instrum Meth B **17**, 300–304

Begemann W., Meiwes-Broer K.H. and Lutz H.O. (1986): Unimolecular decomposition of sputtered Al/sub n//sup +/, Cu/sub n//sup +/, and Si/sub n//sup +/ clusters. Phys Rev Lett **56**, 2248–2251

Belykh S.F., Palitsin V.V., Adriaens A. and Adams F. (2002): Effect of projectile parameters on charge state formation of sputtered atoms. Phys Rev B **66**, 195309-1–195309-10

Berthold W. and Wucher A. (1997): Energy- and angle-dependent excitation probability of sputtered metastable silver atoms. Phys Rev B **56**, 4251–4260

Betz G. (1987): Electronic excitation in sputtered atoms and the oxygen effect. Nucl Instrum Meth B **27**, 104–118

Betz G. and Wehner G.K. (1983): Sputtering of multicomponent materials. In: Behrisch R. (Ed.), Sputtering by Particle Bombardment, Vol. 2. Springer, Heidelberg, pp 11–90

Betz G. and Wien K. (1994): Energy and angular distributions of sputtered particles. Int J Mass Spectrom Ion Proc **140**, 1–110

Bouneau S., Brunelle A., Della-Negra S., Depauw J., Jacquet D., Le Beyec Y., Pautrat M., Fallavier M., Poizat J.C. and Andersen H.H. (2002): Very large gold and silver sputtering yields induced by keV to MeV energy Au/sub n/ clusters ($n = 1$–13). Phys Rev B **65**, 144106–144108

Brizzolara R.A. and Cooper C.B. (1989): Measurements of energy distributions and yields of neutral Cu/sub 2/ and Cu/sub 3/ species sputtered from Cu by low energy Ar/sup +/ ions. Nucl Instrum Meth B **43**, 136–145

Brizzolara R.A., Cooper C.B. and Olson T.K. (1988): Energy distributions of neutral atoms sputtered by very low energy heavy ions. Nucl Instrum Meth B **35**, 36–42

Cheng J. and Winograd N. (2005): Depth profiling of peptide films with TOF-SIMS and a C-60 probe. Anal Chem **77**, 3651–3659

Cheng J., Wucher A. and Winograd N. (2006): Molecular depth profiling with cluster ion beams. J Phys Chem B **110**, 8329–8336

Colla T.J. and Urbassek H.M. (1996): Effect of energy density on cluster formation from energized metals. Comp Mater Sci **6**, 7–14

Coon S.R., Calaway W.F., Pellin M.J. and White J.M. (1993): New findings on the sputtering of neutral metal clusters. Surf Sci **298**, 161–172

Craig B.I., Baxter J.P., Singh J., Schick G.A., Kobrin P.H., Garrison B.J. and Winograd N. (1986): Deexcitation model for sputtered excitation neutral atoms. Phys Rev Lett **57**, 1351–1354

Davidse P.D. and Maissel L.I. (1967): Equivalent dc sputtering yields of insulators. J Vac Sci Technol **4**, 33–36

De Jonge R., Baller T., Tenner M.G., de Vries A.E. and Snowdon K.J. (1986): Rotational, vibrational and translational energy distributions of sputtered S/sub 2/ molecules. Europhys Lett **2**, 449–453

Delcorte A., Poleunis C. and Bertrand P. (2005): Energy distributions of atomic and molecular ions sputtered by C_{60}^+ projectiles. Appl Surf Sci **252**, 6542–6546

Dullni E. (1985): Laser fluorescence measurements of the flux density of titanium sputtered from an oxygen covered surface. Appl Phys A **38**, 131–138

Dzhemilev N.Kh., Goldenberg A.M., Veryovkin I.V. and Verkhoturov S.V. (1991): The influence of unimolecular cluster decompositions in the nanosecond time range on the secondary ion mass spectrum of tantalum. Int J Mass Spectrom Ion Proc **107**, R19–R25

Fayet P., Wolf J.P. and Woeste L. (1986): Temperature measurement of sputtered metal dimers. Phys Rev B **33**, 6792–6797

Flynn C.P. and Averback R.S. (1988): Electron-phonon interactions in energetic displacement cascades. Phys Rev B **38**, 7118–7120

Garrison B.J. (1986): Energy distributions of atoms sputtered from polycrystalline surfaces. Nucl Instrum Meth B **17**, 305–308

Garrison B.J., Winograd N., Chatterjee R., Postawa Z., Wucher A., Vandeweert E., Lievens P., Philipsen V. and Silverans R.E. (1998): Sputtering of atoms in fine structure states: A probe of excitation and de-excitation events. Rapid Commun Mass Sp **12**, 1266–1272

Ghalab S. and Wucher A. (2004): Cluster formation at metal surfaces under bombardment with SF(sub m)(sup +) ($m = 1, \ldots, 5$) and Ar(sup +) projectiles. Nucl Instrum Meth B **226**, 264–273

Gnaser H. (2006): Energy and angular distributions of sputtered species. In: Behrisch R. (Ed.), Sputtering by Particle Bombardment, Vol. 4. Springer, pp 1–92, to be published

Goehlich A. (2001): Investigation of time-of-flight and energy distributions of atoms and molecules sputtered from oxygen-covered metal surfaces by laser-aided techniques. Appl Phys A **72**, 523–529

Grischkowsky D., Yu M.L. and Balant A.C. (1983): The effect of oxygen on the sputtering of metastable atoms and ions from Ba metal. Surf Sci **127**, 315–330

Hansen C.S., Calaway W.F., King B.V. and Pellin M.J. (1998): Energy and yield distributions of calcium atoms and clusters undergoing 4 keV Ar/sup +/ ion bombardment. Surf Sci **398**, 211–220

He C., Postawa Z., Rosencrance S.W., Chatterjee R., Garrison B.J. and Winograd N. (1995): Band structure effects in ejection of Ni atoms in fine structure states. Phys Rev Lett **75**, 3950–3953

Heinrich R. and Wucher A. (2003): Projectile size effects on cluster formation in sputtering. Nucl Instrum Meth B **207**, 136–144

Homolka P., Husinsky W., Nicolussi G., Betz G. and Li X. (1995): Matrix effects of secondary neutrals: laser postionization investigations of particles sputtered from clean and oxidized metals. Phys Rev B **51**, 4665–4667

Husinsky W., Betz G. and Girgis I. (1984): Ground state and excited state sputtering Doppler-shift laser-fluorescence studies of Cr and Ca targets. J Vac Sci Technol **2**, 698–701

Husinsky W., Nicolussi G. and Betz G. (1993): Energy-distributions of sputtered metal Al-clusters. Nucl Instrum Meth B **82**, 323–328

Jorgenson G.V. and Wehner G.K. (1965): Sputtering studies of insulators by means of Langmuir probes. J Appl Phys **36**, 2672–2675

Kobrin P.H., Schick G.A., Baxter J.P. and Winograd N. (1986): Detector for measuring energy- and angle-resolved neutral-particle (EARN) distributions for material desorbed from bombarded surface. Rev Sci Instr **57**, 1354–1362

Lehmann C. and Sigmund P. (1966): On the mechanism of sputtering. Phys Status Solidi **16**, 407–511

Lindenblatt M., Heinrich R., Wucher A. and Garrison B.J. (2001): Self-sputtering of silver by mono- and polyatomic projectiles: A molecular dynamics investigation. J Chem Phys **115**, 8643–8654

Ma Z., Calaway W.F., Pellin M.J. and Nagy-Felsobuki E.I. (1994): Kinetic energy distributions of sputtered indium atoms and clusters. Nucl Instrum Meth B **94**, 197–202

Maboudian R., Postawa Z., El Maazawi M., Garrison B.J. and Winograd N. (1990): Angular distribution of Rh atoms desorbed from ion-bombarded Rh(100): Effect of local environment. Phys Rev B **42**, 7311–7316

Mahoney J.F., Perel J., Ruatta S.A., Martino P.A., Husain S. and Lee T.D. (1991): Massive cluster impact mass spectrometry: A new desorption method for the analysis of large biomolecules. Rapid Commun Mass Sp **5**, 441

Matsunami N., Yamamura Y., Itikawa Y., Itoh N., Kazumata Y., Miyagawa S., Morita K., Shimizu R. and Tawara H. (1984): Energy dependence of the ion-induced sputtering yields of monatomic solids. At Data Nucl Data Tables **31**, 1–80

Matsuo J., Toyoda N., Akizuki M. and Yamada I. (1997): Sputtering of elemental metals by Ar cluster ions. Nucl Instrum Meth B **121**, 459–463

Morozov S.N. and Rasulev U.K. (2004): Non-additive effects in secondary-ion emission from V, Nb and Ta under gold-cluster bombardment. Appl Surf Sci **231–232**, 78–81

Mousel T., Eckstein W. and Gnaser H. (1999): Energy spectra of sputtered species under sub-keV ion bombardment: Experiments and computer simulations. Nucl Instrum Meth B **152**, 36–48

Oechsner H. (1985): Formation of sputtered Molecules. In: Popovic M.M. et al. (Eds), The Physics of Ionized Gases. World Scientific, Singapore, pp 571–598

Oechsner H., Schoof H. and Stumpe E. (1978): Sputtering of Ta_2O_5 by Ar^+ ions at energies below 1 keV. Surf Sci **76**, 343–354

Olson R.R. and Wehner G.K. (1977): Composition variations as a function of ejection angle in sputtering of alloys. J Vac Sci Technol. **14**, 319–321

Philipsen V. (2001): Resonant electron transfer during sputtering of metals studied by resonant laser ionization. PhD Thesis, KU Leuven.

Philipsen V., Bastiaansen J., Lievens P., Vandeweert E. and Silverans R.E. (2000): Resonant electron transfer in the emission of ion-beam sputtered metal atoms studied by double resonance laser ionization. Vacuum **56**, 269–274

Plog C., Wiedmann L. and Benninghoven A. (1977): Empirical formula for the calculation of secondary ion yields from oxidized metal surfaces and metal oxides. Surf Sci **67**, 565–580

Samartsev A. and Wucher A. (2005): Sputtering of indium using Au_m projectiles: Transition from linear cascade to spike regime. Phys Rev B **72**, 115417-1–10

Samartsev A. and Wucher A. (2006a): Kinetic energy distributions of neutral In and In_2 sputtered by polyatomic ion bombardment 2704. Appl Surf Sci **252**, 6470–6473

Samartsev A. and Wucher A. (2006b): Mass spectra and ionization probabilities of Indium species sputtered by atomic and polyatomic ion bombardment. Appl Surf Sci **252**, 6474–6477

Schweer B. and Bay H.L. (1980): Measurements of the population distribution of sputtered Fe-atoms with laser induced fluorescence spectroscopy. In: Fourth International Conference on Solid Surfaces and The Third European Conference on Surface Science, Cannes, 20–26.09.1980 II, pp 721–1448

Sigmund P. (1969): Theory of sputtering. I. Sputtering yield of amorphous and polycrystalline targets. Phys Rev **184**, 383–416

Sigmund P. (1981): Sputtering by ion bombardment: Theoretical concepts. In: Behrisch R. (Ed.), Sputtering by Particle Bombardment, Vol. I. Springer, Berlin, pp 9–72

Sigmund P. and Claussen C. (1981): Sputtering from elastic-collision spikes in heavy-ion-bombarded metals. J Appl Phys **52**, 990–993

Sigmund P. and Lam N.Q. (1993): Alloy and isotope sputtering. In: Sigmund P. (Ed.), Fundamental Processes in Sputtering of Atoms and Molecules (SPUT 92), Det Kongelige Danske Videnskabernes Selskab, Copenhagen, pp 255–350

Sroubek Z., Sroubek F., Wucher A. and Yarmoff J.A. (2003): Formation of excited Ag atoms in sputtering of silver. Phys Rev B **68**, 115426-1–115426-5

Staudt C. and Wucher A. (2002): Generation of large indium clusters by sputtering. Phys Rev B **66**, 075419-1–075419-12

Staudt C., Wucher A., Neukermans S., Janssens E., Vanhoutte F., Vandeweert E., Silverans R.E. and Lievens P. (2001): Internal excitation of sputtered neutral indium clusters. Nucl Instrum Meth B **193**, 787–793

Staudt C., Wucher A., Bastiaansen J., Philipsen V., Vandeweert E., Lievens P., Silverans R.E. and Sroubek Z. (2002): Sputtering of Ag atoms into metastable excited states. Phys Rev B **66**, 085415-1–085415-12

Sun S., Szakal C., Winograd N. and Wucher A. (2005): Energetic ion bombardment of Ag surfaces with C_{60}^+ and Ga^+ projectiles. J Am Soc Mass Spectrom **16**, 1677–1687

Szymczak W., Menzel N., Kreyling W.G. and Wittmaack K. (2006): TOF-SIMS characterisation of spark-generated nanoparticles made from pairs of Ir-Ir and Ir-C electrodes. Int J Mass Spectrom **254**, 70–84

Tempez A., Schultz J.A., Della-Negra S., Depauw J., Jacquet D., Novikov A., Le Beyec Y., Pautrat M., Caroff M., Ugarov M., Bensaoula H., Gonin M., Fuhrer K. and Woods A. (2004): Orthogonal time-of-flight secondary ion mass spectrometric analysis of peptides using large gold clusters as primary ions. Rapid Commun Mass Sp **18**, 371

Thompson M.W. (1968): On the energy spectrum of sputtered Au. Philos Mag **18**, 377

Tu Y.Y., Chuang T.J. and Winters H.F. (1980): The chemical sputtering of fluorinated silicon. In: Varga P., Betz G. and Viehböck F.P. (Eds), Proc. Symp. on Sputtering, Perchtoldsdorf, 28–30.04.1980, pp 337–389

Urbassek H.M. (2006): Sputter theory. Mat Fys Medd Dan Vid Selsk **52**, 433–463

Vandeweert E., Thoen P., Qamhieh Z.N., Lievens P. and Silverans R.E. (1995): The electronic excitation of atoms in atomization processes studied by resonance ionization mass spectrometry. AIP Conf Proc, 91–94

Vandeweert E., Lievens P., Philipsen V., Bastiaansen J. and Silverans R.E. (2001): Measurements of the population partitions and state-selected flight-time distributions of keV ion-beam-sputtered metastable atoms. Phys Rev B **64**, 195417-12

Wahl M. and Wucher A. (1994): VUV photoionization of sputtered neutral silver clusters. Nucl Instrum Meth B **94**, 36–46

Wehner G.K. and Rosenberg D. (1960): Angular distribution of sputtered material. J Appl Phys **31**, 177–179

Winograd N. (2005): The magic of cluster SIMS. Anal Chem **77**, 142A–149A

Winograd N., Kobrin P.H., Schick G.A., Singh J., Baxter J.P. and Garrison B.J. (1986): Energy- and angle-resolved detection of neutral atoms desorbed from ion bombarded single crystals. Rh(111) and p(2*2)O/Rh(111). Surf Sci **176**, L817–L824

Wittmaack K. (2003): Analytical description of the sputtering yields of silicon bombarded with normally incident ions. Phys Rev B **68**, 235211-1–11

Wittmaack K. (2006): A critical review of the electron-tunneling model of secondary ion formation. Mat Fys Medd Dan Vid Selsk **52**,

Wucher A. (1994): Internal energy of sputtered metal clusters. Phys Rev B **49**, 2012–2020

Wucher A. (2002): Formation of clusters in Sputtering. IZV An SSSR Fiz **66**, 499–508

Wucher A. (2006): Molecular secondary ion formation under cluster bombardment: A fundamental review. Appl Surf Sci **252**, 6482–6489

Wucher A., Sun S., Szakal C. and Winograd N. (2004): Molecular Depth Profiling of Histamine in Ice using a Backmininster fullerence probe. Anal Chem **76**, 7234–7242

Yu M.L. (1991): Charged and excited states of sputtered atoms. In: Behrisch R. et al. (Eds), Sputtering by Particle Bombardment, Vol. 3. Springer, Berlin, pp 91–160

Yu M.L., Grischkowsky D. and Balant A.C. (1982): Velocity distributions of sputtered excited atoms. Phys Rev Lett **48**, 427–430

Sputter Theory

Herbert M. Urbassek*

Fachbereich Physik, Universität Kaiserslautern
Erwin-Schrödinger-Straße, D-67663 Kaiserslautern, Germany

Abstract

Progress in the description of energetic-particle-induced sputter processes is predominantly based on computer simulation techniques. This review reports on the progress reached in long standing issues, such as the nature of sputtering from spikes. and highlights research areas which are now actively being investigated, such as topography changes in the irradiated surface induced by sputtering and its consequences upon sputtering.

Contents

1 Introduction: Available Theoretical Tools **434**

2 Collision Cascades **436**
2.1 Yield 436
2.2 Energy Distributions 436
2.3 Angular Distribution 437
2.4 Low-Energy Bombardment 439
2.5 Depth of Origin 440
2.6 Preferential Sputtering 440
2.7 Irradiation-Induced Composition Changes 441
2.8 Creation of Surface Topography 442
2.9 Influence of Surface Topography on Sputtering 443
2.10 Progress in Transport Theory 444

3 Spikes **446**
3.1 Models 446

* E-mail: urbassek@rhrk.uni-kl.de

3.2 Cluster Impact 450
3.3 Crater Formation 452
3.4 Cluster Emission 452
3.5 Sputtering from Swift-Ion Tracks 454

4 Further Topics **455**
4.1 Electronic Excitation 455
4.2 Molecular Targets 455
4.3 Chemical Effects 456

5 Conclusions **457**

Acknowledgements **458**

References **459**

1. Introduction: Available Theoretical Tools

The theoretical understanding of sputter processes has a long history, cf. the introductory chapter of Sigmund (1981). Since the introduction of transport-theoretic methods into this field in the 1960s, and culminating in the seminal paper by Sigmund (1969), a great variety of problems have been analyzed using this method, such as the dependence of the total sputter yield on ion impact energy, angle and species as well as the target materials parameters; the energy and angular distributions of sputtered particles; the preferential sputtering of alloys and compounds; and the depth of origin of emitted particles. Progress in the field of sputtering has been summarized in Behrisch (1981, 1983), Behrisch and Wittmaack (1991) and Sigmund (1993). A recent review over the field is given in the Proceedings of the Grove Symposium (2004), and here in particular in the survey by Baragiola (2004).

These analytical studies allowed to obtain a systematic and explicit quantitative understanding, which in many cases adequately covered the phenomena described above. They were soon supplemented and extended by computer simulation methods (Eckstein, 1991). Here binary-collision codes were among the first to be developed. These are similar in spirit to the analytical transport theory in that they ignore multiple atom interaction, but concentrate on the close collisions dominating projectile slowing down and recoil generation. Prominent examples of these codes are TRIM (Biersack and Haggmark, 1980; Biersack and Eckstein, 1984), in which the target crystal structure is ignored and thus an amorphous target is modelled, and MARLOWE (Robinson and Torrens, 1974), which takes full account of target crystallinity. These codes were developed in the 1970s and 1980s and

applied to the issues of sputter theory mentioned above. The results obtained were generally in good agreement with analytical theory. Additionally, in specific areas, which are difficult to treat using transport theory, these codes brought new insight, such as for low projectile energies, including the regime of single-knockon (near-threshold) sputtering, and in particular when covering the effects of target crystallinity. Also the issue of the fluence dependence of sputtering, which is of particular importance for compound targets, which undergo stoichiometry changes under sputtering, could be naturally included in such codes; here TRIDYN is a prominent example (Möller and Eckstein, 1984). Nowadays, an essential role played by these codes is their widespread availability for experimentalists, which allows them to quickly estimate projectile ranges, sputter yields, etc.

Another theoretical tool consists of the method of molecular-dynamics simulation, in which the interaction of each (projectile or target) atom with all surrounding atoms is taken into account. This method is expected to give the most realistic description of particle slowing down, recoil generation, and sputtering. Molecular dynamics has been employed already in the 1970s, in particular by the pioneering work of Harrison and coworkers (Harrison, 1988). The initial restriction of this method to small target sizes and thus small impact energies – which was dictated by CPU time and memory restrictions – was gradually relieved by the progress in available computer hardware. Thus this method has experienced a considerable progress in the 1990s (Urbassek, 1997), which continues until today. It allowed to attack questions in which multiple atom interaction is important. This applies in particular to the so-called spike regions, which are defined as "a limited volume with the majority of atoms temporarily in motion" (Sigmund, 1974). Since this tool does not only describe repulsive events ("collisions") but also the environment- and configuration-dependent attraction between particles, it has been used to study a variety of sputter phenomena such as the influence of surface topography on sputtering, creation of surface defects by sputtering, cluster emission, or chemical effects in sputtering.

In this review, I will highlight the areas upon which research in sputter theory now focuses. Since most issues of collision-cascade sputtering have been treated satisfactorily, research now generally aims at a detailed quantitative agreement between experiment and theory in specific systems, while most basic questions appear to have been adequately settled. This review will cover the field of projectile impact in the nuclear-stopping regime, while processes of so-called electronic or chemical sputtering are only briefly addressed in Sections 3.5 and 4.3, respectively. Furthermore, with the exception of Section 2.7, which treats

irradiation-induced composition changes, I will concentrate on "static" results, i.e., omit aspects of the fluence dependence of sputtering.

2. Collision Cascades

The concept of a linear collision cascade describes how the projectile energy is distributed among target atoms via a series of collision events; in each of these, an energetic atom collides with an atom at rest and conveys part of its energy to it. We note that early after projectile impact the collision cascade will usually be linear since the density of moving recoil atoms is low. With increasing time, however, this density increases and the cascade becomes nonlinear. Often, however, this latter phase has no influence on sputtering, if the recoil energies are too small (i.e., smaller than the surface binding energy).

2.1. Yield

Linear cascade theory predicts the sputter yield Y to obey

$$Y = \frac{1}{8} \frac{\Gamma_m F_D \Delta x}{U}, \tag{1}$$

where Γ_m is a number, which slightly depends on the low-energy interaction potential, U is the surface binding energy, Δx is the depth of origin of sputtered atoms, and F_D is the energy deposited near the surface. F_D is proportional to the nuclear stopping power of the projectile.

Figure 1 presents a compilation of experimental data of the sputter yields of Si, which shows good quantitative agreement with the ideas underlying Equation (1). This was possible by (i) introducing a reduced energy ϵ, which scales the bombarding energy by parameters depending on the projectile and target atom species, and a reduced stopping power $s_n(\epsilon)$; (ii) writing Equation (1) as $Y = C \cdot s_n(\epsilon)$, where C contains all remaining (energy-independent) factors of Equation (1), (iii) taking threshold effects into account, cf. Section 2.4 below.

So, in general, Equation (1) well describes the physics underlying sputtering in the collision cascade regime.

2.2. Energy Distributions

Collision cascade theory predicts the energy spectrum of sputtered particles to be given by a law

$$f(E) \propto \frac{E}{(E+U)^{3-2m}}, \tag{2}$$

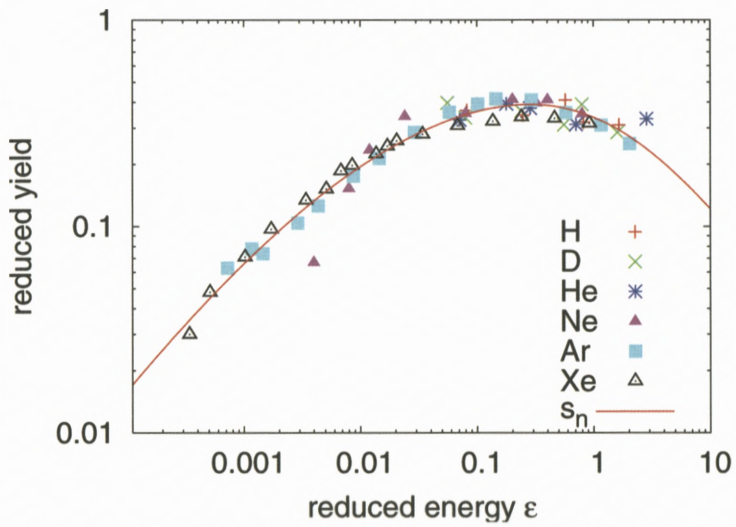

Figure 1. Compilation of experimentally determined sputter yields of Si with normally incident ions. The reduced sputter yields, $y = Y/C$, cf. Section 2.1, have been plotted *versus* the reduced energy ϵ and are seen to align well with the reduced nuclear stopping cross section s_n. Threshold effects have been taken into account via the factor η, Equation (4). Compilation and analysis due to Wittmaack (2003).

where m is a parameter characterizing the repulsive part of the interatomic interaction potential valid in the range of energies of sputtered particles. m is in the range of 0–0.2. Figure 2 gives an example showing that sputtered particle spectra can be well fitted using this law. We note, however, that in such fits, usually both U and m are used as fit parameters. Deviations of the fit value of U to the cohesive energy or sublimation energy of the solid are often ascribed to surface roughness or impurities. From a theoretical point of view, the surface binding energy of single-crystalline flat surfaces is readily calculated; its relevance for describing the energy loss of sputtered particles has been discussed by Gades and Urbassek (1992) for elemental metals and in (1994b) for alloys.

2.3. Angular Distribution

Analytical theory predicts the collision cascade to become isotropic, resulting in a cosine distributed flux of the sputtered atoms. At small projectile energies, below 1 keV, say, the collision cascade still remembers the initial momentum of the projectile; for perpendicular incidence the flux of sputtered atoms is undercosine, i.e., particles are preferentially sputtered at oblique angles rather than perpendicular to the surface. This prediction is in general found to be true.

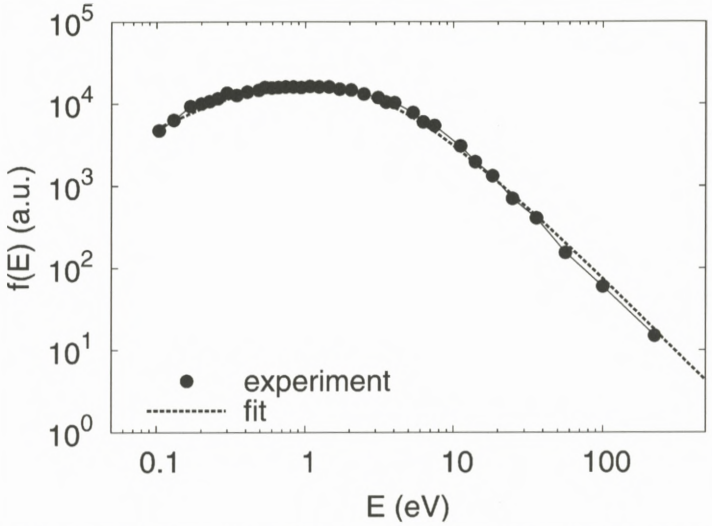

Figure 2. Kinetic energy distribution of neutral Ag atoms sputtered from a polycrystalline Ag sample by bombardment with 5 keV Ar ions at 45° impact angle. Fit to Equation (2) with surface binding energy $U = 2.94$ eV and power exponent $m = 0.15$. Data taken from Wahl and Wucher (1994).

In theoretical terms, this issue has been discussed with the help of the so-called *deposited-momentum* distribution in the collision cascade (Sckerl et al., 1996). In analogy to the well known deposited-energy distribution, it quantifies the space dependence of the average momentum (vector) of recoil atoms, and hence the anisotropy of the collision cascade.

Deviations from the cosine distribution may also be caused by other reasons:

1. Crystal effects play a dominant role in the establishment of the angular distribution (Hofer, 1991; Rosencrance et al., 1995).
2. Impurities present at the surface and also projectiles implanted there disturb the angular distribution.
3. When experiments are performed under high fluences, often a tendency to an over-cosine distribution is found, i.e., a higher emission probability in the normal direction; this feature is usually connected to the evolution of surface topography under higher fluence bombardment.

In particular the first effect mentioned above, viz. the influence of the crystalline structure, is rather complex, as for instance the detailed and systematic experimental investigation of the sputtering of the Au (111) surface in its depen-

dence on ion species, ion energy, and temperature by Szymczak and Wittmaack (1993) demonstrates. The available published modelling, such as the work by Hou and Eckstein (1990), extends only over a small fraction of the parameter space investigated experimentally.

2.4. Low-Energy Bombardment

Small impact energies E_0 lead to characteristic deviations from fully established collision cascades:

1. The energy spectrum is steeper than $1/E^2$.
2. The angular distribution is non-isotropic, favouring emission angles in the direction of the projectile.
3. The sputter yield exhibits a threshold at an energy E_{th}.

In particular the sputter threshold energy E_{th} and the energy dependence of the sputter yield in its vicinity have been the subject of several investigations. Here in general empirical laws have been formulated by various authors. One of these, which has been implemented in Figure 1, is due to Bohdansky (1984) and reads

$$Y_{\text{th}}(E_0) = \left(\frac{1}{8}\,\frac{\Gamma_m F_D \Delta x}{U}\right) \cdot \eta\left(\frac{E_{\text{th}}}{E_0}\right), \tag{3}$$

where the first term in brackets on the right is the sputter yield of Equation (1) and $\eta(x)$ denotes the threshold function

$$\eta(x) = (1 - x^{2/3})(1 - x)^2, \quad (0 < x < 1). \tag{4}$$

The threshold energy, at which sputtering sets in rather sharply, has been derived by Eckstein et al. (1993) to depend on the surface binding energy U and on the mass ratio $\mu = M_2/M_1$ of the target atom mass M_2 to the projectile ion mass M_1 as

$$\frac{E_{\text{th}}}{U} = 7.0\mu^{-0.54} + 0.15\mu^{1.12}. \tag{5}$$

As Figure 1 shows, the inclusion of the threshold function leads to a satisfactory agreement between experiment and theory.

2.5. Depth of Origin

The depth of origin, Δx, has been introduced in Equation (1) as a length characterizing the depth out of which recoils may be ejected. With the exponent m describing the interaction potential of low-energy recoils, it reads

$$\Delta x = \frac{1}{1-2m}\frac{1}{NC_m}U^{2m} \tag{6}$$

and is hence proportional to the range of a recoil of energy U. Since for low-energy recoils, $m = 0$, Equation (6) gives the average depth of origin as

$$\Delta x = \frac{1}{NC_0}. \tag{7}$$

With the original value of the low-energy stopping cross section C_0, this resulted in 5 Å (Sigmund, 1969). However, this value has been recalculated by Vicanek et al. (1989) who found that C_0 should be increased by a factor of 2, thus resulting in a depth of origin of $\Delta x = 2.5$ Å. Glazov et al. (1998) and Shulga and Eckstein (1998) demonstrated by computer simulations that the escape depth is a factor of 4 smaller than the original estimate by Sigmund (1969). This is in reasonable agreement with experimental data by Wittmaack (1997, 2003), who showed particles to be mainly sputtered from the topmost surface layer. We note that the computer simulations of Shulga and Eckstein (1998) predict a dependence on the atomic number density proportional to $N^{-0.86}$ instead of N^{-1} as in Equations (6) and (7).

2.6. Preferential Sputtering

The sputtering behaviour of compounds and alloys is of considerable practical interest. Let us concentrate on the sputtering of a binary system of species i and j which are homogeneously mixed with concentrations c_i, c_j, where $c_i + c_j = 1$. The normalized ratio

$$\delta = \frac{Y_i}{Y_j}\frac{c_j}{c_i} \tag{8}$$

is called the sputter preferentiality, since its deviation from the value 1 indicates over- or under-stoichiometric emission of a particular species. Analytical sputter theory (Sigmund, 1981) predicts δ to depend on the masses $M_{i,j}$ and the surface binding energies $U_{i,j}$ of the respective species in the alloy as

$$\delta = \left(\frac{M_j}{M_i}\right)^{2m}\left(\frac{U_j}{U_i}\right)^{1-2m}. \tag{9}$$

Here m denotes the power exponent describing the interaction potential.

A special case of particular interest is the sputtering of isotopic mixtures. Here sputtering is governed by the mass ratios of the different isotopes in the specimen. Equation (9) thus predicts a preferentiality

$$\delta = \left(\frac{M_j}{M_i}\right)^{2m} . \tag{10}$$

Since this effect is small, in simulations the mass difference is often artificially enhanced. Early work by Shapiro et al. (1988) and Lo et al. (1989) and more recent simulations by Gades and Urbassek (1995) obtained preferentialities compatible with the experimental findings and Equation (10).

Shulga and Sigmund (1995, 1996) performed a series of simulations, where besides binary-collision simulations also molecular dynamics was employed. Molybdenum isotope samples with an artificially increased mass ratio were investigated. These authors studied in particular the dependence of the preferentiality on the bombarding ion energy, and showed that the theoretical result is only retrieved for high energies ($E_0 > 10$ keV in their case). At low bombarding energies, the sputter preferentiality strongly depends on the mass and energy of the bombarding species and varies considerably with the emission angle; this effect could be reduced to the collision kinematics of binary scattering.

2.7. Irradiation-Induced Composition Changes

After long-term bombardment, the surface composition of the target changes. This has several causes: Besides the preferential sputtering effect itself, collisional mixing in the target, radiation-enhanced diffusion and Gibbsian and radiation-induced segregation change the target composition. Furthermore, the altered concentrations and atomic densities in the target may lead to strong local pressures; thus the effect of the relaxation of this pressure needs to be taken into account. The review by Sigmund and Lam (1993) summarizes the underlying physics and presents a comprehensive theoretical framework for analyzing these processes quantitatively. As a consequence of the altered composition profile, also the sputter yields and their preferentiality will be changed as a function of fluence.

Conrad and Urbassek (1992) give a detailed analysis of this effect by taking collisional mixing, preferential sputtering and pressure relaxation in the target self-consistently into account. They investigate a $^{70}Ge/^{76}Ge$ mixture irradiated by 5 keV Ar ions in the framework of a Monte Carlo study. A steady-state concentration profile develops after one ion range has been sputtered away; then the light isotope is depleted at the surface and the sputter preferentiality becomes unity, as

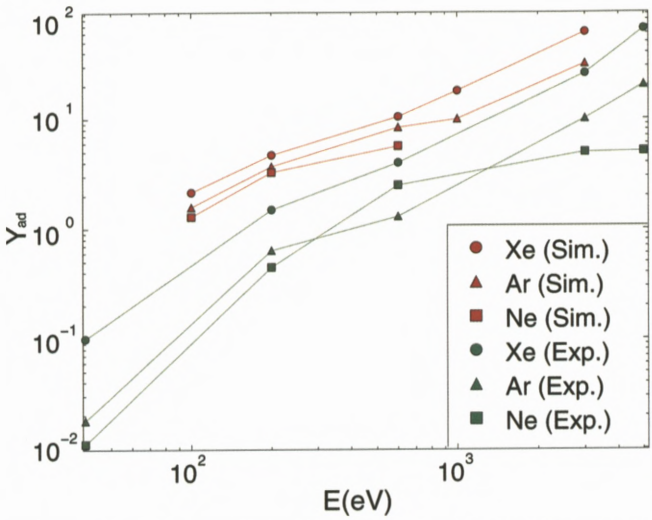

Figure 3. Comparison of simulation data (Gades and Urbassek, 1994a) and experimental data (Michely and Teichert, 1994) of adatoms produced by energetic rare-gas ion bombardment of a Pt (111) surface.

it must be in steady state. These results are in close qualitative agreement with experiments by Gnaser and Oechsner (1990).

In a more comprehensive study, in which all the effects mentioned above are included, Sckerl et al. (1998) investigate in detail the compositional changes in alloys, such as NiCu, and compare to experimental data. Since these authors also allow for higher target temperatures, up to 700°C, the effects of Gibbsian segregation and radiation-enhanced diffusion on the concentration profiles become considerable and even dominant. In a related paper, Vicanek et al. (1998) investigate the effect of composition gradients in alloys on preferential sputtering. This theoretical analysis finds that a surface-depleted species is emitted preferentially in normal direction; they identify a *neutral angle*, where the composition of the sputter flux is representative of the entire flux emitted in the half space.

2.8. Creation of Surface Topography

This topic has gained increasing attention due to the necessity of modelling the evolution of surface topography with ion fluence. Figure 3 gives an example of the formation of adatoms due to keV ion bombardment of a metal surface. An atomistic understanding of the effect of an individual ion-induced collision cascade on the surface topography appears useful, as shown by the contributions

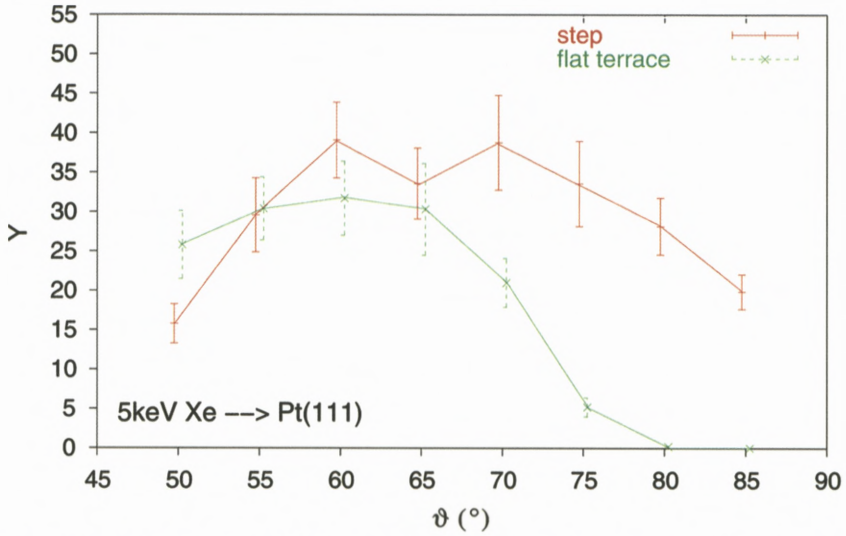

Figure 4. 5 keV Xe impact on a Pt (111) surface: Dependence of the sputter yield Y on the incidence angle ϑ. Data for ion impact on a flat terrace, and on a stepped surface with impact point into the unit cell immediately in front of the step edge. Lines are to guide the eye. Data taken from a molecular-dynamics simulation by Friedrich (2003); for details see also Friedrich and Urbassek (2003).

of Chason and Chan (2006) and Aziz (2006) in these proceedings. One possible approach consists in calculating the *average* surface height profile around the ion impact point using a binary-collision or a molecular-dynamics simulation. Here more work is necessary to obtain this distribution in analytical form and parametrized with the relevant projectile and target materials parameters. Such an analytical representation is necessary for implementation into the (stochastic) equations governing surface evolution.

2.9. Influence of Surface Topography on Sputtering

Both the analytical theory of sputtering and most simulation codes aim at describing sputtering from a planar target surface. However, it has become more and more interesting to describe the effect of target surface structure on sputtering:

1. On a microscopic level, target surfaces are not planar, except in rare cases, where the surface to bombard has been characterized carefully before bombardment. Usually, the surface is atomically rough and full of defects. Conversely, with the advent of scanning tunnelling microscopy techniques, it has become possible to characterize sputtering events individually on an

atomic scale. Figure 4 gives an example of how the presence of a surface step influences the sputter yield, in particular for glancing-ion incidence.

2. After prolonged sputtering, even an initially flat surface will develop roughness. Furthermore, in a number of interesting cases, a surface instability results, which leads to ripple or nanodot formation on the surface.
3. With the advent of nanotechnology, it has become relevant to characterize the sputtering behaviour of nanoscopic structures on surfaces – e.g., trenches, grooves, ridges, edges, etc.

Already quite early, Sigmund (1973) characterized the curvature dependence of the sputter yield. This description is today the basic ingredient of the theories describing surface-structure formation under sputtering (Bradley and Harper, 1988; Michely and Krug, 2004; Chason and Chan, 2006). Figure 5 gives an atomistic example, in which the sputtering of a flat Au surface by 16 keV Au ions is compared to that of a spherical Au cluster with diameter 20 nm. Both the sputter yield and the time evolution of sputtering in the two cases are quite different. The range of the projectile is in this case around of third of the curvature radius of the cluster.

2.10. Progress in Transport Theory

As mentioned in the Introduction, transport theory formed the starting point for sputter theory (for a recent review, see Jakas, 2004). This approach has the obvious advantage of delivering systematic results, in which the important sputter parameters are included in a transparent analytical way, such as for instance in Equation (1). The complexity of the underlying integro-differential equation necessitated several simplifications, notably in the cross sections employed (the so-called *power-law* cross sections are used as a rule) and in the assumption of an *infinite target*, in which the surface only forms a reference plane rather than a boundary. Furthermore, the results obtained apply to the *asymptotic* regime, where the recoil energy E is small compared to the bombarding energy E_0; here, in particular, the cascade becomes isotropic.

It turned out that the dismissal of any of these assumptions requires considerable effort and sometimes the introduction of novel theoretical concepts. However, important progress could be reached in the following areas:

1. Glazov (1994a, 1994b, 1995) reanalyzed the problem of the space dependence of the deposited energy distribution, which is basic to the description of the sputter yield, Equation (1), and of the related concept of the deposited momentum distribution. In particular, he succeeded (1997) to calculate the

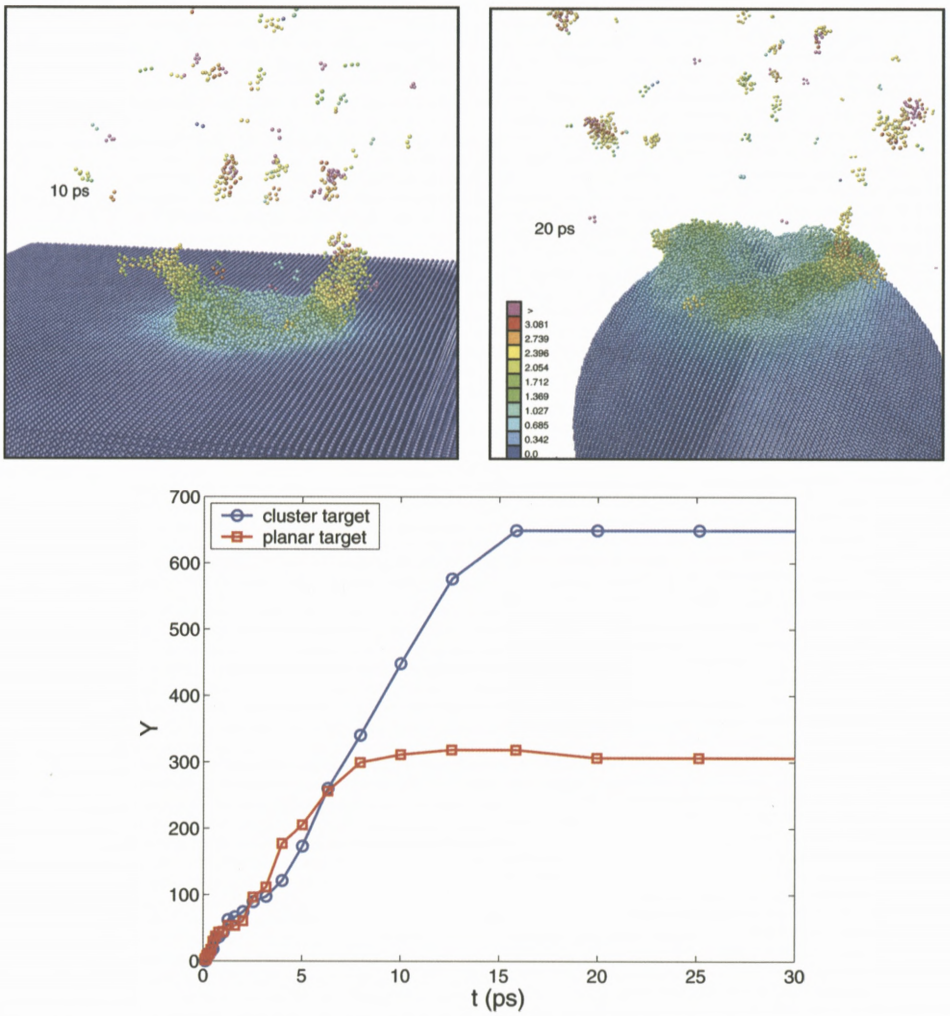

Figure 5. Comparison of the perpendicular impact of a 16 keV Au atom on (a) a planar Au surface, (b) a spherical Au cluster target with diameter 20 nm. The cluster has been bombarded centrally into a region which has a local (111) surface face. Representative sputter events with average sputter yields of 306 and 649, resp., have been selected. Colour denotes local temperature in 1000 K. (c) Comparison of the time evolution of the sputter yields. Courtesy of St. Zimmermann (2006).

sputter flux from a half-space medium. Here, he used the technique of *invariant embedding*, which is well known in other areas of transport theory, and subsequently turned out to be fruitful in several other problems of particle-solid interaction, such as electron (Vicanek, 1999) and positron (Glazov and Paszit, 2004) backscattering from surfaces.

2. The anisotropy of collision cascades – with the exclusion of crystal structure effects – has been analyzed systematically by Sckerl et al. (1996). Its two leading sources were identified as the projectile momentum and the gradient of the deposited energy density. Its relation with the so-called deposited momentum distribution was clarified.
3. Results on the sputtering of binary media, including in particular isotopic systems, have already been discussed in Section 2.6.
4. Asymptotically correct expressions for particle fluxes in binary media could be derived for general, i.e., non-power-law, cross sections by Vicanek et al. (1993).

3. Spikes

A general condition when spikes may contribute to sputtering is given by the criterion

$$E_{\text{atom}} \gtrsim U, \tag{11}$$

where E_{atom} is the energy per atom in the spike volume and U is the cohesive energy of the material. Such a condition may be reached for

1. heavy ion impacts on heavy targets, such as Au on Au,
2. in particular for cluster impact,
3. for weakly bonded solids such as condensed gas targets, weakly bonded molecular targets, etc.,
4. in swift-ion tracks.

3.1. Models

A number of models have been derived already in the 1980s (see Reimann, 1993, for a review) to explain sputtering by spikes with the help of continuum-mechanical, thermo- or hydro-dynamical models:

1. surface evaporation (Johnson and Evatt, 1980; Sigmund and Claussen, 1981),

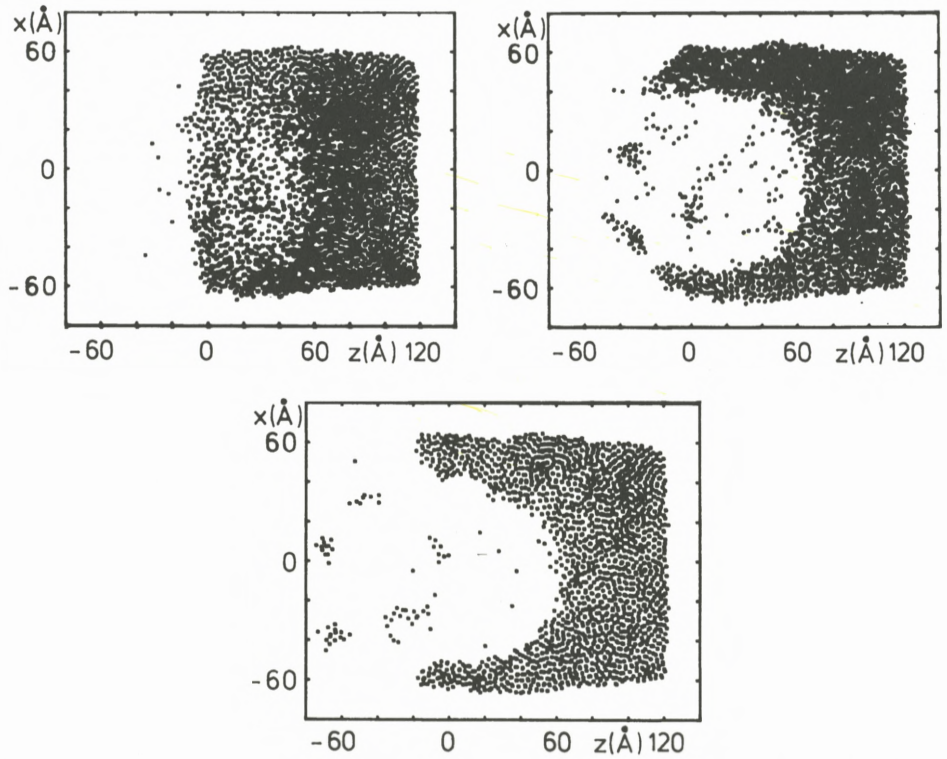

Figure 6. Time evolution of the density in an amorphous Ar solid irradiated at time $t = 0$ by a 1 keV Ar atom. Every dot represents an Ar atom in a layer extending 3.5 Å on both sides of the plane $y = 0$. The surface is initially at $z = 0$. (a) $t = 3.2$ ps after ion impact. (b) $t = 13.8$ ps. (c) $t = 24.7$ ps. Taken from Urbassek and Waldeer (1991).

2. phase explosion, also called bulk evaporation or gas flow (Urbassek and Michl, 1987; Sunner et al., 1988; Kelly, 1990),
3. shock wave (pressure pulse) (Kitazoe et al., 1981; Bitensky and Parilis, 1987; Johnson et al., 1989).

All these models emphasize one aspect which may be relevant for producing sputtering from a spike, while in reality several of the mechanisms proposed above may be operative simultaneously. In this area, molecular-dynamics simulations proved particularly useful in understanding the sputtering mechanisms, since in the simulations the effect of the high energy deposition is taken to account in an atomistic manner.

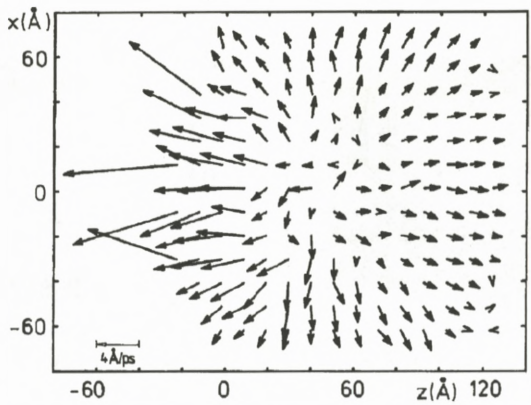

Figure 7. Velocity distribution corresponding to the earliest plot in Figure 6. Velocities are calculated as averages over a cubic cell of dimension $8 \times 7 \times 8$ Å^3. Only the projection of the velocities onto the plane $y = 0$ is plotted. Taken from Urbassek and Waldeer (1991).

In an early simulation of the sputtering of a condensed Ar target by 1 keV Ar atoms, Urbassek and Waldeer (1991) demonstrated the mechanisms of sputtering in a spike regime for the first time. Figure 6 shows that the entire collision-cascade region is filled with a high energy density, such that the kinetic energy surpasses the cohesive energy of an atom; in other words, the volume is heated above the critical point of the liquid-vapour phase transition. The high thermal pressure built up in the target then accelerates the atoms out of the cascade volume. Figure 7 displays the velocity distribution of the sputtered atoms and demonstrates the collective nature of flow. Thus this simulation gives evidence that sputtering occurs via the phase explosion mechanism mentioned as item 2 above. The shock wave plays no role in this case, since it runs *into* the material, thus causing no sputtering from the surface.

Figure 8a displays the energy distribution of sputtered particles for this event. Characteristically, besides a collision cascade contribution – applicable for emission energies above 0.1 eV – a strong low-energy contribution with a broad maximum for energies below around 20 meV is visible. This strong enhancement of low-energy sputtered particle has been found experimentally in many cases of spike sputtering, both for condensed-gas targets (Haring et al., 1984) and also for metals (Figure 8b).

Interestingly, the sputtering of metals under spike conditions follows the same pathway. This is demonstrated in Figure 9, where the sputtering of Au by 16 keV Au_4 cluster impact is shown. Again, the phase explosion mechanism is seen to be operative. Now, however, the liquid phase plays a more important role than in Ar:

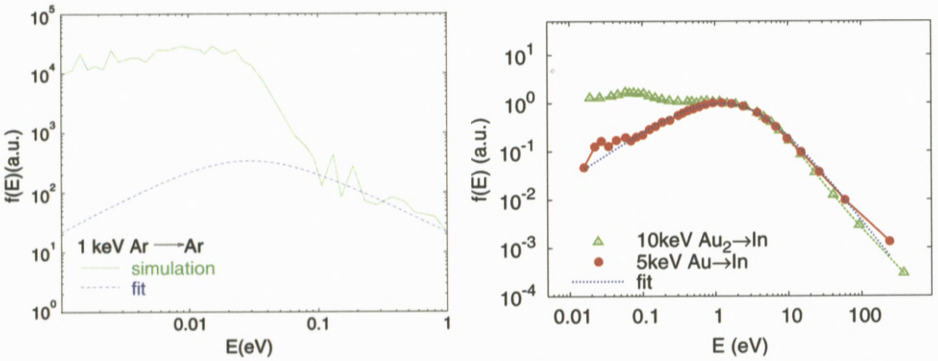

Figure 8. Energy distributions of particles sputtered from a spike, compared to the fit to a Thompson distribution of linear-cascade theory, Equation (2). (a) Molecular-dynamics data for 1 keV Ar → Ar bombardment Urbassek and Waldeer (1991). These data pertain to the individual impact event described in Figures 6 and 7, with a (particularly abundant) sputter yield of 911 atoms. (b) Experimental data Samartsev et al. (2005) of neutral In atoms sputtered from a polycrystalline In sample under impact of a Au atom (green triangles) and a Au_2 dimer (red circles). The impact energy is in both cases 5 keV/atom. The fit describes well the case of atom bombardment, but not the excess of low-energy atoms which are sputtered by dimer impact.

1. The walls of the forming crater are temporarily covered by a liquid film.
2. This liquid is driven out of the crater volume by the expansion; the temporarily forming protrusions or "fingers" (Nordlund et al., 2003) – irregular columns of liquid material protruding above the surface – have little heat contact to the target and therefore stay liquid and mobile for a long time (up to 100 ps). Eventually they may break away from the surface, forming large liquid droplets in the flux of emitted material, or fall back onto the surface forming large adatom islands. Both these phenomena are seen in experiment (Donnelly, 2006).

Effects of shock waves on sputtering do not appear to have been seen in simulations up to now. They may become important when the impact-induced spike is buried under the surface and emits a shock wave to the surface, which leads to the emission of solid chunks of material by a spallation mechanism; or in the bombardment of thin foils, where the shock wave may lead to (spallation) emission from the backside of the material. Such phenomena appear to have been seen by Rehn et al. (2001), cf. also Donnelly (2006). Interestingly the cluster size distribution observed in this group obeys a power law $Y(n) \propto n^{-\alpha}$ with $\alpha = 2$, corresponding to the value predicted by shock wave models (Bitensky and Parilis, 1987), cf. the discussion in Section 3.4.

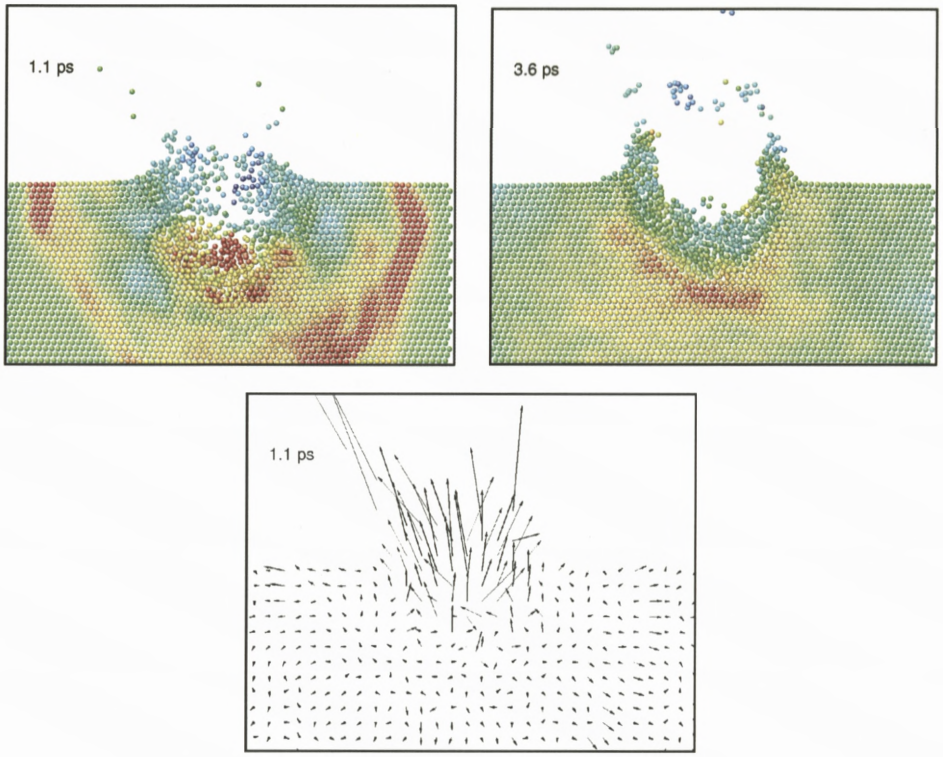

Figure 9. Molecular-dynamics data of a 16 keV Au_4 on Au. A representative event with a sputter yield of $Y = 317$ is shown. The data visualize the pressure distribution inside the target at 1.1 ps (a) and 3.6 ps (b) after impact. Yellow and red denotes compressive pressure, turquoise and blue tensile pressures. (c) Velocity profile of this event at 1.1 ps. Taken from Colla et al. (2000).

3.2. Cluster Impact

Similar considerations hold for the sputter yield due to cluster impact. If the impact velocity is relatively small, such that the energy deposition occurs close to the target surface, the sputter yield is more or less linear in the *total impact energy* of the cluster. This is exemplified in Figure 10 both for a condensed-Ar target and a metal. The sputter yield $Y_n(E)$ of a cluster projectile of size n with total energy E obeys in good approximation the law (Anders et al., 2004)

$$Y_n(E) = a\frac{\epsilon^{1+b}}{(\epsilon_{\mathrm{th}} + \epsilon)^b}, \tag{12}$$

where $\epsilon = E/U$. a, b and ϵ_{th} are constants denoting a "sputter efficiency", the onset of sputtering in the threshold regime, and the threshold energy, respectively.

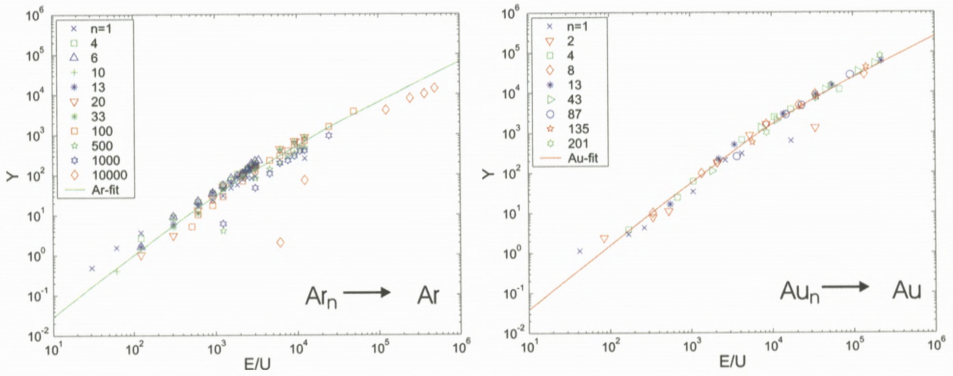

Figure 10. Synoptic display of self-sputter yield of cluster impact of (a) an Ar solid (Anders et al., 2004) and (b) a Au solid (Zimmermann and Urbassek, 2006). The bombarding energy E has been scaled to the cohesive energy of the target U. A fit function, Equation (12), with parameters as given in the text has been included.

Note that the cluster size n does not appear explicitly in Equation (12); it is only the total cluster energy that determines the yield. For high energies, Equation (12) simplifies to a linear law,

$$Y_n(E) = a(\epsilon - b\epsilon_{\text{th}}), \quad \epsilon \gg \epsilon_{\text{th}}. \tag{13}$$

Zimmermann and Urbassek (2006) find that the constants assume similar values for the two systems studied: $a = 0.065$ (0.246), $b = 0.54$ (0.60), and $\epsilon_{\text{th}} = 3160$ (10600) for an Ar (Au) target. The deviations between the two parameter sets may be due to the role of the liquid phase, which is more relevant for metals than for van-der-Waals bonded systems.

However, this simple finding disagrees with experimental data measured by Bouneau et al. (2002), in which the sputtering of a Au surface by Au_n clusters ($n \leq 13$) with total impact energies of up to 5 MeV has been studied. In those experiments a scaling like

$$Y_n(E) = n^2 f\left(\frac{E}{n}\right), \tag{14}$$

has been found, in obvious contrast to Equation (12). The origin of this discrepancy is still under discussion. Possibly, one or several of the following issues are relevant:

1. Under the experimental conditions, the projectile may deposit its energy deeply into the material, and also in the form of subcascades, thus producing buried spikes instead of near-surface spikes in the simulations.

2. In the simulations, no electron-phonon coupling was taken into account with the reasoning that the role of electronic heat transport in the highly disordered spike region is largely unclear from a physical point of view. If, however, spike quenching by electronic heat conduction is relevant, late emission events will be strongly affected. Note, in particular, that the simulated sputter yields – in the range where simulated projectile energies and sizes coincide with the of experimental conditions – are considerably (up to one order of magnitude) larger than experimental values; this might possibly be explained by the role of spike quenching due to electronic heat conduction.
3. Interatomic interaction potentials are poorly tested in the range of high energy densities and pressures and low particle densities relevant for the spike region.

3.3. Crater Formation

Due to the high emission yields and the collective nature of the emission flow, spike sputtering is usually connected to the formation of craters. For spike sputtering in the scenario mentioned above – i.e., where the high energy deposition close to the surface leads to the phase explosion of a near-surface part of the target – crater formation is characterized by the following features (Aderjan and Urbassek, 2000; Colla et al., 2000:

1. above a threshold impact energy E_{th}, the crater volume increases linearly with the total cluster energy;
2. the crater shape is roughly hemispherical;
3. a crater rim is formed, in which the majority of the atoms excavated from the crater are deposited; the rest have been sputtered.

Aderjan and Urbassek (2000) and also Nordlund (2001) note that a similar scaling of the crater size with total impact energy is observed also for macroscopic projectile impact, such as dust particles, bullets, or meteorites.

3.4. Cluster Emission

Both experiments and molecular-dynamics computer simulations show that clusters form an important contribution to the flux of sputtered particles (Urbassek and Hofer, 1993). The abundance distribution of emitted clusters obeys a power law

$$Y(n) \propto n^{-\alpha} \tag{15}$$

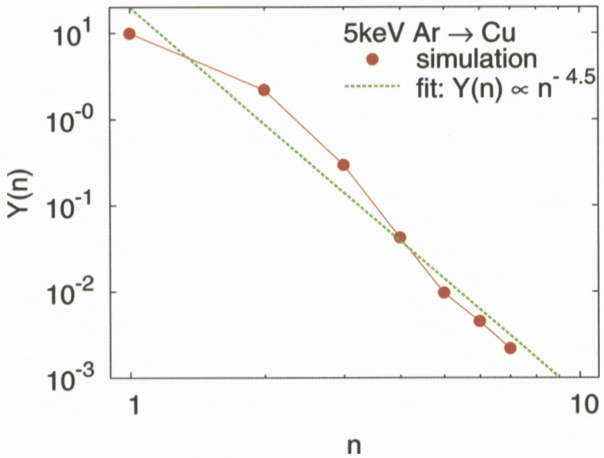

Figure 11. Abundance distribution of sputtered clusters $Y(n)$ *versus* number of atoms contained in the cluster, n. Symbols: Results from molecular-dynamics simulations of 5 keV Ar impact on a Cu (111) surface; fragmentation of metastable clusters after emission has been taken into account. Line: power-law decay, Equation (12), with $\alpha = 4.5$. Data taken from Colla et al. (1998).

in cluster size n; Figure 11 gives an example obtained by molecular-dynamics simulation. The power exponent α has been shown empirically to strongly correlate with the total sputter yield Y; it decreases with Y down to values $\alpha < 4$ and even around 2 (Samartsev et al., 2005). Note that a statistical-combination model for the formation of clusters in the flux of sputtered atoms would predict an exponential abundance distribution. Both the origin of a power-law distribution and of the reason for the strong correlation with the total sputter yield are not entirely clear. Two models exist which predict power-law distributions, albeit with fixed values of the exponent α:

1. The shock wave models mentioned above (Bitensky and Parilis, 1987) in Section 3.1 predict a value of $\alpha = 2$.
2. The gas-flow model (Urbassek, 1988) assumes cluster production to occur in thermodynamic equilibrium; then the highest abundance of large clusters is found in the vicinity of the critical point. Here clusters are distributed according to a power law (15) with α given by the critical exponents of the medium; for a van-der-Waals medium $\alpha = 7/3$.

Note that these models do not predict the power exponent to depend on the total sputter yield. Possibly, such a dependence may be due to the averaging over many impact events: The large-n tail of the distribution will be dominated by particularly

hot near-surface spikes, which abundantly produce clusters, possibly with an exponent α close to the critical value 7/3. An averaging over the properly weighted spike components may then be approximated by a power law Equation (15); the effective value of α will then be lower with increasing total average yield.

3.5. Sputtering from Swift-Ion Tracks

An interesting situation of sputtering under spike conditions occurs when particles are sputtered from a swift-ion track. Such a track is the consequence of the – more or less rectilinear – trajectory of a swift ion, which slows down in the material due to electronic stopping. The highly excited electrons along the cylindrical track impart their energy to the target atoms; for sufficiently high energy densities, a situation characterized by the spike condition, Equation (11), may be established.

Theoretical models for sputtering from these tracks have been set up, cf. the contributions by Toulemonde et al. (2006) and Klaumünzer (2006), and also molecular-dynamics simulations have been employed for investigation. These usually skip the details of how the electronic energy is converted to nuclear motion and immediately assume the excitation energy to be imparted as random kinetic energy to the atoms. The first simulations have been published by Fenyö et al. (1990), Fenyö and Johnson (1992) and Urbassek et al. (1994). More recently, Bringa and Johnson (1998) and Bringa et al. (1999a, 1999b, 2000) analyzed this scenario in greater detail. The following results could be obtained: (i) A regime was identified where at low densities of the energetic excitation events the yield is linear due to the sparse distribution of the excitations. (ii) The high-energy-density linear regime is connected to the formation of a melt and the removal of energy by a pressure pulse. In this regime the size of the yield increases with the initial radial extension of the track and is determined by the removal of energy radially by the pressure pulse and by the transport of energy to the surface.

Beuve et al. (2003) studied two further aspects of fast-ion-induced sputtering by including the dynamics of the electronic subsystem: (i) The energy transfer from the electronic to the atomic system is assumed not to occur instantaneously but to take a period of time Δt. For $\Delta t > 1$ ps it is found that the sputtering yield becomes strongly nonlinear as a function of the stopping power. (ii) The influence of a non-homogeneous spatial distribution of the electronic excitations is modelled. It is shown that such a spatial distribution also leads to a strongly non-linear dependence of the yield on the excitation density.

4. Further Topics

Among further topics in sputter theory, which are presently being investigated, I mention the following:

4.1. Electronic Excitation

Projectiles which are slowed down in the nuclear-stopping regime impart some energy to the electron system of the target; this also holds true for the energetic recoil atoms generated in the target. This energy deposition can be modelled using available quantitative schemes of electronic stopping. In fact, such simulations have been performed with the aim of predicting the probability of sputtered particles to be excited or ionized (Sroubek et al., 2003). However, it might be interesting to know about the fate of the energy given to the electronic system:

1. In metals, swift electronic heat conduction may efficiently quench the collision cascade and in particular long-lived spikes, see Section 3.2 above.
2. As the discussion on ion tracks in Section 3.5 above showed, there exist conditions where energy transfer from the electronic to the atomic system may be important.
3. Since in metals, the electronic degrees of freedom may be assumed to equilibrate quickly, the conditions of excitation and ionization of sputtered particles will be determined by the local electron temperatures around the sputtered particle positions.

Duvenbeck and Wucher (2005) are investigating the latter process by including the electron temperature as a further variable in molecular-dynamics simulations. Their results demonstrate that a detailed knowledge of the dependence of the electron heat diffusivity on the atomic environment (density, temperature, local order) is crucial for progress in this area.

4.2. Molecular Targets

A prototypical example of the sputtering of molecular targets is given by condensed diatomic gas targets (Balaji et al., 1995). Here a variety of phenomena occur beyond those existing in atomic targets:

1. The rotational and vibrational excitation of the target molecules provides a further channel for projectile energy deposition. As a consequence, the (translational) temperature in the cascade volume is smaller than in the case

of sputtering of an atomic target. This effect will reduce the sputter yield in a spike scenario.
2. The possibility of target molecule dissociation operates in the same direction.
3. Upon molecule dissociation, radicals may form and react. These reactions may be exothermic, thus releasing energy and enhancing the sputter yield.

In fact, these possibilities have been seen in experiment and interpreted in this manner by Balaji et al. (1995) and David et al. (2001). Besides the analysis presented in these papers, a detailed quantitative model has not been set up.

In the field of sputtering of organic molecules and polymers some progress has been achieved in particular by the work of Garrison, Delcorte and Postawa. They performed a series of dedicated molecular-dynamics simulations motivated by the needs of organic SIMS; for recent references cf. Czerwinski et al. (2006) for thin organic films and Delcorte et al. (2003) for polymers.

Garrison mentions in her review (2001) that the following features in the sputtering of organic, biological and polymeric solids were demonstrated in the simulations:

- formation of fragments;
- reactions between fragments (radical-radical recombinations);
- molecule emission by a collective mechanism called *molecule liftoff* (Garrison et al., 2000).

4.3. Chemical Effects

Chemical or reactive sputtering occurs when the projectile, or its reaction products, react with the target, thus forming more volatile species which enhance the sputter yield. Analogously, e.g., polymerization reactions occurring in the target and induced by the ion impact, may decrease the sputter yield. Simulations have been performed, e.g., to understand the following specific systems:

1. Schoolcraft and Garrison (1991), Feil et al. (1993) and Feil (1995) studied the reactive sputtering of silicon by halogen ions motivated by the technique of RIBE (reactive ion beaming etching)
2. The sputtering of graphite by hydrogen, motivated by interest in the use of graphite as a first-wall material of fusion reactors (Salonen et al., 2001).

5. Conclusions

In his 1980 review, Jackson poses the following questions to indicate the future directions of sputter theory:

1. What further improvements can be made in transport theory?
2. Can gas-like simulations be used in most practical sputtering calculations?
3. What information can be expected from single-knockon work?
4. Are there surface ejection spike phenomena?
5. What happens in non-linear cascades?
6. How are chunks and large clusters emitted?
7. What effect does pre-existing damage have on sputtering?

Of these, the first three have been answered such that (1) transport theory has reached a mature state of full development, (2) binary collision codes like TRIM or MARLOWE have found widespread use in predicting projectile ranges and sputtering in the collision-cascade and single-knockon regimes, and (3) the interest in near-threshold sputter processes, while of importance in several applications, such as, e.g., in plasma environments, has led to empirical sputter formulae like Equations (3)–(5). Issues 4–6 refer to spike sputtering and are still being actively investigated today. Question 7 is a major issue nowadays, since it affects the fluence dependence of surface modification and erosion, cf. Chason and Chan (2006).

Today the major open problems in sputter theory as addressed in this review can be summarized as follows:

1. *Is there a universal picture of spike sputtering?*
   The regions of validity of available models (shock wave, surface evaporation, gas flow, pressure pulse,...) need to be identified. The role of target materials parameters (in particular that of thermal properties like the critical temperature, importance of a liquid phase, but also the strength of the solid and the surface tension of the liquid) need to be explored. This task is complicated by the fluctuations inherent in the projectile slowing down process.
2. *Scaling laws for cluster impact.*
   While simulations find a scaling of the crater volume and sputter yield proportional to the total cluster energy, in agreement with experiments on macroscopic impacts, experiments with small clusters (Au_n clusters with $n \leq 13$ and total energies $E \leq 5$ MeV) find a different scaling. The origin of this discrepancy is unclear. It is also of interest to delineate more clearly

the parameter region where the energy proportionality of sputter yields and crater sizes hold.

3. *Role of target electrons.*
   While the process of energy transfer to target electrons during projectile slowing down forms a part of stopping theory, the question of how much energy is spent in electronic excitation by high-generation recoils in the collision cascade and in particular in a spike regime does not appear to be clarified. Furthermore, the question needs to be clarified of how efficiently electronic heat conduction can contribute to the quenching of spikes in metals.
4. *How realistic are long time (100 ps) molecular-dynamics simulations of late sputtering events?*
   Besides the role of electrons, also the reliability of interatomic potentials in high-temperature, high-pressure, low-density environments needs to be clarified. The role of boundary conditions to which the simulation volume is subjected may bias simulation results in particular at late times.
5. *What is the origin of the power-law abundance distributions observed for large-cluster emission in sputtering?*
   These hint at a cooperative emission process.
6. *Creation of surface topography by sputtering.*
   A quantification of the spatial dependence of adatoms and surface vacancies after single ion impact would be useful.
7. *Influence of surface topography on sputtering.*
   The ion irradiation of nano-sized objects, and even atomistic patterns like steps or adatom clusters necessitates an understanding of how surface features influence the sputtering process.
8. *Further topics: sputtering of molecular targets, chemical effects in sputtering, etc.*
   An understanding of universal mechanisms beyond the study of specific systems would be useful.

Acknowledgements

Thanks are due to Christian Anders, Yudi Rosandi, Luis Sandoval, and Steffen Zimmermann for preparing figures for this review. I am grateful to Peter Sigmund for a critical reading of the manuscript.

References

Aderjan R. and Urbassek H.M. (2000): Molecular-dynamics study of craters formed by energetic Cu cluster impact on Cu. Nucl Instrum Meth B **164–165**, 697–704

Anders C., Urbassek H.M. and Johnson R.E. (2004): Linearity and additivity in cluster-induced sputtering: A molecular-dynamics study of van der Waals bonded systems. Phys Rev B **70**, 155404-1-6

Aziz M. (2006): Nanoscale morphology control using ion beams. Mat Fys Medd Dan Vid Selsk **52**, 187–206

Balaji V., David D.E., Tian R., Michl J. and Urbassek H.M. (1995): Nuclear sputtering of condensed diatomic gases. J Phys Chem **99**, 15565–15572

Baragiola R.A. (2004): Observations of Sputtering: Survey of Observations and Derived Principles. Phil Trans Roy Soc (London) A **362**, 29

Behrisch R. (Ed.) (1981): Sputtering by Particle Bombardment I, Springer, Berlin

Behrisch R. (Ed.) (1983): Sputtering by Particle Bombardment II, Springer, Berlin

Behrisch R. and Wittmaack K. (Eds) (1991): Sputtering by Particle Bombardment III, Springer, Berlin

Beuve M., Stolterfoht N., Toulemonde M., Trautmann C. and Urbassek H.M. (2003): Influence of the spatial and temporal structure of the deposited-energy distribution in swift-ion-induced sputtering. Phys Rev B **68**, 125423

Biersack J.P. and Eckstein W. (1984): Sputtering studies with the Monte Carlo program TRIM.SP. Appl Phys A **34**, 73

Biersack J.P. and Haggmark L.G. (1980): A Monte Carlo computer program for the transport of energetic ions in amorphous targets. Nucl Instr Meth **174**, 257

Bitensky I.S. and Parilis E.S. (1987): Shock wave mechanism for cluster emission and organic molecule desorption under heavy ion bombardment. Nucl Instrum Meth B **21**, 26

Bohdansky J. (1984): A universal relation for the sputtering yield of monatomic solids at normal ion incidence. Nucl Instrum Meth B **2**, 587

Bouneau S., Brunelle A., Della-Negra S., Depauw J., Jacquet D., LeBeyec Y., Pautrat M., Fallavier M., Poizat J.C. and Andersen H.H. (2002): Very large Au and Ag sputtering yields induced by keV to MeV energy Au_n clusters ($n = 1 - 13$). Phys Rev B **65**, 144106

Bradley R.M. and Harper J.M.E. (1988): Theory of ripple topography induced by ion bombardment. J Vac Sci Technol A **6**, 2390

Bringa E.M. and Johnson R.E. (1998): Molecular dynamics study of non-equilibrium energy transport from a cylindrical track. I. Test of spike models. Nucl Instrum Meth B **143**, 513

Bringa E.M., Johnson R.E. and Dutkiewicz L. (1999a): Molecular dynamics study of non-equilibrium energy transport from a cylindrical track. II. Spike models for sputtering yield. Nucl Instrum Meth B **152**, 267

Bringa E.M., Johnson R.E. and Jakas M. (1999b): Molecular dynamics simulation of electronic sputtering. Phys Rev B **60**, 15107

Bringa E.M., Jakas M. and Johnson R.E. (2000): Spike models for sputtering: effect of the surface and the material stiffness. Nucl Instrum Meth B **164-165**, 762

Chason E. and Chan W.L. (2006): Ion-induced surface evolution in the linear instability regime: Continuum theory and kinetic Monte Carlo simulations. Mat Fys Medd Dan Vid Selsk **52**, 207–225

Colla T.J., Urbassek H.M., Wucher A., Staudt C., Heinrich R., Garrison B.J., Dandachi C. and Betz G. (1998): Experiment and simulation of cluster emission from 5 keV Ar → Cu. Nucl Instrum Meth B **143**, 284–297

Colla T.J., Aderjan R., Kissel R. and Urbassek H.M. (2000): Sputtering of Au (111) induced by 16-keV Au cluster bombardment: Spikes, craters, late emission, and fluctuations. Phys Rev B **62**, 8487–8493

Conrad U. and Urbassek H.M. (1992): Monte Carlo study of fluence dependent mixing and sputtering of isotopic targets under ion bombardment. Surf Sci **278**, 414–426

Czerwinski B., Delcorte A., Garrison B.J., Samson R., Winograd N. and Postawa Z. (2006): Sputtering of thin benzene and polystyrene overlayers by keV Ga and C60 bombardment. Appl Surf Sci **252**, 6419

David D.E., Balaji V., Michl J. and Urbassek H.M. (2001): Sputtering of condensed polyatomic gases by kilo-electron-volt-energy ions. Int J Mass Spectrom **212**, 477–489

Delcorte A., Arezki B. and Garrison B.J. (2003): Matrix and substrate effects on the sputtering of a 2 kDa molecule: Insights from molecular dynamics. Nucl Instrum Meth B **212**, 414

Donnelly S.E. (2006): Some solved and unsolved problems in transmission electron microscopy studies of radiation damage in solids. Mat Fys Medd Dan Vid Selsk **52**, 329–355

Duvenbeck A. and Wucher A. (2005): Low-energy electronic excitation in atomic collision cascades: A nonlinear transport model. Phys Rev B **72**, 115417

Eckstein W. (1991): Computer Simulation of Ion-Solid Interactions. Springer, Berlin

Eckstein W., Garcia-Rosales C., Roth J. and Laszlo J. (1993): Threshold energy for sputtering and its dependence on angle of incidence. Nucl Instrum Meth B **83**, 95

Feil H. (1995): Small free barrier and postdesorption collisions: The keys towards the understanding of reactive ion etching of silicon. Phys Rev Lett **74**, 1879

Feil H., Dieleman J. and Garrison B.J. (1993): Chemical sputtering of Si related to roughness formation of a Cl-passivated Si surface. J Appl Phys **74**, 1303

Fenyö D. and Johnson R.E. (1992): Computer experiments on molecular ejection from an amorphous solid: comparison to an analytic continuum mechanical model. Phys Rev B **46**, 5090

Fenyö D., Sundqvist B.U.R., Karlsson B.R. and Johnson R.E. (1990): Molecular-dynamics study of electronic sputtering of large organic molecules. Phys Rev B **42**, 1895

Friedrich A. (2003): Zerstäubung und Defektentstehung unter schrägem Edelgasionenbeschuss. Diploma thesis, University Kaiserslautern

Friedrich A. and Urbassek H.M. (2003): Effect of surface steps on sputtering and surface defect formation: molecular-dynamics study of 5 keV Xe^+ bombardment of Pt (111) at glancing incidence angles. Surf Sci **547**, 315–323

Gades H. and Urbassek H.M. (1992): Pair versus many-body potentials in atomic emission processes from a Cu surface. Nucl Instrum Meth B **69**, 232–241

Gades H. and Urbassek H.M. (1994a): Molecular-dynamics simulation of adatom formation under keV-ion bombardment of Pt (111). Phys Rev B **50**, 11167–11174

Gades H. and Urbassek H.M. (1994b): Surface binding energies of alloys: a many-body approach. Nucl Instrum Meth B **88**, 218–228

Gades H. and Urbassek H.M. (1995): Preferential sputtering of alloys: a molecular-dynamics study. Nucl Instrum Meth B **102**, 261–271

Garrison B.J. (2001): Molecular dynamics simulations, the theoretical partner to static SIMS experiments. In: Vickerman J.C. and Briggs D. (Eds), ToF-SIMS: Surface Analysis by Mass Spectrometry, Vol. 223, IM Publications, Chichester, UK

Garrison B.J., Delcorte A. and Krantzman K.D. (2000): Molecule liftoff from surfaces. Acc Chem Res **33**, 69

Glazov L.G. (1994a): Solution of the kinetic equation for the deposited energy distribution in the power cross section model. J Phys: Condens Matter **6**, 4181

Glazov L.G. (1994b): Solution of the kinetic equation for the deposited momentum distribution: neglecting threshold energy. J Phys: Condens Matter **6**, 10647

Glazov L.G. (1995): Solution of the kinetic equation for the deposited momentum distribution: II. Threshold energy effects. J Phys: Condens Matter **7**, 6365

Glazov L.G. (1997): Collision cascades and sputter fluxes in bounded random media. Nucl Instrum Meth B **122**, 611

Glazov L.G. and Paszit I. (2004): Applications of invariant embedding: positron backscattering from surfaces. Nucl Instrum Meth B **215**, 509

Glazov L.G., Shulga V.I. and Sigmund P. (1998): Analysis of a perfect sputter experiment. Surf Interface Anal **26**, 512

Gnaser H. and Oechsner H. (1990): Isotopic mass effects in sputtering: dependence on fluence and emission angle. Nucl Instrum Meth B **48**, 544

Grove Symposium (2004): Sputtering: past, present and future. W. R. Grove 150th Anniversary Issue. Phil Trans Roy Soc (London) A **362, no. 1814**, 1–194

Haring R.A., Pedrys R., Haring A. and de Vries A.E. (1984): Sputtering of condensed noble gases by keV heavy ions. Nucl Instrum Meth B **4**, 40

Harrison Jr. D.E. (1988): Application of molecular dynamics simulations to the study of ion-bombarded metal surfaces. Crit Rev Solid State Mater Sci **14**, S1

Hofer W.O. (1991): Angular, energy and mass distribution of sputtered particles. In: Behrisch R. and Wittmaack K. (Eds), *Sputtering by Particle Bombardment III*, 15, Springer, Berlin

Hou M. and Eckstein W. (1990): Anisotropy of momentum distributions in atomic-collision cascades generated in fcc materials. Phys Rev B **42**, 5959

Jackson D.P. (1980): The theory of sputtering. In: Varga P., Betz G. and Viehböck F.P. (Eds), Symposium on Sputtering, 2. Inst. f. Allg. Phys., Wien

Jakas M.M. (2004): Transport theories of sputtering. Phil Trans Roy Soc (London) A **362**, 139

Johnson R.E. and Evatt R. (1980): Thermal spikes and sputtering yields. Radiat Eff **52**, 187

Johnson R.E., Sundqvist B.U.R., Hedin A. and Fenyö D. (1989): Sputtering by fast ions based on a sum of impulses. Phys Rev B **40**, 49

Kelly R. (1990): Thermal sputtering as a gas-dynamic process. Nucl Instrum Meth B **46**, 441

Kitazoe Y., Hiraoka N. and Yamamura Y. (1981): Hydrodynamical analysis of non-linear sputtering yields. Surf Sci **111**, 381

Klaumünzer S. (2006): Thermal-spike models for ion track physics: A critical examination. Mat Fys Medd Dan Vid Selsk **52**, 293–328

Lo D.Y., Tombrello T.A. and Shapiro M.H. (1989): Molecular dynamics simulation of preferential sputtering from isotopic mixtures. Nucl Instrum Meth B **40/41**, 270

Michely T. and Krug J. (2004): Islands, Mounds, and Atoms, Springer Series in Surface Science, Vol. 42, Springer, Berlin

Michely T. and Teichert C. (1994): Adatom yields, sputtering yields, and damage patterns of single-ion impacts on Pt (111). Phys Rev B **50**, 11156

Möller W. and Eckstein W. (1984): TRIDYN – A TRIM simulation code including dynamic composition changes. Nucl Instrum Meth B **2**, 814

Nordlund K. (2001): Ions mimic the impact of meteorites. Phys World **14**, 22

Nordlund K., Tarus J., Keinonen J., Donnelly S.E. and Birtcher R.C. (2003): Atomic fingers, bridges and slingshots: formation of exotic surface structures during ion irradiation of heavy metals. Nucl Instrum Meth B **206**, 189

Rehn L.E., Birtcher R.C., Donnelly S.E., Baldo P.M. and Funk L. (2001): Origin of Atomic Clusters during Ion Sputtering. Phys Rev Lett **87**, 207601

Reimann C.T. (1993): Theoretical models for sputtering and desorption of large bio-organic molecules under collisional and electronic excitation by ion impact. Mat Fys Medd Dan Vid Selsk **43**, 351

Robinson M.T. and Torrens I.M. (1974): Computer simulation of atomic-displacement cascades in solids in the binary-collision approximation. Phys Rev **9**, 5008

Rosencrance S.W., Burnham J.S., Sanders D.E., He C., Garrison B.J., Winograd N., Postawa Z. and DePristo A.E. (1995): A mechanistic study of atomic desorption resulting from the keV ion bombardment of fcc (001) single crystal metals. Phys Rev B **52**, 6006

Salonen E., Nordlund K., Keinonen J. and Wu C.H. (2001): Swift chemical sputtering of amorphous hydrogenated carbon. Phys Rev B **63**, 195415

Samartsev A.V., Duvenbeck A. and Wucher A. (2005): Sputtering of indium using Au_m projectiles: Transition from linear cascade to spike regime. Phys Rev B **72**, 115417

Schoolcraft T.A. and Garrison B.J. (1991): Initial stages of etching of the silicon Si100 (2×1) surface by 3.0-eV normal incident fluorine atoms: a molecular dynamics study. J Am Chem Soc **113**, 8221

Sckerl M.W., Sigmund P. and Vicanek M. (1996): Particle fluxes in atomic collision cascades. Mat Fys Medd Dan Vid Selsk **44**, 1

Sckerl M.W., Lam N.Q. and Sigmund P. (1998): Compositional changes in alloys during ion bombardment at elevated temperatures. Nucl Instrum Meth B **140**, 75

Shapiro M.H., Tombrello T.A. and Harrison Jr. D.E. (1988): Simulation of isotopic mass effects in sputtering, II. Nucl Instrum Meth B **30**, 152

Shulga V.I. and Eckstein W. (1998): Depth of origin of sputtered atoms for elemental targets. Nucl Instrum Meth B **145**, 492

Shulga V.I. and Sigmund P. (1995): Simulation of energy-dependent isotope sputtering. Nucl Instrum Meth B **103**, 383

Shulga V.I. and Sigmund P. (1996): Analysis of the primary process in isotope sputtering. Nucl Instrum Meth B **119**, 359

Sigmund P. (1969): Theory of sputtering 1. Sputtering yield of amorphous and polycrystalline targets. Phys Rev **184**, 383

Sigmund P. (1973): A mechanism of surface micro-roughening by ion bombardment. J Mater Sci **8**, 1545

Sigmund P. (1974): Energy density and time constant of heavy-ion-induced elastic-collision spikes in solids. Appl Phys Lett **25**, 169

Sigmund P. (1981): Sputtering by ion bombardment: Theoretical concepts. In: Behrisch R. (Ed.), Sputtering by Particle Bombardment I, 9, Springer, Berlin

Sigmund P. (Ed.) (1993): Fundamental Processes in Sputtering of Atoms and Molecules (SPUT92). Mat. Fys. Medd. Dan. Vid. Selsk., **43**, Copenhagen

Sigmund P. and Claussen C. (1981): Sputtering from elastic-collision spikes in heavy-ion-bombarded metals. J Appl Phys **52**, 990

Sigmund P. and Lam N.Q. (1993): Alloy and isotope sputtering. Mat Fys Medd Dan Vid Selsk **43**, 255

Sroubek Z., Sroubek F., Wucher A. and Yarmoff J.A. (2003): Formation of excited Ag atoms in sputtering of silver. Phys Rev B **68**, 115426

Sunner J., Ikonomou M.G. and Kebarle P. (1988): SIMS spectra of alcohols and the phase explosion model of desorption ionization. Int J Mass Spectrom Ion Proc **82**, 221

Szymczak W. and Wittmaack K. (1993): Angular distributions of gold sputtered from a (111) crystal: Dependence of spot shapes and of spot and background yields on the primary ion mass and energy and on the target temperature. Nucl Instrum Meth B **82**, 220

Toulemonde M. et al. (2006): Experimental phenomena and thermal spike model description of ion tracks in amorphisable inorganic insulators. Mat Fys Medd Dan Vid Selsk **52**, 263–292

Urbassek H.M. (1988): Sputtered cluster mass distribution, thermodynamic equilibrium and critical phenomena. Nucl Instrum Meth B **31**, 541–550

Urbassek H.M. (1997): Molecular-dynamics simulation of sputtering. Nucl Instrum Meth B **122**, 427–441

Urbassek H.M. and Hofer W.O. (1993): Sputtering of molecules and clusters: Basic experiments and theory. Mat Fys Medd Dan Vid Selsk **43**, 97–125

Urbassek H.M. and Michl J. (1987): A gas-flow model for the sputtering of condensed gases. Nucl Instrum Meth B **22**, 480–490

Urbassek H.M. and Waldeer K.T. (1991): Spikes in Condensed Rare Gases Induced by keV-Atom Bombardment. Phys Rev Lett **67**, 105–108

Urbassek H.M., Kafemann H. and Johnson R.E. (1994): Atom ejection from a fast-ion track: A molecular-dynamics study. Phys Rev B **49**, 786–795

Vicanek M. (1999): Electron transport processes in REELS and XPS. Surf Sci **440**, 1

Vicanek M., Jimenez Rodriguez J.J. and Sigmund P. (1989): Depth of origin and angular spectrum of sputtered atoms. Nucl Instrum Meth B **36**, 124

Vicanek M., Conrad U. and Urbassek H.M. (1993): Energy partitioning and particle spectra in multicomponent collision cascades. Phys Rev B **47**, 617–629

Vicanek M., Sckerl M.W. and Sigmund P. (1998): Effect of composition gradients in alloys on differential sputter parameters. Nucl Instrum Meth B **140**, 61

Wahl M. and Wucher A. (1994): VUV photoionization of sputtered neutral silver clusters. Nucl Instrum Meth B **94**, 36

Wittmaack K. (1997): Energy- and angle-resolved depth of origin of isotopes sputtered from an elemental target. Phys Rev B **56**, R5701

Wittmaack K. (2003): Analytical description of the sputtering yields of silicon bombarded with normally incident ions. Phys Rev B **68**, 235211

Zimmermann S. (2006): Clusterbeschuss auf Oberflächen: Untersuchung des Fragmentations- und Zerstäubungsverhaltens. Ph.D. thesis, University Kaiserslautern

Zimmermann S. and Urbassek H.M. (2006): Sputtering of Au by cluster impact. Nucl Instrum Meth B, submitted

A Critical Review of the Electron-Tunnelling Model of Secondary Ion Formation

Klaus Wittmaack*

GSF – National Research Centre for Environment and Health
Institute of Radiation Protection
85764 Neuherberg, Germany

Abstract

The resonant-electron-tunnelling model of secondary ion formation is based on the assumption that the charge state of an atom departing from the unperturbed surface of a metal is determined by its interaction with the electronic system of the substrate. As a result of the interaction, the height $\varepsilon_a(z)$ of the atomic level and its lifetime, described in terms of the level width $\Delta(z)$, depend strongly on the distance z between the atom and the surface. At large distances $\varepsilon_a(z)$ equals the electron affinity A or the ionisation potential I. The key parameter of the substrate is the work function Φ or Fermi level $\varepsilon_F = -\Phi$. The probability of electron tunnelling from the substrate to the atom or vice versa, i.e. the probability of creating an ion, is controlled by the position of $\varepsilon_a(z)$ relative to ε_F. The probability of survival of the ion on its way to $z \rightarrow \infty$ is determined by the level width $\Delta(z)$ at the so-called crossing distance z_c defined as $\varepsilon_a(z_c) = \varepsilon_F$. Meaningful tests of the tunnelling model have been performed by measuring secondary ion yields $Y^{\pm}$ in dependence of the sample's work function, which was varied in a controlled manner by depositing small quantities of alkali atoms on the surface under study. In accordance with theoretical predictions negative ion yields were found to increase monotonically with decreasing Φ. Positive ion yields of elements with $I < \Phi$, on the other hand, exhibited the predicted decrease with decreasing work function. Previous evaluations of experimental data were based on a simplified version of the tunnelling model according to which $\mathrm{d}\ln P^- / \mathrm{d}\Phi = \text{const}$. The approximation

* E-mail: wittmaack@gsf.de

ignores the observed monotonic change in the slope of $\ln P^-(\Phi)$ and has the additional disadvantage that, on integration, it generates incorrect data for P^-. In this study available experimental data are rationalised without simplifications concerning the Φ-dependence of P^-. The yield saturation frequently observed in negative secondary ion emission from surfaces of very low work function was interpreted as reflecting complete ionisation, i.e. $P^- = 1$. Assuming that $\varepsilon_a(z)$ varies according to the image potential created by the departing ion, experimental $P^-(\Phi - A)$ data were used, for the first time, to determine the z-dependence of the level width which was found to be of the form $\Delta(z) \propto \exp(-\gamma z)$, as often assumed in the literature. Unexpectedly, however, and in contrast to the model, the characteristic inverse distances γ, derived from an analysis of data for various emission energies and angles, turned out to be distinctly different. Qualitatively the same trend was observed with an alternative approximation to $\varepsilon_a(z)$. The importance of γ is evident from the fact that the shape of experimental $P^-(\Phi - A)$ data is determined by this parameter. The apparent variability of γ suggests that the assumption of atom emission from an unperturbed surface is violated by the energetic processes occurring during sputter ejection. The bombardment induced surface perturbations appear to be largely responsible for the lack of agreement between experiment and theory in terms of the velocity dependence of P^-. The deviations from the predicted dependence were found to be moderate in data obtained under bombardment at a low primary ion energy of 0.5 keV. At a relatively high energy of 13 keV, however, a velocity dependence was not evident any more. These observations are in accordance with the idea that the magnitude of surface perturbations will increase with increasing impact energy. The effect of perturbations is also quite pronounced in positive ion emission, in which case P^+ was reported to be almost constant at relatively low emission energies (<8 eV). Furthermore, for $I > \Phi$, the ionisation probability did not approach unity in the limit of infinite velocity. This may be interpreted in terms of the existence of an upper limit in survival probability at small crossing distances (<1.5 Å). Previous attempts to extend the tunnelling model by introducing the concept of a local electron temperature on the order of several thousand Kelvin are discussed.

Contents

1 Introduction **467**

2 Data Basis **468**
2.1 Introductory Remarks 468
2.2 Relevant Examples of Experimental Data 469
2.2.1 Negative Secondary Ions 469
2.2.2 Positive Secondary Ions 472

3 Concept and Predictions of the Electron-Tunnelling Model **473**
3.1 General Features 473
3.2 Basic Formalism for Negative Ion Formation 476
3.3 Linear Approximation to $\ln P^-$ 477
3.4 Rigorous Evaluation 480
3.5 Velocity Dependence 484
3.6 Some Additional Features of the Tunnelling Model 485
3.7 Merging Positive and Negative Secondary Ion Yield Data 488
3.8 Effect of Surface Perturbations and the Infinite-Velocity Issue 490

4 Summary and Conclusions **492**

References **493**

1. Introduction

Bombardment of a solid sample with energetic primary ions can give rise to sputter ejection of atoms and molecules from the near-surface region of the target. The ionised particles in the sputtered flux are referred to as secondary ions. The mass and energy of the ejected secondary ions can be determined rather easily by passing them through an appropriate spectrometer. If this is done for the purpose of analysing the composition of a sample, the method is known as secondary ion mass spectrometry (SIMS). The problem in SIMS is that the ionisation probabilities of sputtered particles can vary by up to seven orders of magnitude (Wittmaack, 1998). High ionisation probabilities ($>10\%$) in sputtering of positive and negative secondary are generally observed only with alkali halides or ionic-like compounds such as oxides or nitrides. In order to achieve a high secondary ion signal from elemental targets or alloys, one must chemically alter the composition of the sample at its surface or within the topmost layers. Positive secondary ion yields are maximized if one manages to generate and maintain an oxide layer at the sputtered (receding) surface. For high yields of negative secondary ions one needs to lower the sample's work function as much as possible. To accomplish this goal, the bombarded surface must be covered with sub-monolayer quantities of electropositive elements like alkali metals. These necessary requirements for achieving high secondary ion yields are easy to design conceptually but are often difficult to implement in practice.

The most successful approach to describing the formation of secondary ions is the tunnelling model. Several groups have contributed to the development of this theory (Nørskov and Lundqvist, 1979; Brako and Newns, 1981; Lang, 1983). In its original form the model applies to sputtering from metallic samples. A simplified

version of the theoretical predictions has been tested for negative as well as positive secondary ion emission (Yu, 1981; Yu and Lang, 1983). The key parameter in the experiments was the sample's work function Φ which was lowered in a controlled manner, by up to 3 eV, using step-wise deposition of either Li or Cs. At secondary ion energies exceeding 20 eV, the observed velocity dependence appeared to be in accordance with simplified predictions of the tunnelling model. Other studies into the Φ-dependence of negative ion yields of atoms sputtered from elemental targets, however, did not show a velocity effect (Bernheim and Le Bourse, 1987). Another problem with the tunnelling model is that it predicts unit ionisation probability to be achievable in the limit of infinite emission velocity. However, as shown by an analysis of relevant data, this prediction is generally not in accordance with experimental findings (Wittmaack, 1999a).

In view of these conflicting results it appeared desirable to take another look at the predictions of the tunnelling model. The aim was to evaluate the strength and the limitations of this promising theory in more detail than before.

2. Data Basis

2.1. Introductory Remarks

Before entering into a discussion of experimental results and a comparison with the predictions of any theory of secondary ion formation, it is worth considering the requirements for a meaningful evaluation of data. An important aspect to note is that, with available instrumentation, absolute measurements of the ionisation probability $P^{\pm}$ are very difficult. Early attempts were based on the assumption that (i) the transmission of the employed SIMS instrument can be calibrated accurately and (ii) the energy distribution of the sputtered neutral atoms can be derived from analytical sputtering theory (Vasile, 1983; van der Heide, 1994). These assumptions have been shown not to be justified (Wittmaack, 1982, 1999a). A more reliable approach is to determine energy dependent yields of secondary ions and sputtered neutrals in the same instrument. Such measurements were originally performed using quadrupole based instruments that allowed mass and energy analysis to be carried out with and without ionisation of sputtered neutrals in a radio-frequency plasma (Wucher and Oechsner, 1988). Very recently laser based instruments were developed that have generated rather promising results (Meyer et al., 2003; Mazarov et al., 2006).

An alternative approach to comparing experimental data with theoretical predictions rests on the idea that, in favourable cases, one can vary the experimental parameters over a wide range so that the measured data include the case $P^{\pm} \approx 1$.

There is evidence that, with clean metallic targets this is possible when sputtering alkali metal atoms like Cs from very dilute overlayers, the reason being that Cs features a very low ionisation potential, lower than the work function of many metals. Meyer et al. (2003) compared the yields of Cs^+ secondary ions and post-ionised Cs atoms ejected from sputter cleaned, initially Cs covered silver. At very low residual Cs coverage, mean ionisation probabilities of Cs^+ as high as 0.8 were derived from velocity integrated spectra. At higher Cs coverage the ionisation probability was lower, presumable due to a Cs induced lowering of the sample's work function. The method of varying the work function of the sample by depositing small quantities of alkali metals on the sample surface for the purpose of systematically changing the ionisation probability of secondary ions was pioneered by Yu (1978, 1981, 1984a, 1984b) and subsequently extended by other groups (Prigge and Bauer, 1980; Bernheim and Le Bourse, 1987). The reported data constitute the most important pieces of information that one can use to test the predictions of the tunnelling model of secondary ion formation.

2.2. Relevant Examples of Experimental Data

2.2.1. *Negative Secondary Ions*

Examples of experimental data illustrating the dependence of negative secondary ion yields on the work function of the sample are compiled in Figures 1 and 2. The two sets of data in Figure 1, which relate to the emission of atomic ions from the respective target elements, were obtained under distinctly different conditions. Figure 1a shows results reported by Yu (1982) who used an ultrahigh-vacuum, quadrupole based SIMS instrument. A broad low-current, low-energy Ne^+ ion beam served to generate secondary ions at a low primary ion fluence of about 3×10^{14} ions/cm^2 per data point. Li or Cs atoms were deposited in a stepwise manner to reduce the work function Φ of the initially cleaned Si(111) sample ($\Phi_{0,Si} = 4.6$ eV; all work functions of clean elemental substrates taken from Michaelson, 1977). The work function changes were derived from the current-voltage characteristics of a low-energy electron beam directed at the sample at normal incidence. After each step of work function change, ion yields were recorded at several emission energies, defined by the pass energy of the energy filter. This approach introduces a systematic error because the changes in work function give rise to a corresponding change in the surface potential of the sample relative to the energy filter and the mass spectrometer (Wittmaack, 1983). The geometrical semi-apex angle of ion detection was 19°, i.e. rather large. The secondary ion yields reported in the original publication were converted to ionisation probabilities P^- assuming that the yields saturated at $P^- = 1$. The data are plotted as a function of $\Phi - A$, where A is the electron affinity of the sputtered

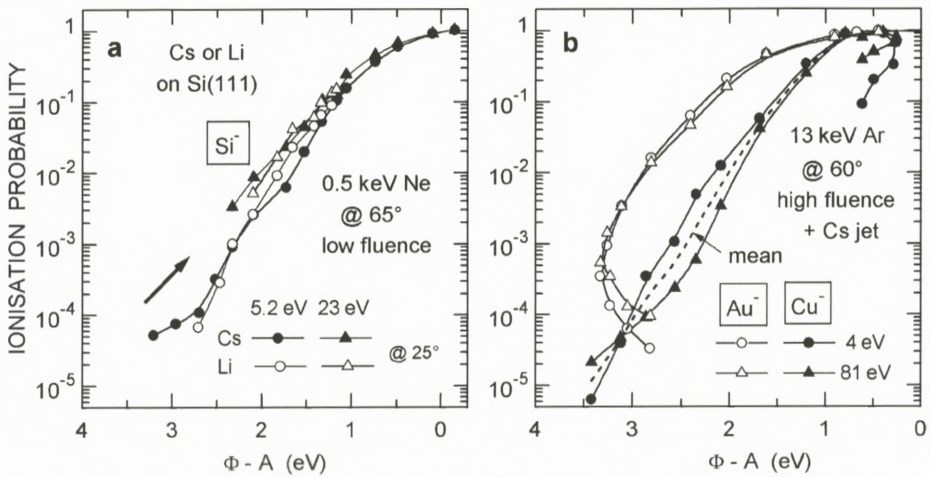

Figure 1. Ionisation probabilities of (a) Si^- and (b) Cu^- and Au^- sputtered from elemental targets (Si, Cu) or a AuCu alloy (Yu, 1982; Bernheim and Le Bourse, 1987). The work function of the targets was varied by depositing Li or Cs. The arrow in (a) denotes the direction of data acquisition. The quoted angles are counted with respect to the surface normal.

atom ($A_{Si} = 1.39$ eV). Note that Φ decreases from left to right. Two aspects of the results in Figure 1a deserve attention. First, within experimental uncertainty, the ionisation probabilities are the same for Li and Cs deposition. Second, at relatively low alkali coverage, i.e. for $\Phi - A > 1.5$ eV, P^- is higher at a (nominal) emission energy of 23 eV than at 5.2 eV. However, the difference is rather small.

The data in Figure 1b were obtained under high-fluence conditions (Bernheim and Le Bourse, 1987), susing a SIMS instrument composed of a magnetic prism and a spherical electrostatic prism. The samples were simultaneously exposed to a beam of Cs vapour and a beam of high-energy Ar^+ ions. Secondary ion yields were recorded after having achieved a dynamical equilibrium between the arrival rate of deposited Cs atoms and the removal rate of Cs atoms sputtered from the sample. The secondary ions were accelerated to the entrance aperture of the secondary ion optics by applying a bias of 3000 V to the target. This approach has the effect that the maximum angle of emission of the secondary ions that were accepted by the spectrometer decreased with increasing emission energy (Wittmaack, 1999a). The changes in work function were derived from the shift of the secondary ion energy spectra associated with the change in the surface potential of the sample relative to the surface potential of the energy analyser. The results for Cu^- emission from polycrystalline Cu ($\Phi_{0,Cu} = 4.65$ eV, $A_{Cu} = 1.23$ eV) are similar to those for Si^- in that the ionisation probability was

found to increase monotonically with decreasing work function. However, a clear dependence of P^- on the emission energy is not evident. If any, P^- is frequently higher at 4 eV than at 81 eV, in contrast to the results for Si^- in Figure 1a. In the data analysis presented below the geometrical mean of the Cu^- data will be used (dashed line).

One should also note that in the Cu^- experiment, the equilibrium Cs coverage was ultimately raised beyond practical limits, i.e. to the point where, after having passed through a well-known minimum in work function observed at about half a monolayer of Cs, Φ increased with increasing Cs coverage, to ultimately approach the work function of bulk Cs ($\Phi_{Cs} = 2.14$ eV). In the region of increasing work function, the Cu^- yield decreased with increasing coverage because the numerous Cs atoms residing at the surface severely inhibited the emission of Cu atoms underneath. The respective data in Figure 1b are ignored in the analysis presented below.

Figure 1b also shows a rather unusual work function dependence of the yields of Au^- sputtered from a $Au_{75}Cu_{25}$ alloy ($A_{Au} = 2.31$ eV). The decrease in work function observed at low Cs fluxes (low "coverage") suggests that due to the high-fluence Ar bombardment most of the Cs atoms were incorporated in the sample rather than staying on the surface, as intended. Under these conditions the method used by the authors for determining the work function seems to break down for currently unknown reasons. Hence the Au^- data are not well suited for a comparison with theoretical predictions. But they are very important because they show, even more convincingly than the Cu^- data, that there was no detectable effect of the secondary ion energy or the emission velocity on the ionisation probability.

The data in Figure 2 are again due to Yu (1981) who investigated the velocity and angular dependence of the yields of O^- ions ($A_O = 1.46$ eV) sputtered from oxygen covered vanadium using the same procedure as in the experiments of Figure 1a. According to Lang (1983) the work function of the oxygen covered V-O sample was 5.2 eV prior to Li deposition. Rather noteworthy is the observation that the ionisation probabilities measured at (nominal) emission energies of 8.3 and 14 eV differ only marginally, if at all, see the data in Figure 2a which relate to an emission angle θ of 55° to the surface normal. A significant velocity dependence was only observed at emission energies exceeding 20 eV, as illustrated by the data for 65 eV. At a constant emission energy of 14 eV, the emission angle was found to have a distinct effect on the ionisation probability, as shown in Figure 2b. The dash-dotted straight line through the experimental data for 14 eV/55° illustrates a linear relation of the form $\ln P^- \propto \Phi$. A closer inspection of the data in Figures 1 and 2, however, shows that the slope $d \ln P^- / d\Phi$ is not constant but changes monotonically as a function of Φ. Nevertheless the approximation

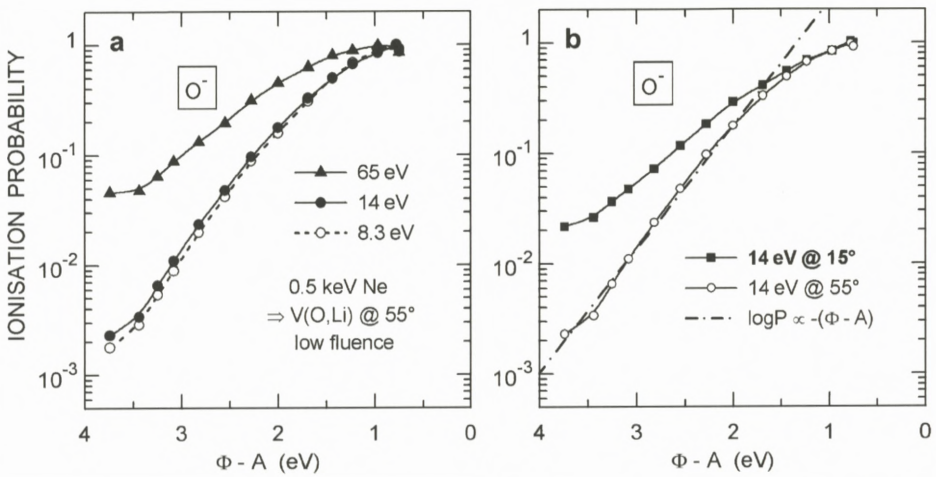

Figure 2. (a) Ionisation probability of O^- sputtered from oxygen on vanadium, for two different emission energies (Yu, 1981). (b) Dependence on emission angle. The dashed line represents a linear fit to log P at low and moderate work function changes.

$d \ln P^-/d\Phi = \text{const}$ was used as the basis for the data evaluation by Yu (1981) and Lang (1983), as discussed in more detail below.

2.2.2. *Positive Secondary Ions*

Experimental data for positive secondary ion emission, suited for a comparison with the predictions of the tunnelling model, are much less abundant than for negative ion emission. Figure 3a shows the work function dependence of the ionisation probability of Cs^+ sputtered from Cs ($I_{Cs} = 3.89$ eV) on polycrystalline Au ($\Phi_{0,Au} = 5.1$ eV), Al ($\Phi_{0,Al} = 4.28$ eV) and Si (Yu and Lang, 1983; Yu, 1984a, 1984b). The data are presented as a function of $I - \Phi$ (note that, in contrast to Figures 1 and 2, Φ decreases from right to left). The small amount of Cs that served as the source of secondary ions was sufficient to introduce a sizable lowering of the work function ($\Delta\Phi = -0.5$ eV for Al and -0.3 eV for Au). Hence the corresponding (first) data points were recorded at $I - \Phi > -1$ eV (compared to $I - \Phi_{0,Au} = -1.21$ eV). Additional changes in Φ were accomplished by depositing Li. The first deposits of Li did not change the initially observed yield of Cs^+, suggesting, in accordance with experimental data of Meyer et al. (2003), that this (maximum) yield corresponded to an ionisation probability $P^+ \approx 1$. This high ionisation probability was retained until Φ had been reduced to the point where $I - \Phi$ for Au and Al had been increased to about 0.6 eV. An additional reduction of Φ resulted in a rapid decrease of the ionisation probability of Cs^+.

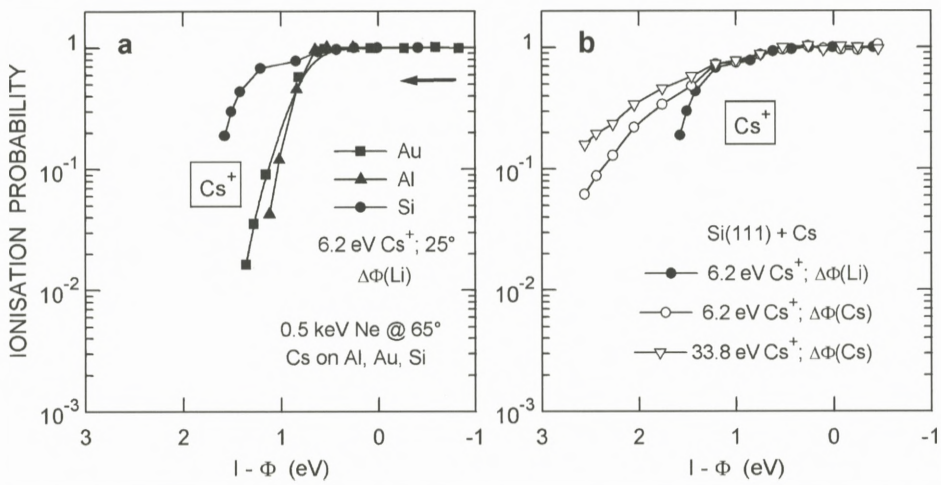

Figure 3. Ionisation probabilities of Cs^+ sputtered from Cs on Au, Al and Si (Yu and Lang, 1983; Yu, 1984a, 1984b). The work function changes were produced by (a) Li and (b) Cs deposition. The arrow in (a) denotes the direction of data acquisition.

The work function dependence of the Cs^+ yields observed in sputtering of Cs from Si exhibited a more complex $(I - \Phi)$-dependence than the data for metal substrates. The initial yield changes observed as $(I - \Phi)$ was raised above 0.6 eV are rather small (see Figure 3b). To produce a more rapid fall-off in Cs^+ yield, $(I - \Phi)$ had to be increased to more than 1 eV. This difference may be related to the fact that Si is a semiconductor. Another problem was encountered when changing Φ by increasing the Cs coverage (rather than by adding Li). As Figure 3b shows, the Cs induced Cs^+ yield changes proceed much more slowly on the $I - \Phi$ scale than the Li induced changes.

3. Concept and Predictions of the Electron-Tunnelling Model

3.1. General Features

The electron-tunnelling model of secondary ion formation involves several important assumptions. (i) The (clean) metal with a work function Φ_0 is at a temperature $T = 0$ K so that all available electron states in the conduction band, considered to be wide, are filled up to the Fermi energy $-\varepsilon_F = \Phi_0$ (see Figure 4). (ii) The sputtering process does not distort the electron distribution, i.e. atoms are emitted from an unperturbed, smooth surface. (iii) The charge state of the departing atom is governed by resonant electron transfer between the atomic level of the atom and

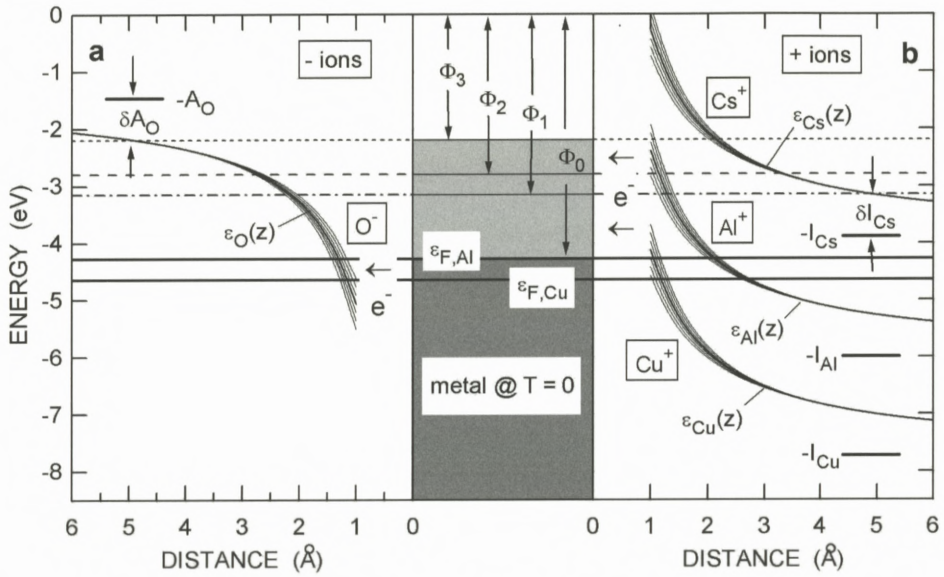

Figure 4. Schematic illustration of the electronic processes occurring as atoms forming (a) negative or (b) positive ions depart from a metal surface. The light-grey areas in the centre denote changes in work function that may be accomplished by the deposition of alkali atoms on the metal surface.

the metal. Electrons can resonantly tunnel in both directions, i.e. from the metal to the atom, thus producing negative secondary ions or neutralising positive ions, or from the atom to the metal, thereby neutralising negative ions or producing positive ions. (iv) The atoms or ions depart from the surface with a constant escape velocity v_n normal to the surface so that time can be easily converted to distance.

The electronic interaction between the atom and the metal has two important consequences: it changes the height $\varepsilon_a(z)$ and the lifetime $\tau(z)$ of the involved atomic level, more so the smaller the distance z between the atom and the surface. The level heights may differ strongly from their respective values at infinity, i.e. from the electron affinity $A = -\varepsilon_A(z \to \infty)$ and the ionisation potential $I = -\varepsilon_I(z \to \infty)$. Very close to the surface accurate calculations of $\varepsilon_a(z)$ and $\tau(z)$ are difficult. Well outside the surface the levels are determined by the image potential $V_{im}(z)$ which shifts $\varepsilon_A(z)$ down and $\varepsilon_I(z)$ up in energy. Examples of $\varepsilon_A(z)$ and $\varepsilon_I(z)$ are sketched, for O^- in Figure 4a and for Cs^+, Al^+ and Cu^+ in Figure 4b. Owing to the finite lifetime $\tau(z)$ of an atomic level near the surface, the level is broadened in energy according to the uncertainty principle, $2\Delta(z)\tau(z) = \hbar$, with $\Delta(z)$ being the half-width of the broadening, indicated by the outermost lines on either side of $\varepsilon_A(z)$ and $\varepsilon_I(z)$. Symmetry with respect to the metal, placed in the

centre of Figure 4, was obtained by allowing the distance in panel (a) to increase from right to left.

The need for the development of the tunnelling model may be appreciated by the results of a simple estimate (Nørskov and Lundqvist, 1979). Let us assume that in course of a sputtering event a secondary ion has been formed somehow. In the immediate vicinity of the surface, the width of the atomic level amounts to about 1 eV or more (see below). This width corresponds to a lifetime $\tau = 2\hbar\Delta \approx 3 \times 10^{16}$ s so that an ion departing from the surface at a normal velocity $v_n = 1$ cm/μs $= 1$ Å/10^{-14} s can travel, on average, only $\tau/v_n \approx 0.03$ Å before being neutralised. Hence the ionisation probability will be very small.

To circumvent this problem, the tunnelling model assumes that, on its way from the surface, the escaping atom can be ionised by resonant tunnelling of an electron from the substrate to the atom, thus creating a negative ion. For this to happen the affinity level must face occupied states in the metal. As the generated ions depart further from the surface, the affinity level increases to cross ε_F at some distance z_c, referred to as the crossing distance. The survival probability at distances $z \geq z_c$, and hence the probability of detecting the ion at large distances ($z \to \infty$), is determined by the lifetime at these distances. In the case of O emission from clean Al or Cu, for example, $\Delta(z)$ is still quite large at z_c (see Figure 4a) so that the ionisation probability is small. If, however, the work function of the sample is gradually reduced, from Φ_0 to Φ_1 or Φ_2, the crossing distance increases. As a result, not only electron tunnelling to the oxygen atom can occur over a wide range of distances from the surface but also the survival probability increases strongly due to the reduced level width (longer lifetime). At some crossing distance the lifetime will be large enough so that essentially all O^- ions formed by resonant tunnelling will be able to survive neutralisation, i.e. tunnelling of an electron from an O^- ion back to empty states above ε_F is then unlikely to occur. In Figure 4a this is assumed to be the case once the work function has been reduced to Φ_3. At that point the affinity level is still well below $-A_O$, by $\delta A_O = \Phi_3 - A_O$.

A different situation is encountered when sputtering Cs from a very thin overlayer of Cs on a metal, as illustrated in Figure 4b. In that case the conditions for secondary ion formation are ideal. Cs features the lowest ionisation potential of all elements, well below the work function of clean Al or Cu. Since $I_{Cs} < \Phi_0$, Cs atoms departing from the surface will always face empty state in the metal so that electrons can tunnel from a Cs atom to the metal at all distances. Hence essentially all sputtered Cs atoms should be able to escape as Cs^+ ions (ionisation probability $P^+ = 1$). The ideal situation changes if the Cs (or Li) coverage is raised to the point where the work function is reduced to Φ_1 or even less. In this range of work

functions, Cs^+ ions formed at small distances will face occupied states in the metal as soon as their separation from the surface exceeds z_c. Therefore, the ionisation probability is expected to decrease rapidly as the work function is reduced below a critical level.

In terms of very low ionisation probability, Cu^+ emission from clean Cu is similar to O^- emission from Cu. With an ionisation potential $I_{Cu} = 7.73$ eV, the condition $-\varepsilon_{I,Cu} < \Phi_{0,Cu}$ applies only at rather small crossing distances z_c, around 1 Å or so, where the survival probability of Cu^+ ions is very small. At distances $z > z_c$, a Cu atom departing from a clean Cu substrate will always face occupied states in the metal from which it was emitted. Hence there is no possibility to form an ion by electron tunnelling from the atom into the metal. The probability for survival would become even smaller if the work function is reduced by depositing alkali atoms.

The third example in Figure 4b, i.e. Al^+ emission from polycrystalline Al ($I_{Al} = 5.99$ eV) constitutes an intermediate case in that $\varepsilon_{I,Al}$ crosses ε_F at a moderate distance $z_c \approx 2$ Å from the surface. Therefore, the survival probability of Al^+ ions generated at $z \leq z_c$ by electron tunnelling from the atom to the substrate is expected to be significantly larger than in the case of Cu^+ emission from Cu.

At this point it is important to note that the well-known enhancement in the ionisation probability of positive (and negative) secondary ions due to surface oxidation of metals and semiconductors (Wittmaack, 1977, 1998) cannot be explained by the tunnelling model. In fact, the pronounced yield enhancement has been observed independent of whether oxidation caused the work function to increase or decrease (Blaise and Slodzian, 1973). Bond breaking was suggested to explain the observed phenomena. In what follows, the effect of oxide formation on the ionisation probability will not be covered.

3.2. Basic Formalism for Negative Ion Formation

In quantitative terms, the ionisation probability P^- calculated in tunnelling theory equals the probability that an atom with the affinity level $|a\rangle$ filled at times $t < t_c$, i.e. before the ion reaches the crossing distance $z_c = z(t_c)$, will survive neutralisation at $t > t_c$, i.e. at $z > z_c$. The probability $\eta(t)\,\mathrm{d}t$ for survival in the time interval $(t, t+\mathrm{d}t)$ is related to the probability $w(t)\,\mathrm{d}t = \mathrm{d}t/\tau(t) = 2\Delta(t)\,\mathrm{d}t/\hbar$ for electron tunnelling back to the substrate as $\eta(t)\,\mathrm{d}t = 1 - w(t)\,\mathrm{d}t = 1 - 2\Delta(t)\,\mathrm{d}t/\hbar$. With the assumption of a constant escape velocity, i.e. with $z = v_n t$, P^- turned out to be (Lang, 1983)

$$P^- \approx P^-(z_c) = \mathrm{e}^{-2\Delta(z_c)/\hbar\gamma v_n}, \tag{1}$$

where γ is a characteristic inverse distance on the order of 1 $Å^{-1}$ and $\hbar$ is Planck's constant. To make use of Equation (1) for predicting ionisation probabilities one needs to know $\Delta(z)$, z_c and γ. In other words, detailed tests of the validity of Equation (1) rest on the availability of theoretical estimates for the input parameters. Here some previously described approaches will be summarised first. Then it is shown that a sizable amount of information concerning the input parameters can be derived directly from the measured work function dependence of the ionisation probability. However, it will be necessary to have detailed *a priori* knowledge concerning the evolution of the affinity level as a function of the atom-surface separation.

3.3. Linear Approximation to $\ln P^-$

In the past, the validity of the tunnelling model has been tested merely on the basis of the straight-line fit to experimental data exemplified in Figure 2b, i.e. by assuming that the complex exponential dependence of P^- on physical parameters of the substrate and the departing atom can be simplified in the form

$$P^-(A, \Phi) \cong \mathrm{e}^{-(\Phi - A - b)/\varepsilon_0}, \tag{2}$$

with ε_0 and b being fitting parameters (note that $P^- = 1$ for $\Phi = A + b$). If Equation (2) applies, the velocity dependence of the ionisation probability, represented by the parameter $\varepsilon_0 \propto v_n$, can be derived from the derivative of $\ln P^-$,

$$\varepsilon_0^{-1} = -\frac{\mathrm{d} \ln P}{\mathrm{d}\Phi} . \tag{3}$$

Lang (1983) used Equation (3) as the starting point for an evaluation of the O^- secondary ion yields from oxygen covered vanadium, as reported by Yu (1981) (see Figure 2). In order to arrive at a theoretical justification for the approximate validity of Equation (2), it was necessary to find a reasonably accurate relation between the work function and the crossing distance. For this purpose an assumption had to be made concerning the z-dependence of the shift, $\delta A(z)$, of the affinity level. The relation between $\varepsilon_A(z)$ and $\delta A(z)$ reads (see Figure 4a)

$$\varepsilon_A(z) = -A - \delta A(z). \tag{4}$$

Lang (1983) used the approximation

$$\delta A(z) = (\Phi - A + E_0)\, \mathrm{e}^{-\alpha z}, \tag{5}$$

where α denotes a characteristic inverse length. E_0 is the affinity level with respect to the Fermi level for the O atom at its equilibrium distance, set to be $z = 0$,

$$\varepsilon_A(0) = \varepsilon_F - E_0 = -(\Phi + E_0). \tag{6}$$

By definition of the crossing distance,

$$\varepsilon_A(z_c) \equiv \varepsilon_F = -\Phi. \tag{7}$$

Hence, with Equation (4),

$$\delta A(z_c) = \Phi - A \tag{8}$$

and, with Equations (4) and (5),

$$z_c = \frac{1}{\alpha} \ln\left(\frac{\Phi - A + E_0}{\Phi - A}\right). \tag{9}$$

Furthermore, Lang (1983) made the common assumption (Nørskov and Lundqvist, 1979) that not only the shift but also the level width $\Delta(z)$ depends exponentially on distance,

$$\Delta(z) = \Delta_0 \, e^{-\gamma z}, \tag{10}$$

where $\Delta_0 = \Delta(z = 0)$. Inserting Equation (10) in Equation (1) yields

$$P^- = \exp\left(-\frac{2\Delta_0}{\hbar\gamma v_n} e^{-\gamma z_c}\right) \tag{11}$$

and, with Equation (9),

$$P^- = \exp\left(-\frac{2\Delta_0}{\hbar\gamma v_n}\left[\frac{\Phi - A}{\Phi - A + E_0}\right]^s\right), \tag{12}$$

with $s = \gamma/\alpha$. Equation (11) exhibits the desired linear dependence of $\ln P^-$ on Φ, provided $s = 1$, i.e. $\alpha = \gamma$, and $E_0 \gg \Phi - A$. The characteristic energy ε_0 derived from Equation (12) according to Equation (3) is

$$\varepsilon_0 = \frac{\alpha\hbar v_n}{2\Delta_0} \frac{(\Phi - A - E_0)^{s+1}}{E_0(\Phi - A)^{s-1}}. \tag{13}$$

Using the same input parameters as Lang (1983), i.e. $\Delta_0 = 1.5$ eV, $\gamma = 1.13$ Å^{-1}, $\alpha = 0.76$ Å^{-1}, and $E_0 = 6$ eV, the ε_0-values derived from Equation (13) are compared in Figure 5a with results obtained by applying Equation (3) to the full range of experimental data. It is evident that the calculated ε_0-values are not constant (16% difference per eV for $\Phi - A$ between 1.5 and 3.5 eV). With few exceptions they differ strongly from the data derived as the derivative of $\ln P^-$. The mean ε_0-values according to Yu (1981), represented by dashed and straight horizontal lines, are in accordance with the results obtained in this study, but only

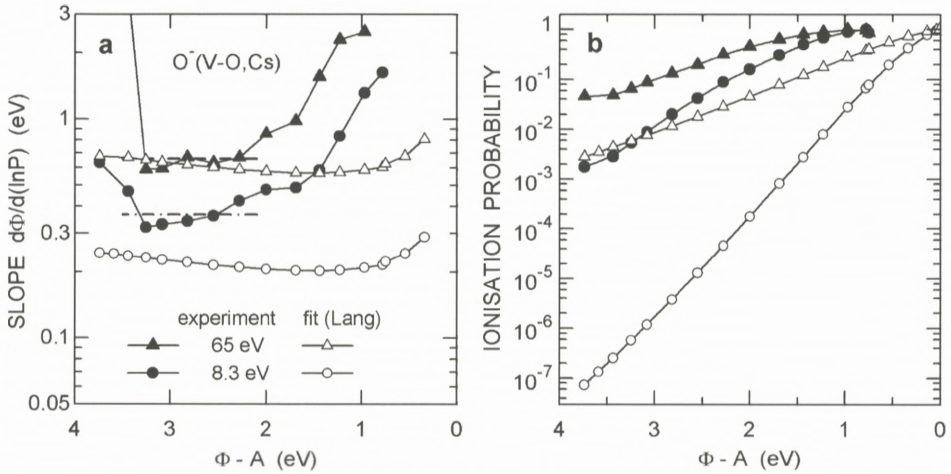

Figure 5. (a) Inverse slope $-1/(\mathrm{d}\ln P/\mathrm{d}\Phi)$ derived from the experimental data and the fit function according to Lang (1983). (b) Ionisation probabilities according to the fit compared with the experimental data. Fit: open symbols; experiment: solid symbols.

within a narrow range of 1 eV or less in terms of work function changes. However, restricting the evaluation to a very narrow range of available data, as done before (Yu, 1981; Lang, 1983) one can hardly arrive at a critical test of the predictions of the tunnelling model.

The poor agreement between the predicted and the experimentally derived ε_0-data can be traced back to the unjustified idea that Equation (2) constitutes a good description of experimental data. As Figure 2b shows, linear sections in graphs of $\log P^-$ (or $\ln P^-$) *versus* Φ can be defined only in narrow ranges of work function changes. Hence ε_0 is neither a constant nor a suitable parameter for describing the work function dependence of the ionisation probability. But this is not the only problem associated with the approach suggested by Lang (1983). Starting with the idea that the derivative of $\ln P^-$ can serve as the leading parameter in the evaluation of experimental data, it should have been clear from the very beginning that one is loosing a potentially important constant contribution to $\ln P^-$ (represented in Equation (2) by $(A + b)/\varepsilon_0$). In the present case this loss of a constant has the dramatic consequence that the ionisation probability calculated according to Equation (12) turns out to be completely wrong, deviating strongly from the experimental data, sometimes by more than four orders of magnitude, as shown in Figure 5b. The reason for the large discrepancy is that the procedure set out to reproduce (only) the slopes $\mathrm{d}\ln P/\mathrm{d}\Phi$. While this has been accomplished in a very approximate manner, but only for $\Phi - A$ between 2 and 3 eV, the absolute values of

P^- do not resemble the experimental data at all. The inevitable conclusion is that the linear approximation to $\ln P^-$ constitutes a completely misleading approach, a scientific meander.

3.4. Rigorous Evaluation

A sufficiently accurate theoretical basis for determining the atom-substrate electronic parameters contained in Equation (1) does not seem to be available presently. Hence it appeared desirable to explore the idea of deriving these parameters from available experimental results. Using Equation (1) we can immediately determine the level width Δ, at least in normalised form and as a function of Φ or $\Phi - A$. Defining an reference level $P_r^- = P^-(\Phi_r)$ which can be chosen arbitrarily, Equation (1) can be rewritten in the form

$$\Delta_r(\Phi) \equiv \frac{\Delta(\Phi)}{\Delta(\Phi_r)} = \frac{\ln P^-(\Phi)}{\ln P^-(\Phi_r)} \,. \tag{14}$$

It is worth noting that, by way of normalisation, the parameters γ and v_n contained in Equation (1) do not appear explicitly in Equation (14). They are contained in hidden form in the experimentally determined parameter $P^-(\Phi_r)$. To proceed we face the same problem as Lang (1983), i.e. we need to correlate the crossing distance with the work function. As an alternative to Equation (5) one can follow Nørskov and Lundqvist (1979) to explore the consequences of the assumption that the shift of the affinity level is determined by the image potential $V_{\mathrm{im}}(z)$,

$$\delta A(z) \equiv V_{\mathrm{im}}(z) = \frac{\mathrm{e}^2}{4(z - z_{\mathrm{im}})} = \frac{3.6}{z - z_{\mathrm{im}}} \,, \tag{15}$$

where z_{im} [Å] denotes the position of the image plane. Using Equations (4), (7) and (15), the conversion of the work function to the crossing distance reads

$$z_{\mathrm{c}} = z_{\mathrm{im}} + \frac{3.6}{\Phi - A} \,, \tag{16}$$

with Φ and A in eV. On this basis the z-dependence of the normalised level width can be determined as

$$\Delta_r(z_{\mathrm{c}}) = \frac{\ln P^-(\Phi)}{\ln P^-(\Phi_r)} \,. \tag{17}$$

Results derived from the data in Figure 2 are presented in Figure 6a. The work function of the alkali-free V-O sample served as the reference point. For simplicity the image plane was assumed to coincide with the origin of the z-scale,

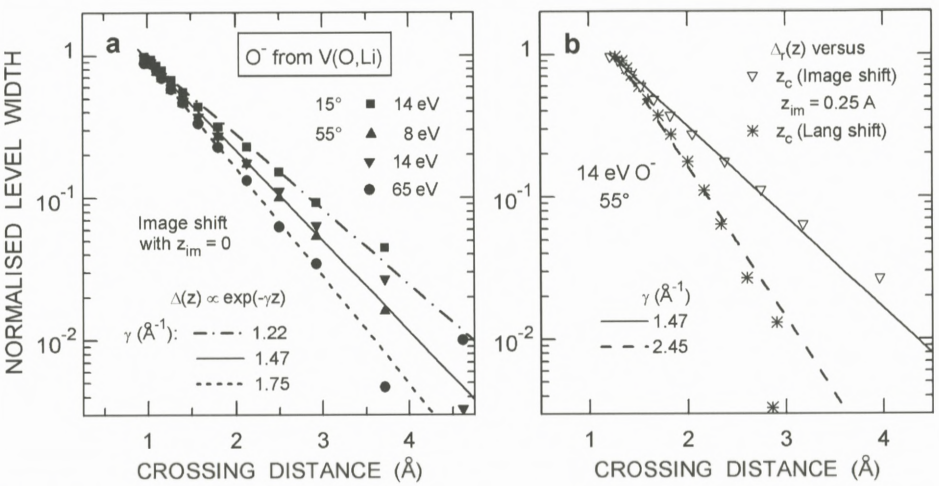

Figure 6. Normalised width of the affinity level of O^- sputtered from oxygen covered vanadium. Data derived according to Equation (17). (a) Crossing distance calculated from the image shift. (b) Comparison of results obtained with the image shift and the shift according to Lang (1983).

$z_{\mathrm{im}} = 0$. The first remarkable result of the evaluation is that, within the limits of accuracy of the data, the affinity level exhibits the commonly assumed exponential dependence on distance, see Equation (10). The increasing scatter of the data for $z_{\mathrm{c}} > 3$ Å is due to the fact that the corresponding P^- values exceed 0.9, in which case Δ_r becomes very sensitive to slight variations of P^-, attributable to statistical errors in the experimental data and uncertainties in the choice of the ion yield corresponding to $P^- = 1$ (note that for $P^- = 1 - \beta$, with $\beta < 0.1$ one can use the approximation $\ln P^- \approx -\beta$). The derived exponential fall-off remains unchanged for $z_{\mathrm{im}} \neq 0$ because $\Delta_r(z)$ is merely shifted by z_{im} in the respective direction, see Equation (16). The evaluated data (solid symbols) can be reproduced quite well inserting γ-values between 1.22 and 1.75 $\mathrm{Å}^{-1}$ in Equation (10), as shown by the straight lines in Figure 6a. Considering the fact that the characteristic inverse distances γ were derived from experimental data for nominal emission energies between 8 and 65 eV and emission angles between 15 and 55°, the different slopes in Figure 6b would imply that γ depends on the normal emission velocity v_n. However, γ is not explicitly contained in the relevant Equation (17). Furthermore, a v_n-dependence of γ would be at variance with the idea that the width of the atomic level depends only on the distance of the atom from the surface. Hence we are led to the preliminary conclusion that a sputtering event involves processes that are not incorporated in the tunnelling model.

One may wonder to what extent the derived data depend on the assumption concerning the z-dependence of the level shift. To address this issue, Figure 6b shows a comparison of normalised level widths derived from the same raw data but by making use of two different analytical descriptions of level shifts, the "image shift" as in Figure 6a (but with $z_{im} \neq 0$) and the "Lang shift" according to Equation (5). In the latter case (the first) 11 data points, out of a total of 14, for P^- between 2×10^{-3} to 0.5 (corresponding to about 90% of the covered $\ln P^-$ scale), are also roughly in accordance with an exponential z-dependence, but with γ as large as 2.45 Å^{-1}. This number is a factor of more than two larger than the estimate of Lang (1983), another piece of evidence supporting the conclusion that the linear approximation to $\ln P^-$ is strongly misleading. As a results of the rapid fall-off of Δ_r, the 11 data points are squeezed together in a rather narrow range of crossing distances between 1.3 and 2.3 Å. With the image-shift concept γ turned out to be much smaller (1.47 Å^{-1}) and the corresponding set of data fall in the range $1.2 < z_c < 3.2$ Å. Note that, to make the two sets of data roughly coincide at small crossing distances, z_{im} had to be set to 0.25 Å. In any case, it is worth noting that all the "action" related to low ionisation probabilities ($P^- < 0.5$) is taking place at distances less than a typical nearest-neighbour distance in a solid.

At this point a direct comparison of the z-dependence of the level shift derived with the two concepts is desirable. Figure 7a shows the Lang shift for two different values of the fitting parameter E_0 and the image shift for two different values of z_{im}. At small crossing distances, i.e. between 1.2 and 2 Å, rather good agreement between the calculated shifts can be obtained for the combination $E_0 = 6$ eV and $z_{im} = 0.25$ Å. Since it has been acknowledged that "far" from the surface the image shift will apply (Lang and Nørskov, 1983), a correction to the image shift may only be necessary below about 2 Å (the term "far" was not defined in any detail). An analytical relation reproducing the Lang shift closely could be achieved by modifying the image shift in the form

$$z_c = \frac{3.4}{\Phi - A} + k[\Phi - A]^m. \tag{18}$$

The thick solid line labelled "fit" in Figure 7a is an example reflecting the case $k = 0.14$ Å and $m = 0.7$. Below 2 Å the resulting shift can be well approximated by the (standard) image shift in combination with $z_{im} = 0.25$ Å.

Extending this exercise on the proper form of the level shift, the next step is to explore the magnitude of the scaling parameter Δ_0 which can be determined from Equation (11) if γ, v_n and z_c are known. Ignoring for the moment the problems associated with the predicted normal-velocity dependence of the ionisation probability, Δ_0 can be written as

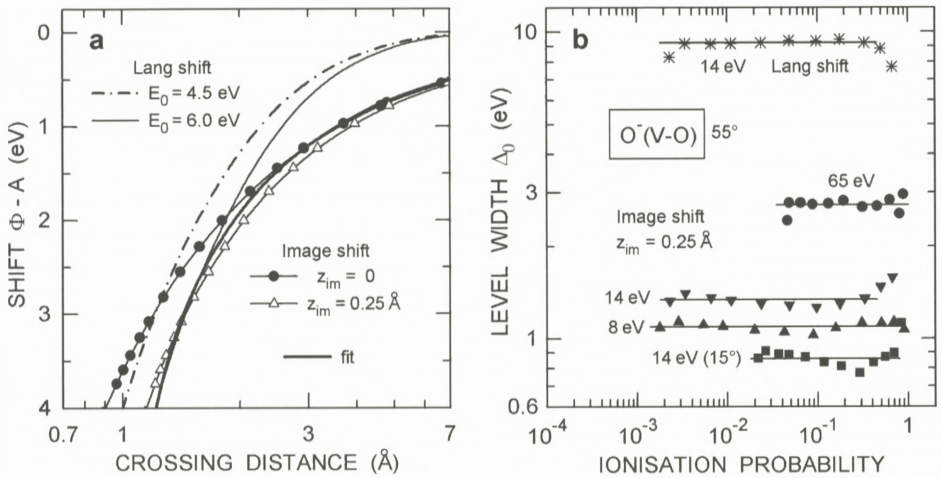

Figure 7. (a) Comparison of the level shifts calculated according to two different approximations. (b) Level width at $z = 0$, derived from experimental data for the ionisation probability of O^- sputtered at different energies.

$$\Delta_0 = -0.5 \ln P^- \hbar\gamma \left(\frac{2E}{M}\right)^{1/2} \cos\theta \, e^{\gamma z_c}, \tag{19}$$

where E and θ are the energy and angle (to the surface normal) of ion emission and M is the ion mass. The results of a data evaluation according to Equation (19) are presented in Figure 7b. Several aspects are noteworthy. First, the results derived for Δ_0 are reasonably constant over a wide range of ionisation probabilities. Deviations are sometimes observed for $P^- > 0.5$. This is either due to the problems of data statistics and calibration, as already discussed with reference to Figure 6, or due to the fact that the z-dependence of Δ_r was not exactly exponential for z_c beyond some critical distance. Second, the derived Δ_0-values exhibit a pronounced dependence on emission energy and angle. Adequate Δ_0-values, which were previously assessed on the basis of surface physical arguments, range between 1 eV (Nørskov and Lundqvist, 1979) and 1.5 eV (Lang, 1983). Hence the results for 8 and 14 eV O^- emission at 55°, obtained using the image shift in combination with $z_{im} = 0.25$ Å ($\langle\Delta_0\rangle = 1.09$ and 1.34 eV, respectively), may be considered quite reasonable. A mean Δ_0-value of 2.73 eV, as derived from the data for emission at 65 eV, appears unreasonably high. This finding may suggest that, in contrast to the interpretation put forward by Yu (1981) and Lang (1983), the most significant deviations from the predictions of the tunnelling model occur at relatively high rather than at low energies. Third, the dependence on the angle

of emission, already observed in deriving Δ_r and γ (Figure 6), is also seen in the data for Δ_0. Emission close to the surface normal (15°) yields smaller numbers for Δ_0 than emission at an oblique angle (55°). Fourth, the Δ_0-value of 9.2 eV, obtained on the basis of the Lang shift for an emission energy of 14 eV, exceeds reasonable numbers by a factor of five. The corresponding number for 65 eV, $\langle\Delta_0\rangle = 27.2$ eV, is completely unrealistic. These results imply that the evaluation of γ and Δ_0-values provides an particularly sensitive test of the validity of the assumed z-dependence of the level shift. The conclusion must be that the Lang shift is not reliable.

Even though proper agreement between the Lang shift and the image shift could be obtained by setting $z_{\mathrm{im}} = 0.25$ Å, the effect of this parameter on the derived values of Δ_0 can serve to assess the possible error in the data of Figure 7b. Using Equation (19) the relation between the two parameters reads

$$\Delta_0(z_{\mathrm{im}}) = \Delta_0(z_{\mathrm{im}} = 0)\, \mathrm{e}^{\gamma z_{\mathrm{im}}}. \tag{20}$$

With $\gamma \approx 1.5$ Å^{-1}, an uncertainty in z_{im} by 0.1 Å corresponds to an uncertainty in Δ_0 by 16%.

3.5. Velocity Dependence

According to the results of Figures 6 and 7 the velocity dependence of the ionisation probability predicted by the tunnelling model may be significantly affected by processes not covered by the underlying assumptions of the model. To discuss the deviations in some detail, we consider the experimental data for 14 eV O^- emitted at 55° from oxygen covered vanadium. The data, shown in Figure 8a as solid symbols, can be reproduced to within typically ±10% or better using Equation (11) in combination with the quoted parameters. This good agreement between experimental data and fit functions was observed for other sets of data as well. Assuming the model to properly predict the velocity dependence of P^-, results expected at some emission energy E_2 can be easily predicted from $P^-(E_1)$ measured at an emission energy E_1,

$$P^-(E_2) = \left(P^-(E_1)\right)^{\sqrt{E_1/E_2}}. \tag{21}$$

Results thus derived from the data for 14 eV are shown in Figure 8a for energies ranging between 5 and 65 eV. The predicted effect of the emission energy on P^- is seen to be quite large, notably at low energies and large work functions.

The procedure according to Equation (21) may also be used to compare the predicted with the measured emission-energy effect on P^-. In Figure 8b the experimental results for 14 and 65 eV at 55° serve as a reference, data measured at

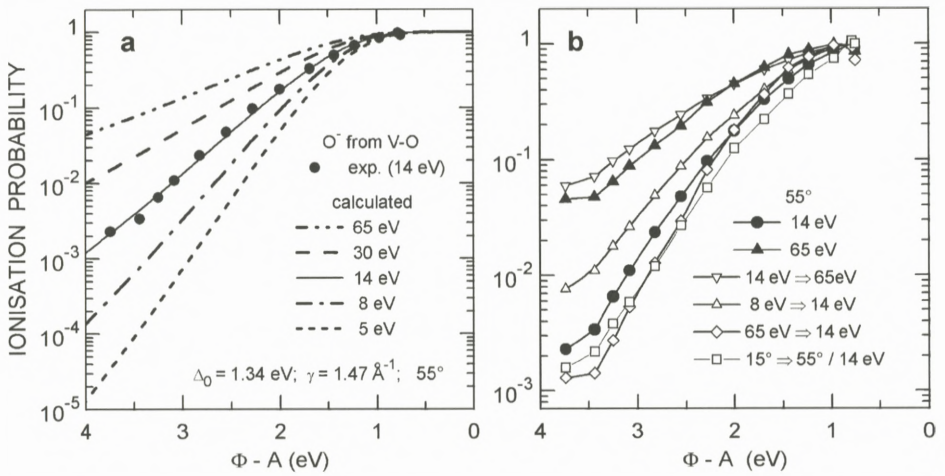

Figure 8. (a) Illustration of the velocity dependence of the ionisation probability P^- predicted by the tunnelling model. The input parameters were derived from a fit to the experimental data for oxygen emission at a nominal energy of 14 eV. (b) Comparison of the measured velocity dependence of P^- (solid symbols) with data obtained using the tunnelling model to convert experimental data from the original emission energy to the reference energies of 14 and 65 eV (open symbols).

other energies were taken as input parameters. The differences between measured and predicted data are significant, sometimes large. The differences are even larger for conversion in more extreme cases like 65 eV → 8 eV (not shown). In analogy to Equation (21) one may also convert data for a given energy and angle to another angle. One example for 15° → 55° is included in Figure 8b. The differences between measured and predicted data, observed at the same nominal energy of 14 eV, imply that the idea of applying corrections to the energy (or velocity) of atom emission cannot resolve existing differences between theory and experiment.

3.6. Some Additional Features of the Tunnelling Model

Even though the tunnelling model may suffer from the fact that some concomitant disturbing effects associated with the sputter emission process are not included, some additional features of the model are worth inspection. Rather than using ratios of $\ln P^-$ to determine the z-dependence of the normalised level width (thus deriving γ), it is worth taking a look at the effect of γ on the shape of $P^-(\Phi - A)$. For this purpose we rewrite Equation (11) as

$$\frac{\ln P^-}{\ln P_r^-} = \mathrm{e}^{\gamma(z_{c,r} - z_c)}. \tag{22}$$

In analogy to Equation (14), Equation (22) does not contain the emission velocity. Furthermore, z_{im} does not appear explicitly in Equation (14). Both parameters are hidden in (the magnitude of) the reference level P_r^-. Using Equation (16) to replace the distance in Equation (22) by the reduced work function, the ionisation probability may be expressed as a function of γ and $\Phi - A$ only

$$P^-(\Phi - A) = \exp\left\{\ln P_r^- \exp\left[3.6\gamma\left(\frac{1}{\Phi_r - A} - \frac{1}{\Phi - A}\right)\right]\right\}. \tag{23}$$

To illustrate the sensitivity of P^- to changes of γ we consider the mean data for Cu^- emission from Cu, which are suited well because they extend over five orders of magnitude in ionisation probability. Somewhat arbitrarily $P_r^-(\Phi_r - A = 2.35\ \mathrm{eV}) = 1.7 \times 10^{-3}$ was selected as the reference level. The results of the fitting procedure are presented in Figure 8a for γ-values ranging between 0.8 and 2.1 $\mathrm{Å}^{-1}$. It is evident that the work function dependence of the ionisation probability is very sensitive to the choice of γ. Hence the optimum value of γ reproducing the experimental data best can be determined rather precisely. In the case of the Cu^- data, $\gamma = 1.2 \pm 0.03\ \mathrm{Å}^{-1}$. The sensitivity of P^- to variations of γ may be considered a proof that resonant tunnelling is the essential process dominating ion formation. If the image potential, with $z_{\mathrm{im}} \neq 0$, is considered to provide a reasonably accurate approximation to the affinity shift, Equation (23) can serve as a very simple means of determining γ directly from experimental data.

As the results of Figure 9a illustrate, γ has a pronounced effect on the way P^- approaches unity. This aspect may be discussed more conveniently by presenting the results on a probability scale, as shown in Figure 9b. The reduced work function $\delta A = \Phi - A$, at which P^- exceeds a certain limit, say 95 or 99%, is seen to depend strongly on γ. More specifically, $\delta A(99\%)$ ranges between 0.38 and 0.78 eV, a difference by as much as 0.4 eV. We note that δA is quite large, amounting to typically one third of the electron affinity of oxygen. The rather large values of δA are due to the fact that the survival probability of a generated ion approaches 100% already at ion-surface distances of about 5 Å (see Figure 4a).

To discuss ionisation probabilities >10% somewhat more, Figure 10a shows O^- data as a function of the crossing distance, with P^- on a linear and z_c on a logarithmic scale. In this kind of presentation the ionisation probabilities have shapes that can be approximated by error functions. Hence the derivatives $P' = \mathrm{d}P/\mathrm{d}z_c$ closely resemble lognormal distributions (see Figure 10b). It was found that, with P according to Equation (11), P' is proportional to the weight function $\Delta_c P$ introduced by Nørskov and Lundqvist (1979),

$$\Delta_c P \equiv \Delta(z_c)P = \frac{\hbar v_n}{2} P'. \tag{24}$$

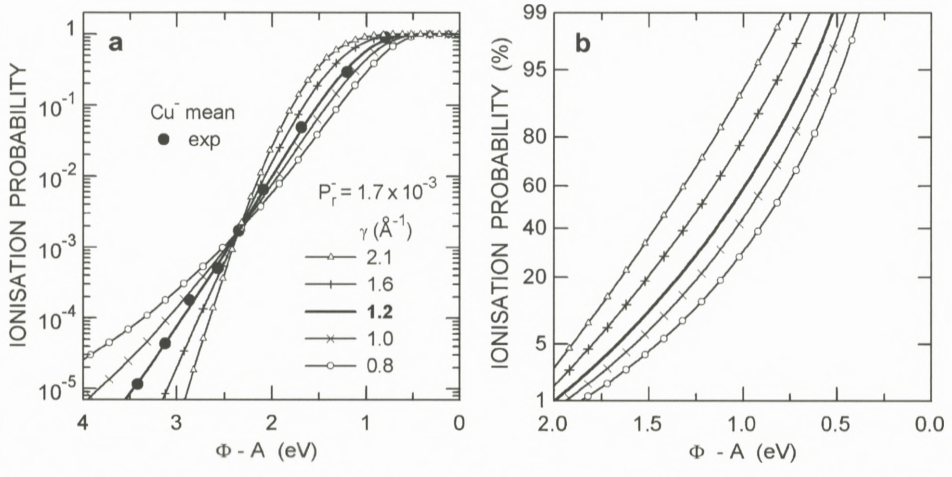

Figure 9. Illustration of the effect of the parameter γ on the work function dependence of the ionisation probability P^-, as predicted by the tunnelling model. The solid symbols represent the mean data for emission of Cu^- from polycrystalline Cu. (a) P^- on a logarithmic scale, (b) on a probability scale. Note the expanded work function scale in (b).

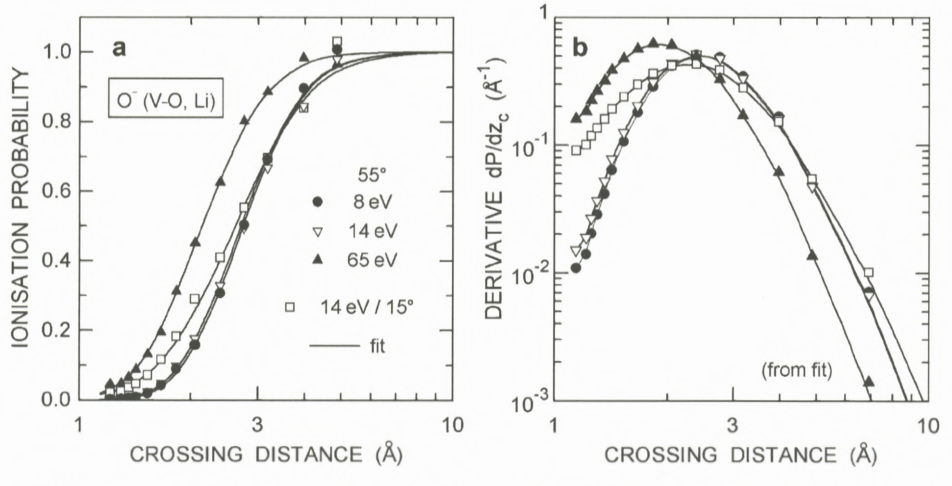

Figure 10. (a) Ionisation probability of O^- *versus* the crossing distance ($Z_{im} = 0.25$ Å). Solid symbols: experimental data for different emission energies, solid lines: fit according to the tunnelling model. (b) Derivatives of the fit functions in (a).

The maximum of the weight function was considered to reflect the "balance" between the excitation probability represented by $\Delta(z_c)$ and the probability $P(z_c)$ that the excitation will survive. The derivatives P' feature a maximum $\hat{P}'$ at

$$z_c(\hat{P}') = -\gamma^{-1} \ln \frac{\hbar \gamma v_n}{2\Delta_0}, \tag{25}$$

with a peak height $\hat{P}' = \gamma/e$. At $z_c(\hat{P}')$ the ionisation probabilities are the same $P(\hat{P}') = 1/e = 0.368$. The deviation from 0.5 reflects the deviation from an exact error function.

3.7. Merging Positive and Negative Secondary Ion Yield Data

One of the particularly interesting aspects of the tunnelling model is that the same formalism can be used to calculate ionisation probabilities of negative as well as of positive secondary ions. Unfortunately, the main body of available experimental data relates only to negative ions. Data for both charge states are rare. An exception are the data of Figures 1a and 3b for the emission of Si^- and Cs^+ from alkali covered Si (Yu, 1982, 1984a, 1984b; Yu and Lang, 1983). The problem with these data is that Si is a semiconductor. The presence of a band gap in this kind of materials introduces uncertainties problems because the definition of an "effective" work function is a subject to ongoing debate (Wittmaack, 1999b). The approach taken here is a pragmatic one: It is assumed that the "effective" work function Φ^* is related Φ, the value determined experimentally, as $\Phi^* = \Phi + \delta\Phi$, with $\delta\Phi$ being a fitting parameter. To illustrate the approach, the normalised level widths derived from the Si^- data in Figure 1a, in analogy to the data in Figure 6, are presented in Figure 11a. With the "standard" assumption, i.e. $\delta\Phi = 0$, the characteristic fall-off parameter γ, derived from the first 11 data points in the range $P^- < 0.25$ is unusually low (0.75 $Å^{-1}$; triangles in Figure 11a). The crossing distance for a moderate ionisation probability of about 0.6 was found to be as large as 7.4 Å. Furthermore, for $P^- \approx 0.9$, the completely unrealistic result $z_c = 36$ Å was obtained (data point not shown in Figure 11a). A much more realistic number, $\gamma = 1.3$ $Å^{-1}$, was derived with $\delta\Phi = 0.6$ eV (circles in Figure 11b). Clearly, this method of deriving $\delta\Phi$ can only be considered a very approximate one. It mainly serves to show that $\delta\Phi > 0$.

It is worth noting that, in contrast to the results of Figure 6, the γ-values derived from the Si^- data in Figure 11a are the same (but the velocity effect seen in Figure 1a is much too small). One presumably important difference between the Si^- and the O^- experiment is that in the former case the ions originated from the substrate, in the latter case from the adsorbed layer. The effect of the

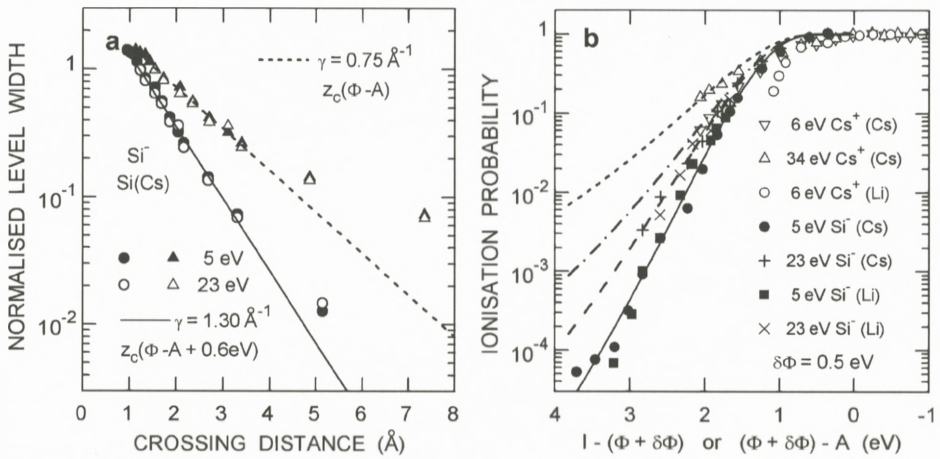

Figure 11. (a) Normalised width of the affinity level of Si^- sputtered from Si. Data derived according to Equation (17). The triangles were obtained assuming the ionisation probability to be controlled by the measured work function. The circles relate to an "effective" work function that is larger by 0.6 eV than the measured value. (b) Comparison of the ionisation probabilities of positive and negative ions sputtered from alkali covered Si. The "effective" work function was assumed to be larger by 0.5 eV than the measured number.

starting position of the analysed ion on the tunnelling probabilty remains to be investigated.

An alternative and probably even more convincing way of assessing the effective work function is to merge ionisation probabilities for positive and negative secondary ions in one graph. Figure 11b shows a compilation of ionisation probabilities for Cs^+ *versus* $I - \Phi^*$ and for Si^- *versus* $\Phi^* - A$. Here the criterion for selecting the optimum value of $\delta\Phi$ was the fall-off in ionisation probability from the level $P^- \approx 1$ which, according to Figure 9, determines γ. For $\delta\Phi = 0.5$ eV the fall-off points for positive and negative secondary ion emission coincided reasonably well (with $\gamma(Si^-) = 1.3$ Å^{-1} and $\gamma(Cs^+) = 1.2$ Å^{-1}). Most of the uncertainty is due the fact that, with available knowledge, no distinction can be made as to whether the Cs^+ data are more reliable for Li or Cs induced work function changes (see Figure 3b). Given these uncertainties, the results of Figure 11b suggest that it is possible to incorporate the ionisation probabilities of positive and negative ions emitted from the same substrate into one graph, thus supporting one of the basic predictions of the tunnelling model. Studies of this kind using metallic substrates would be highly desirable.

3.8. Effect of Surface Perturbations and the Infinite-Velocity Issue

The last issue to be addressed is the origin of the deviations from the tunnelling model which have been quantified, for example, by the results of Figures 6 and 8b. The differences may be due to experimental problems, due to simplifying assumptions of the model or both. On the experimental side there are several uncertainties. In the experiments of Yu (1981, 1982, 1984a), the large acceptance cone, with a geometrical semi-apex angle as large as 19°, prevents a proper definition of emission velocities. Notably at oblique angles of emission (e.g., 55°), the quoted angle may deviate significantly from an appropriate mean value. Additional problems may be brought about by the pronounced angular dependence of the transmission of a quadrupole mass filter (Wittmaack, 1982). With reference to the definition of emission energies, one should note that the surface potential was changing with decreasing work function, and so did the true ion energy (Wittmaack, 1983). Hence it is probably not justified to assign the same energy to all data recorded at different work functions. As to the work of Bernheim and Le Bourse (1987), the issues there are the high primary ion energy, the high bombardment fluence (generating a large surface roughness on polycrystalline metal targets) and the energy dependent maximum angle of ion detection. In future experimental studies attempts should be made to minimise the problems from which the pioneering studies of theses two groups suffered.

On the side of the theory the assumption of a constant emission velocity may cause some problems, as already discussed by Lang (1983). But this aspect does not appear to be capable of explaining the pronounced difference in γ, discussed with reference to Figure 6. Other aspects of the sputtering process, not covered by the assumptions of the tunnelling model, must be of relevance. The notation "surface perturbation" has been used above to describe the origin of the deviations rather vaguely. Nourtier et al. (1988) have considered the sputtering process in more detail in order to explain previously reported ionisation probabilities of Cu^+, which were significantly higher than expected on the basis of the tunnelling model. They questioned the picture of an atom gently desorbing from a flat surface and pointed out that distorted atomic configurations will strongly alter the local electronic structure as well as the relative importance of the various charge exchange channels. Ion scattering in the last collision has also been considered an important deviation from the simple model (Lang, 1983; Lang and Nørskov, 1983; Nourtier et al., 1988). Such aspects and processes could well provide a route to explaining the different γ-values derived in this study. It may also be of interest

to investigate whether the presence of surface inhomogeneities has a significant effect on the model parameters.

One of the frequently discussed predictions of the tunnelling model relates to the question of ionisation probabilities in the limit of infinite velocity. According to Equation (11) we should have $P^-(v_n \rightarrow \infty) = 1$. The same should hold true for P^+. In general, however, as a detailed analysis of literature data has shown, this prediction is at variance with experimental results (Wittmaack, 1999a). Very recent velocity dependent measurements of the yields of secondary ions and laser post-ionised neutrals sputtered from In (Mazarov et al., 2006) support the conclusions of the previous evaluation ($\Phi_{0,\mathrm{In}} = 4.12$ eV; $I_{\mathrm{In}} = 5.79$ eV). The reported ionisation probabilities are depicted in Figure 12 as a function of (a) the emission energy and (b) the inverse emission velocity. The results differ from the predictions of the tunnelling model in two ways. First, the ionisation probabilities observed at low emission energies do not decrease monotonically (and rapidly) but tend to approach some stable level in the limit $E \rightarrow 0$. The low-energy data can be approximated by $P^+ \propto E^{0.05}$, i.e. by a function that increase only marginally with increasing energy. Subtracting this contribution from the raw data, a second, strongly energy dependent contribution is obtained, which is represented by open circles. This contribution (straight dashed line in Figure 12b) exhibits an exponential inverse-velocity dependence, in accordance with the predictions of the tunnelling model. However, the ultimate ionisation probability derived by extrapolation to a vanishing inverse velocity is only $(2 \pm 0.2) \times 10^{-2}$, i.e. much lower than unity. Clearly, the tunnelling model fails to reproduce this observation. The comparatively low ionisation probability derived in the limit of infinite velocity could indicate that, beyond some limit in velocity, the "balance" between ion formation and survival may arrive at an upper limit.

The excess ionisation probabilities observed at In^+ energies below 5 eV may again be indicative of those sputtering events in which atoms (and molecules) were emitted from strongly surface perturbed areas. This kind of distortion appears to be responsible for the observation, reported independently by Wittmaack (1979) and Šroubek (1983), that the ionisation probability in low-energy secondary ion emission from clean samples depends rather strongly on the primary ion energy. The tunnelling model does not include such an energy dependence. Šroubek et al. (1980) were the first to explore the consequences of perturbation due to the ion impact. Using a very simple atomic model, they arrived at ionisation probabilities that increased only very slowly with increasing emission energy, similar to the results in Figure 12a at energies below 5 eV. The excitation of the sample was described in terms of a local electronic temperature generated by the ion impact. The model has been extended more recently (Šroubek and Lörinčik, 2000; Duvenbeck

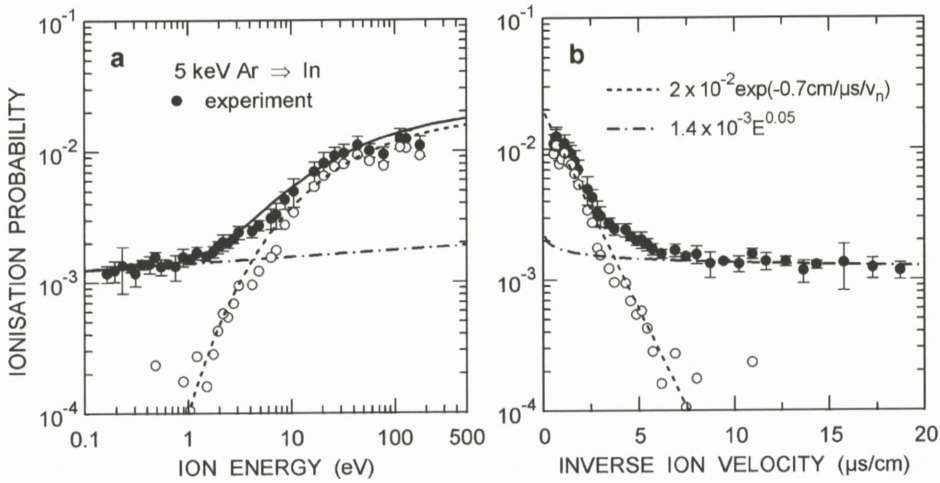

Figure 12. Ionisation probability of In^+ sputtered from clean In, (a) *versus* the energy, (b) *versus* the inverse velocity of the In^+ ions (Mazarov et al., 2006). The dotted lines represent a high-energy fit functions according to the tunnelling model, but with a maximum ionisation probability of only 2×10^{-2}. The dash-dotted line is assumed to represent the contribution of surface perturbations to the total ionisation probability.

et al., 2005; Duvenbeck and Wucher, 2005), but the theory does not seem to have arrived at a mature level yet. It should be noted that, in order to produce effects with a probability on the order of 10^{-3}, only a very small fraction of the sputtering events need to involve strong "perturbation" and "excitation". Molecular dynamics simulations might help to identify the structure of those collision cascades that could act as an additional source of secondary ions.

4. Summary and Conclusions

This study has clarified a number of issues related to the question to what extent the tunnelling model can provide a useful description of secondary ion formation, in qualitative as well as in quantitative form. The strength of the model is that, on principle, it involves a rather simple picture of the electronic processes determining the charge state of an atom that departs from a metallic surface. The results of the experiments performed by Yu (1981, 1984a, 1984b) have provided rather convincing evidence that the basic concept of the model is correct. The evaluation presented here has shown that the ion yields and the derived ionisation probabilities, presented as a function of the alkali induced changes in the sample's work function, are basically in accordance with the predictions of the tunnelling

model, not only for small changes but over the full range of changes. Within experimental uncertainty, the measured ion yields can be reproduced using reasonable input parameters. Inverting the problem, it has been shown for the first time that one can derive relevant input parameters from the experimental data, notably the parameter γ which quantifies the z-dependence of the level width.

There are, however, many unsolved questions relating to the finer details of the tunnelling model. Progress in the theory of electronic interactions between departing atoms and a metallic substrate would be highly desirable, the aim being to calculate the width and the shift of the atomic level from first principles rather than making recourse to reasonable estimates. The calculations should cover the whole range of relevant distances. Of particular importance is the fact that the charge state of a departing atom is determined at distances on the order of or even smaller than a lattice spacing. Hence, intuitively, one would expect the charge states of atoms starting either *on* or *in* the surface to be quite different. Another open questions concerns the absolute value of the ionisation probability. Is it really possible to produce conditions such that all sputtered atoms can escape as ions? This aspect needs to be addressed in much more detail than before.

Undoubtedly, progress in the field will require significant improvements on the experimental side as well. One particular problem with the previous work, both in the low-fluence and the high-fluence studies, is the wide angular distribution accepted by the employed spectrometers. As a result, a well-defined normal velocity cannot be assigned safely to the recorded secondary ions. This uncertainty severely limits the ability to evaluate the predictions of the tunnelling model in terms of the normal-velocity dependence.

The results presented in Figure 12 as well as some other cited results, published more than 20 years ago, imply that perturbations of the surface can give rise to secondary ion yields significantly above the predictions of the tunnelling model. This additional source of secondary ions becomes significant whenever the probability of ion formation due to resonant electron tunnelling is low, typically below 10^{-3}. However, specific limits of validity of the tunnelling model still need to be determined.

References

Bernheim M. and Le Bourse F. (1987): On the velocity dependence for negative ionization of atoms sputtered from cesiated surfaces: An experimental study. Nucl Instrum Meth Phys Res B **27**, 94–103

Blaise G. and Slodzian G. (1973): Effets comparés de l'oxygène sur l'émission ionique et le potentiel de surface des metaux. Surf Sci **40**, 708–714

Brako R. and Newns D.M. (1981): Charge exchange in atom-surface scattering: Thermal versus quantum mechnical non-adiabaticity. Surf Sci **108**, 253–270

Duvenbeck A. and Wucher A. (2005): Low energy electronic excitation in atomic collision cascades: a nonlinear transport model. Phys Rev B **72**, 165408

Duvenbeck A., Šroubek Z. and Wucher A. (2005): Electronic excitation in atomic collision cascades. Nucl Instrum Meth Phys Res B **228**, 325–329

Lang N.D. (1983): Ionization probability of sputtered atoms. Phys Rev B **27**, 2019–2029

Lang N.D. and Nørskov J.K. (1983): The theory of ionization probability in sputtering. Physica Scripta **T6**, 15–18

Mazarov P., Samartsev A.V. and Wucher A. (2006): Determination of energy dependent ionisation probabilities of sputtered particles. Appl Surf Sci **252**, 6452–6455

Meyer S., Staudt C. and Wucher A. (2003): Ionization probability of atoms and molecules sputtered from a cesium covered silver surface. Appl Surf Sci **203–204**, 48–51

Michaelson H.B. (1977): The work function of the elements and its periodicity. J Appl Phys **48**, 4729–4733

Nørskov J.K. and Lundqvist B.I. (1979): Secondary-ion emission probability in sputtering. Phys Rev B **19**, 5661–5665

Nourtier A., Jardin, J.-P. and Quazza, J. (1988): Ionization probability of sputtered atoms: Band-structure and collisional effects. Phys Rev B **37**, 10628–10636

Prigge, S. and Bauer, E. (1980): Static SIMS studies of metal-covered W(110) surfaces. Adv Mass Spectrom **8**, 543–552

Šroubek Z. (1983): Substrate surface excitations and ionisation of particles sputtered from GaAs. Appl Phys Lett **42**, 514–516

Šroubek Z. and Lörinčik J. (2000): Electronic excitations in solids during impact of atomic particles. Vacuum **56**, 263–267

Šroubek Z., Ždánsky K. and Zavadil J. (1980): Ionization of atomic particles sputtered from solids. Phys Rev Lett **45**, 580–583

Van der Heide P.A.W. (1994): Inverse velocity trends in secondary ion mass spectrometry: A new method of quantification? Nucl Instrum Meth Phys Res B **86**, 373–379

Vasile M.J. (1983): The velocity dependence of secondary ions. Nucl Instrum Methods **218**, 319–323

Wittmaack, K. (1977): Secondary ion production due to ion-surface bombardment. In: Tolk N.H., Tully J.C., Heiland W. and White C.W. (Eds), Inelastic Ion-Surface Collisions. Academic, New York, pp 153–199

Wittmaack K. (1979): Secondary-ion emission from silicon bombarded with atomic and molecular noble-gas ions. Surf Sci **90**, 557–563

Wittmaack K. (1982): Design and performance of quadrupole-based SIMS instruments: A critical review. Vacuum **32**, 65–89

Wittmaack K. (1983): The effect of work function changes on secondary ion energy spectra. Physica Scripta **T6**, 71–75

Wittmaack K. (1998): Physical and chemical parameters determining ion yields in SIMS analyses: A closer look at the oxygen induced yield enhancement effect. In: Gillen G., Lareau R., Bennett J. and Stevie F. (Eds), Secondary Ion Mass Spectrometry SIMS XI. Wiley, Chichester, pp 11–18

Wittmaack K. (1999a): The 'infinite velocity method': A means of concentration calibration in secondary ion mass spectrometry? Surf Sci **429**, 84–101

Wittmaack K. (1999b): Ion induced electron emission as a means of studying energy- and angle-dependent compositional changes of solids bombarded with reactive ions: I. Oxygen bombardment of silicon. Surf Sci **419**, 249–264

Wucher A. and Oechsner H. (1988): Emission energy dependence of ionisation probabilities in secondary ion emission from oxygen covered Ta, Nb and Cu surfaces. Surf Sci **199**, 567–578

Yu M.L. (1978): Work-function dependence of negative-ion production during sputtering. Phys Rev Lett **40**, 574–577

Yu M.L. (1981): Velocity dependence of the ionisation probability of sputtered atoms. Phys Rev Lett **47**, 1325–1328

Yu M.L. (1982): Matrix effects in the work-function dependence of negative secondary ion emission. Phys Rev B **26**, 4731–4734

Yu M.L. (1984a): Anomalous coverage dependence of secondary-ion emission from overlayers. Phys Rev B **29**, 2311–2313

Yu M.L. (1984b): On the velocity dependence of secondary ion emission from metallic surfaces. Rad Eff Defects Sol **109**, 259–264

Yu M.L. and Lang N.D. (1983): Direct evidence of electron tunnelling in the ionisation of sputtered atoms. Phys Rev Lett **50**, 127–130

Electron Emission from Solids Irradiated with Swift Ion Beams

Hermann Rothard* and Benoit Gervais

Centre Interdisciplinaire de Recherche Ions Lasers
UMR 6637 (CEA/CNRS/ENSICAEN/Université de Caen)
CIRIL-Ganil, Boulevard Henri Becquerel
BP 5133, F-14070 Caen Cedex 05, France

Abstract

We present basic features, important results obtained so far, and open questions on electron ejection from solids induced by swift ion beams in the "electronic stopping" regime, where the transfer of kinetic energy to target electrons dominates over effects related to potential energy or elastic stopping. Topics include primary ionization in binary collisions, transport of fast and slow electrons, multiple collision sequences (Fermi shuttle), collective excitations (wake, plasmons), effects related to strong perturbation (high charge effects on primary ionization and electron transport, multiple ionization), Auger electron spectroscopy (track potential, electronic temperatures), statistics and correlated emission of electrons, electron ejection in channeling, and charging effects in insulating targets.

Contents

1 Introduction: Present Knowledge **498**

2 Experimental Techniques: New Developments **500**

3 Overview: Basic Mechanisms **501**

4 Primary Ionization, Fast Electron Transport and Collision Sequences **505**

* E-mail: rothard@ganil.fr

5 Low Energy Electrons: Collective Excitations **507**

6 Electron Yields: Scaling Laws **508**

7 Strong Perturbation: High Charge Effects **511**

8 Auger Electrons: Electronic Temperatures **514**

9 Insulators: Charging Effects **516**

10 Channeling and Emission Statistics **517**

11 Other Intriguing Topics: An Open End **518**

Acknowledgements **519**

References **520**

1. Introduction: Present Knowledge

The major part of the energy deposited in matter by swift ions in the "electronic stopping" regime leads to ionization of the target atoms. In condensed matter, ejected electrons may then suffer elastic scattering or inelastic scattering by target atoms during their transport through the medium. A cascade of secondary electrons is created in this way. Electrons induced by swift ions are often called "delta-rays", and the zone of high ionization density close to the ion trajectory is referred to as "track core". The detailed knowledge of the microscopic structure of ion tracks is necessary for understanding radiation effects in condensed matter such as track formation, radiolysis, relative biological effectiveness (RBE) calculations for hadron-therapy to name a few. In these examples, doubly differential electron ejection cross sections are a key input parameter for numerical simulations (Spohr, 1990; Kraft, 2000). Useful books containing comprehensive reviews on electron emission from solids include Devooght et al. (1991) for theoretical aspects, Hasselkamp et al. (1991) for experimental aspects and Baragiola (1993). Electron ejection in single collisions (gas targets, primary ionization) was treated by Stolterfoht et al. (1997). A large number of reviews in common journals are also available.

Important parameters which can be varied in experiments or calculations are first of all the properties of the projectile such as its velocity v_P, atomic number Z_P or charge q_P, and the number n of constituents in the case of cluster projectiles. In the following, we exclude "molecular (cluster) effects" and refer the reader to

the review by Fallavier (1996). Also, we restrict our discussion to the high velocity regime (electronic stopping) and exclude effects related to elastic ("nuclear") stopping or effects related to the potential energy (see the contribution by Winter et al. in this book for information about electron emission in the low velocity regime). The impact angle δ between the beam and the target surface normal may range from $\delta = 0°$ (perpendicular incidence) to δ close to 90° (grazing incidence). Basic properties of the target are its atomic number Z_T (keeping in mind that many materials are made of atoms of different kinds) and the thickness d. The target surface has a great influence on low energy electron emission (structure, topography, surface impurities due to physisorption and chemisorption). Furthermore, effects related to the orientation of either incoming beam or outgoing electrons with respect to a crystal direction (channeling, etc.) or the target temperature (surface modification, phase transitions) may arise.

Electron emission from solid surfaces under electron and ion impact was first observed at the end of the 19th century along with all the major discoveries concerning cathode rays, canal rays and radioactivity. The first systematic studies were performed by Füchtbauer (1906a, 1906b) exactly one hundred years ago. In his quite remarkable papers, Füchtbauer (1906a, 1906b) already described most of the basic features concerning electron yields, angular distributions and even velocity distributions. Nowadays, electron emission from solids is fairly well understood. Generally, a three step process is assumed: (1) primary ionization (both of target and projectile), (2) transport (elastic scattering, inelastic processes, secondary electron cascade multiplication), (3) transmission through the surface potential barrier. We should keep in mind that we are dealing with a complex phenomenon (many particles, target properties, surface phenomena). Theoretically, the phenomenon can be described at different levels of sophistication. A basic description is provided by the semi-empirical theory based on the classical paper by Sternglass (1957) with possible extensions for forward and backward emission from thin foil targets (Jung et al., 1996).

All theoretical approaches are based on master phase space equations. Most of them require first the knowledge of ion-solid interaction cross sections to model the primary excitation which gives rise to secondary electron cascades. They also need electron transport cross sections to account for electron transport and escape from the solid. These cross section are not easy to calculate and at the simplest level of modeling, they are eliminated to the benefits of empirical parameters like stopping power and transport or escape length (Sternglass, 1957). More involved models make an attempt to introduce explicitly the cross section in the master equation. Various approximations have been used to determine them. They are usually deduced from first order perturbation theory (see, e.g., Beuve et al., 2002,

and references therein) at various levels of sophistication to account for solid state effects. We can distinguish three approaches: (1) approximations which neglect the electronic structure of the target and where transport is considered as a series of atomic collisions (Schou, 1980; Schiwietz et al., 1990), (2) models based on jellium theory which are able to account for collective effects like plasmon excitation (Devooght et al., 1987; Dubus et al., 1993; Juaristi et al., 1998), and (3) models where the electronic structure is taken into account explicitly (Willis et al., 1974; Chung and Everhart, 1977; Rösler and Brauer, 1981, 1988) or empirically (Beuve et al., 2002). The master phase space equation has been solved by direct integration in the case of stationary flux approximation (Schou, 1980; Devooght et al., 1987; Rösler and Brauer, 1981, 1988) or by Monte Carlo simulation (Lencinas et al. 1990, Dubus et al. 1993, Beuve et al. 2002). The latter method provides more freedom regarding the geometry and interaction with the surfaces of the target. The calculated (total and differential) electron yields are in good qualitative agreement with experiments and allow interpretation of many experimentally observed features.

2. Experimental Techniques: New Developments

Experimentally, doubly differential electron yields (in single collisions with gas targets, doubly differential cross sections) are recorded with the help of both magnetic or electrostatic spectrometers, and time-of-flight techniques. The spectrometer is placed at a certain observation angle θ, and the doubly differential electron yields, i.e. energy or momentum spectra, are measured by varying the electric or magnetic field of the analyzer. The ejection angle θ is usually measured with respect to the beam direction, i.e. $\theta = 0$ deg. denotes emission in the direction of the beam. Secondary electron yields (the mean number of electrons emitted per projectile) can be obtained from current measurements or from the measurement of electron emission statistics, i.e. the probability $P(n)$ that $0, 1, 2, \ldots, n$ electrons are emitted. More details on experimental techniques can be found in e.g. Hasselkamp et al. (1991) and Stolterfoht et al. (1997). During the last 10 years, important new experimental techniques were applied to electron ejection. Advanced electrostatic spectrometers (toroidal geometry of the deflection plates; see Bechthold et al., 1998) allow to simultaneously measuring the complete electron angular distribution at given electron energy with good angular resolution. This feature allowed to identify never before seen spike-like narrow electron jets along the beam axis in electron emission from thin foils, which may possibly be due to a plasma-lens (track guiding) effect (Zäpfel et al., 2002).

The multi-detector ARGOS, initially designed for studying nuclear reaction products, was adapted for the measurement of fast electrons (Lanzanò et al., 1998; De Filippo et al., 2004). With this multi-detector, in comparison to conventional spectroscopic methods used in atomic collisions up to now, three important advantages are achieved: (1) doubly differential velocity spectra can be measured simultaneously at many ejection angles (up to 120 detectors), (2) absolute ejection yields and cross sections can be measured with great accuracy thus allowing a stringent test of ionization theory, and (3) (multi-) coincidences can be measured. This latter feature opens the door for studies of processes which have not yet been accessible, e.g. correlated emission of two or more electrons. Such studies become also feasible for low energy electrons via the measurement of the time-of-flight of electrons combined with imaging techniques (derived from the "reaction microscope", see e.g. Ullrich et al., 2003), a technique that has been successfully applied to study particle ejection in ion-atom and ion-molecule collisions. A combination of electric and magnetic fields guide the ejected electrons onto a position sensitive detector. The full differential emission characteristics of up to 10 electrons per single incoming ion can be extracted (Rothard et al., 2007).

3. Overview: Basic Mechanisms

Basic mechanisms of electron ejection such as primary ionization in binary encounter collisions, multiple collision sequences, electrons transport and collective excitation (wake, plasmons) are summarized in Figure 1 and explained in more detail throughout the text. Primary ionization in close collisions leads to ejection of fast (δ-) electrons from the target atoms (binary encounter, denoted P in Figure 1). Low energy electrons stem from ionization in distant collisions or from collective effects such as plasmon decay or directed emission of shock electrons from the ion-induced wake. On their way through the solid towards the surface, electrons suffer inelastic collisions or angular scattering (electron transport). The projectile can be ionized (electron loss, denoted T in Figure 1). Higher order collision sequences (P-T-P-..., referred to as "Fermi shuttle") may also occur. Figures 2 and 3 show examples of doubly differential spectra of low energy ($E < 3$ keV) electrons in backward and forward direction (Figure 2) and of high energy electrons ($E > 10$ keV) in forward direction (Figure 3).

A prominent feature in these latter spectra are "binary encounter electrons" with a broad distribution around a velocity of $v_{\mathrm{BE}} = 2v_{\mathrm{P}} \cos\theta$. Another feature are "convoy electrons" (CE) from either electron loss or capture to low-lying projectile continuum states. The paper by Breinig et al. (1982) still is an excellent introduction to CE. Their energy is close to zero in the projectile frame, and they

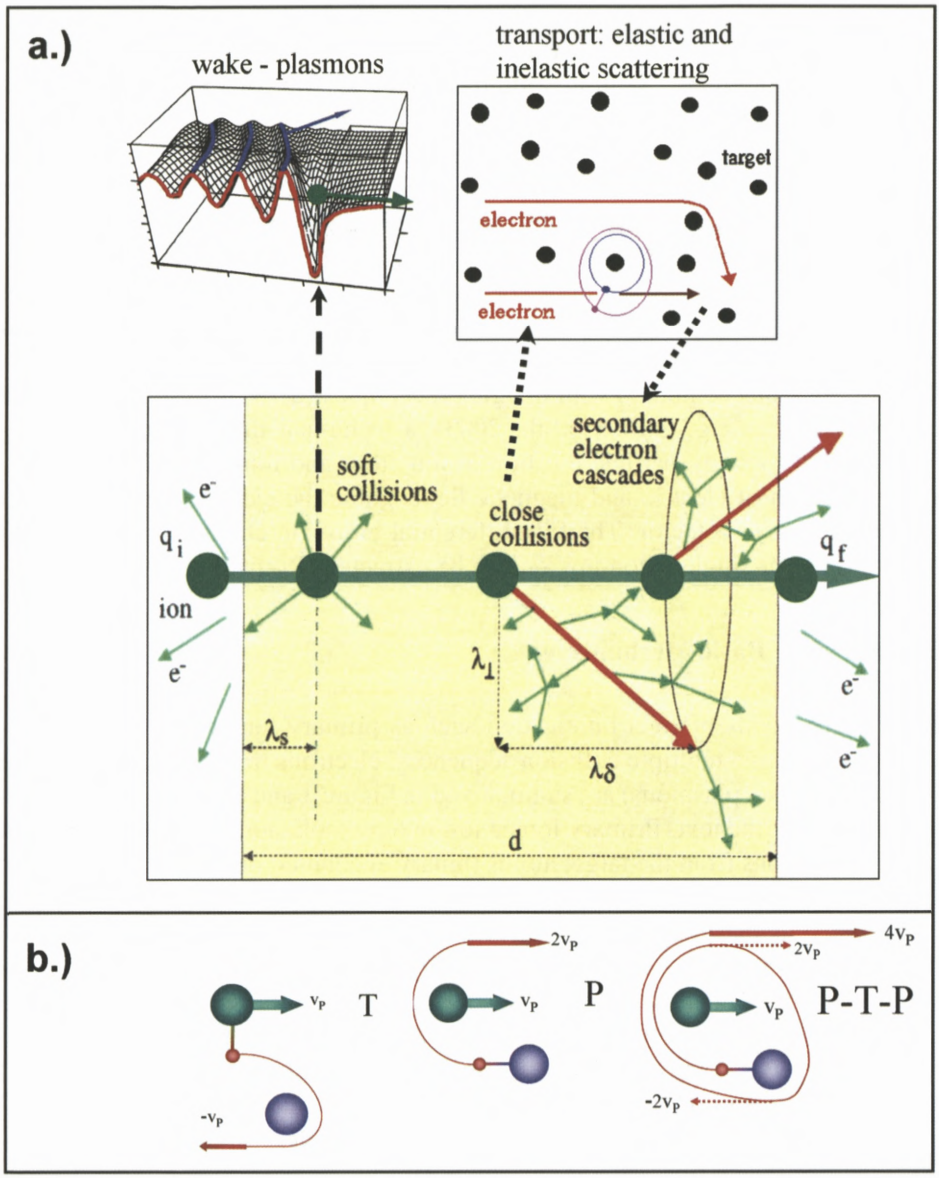

Figure 1. (a) Basic mechanisms of electron ejection from a thin foil of thickness d bombarded with an ion beam of incoming charge q_i and outgoing charge q_f. Low energy electrons stem from ionization in distant collisions or collective effects (plasmon decay and wake, upper left part). Primary ionization in close collisions leads to ejection of fast (δ-) electrons from the target atoms. On their way through the solid towards the surface, electrons suffer inelastic collisions without angular deflection or angular scattering (upper right part) and may create secondary electron cascades. (b) Target ionization by a binary encounter projectile-electron collision (P), projectile ionization by the target (electron loss, T) and higher order collision sequences (Fermi shuttle P-T-P-...).

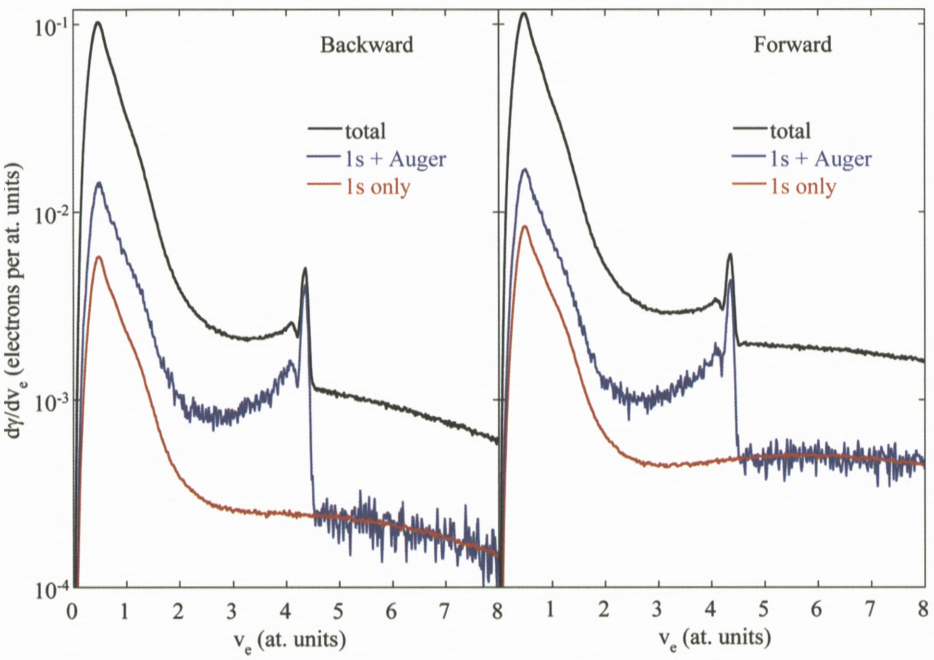

Figure 2. Low energy electron spectra) for H^+ (9 MeV/u) penetrating a thin carbon foil (4 μg/cm^2) in backward (beam entrance side, left) and forward (beam exit side, right) direction. The numerical simulation (Beuve et al., 2002) is based on the Monte Carlo method, therefore, statistical fluctuations naturally arise and can be seen in the spectra. Shown are the total velocity differential spectra, the contribution of the K-shell 1s ionization, and the contribution of KLL Auger electron emission. The most prominent feature is the peak of low energy often so-called "secondary electrons" at typically a few eV which stem from both primary ionization and cascade multiplication. Also, a shoulder from the decay of volume plasmons (at $E < 20$ eV for C targets) is visible.

form a characteristic cusp shaped peak in fast forward electron spectra. Recently, absolute cross sections for convoy electron emission from thin foils in a wide range of Z_T (C ... Bi) by fast projectiles (23–95 MeV/u) were measured with the ARGOS multi-detector (De Filippo et al., 2004). A numerical description of convoy electron transport through solids in the vicinity of the projectile Coulomb field was developed by Burgdörfer and Gibbons (1990). Note that the production of CE in low lying projectile continuum states, the population of highly excited bound (Rydberg-) states of (heavy) ions in solids and the evolution of the ion charge states are related. A further electron ejection mechanism is the Auger effect. Projectile Auger electrons from in-flight de-excitation of heavy ions carrying electrons in bound excited states can be observed (Figure 3). A review on this

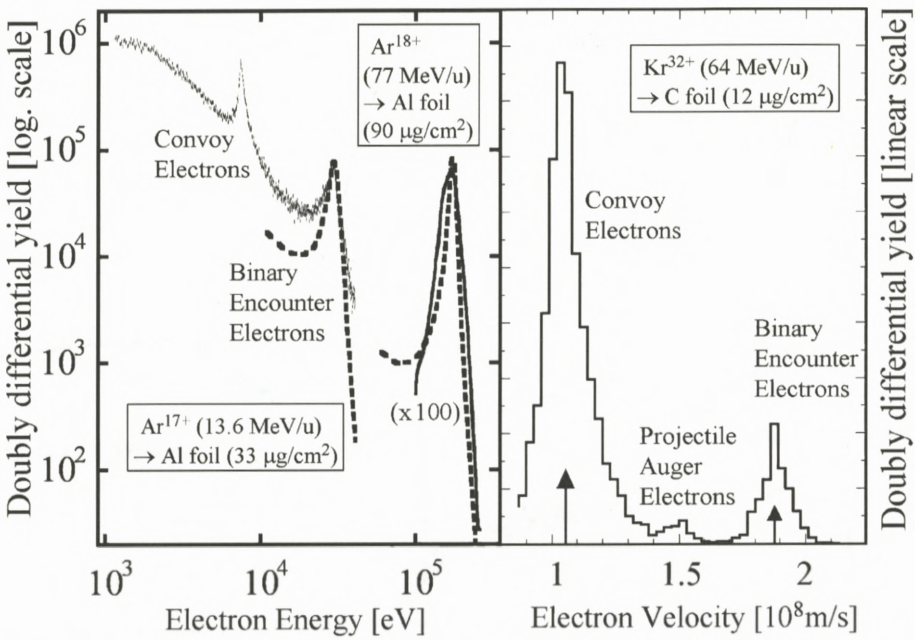

Figure 3. Fast-electron spectra emitted in forward direction (beam exit side, near $\theta = 5$ deg.) from thin foils, showing convoy- and binary encounter electrons. Left-hand side: doubly differential electron yields $d^2\sigma/(dE\, d\Omega)$ plotted as a function of the electron energy for the collision system Ar on Al foil. Comparison of experimental spectra at 13.6 MeV/u (thickness 33 μg/cm^2, Rothard et al., 1998) and at 77 MeV/u (thickness 90 μg/cm^2, Lanzanò et al., 1998) to the EIA calculation (dotted lines). In this latter case, the left-hand scale corresponds to units of barn/(keV sr). Right-hand side: Forward electron velocity spectrum induced by Kr^{32+} (64 MeV/u) from a C foil of approx. 50 nm (experimental data). Note the projectile Auger electrons.

topic was given by Stolterfoth (1987). Target Auger electrons (typically at low energies $E < 3$ keV) appear in the low energy electron spectra (Figure 2).

The low energy electron spectra from a calculation according to Beuve et al. (2001, 2002) for H^+ (9 MeV/u) penetrating a thin carbon foil (4 μg/cm^2) in backward and forward direction (Figure 2) show as most prominent feature the peak of often so-called "secondary electrons" at typically a few eV. This broad distribution stems from both primary ionization and cascade multiplication (secondary electrons). Also, a shoulder from the decay of volume plasmons (at $E < 20$ eV for C targets) is visible. An interesting feature of theoretical calculations is that different contributions to electron ejection can be separated. Therefore, in Figure 2, we show the total velocity differential spectra in comparison to the contribution of the K-shell 1s ionization and the contribution of KLL Auger electron emission.

The overall intensity is slightly higher for forward emission. Experimental data may also serve as a benchmark for the development of numerical simulations of electronic energy deposition in matter and electron emission. After this rapid overview, we now discuss some special topics in more detail. We do not attempt at an exhaustive review, but rather would like to highlight the most important basic features, recent important new developments and findings, and open questions.

4. Primary Ionization, Fast Electron Transport and Collision Sequences

A "binary encounter" (BE) collision between projectile and target electron leads to ejection of electrons with a velocity of $v_{\mathrm{BE}} = 2v_{\mathrm{P}} \cos\theta$ if the interaction with the target nucleus is neglected. The momentum $p = \gamma v$ with $\gamma = (1-(v/c)^2)^{-1/2}$ is the relevant quantity (instead of v_p) for relativistic projeciles. The observed BE electron peak shows a broadening due to the initial momentum distribution of the bound target electrons known as Compton profile (Figure 3). The BE process is theoretically well understood. The relativistic theory is based on the electron impact approximation (EIA), where ionization takes place via electron transfer to the projectile continuum in a quasi-elastic scattering of the target electron by the projectile Coulomb field (Jakubassa-Amundsen, 1997; see also Rothard et al., 1998a). The corresponding cross section is then folded with the Compton profile in the initial state.

Measurements of electron spectra as a function of the target thickness allowed observing how electron emission evolves from single collisions (as in atomic collisions with low density gas targets) up to multiple collisions (as in the bulk of solids, where electron transport phenomena become important) and thus to link single collisions to effects in condensed matter. A transport theory, based on the "Separation of Energy Loss and Angular Straggling" approximation (Tougaard and Sigmund, 1982; Schiwietz et al., 1990), was developed. It was tested for different collision systems (13.6 MeV/u and 95 MeV/u Ar^{18+} GANIL, and 45 MeV/u Ni^{28+}, LNS Catania) (Rothard et al., 2001; De Filippo et al., 2004). Singly differential cross sections, which vary with ejection angle θ as $\mathrm{SDCS}(\theta) \sim \cos^{-3}\theta$, obtained from measurement and calculation agree within some percent for thin foils, and so do doubly differential electron yields (as can be seen in Figure 3, left-hand side). The evolution of the shape of the spectra is reasonably well reproduced. Another important result concerns the target material dependence of BE electrons. It was found experimentally that they roughly follow a very simple scaling law: the BE electron yield is proportional to the number of target electrons "seen" by the projectile (Bechthold et al., 1998; Rothard et al., 1998a; De Filippo et al., 2004).

Another interesting result is the observation of unexpectedly high cross sections for electron emission at energies far beyond the BE peak, at large angles and even in backward direction. Possibly, this can be explained by the so-called "Fermi-shuttle" process, which was introduced to explain the origin of high-energy cosmic radiation due to acceleration of charged particles by repeated collisions with moving magnetic fields in interstellar space. Evidence for such acceleration schemes were found in ion-solid collisions (Lanzanò et al., 1999) and ion-atom collisions (Sulik et al., 2002). From the basic BE process (ionization of the target by the projectile, P) and its counterpart in the projectile frame (T, ionization of the projectile by the target: electron loss), collision sequences (consecutive scattering events on the target nucleus and the projectile nucleus) can build up such as e.g. P-T, P-T-P, T-P, etc. as shown schematically in Figure 1b. It was shown that the Fermi shuttle electron yield increases with the perturbation parameter Z_P/v_P, and also with the more realistic scaling parameter $Z_P^2 Z_T/6v_P^3$, which takes into account re-bouncing of the electrons on target and projectile. This finding points towards the important role of the combined projectile-target system (Rothard et al., 2005).

The velocity distribution $N(v)$ of the fast Fermi shuttle electrons is exponentially decreasing, i.e. $N(v) \sim \exp(-nv)$, and exhibits the same evolution of n with projectile velocity as in the case of Fermi accelerated target deuterons. The Fermi shuttle acceleration should become of particular importance in ion-solid collisions compared to ion-atom collisions, because of the high target nucleus density. In this case, there should be an enhanced probability of re-scattering of electrons all along the projectile trajectory, since the projectile sees the projected density of backscattered electrons along the ion track. But this is an open question, since a direct comparison of data from thin foils and gas targets is still missing. Furthermore, when heavy collision partners (heavy target atoms, heavy ions) are involved, the re-scattering probability increases. This may have consequences for the microscopic structure of ion tracks (micro-dosimetry) and radiation induced energy deposition in both inert and living matter. We note that collision sequences of orders higher than P-T-P were observed (Sulik et al., 2003). A further problem to be solved lies in quantification of the absolute contribution of such Fermi shuttle processes to electron ejection yields and to radiation effects. Monte Carlo simulations are useful in this respect (Sulik et al., 2003).

As far as primary ionization is concerned, an important recent theoretical development is the application of the binary stopping theory in a straightforward way to calculate ejected electron spectra (Weng et al., 2006). In this treatment, the contributions of target and projectile ionization are included. From an experimental point of view, the application of the "reaction microscope" to electron emission

in primary ionization allowed in particular studying the low energy part of the spectra down to less than eV energies (Ullrich et al., 2003). In the low electron energy limit (soft collisions with low momentum transfer), the influence of the target nucleus increases (two center effects). Also, for a realistic description of soft electron emission, quantum mechanical treatments are necessary. The emission of low energy electrons is governed by dipole transitions. For example, for a simple hydrogen target, most low energy electrons are emitted around $\theta = 90$ deg., i.e. $\cos\theta = 0$. Nevertheless, the Compton profile, the initial momentum distribution of the bound electrons, broadens the distribution and leads to emission towards all angles. For complex targets (molecules with many electrons), the angular dependence is much weaker than for hydrogen, and smeared out over all angles.

5. Low Energy Electrons: Collective Excitations

Low energy electron emission (below 1 keV) strongly depends on surface properties, and bears features of collective excitation (plasmons, wake), of transport effects (cascade multiplication, low energy "secondary" electron peak, Figure 2) and of effects connected to strong perturbation ("high charge effects", see below, Figure 6). Plasmon excitation and subsequent electron emission following plasmon decay is well known (see Figure 2) and well treated theoretically in particular for Al. Collective plasmon-like excitations were also observed for Be, C, Mg, Si, Ti, Nb and Au (Hasselkamp et al., 1991). Low energy electron emission from metals in backward direction was intensively studied by the Giessen group (Hasselkamp et al., 1990).

The collective response of the ensemble of target electrons to a moving charge shows up as electron density fluctuation with a Mach cone-like spatial structure (Echenique et al., 1979). This so-called "wake" is related to plasmon excitation, and may lead to a directed emission of low energy electrons perpendicular to the shock front as shown in Figure 1 (top left part). For theoretical treatments see Schäfer et al. (1980) and Brice and Sigmund (1980), the first experiment with controlled surfaces was performed by Burkhard et al. (1987b). An open problem here is the coupling to the surface and the de-excitation from a collective state inside the solid to a single electron continuum state outside the solid (Griepenkerl et al., 1995). A search for the possible influence of a superconducting phase transition on collective electron emission (Rothard et al., 1992) was performed but did not reveal an important dependence of electron emission characteristics on the target temperature above and below the transition temperature.

Another phenomenon was searched for: the existence of bound states of electrons in the wake of ions inside the solid and the possible trapping of electrons

as suggested by Neelavathi et al. (1974). Experimental searches for such "wake-riding" electrons in connection with experimental studies of the convoy electron peak remained without success. However, the wake of negatively charged particles heavier than electrons may lead to an enhanced probability of single electron trapping in wake-bound states (Burgdörfer et al., 1989). Experimental investigations by Yamazaki et al. (1990) showed evidence for an additional "wake" related mechanism for electron emission in forward electron spectra induced by antiprotons passing through thin carbon foils. Interestingly, in contrast to the case of positively charged particles, there is no convoy electron peak at $v_e \approx v_P$ with negatively charged projectiles, but an "anticusp" caused by the repulsive interaction between the antiproton and the electrons. However, the anti-cusp is filled up by scattered electrons in the case of solid foils.

6. Electron Yields: Scaling Laws

During the ION06 meeting, it became clear that there is interest in knowing the behaviour of electron emission and to find simple scaling laws as a function of v_P, Z_P and target thickness d for applications. First of all, since very often thin foils are used as electron source for e.g. beam monitors and dosimetry, let us have a look at the target thickness dependence of electron emission. Forward and backward electron yields are plotted as a function of the target thickness in Figure 4 for Cu ions of 9.6 MeV/u, and for Ni ions of 74 MeV/u. These experiments are based on current measurements as described by e.g. Clouvas et al. (1997) and Beuve et al. (2001). Also, yields for proton impact at 0.5 MeV/u and 9 MeV/u, calculated by means of a numerical simulation based on the Monte Carlo method, are shown (Beuve et al., 2001). Forward yields γ_F evolve over a large target thickness range and finally reach a plateau $\gamma_F(\infty)$. This is related to cascade multiplication by high energy δ-electrons which are mainly emitted in the forward direction. Backward yields rapidly reach a saturation value $\gamma_B(\infty)$ except at 74 MeV/u, where a second plateau is observed. In the case of forward electron yields, one must be careful and take into account that the ions loose energy in the foil. Their energy upon exit $E_P - \Delta E_P$ may considerably differ from the initial energy E_P upon entrance. The energy loss ΔE_P increases with target thickness. At high projectile energies, forward electron yields are "in equilibrium" (Figure 4) for foils thin enough to ensure that the energy loss is small compared to the initial energy $\Delta E_P \ll E_P$. However, such effects may become important at energies below the stopping power maximum (Clouvas et al., 1997; Beuve et al., 2001).

Electron transport can be studied by an analysis of measured electron yields as a function of foil thickness within the framework of an empirical theory (Stern-

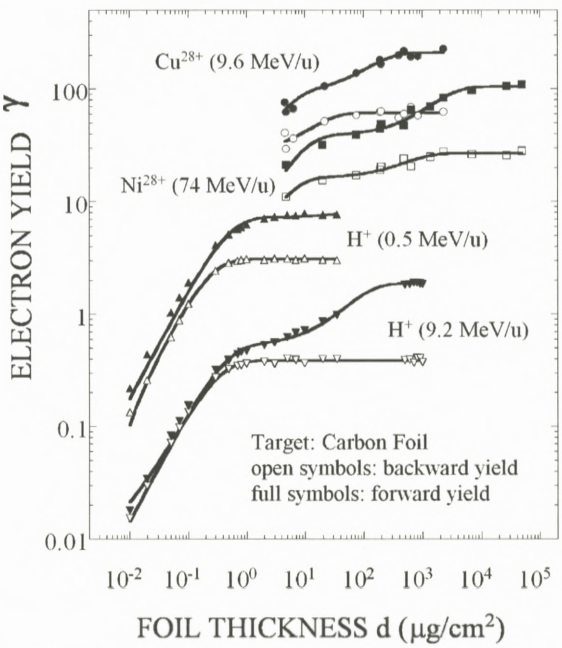

Figure 4. Forward (full symbols) and backward (open symbols) electron yields (γ_F, γ_B) as a function of carbon target thickness d. The lines drawn through the experimental data are fits of Equation (1) to γ_F and with Equation (2) to γ_B. A thickness of $d = 1$ μg/cm^2 corresponds to about 61 Å for a carbon foil density of $\rho = 1.65$ g/cm^3. Projectiles: Cu^{28+} (9.6 MeV/u, circles, experiment, Jung et al., 1996), Ni^{28+} (74 MeV/u, squares, experiment, Jung et al., 1996), H^+ (0.5 MeV/u, triangles, numerical simulation, Beuve et al., 2002), H^+ (9.2 MeV/u, upside-down triangles, numerical simulation, Beuve et al., 2002).

glass, 1957; Jung et al., 1996). The following equations are deduced for the target thickness (d) dependent forward (γ_F) and backward (γ_B) low energy electron yields:

$$\gamma_F(d) = \Lambda_F \frac{dE}{dx}\left(1 - \beta_S\, e^{-d/\lambda_S} - \beta_\delta\, e^{-d/\lambda_\delta}\right), \tag{1}$$

$$\gamma_B(d) = \Lambda_B \frac{dE}{dx}\left(1 - F_1\, e^{-d/\lambda_S} - F_2\, e^{-d/\lambda'_\delta}\right). \tag{2}$$

Here, Λ_F and Λ_B are constants and dE/dx is the electronic energy loss per unit path length. The curves shown in Figure 4 are fits with Equation (1) to the forward yields and with Equation (2) to the backward yields. The evolution of both theoretical and experimental data with target thickness is remarkably well reproduced

by these simple formulae. By means of this fitting procedure, one can deduce the mean *diffusion length for slow electrons* λ_S and the mean *transport (attenuation) length* for high energy electrons (in forward direction: λ_δ, in backward direction for backscattered fast electrons: λ'_δ). The meaning of these quantities is shown schematically in Figure 1 (central part). One also can deduce the "partition factor" β_δ, which measures the fraction of projectile energy lost in close collisions with subsequent high energy δ electron emission. The fraction dissipated in soft collisions, leading to direct production of low energy electrons or to plasmon excitation with subsequent plasmon decay, is given by $\beta_S = (1 - \beta_\delta)$. Under the assumption that $\lambda_S \ll \lambda'_\delta \ll \lambda_\delta$, it can be shown that

$$F_1 = 1 - F_2,$$

$$F_2 = -\beta_\delta \lambda'^2_\delta (\lambda_\delta + \lambda'_\delta + \beta_\delta \lambda_\delta)^{-1} (\lambda_S - \lambda'_\delta)^{-1},$$

see Jung et al. (1996).

The low energy electron diffusion length λ_S does not depend on the ion species or projectile energy and is of the order of 30 Å for carbon, whereas λ_δ increases strongly with increasing projectile velocity. This explains the "velocity effect" where different damage in solids occurs at the same electronic energy loss dE/dx, but at different ion velocities. The energy having been taken away from the track core by fast electrons increases with ion velocity for faster ions. This leads to a reduced density of energy deposition close to the ion track. Such a velocity effect was also observed in ion induced electron emission by Neugebauer et al. (1999). Due to the high projectile velocity, it is possible to clearly distinguish λ_S, λ'_δ and λ_δ at 74 MeV/u, but not around 10 MeV/u, where both exponential functions of Equation (2) merge and the backward yield increase can be described by one single exponential function.

The partition factor β_δ does not depend significantly on the ion energy, but rather increases strongly with Z_P from 0.35 with protons up to 0.75 with Ni/Cu. This finding is related to so-called "saturation effects" (see below, discussion of high charge effects, Figure 6), since for heavy ions, the proportion of low energy electron emission in primary ionization (from soft collisions with large impact parameter) decreases with Z_P compared to high energy electron emission (from violent collisions at small impact parameters). This leads to reduced electron emission in backward direction and enhanced emission in forward direction. Indeed, the ratio of forward to backward yields $R = \gamma_F/\gamma_B$ for "thick" targets strongly increases with projectile atomic number from approx. $R = 1.2$ for protons up to $R = 5$ for the heaviest ions.

Coming back to relevant scaling, the electronic energy loss per unit path length dE/dx immediately comes into mind as a first choice of an appropriate scaling

parameter. Such a proportionality is indeed suggested in several theoretical approaches (Sternglass, 1957; Sigmund and Tougaard, 1981). To test this hypothesis, we can compare electron yields to $\mathrm{d}E/\mathrm{d}x$ by defining a ratio

$$\Lambda_i(Z_\mathrm{P}, v_\mathrm{P}) = \frac{\gamma_i}{\mathrm{d}E/\mathrm{d}x} \,. \tag{3}$$

The index i stands for B, F or T if backward (from the beam entrance side), forward (the beam exit side in the case of thin foils), or total electron yields are concerned ($\gamma_\mathrm{T} = \gamma_\mathrm{F} + \gamma_\mathrm{B}$). In practice, rather $\mathrm{d}E/\mathrm{d}(\rho x)$ measured in keV/(μg/cm^2) than $\mathrm{d}E/\mathrm{d}x$ is used and tabulated. The parameter Λ is often called "material parameter" in the literature and it is assumed that it depends on the target material only. This is wrong, as we will see in the following, since it also depends on the projectile parameters v_P and Z_P. It should be kept in mind that, if the condition $\Delta E_\mathrm{P} \ll E_\mathrm{P}$ is not fulfilled, ΔE_P may lead to a different $\mathrm{d}E/\mathrm{d}x$ at the beam exit side. This should be taken into account when calculating Λ_F with Equation (3) (Beuve et al., 2001).

The dependence of the ratios Equation (3) for protons, carbon ions, nickel (copper) ions and uranium ions is shown in Figure 5. The foils are thick enough to assure that the plateaus $\gamma_\mathrm{F}(\infty)$ and $\gamma_\mathrm{B}(\infty)$ are reached. In all cases, an increase of Λ_i is observed. It is more pronounced the heavier the ion, and stronger for forward than for backward yields. Note that Λ values are different above and below the electronic stopping power maximum (see above, velocity effect, Neugebauer et al., 1999). Finally, we mention that a simple empirical law for the charge dependence of backward emission was proposed by Beuve et al. (2000):

$$\Lambda_\mathrm{B}(q_\mathrm{P}) = \Lambda_\mathrm{B}(q_\mathrm{P} = 1)\left(2 - q_\mathrm{P}^2 \frac{\mathrm{d}E/\mathrm{d}x(q_\mathrm{P} = 1)}{\mathrm{d}E/\mathrm{d}x(q_\mathrm{P})}\right). \tag{4}$$

If low energy electron energy distributions (singly or doubly differential yields) are needed, the above scaling of the integrated forward and backward emission yields (Jung et al., 1996; Rothard et al., 1998b; Beuve et al., 2000, 2001) can be combined with doubly differential low energy electron spectra for fast proton impact as measured by Drexler and Dubois (1996).

7. Strong Perturbation: High Charge Effects

Several specific effects connected to the high projectile charge of swift heavy ions in electron emission were observed. Examples are the saturation of low energy electron yields, appearance of hypersatellite lines due to multiple ionization of inner shells and a broadening of Auger lines (see e.g. Rothard, 2004; Schiwietz

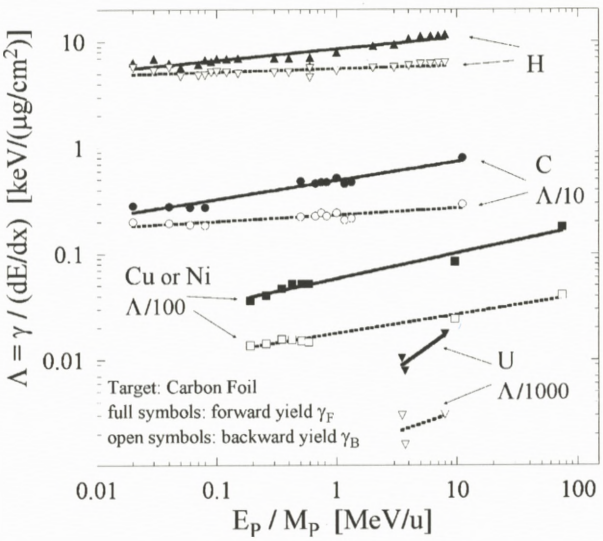

Figure 5. The ratios of forward electron yields (full symbols) and backward yields (open symbols) to the (electronic) energy loss per unit path length (Equation 3) as a function of the projectile energy divided by ion mass, E_P/M_P, for protons (triangles), carbon (circles), nickel/copper (squares) and uranium ions (upside-down triangles). The Λ-values were divided by the indicated factors. The lines are fits of a power law $\Lambda = C(E_P/M_P)^n$ to the data (similar plots shown in Rothard et al., 1998, here revisited and enriched with new data where available). The target thickness was chosen so that electron yields have reached the (projectile velocity dependent) asymptotic equilibrium value (see Figure 4, typically 500 μg/cm^2 at 10 MeV/u). The charge state of the incoming ions is close to the mean final charge.

et al., 2004, and references therein). Important results on high charge effects were obtained from measurements and theoretical calculations of low energy electron spectra. In ionization theory, the ratio q/v_P of charge and projectile velocity measures the strength of perturbation induced by the projectile (see e.g. Stolterfoth et al., 1997; Beuve et al., 2002). We can vary this parameter in a straightforward way by performing experiments with projectiles of different charge or atomic number while keeping the projectile velocity constant. In order to avoid effects connected to charge exchange or screening, it is important to do the experiments aimed at exploring the influence of the perturbation parameter with ions of charge states close to the mean equilibrium charge. The role of projectile electrons (active and passive screening) was e.g. discussed by Clouvas et al. (1997).

In Figure 6, the ratios of backward electron energy spectra obtained with Mo^{39+} and spectra obtained with C^{6+} (at constant projectile velocity of 9.2 MeV/u, about 19 atomic velocity units) are shown. Here, the perturbation

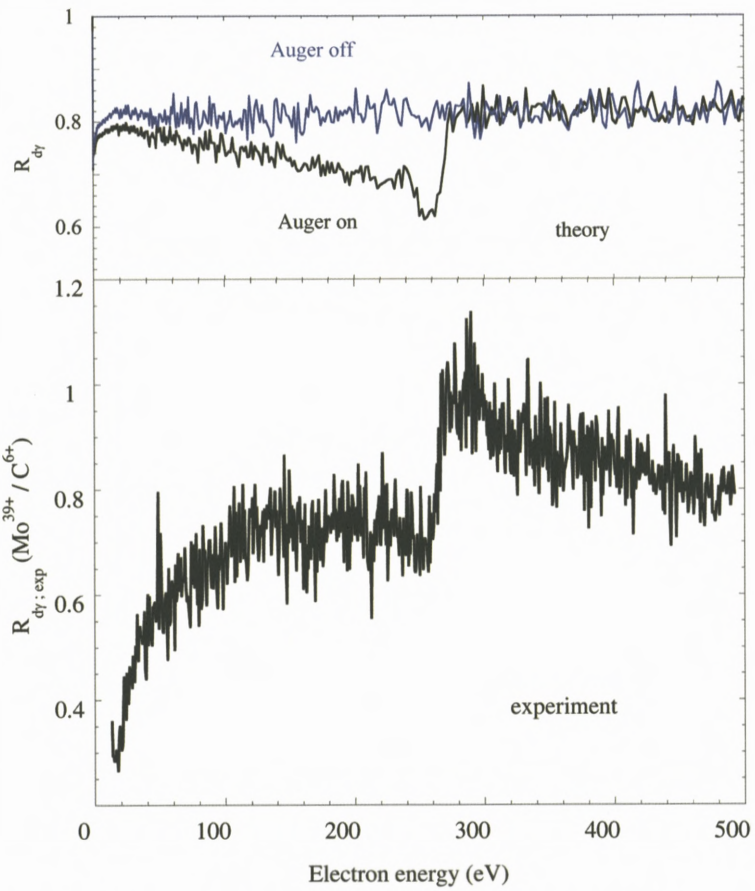

Figure 6. The ratios of backward electron energy spectra obtained with Mo^{39+} and spectra obtained with C^{6+} (at constant projectile velocity of 9.2 MeV/u, about 19 atomic velocity units) on carbon. The differential emission yields are divided by q_P^2. Top: numerical simulation (Beuve et al., 2002) including the carbon KLL Auger emission ("on") and without carbon KLL Auger ("off"). The numerical simulation is based on the Monte Carlo method, therefore, statistical fluctuations naturally arise and can be seen in the spectra. Bottom: experiment (Caron et al., 2001).

strength (given in atomic units) was varied from $q/v_P = 0.065$ (weak perturbation) to $q/v_P = 2$ (strong perturbation). The differential emission yields were divided by q_P^2, since in first-order theory one would expect such a q_P^2 scaling. If no high charge effects were present, the ratio should be constant and equal to one. This is not observed: the shape of these ratios varies with energy, and thus electron spectra depend on q_P. At large electron energy, a q_P^2 scaling law is observed: the

ratios, divided by q_P^2, are approximately equal to unity within the experimental uncertainty. In contrast, at lower energy (below the 1s ionization threshold) a strong deviation from a simple q_P^2 scaling occurs. This high charge effect (reduction of low energy electron yields with respect to a q_P^2 scaling) saturates with increasing q_P: the ratios of low energy electron yields divided by q_P^2 decrease with q_P and approach a constant saturation value.

The experimental results thus show a "reduction effect" with respect to a q_P^2 scaling for low energy electron emission under strong perturbation by heavy projectiles. Such an effect is mainly connected to low energy electron emission, below the K-shell ionization threshold (carbon KLL Auger electron emission, see Figures 2 and 6). In Figure 6, both calculation (top) and experimental data (bottom) are shown. The numerical simulations allow studying the influence of the contribution of carbon KLL Auger electron emission ("Auger on/off"). An important result is that the experimentally observed variation of the ratios can only be qualitatively reproduced by theory if Auger emission is taken into account.

In the present case of high projectile velocities, the saturation cannot be explained in terms of screening of the projectile's charge by polarized target electrons for distant collisions as suggested by Koyama et al. (1986). Reduction effects could rather arise from either (1) specific high charge effects in primary ionization, or (2) collective effects on electron transport in the vicinity of the projectile (Borovsky and Suszcynski, 1991; Benka et al., 1995). The ion creates a positively charged zone in its wake, leading to an attractive track potential which results in an attractive force on the electrons moving away from the ion track. Recent theoretical investigations rather point towards "saturation effects" of ionization cross sections with increasing ion charge (Beuve et al., 2002). This model going beyond first order theory by using a distorted wave approach (CDW-EIS) for the primary ionization allows reproducing qualitatively (but not yet quantitatively) the electron yield reductions (Figure 6). The model takes into account two-center effects (the electron moves in the combined fields of projectile and target nuclei) and can be further amended by taking into account multi-electron effects (Gervais et al., 2003). In particular, modification of the binding energies occurs. This is caused by multiple ionization, a specific feature observed with heavy ions. It can directly be observed in electron spectra, where complete K-shell ionization leads to the appearance of Auger hypersatellite lines.

8. Auger Electrons: Electronic Temperatures

It was observed that ion induced Auger electron lines become broader with increasing projectile charge. Schiwietz et al. (1999) suggested that this broadening

of Auger lines could be due to increasing "electronic temperatures" of valence electrons. The width of the Auger lines is connected to the energy width of the occupied density of states at the time of the Auger decay. It is possible to deduce the mean "electronic temperature" of the target for the corresponding Auger decay time (typically about 10 fs for carbon) from the primary Auger spectra, taking into account instrumental resolution and slowing down of Auger electrons during their transport to the surface by means of a numerical simulation. The "background" consisting of ionization electrons (continuous decrease) and possibly hypersatellite lines is subtracted. The total electron energy distribution $n(\varepsilon, T) = D(\varepsilon) f(\varepsilon, T)$ of the valence electrons is obtained from the convolution of the temperature-dependent Fermi distribution $f(\varepsilon, T)$ and the calculated band structure (density of states) $D(\varepsilon)$. Finally, one can adjust the temperature T of the Fermi–Dirac distribution $f(\varepsilon, T)$ so that the total width (not the FWHM) of the calculated electron energy distribution $n(\varepsilon)$ best fits the measured width of the primary Auger spectrum. This procedure, applied by Caron et al. (2001, 2006), differs from the one used by Schiwietz et al. (1999, 2000), the latter one being based on a comparison to electron induced spectra and fitting of calculated spectra (with temperature T as only free parameter) to the slope of the high-energy side of measured spectra.

The energy width of the primary Auger ΔE spectra increases as a function of the projectile charge: at 9.2 MeV/u, for example, $\Delta E = 42$ eV with C^{6+} and $\Delta E = 50$ eV with Ni^{27+}. In this case, the best fit of the width is obtained at two different temperatures of $T = 11600$ K and $T = 24000$ K, for C and Ni impact, respectively. The measured temperature values can now be compared to the predictions of "thermal spike" numerical simulations. The calculations reproduce the evolution of the temperature with projectile charge, but, depending on the model, may underestimate the temperatures by up to a factor of three. We refer the reader to Schiwietz et al. (2000) and Caron et al. (2006) for detailed discussions of the corresponding thermal spike models and comparison to experiment. The spectroscopy of ion-induced Auger electrons is an experimental method to obtain quantitative information about the onset of the thermal spike. Information about the "track temperature" at later times and its evolution may be accessible via the measurement of the velocity of sputtered and desorbed particles from the surface. We finally note that his method was mainly applied to carbon targets (see Schiwietz et al., 1999, 2000, 2004; Rothard, 2004; Caron et al., 2001, 2006). Also, heavy ion induced Auger electron spectra from other target materials such as Al, Si, Be etc. were analyzed (see Staufenbiel et al., 2005, for a recent summary), but the complexity of the spectra for materials heavier than Be or C renders the interpretation more difficult.

9. Insulators: Charging Effects

Most of the results discussed in the previous chapters were obtained for metallic (conductive) targets or with thin carbon foils. Carbon foils are available in a wide target thickness range and are more or less easy to handle, even as free standing target with sufficient surface area. Metals are also relatively easy to handle and preparation of clean surfaces in ultrahigh vacuum is possible. Therefore, target-specific characteristic features of low energy electron emission (such as plasmon decay and Auger electrons) were intensively studied with metal targets. The Z_T-dependence of electron yields is relatively weak. Also, data about fast electron ejection (convoy- and binary encounter electrons) were obtained with thin metallic foils (e.g. De Filippo et al., 2004). Main dependencies on Z_T stem from the Compton profile which is much larger for high-Z_T targets and which shows up in the width of the binary encounter electron peak, and from the Z_T-dependence of electron capture and loss, which partly determine the convoy electron yield. Also, electron transport and cascade multiplication depend on Z_T. Besides the Z_T-dependence, other target properties such as conductivity or crystalline structure may have a more important influence on electron ejection.

With insulators, a build-up of charge on the target surface occurs, which makes experiments difficult. Therefore, only few experiments were performed with high velocity ions, for example with aluminum oxide Al_2O_3 under standard vacuum conditions (Borovsky and Suszinsky, 1991). Charging has been studied widely for electron beam impact (see e.g. Cazaux, 2006, and references therein), since it is of importance for electron microscopy. Charging phenomena should be even more important for heavy ion beams, because electron yields are much higher for high-Z_P ions than in the case of electron or proton impact. As a main result, electron yields from insulators are higher than those obtained with metals of comparable atomic number. This was often interpreted in terms of a reduced work function and enhanced electron escape depth.

A few studies of electron energy spectra induced by swift (MeV/u) ions were performed. With fast protons beams, a reduction of low energy electron yields with insulators was observed by Burkhard et al. (1987a) as a function of the ion current density. These experiments were performed with amorphous hydrogen loaded (>20 at%) α-C:H targets, which are good insulators in contrast to ordinary conducting carbon foils (with a hydrogen content of typically <1 at%). Furthermore, a shift to lower energies of the convoy electron peak with increasing flux density was observed (Burkhard et al., 1987a). An energy shift of Carbon KLL Auger electrons towards lower energies with respect to Auger emission from carbon foils was observed with polypropylene foils. This was attributed to

the influence of the heavy ion nuclear track potential (Schiwietz et al., 1992). Note that in this latter case, we are dealing with a microscopic effect related to a single track, and not with a macroscopic charging effect. Measurements of particle emission with the ion flux density as parameter may be a means to distinguish between macroscopic and microscopic (track) charging. A shift of the convoy electron peak energy and a "focusing effect" of the charged ion track leading to "nuclear track guiding" of convoy electrons with polymer foils was reported by Xiao et al. (1997). In a quite recent experiment (2005) at GANIL, shifts of the convoy and the binary encounter electron peak with Kr ions at 64 MeV/u traversing mylar foils were observed.

10. Channeling and Emission Statistics

An interesting possibility to probe electron emission in relation to energy loss and charge exchange is ion channeling in crystals (see Cohen and Dauvergne, 2004, and references therein). By comparing electron emission under random impact and channeling conditions, one can study the dependence of electron production on the electron density encountered by the projectile. For well channeled ions, collisions with inner shell target electrons are strongly reduced. Therefore, the energy loss of channeled ions is only about half of that in random direction. These effects lead e.g. to a reduction of convoy electron yields (Breinig et al., 1982) and binary encounter electron ejection (Kudo, 2001). Directional effects do not only occur as far as the projectile interaction is concerned, but also have an influence on electron transport and escape from the surface (Brusilovsky, 1985).

Recently, new interest in electron emission under channeling conditions has arisen. The distribution $P(n)$ (electron emission statistics, which allows to deduce electron yields) was measured in coincidence with the energy loss $\mathrm{d}E/\mathrm{d}x$ and emerging charge states of Pb ions (29 MeV/u) after interaction of the beam with a thin Si crystal. This powerful technique allows observing correlations of forward and backward electron emission and the correlation of electron emission to a particular ion trajectory and corresponding energy loss and charge. A strong reduction of energy loss and electron emission for hyper-channeled ions (which interact mainly with target valence electrons) is observed. Furthermore, enhanced electron emission due to projectiles entering the crystal very close to atomic strings (leading to enhanced energy loss compared to random impact) occurs (Barrué et al., 2004).

The measurement of the multiplicity distribution $P(n)$ was also applied for amorphous targets without directional effects (Kozochina et al., 1993). Here, the electron emission for fixed in- and outgoing ionic charge states (Vidović et al.,

1997), the relation of electron emission and energy loss (Benka et al., 1995) and the correlation of forward and backward emission (Smidts et al., 1999) can be probed. Yamazaki et al. (1993) also measured $P(n)$ and reported a correlation of forward and backward electron emission in collisions of Ar (1.8 MeV/u) with foils as thick as 500 Å, possibly due to plasmon decay taking place all over the target thickness.

11. Other Intriguing Topics: An Open End

Let us now have a look at a choice of topics marking interesting approaches or bearing unsolved questions which therefore could be of interest as directions of future research. Further new horizons appear with experimental techniques allowing a one-ion by one-ion measurement of ejected electrons and multi particle coincidences. Examples are the reaction microscope (Ullrich et al., 2003), which was applied for studying differential multi-electron ejection from heavy ion-solid collisions (Rothard et al., 2007), and the multi-detector ARGOS (Lanzanò et al., 1998), which allows the coincident ejection of two or more electrons (Lanzanò et al., 2003). In a recent experiment, hints for an inelastic binary encounter process with simultaneous target and projectile ionization were found. This particular ionization process with a specific kinematic signature is related to so-called $(e, 2e)$ experiments allowing a stringent test of ionization theories.

Few studies exist on temperature dependence of electron emission (see e.g. Hasselkamp et al., 1991; Benka and Steinbatz, 2003). A problem here, in particular at low temperatures, is surface contamination and the relation to structural phase transitions at the surface (Benka and Steinbatz, 2004; Rothard et al., 1992). Experiments at low temperature with thin layers of frozen gases or biomolecules could be useful for radiobiology (DuBois and Drexler, 1994). Also, electron emission from insulators with microscopic and macroscopic charging phenomena will be of further interest in the future. The measurement of "electronic temperatures" via target Auger electrons from the conduction band might be a tool as probe for the femtosecond dynamics of energy deposition (Schiwietz et al., 2004). For a complete picture of energy deposition in condensed matter, however, we need to go beyond electron spectroscopy. Possibly, measurements of the velocity distribution of neutral and charged particles (secondary ions) from solid surfaces will allow to study the evolution of the "ionic temperature" of the track core at a somewhat later stage (picoseconds) depending on the electron-phonon interaction time.

Electron emission is a relatively stringent test of transport theory and modeling of specific target properties as needed in track structure calculations. However,

for strong perturbation, improved ionization theory is needed (Gervais et al., 2003). As also discussed during ION06, there is still a need for doubly differential electron emission cross sections in particular for applications in radiobiology or radiation chemistry. The microscopic dose distribution is crucial for understanding specific effects connected to light ions and heavy ions (e.g. for hadron-therapy, irradiation of polymers, radiolysis, aerospace applications) as compared to photon or high energy electron irradiation. One reason is that damage of biological tissue as well as material modification in condensed matter can be induced not only by the primary ionization of the target atoms or molecules itself, but also by secondary ionization caused by the fast δ-electrons. Even low energy electrons may be of crucial importance if such effects as electron attachment play a significant role in condensed matter. Probably, multiple ionization and possibly, inner shell Auger electron ejection may play an important role for damage induced by heavy ion beams. These topics are at the present time under vivid discussion. It is important to first study "simple" targets (atoms, small molecules) such as rare gases and then go to more complex targets (biomolecules, clusters, droplets) and finally, surfaces, thin films (or foils) and bulk condensed matter.

Due to the worldwide availability of single stage and tandem Van-de-Graff accelerators, electron ejection was widely studied in the corresponding relatively low projectile energy range of keV/u to 1 MeV/u. Studies at 1–400 MeV/u energies are more scarce because they need large accelerator facilities. However, ultra-relativistic projectiles with energies as high as 6.4 TeV were used by Vane et al. (1993), who studied high energy "knock-on" electrons ($E = 0.6$–12 MeV) from collisions of S ions (200 GeV/u) with target electrons in polypropylene targets. New accelerator facilities such as GSI-FAIR will help to close the gap between such ultra-relativistic projectile and "conventional" energies up to 400 MeV/u as studied up to now.

Acknowledgements

We are indebted to many colleagues who contributed to our involvement in ion beam interaction with matter in general and electron emission in particular. It was interesting to discuss and work with you! With our apologies not to name all of you, we thank as representatives Alexander Clouvas (Thessaloniki) and Gaetano Lanzanò (Catania) and their groups, since important parts of the experimental work presented here was obtained in close collaboration with them. Special thanks are due to our former Ph.D. students Matthias Jung, Michaël Beuve and Michel Caron.

References

Baragiola R.A. (Ed.) (1993): Ionization of Solids by Heavy Particles. NATO ASI Series B, Vol. 306. Plenum Publishing Corporation

Barrué F., Chevallier M., Dauvergne D., Kirsch R., Poizat J.C., Ray C., Adoui L., Cassimi A., Rothard H., Toulemonde M., Cohen C., L'Hoir A., Vernhet D., Demonchy C., Giot L., Mittig W., Pita S., Roussel-Chomaz P. and Billebaud A. (2004): Electron emission induced by fast heavy ions in a thin Silicon crystal. Phys Rev A **70**, 032902

Bechthold U., Ullrich J., Ramm U., Kraft G., Hagmann S., Schultz D.R., Reinhold C.O. and Schmidt-Böcking H. (1998): Binary-encounter electron emission after fast heavy-ion impact on complex rare- and molecular-gas targets. Phys Rev A **58**, 1971–1979

Benka O. and Steinbatz M. (2003): Temperature dependence of the electron and ion induced electron emission yield of Al, Cu and Ag. Nucl Instrum Meth B **201**, 296–404

Benka O., Schinner A., Fink T. and Pfaffenlehner M. (1995): Electron emission yield of Al, Cu, and Au for the impact of swift bare ions. Phys Rev A **52**, 3959–3965

Beuve M., Caron M., Gervais B. and Rothard H. (2000): Charge dependence of electron emission in swift heavy ion collisions with carbon. Phys Rev B **62**, 8818–8823

Beuve M., Caron M., Gervais B., Rothard H., Clouvas A. and Potiriadis C. (2001): Experimental study and Monte Carlo simulation of the correlation between electron emission and stopping power for swift proton impact on amorphous carbon target. Eur Phys J D **15**, 293–300

Beuve M., Caron M., Fainstein P.D., Galassi M., Gervais B., Rivarola R.D. and Rothard H. (2002): Monte Carlo simulation of electron emission induced by swift highly charged ions: Beyond the linear response approximation. Eur Phys J D **21**, 125–135

Borovsky J.E. and Suszcynsky D.M. (1991): Reduction of secondary-electron yields by collective electric fields within metals. Phys Rev A **43**, 1433–1440

Breinig M., Elston S.B., Huldt S., Liljeby L., Vane C.R., Berry S.D., Glass G.A., Schauer M., Sellin I.A., Alton G.D., Datz S., Overbury S., Laubert R. and Suter M. (1982): Experiments concerning electron capture and loss to the continuum and convoy electron production by highly ionized projectiles in the 0.7–8.5 MeV/u range traversing the rare gases, polycrystalline solids, and axial channels in gold. Phys Rev A **25**, 3015–3048

Brice D.K. and Sigmund P. (1980): Secondary electron spectra from dielectric theory. K Dan Vidensk Selsk Mat Fys Medd **40, no. 8**

Brusilovsky B.A. (1985): Directional effects in kinetic ion-electron emission. Vacuum **36**, 595–615

Burgdörfer J. and Gibbons J. (1990): Electron transport in the presence of a Coulomb field. Phys Rev A **42**, 1206–1221

Burgdörfer J., Wang J. and Müller J. (1989): Forward electron production in antimatter-solid collisions. Phys Rev Lett **62**, 1599–1602

Burkhard M., Rothard H., Biedermann C., Kemmler J., Koschar P. and Groeneveld K.O. (1987a): Strong convoy electron yield dependence on surface properties. Nucl Instrum Meth B **24/25**, 143–146

Burkhard M., Rothard H., Biedermann C., Kemmler J., Kroneberger K., Koschar P., Heil O. and Groeneveld K.O. (1987b): Heavy-ion-induced shock electrons from sputter-cleaned solid surfaces. Phys Rev Lett **58**, 1773–1775

Caron M., Rothard H., Beuve M. and Gervais B. (2001): Shape analysis of Auger electron spectra induced by highly charged ion impact on carbon. Phys Scripta T **92**, 281–283

Caron M., Rothard H., Toulemonde M., Beuve M. and Gervais B. (2006): Theoretical and experimental study of electronic temperatures in heavy ion tracks from Auger electron spectra and thermal spike calculations. Nucl Instrum Meth B **245**, 36–46

Cazaux J. (2006): E-induced secondary electron emission yield of insulators and the charging effect. Nucl Instrum Meth B **244**, 307–322

Chung M.S. and Everhart T.E. (1977): Role of plasmon decay in secondary electron emission in the nearly-free-electron metals. Application to aluminium. Phys Rev B **15**, 4699–4715

Clouvas A., Potiriadis C., Rothard H., Hofmann D., Wünsch R., Groeneveld K.O., Katsanos A. and Xenoulis A.C. (1997): Role of projectile electrons in secondary electron emission from solid surfaces under fast ion bombardment. Phys Rev B **55**, 12086–12098

Cohen C. and Dauvergne D. (2004): High energy ion channeling: Principles and typical applications. Nucl Instrum Meth B **225**, 40–71

De Filippo E., Lanzanò G., Rothard H., Volant C., Aiello S., Anzalone A., Arena N., Geraci M., Giustolisi F. and Pagano A. (2004): Fast electron ejection from C, Ni, Ag and Au foils by $^{36}Ar^{18+}$ (95 MeV/u): Measurement of absolute cross sections. Eur Phys J A **21**, 169–174

Devooght J., Dubus A. and Dehaes J.C. (1987): Improved age-diffusion model for low-energy electron transport in solids. I. Theory. Phys Rev B **36**, 5093–5109

Devooght J., Dehaes J.C., Dubus A., Cailler M., Ganachaud J.P., Rösler M. and Brauer W. (1991): Particle Induced Electron Emission I. Springer Tracts in Modern Physics, Vol. 122

Drexler C.G. and DuBois R.D. (1996): Energy- and angle-differential yields of electron emission from thin carbon foils after fast proton impact. Phys Rev A **53**, 1630–1636

DuBois R.D. and Drexler C.G. (1994): Electron emission from fast ion impact on thin metal foils: Implications of these data for development of track structure models. In: Varma M.N. and Chatterjee A. (Eds.), Computational Approaches in Molecular Radiation Biology. Plenum Press, New York, pp 49–63

Dubus A., Dehaes J.C., Ganachaud J.P., Hafni A. and Cailler M. (1993): Monte Carlo evaluation of the influence of the interaction cross sections on the secondary-electron-emission yields from polycrystalline aluminum targets. Phys Rev B **47**, 11056–11073

Echenique P.M., Ritchie R.H. and Brandt W. (1979): Spatial excitation patterns induced by swift ions in condensed matter. Phys Rev B **20**, 2567–2580

Fallavier M. (1996): Secondary electron emission of solids by impact of molecular ions and clusters. Nucl Instrum Meth B **112**, 72–78

Füchtbauer C. (1906a): Über eine von Kanalstrahlen erzeugte Sekundär-Strahlung und über eine Reflexion der Kanalstrahlen. Phys Zeitschr **7, no. 5**, 153–157

Füchtbauer C. (1906b). Über die Geschwindigkeit der von Kanalstrahlen und von Kathodenstrahlen beim Auftreffen auf Metalle erzeugten negativen Strahlen. Phys Zeitschr **7, no. 21**, 748–750

Gervais B., Beuve M., Caron M. and Rothard H. (2003): Saturation effects in highly charged ion interaction with thin carbon foils. Nucl Instrum Meth B **205**, 835–840

Griepenkerl K., Schäfer A. and Greiner W. (1995): Mach schock waves and surface effects in metals. J Phys: Condens Matter **7**, 9465–9473

Hasselkamp D., Hippler S., Scharmann A. and Schmehl T. (1990): Electron emission from clean solid surfaces by fast ions, Ann Phys **47** (7. Folge), 555–567

Hasselkamp D., Rothard H., Groeneveld K.O., Kemmler J., Varga P. and Winter Hp. (1991): Particle Induced Electron Emission II, Springer Tracts in Modern Physics, Vol. 123

Jakubassa-Amundsen D.H.(1997): Relativistic theory for binary encounter electron emission. J Phys B: At Mol Opt Phys **30**, 365–385

Juaristi J.I., Rösler M. and García de Abajo F.J. (1998): Contribution of the excitation of conduction band electrons to the kinetic electron emission induced by slow ions in metals. Phys Rev B **58**, 15838–15846

Jung M., Rothard H., Gervais B., Grandin J.P., Clouvas A. and Wünsch R. (1996): Transport of electrons induced by highly charged Ni (74 MeV/u) and Cu (9.6 MeV/u) ions in carbon: A study of target thickness dependent electron yields. Phys Rev A **54**, 4153–4161

Koyama A., Benka O., Sasa Y. and Uda M.(1986): Energy spectra of secondary electrons from Al induced by heavy-ion impact. Phys Rev B **34**, 8150–8152

Kozochina A.A., Leonas V.B. and Fine V.E. (1993): Statistics of heavy particle-induced electron emission from a foil. In: Baragiola R.A. (Ed.), Ionization of Solids by Heavy Particles. NATO ASI Series B, Vol. 306. Plenum Publishing Corporation, pp 223–237

Kraft G. (2000): Tumor therapy with heavy charged particles. Progr Part Nucl Phys **45**, S473–S544

Kudo H. (2001): Ion-Induced Electron Emission from Crystalline Solids. Springer Tracts in Modern Physics, Vol. 175

Lanzanò G., De Filippo E., Aiello S., Geraci M., Pagano A., Cavallaro Sl., LoPiano F., Pollaco E.C., Volant C., Vuillier S., Beck C., Mahboub D., Nouicer R., Politi G., Rothard H. and Jakubassa-Amundsen D.H. (1998): Fast electron production in atomic collisions induced by 77 A-MeV ^{40}Ar ions studied with a multidetector. Phys Rev A **58**, 3634–3641

Lanzanò G., De Filippo E., Mahboub D., Rothard H., Aiello S., Anzalone A., Cavallaro Sl., Elanique A., Geraci E., Geraci M., Giustolisi F., Pagano A. and Politi G. (1999): Fast electron production at intermediate energies: Evidence for Fermi shuttle acceleration and for deviations from simple relativistic kinematics. Phys Rev Lett **83**, 4518–4521

Lanzanò G., De Filippo E., Anzalone A., Arena N., Geraci M., Giustolisi F., Pagano A., Rothard H. and Volant C. (2003): Recent results on fast intermediate velocity electron production induced by 19+ 45 A.MeV ^{58}Ni highly charged ions on thin solid targets. Nucl Instrum Meth B **205**, 841–846

Lencinas S., Burgdörfer J., Kemmler J., Heil O., Kroneberger K., Keller N., Rothard H. and Groeneveld K.O. (1990): Transport of fast electrons through thin foils. Phys Rev A **41**, 1435–1443

Neelavathi V.N., Ritchie R.H. and Brandt W. (1974): Bound electron states in the wake of swift ions in solids. Phys Rev Lett **33**, 302–305

Neugebauer R., Wünsch R., Jalowy T., Groeneveld K.O., Rothard H., Clouvas A. and Potiriadis C. (1999): Secondary electron emission near the electronic stopping power maximum. Phys Rev B **59**, 11113–11116

Rösler M. and Brauer W. (1981): Theory of secondary electron emission. I. General theory for nearly-free-electron metals. Phys Stat Sol (b) **104**, 161

Rösler M. and Brauer W. (1988): Theory of electron emission from solids by proton and electron bombardment. Phys Stat Sol (b) **148**, 213

Rothard H. (2004): Electron ejection by heavy particles as precursor of track formation in condensed matter. Nucl Instrum Meth B **225**, 27–39

Rothard H., Schosnig M., Kroneberger K. and Groeneveld K.O. (1992): Ion induced electron emission study of high Tc superconductors and phase transitions. Phys Rev B **46**, 11847–11853

Rothard H., Jakubassa-Amundsen D.H. and Billebaud A. (1998a): Solid state effects in binary encounter electron emission from 13.6 MeV/u Ar^{17+} collisions with C, Al, Cu and Au foils. J Phys B: At Mol Opt Phys **31**, 1563–1578

Rothard H., Jung M., Caron M., Grandin J.P., Gervais B., Billebaud A., Clouvas A. and Wünsch R. (1998b): Strong projectile dependent forward/backward asymmetry of electron ejection by swift heavy ions in solids. Phys Rev A **57**, 3660–3664

Rothard H., Lanzanò G., Jakubassa-Amundsen D.H., De Filippo E. and Mahboub D. (2001): Theory and measurement of absolute doubly differential cross sections of binary encounter electron ejection in collisions of swift heavy ions with solids. J Phys B: At Mol Opt Phys **43**, 3261–3274

Rothard H., Lanzanò G., De Filippo E. and Volant C. (2005): Fermi shuttle acceleration in atomic collisions: The case of ion induced electron emission. Nucl Instrum Meth B **230**, 419–425

Rothard H., Moshammer R., Ullrich J., Kollmus H., Mann R., Hagmann S. and Zouros T.J.M. (2007): Differential multi-electron emission induced by swift highly charged gold ions penetrating carbon foils. Nucl Instrum Meth B, to appear

Schäfer W., Stöcker H., Müller B. and Greiner W. (1980): Mach shock electron distributions from solids. Z Phys B **36**, 319–322

Schiwietz G., Biersack J.P., Schneider D., Stolterfoht N., Fink D., Montemayor V. and Skogvall B. (1990): Investigation of δ-electron emission in collisions of highly charged fast Ne projectiles with carbon-foil targets. Phys Rev B **41**, 6262–6271

Schiwietz G., Grande P., Skogvall B., Biersack J.P., Köhrbrück R., Sommer K., Schmoldt A., Goppelt P., Kadar I., Ricz S. and Stettner U. (1992): Influence of nuclear track potentials in insulators on the emission of target Auger electrons. Phys Rev Lett **69**, 628–631

Schiwietz G., Xiao G., Grande P.L., Luderer E., Pazirandeh R. and Stettner U. (1999): Determination of the electron temperature in the thermal spike of amorphous carbon. Europhys Lett **47**, 384–390

Schiwietz G., Xiao G., Luderer E. and Grande P.L. (2000): Auger electrons from ion tracks. Nucl Instrum Meth B **164/165**, 353–364

Schiwietz G., Czerski K., Roth M., Staufenbiel F. and Grande P.L. (2004): Femtosecond dynamics – snapshots of the early ion-track evolution. Nucl Instrum Meth B **226**, 683–704

Schou J. (1980): Transport theory for kinetic emission of secondary electrons from solids. Phys Rev B **22**, 2141–2174

Sigmund P. and Tougaard S. (1981). Electron emission from solids during ion bombardment: Theoretical aspects. In: Taglauer E. and Heiland W. (Eds), Inelastic Particle-Surface Collisions. Springer Series in Chemical Physics, Vol. 17, pp 2–37

Smidts O.F., Dubus A., Vidović Z., Billebaud A., Fallavier M., Kirsch R., Poizat J.C., Remillieux J. and Rösler M. (1999): Theoretical and experimental study of the correlation between forward and backward electron emissions induced by H^0 or H^+ projectiles incident on carbon foils. Nucl Instrum Meth B **157**, 239–245

Sternglass E.J. (1957): Theory of secondary electron emission by high-speed ions. Phys Rev **108**, 1–12

Spohr R. (1990): Ion Tracks and Microtechnology. Friedr. Vieweg & Sohn Verlags GmbH, Braunschweig

Staufenbiel F., Schiwietz G., Czerski K., Roth M. and Grande P.L. (2005): Electronic energy-density effects in ion tracks of metals. Nucl Instrum Meth B **230**, 426–430

Stolterfoht N., (1987): High resolution Auger spectroscopy in energetic ion collisions. Phys Rep **146**, 315–424

Stolterfoht N., Dubois R.D. and Rivarola R.D., (1997): Electron Emission in Heavy-Ion-Atom Collision. Springer Series on Atoms and Plasmas, Vol. 20

Sulik B., Koncz Cs., Tökési K., Orbán A. and Berényi D. (2002): Evidence for Fermi-shuttle ionization in intermediate velocity C^++Xe collisions. Phys Rev Lett **88**, 073201

Sulik B., Stolterfoht N., Hellhammer R., Pésiç Z., Koncz Cs., Tökési K. and Berényi D. (2003): Fermi-shuttle acceleration of electrons in ion–matter interaction. Nucl Instrum Meth B **212**, 33–44

Tougaard S. and Sigmund P. (1982): Influence of elastic and inelastic scattering on energy spectra of electrons emitted from solids. Phys Rev B **25**, 4452–4460

Ullrich J., Moshammer R., Dorn A., Dörner R., Schmidt L.P. and Schmidt-Böcking H. (2003): Recoil-ion and electron momentum spectroscopy: Reaction-microscopes. Rep Prog Phys **66**, 1463–1545

Vane C.R., Datz S., Dittner P.F., Krause H.F., Schuch R., Gao H. and Hutton R. (1993): Knock-on electrons produced in collisions of 6.4 TeV sulfur ions with fixed targets. Nucl Instrum Meth B **79**, 26–29

Vidović Z., Billebaud A., Fallavier M., Kirsch R., Poizat J.C. and Remillieux J. (1997): Backward- and forward-electron-emission measurements for MeV H^0 projectiles incident on thin carbon foils: Correlation with the charge state of the emergent projectile. Phys Rev A **56**, 4807–4814

Yamazaki Y., Kuroki K., Komaki K.J., Andersen L.H., Horsdal-Pedersen E., Hvelplund P., Knudsen H., Moller S.P., Uggerhoj E. and Elsener K. (1990): Measurements of electron spectra in the forward direction in slow antiproton-carbon foil collisions. J Phys Soc of Japan **59**, 2643–2646

Yamazaki Y., Kuroki K., Azuma T., Komaki K., Watanabe H., Kakutani N., Hasegawa T., Sekiguchi M. and Hattori T. (1993): Correlated electron emission from thin carbon foils bombarded by 1.8 MeV/u Ar ions. Phys Rev Lett **70**, 2702–2705

Weng M.S., Schinner A., Sharma A. and Sigmund P. (2006): Primary electron spectra from swift heavy-ion impact: Scaling relations and estimates from modified Bohr theory. Eur Phys J D **39**, 209–221

Willis R.F., Fitton B. and Painter G.S. (1974): Secondary-electron emission spectroscopy and the observation of high-energy excited states in graphite: Theory and experiment. Phys Rev B **9**, 1926–1937

Xiao G., Schiwietz G., Grande P.L., Stolterfoht N., Schmoldt A., Grether M., Kohrbruck R., Spieler A. and Stettner A. (1997): Indications of nuclear-track-guided electrons induced by fast heavy ions in insulators. Phys Rev Lett **79**, 1821–1824

Zäpfel T., Hagmann S., Rothard H., Ullrich J., Kraft G., Schmidt-Böcking H. and Groeneveld K.O. (2002): Experimental study of electron ejection by heavy ion irradiation of solids: Observation of forward and backward emitted electron jets. Nucl Instrum Meth B **193**, 651–655

Recent Advances in Slow Heavy Particle Induced Electron Emission

HP. Winter[1,⋆], F. Aumayr[1], H. Winter[2] and S. Lederer[1]

[1]Institut für Allgemeine Physik, TU Wien, A-1040, Austria
[2]Institut für Physik, Humboldt-Universität zu Berlin, Germany

Abstract

We present recent developments for electron emission induced by impact of slow (projectile velocity $\leq$ 1 a.u. = 2.18×10^6 m/s) atoms, molecules, and singly and multiply charged ions on atomically clean monocrystalline metal and insulator surfaces. We show, in particular, that with grazing incident projectiles on monocrystalline flat surfaces the coincident measurement of projectile energy loss with the number of emitted electrons, the electron yields caused by potential and kinetic emission can be distinguished. Furthermore, for grazing impact of neutral ground state atoms on monocrystalline flat metal surfaces a very precise determination of the small total electron yield near the kinetic emission threshold can be achieved, and the measured yields are in good agreement with a classical model for electron emission from binary collisions of projectiles with quasi-free metal electrons above the target surface. We also present some results on slow molecular projectile non-proportionality effects in kinetic emission. Finally, we mention as two novel applications of KE a surface structure determination based on KE by grazing-incident ions or atoms, and a method for evaluation of mixed ion beam fractions for different ion species with nearly equal charge-to-mass ratios.

Contents

1 General Aspects of Kinetic Emission (KE) and Potential Emission (PE) – Scope of the Present Report **526**
1.1 Kinetic Electron Emission (KE) 526

⋆ E-mail: winter@iap.tuwien.ac.at

1.2 Potential Electron Emission (PE) 528
1.3 Combined Kinetic and Potential Electron Emission 531

2 KE and PE for Grazing Incidence of Slow MCI on Single Crystal Surfaces 532
2.1 Experimental Aspects 532
2.2 MCI Impact at Grazing Incidence on Au(111) 535
2.3 MCI Impact at Grazing Incidence on LiF(001) 538

3 Near-Threshold Studies for KE from Grazing Incidence of Slow Atoms on Single-Crystalline Metal and Insulator Surfaces 540
3.1 Near-Threshold KE Studies for a LiF(001) Surface 541
3.2 Near-Threshold KE Studies for an Al(111) Surface 542

4 Non-Proportionality Effects for Slow Molecular-Ion Induced KE 545

5 Novel Applications of KE and PE 546
5.1 Surface Triangulation by Means of KE from Grazing Incident Atoms . . . 546
5.2 m/q Discrimination for Mixed Multicharged Ion Beams 549

6 Summary and Open Questions 550

Acknowledgements 553

References 553

1. General Aspects of Kinetic Emission (KE) and Potential Emission (PE) – Scope of the Present Report

Processes induced by impact of slow heavy particles on solid surfaces (neutral/ionized atoms or molecules; impact velocity typically far below 1 a.u. = 25 keV/amu = 2.18×10^6 m/s) are highly relevant for plasma- and surface physics and -technology (Hasselkamp, 1992). Nature and intensity of these processes depend both on the kinetic and the potential (i.e. internal) energy carried by the projectile toward the surface.

1.1. Kinetic Electron Emission (KE)

In most practical applications the kinetic energy of a projectile is of higher relevance than the potential energy, as, e.g., for kinetic emission (KE) (Hasselkamp, 1992; Schou, 1988; Rösler and Brauer, 1991; Baragiola, 1993), ion-surface scattering and kinetic sputtering (Sigmund, 1993; Gnaser, 1999). For inducing KE, the projectile needs a minimum velocity or kinetic energy (KE

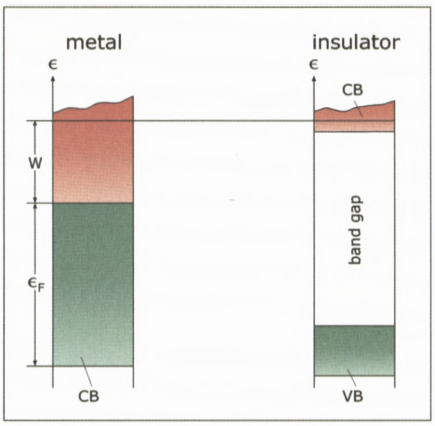

Figure 1. Energy levels for quasi-free electron metal (left) and wide-band gap insulator (right). CB: conduction band (with empty region in red), VB: valence band. Horizontal line: vacuum level, EF: Fermi energy, W: surface work function.

threshold) which depends on the projectile and target species. In general, this KE threshold cannot be clearly identified. Precise determination of the electron yield which disappears at the KE threshold is not a simple task, because common techniques for electron yield measurement involve the electrical currents of impinging projectiles and ejected electrons. The absolute measurement of neutral projectile fluxes requires rather specific methods. Different processes can contribute to KE and their relative importance depends strongly on the given situation.

For normal incidence on metal targets, both the momentum transfer from projectiles onto quasi-free metal electrons and electron promotion into the continuum in close collisions with target atom cores may excite electrons inside the target bulk. In insulator targets there are no quasi-free electrons and KE can then only arise from close projectile-target particle collisions. Figure 1 compares the principally different surface-densities-of-states of a quasi-free electron metal and a wide-band gap insulator surface.

In the present review we deal with recent studies for grazing incidence of neutral atoms and singly and multiply charged atomic ions on exclusively atomically clean metal and insulator surfaces. We discuss related total electron yields derived from measured electron number statistics (ES), without considering energy and angular distributions of the emitted electrons. The considered projectile impact energy is restricted to a few keV/amu (for electron emission induced by faster ions we refer to the review of H. Rothart in this book).

Sections 2 and 3 deal with KE and PE studies for monocrystalline Au(111), Al(111) and LiF(001) surfaces where differences in the surface-density-of-states

play a decisive role. In either case, electrons excited inside the solid diffuse toward the surface and only a fraction of them can escape into vacuum. KE involves at least three steps, i.e. electron excitation in the target bulk, transport of some of these electrons to the surface and passage of a fraction of the originally excited electrons over the solid-vacuum barrier (Hasselkamp, 1992; Rösler and Brauer, 1991). We have restricted ourselves to measurements for PE and KE from *collisions in the surface selvedge* (region at and above the topmost plane of surface atoms). In this case the KE yield depends almost exclusively on the primary excitation mechanism (step 1), and in contrast to the more common near-normal incidence conditions the two other steps for KE are of minor importance.

Grazing incidence conditions permit a fine tuning of the distance of closest projectile approach toward the surface, corresponding to an impact parameter selection in atomic collisions. Combined with the technique of electron emission statistics (ES, see Section 2) this opens the possibility for KE measurements with a so far not achieved sensitivity and accuracy, being of foremost importance for near-KE threshold studies.

In addition to their kinetic energy, singly and multiply charged ions (MCI) Z^{q+} also carry the potential energy which had to be spent for removing the respective number of electron(s) from the initially neutral atom. The same potential energy will be released if the charged projectiles are neutralized upon impact on the surface, giving rise to (additional) potential electron emission (PE) (Baragiola, 1993; Hagstrum, 1954a, 1954b; Arnau et al., 1997; Winter, 2002); see also Figure 2. Apart from producing PE, the potential ion energy causes for some materials desorption of near-surface particles ("potential sputtering") (Neidhart et al., 1995; Sporn et al., 1997; Aumayr and Winter, 2004).

1.2. Potential Electron Emission (PE)

PE results from fast electronic transitions (rates $\geq 10^{14}$ s^{-1}) between surface and empty projectile states, which require no minimum impact velocity and start before the ion has actually touched the surface (Hagstrum, 1954a, 1954b). The PE yield increases strongly with the projectile potential energy, i.e. its charge state q. At higher impact velocity also KE will produce slow electrons which cannot simply be distinguished from the PE contribution. Various one- and two-electron transitions can be relevant for PE.

Resonant neutralization transfers electrons into empty states of the ion which overlap occupied surface valence band states. For MCI impact sequential resonance neutralization generates multiply-excited particles (Arifov et al., 1973) termed "hollow atoms" (Briand et al., 1990).

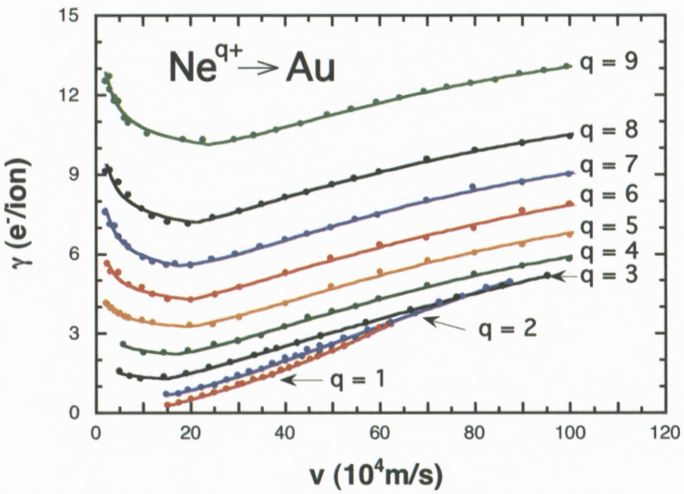

Figure 2. Total electron yields γ *versus* ion velocity v measured for impact of singly and multiply charged Ne ions on atomically clean polycrystalline gold (Eder et al., 1999). Observed electron yields result from KE (yield increases monotonically with impact velocity from the threshold on) and PE (respective yield increases with ion charge state but slightly decreases with impact energy).

Resonant ionization as the inverse process to resonance neutralization transfers electrons from projectile states into empty states with binding energy below the surface work function W.

Auger neutralization (sometimes named *Auger capture*) can give rise to electron ejection from the surface valence band if the available potential energy exceeds twice the surface work function W. One electron is captured by the ion and another one ejected with a kinetic energy defined by the common energy balance. The electron energy distribution corresponds to the self-convolution of the surface-electronic-density-of-states.

Auger de-excitation of projectiles can take place if after resonance or Auger neutralization their excitation energy is still larger than W. Excited projectile electrons interact with target electrons and the latter are ejected and the former demoted, or other target electrons are captured into the projectile and originally excited electron of the projectile ejected. In contrast to Auger neutralization, electron energy distributions resulting from Auger de-excitation are directly correlated with the surface-density-of states.

By incorporating these different electronic transitions into an adiabatic model (no coupling between electronic and nuclear motion), the total slow electron yield can be calculated (Hagstrum, 1954a, 1954b, 1956). Transition rates increase exponentially with decreasing ion-surface distance, according to the overlap between

the surface-density-of-states and the projectile-based electronic wave functions. Consequently, these transitions start most probably from the Fermi edge of the surface-density-of-states. Assuming transition probabilities as independent of the impact velocity, neutralization of singly charged ions occurs most probably at a distance of a few Angstroms. Neutralization of an MCI Z^{q+} can, however, already start at a considerably larger distance which increases with the charge state q (see below). MCI may capture a sizeable number of electrons from the surface within a rather short time (typically about ten fs), which will give rise to *autoionization* of the transiently multiply-excited particles. Here, one or more electrons are ejected into vacuum, while other projectile electrons are demoted into lower lying states. Projectile autoionization was first observed for transiently formed doubly-excited atoms in the surface impact of He^{2+} or metastable He^{+} (Hagstrum and Becker, 1973). Electron energy distributions resulting from autoionization are not related to the target surface-density-of-states.

Quasi-resonant neutralization is a near-resonant transition between target- and projectile core states which can only occur in close collisions by a strong overlap of the inner electronic orbitals. This process may occur in the late stage of MCI neutralization in the bulk.

Radiative de-excitation of excited projectile states formed by resonance of Auger neutralization of singly charged ions is much less probable than Auger de-excitation, since the respective transition rates are orders of magnitude smaller than for Auger transitions. However, the radiative transition rates increase with about the fourth power of the projectile core charge (Bethe and Salpeter, 1957), whereas the Auger transition rates are not strongly affected by electron-core interaction. Therefore, in the final steps of the MCI de-excitation which involve the recombination of inner-shell vacancies, apart from Auger electron emission also soft X-ray emission can become probable (see below).

Based on the above concepts our present understanding of MCI-surface interaction has been sketched in Figure 3. Neutralization of MCI starts by forming transient multiple-excited species which carry empty inner shells and have thus been called a "Hollow Atom". This name was first used (Briand et al., 1990) for explaining the projectile-characteristic soft X-ray emission observed in the surface impact of MCI. The X-rays are produced in the late stage of the hollow-atom decay inside the target bulk, whereas most of the slow electrons will be emitted already before the hollow atom has touched the surface (Arnau et al., 1997). In this way a MCI extracts a number of electrons from the surface and eventually becomes neutral. During this neutralization, slow electrons are emitted via autoionzation. Eventually, the full MCI potential energy will be deposited during a rather short time (typically less than hundred femtoseconds) within a very small

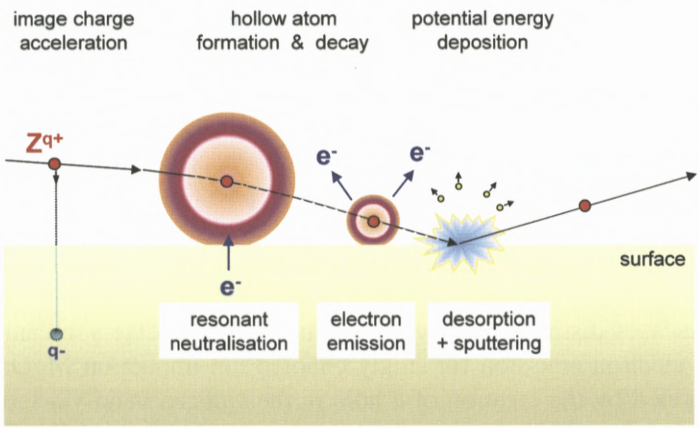

Figure 3. Schematic characterization of neutralization steps for a slow MCI approaching a surface, with formation of a hollow atom, its decay and possible KE (Winter and Aumayr, 2002).

area (typically one nm squared). This neutralization sequence can be explained by the so-called "classical over-the-barrier model" (Burgdörfer et al., 1991). If the hollow atom gets closer to the surface, it will become screened by target electrons which further accelerates its neutralization and de-excitation sequence.

Desorption and potential sputtering (Neidhart et al., 1995; Sporn et al., 1997; Aumayr and Winter, 2004) do only occur for certain insulator materials and gas-covered surfaces.

Once inside the solid, the so far remained inner shell vacancies in the strongly screened hollow atom will now also be filled, which gives rise to emission of projectile-characteristic fast Auger electrons and/or soft X-rays (see above), depending on the respective fluorescence yield. The different projectile recombination- and relaxation processes cannot be easily distinguished from each other, since some of the fast Auger electron emission may already occur before close surface contact and slow electron emission can continue after penetration of the surface. However, the slow electrons carry the information about the hollow-atom development above and at the target surface, whereas the fast Auger electrons and/or soft X-rays are signatures for the final hollow-atom development below the surface (Arnau et al., 1997).

1.3. Combined Kinetic and Potential Electron Emission

If the ion kinetic energy stays well above the KE threshold (Hasselkamp, 1992), total electron yields will result both from PE and KE, and the relative importance of both contributions will be difficult to distinguish except in the following cases.

(a) For projectile ions with a kinetic energy well below the KE threshold (exclusive PE);
(b) if the potential energy greatly exceeds the kinetic energy (dominant PE);
(c) for neutral ground-state projectiles of any velocity (exclusive KE).

In Section 2 we will demonstrate how for the special case of grazing projectile incidence the coincident measurement of electron emission and projectile energy loss permits separation of PE and KE contributions, even if both are of comparable size.

In some cases distinction between KE and PE is not very meaningful. One example is electron emission for singly charged ion impact on MgO, which has been interpreted by the creation of a hole in the valence band via resonant electron capture, followed by Auger neutralization of this hole (PE related effect) (Matulevich and Zeijlmans van Emmichoven, 2004). An alternative explanation involves production of a surface exciton via electron promotion in collisions with O^- target ions (a kinetic effect) followed by autoionization of the exciton (an Auger-type effect) (Riccardi et al., 2004).

Another effect concerns the excitation of plasmons. Sufficiently fast particles (electrons, ions) can excite plasmons in a solid (Raether, 1988). Another plasmon excitation process has recently been observed for slow ion impact on metal surfaces (Baragiola and Dukes, 1996; Stolterfoht et al., 1998).

For this to occur, either the ion potential energy needs to be sufficiently high ("potential excitation of plasmons"), or it proceeds as a secondary process which is caused by fast electrons from KE. Clear signature for plasmon excitation is the subsequent one-electron decay with a characteristic feature in the electron energy distribution (Raether, 1988; Baragiola and Dukes, 1996; Stolterfoht et al., 1998; Eder et al., 2001). Slow-ion induced plasmons can therefore result from the potential and/or the kinetic projectile energy.

2. KE and PE for Grazing Incidence of Slow MCI on Single Crystal Surfaces

2.1. Experimental Aspects

The total electron yield γ (mean number of electrons emitted for single projectile impacts) from KE and/or PE is usually determined from the fluxes of projectiles I_p and emitted electrons $I_e = \gamma \cdot I_p/q$ ("current measurement"; see Hasselkamp, 1992). For charged projectiles this can be simply accomplished by the measurement of target currents for different target bias (with and without electrons leaving

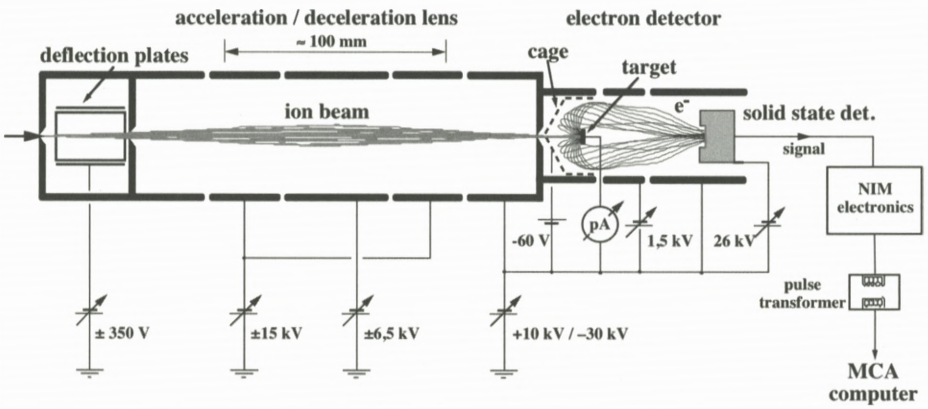

Figure 4. Experimental setup for measuring the electron number statistics (ES) (Eder et al., 1997).

the surface). Here one must avoid possible contributions from charged particle reflection, secondary ion emission and spurious electron production by reflected or scattered projectiles or electrons. Primary ion currents should be at least in the nA range which can become a problem for highly charged ions. Neutral projectile fluxes can either be determined via KE if the respective yield is already known, or by means of sensitive calorimetry with a bolometer.

Another very useful method for total electron yield measurements utilizes the electron number statistics (ES), i.e. the probability distribution W_n for ejection of $1, 2, \ldots, n$ electrons per incident projectile. From this ES the total electron yield γ is simply obtained as the first moment of the W_n distribution, if the probability W_0 for no electron emission is also known (see below; Lakits et al., 1989a; Aumayr et al., 1991; Kurz et al., 1992, 1993; Eder et al., 1997). Figure 4 shows a setup for ES measurements for near-normal particle incidence. Incoming ions are brought to the desired impact energy by a four-cylinder lens before hitting the target surface, but their lowest achievable impact energy is determined by image charge acceleration toward the surface (Aumayr et al., 1993a; Winter et al., 1993). Electrons ejected from the target with an energy below about 50 eV into the full 2π solid angle are back-bent by a highly transparent (96%) conical electrode and accelerated toward a surface barrier detector at 20 kV with respect to the target. The probability W_0 that no electron is emitted cannot be directly measured but becomes practically negligible for $\gamma \geq 3$. However, for small electron yields W_0 is the dominant ES component, and without its knowledge no accurate determination of γ by the ES technique is possible.

In Sections 2.2, 2.3 and 3 below we describe ES measurements in coincidence with grazing scattered projectiles, which permit a straightforward evaluation of

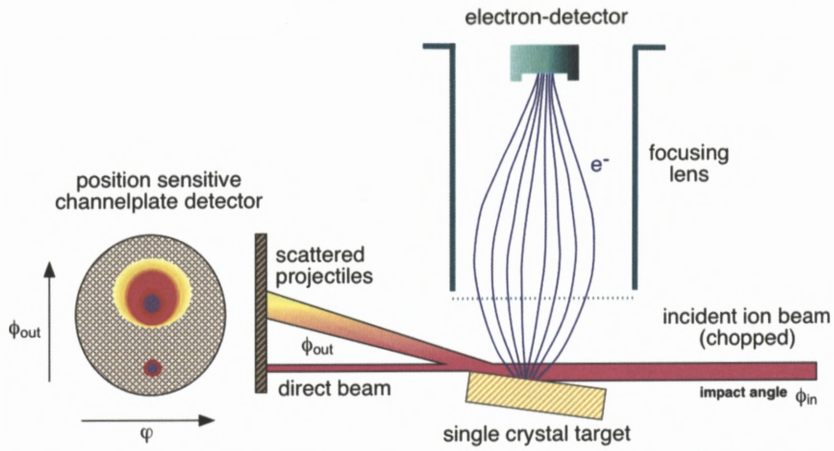

Figure 5. Experimental setup (schematic) for measuring electron number stastistics (ES) in coincidence with scattered projectiles for grazing incidence of slow MCI on a monocrystalline flat target surface (Lemell et al., 1998; Lemell et al., 1999).

W_0 and therewith the precise measurement of very small electron yields. As two other attractive features, the ES technique is also applicable for neutral projectiles and it requires only very small projectile flux (less than 10^4 projectiles/s), which avoids the disturbing charge-up of insulator surfaces (Vana et al., 1995a, 1995b). Apart from its application for measuring γ, the ES are of interest in their own, as they give information on the total number of electrons involved in the particular emission process, and on the related mean single electron emission probability. These two parameters differ significantly for KE and PE processes (Lemell et al., 1995, 1996a; Vana et al., 1995c).

For determination of the relative importance of PE and KE we have performed measurements with slow MCI impinging under a grazing angle of incidence on atomically clean flat monocrystalline target surfaces. In this particular scattering geometry the projectiles interact with the surface along well-defined trajectories (surface channeling; see Winter, 2002). Rather detailed information can be obtained if the electron emission is measured in coincidence with the angular distribution of scattered projectiles (Lemell et al., 1998, 1999), and further insight can be gained if the energy loss of scattered projectiles is also taken into account (Stöckl et al., 2004).

Figure 5 schematically shows a setup by which the energy- and angular distributions of projectiles scattered under grazing incidence from a flat monocrystalline target surface can be observed in coincidence with the ES of ejected electrons. In such a situation neutral scattered projectiles are usually more abundant than

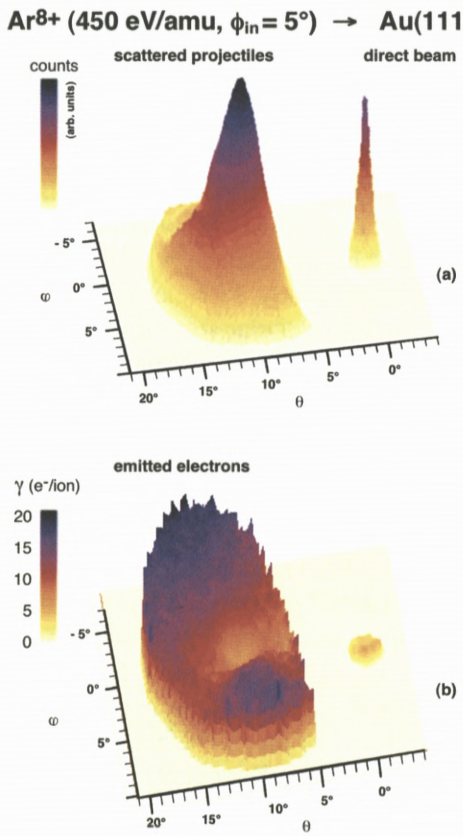

Figure 6. Top: Intensity distribution of scattered projectiles recorded with a position sensitive detector for 0.45 keV/amu Ar^{8+} ions impinging under a grazing angle $\phi_{in} = 5°$ onto a clean Au(111) surface (Lemell et al., 1998). *Bottom*: Mean number of emitted electrons measured in coincidence with projectiles scattered into different exit angles (positions corresponding to the top of figure).

charged ones. Kinetic energy distributions of both neutral and charged particles can be determined by means of time-of-flight (TOF) techniques which require a well-defined time structure (short pulsing) of the projectile beam.

2.2. MCI Impact at Grazing Incidence on Au(111)

Coincidence measurements beween ES and scattered projectiles have been performed for grazing impact of slow MCI on clean monocrystalline Au(111) with an experimental setup sketched in Figure 5 (Lemell et al., 1999; Stöckl et al., 2004). Figure 6 shows the intensity distribution of scattered projectiles recorded with a

position sensitive detector for 0.45 keV/amu Ar^{8+} ion impact under an angle of incidence of 5° onto a Au(111) surface (Lemell et al., 1998). The peaked feature on the top right hand side represents a small fraction of the primary ion beam that has passed above the target (see Figure 5), whereas the broad peak results from scattered projectiles. Specularly reflected projectiles contribute to the central peak, while scattering from surface imperfections (e.g. steps) is responsible for the tail of the scattered particles distribution. On the bottom of Figure 6 one sees the mean number of electrons emitted in coincidence with different parts of the angular distribution shown on top. Apparently, less electrons are emitted for specularly reflected projectiles than for non-specular scattering.

In Figure 7 we show the ES from these measurements. The upper panel depicts "non-coincident ES" resulting from all impinging projectiles without selection. "Coincident ES" are obtained in coincidence with projectiles for the complete scattering distribution shown in the top part of Figure 6. From the difference we see that a considerable fraction of the projectiles has not been specularly scattered and apparently produced a comparably higher electron yield.

In the center of Figure 7 ES labelled (1) results from truly specularly reflected projectiles into the central peak in the top part of Figure 6. ES labelled (2) was measured coincidently for projectiles scattered out of the specular direction into the tail shown in the top part of Figure 6. ES(2) clearly gives a higher electron yield than ES(1) [40]. Finally, in the bottom part of Figure 7 an ES is shown for Ar^{8+} impact under normal incidence on polycrystalline Au with a total impact energy of 2.5 eV/amu (Kurz et al., 1992), which is comparable to the 3.4 eV/amu kinetic energy component normal to the surface for grazing incidence of 450 eV/amu projectiles at 5o with respect to the surface. Since 100 eV (2.5 eV/amu) Ar projectiles ($v = 2.2 \times 10^4$ m/s) can hardly produce any KE, the ES shown in the bottom part of Figure 7 results exclusively from PE by Ar^{8+} ions which release a total potential energy of about 600 eV upon their surface impact. The similarity of this ES and the one labeled (1) in the center of Figure 7 proves that specular scattering from a metal surface produces approximately the same PE yield as the same ions if impinging perpendicular with an energy comparable to the surface-normal impact energy component for grazing incidence. ES(1) can therefore be related to PE from projectiles which approach the top-most surface layer not closer than about 1 a.u. Another conclusion from this observation is that the PE contribution from hollow-atom relaxation above a metal surface only depends on the respective perpendicular impact velocity component.

We remark that the tail toward higher eletron numbers in ES(1) (center of Figure 7) results from projectiles which have produced KE on some surface steps and were then just randomly scattered into the specular direction.

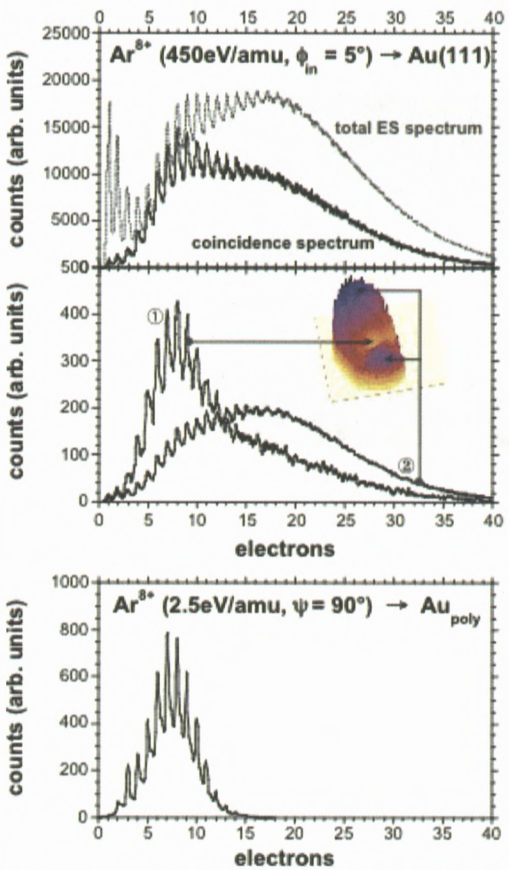

Figure 7. Top: ES for 0.45 keV/amu Ar^{8+} ions impinging under a grazing angle $\phi_{in} = 5°$ onto a Au(111) surface, measured non-coincidently and in coincidence with all scattered projectiles (Lemell et al., 1998), respectively. *Center*: ES for 0.45 keV/amu Ar^{8+} ion impact under a grazing angle $\phi_{in} = 5°$ onto a Au(111) surface, measured in coincidence with the central part (1) and the wings (2) of the projectile scattering distribution shown on top of Figure 6, respectively. *Bottom*: ES for 2.5 eV/amu normal incidence of Ar^{8+} on polycrystalline Au (Kurz et al., 1992).

In this context we note that for grazing scattering of MCI on flat surfaces the entrance angle of the MCI and therefore also the exit angle of specularly reflected neutralized projectiles are increased by the image charge attraction on the incoming trajectory (Aumayr et al., 1993a; Lemell et al., 1996b; Meyer et al., 1995; Winter, 1992). For example, near a Au surface (work function $W = 5.1$ eV) Ar^{8+} ions gain about 30 Ev, which is a considerable fraction of their initial perpendicular energy of about 140 eV in the above discussed case. For

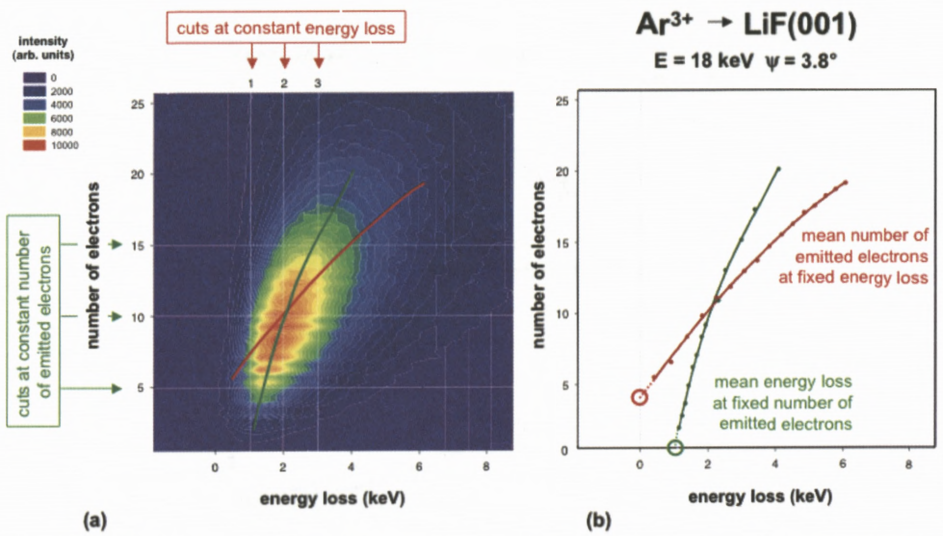

Figure 8. (a) Coincidence spectra of the number of emitted electrons *versus* projectile energy loss for 18 keV Ar^{3+} impact on a LiF(001) surface (angle of incidence 3.8°) (Stöckl et al., 2004). Red and green curves as explained in (b). (b) Cuts through these coincidence spectra at constant mean energy loss (red curve) provide the related mean number of emitted electrons, and cuts for a given mean number of emitted electrons (green curve) provide the related mean energy loss. The two curves have been extrapolated to zero energy loss and zero number of emitted electrons (red and green circle), respectively (for further explanations, see text).

higher ion charge states the increasingingly stronger image charge acceleration will eventually prohibit access to the grazing incidence regime. Secondly, faster grazing incident projectiles can produce KE by elastic collisions with quasi-free electrons above the surface (see Section 3). However, in the here discussed case the Ar ions with about 0.1 a.u. velocity give rise to a KE yield of less than 2% (Kurz et al., 1992), which is negligible in comparison to the resulting PE yield.

2.3. MCI Impact at Grazing Incidence on LiF(001)

We now consider a case where the PE and KE yields are of comparable importance. In order to separate these KE and PE contributions, we use the close relationship between KE and the inelastic energy loss of scattered projectiles (see Section 3). For grazing incidence conditions and with a time-of-flight (TOF) unit added to the setup shown in Figure 5 we have performed ES measurements in coincidence with the projectile energy loss (Stöckl et al., 2004). Figure 8 depicts a correlation of the mean number of emitted electrons with the projectile energy loss. Extrapolation of the resulting curve to the hypothetical case of projectiles

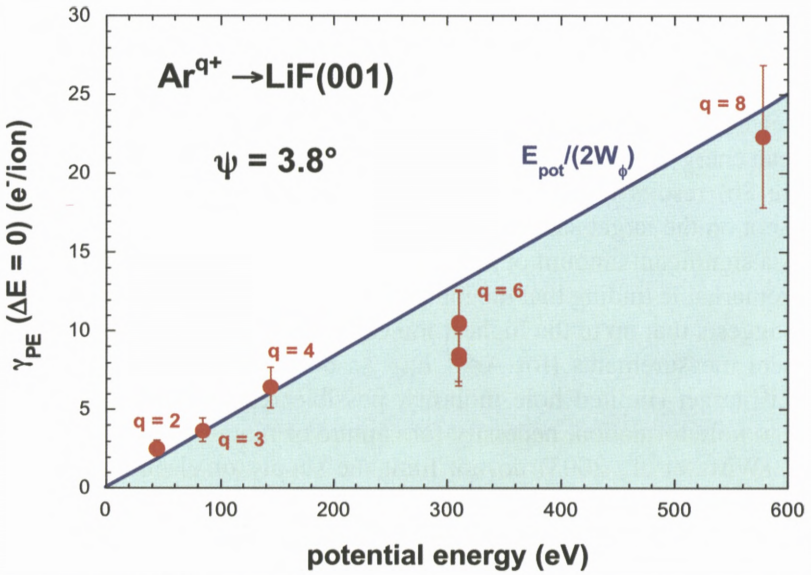

Figure 9. "Pure" PE yields *versus* MCI potential energy (data points) for grazing impact of Ar^{q+} (angle of incidence $\psi = 3.8°$) compared with theoretical limitation by potential energy conservation (solid line) (Stöckl et al., 2004).

without energy loss (red circle in Figure 8; not directly accessible in our experiment) leads to an electron emission yield which is not accompanied by a kinetic energy loss ΔE of the projectile (Stöckl et al., 2004). Therefore, this extrapolated electron yield could only result from the projectile potential energy Epot as a "pure" potential electron emission yield γ_{PE} ($\Delta E \rightarrow 0$). Plotting this extrapolated data for different Ar^{q+} projectiles as a function of the related potential energy supports our interpretation quite convincingly. As shown in Figure 9, we find a linear relationship between this "pure" PE yield and the potential energy carried by different MCI towards the surface. There is no dependence on the kinetic projectile energy which has been varied between 18 and 54 keV (Stöckl et al., 2004). Most notably, the data points are close to the limit of potential energy conservation (solid line in Figure 9). Auger processes resulting in PE (see Section 1) require a potential energy of at least twice the minimum electronic binding energy W at the surface (corresponding to the work function of metal targets). The maximum possible number of electrons emitted via PE is therefore given by $n_{max} = E_{pot}/2W$. This number of PE electrons is indeed evaluated from our extrapolated data, taking into account a binding energy of about 12 eV (Ochs et al., 1997) for the highest occupied states in the $F^-(2p)$ valance band of LiF (solid line in Figure 9).

Here we have assumed 100% probability for electron escape from the surface. This assumption seems not unreasonable considering the large band gap of LiF(001) which extends above the vacuum energy and thus blocks the absorption of slow electrons inside the solid. We also remark that the extrapolated relatively large mean energy loss of 1 keV correlated with no electron emission (green circle in Figure 8b) results from the relatively small distance of 13 cm between the impact spot on the target surface and the projectile detector, which therefore also registers a significant amount of scattering events from deeper surface layers.

Our remarkable finding that the ion potential energy is utilized by almost 100% for PE suggests that up to the highest ion charge state/potential energy applied in the present measurements (for Ar^{8+} $E_{pot} \approx 600$ eV), the electronic properties of the LiF target (limited hole mobility, possible reduction of electron capture rate due to hole formation, necessity for capture of more tightly bound electrons, see, e.g., Wirtz et al., 2003) do not limit the supply of electrons for complete neutralization and de-excitation within the given short surface interaction time.

In particular, the PE yields observed for grazing Ar^{q+} impact are by more than a factor of two larger than earlier measured for normal incidence of Ar^{q+} on polycrystalline LiF (Vana et al., 1995b). In grazing collisions the projectiles interact with many different F^- sites over a relatively long way. On the other hand, for normal impact the rates for electron capture from neighboring sites are considerably (typically one order of magnitude) smaller than for capture from the F^- ion closest to the projectile impact site, and multiple capture from a single site would also involve more tightly bound electrons (Wirtz et al., 2003). Our present findings are consistent with image charge acceleration measurements for grazing scattering of MCI on a monocrystalline LiF surface (Auth et al., 1995), from which result a complete projectile neutralization along the particle trajectory can be concluded.

Since surface-channeled projectiles interact with the surface along well defined and calculable trajectories (Winter, 2002), the here presented technique allows, at least in principle, investigations of the PE yield as a function of the closest distance of projectile approach toward the surface, which also permits studies of distance dependent Auger transition rates (Hecht et al., 1997; Monreal et al., 2003; Bandurin et al., 2004).

3. Near-Threshold Studies for KE from Grazing Incidence of Slow Atoms on Single-Crystalline Metal and Insulator Surfaces

For these measurements fast neutral atoms have been produced by passing the respective singly charged ions through a gas-filled charge-exchange cell and suf-

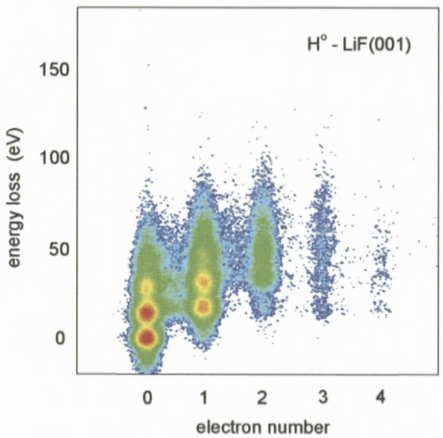

Figure 10. Raw data for projectile time-of-flight *versus* electron number for 1 keV H^0 impact on LiF(001) at $\phi_{in} = 1.8°$ (colour code indicates from blue to red increasing relative intensities; Winter et al., 2002).

ficiently close collimation. With similar techniques as described in Section 2.3, coincident measurements of electron number statistics (ES) with projectile time-of-flight have been performed for grazing scattering of neutral ground state hydrogen atoms (avoiding any PE) on LiF(001) (Winter et al., 2002), and of neutral ground state hydrogen and noble gas atoms on Al(111) (Lederer et al., 2003). This permitted precise measurements down to very small electron yields ($\leq 10^{-4}$ electrons per projectile) and also projectile energy loss measurements without electron emission, as necessary near the KE threshold.

3.1. Near-Threshold KE Studies for a LiF(001) Surface

Figure 10 shows a 2D plot of raw data for ES *versus* projectile time-of-flight (TOF) for grazing impact of 1 keV H^0 on LiF(001) (Winter et al., 2002). Events without electron emission (left column) belong to elastically scattered projectiles (lowest mark) or to a different number of discrete energy losses of 12 eV each, which are related to excitation of the corresponding number of surface excitons (Roncin et al., 1999). One- and more electron emission events (other columns) can be accompanied by production of no or of different numbers of excitons.

Figure 11 shows the electron yield and fractions of excitons and negative ions after H^0 scattering under $\phi_{in} = 1.8°$ with different impact energies. Scattered negative ions have been registered with biased electric field plates and a second particle detector (Mertens et al., 2002).

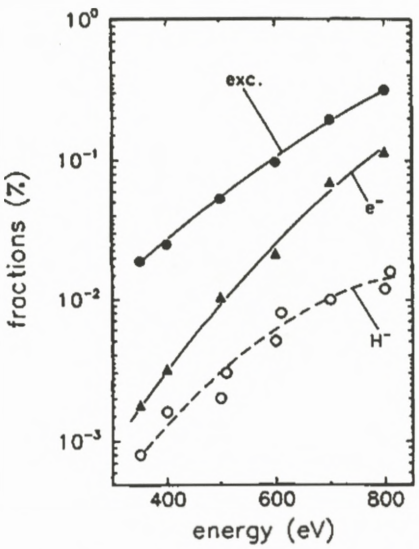

Figure 11. Fraction of excitons (full circles), electrons (full triangles) and H^- ions (open circles) *versus* impact energy, for scattering of H^0 atoms under $\phi_{in} = 1.8°$ from LiF(001) (Mertens et al., 2002).

Interpretation of these results involves the binary collision of H^0 atoms with F^- ions at LiF crystal lattice sites (Winter et al., 2002; Roncin et al., 1999; Mertens et al., 2002). In such collisions an electron can be captured from an F^- ion into a negative hydrogen state which then is shifted to a crossing with a F^{-*} surface exciton state at about 2 eV below the vacuum level. At this crossing the electron may either be recaptured for forming a surface exciton, or the negative ion prevails and acts as precursor for electron emission by detachment at the surface, or it can survive the scattering event. For grazing scattering on LiF(001) the projectile energy loss is exclusively caused by discrete contributions for exciton production (about 12 eV each) and/or negative ion formation which primarily ends up in electron detachment (about 14 eV). Toward higher impact energy the discrete energy losses gradually change into quasi-continua which however still constitute a relatively small part of the total projectile energy.

3.2. Near-Threshold KE Studies for an Al(111) Surface

The situation is rather different for a quasi-free electron metal surface such as Al(111). Figure 12 shows measured projectile energy loss distributions for emission of no and of one electron (Lederer et al., 2003). In striking contrast to

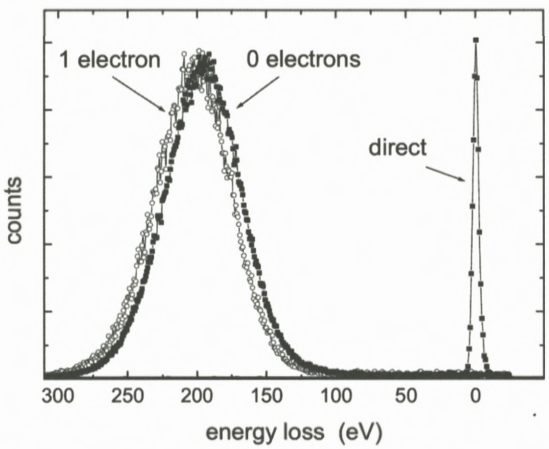

Figure 12. Energy loss spectra for emission of no (full circles) and one (open circles) electron from scattering of 1.5 keV H^0 atoms at $\phi_{in} = 1.88°$ on an Al(111) surface (Lederer et al., 2003).

scattering from LiF(001), for the metal surface the projectile mean energy loss is considerably larger but not strongly different for cases without or with emission of electrons. Apparently, most of the projectile energy loss results from friction in the quasi-free electron gas in the solid, a situation not applicable for an insulator.

The fact that without electron emission a much larger mean projectile energy loss is found for scattering from Al(111) than from LiF(001) (see Figure 10) can be satisfactorily explained with a simple classical model for binary elastic collisions of the projectile in the quasi-free electron gas at the selvedge above the Al(111) surface (Winter and Winter, 2003). The maximum velocity of electrons here is the Fermi velocity v_F which depends on the electron density. The majority of collisions takes place at a relatively large distance from the surface (typically some a.u.) and therefore results only in small projectile energy transfers which, however, for an appreciably large number of collisions along the projectile trajectory add up to the here observed total energy loss. The KE threshold velocity

$$v_{th} = \frac{v_F}{2}\left(\sqrt{1 + W/E_F} - 1\right)$$

for electron emission is reached if the energy transfer in a binary collision is sufficiently large to excite an electron from the Fermi level (EF: Fermi energy) into vacuum (Baragiola et al., 1979). Measurements performed with H^0 and He^0 projectiles agree on a quantitative level with these simple model calculations, both with respect to the KE threshold velocity vth and the dependence of the KE yield on the projectile velocity near vth (see Figure 13).

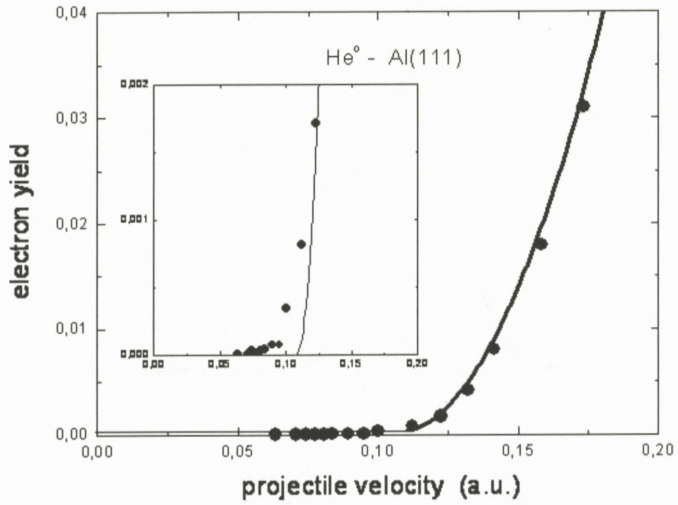

Figure 13. Full circles: Total electron yields *versus* projectile energy for He^0 atoms scattered from Al(111) under $\phi_{in} = 1.88°$. Solid curve: Model calculations as explained in the text (Lederer et al., 2003; Winter and Winter, 2003). Insert: Vertical scale enlarged by a factor of 20, with the small contribution below $v = 0.1$ a.u. presumably caused by scattering events on surface imperfections.

Recently, similar measurements have been conducted for grazing incidence of Ne and Ar atoms on Al(111). They revealed defined but very small KE contributions below the here discussed KE threshold for quasi-free electron metals. Such "subthreshold KE" has recently been explained by higher-momentum components in the local S-DOS as the result from surface corrugation and electron correlation effects (Winter et al., 2005).

Comparing Figure 11 for impact of H^0 on LiF(001) with Figure 13 for He^0 on Al(111) shows a clearly different behaviour of KE yields towards low impact energy. There is a quite well defined threshold for Al(111), whereas for LiF(001) no such clear threshold can be found even at lower impact energy than covered by Figure 11.

For insulators KE can still occur at very low impact energy, despite the generally higher electron binding energy in comparison with metal surfaces. This explains why bombardment of oxidized ("dirty") metal surfaces with slow projectiles gives a higher chance to emit electrons than for atomically clean metal surfaces. However, for non-grazing impact the observed relatively higher electron yields for insulators then for metals are mainly caused by a larger mean free

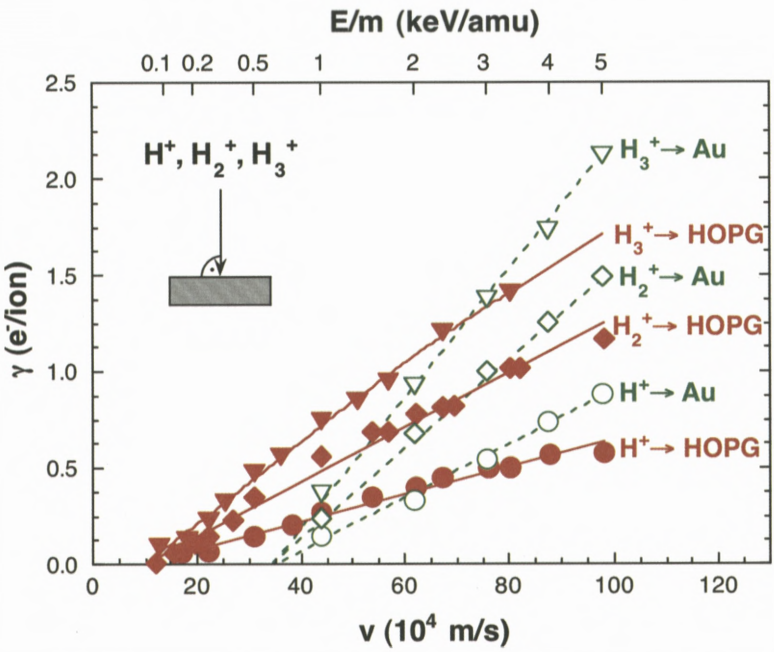

Figure 14. Comparison between total electron yields *versus* impact velocity for normal impact of H^+, H_2^+ and H_3^+ on Au and highly oriented pyrolytic graphite (HOPG) (from Cernusca et al., 2002).

path for inelastic electron collisions (KE step 2) (Hasselkamp, 1992; Schou, 1988; Rösler and Brauer, 1991).

4. Non-Proportionality Effects for Slow Molecular-Ion Induced KE

In the present context we understand as "non-proportionality" or "non-additivity" in KE a discrepancy between the KE yield for a certain molecular projectile and for the sum of KE yields produced by its constituent particles with equal impact velocity. Such effects are generally explained by differences in the projectile ion charge shielding inside the target bulk. The most simple case is KE for H_2^+ and H_3^+ molecular ions in comparison with protons. Figure 14 shows related data for normal impact of H_n^+ ($n = 1, 2, 3$) on gold (Lakits et al., 1989b) and HOPG (highly oriented graphite) (Cernusca et al., 2002). In both cases the measured electron yields are not subject to any PE contribution. Respective KE thresholds are the same for all three projectile ion species, but the KE yields themselves exhibit a clearly apparent non-proportionality. This behaviour has been explained

(Lakits et al., 1989b) by the different number of electron(s) per proton for the three projectile ions, which causes accordingly different shielding of proton(s) inside the solid. In essence, the following simple relation holds at a given impact velocity:

$$\gamma(H_n^+) = \gamma(H^+) + (n-1)\gamma(H^0).$$

This relation permits determination of KE yields for impact of neutral hydrogen atoms (which have actually been measured for a gold surface by means of the ES method; see Lakits et al., 1989b) from the much easier measurable KE yields for charged projectiles. We do not claim, however, that the same relation holds for other chemical species, which would be worthwhile to check.

A rather strong non-proportionality into the other direction has been identified for impact of singly and multiply charged fullerene ions (C_{60}^{q+}) on clean polycrystalline gold. Multicharged C_{60}^{q+} ions do not produce any PE, even if their potential energy becomes sufficiently large (about 22 eV for $q = 4$), since this potential energy is apparently used for enhanced fragmentation upon surface impact (Winter et al., 1997). The KE yield for impact of ground state C^+ ions on Au (no PE) at an impact velocity of 1.2×10^5 m/s is about 0.03 electrons/ion (Eder et al., 1999). At the same impact velocity, a single C_{60}^{q+} ion produces an average of about 9 electrons, corresponding to 0.15 electrons per carbon atom! Measurements for differently charged fullerene fragments down to $n = 15$ showed practically no deviation from the KE yield proportionality with the intact fullerene molecule. It would be of interest to investigate the behaviour of KE yields toward still lower numbers of carbon constituents, in order to explain the reason for this quite huge non-proportionality effect.

5. Novel Applications of KE and PE

5.1. Surface Triangulation by Means of KE from Grazing Incident Atoms

Measurements involving grazing incident projectiles on monocrystalline target surfaces as described in Sections 2 and 3 have been conducted for planar channeling conditions. In this scattering regime the projectile trajectories can be derived from an approximated continuum potential with planar symmetry. This results in specular reflection of projectiles in front of the topmost surface layer, with an energy loss and electron emission as explained above. The scattering conditions are drastically changed if the incident beam is aligned to a low index direction of the crystal lattice. Then the projectiles will be steered along atomic strings

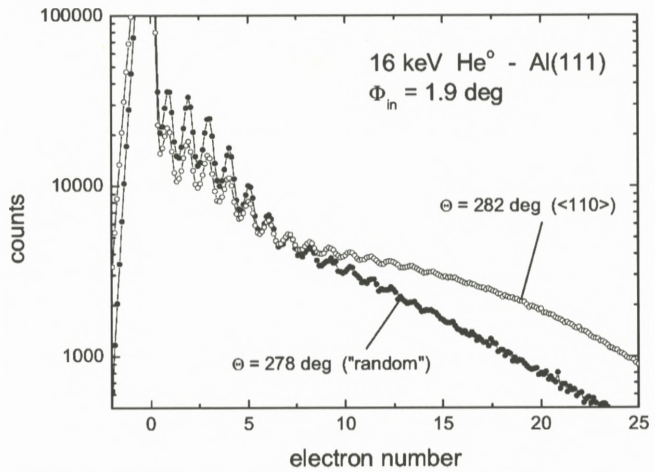

Figure 15. Non-coincident ES for scattering of 16 keV H^0 atoms from Al(111) under $\phi_{in} = 1.9°$, for azimuthal orientation angles of 282° (axial channeling) and 278° (planar scattering), respectively (Winter et al., 2004).

in the surface plane ("axial channeling"), governed by a continuum potential of axial symmetry. In such cases the probability for projectiles to penetrate into the bulk of the target becomes enhanced. Consequently, one expects for transition from planar to axial surface channeling enhanced electron yields, because of a higher chance for trajectories leading into the subsurface region. In Figure 15 we show non-coincident ES for scattering of 16 keV He atoms from Al(111) under $\phi_{in} = 1.9°$ along two different azimuthal directions (Winter et al., 2004). Data for scattering from the target surface along the ⟨110⟩ direction ($\Theta_{in} = 282°$, open circles) reveals a substantial enhancement of events with higher electron numbers, compared to a "random" azimuthal orientation ($\Theta_{in} = 278°$, full circles). This striking difference is interpreted in simple terms by a relatively small fraction of projectiles which under axial surface channeling conditions can enter the subsurface region, resulting in an increase of the total electron yield.

The such enhanced electron yield can also be observed by an increase of the (uncompensated) target current. Low index crystallographic directions can be deduced from this current as a function of the azimuthal orientation of the target surface. This "ion beam triangulation" (Pfandzelter et al., 2003) allows one to investigate the structure of clean surfaces and, in particular, ultrathin films.

Note that the data displayed in Figure 15 do not reveal a shift of ES with low electron numbers, but rather an enhancement for high electron numbers, caused by a small part of projectiles which produce a considerably larger number of

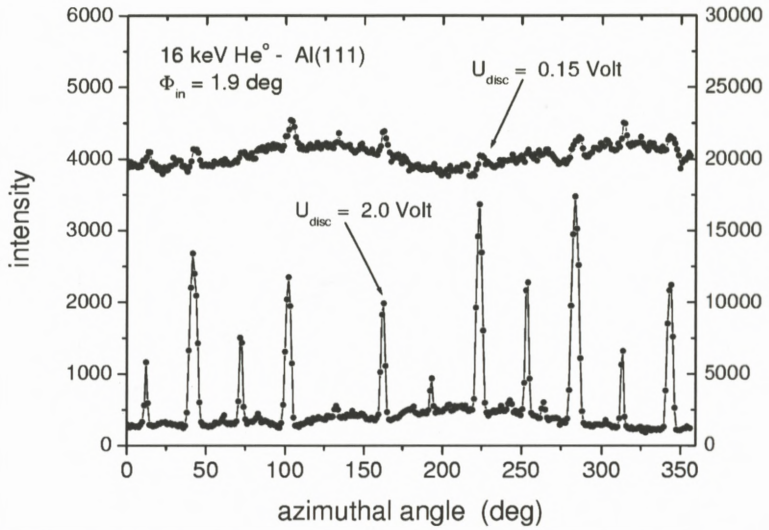

Figure 16. Electron detector count rate as function of azimuthal target angle for scattering of 16 keV He^0 atoms from Al(111) under $\phi_{in} = 1.9°$. Upper curve: discriminator level 0.15 V, lower curve: discriminator level 2.0 V (Winter et al., 2004).

electrons. With ion beam triangulation based on target current measurements, the structure of Co and Mn films epitaxially grown on Cu(001) has been studied. For these systems a variety of complex superstructures is present and, in particular, for the Mn c(12×8) Cu(001) system a new structural model has been derived (Bernhard et al., 2003). If the same method is applied by recording ES instead of the target current, important advantages will be gained. The number of impinging projectiles can be reduced to an extremely low limit of some 1,000 projectiles per second (equivalent to currents of sub-fA), so that even for ultrathin films any damage by the fast projectiles can be excluded. In addition, by selecting emission events with a higher number of electrons (see Figure 15), the "signal to noise ratio" will be substantially enhanced. This was demonstrated in the scattering experiments mentioned above by different settings of the signal discriminator level for the surface barrier detector (Winter et al., 2004). In Figure 16 resulting counts are plotted as function of the azimuthal angle for $U_{disc} = 0.15$ Volt (just above the detector noise level, upper curve) and 2.0 Volt (only detection of events with electron number $n > 9$, lower curve). Recently this new technique was successfully applied to studies on the structure of ultrathin Fe films on Cu(001) (Bernhard et al., 2005).

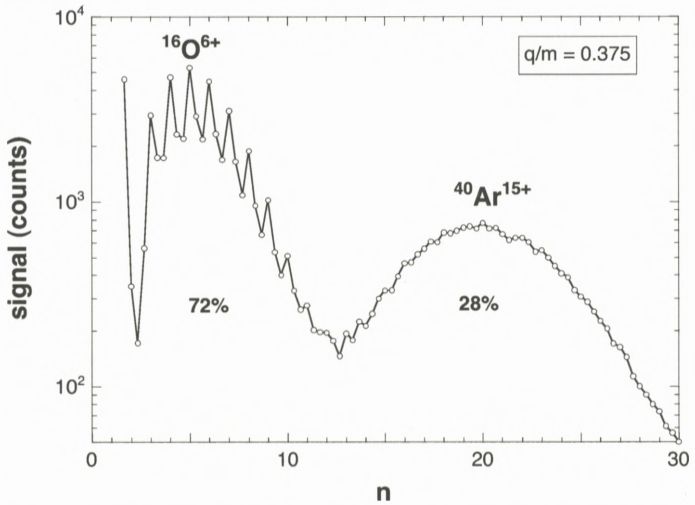

Figure 17. ES for impact of a mixed MCI beam ($^{16}O^{6+}/^{40}Ar^{15+}$) from an electron beam ion trap (EBIT) (Schneider et al., 1991). The fractions of the two ion species can be determined after evaluation of raw ES data (open circles) according to Lakits et al., 1989b and Aumayr et al., 1993b.

5.2. m/q Discrimination for Mixed Multicharged Ion Beams

Ion beams from MCI sources often comprise a mixture of ion species from different elements in different charge states. No standard methodology for ion analysis (electrostatic or magnetic field selectors, time-of-flight measurement) can distinguish between different ion species with (nearly) equal mass to charge (m/q) ratio accelerated by the same potential difference. However, one can utilize surface impact of the ions in question, as soon as they produce strongly different electron emission yields. In this way we could accurately determine the fractions of different ion species with equal q/m in mixed ion beams, both for highly charged atomic ions (different PE yields; see Figure 17 from Aumayr et al., 1993b) and for fullerene ions and their fragments (different KE yields; see Section 4 and Figure 18 from Aumayr et al., 1997).

Recently we have built a simple setup that exploits the strongly different PE yields for highly charged ions extracted from an electron beam ion trap (EBIT) of the distributed "LEIF" (low-energy ion beam facility) infrastructure in Heidelberg (Crespo López-Urrutia, 2003). An ES detector (see Section 2.1) registers short electron pulses which are created from individual ion impacts on a sputter-cleaned single-crystalline gold surface in UHV.

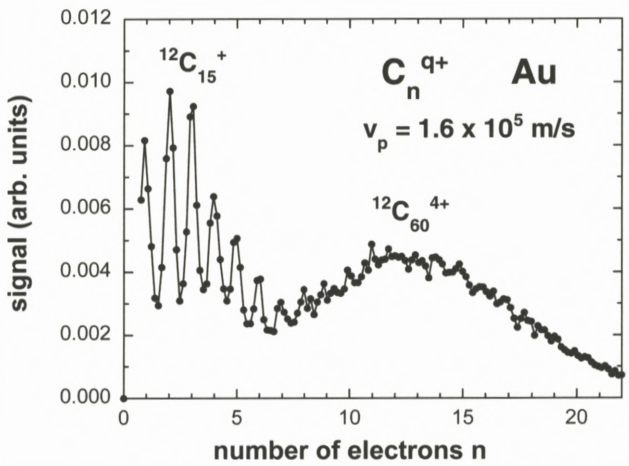

Figure 18. ES for impact of quadruply charged fullerene ions $^{12}C_{60}^{4+}$ and their singly charged fragment ions $^{12}C_{15}^{+}$ (from Aumayr et al., 1997).

The heights of these pulses are directly proportional to the number of ejected electrons. Therefore, the pulse height spectra allow for separation and quantitative analysis of different ion species with equal or nearly equal m/q. We demonstrate the power of this method by characterizing a full scan of the analyzing magnet by correlation of the pulse heights from the ES detector with the analyzing magnetic field strength. The resulting 2-D plot is shown in Figure 19 and allows one to distinguish the here desired $^{129}Xe^{q+}$ ions from various residual gas ions like Ar^{q+}, O^{q+} and N^{q+}, and to identify minute admixtures like W^{q+}, Ba^{q+} and Cu^{q+} (Meissl et al., 2006).

The target crystal was mounted on a manipulator and could easily be retracted after the here described ion identification, in order to allow the MCI beam from the electron beam ion trap to enter an experimental chamber for other measurements of interest.

6. Summary and Open Questions

R.A. Baragiola, one of the pioneers in the field of ion-induced electron emission from solid surfaces, has recently listed the following five "unsolved problems" (Baragiola, 2005):

(a) threshold behavior for heavy ions;

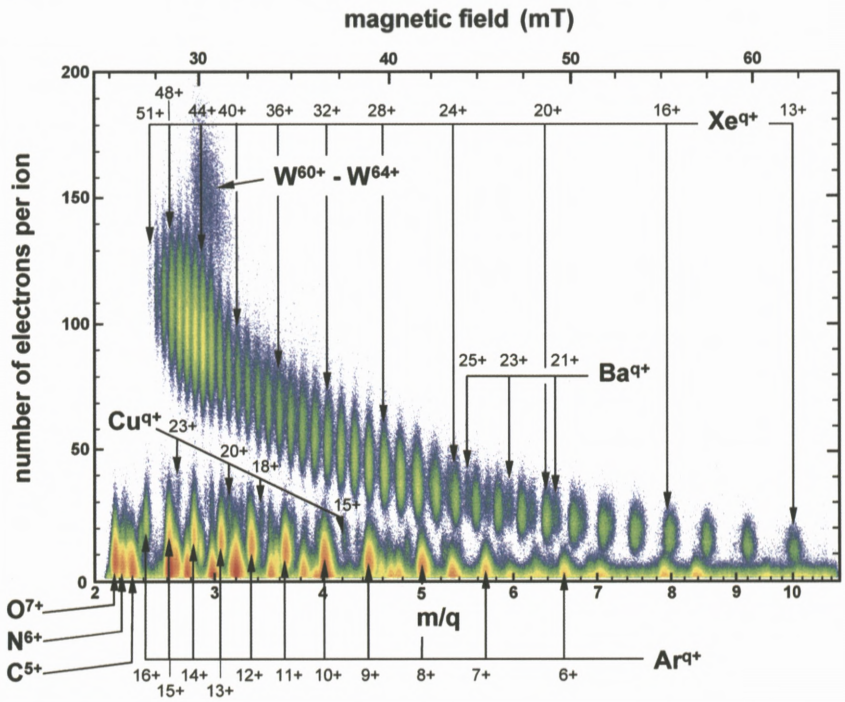

Figure 19. Plot of the number of emitted electrons for ion impact events *versus* analyzer magnet field strenght converted to ion charge-to-mass ratio (total scanning time 30 min) (Meissl et al., 2006).

(b) non-additivity in molecular impact;

(c) dependence of material properties for insulators;

(d) dynamics of plasmon decay;

(e) non-Poissonian probability for non-electron emission.

In this review we have demonstrated how the measurement of electron number statistics (ES) can benefit experimental studies on slow ion induced electron emission in a number of ways. Combination of the ES technique with grazing incidence scattering of slow atoms and singly and multiply charged ions on flat monocrystalline metal and insulator surfaces permits rather detailed studies on potential electron emission (PE) and kinetic electron emission (KE) with the following achievements.

Section 2: For impact of multiply charged ions contributions by PE and KE can be separated and quantitatively explained in terms of simple model considerations.

In contrast to metal surfaces, PE yields for insulator surfaces are considerably higher for grazing incidence than for larger angle impact, which is possibly caused by incomplete hollow-atom formation in the latter case. Systematic trajectory-dependent investigations of PE may eventually permit the mapping of Auger transition rates *versus* surface distance.

Section 3: Total electron yields for KE could be reliably measured in coincidence with the energy loss of scattered projectile down to less than 10^{-4} electrons/particle near the KE threshold. Atom trajectories with different, well defined distances of closest approach to the surface lead to KE thresholds that depend sensitively on the electron density in the surface selvedge. With these results important contributions for the solution of Baragiola's problems (a), (c) and (e) have been made.

Section 4: Examples for non-additive electron yields from molecular ion impact (problem b) suggest more systematic experiments and attention from theory. The same applies to slow ion induced plasmon excitation (problem d).

Furthermore, two interesting applications of KE and PE have been presented in *Section 5*:

(1) Based on clearly changing ES for transition from planar to axial surface channelling, a new non-destructive technique for structural characterization of surfaces and thin films ("surface triangulation") has been developed.
(2) Strongly different PE and/or KE yields permit the identification of different ion species with equal or similar q/m in mixed ion beams.

At least three other interesting points should be mentioned.

(1) The still unresolved question of a possible "trampoline effect" (Briand et al., 1996): During the approach of a slow MCI toward an insulator surface a situation could be envisaged, where still incompletely neulralized ions become stopped and reflected from the temporarily electron-depleted and thus positively charged surface.
(2) Strong electron emission from slow fullerene surface impact is not understood (Winter et al., 1997).
(3) What can be expected for grazing scattering of molecules on monocrystalline metal surfaces – will there be some kind of "snowplough" effect?

Acknowledgements

Work carried out at TU Wien has been supported by Austrian Science Foundation FWF and was carried out within Association EURATOM-ÖAW.

Work carried out at Humboldt Universität zu Berlin was supported by the Deutsche Forschungsgemeinschaft DFG (Projekt Wi 1336). HPW thanks the Alexander-von-Humboldt Foundation for generous support.

References

Arifov U.A., Kishinevskii L.M., Mukhamadiev E.S. and Parilis E.S. (1973): Auger neutralization of highly charged ions at the surface of a metal. Zh Tekh Fiz **43**, 181–187 [Sov Phys Tech Phys **18**, 118–122]

Arnau A. et al. (1997): Interaction of slow multicharged ions with solid surfaces. Surf Sci Rep **27**, 113–239

Aumayr F. and Winter HP. (2004): Potential sputtering. Phil Trans Roy Soc (London) **362**, 77–102

Aumayr F., Lakits G. and HP. Winter HP. (1991): On the measurement of statistics for particle-induced electron emission from a clean metal surface. Appl Surf Sci **47**, 139–147

Aumayr F., Kurz H., Schneider D., Briere M.A., McDonald J.W., Cunningham C.E. and Winter HP. (1993a): Emission of electrons from a clean gold surface induced by slow, very highly charged ions at the image charge acceleration limit. Phys Rev Lett **71**, 1943–1946

Aumayr F., Kurz H., Winter HP., Schneider D., Briere M.A., McDonald J.W. and Cunningham C.E. (1993b): Distinction between multicharged ion species with equal q/m. Rev Sci Instrum **64**, 3499–3502

Aumayr F., Vana M., Winter HP., Drexel H., Grill V., Senn G., Matt S., Scheier P. and Märk T.D. (1997): Distinction between multicharged fullerene ions and their fragment ions with equal charge to mass. Int J Mass Spectrom Ion Proc **163**, 9L–14L

Auth C., Hecht T., Igel T. and Winter H. (1995): Image charge acceleration of multicharged ions in front of the surface of an insulator. Phys Rev Lett **74**, 5244–5247

Bandurin Y., Esaulov V.A., Guillemot L. and Monreal R.C. (2004): Surface Miller index dependence of Auger neutralization of ions on surfaces. Phys Rev Lett **92**, 017601

Baragiola R. (1993): Electron emission from slow ion-solid interactions. In: Rabalais J.W. (Ed.), Low Energy Ion-Surface Interactions. Wiley, Chap. IV

Baragiola R.A. (2005): Some challenging unsolved problems in atomic collisions in solids. Nucl Instrum Meth Phys Res B **237**, 520–524

Baragiola R.A. and Dukes C.A. (1996): Plasmon-assisted electron emission from Al and Mg surfaces by slow ions. Phys Rev Lett **76**, 2547–2550

Baragiola R.A., Alonso E.V. and Olivia-Florio A. (1979): Electron emission from clean metal surfaces induced by low-energy light ions. Phys Rev B **19**, 121–129

Bernhard T., Pfandzelter R. and Winter H. (2003): Growth and structure of Mn and CoMn on Cu(001) studied by ion scattering. Surface Sci **543**, 36–46

Bernhard T., Baron M., Gruyters M. and Winter H. (2005): Surface structure of ultrathin Fe films on Cu(001) revisited. Phys Rev Lett **95**, 087601

Bethe H.A. and Salpeter E.E. (1957): Quantum Mechanics of One- and Two Electron Systems, Academic Press, New York

Briand J.P., de Billy L., Charles P., Essabaa S., Briand P., Geller R., Desclaux J.P., Bliman S. and Ristori C. (1990): Production of hollow atoms by the excitation of highly charged ions in interaction with a metallic surface. Phys Rev Lett **65**, 159–162

Briand J.P., Thuriez S., Giardino G., Borsoni G., Froment M., Eddrief M. and Sebenne C. (1996): Observation of hollow atoms or ions above insulator and metal surfaces. Phys Rev Lett **77**, 1452–1455

Burgdörfer J., Lerner P. and Meyer F.W. (1991): Above-surface neutralization of highly charged ions: The classical over-the-barrier model. Phys Rev A **44**, 5674–5685

Cernusca S., Diem A., Winter HP., Aumayr F., Lörincik J. and Sroubek Z. (2002): Kinetic electron emission from highly oriented pyrolytic graphite surfaces induced by singly charged ions. Nucl Instrum Meth Phys Res B **193**, 616–620

Crespo López-Urrutia J.R., Bapat B., Feuerstein B., Fischer D., Lörch H., Moshammer R. and Ullrich J. (2003): Physics with highly-charged ions in an EBIT. Hyperfine Interactions **146/147**, 109–118

Eder H., Vana M., Aumayr F. and Winter HP. (1997): Precise total electron yield measurements for impact of singly or multiply charged ions on clean solid surfaces. Rev Sci Instrum **68**, 165–169

Eder H., Aumayr F. and Winter HP. (1999): Search for projectile charge dependence of kinetic electron emission from clean polycrystalline gold. Nucl Instrum Meth B **154**, 185–193

Eder H., Aumayr F., Berlinger P., Störi H. and Winter HP. (2001): Excitation of plasmons by impact of slow ions on clean mono- and polycrystalline aluminum. Surf Sci **472**, 195–204

Gnaser H. (1999): Low-Energy Ion Irradiation of Solid Surfaces. Springer, Berlin

Hagstrum H.D. (1954a): Auger ejection of electrons from tungsten by noble gas ions. Phys Rev **96**, 325–335

Hagstrum H.D. (1954b): Theory of Auger ejection of electrons from metals by ions. Phys Rev **96**, 336–365

Hagstrum H.D. (1956): Auger ejection of electrons from molybdenum by noble gas ions. Phys Rev **104**, 672–683

Hagstrum H.D. and Becker G.E. (1973): Resonance, Auger, and autoionization processes involving $He^{+}(2s)$ and He^{++} near solid surfaces. Phys Rev B **8**, 107–121

Hasselkamp D. (1992): Kinetic electron emission from solid surfaces under ion bombardment. In: Höhler G. (Ed.), Particle Induced Electron Mission II. Springer, Heidelberg, Vol. 123, p 1

Hecht T., Winter H. and McCullough R.W. (1997): New method to analyze fast metastable atomic beams. Rev Sci Instrum **68**, 2693–2697

Kurz H., Töglhofer K., Winter HP., Aumayr F. and Mann R. (1992): Electron emission from slow hollow atoms at a clean metal surface. Phys Rev Lett **69**, 1140–1143

Kurz H., Aumayr F., Lemell C., Töglhofer K. and Winter HP. (1993): Neutralization of slow multicharged ions at a clean gold surface: Total electron yields. Phys Rev A **48**, 2182–2191

Lakits G., Aumayr F. and Winter HP. (1989a): Statistics of ion-induced electron emission from a clean metal surface. Rev Sci Instrum **60**, 3151–3159

Lakits G., Aumayr F. and Winter HP. (1989b): Electronic effects in slow heavy-particle-induced electron emission from a clean metal surface. Europhys Lett **10**, 679–685

Lederer S., Maass K., Blauth D., Winter H., Winter HP. and Aumayr F. (2003): Kinetic electron emission from the selvage of a free-electron-gas metal. Phys Rev B **67**, 121405(R)

Lemell C., Winter HP., Aumayr F., Burgdörfer J. and Reinhold C. (1995): Escape probabilities for electrons emitted during the interaction of slow highly charged ions with metal surfaces. Nucl Instrum Meth Phys Res B **102**, 33–36

Lemell C., Winter HP., Aumayr F., Burgdörfer J. and Meyer F.W. (1996a): Image acceleration of highly charged ions by metal surfaces. Phys Rev A **53**, 880–885

Lemell C., Winter HP., Aumayr F., Burgdörfer J. and Meyer F.W. (1996b): Image acceleration of highly charged ions by metal surfaces. Phys Rev A **53**, 880–885

Lemell C., Stöckl J., Burgdörfer J., Betz G., Winter HP. and Aumayr F. (1998): Multicharged ion impact on clean Au(111): Suppression of kinetic electron emission in glancing angle scattering. Phys Rev Lett **81**, 1965–1968

Lemell C., Stöckl J., Winter HP. and Aumayr F. (1999): A versatile electron detector for studies on ion-surface scattering. Rev Sci Instrum **70**, 1653–1657

Matulevich Y.T. and Zeijlmans van Emmichoven P.A. (2004): Electron emission from low-energy Xe^+ ions interacting with a MgO thin film deposited on a Mo substrate. Phys Rev B **69**, 245414

Meissl W., Simon M.C., Crespo Lopez-Urrutia J.R., Tawara H., Ullrich J., Winter HP. and Aumayr F. (2006): Novel method for unambiguous ion identification in mixed ion beams extracted from an EBIT. Rev Sci Instrum **77**, 093303

Mertens A., Winter H., Stöckl J., Winter HP. and Aumayr F. (2002): Excitation vs. electron emission near the kinetic thresholds for grazing impact of hydrogen atoms on LiF(001). Phys Rev B **65**, 132410

Meyer F.W., Folkerts L., Folkerts H.O. and Schippers S. (1995): Projectile image acceleration, neutralization and electron emission during grazing interactions of multicharged ions with Au(110). Nucl Instrum Meth Phys Res B **98**, 441–444

Monreal R.C., Guillemot L. and Esaulov V.A. (2003): On Auger neutralization of He^+ ions on a Ag(111) surface. J Phys: Condens Matter **15**, 1165–1171

Neidhart T., Pichler F., Aumayr F., Winter HP., Schmid M. and Varga P. (1995): Potential sputtering of lithium fluoride by slow multicharged ions. Phys Rev Lett **74**, 5280–5283

Ochs D., Brause M., Stracke P., Krischok S., Wiegershaus F., Maus-Friedrichs W., Kempter V., Puchin V.E. and Shluger A.L. (1997): The surface electronic structure of stoichiometric and defective LiF surfaces studied with MIES and UPS in combination with ab-initio calculations. Surf Sci **383**, 162–172

Pfandzelter R., Bernhard T. and Winter H. (2003): Ion beam triangulation of ultrathin Mn and CoMn films grown on Cu(001). Phys Rev Lett **90**, 036102

Raether H. (1988): Excitation of plasmons and interband transitions by electrons. In: Surface Plasmons on Smooth and Rough Surfaces and on Gratings. Springer Tracts in Modern Physics, Vol. 111. Springer, Berlin

Riccardi P., Ishimoto M., Barone P. and Baragiola R.A. (2004): Ion-induced electron emission from MgO exciton decay into vacuum. Surf Sci **571**, L305–310

Roncin P., Villette J., Atanas J.P. and Khemliche H. (1999): Energy loss of low energy protons on LiF(100): Surface excitation and H-mediated electron emission. Phys Rev Lett **83**, 864–867

Rösler M. and Brauer W. (1991): Theory of electron emission from nearly-free-electron metals by proton and electron bombardment. In: Höhler G. (Ed.), Particle Induced Electron Mission I. Springer, Berlin, Vol. 122

Schneider D., Clark M.W., Penetrante B., McDonald J., DeWitt D. and Bardsley J.N. (1991): Production of high-charge-state thorium and uranium ions in an electron-beam ion trap. Phys Rev A **44**, 3119–3124

Schou J. (1988): Secondary electron emission from solids by electron and proton bombardment. Scanning Microsc **2**, 607–632

Sigmund P. (1993): Fundamental processes in sputtering of atoms and molecules. Mat Fys Medd Dan Vidensk Selsk **43**, 2

Sporn M., Libiseller G., Neidhart T., Schmid M., Aumayr F., Winter HP., Varga P., Grether M. and Stolterfoht N. (1997): Potential sputtering of clean SiO_2 by slow highly charged ions. Phys Rev Lett **79**, 945–948

Stöckl J., Suta T., Ditroi F., Winter HP. and Aumayr F. (2004): Separation of potential and kinetic electron emission for grazing impact of multiply charged Ar ions on a LiF(001) surface. Phys Rev Lett **93**, 263201

Stolterfoht N., Niemann D., Hofmann V., Rösler M. and Baragiola R.A. (1998): Plasmon excitation by multiply charged Ne^{q+} ions interacting with an Al surface. Phys Rev Lett **80**, 3328–3331

Vana M., Aumayr F., Varga P. and Winter HP. (1995a): Electron emission from polycrystalline lithium fluoride induced by slow multicharged ions. Europhys Lett **29**, 55–60

Vana M., Aumayr F., Varga P. and Winter HP. (1995b): Electron emission from polycrystalline lithium fluoride bombarded by slow multicharged ions. Nucl Instrum Meth Phys Res B **100**, 284–289

Vana M., Aumayr F., Lemell C. and Winter HP. (1995c): Ion induced electron emission from solid surfaces: Information content of the electron number statistics. Int J Mass Spectr Ion Proc **149/150**, 45–57

Winter H. (1992): Image charge acceleration of multi-charged argon ions in grazing collisions with an aluminum surface. Europhys Lett **18**, 207–212

Winter H.: (2002): Collisions of atoms and ions with surfaces under grazing incidence. Phys Rep **367**, 387–582

Winter H. and Winter HP. (2003): Classical model of kinetic electron emission near threshold induced by impact of atomic projectiles on a free-electron gas metal. Europhys Lett **62**, 739–745

Winter H., Auth C., Schuch R. and Beebe E. (1993): Image acceleration of highly charged xenon ions in front of a metal surface. Phys Rev Lett **71**, 1939–1942

Winter H., Lederer S., Maass K., Mertens A., Aumayr F. and Winter HP. (2002): Statistics of electron and exciton production for grazing impact of keV hydrogen atoms on a LiF(001) surface. J Phys B: At Mol Opt Phys **35**, 3315–3325

Winter H., Maass K., Lederer S., Winter HP. and Aumayr F. (2004): Kinetic electron emission for planar versus axial surface channeling of He atoms and ions. Phys Rev B **69**, 054110

Winter H., Lederer S., Winter HP., Lemell C. and Burgdörfer J. (2005): Kinetic electron emission induced by grazing scattering of slow atoms: Local probe of the Compton profile near the Fermi edge. Phys Rev B **72**, 161402(R)

Winter HP. and Aumayr F. (2002): Slow multicharged ions hitting a solid surface: From hollow atoms to novel applications. Euro Phys News **33**, 215–218

Winter HP., Vana M., Betz G., Aumayr F., Drexel H., Scheier P. and Märk T.D. (1997): Suppression of potential electron emission for impact of slow multicharged fullerenes on clean gold. Phys Rev A **56**, 3007–3010

Wirtz L., Reinhold C.O., Lemell C. and Burgdörfer J. (2003): Liouville master equation for multielectron dynamics: Neutralization of highly charged ions near a LiF surface. Phys Rev A **67**, 12903

Stopping of Swift Ions: Solved and Unsolved Problems

Peter Sigmund*

Department of Physics and Chemistry
University of Southern Denmark
DK-5230 Odense M, Denmark

Abstract

Despite intense research in penetration of charged particles over almost a century, several central problems remain unsolved. In this paper I am trying to point out recent solutions to problem areas of long standing and, at the same time, identify specific needs from important application areas where new ideas and an increased effort are desirable. For more tutorial introductions the reader is referred to two recent monographs (Sigmund, 2004, 2006).

Contents

1 General Considerations **558**
1.1 Particle Penetration: Standard Description 558
1.2 Energy Loss, Energy Deposition and Related Quantities 559

2 Stopping: High and Intermediate Speed **562**
2.1 Stopping of Point Charges 562
2.1.1 Bohr and Bethe Theory 562
2.1.2 Additions 565
2.2 Stopping of Dressed Ions 569
2.2.1 Effective Ion Charge: A Misleading Concept 570
2.2.2 Charge-Dependent Stopping and Gas-Solid Paradox 571
2.2.3 Projectile Excitation/Ionization; Antiscreening 573
2.2.4 Charge Exchange 574
2.3 Valence Structure Effects 574
2.4 Channeling 575

* E-mail: sigmund@ifk.sdu.dk

3 Straggling **576**
3.1 Variance and Straggling Parameter 576
3.1.1 Factors Affecting Straggling 576
3.1.2 Shell and Barkas–Andersen Correction 577
3.1.3 Bunching and Correlation 578
3.2 Energy-loss spectra 581

4 Low-Velocity Stopping **583**
4.1 Application Areas 583
4.2 Standard Descriptions 583
4.3 Open problems 584

5 Velocity Effect for Swift Ions **585**

6 Conclusions **587**

Acknowledgements **588**

References **588**

1. General Considerations

1.1. Particle Penetration: Standard Description

Figure 1 shows a cloud chamber photograph of the slowing down of alpha particles in air. Implicitly or explicitly, many of us have such a situation in mind when addressing penetration of swift charged particles.[1] Characteristic features are almost straight trajectories of fairly uniform length, i.e., negligible multiple scattering and straggling, dependent on the accuracy aimed at. The key quantity in such a description, the continuum-slowing-down approximation, is the energy loss per travelled pathlength, usually called stopping power although stopping force is more precise, from which the total range can be determined by integration.

As a first step of a more sophisticated description, one may take into account multiple scattering and straggling in the Gaussian approximation, both being treated as minor perturbations. Such a description is employed routinely in ion beam analysis at low and intermediate resolution as well as in particle therapy (Jäkel, 2006). Conversely, such a description is insufficient in high-resolution ion beam analysis, as documented by Grande et al. (2006) and, more generally, in the study of energy transfer in thin layers or small volumes (microdosimetry).

[1] In accordance with common nomenclature, the term "swift" denotes projectile speeds above the Bohr velocity $v_0 = c/137$.

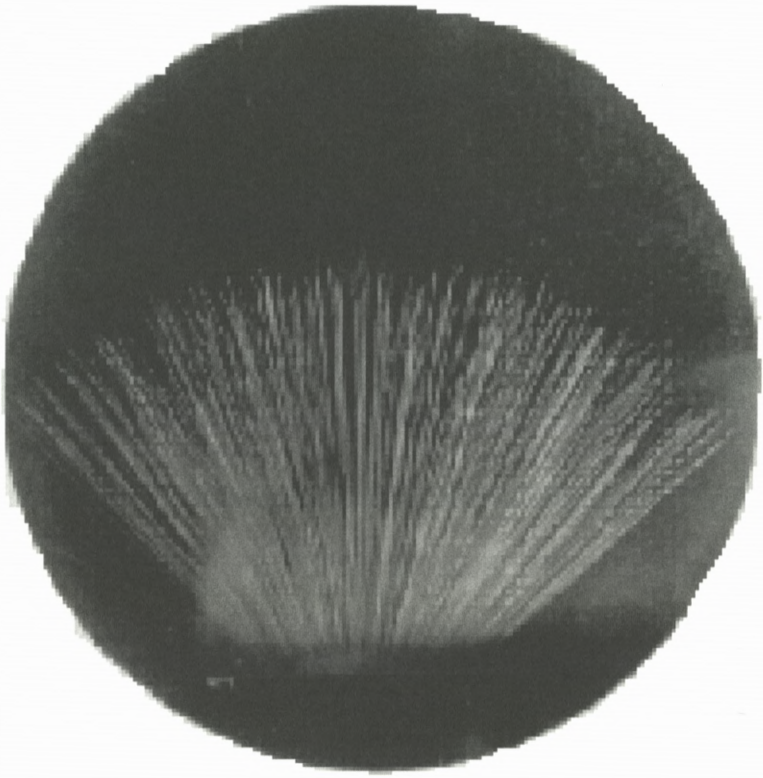

Figure 1. Cloud chamber photograph of the slowing down of alpha particles in air. From Meitner and Freitag (1926).

The model is well known to break down in case of electron and positron penetration, not the least because of excessive angular scattering, but even in light-ion penetration at low beam velocities, angular scattering is known to be a major disturbance (Schiøtt, 1966). Further complications arise in the presence of charge exchange and/or nuclear stopping.

1.2. Energy Loss, Energy Deposition and Related Quantities

Energy *lost* by the beam is the quantity of interest in ion beam analysis, but in numerous other application areas, the quantity needed is the energy *deposited* by the beam. Typical stopping measurements address energy loss, even though some of the most precise stopping data are based on measurement of deposited energy (Andersen et al., 1966).

The difference between energy loss and energy deposition is worthwhile to keep in mind, partly because energy deposition may involve energy transport by secondary particles, especially by secondary electrons but, occasionally, also by recoil atoms (Holmén et al., 1979). Serious conceptional problems may arise when potential energy becomes important, as is the case for secondary electron emission at low beam velocities (Winter et al., 2006) and, more generally, for bombardment with highly charged ions. Clearly, it does not make sense to describe the energy deposition by a slow highly charged ion in terms of an energy loss per pathlength when the travelled pathlength is essentially zero. Failure to realize this leads to misconceptions such as negative stopping powers of keV ions (Cabrera-Trujillo et al., 2002).

The prototype of an energy-loss profile is the so-called Bragg curve which, in the simplest case, is a plot of stopping force *versus* penetration depth, possibly corrected for Gaussian straggling. More appropriate for applications is a plot of the number of ionization events per travelled pathlength. This would be of interest, for example, in a detailed analysis of the particle tracks shown in Figure 1. You may be inclined to take the two quantities as proportional to each other. After all, the number of ions ν generated by a primary particle of energy E is most often estimated as $\nu = E/W$, where the "W-value" is, by and large, a constant characteristic of the stopping medium.

Figure 2 shows the stopping cross section

$$S = \sum_j \left(\int_0^{T_{\max}} T \, \mathrm{d}\sigma(T) \right)_j \tag{1}$$

and the *ionization stopping cross section*

$$S_{\mathrm{ioniz}} = \sum_j \left(\int_{U_j}^{T_{\max}} T \, \mathrm{d}\sigma(T) \right)_j \tag{2}$$

for argon in silicon, where $\mathrm{d}\sigma(T)$ indicates the cross section for energy transfer $(T, \mathrm{d}T)$ in a single collision event, j is a label for the silicon subshells involved and U_j the subshell binding energy. Calculations are performed by the PASS code based on binary stopping theory (Sigmund and Schinner, 2000) with input data from ICRU (2005).

Evidently, the two curves are not proportional. The ratio S_{ioniz}/S comes close to 1 somewhat below the stopping maximum. While the dropoff at low velocities due to threshold effects may be expected, a more pronounced dropoff at high speed may seem surprising. It reflects the relative significance of very soft collisions – or a large interaction volume – at high projectile speed. In order to demonstrate that

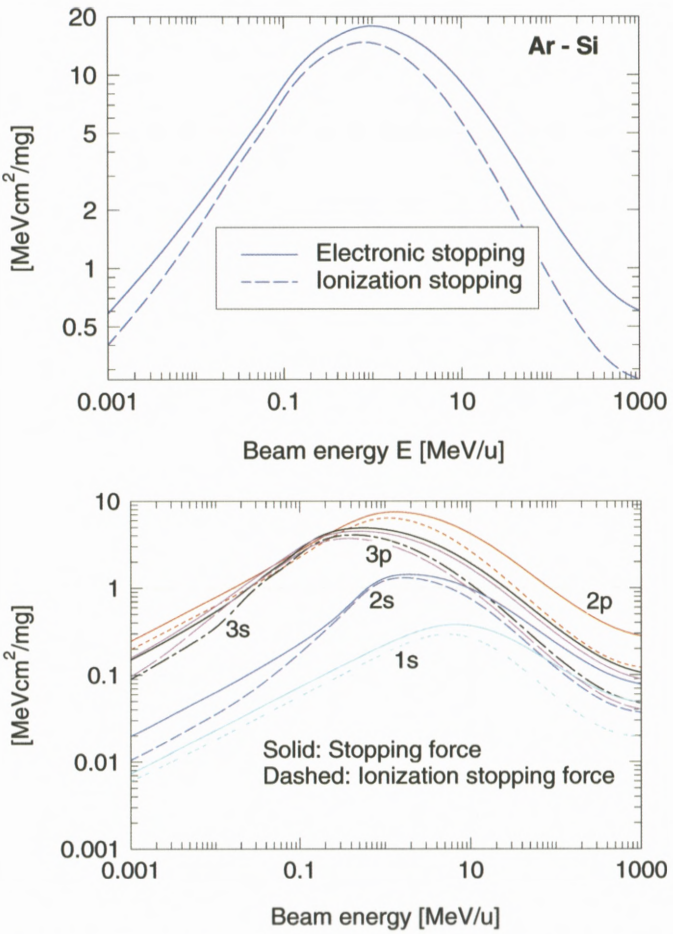

Figure 2. Stopping force on argon in silicon (solid lines) calculated from binary theory. Only target excitations considered. Dashed lines: Only energy losses exceeding the subshell binding energy included. Upper graph: All shells; lower graph: contributions from individual subshells.

this feature is unrelated to the magnitude of the shell binding energy, the lower graph shows the same information but split up into contributions from the five subshells of silicon. This feature appears important for dose planning in hadron therapy.

While energy-loss measurements typically offer less challenge to experimentalists than measurements of energy deposition, optimistic estimates of experimental error seem to be the rule rather than the exception. Figure 3 shows a typical graph of stopping data compiled by Paul (2005). Data for oxygen in gold

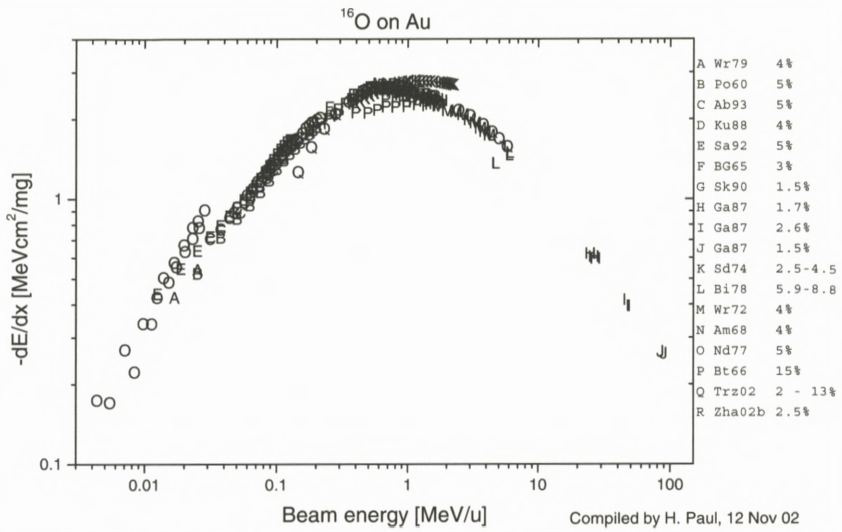

Figure 3. Measured stopping forces on oxygen in gold from numerous sources compiled by Paul (2005). Numbers on the right margin show experimental errors assigned by the respective authors.

are shown from 18 different sources. Experimental errors given in the margin are supposed to be a few per cent, while discrepancies of 20–30% between different sources are evident not only at low projectile speed but also around the Bragg peak.

2. Stopping: High and Intermediate Speed

2.1. Stopping of Point Charges

2.1.1. *Bohr and Bethe Theory*

The stopping cross section for a point charge is conventionally written in the form[2]

$$S = \frac{4\pi Z_1^2 Z_2 e^4}{mv^2} L, \tag{3}$$

where the stopping number L reads

$$L = \begin{cases} \ln \dfrac{2mv^2}{I} & \text{(Bethe)} \\ \ln \dfrac{Cmv^3}{Z_1 e^2 \omega} & \text{(Bohr)} \quad \omega = I/\hbar \end{cases} \tag{4}$$

[2] Gaussian units are employed throughout this paper.

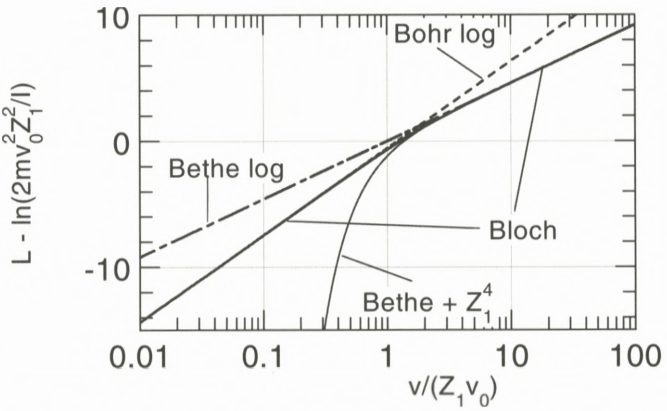

Figure 4. The stopping number according to Bloch (1933) (solid line) approaches the Bohr and Bethe logarithms at low and high projectile speed, respectively. Also included is a curve consisting of the Bethe logarithm and the Z_1^4 correction which often, erroneously, is called the Bloch correction. $v_0 = c/137$ is the Bohr velocity. From Sigmund (1997).

in the simplest versions of Bethe and Bohr stopping theory, rerspectively. Figure 4 shows the two expressions in a plot which, within the range of validity of the two schemes, is universally valid for all point charges Z_1 and all elemental materials with atomic number Z_2.

According to Bohr (1948), the classical expression L_{Bohr} applies to the regime $\kappa = 2Z_1e^2/\hbar v > 1$, while L_{Bethe}, based on the Born approximation, has a complementary range of validity specified by $\kappa/2 = Z_1e^2/\hbar v < 1$. The curve labelled "Bloch" combines the two limits, the transition between which is seen to be rather abrupt. Also shown is a curve labeled "Bethe + Z_1^4", which approximates the Bloch curve in the region of small deviations from the Bethe logarithm, but which leads to absurd results at lower projectile speeds. The Z_1^4 term is often erroneously called Bloch correction.

The central empirical parameter entering both Bethe's and Bohr's expression for the stopping number is the I-value, the mean logarithmic excitation energy or, equivalently, the effective resonant frequency $\omega = I/\hbar$. There are, roughly spoken, four ways available to determine I-values:

- The local-plasma model proposed by Lindhard and Scharff (1953), where a logarithmic average of the plasma frequency is taken over the density profile of the target atom. The latter may be described either by the Thomas–Fermi model (Bonderup, 1967) or by atomic charge distributions (Chu and Powers, 1972).

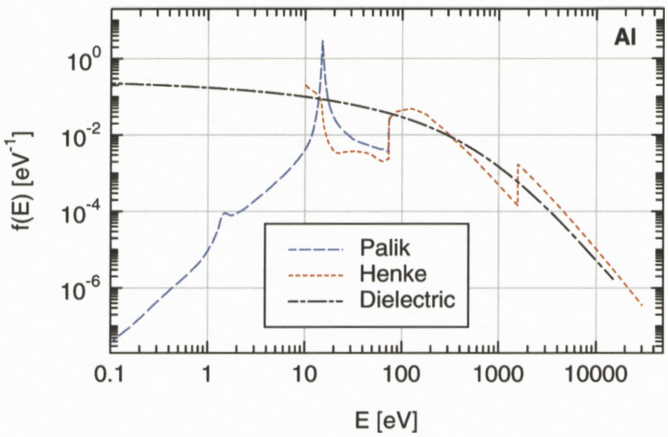

Figure 5. Oscillator-strength spectrum for metallic aluminium according to Palik (2000) and Henke et al. (1993). Also included is a curve found from the local-plasma model on the basis of the Thomas–Fermi function of a neutral aluminium atom. From Sigmund (2006).

- Fitting to measured stopping cross sections. This procedure requires reliable estimates of shell and Barkas–Andersen corrections (Andersen et al., 1969b).
- Calculation from atomic wave functions (shellwise) (Dehmer et al., 1975).
- Integration of measured oscillator strengths and photoabsorption cross sections (shellwise) (ICRU, 2005).

Figure 5 shows oscillator strength spectra for metallic aluminium from available tabulations (Palik, 2000; Henke et al., 1993), compared with a spectrum underlying the local plasma approximation, evaluated on the basis of the Thomas–Fermi density profile for a neutral atom. Evidently, the latter curve cannot reproduce the shell structure, nor does it properly describe low excitations in the free electron gas. However, it does produce a feasibly smooth average above $\sim$10 eV.

Oscillator strengths calculated from Slater orbitals by Dehmer et al. (1975) have been bundled into subshell I-values and weight factors by Oddershede and Sabin (1984). Figure 6 shows K-shell I-values tabulated by Oddershede and Sabin (1984) *versus* Z, compared with a recent evaluation on the basis of tabulated oscillator-strength spectra like those shown in Figure 5. A discrepancy is observed which approaches a factor of 5 at $Z = 36$. It is seen that for $Z > 10$, the predictions of Oddershede and Sabin (1984) even fall below the K-shell binding energy.

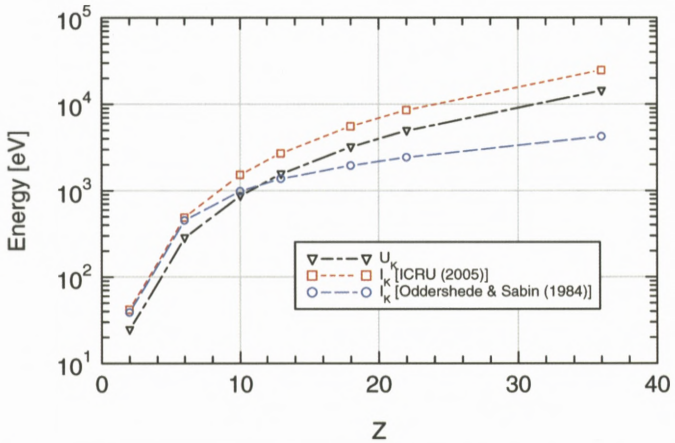

Figure 6. I-values for the K shell as a function of atomic number according to Oddershede and Sabin (1984) and ICRU (2005). Also included are K-shell binding energies. From Sigmund (2006).

2.1.2. *Additions*

The predictions of Equation (4) can only rarely stand alone but need additions. For swift point charges, such additions are conventionally classified into

1. Barkas–Andersen correction,
2. Shell correction,
3. Relativistic correction,
4. Density correction, and
5. High-Z_1 correction.

Recent progress concerns items (1), (2) and (5).

Barkas–Andersen correction The Barkas effect denotes the difference in stopping cross section between a particle and its antiparticle. Figure 7 shows that this difference is not just a small correction $\propto Z_1^3$ to the Bethe stopping formula, as it was thought for a long time. On the contrary, it becomes exceedingly large around and below the stopping maximum. Early measurements identified a closely related effect by comparison of measured stopping cross sections for alpha particles and protons (Andersen et al., 1969a). The fact that those measurements could be described in terms of a Z_1^3 contribution suggested a very large Barkas–Andersen correction for high-Z_1 ions. However, Lindhard (1976) predicted, on the basis of a dimensional argument, a similar behavior for all projectiles in terms of the

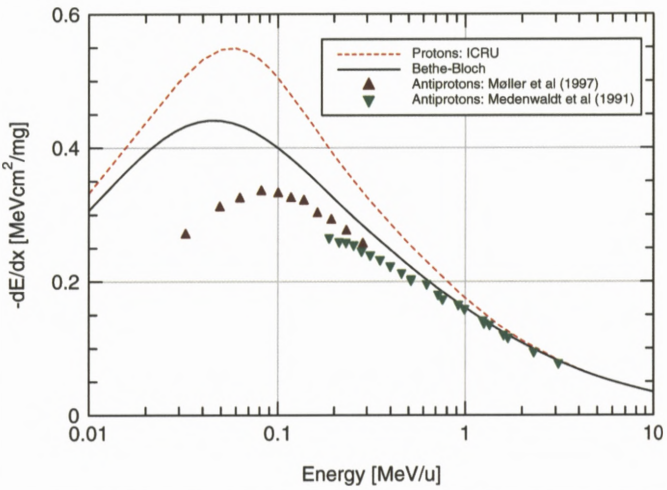

Figure 7. Barkas effect in silicon: The dotted curve represents tabulated stopping forces on protons according to ICRU (1993). Points refer to measured stopping forces on antiprotons (Medenwaldt et al., 1991; Møller et al., 1997). The solid line was found by taking the average of stopping forces calculated from binary theory for antiprotons and protons.

Bohr scaling variable $mv^3/Z_1e^2\omega$. This prediction has been confirmed in recent calculations by Sigmund and Schinner (2003).

Reliable estimates of the Barkas–Andersen corrections for protons and antiprotons on the basis of several theoretical schemes have become available in recent years, cf. ICRU (2005) or Sigmund (2006) for reviews.

A particularly controversal topic was the question of whether the Barkas–Andersen correction received contributions from distant collisions only, as asserted by Ashley et al. (1972) or, following an argument by Lindhard (1976), also from close collisions. Figure 8 shows calculations for a target atom modelled as a spherical harmonic quantum oscillator. The upper graph shows the mean energy loss *versus* impact parameter in the first Born approximation ($\propto Z_1^2$), while the lower graph shows the contribution from the second Born approximation ($\propto Z_1^3$), for a wide range of the Bethe parameter $2mv^2/\hbar\omega$. While there are quantitative differences, there is clear evidence for a contribution also from close collisions in the graph on the bottom. This behavior has been confirmed in all recent studies, with the exception of a classical-trajectory Monte Carlo simulation by Grüner et al. (2004). Possible origins of that discrepancy are still being discussed.

Shell correction The shell correction prevents the stopping number from becoming negative at low speed, as would be the case if it were estimated from

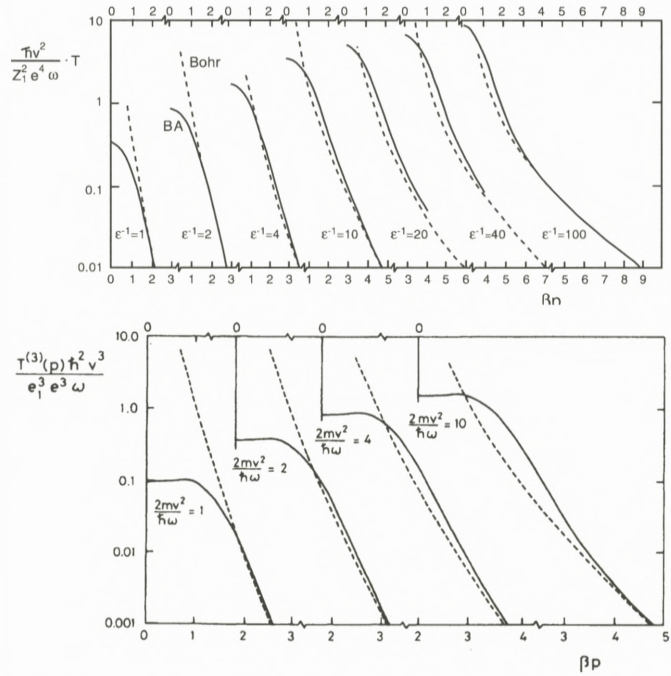

Figure 8. Energy loss in single collision *versus* impact parameter for a spherical harmonic oscillator. Upper graph: First Born approximation (Mikkelsen and Sigmund, 1987); lower graph: contribution from second Born approximation (Mikkelsen and Sigmund, 1989).

the Bethe logarithm alone. Following a tradition established by Walske (1952), this correction is evaluated separately for each principal shell of the target. This implies that in particular for high-Z_2 materials, shell corrections may be non-negligible even at rather high projectile speeds.

Several theoretical schemes have been proposed, and utilized successfully, for evaluating shell corrections. For reviews see Fano (1963) and Sigmund (2006). A point of discussion, however, has been the origin of the correction. An asymptotic expansion for high but non-relativistic projectile speed yields $-\langle v_e^2\rangle/v^2$ as the leading correction in the stopping number, where v_e denotes the orbital speed of a target electron. On this basis, the primary cause of the shell correction has been understood to be the neglect of the orbital velocity in comparison to the beam velocity, when the transition is made from the rigorous Born approximation to the Bethe logarithm.

However, the Bohr formula also shows a logarithmic dependence on projectile speed, even though the classical Bohr model operates with an initially stationary

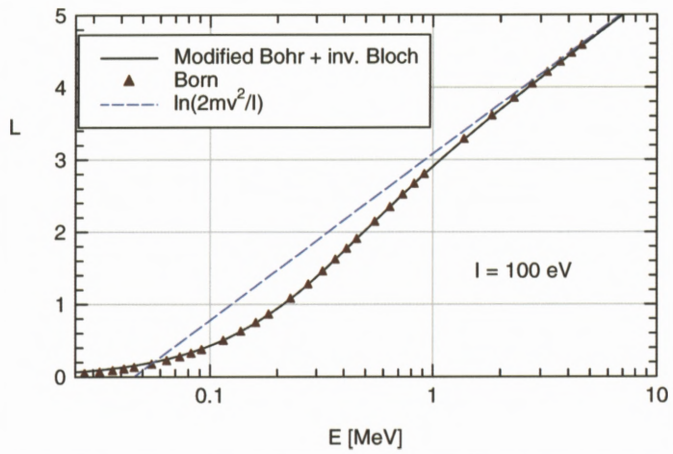

Figure 9. Stopping number of a spherical harmonic oscillator. Triangles: Born approximation for quantum oscillator (Sigmund and Haagerup, 1986). Dashed line: Bethe logarithm. Solid line: Bohr theory (logarithmic expansion avoided) plus inverse-Bloch correction. Orbital motion included via kinetic transformation (Sigmund, 1982). From Sigmund and Schinner (2006).

target electron. In that case, it is easily seen that the logarithmic dependence arises purely mathematically from an asymptotic expansion of a Bessel function, which can readily be avoided (Sigmund, 1996).

Figure 9 illustrates the situation on a target modeled as a spherical harmonic oscillator. The straight line represents the Bethe logarithm. The triangles represent the rigorous result for the Born approximation (Sigmund and Haagerup, 1986), while the solid line reflects the sum of an accurate evaluation of the Bohr stopping number – i.e. beyond the logarithmic approximation – plus the inverse-Bloch correction – which ensures that the Bethe formula is approached for $\kappa < 1$ – both terms being kinematically corrected in accordance with the velocity spectrum of the quantum oscillator.

Sigmund and Schinner (2006) concluded from the perfect agreement that the shell correction is made up by two distinct contributions: A mathematical correction that can be repaired in the classical Bohr expression, and a kinematic correction taking into account the velocity spectrum of the target atom.

Relativistic corrections within the Born approximation have been known for a long time and reviewed by Fano (1963). Corrections beyond the Born approximation were found experimentally by several groups (Tarlé and Solarz, 1978; Scheidenberger et al., 1994). Theoretical attacks go back to Ahlen (1980, 1982) and Scheidenberger et al. (1994). A powerful analysis on the basis of the

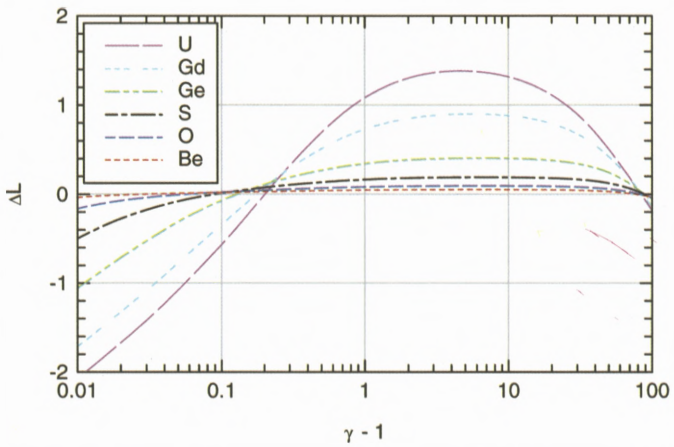

Figure 10. Correction to relativistic Bethe formula according to Lindhard and Sørensen (1996). $\gamma = 1/\sqrt{1 - v^2/c^2}$. From (Sigmund, 2006).

phase shifts for relativistic Coulomb scattering was presented by Lindhard and Sørensen (1996). This analysis does not only comprise the Mott correction and what was called the relativistic Bloch correction, but also allows for deviations from Coulomb scattering due to the non-vanishing size of the projectile nucleus. Figure 10 shows the relativistic high-Z_1 correction for several values of Z_1. While it is quite small for the lightest ions, it is very substantial for $Z_1 > 10$, once the kinetic energy of the projectile approaches or exceeds its rest energy.

2.2. Stopping of Dressed Ions

For ions carrying electrons, additional effects need to be considered,

1. Screening of the Coulomb interaction by electrons accompanying the projectile,
2. Excitation amd ionization of the projectile by collisions with target atoms,
3. Energy loss by charge exchange.

While the second and third process have received comparatively little attention in the literature, the first one represents one of the most lively discussed topics in the field of particle penetration, with the central keywords being the effective ion charge and the so-called gas-solid paradox.

2.2.1. *Effective Ion Charge: A Misleading Concept*

In a first attempt to estimate the stopping of fission fragments after the discovery of uranium fission, Bohr (1940) employed his classical stopping formula but inserted an effective ion charge $q_1 e$ instead of the nuclear charge $Z_1 e$. The magnitude of q_1 was estimated from a simple adiabaticity criterion.

While this appears reasonable in the absence of a more accurate estimate, Northcliffe (1963) suggested to apply the same procedure but implying validity of the Bethe stopping cross section, with an effective charge defined by

$$q^2_{1,\mathrm{eff}} = Z^2_{1,\mathrm{ref}} \frac{S(Z_1, v)}{S(Z_{1,\mathrm{ref}}, v)}\,, \tag{5}$$

where $S(Z_1, v)$ represents the stopping cross section in charge equilibrium of an ion with atomic number Z_1 as a function of speed, and $Z_{1,\mathrm{ref}}$ a reference ion, typically a proton or an alpha particle.

Equation (5) is highly problematic in several respects,

- Screening is important for $v \lesssim Z_1^{2/3} v_0$, while Bethe theory is valid for $v > Z_1 v_0$. Thus, Bethe theory cannot be assumed to be valid in the velocity regime of substantial screening.
- A more accurate description of stopping in the screening regime would have to start at the Bohr formula which does not predict a stopping cross section $\propto Z_1^2$.
- Both Bethe's and Bohr's formulae have been derived for point projectiles. For screened-Coulomb interaction, neither formula can be taken to be valid.

In Figure 11, the solid line represents a calculated effective-charge ratio $q^2_{1,\mathrm{eff}}/Z_1^2$ for oxygen in amorphous carbon with helium as the reference ion. It shows a characteristic S shape with an approach toward unity at high velocities for vanishing screening, and a drop-off to almost 0.1 at low projectile speed. The experimental points in the graph – which refer to a large number of target materials – show that this behavior is also found by inserting measured stopping cross sections for both the ion of interest and the reference ion. It has almost universally been ascribed to projectile screening in the literature. However, as is seen from the dashed line in Figure 11, a similar, almost as pronounced S shape is found when calculated stopping cross sections for bare ions are inserted both for the ion of interest and the reference ion. If the effective-charge concept were valid, a constant = 1 would be expected. From the location of the classical limit $\kappa = 1$, we may conclude that *the effective-charge model ascribes effects to projectile screening which are actually caused by the breakdown of Bethe theory and the transition to the classical regime.*

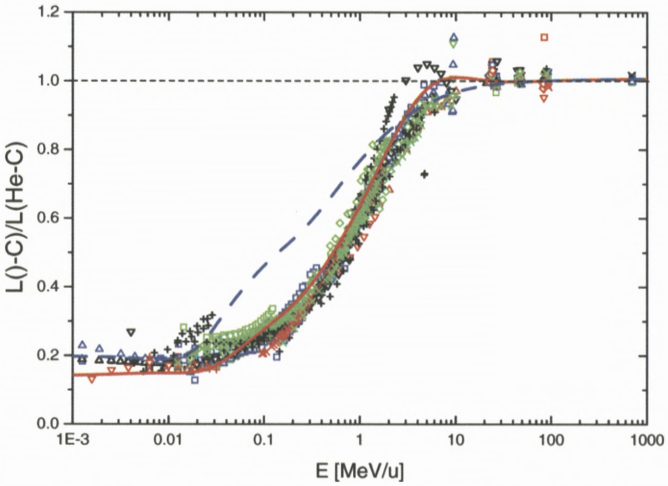

Figure 11. Stopping ratio O-C/He-C calculated from binary theory. Solid red line: Both ions in charge equilibrium. Dashed blue line: Both ions bare. From Sigmund and Schinner (2001a) and ICRU (2005). Experimental points for oxygen ions on a large number of targets according to Paul (2005).

Thus, while Equation (5), when utilized as a purely empirical relation to scale measured stopping cross sections with the aim of interpolation, may be useful at least for (Z_1, Z_2) pairs in the neighborhood of experimental data, it grossly misrepresents the physics involved, the error being up to a factor of 5 in the case depicted in Figure 11. This immediately explains why attempts to relate the effective charge to the actual ion charge were notoriously unsuccessful. Furthermore, there is no reason to expect the effective charge to exhibit Thomas–Fermi scaling behavior of the kind obeyed by the equilibrium ion charge, an assumption underlying e.g. the popular SRIM code (Ziegler, 2005).

2.2.2. *Charge-Dependent Stopping and Gas-Solid Paradox*

Several theoretical schemes have become available during the past decade to estimate stopping cross sections for dressed ions, in particular

- the convergent kinetic theory scheme by Maynard et al. (2001),
- the binary theory by Sigmund and Schinner (2000, 2002b),
- the unitary convolution approximation by Grande and Schiwietz (2002), and
- the scheme of Arista (2002) based on a generalization of the Friedel sum rule.

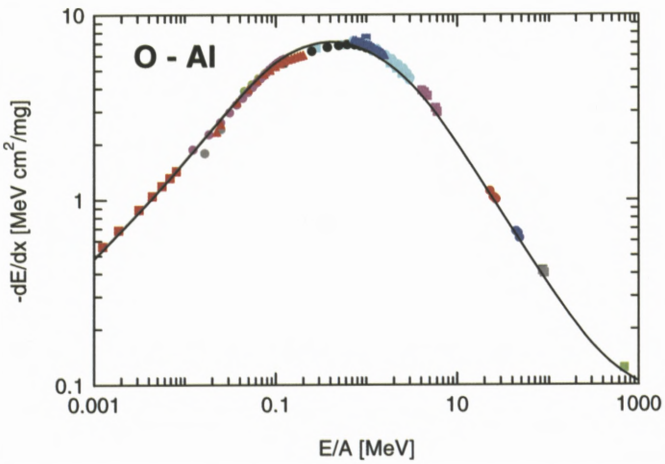

Figure 12. Stopping of oxygen in aluminium. Experimental data compiled by Paul (2005). Theoretical prediction from binary theory. From Sigmund and Schinner (2002b).

Apart from the theoretical tools applied, the schemes also differ in the way how various corrections to equivalents of the Bohr or Bethe formula are taken into account. For details the reader is referred to Sigmund (2004).

Any of the above schemes can be utilized to estimate stopping cross sections in charge equilibrium by using suitable data for mean equilibrium charges or, preferrably, equilibrium charge fractions. Figure 12 shows, as an example, a comparison of measured equilibrium stopping cross sections for oxygen in aluminium with the prediction of the binary theory.

It was found experimentally by Lassen (1951b) that equilibrium charge states of fission fragments tend to be significantly higher in solids than in gases. Moreover, for gases, a weak increase with gas pressure was found (Lassen, 1951a). An explanation of this phenomenon was presented by Bohr and Lindhard (1954) who ascribed it to short free pathlengths for electronic collisions in condensed matter, where excited projectiles would not have time to deexcite into their ground states and thus would exhibit higher ionization cross sections.

A seeming problem with this explanation was considered to be the lack of a corresponding enhancement in the measured stopping cross sections. Although such an enhancement was found subsequently (Geissel, 1982; Bimbot et al., 1989a, 1989b), it was smaller than expected. A proposed explanation of this so-called charge-state paradox was the assertion that there was no difference between charge states in solids and gases, and that the enhanced charge state in case of solids was a post-foil effect due to emission of Auger electrons (Betz and

Grodzins, 1970). That assertion, however, could not be verified, since the required number of Auger electrons was never found in pertinent experiments.

While the claim of a paradox presumably was justified until 1982, where no evidence of enhanced stopping cross sections was available, the main problem afterwards was the more or less explicit belief in the validity of a q_1^2 dependence of the stopping cross section on the ion charge. The problem evaporated, once it was recognized that the actual dependence was weaker and that even for bare ions, Bohr theory does not predict a Z_1^2 dependence because of the occurrence of Z_1 in the logarithm. For explicit discussions the reader is referred to Sigmund (1997) or Maynard et al. (2000).

2.2.3. *Projectile Excitation/Ionization; Antiscreening*

A projectile carrying bound electrons does not only lose energy by excitation of the target but also by excitation of its own electrons. As a first approximation one may treat this process as the interaction between a screened (neutral) target nucleus and a partially screened projectile. For $Z_1 = Z_2$, this process will be less important than target excitation because

- a neutral particle represents a weaker perturbation than a partially stripped one,
- there are fewer electrons to be excited on the projectile than on the target, and
- electrons on the projectile are more strongly bound in the average.

It is also clear that projectile excitation decreases in importance with increasing projectile speed because of a decreasing number of bound electrons. However, the effect must be expected to increase in importance for ions with Z_1 exceeding Z_2.

An interesting difference between atomic-collision physics and particle stopping was pointed out recently by Sigmund and Glazov (2003). In atomic-collision physics, the quantity of interest is the inelastic energy loss,

$$6Q = \epsilon_{\text{target}} + \epsilon_{\text{projectile}}, \tag{6}$$

where ϵ represents the excitation energy of the target and projectile, respectively, from their respective initial states. This relation also holds for excitation into the continuum.

In particle stopping, somewhat contradictory to common nomenclature, it is actually not the total energy loss per pathlength that defines the stopping force but the change in velocity or momentum of the projectile nucleus. This implies that Equation (6) holds for discrete excitations while for the continuum, i.e., projectile

ionization, the matter is more complex. Indeed, for screened-Coulomb interaction with the target atom, electrons are ejected from the projectile predominantly in the backward direction, seen in a reference frame moving with the ion, and hence move more slowly than the ion, seen in the laboratory frame of reference. Thus, such electrons actually give rise to an *increase* in projectile speed instead of a decrease. However, the effect is small. As a consequence, and in accordance with the conclusion of Sigmund and Glazov (2003), only projectile *excitation* is taken into account in tabulations of stopping cross sections (ICRU, 2005), while the effect of projectile ionization is simply ignored.

Stimulated by experience in atomic-collision physics, an effect called anti-screening has occasionally been discussed in connection with particle penetration (Kabachnik, 1993). It denotes the phenomenon that a projectile electron, rather than screening the charge of the projectile nucleus, may cause excitation of target electrons by electron-electron interaction, while the nuclei act as spectators. In this way, energy losses exceeding those estimated for Coulomb interaction with a bare ion may be achievable. Clearly, target excitation by such processes is intimately coupled to projectile excitation. I have presented estimates (Sigmund, 1997) indicating that the effect decreases rapidly as Z_1 becomes > 1. The effect has been ignored in all quantitative estimates of stopping cross sections to the author's knowledge. It has been considered in a recent study by Montanari et al. (2003). Those results, however, seem questionable because of the failure to recognize the essential difference between projectile excitation and ionization.

2.2.4. *Charge Exchange*

Charge exchange is known to contribute to the mean energy loss mainly below the stopping maximum, in particular for light ions (Golser and Semrad, 1991; Schiwietz, 1990). In the model of Firsov (1959) for inelastic energy losses of heavy ions, all energy transfer is assumed to be due to electron capture by the projectile from the target. A comprehensive study of the influence of charge exchange *on the stopping cross section*, in particular a specification of conditions under which the effect is negligible, would be desirable.

2.3. Valence Structure Effects

The valence structure of the target has unquestionably an influence on atomic stopping cross sections and may produce

1. non-monotonic variations with atomic number, commonly called Z_2 structure or Z_2 oscillations,

2. atom-molecule differences, commonly denoted as deviations from Bragg additivity,
3. gas-solid differences, and
4. conductor-insulator differences.

While the first two effects are well established experimentally, little quantitative information is available regarding the latter two, not the least because it may be hard to separate them from the others, both experimentally and theoretically.

As a general rule, one may assume that valence structure effects are most pronounced for light target materials, simply because of a large fraction of valence electrons (ICRU, 1993).

Z_2 structure and deviations from Bragg additivity have commonly been analysed in terms of pertinent I-values (Chu and Powers, 1972; Thwaites, 1984; ICRU, 1993). This is justified in the range of beam velocities where these effects are small. However, the logarithmic dependence of both Bohr and Bethe stopping cross section on I suggests valence effects to increase with decreasing projectile speed. This trend is enhanced by the gradually decreasing influence of inner taget shells on the stopping cross section as the velocity decreases. A recent study (Sigmund et al., 2005) indicates that in the velocity regime of pronounced valence effects, shell and Barkas–Andersen corrections are at least as important as I-values in quantitative predictions.

In view of the absence of experimental data, predicted deviations from Bragg additivity for heavy ions have usually been determined by scaling experimental results for proton and alpha-particle bombardment (Ziegler, 2005). This assertion has not been corroborated by theory: In the velocity range where valence structure effects become significant for protons and helium ions, heavier ions are strongly screened. This implies a drastic reduction of the contribution of distant collisions to the stopping cross section, and hence much less pronounced valence structure effects. Conversely, the most pronounced effects were found in the stopping of antiprotons (Sigmund et al., 2003).

2.4. Channeling

Early studies of energy loss in channeling (Lindhard, 1965) were handicapped by the absence of reliable estimates of impact-parameter-dependent energy losses. Therefore, most estimates going beyond the use of the equipartition rule employed the local-plasma picture, even though this picture is much more questionable for impact-parameter-dependent energy losses than for stopping cross sections.

Several of the theoretical schemes mentioned above allow to estimate impact-parameter dependencies, in particular so the harmonic-oscillator model

(Mikkelsen and Mortensen, 1990), binary theory (Sigmund and Schinner, 2001b), and the unitary-convolution approximation (Azevedo et al., 2000). Considering the large number of available experimental data, here is a widely open area for thorough and comprehensive study.

A problem of long standing in this area is the Barkas–Andersen effect for channeled ions. In experiments with heavy ions in "frozen charge states", Datz et al. (1977) and Golovchenko et al. (1981) found energy losses strictly proportional to the square of the charge state, i.e., seemingly no Barkas–Andersen correction. We have looked into this problem (Sigmund and Schinner, 2001b) and arrived at some degree of understanding. Conversely, Azevedo et al. (2001) found what they call a giant Barkas effect for low-Z_1 ions with a maximum for channeled lithium ions. For random stopping, on the other hand, the maximal Barkas–Andersen effect was predicted to be observable for protons (Sigmund and Schinner, 2003). Some clarification is evidently needed here.

3. Straggling

The term "energy-loss straggling" is commonly used either for the variance of an energy-loss profile,

$$\Omega^2 = NxW = \left\langle (\Delta E - \langle \Delta E \rangle)^2 \right\rangle, \tag{7}$$

which is proportional to the travelled path length x and atom density N for random stopping, or for the energy-loss profile $F(\Delta E, x)\,\mathrm{d}(\Delta E)$ itself.

In principle. also higher cumulants $\langle (\Delta E - \langle \Delta E \rangle)^n \rangle$ with $n \geq 3$ are of interest, although measured results are scarce in the literature: These quantities are sensitive to the high-loss tail of the spectrum and, hence, to background noise.

Straggling is a complex topic and has been much less studied than the mean energy loss. One reason is that straggling is not the only reason for observed broadening of an energy-loss profile: Non-uniform layer thickness and target inhomogeneities may compete and sometimes become dominant, and separating these effects from straggling is by no means trivial.

This survey is rather brief. For a more comprehensive account the reader is referred to Sigmund (2006, chapters 8 and 9).

3.1. Variance and Straggling Parameter

3.1.1. *Factors Affecting Straggling*

The generally accepted reference standard in straggling is "Bohr straggling",

$$W_\mathrm{B} = 4\pi Z_1^2 Z_2 e^4, \tag{8}$$

which represents the fluctuation of the energy loss of a point charge $Z_1 e$ penetrating through a medium filled randomly with free electrons at a density of $Z_2 N$ [electrons/volume]. Note that Bohr straggling does *not* represent the prediction of the Bohr stopping model for straggling: Binding of target electrons is neglected here.

In principle, all factors influencing the stopping cross section also affect the straggling parameter, i.e.,

- Binding,
- Orbital motion (shell correction),
- Barkas–Andersen effect,
- Projectile screening and excitation, and
- Relativity.

Lindhard and Sørensen (1996) have shown that there is no non-relativistic Bloch correction in straggling, i.e., similar predictions ought to emerge from the Born approximation on the one hand and the Bohr model on the other. However, in the same work it was demonstrated that the relativistic high-Z_1 correction is quite important also in straggling.

Moreover, charge exchange has long been known to produce drastic effects in straggling. In addition, bunching and correlation are effects which are of no significance to the mean energy loss for a uniform beam but can be substantial in straggling.

3.1.2. *Shell and Barkas–Andersen Correction*

Figure 13 shows a set of recent predictions for protons and antiprotons in silicon, split up into contributions from the principal target shells. All curves have been normalized to Bohr straggling. In addition to the curves for protons and antiprotons, also average curves are shown, i.e., results ignoring the Barkas–Andersen correction.

In the high-speed limit, Bohr straggling is approached, with the contributions from individual shells reflecting the number of electrons in those shells. A pronounced overshoot, the Bethe–Livingston shoulder, is observed at intermediate speed, in particular for protons interacting with the L-shell. This is a manifestation of the shell correction (Fano, 1963). Figure 14 shows an experimental verification of this effect.

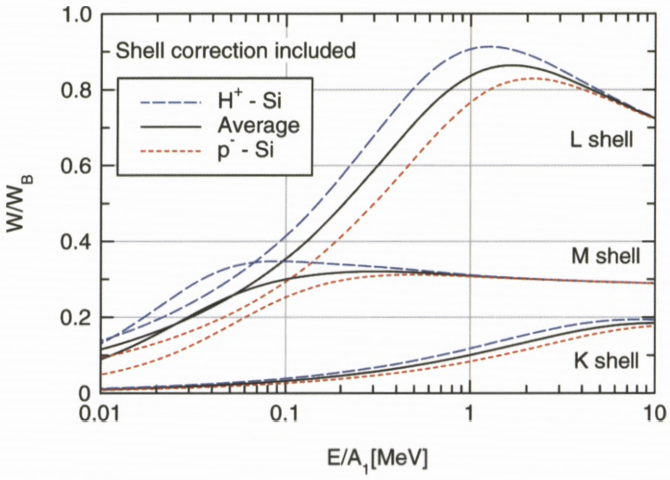

Figure 13. Straggling for protons and antiprotons in silicon predicted from binary theory, split into contributions from the principal shells. From Sigmund and Schinner (2002a).

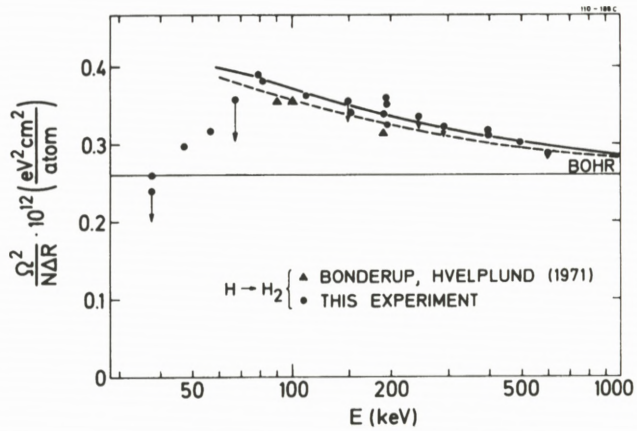

Figure 14. Straggling for protons in hydrogen. Measurements by Besenbacher et al. (1981) compared to calculations by Bonderup and Hvelplund (1971). The solid and dashed line represent two versions of the Thomas–Fermi description of the I-value. From Besenbacher et al. (1981).

3.1.3. *Bunching and Correlation*

As mentioned above, Bohr straggling assumes electrons distributed at random. Deviations from Poisson behavior occur when electrons are not distributed randomly in space.

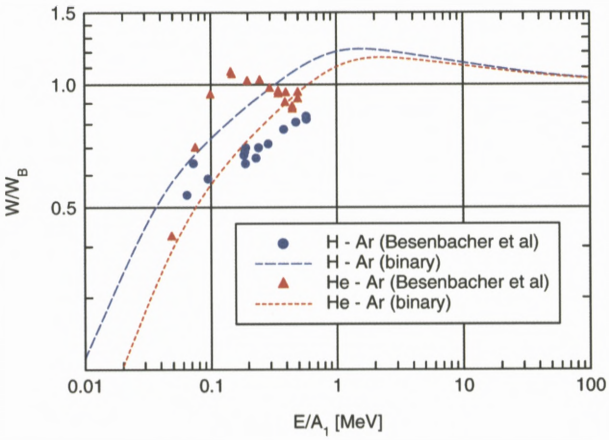

Figure 15. Straggling of protons and helium ions in argon gas. Measurements from Besenbacher et al. (1981). Calculations from binary theory. From Sigmund and Schinner (2002a).

- The *bunching effect* takes into account enhanced straggling due to the proximity of electrons in a target atom.
- *Correlation*, on the other hand means
  - Enhanced straggling due to proximity of atoms in the molecules of a gas, or
  - Diminished straggling due to dense packing of atoms in (amorphous) solids (Sigmund, 1978).

Contributions of bunching and correlation to straggling go roughly with the square of the atomic stopping cross section (Sigmund, 1976, 2006; Besenbacher et al., 1980). Figure 15 shows measured straggling parameters for protons and helium ions in argon gas. It seen that due to bunching, the curve for helium shows a pronounced enhancement near the stopping maximum. Theoretical curves, calculated from binary theory, have been determined by ignoring the bunching effect.

Figure 16 demonstrates the existence of the molecular correlation effect, i.e., enhanced straggling roughly $\propto S^2$ for a molecular gas (N_2) as compared to a similar atomic gas (Ne).

Figure 17 shows measured straggling parameters for light ions in germanium. Binary theory predicts a pronounced Bethe–Livingston shoulder, which is not found experimentally. One possible explanation is the correlation effect which, in a solid, gives rise to decreased straggling (Sigmund, 1978), and which has not been included in the theoretical curves.

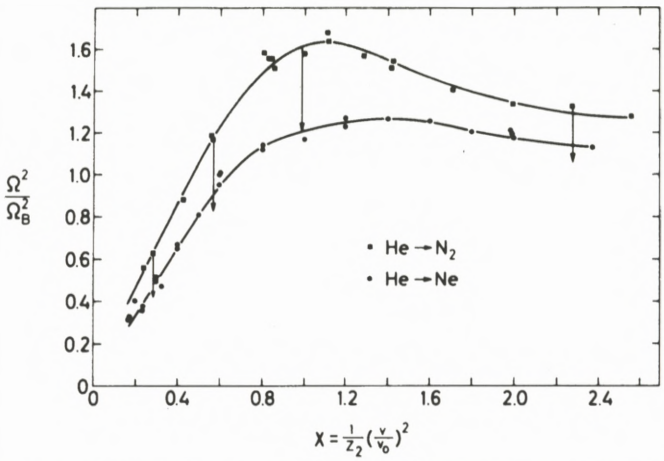

Figure 16. Straggling of helium ions in neon gas and molecular nitrogen. Curves drawn to guide the eye. Upper line: N_2; lower line: Ne. Arrows indicate a theoretical estimate of the correction for molecular correlation. From Besenbacher et al. (1977).

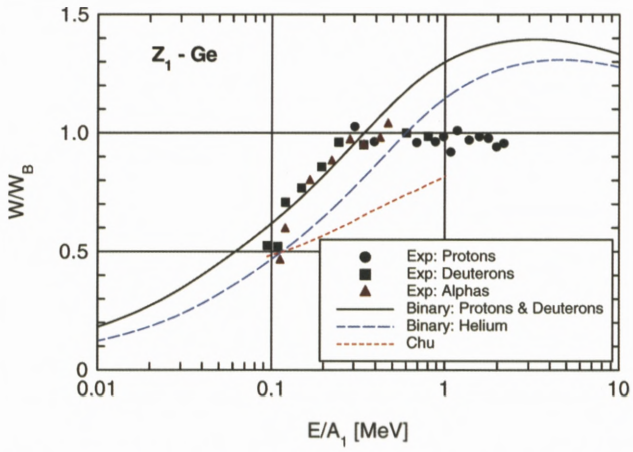

Figure 17. Straggling of light ions in solid germanium. Measurements from Malherbe and Albertz (1982). Calculations from binary theory and from Chu (1976). From Sigmund and Schinner (2002a).

Careful straggling measurements on foils with a well-controlled thickness, with ion-target combinations and velocities chosen such as to specifically test the roles of shell and Barkas–Andersen corrections, bunching and correlation, are highly desirable.

3.2. Energy-loss spectra

According to Bohr (1948), an energy-loss profile approaches Gaussian shape for $\Omega^2 \gg T_{\max}^2$, where $T_{\max}$ is the maximum energy transfer in an individual collision event. For a penetrating point charge this implies

$$4\pi Z_1^2 Z_2 e^4 N x \gg (2mv^2)^2. \tag{9}$$

Evidently, the lower limit in layer thickness for the Gaussian approximation to apply depends most sensitively on Z_1 and on the projectile speed. Specifically, deviations from Gaussian shape are expected to be most pronounced for protons and antiprotons at high speed.

For a detailed discussion, the reader is referred to Sigmund (2006) and a forthcoming paper by Glazov and Sigmund (2006). Here I shall briefly go through the various regimes and the way to treat them theoretically, in the order of increasing thickness:

1. For the thinnest targets, the observed spectrum will resemble the differential scattering cross section and reveal the shell structure of the excitation spectrum of the target. Spectra may be predicted by the convolution method (Bichsel and Saxon, 1975).
2. With increasing layer thickness, shell structure effects will be wiped out, and a more continuous spectrum will emerge which may be approximated by the Landau formula based on Coulomb scattering (Landau, 1944).
3. While the validity of the Landau formula is limited to rather small target thicknesses, an extension of the scheme by Glazov (2000) has proven to be very powerful.
4. The approach to Gaussian shape, which happens to be rather slow, is well described by the method of steepest descent as outlined by Sigmund and Winterbon (1985).
5. As indicated above, Gaussian profiles are more common for $Z_1 \gg 1$, even at high speed, but
6. Non-stochastic broadening may cause deviations from Gaussian shape for large target thicknesses. This effect will occur even in the absence of straggling: Since the initial spectrum always has a non-zero width, the very dependence of the stopping cross section on beam energy will eventually cause the spectrum to broaden in a way that does not preserve an initial Gaussian shape (Payne, 1969).

Figure 18 shows parameters characterizing the energy-loss profile of a point charge according to Glazov (2002a). The abscissa variable $\Omega_B^2/T_{\max}^2$ represents a

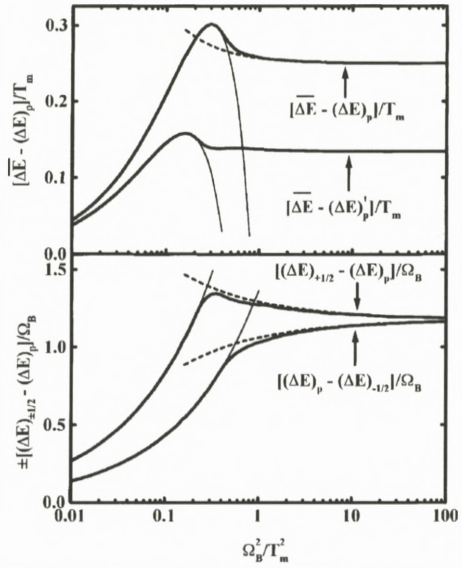

Figure 18. Quantities characteristic of energy-loss spectra calculated for truncated-Coulomb interaction. Thick lines: Numerical from Bothe–Landau equation. Thin lines: Extended Landau approximation due to Glazov (2000). Dotted lines: Steepest-descent method due to Sigmund and Winterbon (1985). $\overline{\Delta E}$ represents the mean energy loss, $(\Delta E)_p$ the peak position, and $(\Delta E)'_p$ the mean value between the left and the right half-value $(\Delta E)_{\pm 1/2}$. From Glazov (2002a).

measure of the target thickness. According to Bohr (1948), the abscissa value 1 represents the dividing point between non-Gaussian and close-to-Gaussian behavior. The upper graph shows the deviation from the peak energy loss ΔE_p from the mean energy loss $\overline{\Delta E}$, as well as the same quantity for a modified peak energy loss $(\Delta E_p)'$, found by taking the average between the upper and lower halfwidth. The difference is striking. The lower graph shows the upper and the lower halfwidth of the projectile. The difference between the two is a measure of the skewness of the profile, which is seen to vanish only at $\Omega^2/T^2_{\max} \geq 100$.

Thick solid lines represent numerical solutions of the Bothe-Landau equation, which comprises the statistical aspects for random stopping under the condition of small total energy loss $\overline{\Delta E} \ll E$. Thin lines represent Glazov's extension of the Landau scheme, while dotted lines represent results of the steepest-descent method. It is seen that combination of the latter two approaches makes up a very satisfactory description, with only a very small error in the immediate vicinity of the cross-over.

Much more drastic deviations from Gaussian shape have been studied extensively in situations where charge exchange plays a significant role. Experimental

studies were performed both for light and heavy ions (Cowern et al., 1984; Ogawa et al., 1991, 1993; Blazevic et al., 2002), and efficient formalisms have been established for theoretical analysis (Winterbon, 1977; Sigmund, 1992; Glazov, 2002b).

4. Low-Velocity Stopping

Some aspects of low-velocity stopping ($v < v_0$) are discussed in the contribution by Arista (2006). In this contribution I shall primarily try to identify needs for information on stopping data for low-speed ions.

4.1. Application Areas

With the exception of the lightest ions, nuclear stopping represents the dominating loss mechanism for $v \ll v_0$. This represents a complication with regard to extracting accurate data on electronic stopping from energy-loss measurements (Fastrup et al., 1966). Data on electronic losses are needed primarily for the understanding of radiation effects such as secondary electron emission, particle detectors, and electronic sputtering.

A topic of particular interest is that of elastic-collision spikes (Sigmund, 1974): A spike is a limited volume in a medium exposed to irradiation, where the majority of the atoms is temporarily in motion. Elastic collisions in such a spike lead to redistribution of kinetic energy amongst the atoms, whereas the slowing-down process is very inefficient. Under these circumstances, electronic energy loss may be the main cooling mechanism of a spike, together with energy transport by phonons, even though the electronic stopping cross section may be significantly smaller than the cross section for nuclear stopping which is conventionally determined for a target atom initially at rest.

4.2. Standard Descriptions

Electronic stopping cross sections have traditionally been evaluated from the Thomas–Fermi models of Lindhard and Scharff (1961) and Firsov (1959). Several attempts have been made to incorporate experimentally observed Z_1 structure into these models, with limited success. For summaries, the reader is referred to Sigmund (2004) or ICRU (2005). More recent work focused almost exclusively on stopping in an electron gas. An early attempt by Finnemann (1968) to describe low-velocity stopping in terms of quantum mechanical phase shifts has proven very successful, both in linear (Briggs and Pathak, 1974) and nonlinear

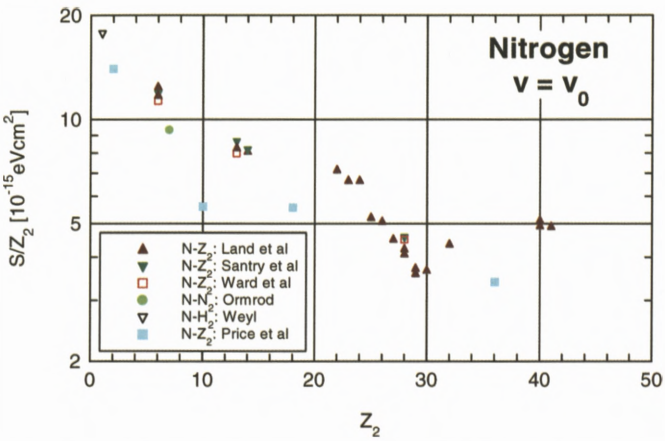

Figure 19. Stopping cross sections for nitrogen ions at $v = v_0$ measured by Land et al. (1985), Santry and Werner (1991), Ward et al. (1979), Ormrod (1968), Weyl (1953) and Price et al. (1993). Data not referring to exactly $v = v_0$ were scaled assuming velocity-proportional stopping. From ICRU (2005).

(Echenique et al., 1981) versions. Interestingly, while relatively weak Z_1 oscillations for random stopping seem to have escaped accurate theoretical description, much more pronounced structure observed in channeling (Bøttiger and Bason, 1969) has received a satisfactory explanation in terms of phase shifts calculated from density functional theory (Ashley et al., 1986) .

4.3. Open problems

First of all, theory for low-velocity stopping in *insulators* is essentially nonexisting. Existing experience in atomic-collision physics suggests electron promotion to be of prime importance, but even for collisions in the gas phase, valid theoretical predictions seem to address mainly inner-shell phenomena.

Second, the problem of the threshold for electronic energy transfer is essentially unsolved, not only for heavy ions but even for protons and antiprotons, as is manifest in a recent series of publications on stopping in lithium fluoride (Eder et al., 1997; Møller et al., 2002). Experiments indicate, however, that the stopping cross section for protons and antiprotons in LiF is proportional to projectile speed significantly below the binary-collision threshold.

Finally, the suggestion has been made that there is a gas-solid effect in low-velocity stopping of heavy ions (Paul, 2004). Figure 19 shows measured stopping cross sections from various sources for nitrogen ions at $v = v_0$. Evidently, the noble gases He, Ne, Ar and Kr show lower stopping cross sections than numerous

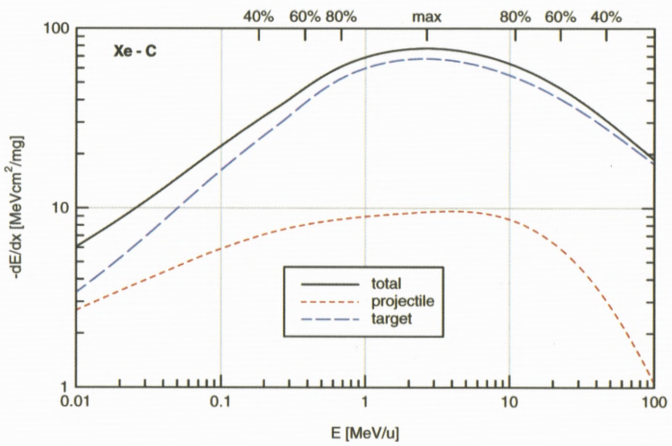

Figure 20. Stopping force of amorphous carbon for xenon ions, calculated from binary theory. Contributions due to target and projectile excitations are shown separately, as well as their sum.

other elements. However, it is not clear whether this is an effect of Z_2 structure or a gas-solid effect. Note in particular that nitrogen gas – according to a different source – shows a much less pronounced effect.

5. Velocity Effect for Swift Ions

Several contributions to this volume mention the so-called velocity effect, i.e., the experimental finding that radiation effects originating in electronic energy loss do not necessarily scale with the stopping cross section. A common feature for such phenomena is the double-valuedness of the physical quantity of interest, such as a sputter yield of a solid or an inactivation rate of a cell culture, when plotted as a function of the stopping cross section.

Clearly, the differential energy-transfer cross section at two different values of the beam energy will not be the same, even if the stopping cross sections happen to coincide. But how large is the difference, and in which part of the excitation spectrum is it most pronounced?

Figure 20 shows the calculated equilibrium stopping force on xenon in carbon. Contributions from target and projectile excitation are shown separately. The upper abscissa scale shows the position of the maximum as well as the 80, 60 and 40% levels below the maximum.

Figure 21 shows single-differential cross sections for electron emission – i.e. integrated over emission angle – for target excitation/ionization and the whole spectrum, respectively. Cross sections were calculated from the PASS code ac-

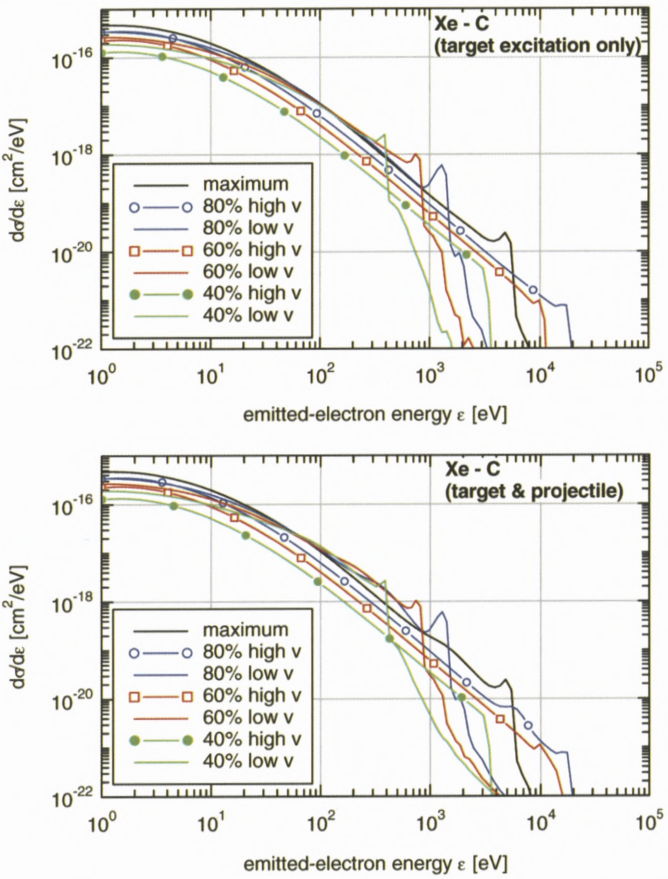

Figure 21. Energy spectra of electrons emitted in a single Xe-C collision. Beam energies chosen at maximum stopping as well as the 80, 60 and 40% level indicated in figure 20. Upper graph: Target excitation only. Lower graph: Total spectrum.

cording to a theoretical scheme described by Weng et al. (2006). Spectra for the various levels are distinguished by their colors.

As expected, the spectrum reflecting the higher beam energy extends to a higher electron energy ϵ than that for the lower beam energy. That difference, however, is compensated by a pronounced shoulder of the low-energy spectrum near its kinematic limit. Conversely, only minor differences are observed at the low-energy end of the spectra, despite a factor of 10–100 difference between the respective beam energies. Note that from Rutherford's law – which is the standard theoretical tool in this kind of analysis (Kobetich and Katz, 1968; Wilson and

Paretzke, 1981; Scholz and Kraft, 1995) one would expect a difference in the two spectra at the lower end of one to two orders of magnitude!

6. Conclusions

Although I have not dwelled on this aspect, I like to emphasize that classical mechanics is a powerful tool in the description of electronic stopping and related problems. This has proven particularly true for ions heavier than helium, but even in the velocity range that is commonly identified as the Born regime, not much more quantum physics is needed to achieve a valid description than what is contained in the Bloch correction, which does not contain target parameters.

Amongst longstanding problems which may be considered "solved" at least in principle, I like to mention

- the gas-solid effect in the stopping force on heavy ions, except at low speed,
- the (lacking) role of the effective charge in heavy-ion stopping,
- the magnitude of the Barkas–Andersen effect in close collisions,
- the physics of the shell correction, and
- deviations from Bragg additivity and other valence effects.
- Efficient tools are available to analyse the role of charge exchange in straggling, but the potential of utilizing information from pertinent experiments has not been fully utilized yet.

Amongst aspects that I believe need adequate attention I should like to mention

- careful distinction between energy loss and deposition,
- low-velocity stopping in insulators,
- the role of electron promotion in stopping and straggling,
- clear criteria for the significance of charge exchange in stopping,
- the Barkas–Andersen effect in channeling,
- the gas-solid effect in straggling,
- the role of bunching and correlation in straggling, mostly in solids, and the competition with the Bethe–Livingston shoulder.

Acknowledgements

Most of the calculations performed specifically for this article were carried out by the PASS code developed in cooperation with Andreas Schinner. This work has been supported by the Danish Natural Science Research Council (FNU).

References

Ahlen S.P. (1980): Theoretical and experimental aspects of the energy loss of relativistic heavily ionizing particles. Rev Mod Phys **52**, 121–173

Ahlen S.P. (1982): Calculation of the relativistic Bloch correction to stopping power. Phys Rev A **25**, 1856–1867

Andersen H.H., Garfinkel A.F., Hanke C.C. and Sørensen H. (1966): Stopping power of aluminium for 5-12 MeV protons and deuterons. Mat Fys Medd Dan Vid Selsk **35, no. 4**, 1–24

Andersen H.H., Simonsen H. and Sørensen H. (1969a): An experimental investigation of charge-dependent deviations from the Bethe stopping power formula. Nucl Phys A **125**, 171–175

Andersen H.H., Sørensen H. and Vajda P. (1969b): Excitation potentials and shell corrections for elements $Z_2 = 20$ to $Z_2 = 30$. Phys Rev **180**, 373–380

Arista N.R. (2002): Energy loss of heavy ions in solids: -linear calculations for slow and swift ions. Nucl Instrum Methods B **195**, 91–105

Arista N.R. (2006): Charge states and energy loss of ions in solids. Mat Fys Medd Dan Vid Selsk **52**, 595–623

Ashley J.C., Ritchie R.H. and Brandt W. (1972): Z_1^3 Effect in the stopping power of matter for charged particles. Phys Rev B **5**, 2393–2397

Ashley J.C., Ritchie R.H., Echenique P.M. and Nieminen R.M. (1986): Nonlinear calculations of the energy loss of slow ions in an electron gas. Nucl Instrum Methods B **15**, 11–13

Azevedo G.M., Grande P.L., Behar M., Dias J.F. and Schiwietz G. (2001): Giant Barkas effect observed for light ion channeling in Si. Phys Rev Lett **86**, 1482–1485

Azevedo G.M., Grande P.L. and Schiwietz G. (2000): Impact-parameter dependent energy loss of screened ions. Nucl Instrum Methods B **164-165**, 203–211

Besenbacher F., Andersen J.U. and Bonderup E. (1980): Straggling in energy loss of energetic hydrogen and helium ions. Nucl Instrum Methods **168**, 1–15

Besenbacher F., Andersen H.H., Hvelplund P. and Knudsen H. (1981): Straggling in energy loss of swift hydrogen and helium ions in gases. Mat Fys Medd Dan Vid Selsk **40, no. 9**, 1–42

Besenbacher F., Heinemeier J., Hvelplund P. and Knudsen H. (1977): Energy-loss straggling for protons and helium ions. Phys Lett A **61**, 75–77

Betz H.D. and Grodzins L. (1970): Charge states and excitation of fast heavy ions passing through solids: a new model for the density effect. Phys Rev Lett **25**, 211–214

Bichsel H. and Saxon R.P. (1975): Comparison of calculational methods for straggling in thin absorbers. Phys Rev A **11**, 1286–1296

Bimbot R., Cabot C., Gardès D., Gauvin H., Hingmann R., Orliange I., De Reilhac L. and Hubert F. (1989a): Stopping power of gases for heavy ions: as-solid effect I. 2-13 MeV/u Ne and Ar projectiles. Nucl Instrum Methods B **44**, 1–18

Bimbot R., Cabot C., Gardès D., Gauvin H., Orliange I., DeReilhac L., Subotic K. and Hubert F. (1989b): Stopping power of gases for heavy ions: gas-solid effect II. 2-6MeV/u Cu, Kr and Ag projectiles. Nucl Instrum Methods B **44**, 19–34

Blazevic A., Bohlen H.G. and von Oertzen W. (2002): Stopping power of swift neon ions in dependence on the charge state in the non-equilibrium regime. Nucl Instrum Methods B **190**, 64–68

Bloch F. (1933): Zur Bremsung rasch bewegter Teilchen beim Durchgang durch Materie. Ann Physik **16**, 285–320

Bohr N. (1940): Scattering and stopping of fission fragments. Phys Rev **58**, 654–655

Bohr N. (1948): The penetration of atomic particles through matter. Mat Fys Medd Dan Vid Selsk **18, no. 8**, 1–144

Bohr N. and Lindhard J. (1954): Electron capture and loss by heavy ions penetrating through matter. Mat Fys Medd Dan Vid Selsk **28, no. 7**, 1–31

Bonderup E. (1967): Stopping of swift protons evaluated from statistical atomic model. Mat Fys Medd Dan Vid Selsk **35, no. 17**, 1–20

Bonderup E. and Hvelplund P. (1971): Stopping power and energy straggling for swift protons. Phys Rev A **4**, 562–589

Bøttiger J. and Bason F. (1969): Energy loss of heavy ions along low-index directions in gold single crystals. Radiat Eff **2**, 105

Briggs J.S. and Pathak A.P. (1974): The stopping power of solids for low-velocity channelled heavy ions. J Phys C **7**, 1929–1936

Cabrera-Trujillo R., Sabin J.R., Deumens E. and Öhrn Y. (2002): Stopping cross sections for $N^{4+} \rightarrow H$ at low velocity. Phys Rev A **66**, 022706, 1–7

Chu W.K. (1976): Calculation of energy straggling for protons and helium ions. Phys Rev A **13**, 2057–2060

Chu W.K. and Powers D. (1972): Calculations of mean excitation energy for all elements. Phys Lett **40A**, 23–24

Cowern N.E.B., Read P.M., Sofield C.J., Bridwell L.B. and Lucas M.W. (1984): Charge-changing energy loss, higher-order Z_1 dependence, and pre-equilibrium behavior in the stopping power for energetic ions in solids. Phys Rev A **30**, 1682–1691

Datz S., DelCampo J.G., Dittner P.F., Miller P.D. and Biggerstaff J.A. (1977): Higher-order Z_1 effects and effects of screening by bound K electrons on the electronic stopping of channeled ions. Phys Rev Lett **38**, 1145–1148

Dehmer J.L., Inokuti M. and Saxon R.P. (1975): Systematics of dipole oscillator-strength distributions for atoms of the first and second row. Phys Rev A **12**, 102–121

Echenique P.M., Nieminen R.M. and Ritchie R.H. (1981): Density functional calculation of stopping power of an electron gas for slow ions. Sol St Comm **37**, 779–781

Eder K., Semrad D., Bauer P., Golser R., Maier-Komor P., Aumayr F., Peñalba M., Arnau A., Ugalde J.M. and Echenique P.M. (1997): Absence of a "threshold effect" in the energy loss of slow protons traversing large-band-gap insulators. Phys Rev Lett **79**, 4112–4115

Fano U. (1963): Penetration of protons, alpha particles, and mesons. Ann Rev Nucl Sci **13**, 1–66

Fastrup B., Hvelplund P. and Sautter C.A. (1966): Stopping cross section in carbon of 0.1–1.0 MeV atoms with $6 < Z_1 < 20$. Mat Fys Medd Dan Vid Selsk **35, no. 10**, 1–28

Finnemann J. (1968): En redegørelse for resultaterne af beregninger over spredning af elektroner med lav energi på afskærmede Coulombfelter. Master's thesis, Aarhus University

Firsov O.B. (1959): A qualitative interpretation of the mean electron excitation energy in atomic collsions. Zh Eksp Teor Fiz **36**, 1517–1523. [English translation: Sov. Phys. JETP **9**, 1076-1080 (1959)]

Geissel H. (1982): Untersuchungen zur Abbremsung von Schwerionen in Materie im Energiebereich von (0,5–10) MeV/U. GSI-Report **82-12**, 21–29

Glazov L.G. (2000): Energy-loss spectra of swift ions. Nucl Instrum Methods B **161**, 1–8

Glazov L.G. (2002a): Energy-loss spectra of swift ions: Beyond the Landau approximation. Nucl Instrum Methods B **192**, 239–248

Glazov L.G. (2002b): Multiple-peak structures in energy-loss spectra of swift ions. Nucl Instrum Methods B **193**, 56–65

Glazov L.G. and Sigmund P. (2006): Energy-loss spectra of swift point charges at relativistic velocities. Nucl Instrum Methods B, in press

Golovchenko J.A., Goland A.N., Rosner J.S., Thorn C.E., Wegner H.E., Knudsen H. and Moak C.D. (1981): Charge state dependence of channeled ion energy loss. Phys Rev B **23**, 957–966

Golser R. and Semrad D. (1991): Observation of a striking departure from velocity proportionality in low-energy electronic stopping. Phys Rev Lett **66**, 1831–1833

Grande P.L. and Schiwietz G. (2002): The unitary convolution approximation for heavy ions. Nucl Instrum Methods B **195**, 55–63

Grande P.L., Hentz A., Pezzi R.P., Baumvoll I.J.R. and Schiwietz G. (2006): Solved and unsolved problems in ion-beam analysis: The influence of single collisions. Mat Fys Medd Dan Vid Selsk **52**, 151–185

Grüner F., Bell F., Assmann W. and Schubert M. (2004): Integrated approach to the electronic interaction of swift heavy ions with solids and gases. Phys Rev Lett **93**, 213201

Henke B.L., Gullikson E.M. and Davies J.C. (1993): X-ray interactions: photoabsorption, scattering, transmission, and reflection at E = 50-30,000 eV, Z = 1-92. At Data & Nucl Data Tab **54**, 181–342

Holmén G., Svensson B.G., Schou J. and Sigmund P. (1979): Direct and recoil-induced electron emission from ion-bombarded solids. Phys Rev B **20**, 2247–2254

ICRU (1993): Stopping Powers and Ranges for Protons and Alpha Particles, Vol. 49 of ICRU Report. International Commission of Radiation Units and Measurements, Bethesda, Maryland

ICRU (2005): Stopping of Ions Heavier Than Helium, Vol. 73 of ICRU Report. Oxford University Press, Oxford

Jäkel O. (2006): Hadron therapy: Radiotherapy using fast ion beams. Mat Fys Medd Dan Vid Selsk **52**, 37–57

Kabachnik N.M. (1993): Screening and antiscreening in the semiclassical description of ionization in fast ion-atom collisions. J Phys B **26**, 3803–3814

Kobetich E.J. and Katz R. (1968): Energy deposition by electron beams and delta rays. Phys Rev **170**, 391–396

Land D.J., Simons D.G., Brennan J.G. and Glass G.A. (1985): Range distributions and electronic stopping power of nitrogen ions in solids. Nucl Instrum Methods B **10/11**, 234–236

Landau L. (1944): On the energy loss of fast particles by ionization. J Phys USSR **8**, 201–205

Lassen N.O. (1951a): Total charges of fission fragments as functions of the pressure in the stopping gas. Mat Fys Medd Dan Vid Selsk **26, no. 12**, 1–19

Lassen N.O. (1951b): The total charges of fission fragments in gaseous and solidstopping media. Mat Fys Medd Dan Vid Selsk **26, no. 5**, 1–28

Lindhard J. (1965): Influence of crystal lattice on motion of energetic charged particles. Mat Fys Medd Dan Vid Selsk **34, no. 14**, 1–64

Lindhard J. (1976): The Barkas effect – or Z_1^3, Z_1^4-corrections to stopping of swift charged particles. Nucl Instrum Methods **132**, 1–5

Lindhard J. and Scharff M. (1953): Energy loss in matter by fast particles of low charge. Mat Fys Medd Dan Vid Selsk **27, no. 15**, 1–31

Lindhard J. and Scharff M. (1961): Energy dissipation by ions in the keV region. Phys Rev **124**, 128–130

Lindhard J. and Sørensen A.H. (1996): On the relativistic theory of stopping of heavy ions. Phys Rev A **53**, 2443–2456

Malherbe J.B. and Albertz H.W. (1982): Energy-loss straggling in C and Ge of p, D and alpha particles in the energy region 0.2 to 2.4 MeV. Nucl Instrum Methods **192**, 559–563

Maynard G., Chabot M. and Gardès D. (2000): Density effect and charge dependent stopping theories for heavy ions in the intermediate velocity regime. Nucl Instrum Methods B **164-165**, 139–146

Maynard G., Zwicknagel G., Deutsch C. and Katsonis K. (2001): Diffusion-transport cross section and stopping power of swift heavy ions. Phys Rev A **63**, 052903-1–14

Medenwaldt R., Møller S.P., Uggerhøj E., Worm T., Hvelplund P., Knudsen H., Elsener K. and Morenzoni E. (1991): Measurement of the stopping power of silicon for antiprotons between 0.2 and 3 MeV. Nucl Instrum Methods B **58**, 1–5

Meitner L. and Freitag K. (1926): Über die Alpha-Strahlen des ThC+C' und ihr Verhalten beim Durchgang durch verschiedene Gase. Z Physik **37**, 481–517

Mikkelsen H.H. and Mortensen E.H. (1990): The extended oscillator model of atomic stopping - application to proton stopping in noble gases. Nucl Instrum Methods B **48**, 39–42

Mikkelsen H.H. and Sigmund P. (1987): Impact parameter dependence of electronic energy loss: Oscillator model. Nucl Instrum Methods B **27**, 266–275

Mikkelsen H.H. and Sigmund P. (1989): Barkas effect in electronic stopping power: Rigorous evaluation for the harmonic oscillator. Phys Rev A **40**, 101–116

Møller S.P., Uggerhøj E., Bluhme H., Knudsen H., Mikkelsen U., Paludan K. and Morenzoni E. (1997): Direct measurement of the stopping power for antiprotons of light and heavy targets. Phys Rev A **56**, 2930–2939

Møller S.P., Csete A., Ichioka T., Knudsen H., Uggerhoj U.I. and Andersen H.H. (2002): Antiproton stopping at low energies: confirmation of velocity-proportional stopping power. Phys Rev Lett **88**, 193201-1–4

Montanari C.C., Miraglia J.E. and Arista N.R. (2003): Antiscreening mode of projectile-electron loss. Phys Rev A **67**, 062702

Northcliffe L.C. (1963): Passage of heavy ions through matter. Ann Rev Nucl Sci **13**, 67–102

Oddershede J. and Sabin J.R. (1984): Orbital and whole-atom proton stopping power and shell corrections for atoms with $Z < 36$. At Data Nucl Data Tab **31**, 275–297

Ogawa H., Katayama I., Ikegami H., Haruyama Y., Aoki A., Tosaki M., Fukuzawa F., Yoshida K., Sugai I. and Kaneko T. (1991): Direct Measurement of fixed-charge stopping power for 32-MeV He^{3+} in a charge-state nonequilibrium region. Phys Rev B **43**, 11370–11376

Ogawa H., Katayama I., Sugai I., Haruyama Y., Saito M., Yoshida K., Tosaki M. and Ikegami H. (1993): Charge state dependent energy loss of high velocity oxygen ions in the charge state non-equilibrium region. Nucl Instrum Methods B **82**, 80–84

Ormrod J.H. (1968): Low-energy electronic stopping cross sections in nitrogen and argon. Can J Phys **46**, 497–502

Palik E.D. (2000): Electronic Handbook of Optical Constants of Solids – Version 1.0. SciVision – Academic Press

Paul H. (2004): A note on the density effect in the stopping power for positive ions. Nucl Instrum Methods B **217**, 7–11

Paul H. (2005): Stopping power graphs. `www.exphys.uni-linz.ac.at/stopping/`

Payne M.G. (1969): Energy straggling of heavy charged particles in thick absorbers. Phys Rev **185**, 611–622

Price J.L., Simons D.G., Stern S.H., Land D.J., Guardala N.A., Brennan J.G. and Stumborg M.F. (1993): Stopping powers of the noble gases for (0.3-10)-MeV nitrogen ions. Phys Rev A **47**, 2913–2918

Santry D. and Werner R. (1991): Measured stopping powers of ^{12}C and ^{14}N ions in thin elemental foils. Nucl Instrum Methods B **53**, 7–14

Scheidenberger C., Geissel H., Mikkelsen H.H., Nickel F., Brohm T., Folger H., Irnich H., Magel A., Mohar M.F., Pfützner G.M.M. et al. (1994): Direct observation of systematic deviations from the Bethe stopping theory for relativistic heavy ions. Phys Rev Lett **73**, 50–53

Schiøtt H.E. (1966): Range-energy relations for low-energy ions. Mat Fys Medd Dan Vid Selsk **35, no. 9**, 1

Schiwietz G. (1990): Coupled-channel calculation of stopping powers for intermediate-energy light ions penetrating atomic H and He targets. Phys Rev A **42**, 296–306

Scholz M. and Kraft G. (1995): Track structure and the calculation of biological effects of heavy charged particles. Adv Space Res **18**, 5–14

Sigmund P. (1974): Energy density and time constant of heavy-ion-induced elastic-collision spikes in solids. Appl Phys Lett **25**, 169–171

Sigmund P. (1976): Energy loss of charged particles to molecular gas targets. Phys Rev A **14**, 996–1005

Sigmund P. (1978): Statistics of particle penetration. Mat Fys Medd Dan Vid Selsk **40, no. 5**, 1–36

Sigmund P. (1982): Kinetic theory of particle stopping in a medium with internal motion. Phys Rev A **26**, 2497–2517

Sigmund P. (1992): Statistical theory of charged-particle stopping and straggling in the presence of charge exchange. Nucl Instrum Methods B **69**, 113–122

Sigmund P. (1996): Low-velocity limit of Bohr's stopping-power formula. Phys Rev A **54**, 3113–3117

Sigmund P. (1997): Charge-dependent electronic stopping of swift nonrelativistic heavy ions. Phys Rev A **56**, 3781–3793

Sigmund P. (2004): Stopping of Heavy Ions, Springer Tracts of Modern Physics, Vol. 204. Springer, Berlin

Sigmund P. (2006): Particle Penetration and Radiation Effects, Springer Series in Solid-State Sciences, Vol. 151. Springer, Berlin

Sigmund P. and Glazov L.G. (2003): Interplay of charge exchange and projectile excitation in the stopping of swift heavy ions. Europ Phys J D **23**, 211–215

Sigmund P. and Haagerup U. (1986): Bethe stopping theory for a harmonic oscillator and Bohr's oscillator model of atomic stopping. Phys Rev A **34**, 892–910

Sigmund P. and Schinner A. (2000): Binary stopping theory for swift heavy ions. Europ Phys J D **12**, 425–434

Sigmund P. and Schinner A. (2001a): Effective charge and related/unrelated quantities in heavy-ion stopping. Nucl Instrum Methods B **174**, 535–540

Sigmund P. and Schinner A. (2001b): Resolution of the frozen-charge paradox in stopping of channeled heavy ions. Phys Rev Lett **86**, 1486–1489

Sigmund P. and Schinner A. (2002a): Barkas effect, shell correction, screening and correlation in collisional energy-loss straggling of an ion beam. Europ Phys J D 201–209

Sigmund P. and Schinner A. (2002b): Binary theory of electronic stopping. Nucl Instrum Methods B **195**, 64–90

Sigmund P. and Schinner A. (2003): Anatomy of the Barkas effect. Nucl Instrum Methods B **212**, 110 – 117

Sigmund P. and Schinner A. (2006): Shell correction in stopping theory. Nucl Instrum Methods B **243**, 457–460

Sigmund P. and Winterbon K.B. (1985): Energy loss spectrum of swift charged particles penetrating a layer of material. Nucl Instrum Methods B **12**, 1–16

Sigmund P., Fettouhi A. and Schinner A. (2003): Material dependence of electronic stopping. Nucl Instrum Methods B **209**, 19–25

Sigmund P., Sharma A., Schinner A. and Fettouhi A. (2005): Valence structure effects in the stopping of swift ions. Nucl Instrum Methods B **230**, 1–6

Tarlé G. and Solarz M. (1978): Evidence for higher-order contributions to the stopping power of relativistic iron nuclei. Phys Rev Lett **41**, 483–486

Thwaites D.I. (1984): Current status of physical state effects on stopping power. Nucl Instrum Methods B **12**, 84–89

Walske M.C. (1952): The stopping power of K-electrons. Phys Rev **88**, 1283–1289

Ward D., Andrews H.R., Mitchell I.V., Lennard W.N., Walker R.B. and Rud N. (1979): Systematics for the Z_1-oscillation in stopping powers of various solid materials. Can J Phys **57**, 645–656

Weng M.S., Schinner A., Sharma A. and Sigmund P. (2006): Primary electron spectra from swift heavy-ion impact: Scaling relations and estimates from modified Bohr theory. Europ Phys J D **39**, 209–221

Weyl P.K. (1953): The energy loss of hydrogen, helium, nitrogen, and neon ions in gases. Phys Rev **91**, 289–296

Wilson W.E. and Paretzke H.G. (1981): Calculation of distributions for energy imparted and ionization by fast protons in nanometer sites. Radiat Res **87**, 521–537

Winter HP., Aumayr F., Winter H. and Lederer S. (2006): Recent advances in slow heavy particle induced electron emission. Mat Fys Medd Dan Vid Selsk **52**, 525–556

Winterbon K.B. (1977): Electronic energy loss and charge-state fluctuations of swift ions. Nucl Instrum Methods **144**, 311–315

Ziegler J.F. (2005): Particle interactions with matter. `www.srim.org`

Charge States and Energy Loss of Ions in Solids

N.R. Arista*

División Colisiones Atómicas
Centro Atómico Bariloche, Instituto Balseiro
RA-8400 S.C. Bariloche, Argentina

Abstract

The interrelation between electronic energy loss and charge states of ions in solids is analyzed with particular attention to the cases of hydrogen and heavy ions. Different theoretical schemes and empirical evidences are discussed. Various approaches to describe the behavior of slow protons in metals are reviewed and compared with alternative experimental evidences obtained with other subatomic projectiles. Recent developments in theoretical evaluations of the energy loss of heavy ions using non-perturbative methods are compared with previous linear approaches using different ion charge models. Important differences in the ion charges assumed in previous models are explained by the influence of saturation effects which are absent in the linear and perturbative methods (and contained in the non-linear approach).

Contents

1 Introduction **596**

2 Light Ions: The Case of Hydrogen **597**
2.1 Experimental Evidences: Positrons, Positive Muons and Pions 606
2.2 Discussion 609

3 Heavy Ions **610**
3.1 Saturation Effects in the Energy Loss 617

* E-mail: arista@cab.cnea.gov.ar

4 Summary **618**

Acknowledgements **619**

References **619**

1. Introduction

The question of the energy loss of light and heavy ions in solids is intimately connected with the question of the charge state of the ions inside the medium. The two problems have been present in the studies of ion penetration in matter for many years (Betz, 1972; Kumakhov and Komarov, 1981). The early developments based on classical and quantum perturbation theory provided close analytical expressions for the mean energy loss only for the case of bare ions, but nevertheless have served for qualitative analysis and applications in various fields. The recent books by Sigmund (2004, 2006) together with an ICRU Report (2005) provide a very complete coverage of the field.

In this context, it is also a nice opportunity to make a special recognition in these Proceedings to the masterful contribution done by Peter Sigmund along many years in almost all the fields of ion-matter interactions covered in this volume.

For many years, the problem of dressed ions was approached from the perspective of statistical atomic models (Firsov, 1959; Lindhard and Scharf, 1953; Yarlagadda et al., 1978) and also by the introduction of effective charge models, where the emphasis was more on providing phenomenological scaling properties than formulating a complete theory of the complicated process of electronic energy loss of partially stripped ions. The greatest difficulties appeared of course in the case of heavy ions. In particular, the range of low energies proved to be much more complex than the statistical models predicted as clearly evidenced by the discovery of the oscillatory Z_1 dependence of the stopping coefficients for different ions (Ormrod and Duckworth, 1963; Ormrod et al., 1965).

Important advances were made in more recent years with the development of non-perturbative methods that include in the calculations terms of all orders in the interaction strength (Briggs and Pathak, 1973, 1974; Echenique et al., 1981, 1986, 1990; Grande and Schiwietz, 1991, 1993, 2002; Maynard et al., 2000, 2002; Sigmund and Schinner, 2000, 2002; Lifschitz and Arista, 1998; Arista, 2002). In various ways, these non-perturbative approaches hinge on nearly exact calculations of the energy loss either by directly solving Schrödinger's equation or by using alternative methods of approximation. In these approaches, the charge state of the ion plays a determinant role as a relevant input parameter.

While these aspects have been studied for a long time, various fundamental issues are still not properly understood. Different approaches have been proposed, but problems still remain and discrepancies between different views are important; this situation affects both light and heavy ions. In this work I will discuss the current state of the knowledge on some relevant questions concerning the charge state of ions moving in solids and its relevance to the stopping power problem. Following a usual convention, I will distinguish between light (hydrogen and helium) and heavy ions (everything heavier than helium). The discussion of light ions, however, will be centered on the case of hydrogen, since helium does not present significant problems compared with the rest of the cases.

2. Light Ions: The Case of Hydrogen

In spite of being the simplest case of a free ion, the question of protons moving in solids is one of the most elusive ones. The existing pictures for slow hydrogen in metals go from the simplest view of the protons remaining as unbound point particles, strongly screened by the conduction electrons, to the opposite extreme of considering the proton binding two electrons and forming H^- as the stable system for low energies. To try to understand the difficulties and subtleties encountered in this area it is useful to review some of the ideas and discussions that took place in the last three decades.

About 30 years ago Brandt (1975) conjectured that a proton would not be able to bind an electron in a metal due to the strong screening conditions. This conjecture was based on theoretical evidences of the time (Friedel, 1952, 1954, 1958; Langer and Vosko, 1959; Payne, 1970; Rogers et al., 1970). In particular, exact calculations of the effects of screening on the bound states of hydrogenic systems by Rogers et al. (1970), showed that, for the typical screening distances in metals, a bound state of hydrogen would not be possible. While the analysis for protons at low energies was reasonably well supported on physical grounds, the extension of the same picture to protons at all energies was not obvious. These conclusions were then objected by Cross (1977) who analyzed the case of swift protons and gave arguments to support the view of collisional equilibrium between protons and neutral hydrogen, dynamically connected by capture and loss processes. It should be noted that the criticism by Cross in principle does not apply to slow protons, as it presumes a dynamical decoupling between projectile and target states (ignoring also screening effects that play a dominant role at low energies) using a picture that is appropriate for swift ions.

Later on, and from a different perspective, self energy calculations based on a dielectric model (Guinea et al., 1981, 1982) predicted that both hydrogen and

helium in metals would be neutralized at low energies. It may be noted however that one should take these results with caution since the use of perturbative models for velocities below one atomic unit is quite risky (Mann and Brandt, 1981).

A different view emerged in the following years (Peñalba et al., 1992), inspired by the new methods of density functional theory (Hohenberg and Kohn, 1964; Kohn and Sham, 1965). According to this view, the ground state of hydrogen in metals (represented by a jellium model) would be a state with two bound electrons, resembling H^-. This rather unexpected picture (considering the very low binding energy of H^- in vacuum, $E_0 \sim 0.75$ eV) emerged from the analysis of the eigenvalues of the Kohn-Sham equations which arise in the density functional theory when the wavefunction of the total system is represented by a Slater determinant, using an independent particle approach (but including exchange and correlation effects in the effective potential through a local approximation). In this representation, an eigenvalue corresponding to a doubly occupied Kohn–Sham state with an energy slightly below the bottom of the conduction band is obtained. The interpretation of this eigenvalue as an evidence of a real physical state of H^- is, however, a doubtful point, since, as is well known, the only physically meaningful quantity in density functional theory is the density itself. In particular, there is a specific mention that the KS eigenvalues do not represent the actual energies of the real system (Sham and Kohn, 1966).

One of the shortcomings of the jellium model is the failure of including lattice structure effects. While these effects may not be extremely important for the description of static interstitial ions, they may become of paramount importance for moving ions. A more complete picture that includes both band structure and lattice structure effects is the one given by the linear-muffin-tin-orbital (LMTO) or related formulations (Vargas et al., 1986; Vargas and Christensen, 1987). An illustrative picture emerging from these studies is shown in Figure 1. The figure illustrates the localized state around the proton, which is located in an interstitial position within the lattice. Here we should call the attention on two points. First, the density of states shown on the right-hand scale shows that the localized state is degenerate in energies with the unlocalized states of the conduction band. This is typically the case for screening of ionized impurities (or scattering resonances) rather than a bound state. The physical image that emerges from these calculations is that of a strongly screened, or overscreened, proton with a non-integer value of screening charge larger than 1 (note that the excess screening charge is compensated at larger distances by Friedel oscillations). Secondly, we note the shape of the effective lattice potential in this figure, which, although qualitative, is representative of the real behavior predicted by extensive calculations (Vargas and Christensen, 1987). It produces important energy barriers that break

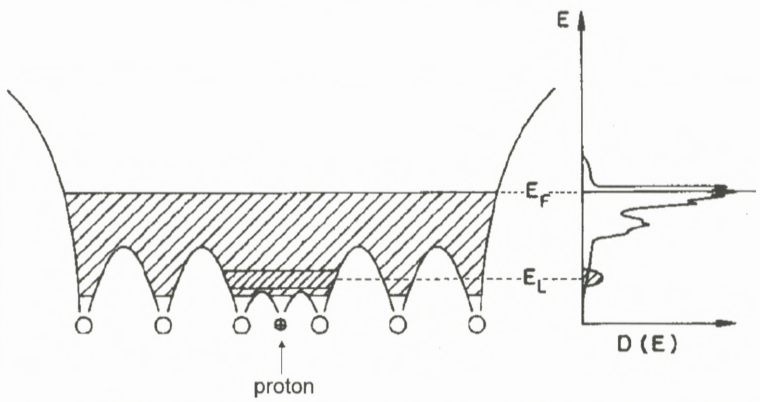

Figure 1. Illustrative picture of the properties of the localized states around protons in metals according to band structure calculations by (Vargas et al., 1986; Vargas and Christensen, 1987).

the translational symmetry assumed in the jellium model. Because of these potential barriers, the possibility of bound electrons following adiabatically the motion of the ion through the solid is ruled out. The wavefunction of the localized states will suffer scattering by the potential barriers and will be dispersed, leaving the proton as a single ion moving through the solid (subject to the strong screening by the free electrons).

Going back to the historical summary, it should be mentioned that while some calculations have stressed the picture of three ionic components (H^+, H^0, H^-) most of the calculations have used the standard view of two charge states: H^0 and H^+ (Guinea et al., 1981, 1982; Lakits et al., 1990; Alducin et al., 2003); the most complete non-linear screening and stopping calculation for protons using the jellium model is the one made by Salin et al. (1999) including dynamical effects for slow ions.

While the intention of this paper is not to give a final conclusion on these intricate questions, it may be useful to perform a simplified but physically revealing analysis of the problem on the basis of recent approaches emerging from self consistent models of proton-solid interactions, including the relevant question of non-linear treatments of screening and scattering processes.

Following a previous proposal (Lifschitz and Arista, 1998), the interaction between the proton and the free electron gas will be approximated by an effective (self consistent) model potential $V(r)$ which, for analytical convenience, will take either of the following forms:

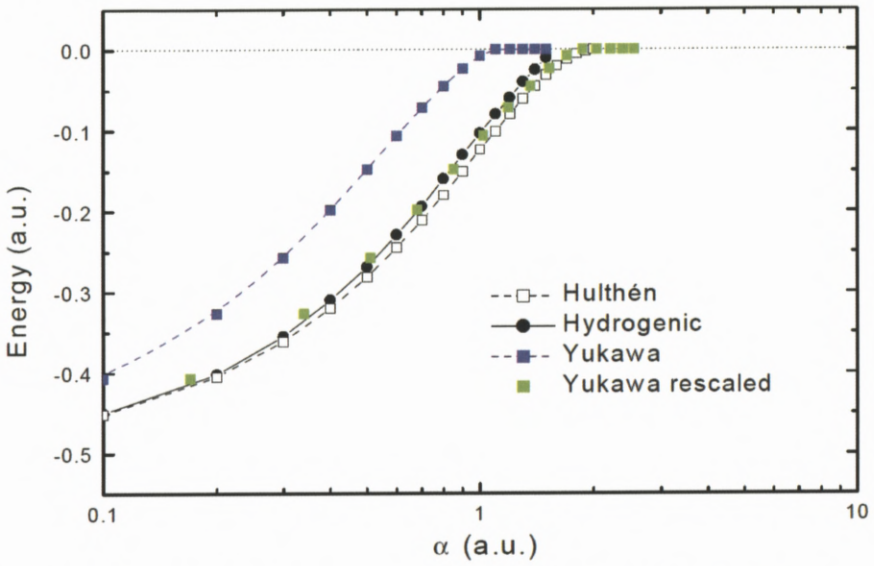

Figure 2. Energy eigenvalues, in atomic units, corresponding to the $1s$ state of three screened potentials: Hydrogenic, Hulthén and Yukawa, as a function of the screening parameter α, obtained by numerical solution of the Schrödinger equation. The rescaled points for the Yukawa potential are obtained by multiplying the corresponding α values by a fixed factor 1.7.

(a) Yukawa potential:

$$V(r) = -\frac{e^2}{r}\,\mathrm{e}^{-\alpha r},$$

(b) Hydrogenic potential,

$$V(r) = -\frac{e^2}{r}\left(1+\alpha\frac{r}{2}\right)\mathrm{e}^{-\alpha r},$$

(c) Hulthén potential

$$V(r) = -e^2\alpha\,\frac{\mathrm{e}^{-\alpha r}}{1-\mathrm{e}^{-\alpha r}}\,.$$

First I consider the question of determining the conditions for the existence of bound states in the indicated potentials, taking as a parameter the screening constant α. To this end, I have solved by numerical methods the corresponding Schrödinger equation, obtaining the energy eigenvalue for the ground ($1s$) state as a function of α. Note that only for the Hulthén potential there are exact analytical solutions, both for the wavefunctions and energies (Hulthén, 1942). The results

of the calculations are shown in Figure 2. It is observed that as the equivalent screening distance, $\Lambda = 1/\alpha$, decreases (α increases) the state becomes more loosely bound and finally disappears. This occurs for values of α close to one atomic unit, and hence in the range of screening conditions in real metals. As a guide, a first approximation to the value of the screening constant for fixed impurities in a free electron gas is given by the Thomas–Fermi (or RPA) approximation as $\alpha_{\mathrm{RPA}} = \sqrt{3}\,\omega_{\mathrm{P}}/v_F$, where ω_{P} and v_F are the plasma frequency and Fermi velocity of the electron gas. Introducing the usual r_{s} parameter of the electron gas by $(4\pi/3)r_{\mathrm{s}}^3 n = 1$, in terms of the electron density n, the value of α_{RPA} is given by $\alpha_{\mathrm{RPA}} = 1.563/\sqrt{r_{\mathrm{s}}}$ a.u. (in the following the values indicated by a.u. refer to atomic units).

However, this value is not a very good one from the point of view of a non-linear representation of impurity screening in solids. A more appropriate value of α is the one that may be obtained in a self-consistent way by applying the Friedel sum rule (Friedel, 1952). This rule expresses the condition of overall charge neutrality when an impurity is immersed in a metal. The mathematical condition is expressed in terms of the scattering phase shifts δ_l (corresponding to the scattering of electrons at the Fermi surface) by

$$\frac{2}{\pi}\sum_{l=0}^{\ell_{\max}}(2l+1)\delta_\ell(k_{\mathrm{F}}) = 1, \tag{1}$$

where $k_{\mathrm{F}} = 1.919/r_{\mathrm{s}}$ is the Fermi wavenumber.

In a full non-linear representation of the screening problem the phase shifts are calculated by numerical integration of the Schrödinger equation corresponding to the scattering of partial waves with angular momentum l in the self-consistent potential $V(r)$. The maximum value of ℓ required in this sum ($\ell_{\max}$) depends on the value of r_{s}, and it has been numerically determined for each r_{s} so as to obtain an accuracy better than 10^{-5} in the total sum.

The resulting values of α obtained from this procedure for each of the indicated potentials are plotted in Figure 3 as a function of r_{s}. In the case of the hydrogenic potential the present result coincides with calculations by Apagyi and Nagy (1987).

By combining the results of the two previous figures we obtain the expected values of binding energy for static protons, as a function of r_{s}; the results are shown in Figure 4. In the case of the Hydrogenic potential this procedure yields no bound states for any value of r_{s}. Moreover, the figure shows a very restricted window of possible r_{s} values, and also, the values of binding energies are so small that they almost preclude the possibility of bound states at any density. These results, although mathematically correct, are physically misleading, as it

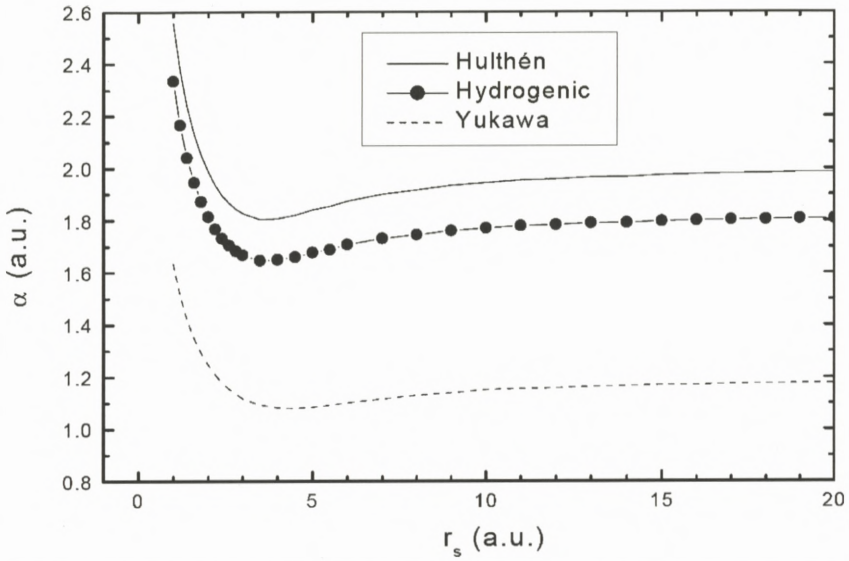

Figure 3. Values of the screening constant α calculated from the Friedel sum rule as described in the text, for the three model potentials: Hydrogenic, Hulthén and Yukawa *versus* the electron gas parameter r_S.

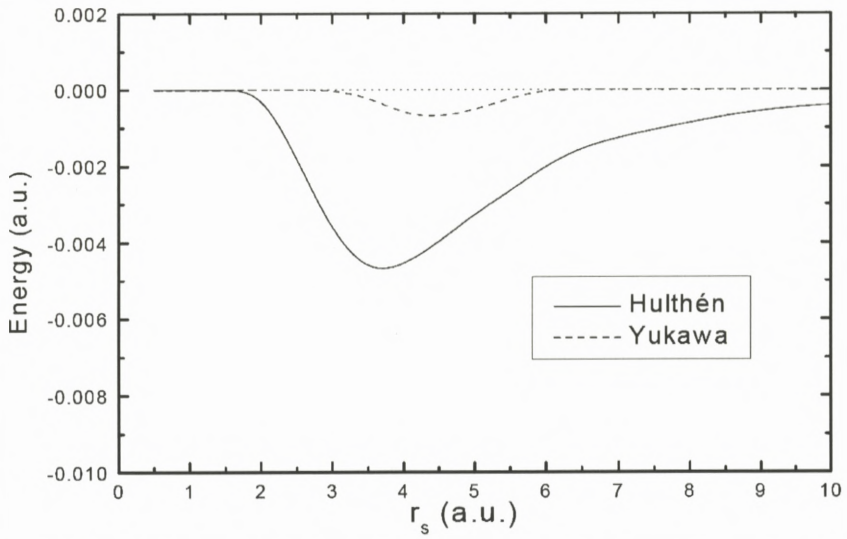

Figure 4. Binding energy of 1*s* state around protons in a jellium taking into account the values of the screening constant α that satisfies the Friedel sum rule (Figure 3) and the energy of the bound state for the corresponding values of α (Figure 2). No bound states are obtained in the case of the Hydrogenic potential (note also the very small values of binding energies obtained here).

becomes obvious when considering the high r_s limit. It is physically clear that for a dilute electron gas the ground state of the system should be that with one electron captured by the proton in a hydrogenic bound state. However this limit is not obtained with the present approach. A nice physical discussion of the problem was given some time ago by Ferrell and Ritchie (1977). They identify the origin of the problem in the absence of an important many-body effect that comes from a self interaction of the electron mediated by the polarization induced in the electron gas by the same individual electron. In order to take into account this effect they formulated a simple model, using still a one-electron Hamiltonian, and showing that the new result reproduces the bound state with the correct binding energy of the free hydrogen atom when $r_s \to \infty$. (The original calculations by Ferrell and Ritchie were made for helium ions but it is easy to check using their analytical expressions that the same property applies to protons).

Nevertheless, in the range of metallic densities the Ferrell–Ritchie approach would not guarantee a bound state for protons since one should add a correction term to the energy due to the difference between the Fermi and the vacuum level (i.e., the work function value) (Ferrell and Ritchie, 1977).

As indicated, the calculations mentioned so far were restricted to the case of ions at rest. Therefore, the possibility arises that by considering the relaxation of the screening conditions due to dynamical effects on moving ions, new conditions for the existence of bound states may arise.

To study this possibility I have extended the analysis to the case of moving ions, applying in this case the extended Friedel sum rule (Lifschitz and Arista, 1998) as a new constraining condition to determine in a self-consistent way the values of α for each type of potential, as a function of the proton velocity v, i.e. $\alpha = \alpha(v)$.

The values of α obtained from these adjustments are shown in Figure 5, for $r_s = 2$, corresponding to typical electron densities in metals. The results show two clear regimes: a low-energy range ($v < v_F$) where α is basically constant, and a high-velocity range where it drops quite rapidly (dynamical screening regime); the asymptotic behavior for the Yukawa potential is of the form $\alpha \sim \omega_P / v$. Using the values of $\alpha(v)$ so determined, and the previous results for the binding energy as a function of α (Figure 2) we finally determine the binding energies as a function of velocity for the three potential models. The results are shown in Figure 6. We note that, in spite of the *a priori* independence of the three potential models (note in particular the differences in the values in Figure 5) the final results for the binding energies show a remarkably close agreement. The reason for this agreement lies in the use of the Friedel sum rule to adjust in a self-consistent way the three potentials.

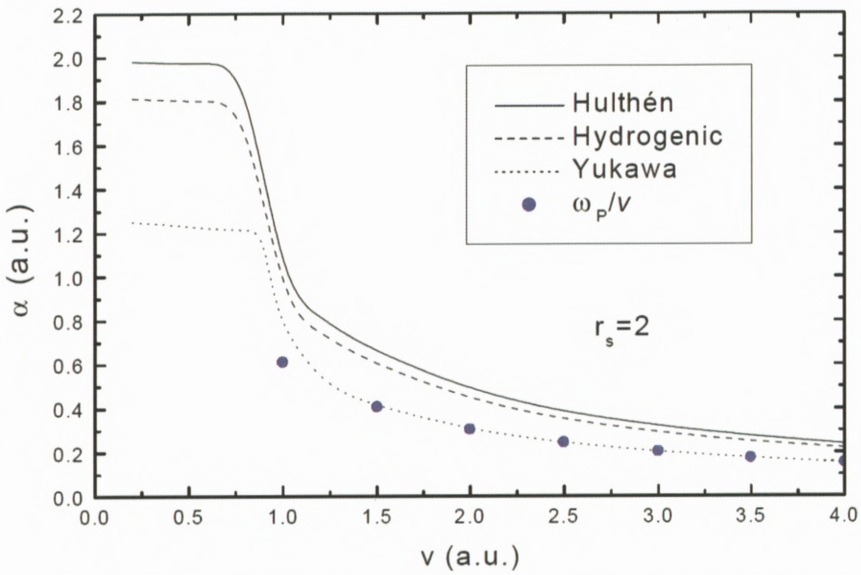

Figure 5. Values of the screening constant α *versus* proton velocity v for the three model potentials considered in the text, for a typical electron density in metals corresponding to $r_S = 2$. The solid symbols show the values of ω_P/v.

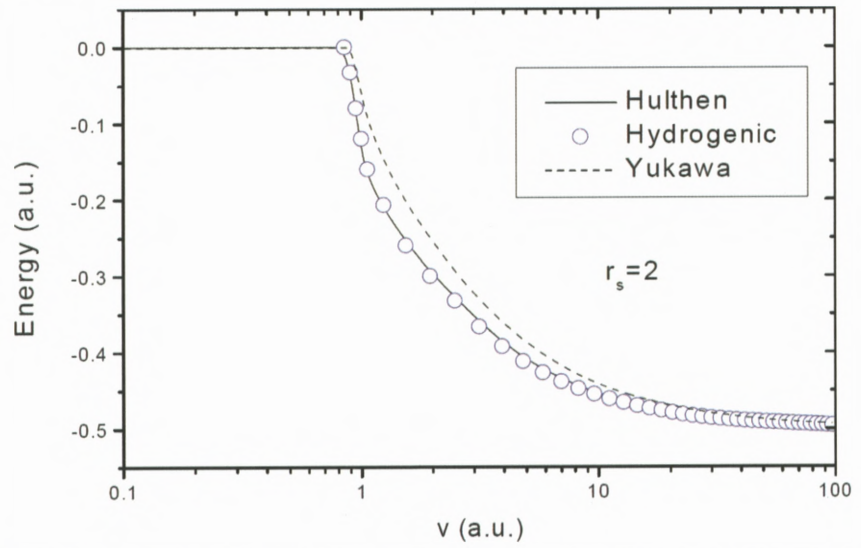

Figure 6. Binding energy of an electron state around a moving proton as a function of proton velocity v for the three potential models indicated in the text, for an electron density corresponding to $r_S = 2$. Bound states appear for velocities larger than about 1 a.u. For high velocities the binding energy converges to the normal value for the hydrogen atom, $E_0 = -0.5$ a.u.

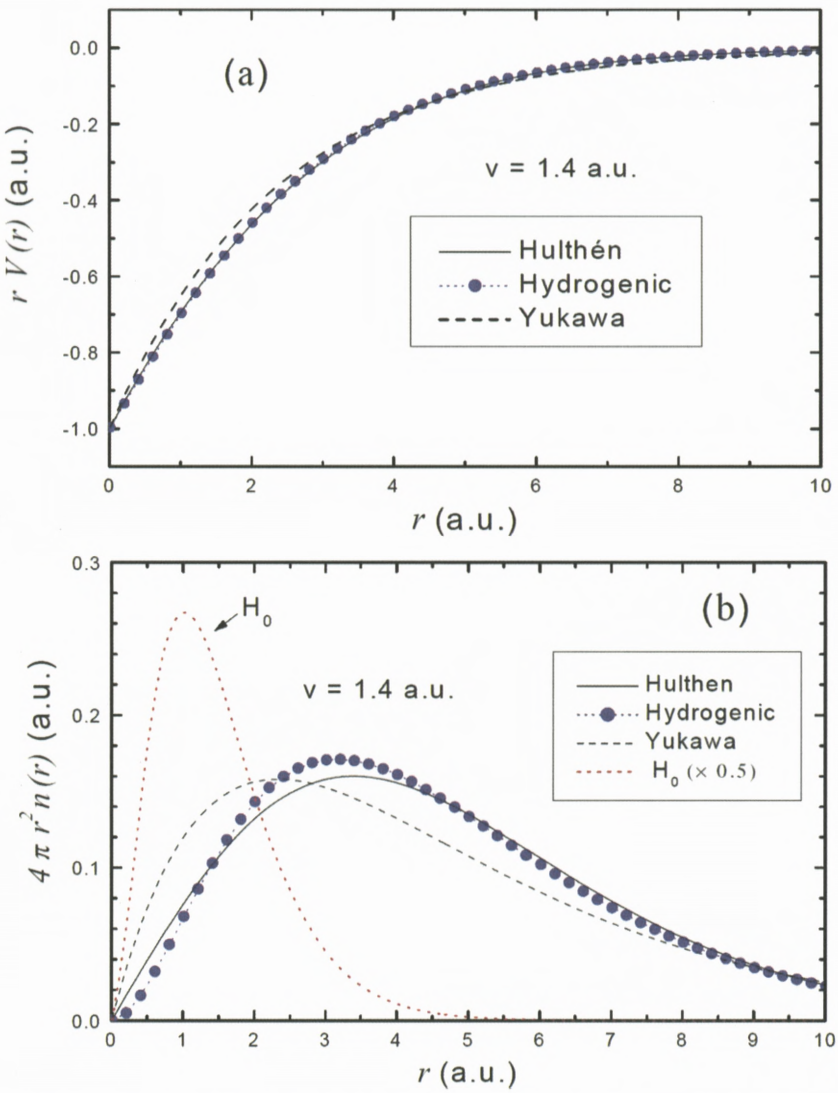

Figure 7. Values of the potentials (part a), and corresponding screening densities (part b) for the three potential models (Hydrogenic, Hulthén and Yukawa), with screening constants α adjusted by the extended Friedel sum rule method as discussed in the text.

For further illustration, Figure 7 shows the values of the potentials (part a), and the corresponding screening densities (part b) for the three adjusted potentials indicated before (with the α-values determined by the extended Friedel sum rule). Also included in this figure is the normal electron density for the free hydrogen atom (reduced by a factor 0.5). One observes a remarkably close agreement between the three potentials (as a result of the adjustment made by the extended Friedel sum rule); second, the screening cloud is much more spread than the normal density of the hydrogen atom; this is a dynamical effect on the screening charge. Of course the present results yield only a spherically averaged view of the screening phenomenon but they are still useful for illustrative purposes.

Similar calculations for slow ions ($v < v_F$) show that the screening densities become similar to the normal hydrogen density (although in these calculations they represent the density of free electrons undergoing scattering). Under these conditions, the corresponding phase shifts and stopping coefficients obtained with the different models are also expected to be quite similar (see Lifschitz and Arista, 1998, for specific calculations).

The conclusion drawn from these calculations is that slow protons in metals behave as free particles dressed by a screening cloud of conduction electrons; this conclusion is backed by full size band structure calculations as indicated earlier (Vargas et al., 1986; Vargas and Christensen, 1987). At higher velocities ($v > v_F$) bound states appear, and at the same time the coupling between the projectile and the target weakens, so that a good approximation may be to consider a base of states composed by the separate projectile and free-electron-gas wavefunctions (in the sense of the zero-order approximation of time-dependent perturbation theory), and then calculate the transition probabilities corresponding to capture and loss processes (Cross, 1977; Lakits et al., 1990; Alducin et al., 2003).

2.1. Experimental Evidences: Positrons, Positive Muons and Pions

According to the previous analysis, no bound states of protons in metals would be expected for velocities smaller than about one atomic unit. In principle, it might be expected that the energy loss of slow protons would yield information to confirm this. However, the theoretical evaluation of stopping powers at low energies is not currently as accurate as it is at high energies (in the perturbative regime) and so it seems that for the moment it cannot provide a final test of this point (for instance, the best available calculations using density functional theory for protons and helium ions do not show a very satisfactory agreement with experiments (Martínez-Tamayo et al., 1996).

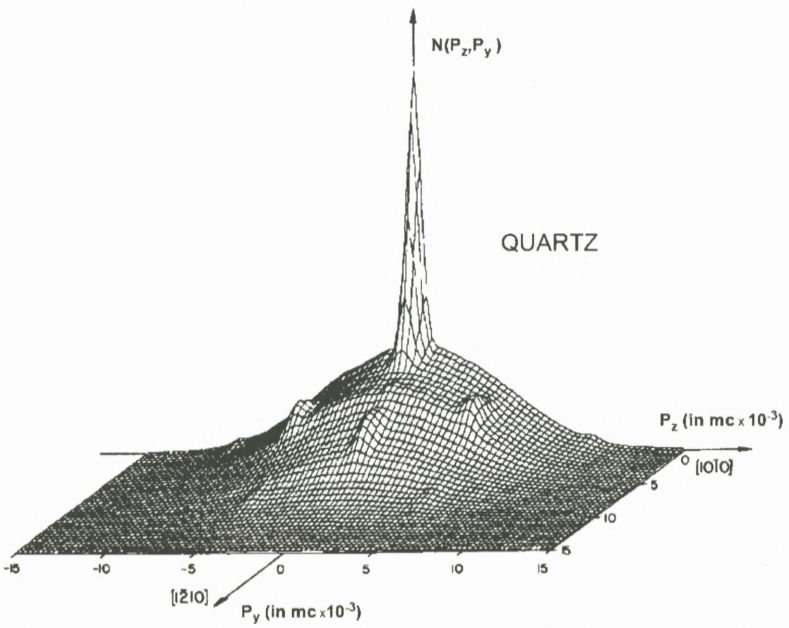

Figure 8. Angular-correlation distribution of gamma rays corresponding to positronium annihilation in crystalline quartz (experiment by Berko et al., 1977).

But there are other experimental methods that are more sensitive to the electronic environment around an impurity ion and could provide more conclusive information on the charge state problem. In particular, such is the case of experiments done with positrons and positive muons or pions.

Experiments on positron annihilation in solids reveal a sharp distinction between metals and semiconductors or insulators (West, 1973, 1974; Brandt and Dupasquier, 1983). Figures 8 and 9 show two typical spectra (Berko et al., 1977) of angular correlations between the two gamma rays (emerging in opposite directions) produced by the annihilation of individual positrons in solids. In these experiments the positrons, coming from an external source, are completely slowed down and approach thermal equilibrium with the lattice before annihilating (Brandt and Arista, 1982). Figure 8 corresponds to an insulator (a quartz crystal) while Figure 9 is for a metal (Al, with $r_s = 2.07$). The prominent and narrow peak observed in Figure 8 is explained by the mechanism of electron capture (positronium formation) prior to annihilation; here the angular width corresponds to the momentum distribution of the positronium wavefunction (the small periodic crispations are produced by the effects of the lattice on this wavefunction). By contrast, the wider shape in Figure 9 corresponds to the spectrum of positron an-

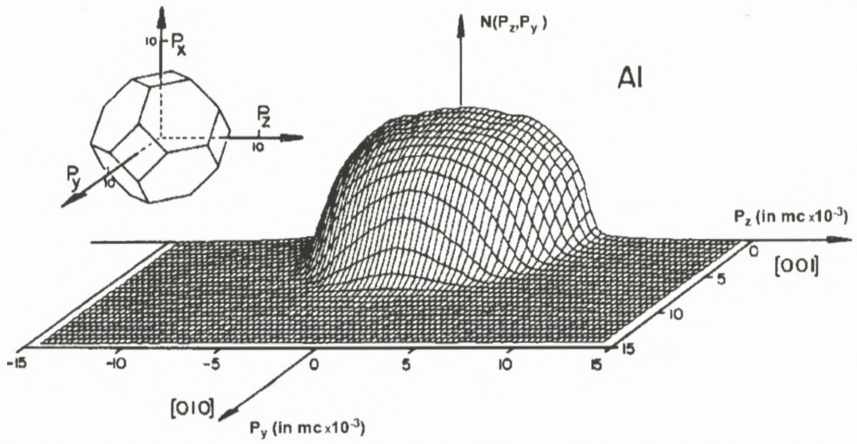

Figure 9. Angular-correlation distribution of gamma rays corresponding to the annihilation of free positrons in aluminum (experiment by Berko et al., 1977).

nihilation in metals; this result is representative of similar spectra found for other metals (Donaghy and Stewart, 1967a, 1967b; Stewart et al., 1962; West, 1973, 1974). In this case the width of the angular distribution is directly related to the radius of the Fermi sphere, indicating that the positron does not capture an electron but annihilates as a free particle with the conduction electrons of the metal. The usual explanation given to this different behavior is that positrons cannot bind electrons in metals due to the strong screening produced by free electrons (West, 1973, 1974; Brandt and Dupasquier, 1983).

It could be argued that these results do not apply directly to protons due to the significant mass difference (in fact, the relevant parameter is the reduced mass of the system which is only affected by a factor 1/2). Hence we may turn to consider additional evidences arising from experiments on spin rotation and relaxation of positive muons and pions stopped in different materials (Patterson, 1988; Morenzoni, 1992; Morenzoni et al., 2002; Major et al., 1992). The evidence arising from these experiments is fully consistent with the previous picture of positrons: in the case of metals the muons/pions decay (by positron/muon emission) as free particles, whereas in the case of insulators, semiconductors, or organic materials, they capture an electron, forming a stable bound state, before decaying. Also, the charge distribution around muons in interstitial positions in Ni and other metals, measured by the intensity of the hyperfine field, demonstrated a strong screening of muons by conduction electrons, but not a bound state (Vargas and Christensen, 1987). The explanation of the different behavior

between metals and non-metals is, as in the case of positrons, based on the strong screening effect that avoids the formation of bound states in metals.

2.2. Discussion

As illustrated, there is a consistent explanation of the behavior of positrons and positive pions and muons in the different types of solids, irrespective of the different masses between these particles. Thus, one would expect a similar behavior in the case of slow protons. The closest comparison is of course between protons and positive muons/pions.

The theoretical analysis provides physical arguments to expect that no bound states would be formed for velocities below the Fermi velocity in metals. There is no consensus on this point in the ion-beam community, but it should be noted that it is in agreement with all the experimental evidence coming from positron, muon and pion experiments.

According to this view, the physical picture of the behavior of protons in solids would be the following.

(a) Metals: one may distinguish two ranges:

  (i) for $v < v_F$: bound states are not formed (except perhaps for high-r_s materials) and the protons propagate through the lattice as strongly screened ions;
  (ii) for $v > v_F$: bound states appear and a collisional equilibrium between H^0 and H^+, determined by capture and loss processes, is established. The neutral and negative fractions observed when slow (1–20 keV) hydrogen beams emerge from metals may be explained by electron capture processes taking place at the exit surface (Bhattacharya et al., 1980; Verbeek et al., 1980).

(b) Insulators, semiconductors and organic materials: here an equilibrium between H^0 and H^+ is expected at all energies (with a predominant fraction of H^0 at low energies).

While for the moment a complete theoretical proof of this picture cannot be given (a full size theoretical model would require self-consistent many-body calculations including non-linear screening plus dynamical and lattice-potential effects), we may note that it is consistent with all the existing experimental evidences cited before.

3. Heavy Ions

The question of the charge states of heavy ions in solids is one of the main problems in trying to achieve a definitive theoretical framework for the evaluation of ion stopping and ranges. As in the case of light ions, one common difficulty is the fact that measurements of the charge states of ions emerging from solid targets provide only indirect information on the internal charge state distributions. Yet, alternative methods to measure the equilibrium charge state of ions in solids (Della-Negra et al., 1987) may yield useful information in this respect.

There are extensive experimental studies that provide detailed information on the charge state distributions (Shima et al., 1986, 1992), as well as convenient empirical fittings to the data (Nikolaev and Dmitriev, 1968; Schiwietz and Grande, 2001). But the question of charge states of ions moving within a solid was for many years an open issue. In particular we may note the old controversy between two models that has remained open through the years: the Bohr–Lindhard (BL) (1954) and the Betz–Grodzins (BG) models (Betz, 1972).

The BL model considers that the fast sequence of collisions experienced by the ion within a solid produces an enhancement in the excitation and ionization probabilities, leading to an increased equilibrium charge. The effect of the passage through the surface, in the case of swift ions, is not considered to be very relevant, due to the high velocity condition, and so the mean exit charge $\bar{q}_{\rm exit}$ is expected to be close to the mean charge $\bar{q}$ inside the solid. Instead, the BG model considers that the effect of repeated collisions within the solid produces ions with several excited electrons in outer shells, but those electrons remain mostly attached to the ion until it emerges into vacuum; after this, the ion would decay by emitting electrons *via* Auger processes. According to this model, the mean charge states $\bar{q}$ of the ion inside the solid should be significantly smaller than the exit values $\bar{q}_{\rm exit}$. A detailed discussion of this problem within the context of non-linear calculations of the energy loss has been given recently (Lifschitz and Arista, 2004); the results of this study show a disagreement with the BG model and provide a plausible explanation to the old controversy.

It may be noted that the BG model was initially inspired in the apparent lack of gas-solid differences in the energy loss values, which was associated to similar values of charge states. However, small gas-solid differences in the stopping were found later on by Geissel et al. (1982), whereas, on the other hand, the Auger electrons predicted by the BG model were not found.

The study of the charge states of ions moving in solids is thus a fundamental aspect in the field of ion-solid interactions. An important problem in this respect is the wide discrepancy among the values assumed in different places. An example

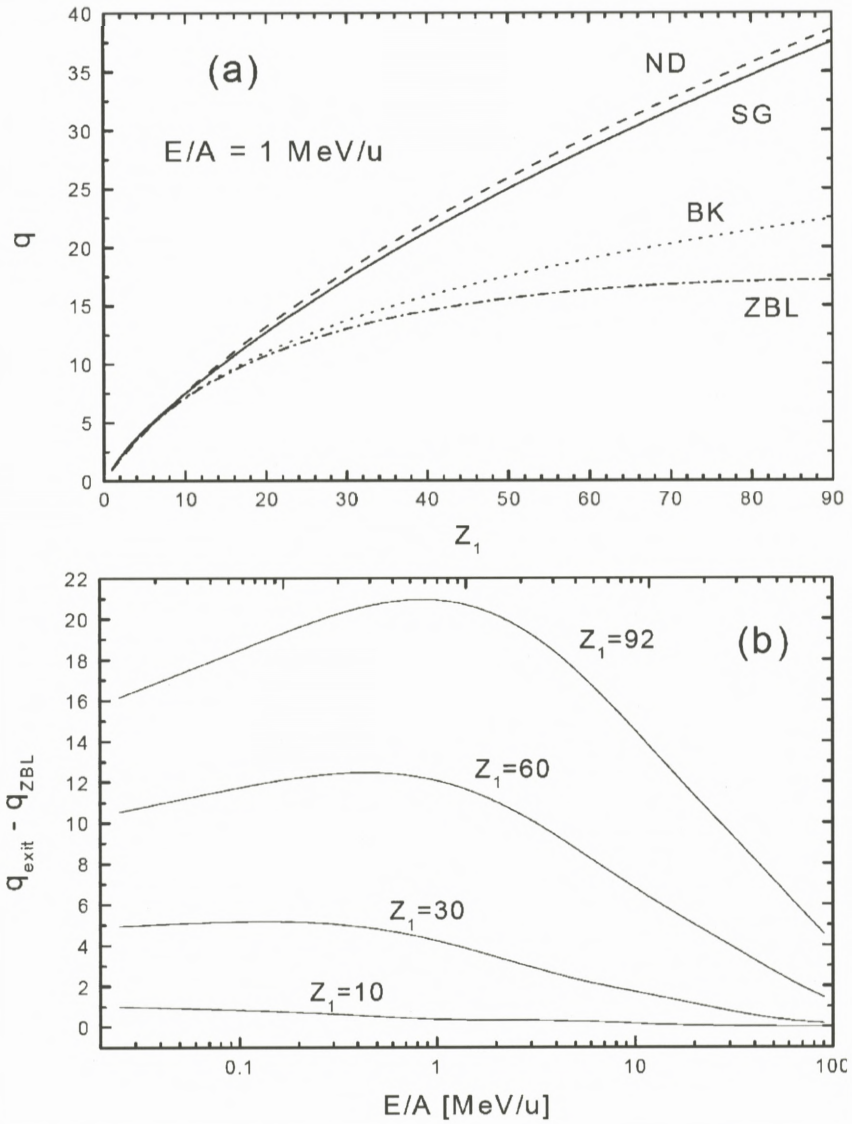

Figure 10. (a) Different approaches to the mean charge of ions in solids. Curves ND and SG: fitting values to the mean charge of ions emerging from solid foils according to Nikolaev and Dmitriev (ND) and Schiwietz and Grande (SG) respectively; BK: ion charge values calculated by Brandt (1975) and used in the Brandt–Kitagawa model; ZBL: recommended values by Ziegler et al. (ZBL) (1985) obtained by fitting stopping power values with the BK model. (b) Difference between the mean exit charge q_{exit} (represented by the empirical SG values), and the average ionization values by Ziegler et al. q_{ZBL}, for various atomic numbers, as a function of ion energy.

of the most frequent assumptions is shown in Figure 10. Part (a) of this figure shows the fitting expressions to the mean charge of ions emerging from a solid foil obtained by Nikolaev–Dmitriev (ND) and Schiwietz–Grande (SG), the q-values of the Brandt–Kitagawa (BK) model (Brandt, 1975; Brandt and Kitagawa, 1982), and the expression for the "ionization" values given by Ziegler et al. (ZBL) (Ziegler et al., 1985). The BK model calculates the mean ion charge using a previous model by Brandt (1975) based on the velocity-stripping criterion by Bohr and assuming a Thomas–Fermi model for the electron velocities in the atom. The ZBL formula is the result of a large number of fittings based on the BK model for heavy ions scaled to equal-velocity proton values. As observed in the figure, large discrepancies arise for heavy ions. Part (b) of this figure shows the difference between the mean charge values measured at the exit of solid foils and the charge values recommended in the ZBL approach. As observed, very large differences arise for heavy ions on a wide range of energies below and over 1 MeV/u. Hence, this range of energies is of central interest for the present analysis.

The purpose of the following is to try different stopping models, together with different q-values, in order to analyze some basic differences dealing with linear *versus* non-linear approaches, and finally, to discuss the origin of these discrepancies.

First, I will briefly recall the calculation of the stopping power for dressed ions according to the dielectric function formulation (Lindhard, 1954; Ferrell and Ritchie, 1977; Brandt and Kitagawa, 1982). The energy loss in this case is given in terms of the dielectric function $\varepsilon(k, \omega)$ by the expression

$$\frac{\mathrm{d}E}{\mathrm{d}x} = \frac{2e^2}{\pi v^2} \int_0^\infty \frac{\mathrm{d}k}{k} |f(k)|^2 \int_0^{kv} \omega \, \mathrm{d}\omega \, \mathrm{Im} \frac{-1}{\varepsilon(k, \omega)}, \tag{2}$$

where $f(k)$ is the ion form factor, which is calculated from the Fourier transform of the ion-charge density $\rho_{\mathrm{ion}}(\vec{r})$, by

$$f(k) = \int d^3r \, \mathrm{e}^{i\vec{k}\cdot\vec{r}} \rho_{\mathrm{ion}}(\vec{r}) \, . \tag{3}$$

In particular, in the BK model $f(k)$ may be expressed analytically, for any ion charge q and atomic number Z_1, by

$$f_{\mathrm{BK}}(k) = Z_1 \frac{q/Z_1 + k^2\Lambda^2}{1 + k^2\Lambda^2} \, , \tag{4}$$

where Λ is the screening radius of the ion (which depends also on q and Z_1). In the simplest case of bare nuclei, $f(k) = Z_1$.

The use of a dielectric description, as well as the use of a free electron gas picture, is more adequate to deal with the excitation of conduction electrons in

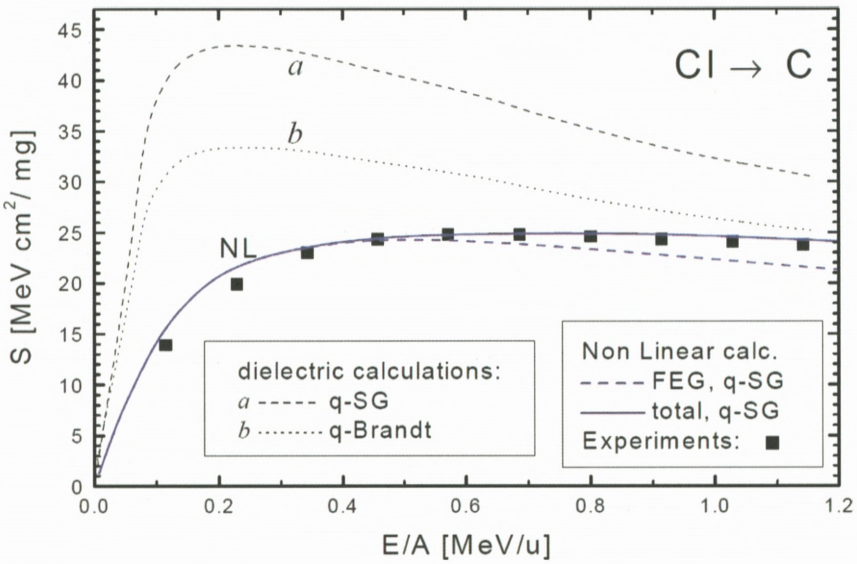

Figure 11. Calculations of stopping cross sections for Cl ions in carbon using linear and non-linear models. Curves *a* and *b*: dielectric calculations corresponding to the following assumptions on the ion charge: (a) empirical values by Schiwietz–Grande (SG), (b) Brandt statistical-ion model (Brandt, 1975). The two blue curves denoted NL are the results of the non-linear calculations using the SG values of ion charges, considering only the electron gas contribution (dashed line) and including K-shell ionization (continuous line). The solid symbols are experimental values (Boot and Grant, 1965; Paul, 2006).

metals or valence electrons in semiconductors. A more comprehensive scheme may be built using a description in terms of Mermin functions derived from optical data and including also inner shells (Abril et al., 1998). The present calculations will be restricted to a carbon target where the dominant energy loss is produced by the excitation of valence electrons, and the contribution of the K-shell may be included as a separate correction.

The calculations were made using the dielectric function obtained by (Lindhard, 1954) for the free electron gas. To integrate Equation (2) according to this formulation one must separate the contributions of plasmon (given by a line integral) and single particle excitations. The numerical method was described in a previous publication (Arista, 1978).

Results of these calculations are shown in Figures 11 and 12, for Cl and Ni ions in carbon foils ($r_s = 1.6$). The figures show the results of the linear (dielectric) formulation and of the non-linear quantal calculations considering different ion charge values. The curves denoted *a* and *b* are dielectric calcu-

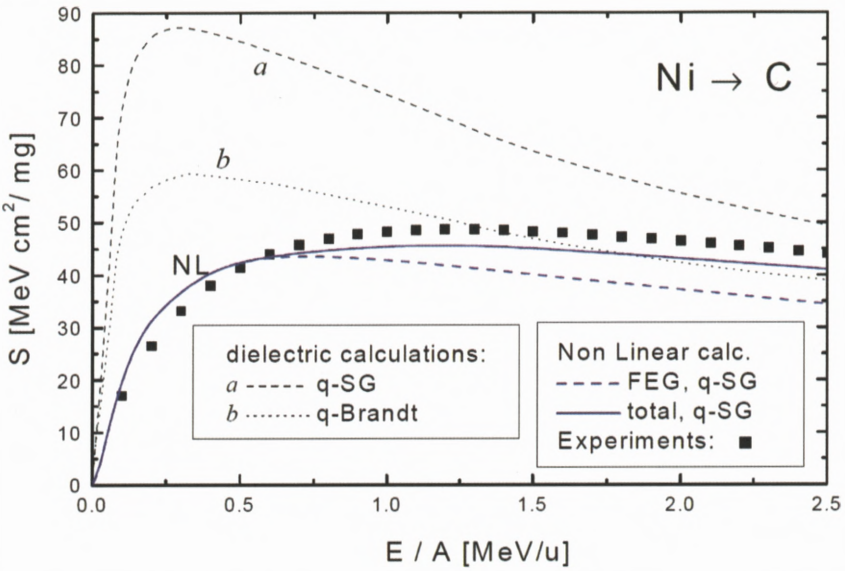

Figure 12. Same as in Figure 11 for Ni ions in carbon; the solid symbols are empirical values according to the fitting by Konac et al. (1998).

lations corresponding to the following assumptions on the equilibrium charge states $\bar{q}$ of the ions: (a) empirical values by Schiwietz and Grande (2001) (derived from experiments with emerging ion beams), (b) Brandt statistical-ion model (Brandt, 1975; Brandt and Kitagawa, 1982). The curves denoted NL are the results of non-linear calculations based on the extended Friedel sum rule according to the method described in Arista (2002) and using the Schiwietz–Grande values of ion charges (Schiwietz and Grande, 2001). This method is fully non-perturbative and based on numerical integrations of the Schrödinger equation for the scattering of electrons by the field of the moving ion. A correction due to K-shell ionization has been included in the non-linear calculations following Arista (2002) and Arista and Lifschitz (2004) yielding the result indicated by the solid blue line. The solid symbols are experimental values from Boot and Grant (1965) and Paul (2006).

As it may be observed, the calculations based on the linear formulation overestimate the values of the stopping power. The reason for this behavior is simple: the basic assumption of the dielectric approach is the linear response of the medium, which produces a quadratic dependence of the stopping power on the ion form factor $f(q)$, Equation (2), and is the same reason why the stopping of bare ions in the Bethe model increases with Z_1^2. In the case of

heavy ions this produces a significant overestimation of the energy transfer to the medium. A more realistic description, such as the non-linear method for heavy ions (Arista, 2002; Arista and Lifschitz, 2004), takes into account the effect of "saturation" in the energy transfer. In the ZBL method, the values of $\bar{q}$ are fitted to the experiments by a calculation procedure that is based on the BK model; in this way it compensates the intrinsic overestimation of the linear approach by using a reduced value of $\bar{q}$. Instead, the non-linear calculation shows a good agreement with the experiments when the SG values of $\bar{q}$ are used. Conversely, if the non-linear calculations were made using the ZBL values for $\bar{q}$ the results would be too low (Arista and Lifschitz, 2004).

It may be noted that other non-perturbative methods (Grande and Schiwietz, 1993, 2002; Maynard et al., 2000, 2002; Sigmund and Schinner, 2000, 2002) may be used to obtain appropriate stopping power values in this energy range, although the present aim is not to perform a fine test of stopping evaluation methods but to illustrate the relevance of charge state assumptions on these calculations.

Another illustrative comparison is made in Figure 13 which shows the calculated values of the stopping cross sections for a fixed ion velocity ($v = 10$ a.u.) as a function of the atomic number Z_1 (which may be thought of as representing the interaction strength). Calculations using the two referred methods are included. The letter L here refers to linear calculations (using the described approach, Equations (2–4)) for two different ion charge values: the empirical SG values ($\bar{q}_{\mathrm{SG}}$) (Schiwietz and Grande, 2001) and the Brandt model ($\bar{q}_{\mathrm{Brandt}}$). The NL curves correspond to the non-linear calculations according to the method of Arista (2002) and Arista and Lifschitz (2004)); curve (a) corresponds to the stopping power of a free electron gas (FEG) for the case $\bar{q} = \bar{q}_{\mathrm{SG}}$, while curve (b) includes the contribution due to K-shell ionization. The additional curve (c) is the result of stopping calculations with the non-linear method using the heavy-ion charge model by Brandt ($\bar{q}_{\mathrm{Brandt}}$). The data symbols are the fittings to experimental values according to Konac et al. (1998) and Hubert et al. (1990). A good agreement between the non-linear calculations (curve (b)) and the empirical values is observed for atomic numbers below 50, but for higher Z_1 an increasing discrepancy is observed. This behavior was also observed in previous calculations and probably indicates a deficiency in the ion-potential model (a modified Molière potential) for the heaviest ions (Arista, 2002). We note also a fair agreement between the non-linear curve (a) and the linear calculation using $\bar{q} = \bar{q}_{\mathrm{Brandt}}$. However, a significant disagreement (which grows with Z_1) is observed between the non-linear calculations corresponding to $\bar{q}_{\mathrm{SG}}$ and $\bar{q}_{\mathrm{Brandt}}$ (curves (a) and (c)). This is a consequence of the important differences in the ion charge values already noted in

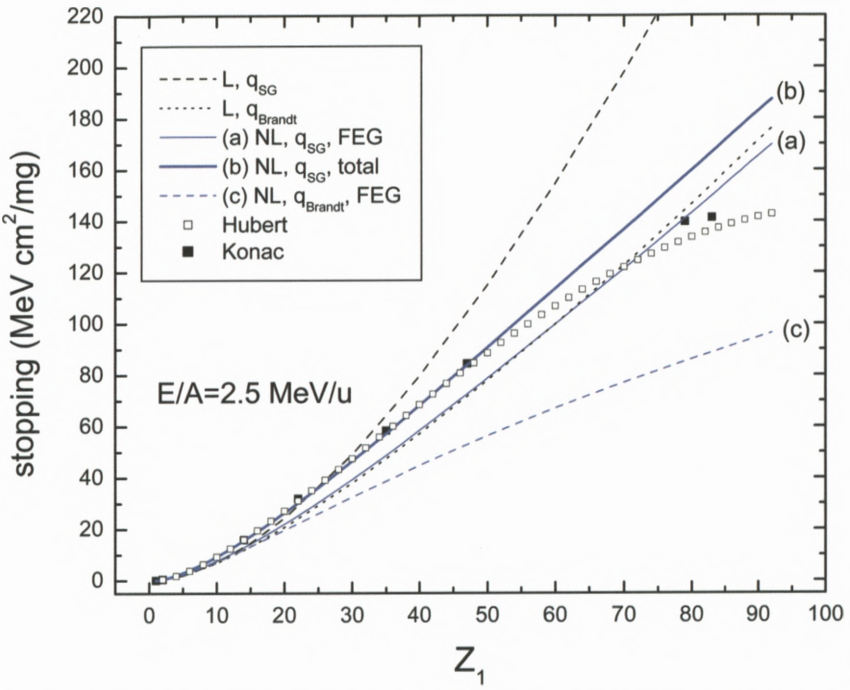

Figure 13. Calculated and empirical values of stopping cross sections for a fixed ion velocity ($v = 10$ a.u.) as a function of the atomic number Z_1. Letter L denotes linear calculations (dielectric approach) for two different ion charge values: the empirical values by Schiwietz and Grande ($\bar{q}_{SG}$), and the values of the Brandt model ($\bar{q}_{Brandt}$). The solid lines are the non-linear (NL) calculations described in the text: curve (a) corresponds to the stopping power of a free electron gas (FEG) for the case $\bar{q} = \bar{q}_{SG}$, curve (b) includes the contribution to the energy loss due to K-shell ionization, and curve (c) is the result of non-linear calculations using the ion charge model proposed by Brandt ($\bar{q} = \bar{q}_{Brandt}$). The data symbols are the fittings to experimental values using the approaches by Konac et al. (1998) and Hubert et al. (1990).

Figures 10a and 10b. A similar disagreement was found in previous calculations when the ZBL values for $\bar{q}$ were used (Arista and Lifschitz, 2004).

The fact that the NL results in these figures are in reasonably good agreement with the experiments suggests that the approximation of the ion charge inside the solid by the value of the corresponding emerging ion charge is fairly good (although a difference of a few units of charge, but much smaller than the differences shown in Figure 10b, may not be excluded). In this way the results of the non-linear approach show a disagreement with the Betz, Brandt and ZBL models of ion charge, being instead compatible with the BL model (Lifschitz and Arista, 2004).

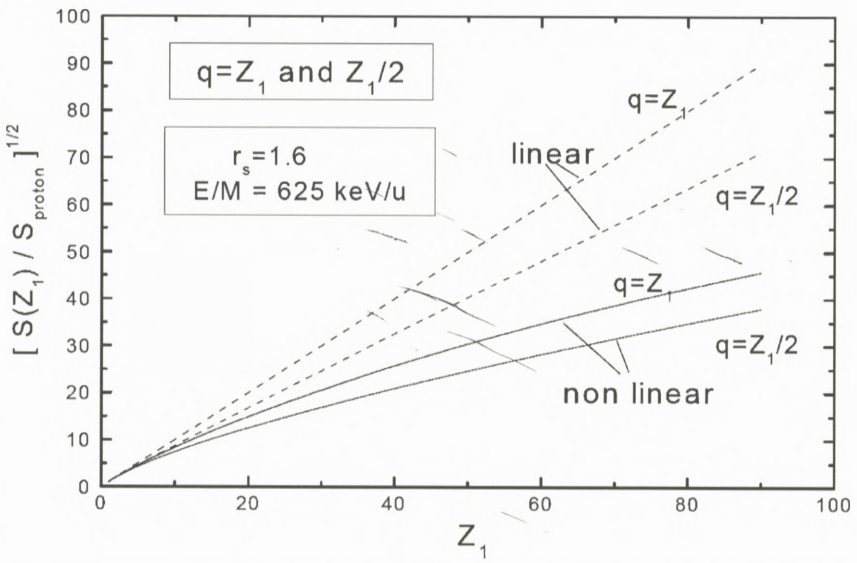

Figure 14. Illustrative calculations of stopping power ratios, shown as $[S(Z_1)/S_{\text{proton}}]^{1/2}$, where $S(Z_1)$ and S_{proton} are the stopping powers of ions and protons at the same velocity, $v = 5$ a.u. The present calculations correspond to fully charged ($q = Z_1$) and half-charged ($q = Z_1/2$) ions, using the linear (dashed lines) and non-linear (continuous lines) methods described in the text.

3.1. Saturation Effects in the Energy Loss

As already mentioned, a very basic difference between linear and non-linear approaches for swift heavy ions is the possibility – in the non-linear approach – of accounting for the saturation effect in the energy loss (Arista, 2002; Arista and Lifschitz, 2004). This effect arises from a more complete description that includes the effects of higher-order terms in the interaction.

To illustrate this effect I include in Figure 14 various simplified calculations assuming frozen ion charges: full charge ($q = Z_1$) and half charge ($q = Z_1/2$), according to the linear (dashed lines) and non-linear (continuous lines) models. Here the results are plotted in the form of "effective charge ratios": $[S(Z_1)/S_{\text{proton}}]^{1/2}$, where $S(Z_1)/S_{\text{proton}}$ is the ratio of the corresponding ion and proton stoppings for the same velocity. Clearly the linear calculation for $q = Z_1$ yields a straight line ($S \propto Z_1^2$ behavior). The non-linear results show a more moderate increase with ion charge in both cases. It should be noted that in most of this range the interaction parameter $\eta = Z_1 e^2/\hbar v$ is larger than 1, and therefore in the case of bare ions the behavior of the non-linear calculations may be well explained by a simple estimation based on the Bloch approximation. Thus, in the case of bare

ions the effect of saturation in the energy loss is already contained in the Bloch formula. The main new feature of the non-linear approach is that in contains both Bloch and Barkas corrections for dressed ions.

4. Summary

The question of charge states of light and heavy ions in solids remains being one of the most challenging problems in the field of ion-solid interactions. Two main difficulties combine to make this question a very tough one both from experimental and theoretical sides. The main experimental problem lies in the impossibility of obtaining precise values of the charge states of the ions inside the solid, at least from the conventional type of experiments using ion beams, so that one has to rely on indirect or external evidences. In the case of protons there are some alternative sources of information using subatomic particles, which consistently produce a rather well defined picture separating the cases of metallic and non-metallic materials. In the case of metals, the evidences support Brandt's conjecture in a more restricted sense: slow protons, as well as other positive point particles, would not bind electrons due to the strong screening conditions imposed by the metallic environment and so the protons remain as free but strongly screened ions. However, when the proton velocity increases the screening weakens and hydrogenic bound states appear. On the other hand, in the case of non-metallic materials, the screening is lower, and so it allows the existence of both free protons as well as neutral hydrogen atoms at all velocities, with corresponding charge state fractions determined by capture and loss processes.

Heavy ions are in principle still more complicated systems due to the much larger number of possible charge states and corresponding capture and loss processes that may take place (Echenique et al., 1990). A complete theoretical analysis of charge equilibrium and charge state fractions is a highly complicated issue since the cross section values for the elementary processes are not precisely known, having to deal in most cases with only rough estimations. The experimental side of this question is much more evolved; in particular, there are extensive sets of measurements of charge state distributions and mean values (q_{exit}) for ions emerging from solid foils (Shima et al., 1986, 1992). An important question that arises from these studies is the striking difference that may be found in some cases between these experimental values and those of the ion charges used in some phenomenological approaches and computer codes. The origin of this problem has been clarified by the recent calculations based on non-perturbative approaches (Arista, 2002; Arista and Lifschitz, 2004; Lifschitz and Arista, 2004). A very important difference between linear (or perturbative) and non-linear

(non-perturbative) methods is the absence of saturation effects (Bloch type of corrections) in the former case, which tends to enhance the stopping power values calculated with the linear/perturbative approach. This deficiency has been compensated in a heuristic way in the past by using comparatively lower values of ionization charges (like in the ZBL approach). It should be stressed that these values do not physically represent the real charge of ions travelling through a solid, and it follows that the use of these values in a different context may lead to erroneous results.

It should be noted that the question of slow heavy ions has not been included in this analysis. The most appropriate methods currently available for electronic energy loss calculations appear to be those based on density functional theory (for metallic targets) or alternative quantum methods. There are also a few recent calculations that describe changes in the electronic energy loss of slow ions due to inner-shell vacancies (Juaristi and Arnau, 1996; Juaristi et al., 1999).

The areas of ion charge states in solids and related energy loss processes still offer many open questions to be clarified from the theoretical point of view. Among these, an accurate theoretical treatment of capture and loss processes is one of the most challenging issues. A quantitative description of these processes may be the key to access the problem of charge state distributions and charge equilibrium in solids. The use of non-perturbative methods and the inclusion of dynamical effects should be considered as essential requirements for future studies on this line.

Acknowledgements

The author is grateful to Dr. P. Vargas by several insightful comments. This work was partially supported by ANPCYT of Argentina, Project PICT-R122/02.

References

Abril I., García-Molina R., Denton C.D., Pérez F.J. and Arista N.R. (1998): Dielectric description of wakes and stopping powers in solids. Phys Rev A **58**, 357–366

Alducin M., Arnau A. and Nagy I. (2003): Role of the bound-state wave function in capture-loss rates: Slow proton in an electron gas. Phys Rev **68**, 014701/1–4

Apagyi B. and Nagy I. (1987): A simple calculation of the stopping power of an electron gas for slow protons. J Phys C **20**, 1465–1468

Arista N.R. (1978): Energy loss of correlated charges in an electron gas. Phys Rev B **18**, 1–8

Arista N.R. (2002): Energy loss of ions in solids: Non-linear calculations for slow and swift ions. Nucl Instr Meth B **195**, 91–105

Arista N.R. and Lifschitz A.F. (2004): Non-linear approach to the energy loss of ions in solids. In: Cabrera-Trujillo R. and Sabin J. (Eds), Theory of the Interaction of Swift Ions with Matter, Part 1, Advances in Quantum Chemistry, Vol. 45. Elsevier, pp 47–77

Berko S., Haghgooie M. and Mader J.J. (1977): Momentum density measurements with a new multicounter two-dimensional angular correlation of annihilation radiation apparatus. Phys Lett A **63**, 335–338

Betz H.-D. (1972): Charge states and charge-changing cross sections of fast heavy ions penetrating through gaseous and solid media. Rev Mod Phys **44**, 465–539

Bhattacharya R.S., Eckstein W. and Verbeek H. (1980): Positive charge fractions of H, D, and He backscattered from solid surfaces. Surface Sci **93**, 563–581

Bohr N. and Lindhard J. (1954): Electron capture and loss by heavy ions penetrating through matter. K Danske Vidensk Selsk, Ma-Fys Meddr **28, no. 7**, 1–31

Boot W. and Grant I.S. (1965): The energy loss of oxygen and chlorine ions in solids. Nucl Phys **63**, 481–495

Brandt W. (1975): Ion screening in solids. In: Datz S., Appleton B.R. and Moak C.D. (Eds), Atomic Collisions in Solids. Plenum, New York, pp 261–288

Brandt W. and Arista N.R. (1982): Thermalization and diffusion of positrons in solids. Phys Rev B **26**, 4229–4238

Brandt W. and Dupasquier A. (Eds) (1983): Positron Solid-State Physics, Proceedings of the International School of Physics "Enrico Fermi", Course 83. North Holland Publishing

Brandt W. and Kitagawa M. (1982): Effective stopping-power charges of swift ions in condensed matter. Phys Rev B **25**, 5631–5637

Briggs J. and Pathak A. (1973): Momentum transfer cross section and the Z1 oscillations in stopping power. J Phys C **6**, L153–157

Briggs J. and Pathak A. (1974): The stopping power of solids for low-velocity channelled heavy ions. J Phys C **7**, 1929–1936

Cross M.C. (1977): Charge states of fast protons in solids. Phys Rev B **15**, 602–607

Della-Negra S., Le Beyeq Y., Monart B., Standing K. and Wien K. (1987): Measurements of the average equilibrium charge of fast heavy ions in a solid by H^+ emission at the exit surface. Phys Rev Lett **58**, 17–20

Donaghy J.J. and Stewart A.T. (1967a): "Enhancement factor" for positrons in sodium. Phys Rev **164**, 396–398

Donaghy J.J. and Stewart A.T. (1967b): Fermi surface of lithium by positron annihilation. Phys Rev **164**, 391–395

Echenique P.M., Nieminen R.M. and Ritchie R.H. (1981): Density functional calculation of stopping power of an electron gas for slow ions. Solid State Commun **37**, 779–781

Echenique P.M., Nieminen R.M., Ashley J.C. and Ritchie R.H. (1986): Nonlinear stopping power of an electron gas for slow ions. Phys Rev A **33**, 897–904

Echenique P.M., Flores F. and Ritchie R.H. (1990): Dynamical screening of ions in condensed matter. Sol State Phys **43**, 229–311

Ferrell T.L. and Ritchie R.H. (1977): Energy losses by slow ions and atoms to electronic excitations in solids. Phys Rev B **16**, 115–123

Firsov O.B. (1959): A qualitative interpretation of the mean excitation energy in atomic collisions. Sov Phys JETP **9**, 1076–1080

Friedel J. (1952): The distribution of electrons round impurities in monovalent metals. Phil Mag **43**, 153–189

Friedel J. (1954): Electronic structure of primary solid solutions in metals. Adv Phys **12**, 446–507
Friedel J. (1958): Metallic alloys. Nuovo Cimento, Suppl. **2**, 287–311
Geissel, H., Laichter Y., Schneider W.F.W. and Armbruster P. (1982): Energy loss and energy loss straggling of fast ions in matter. Nucl Instr Meth B **194**, 21–29
Grande P.L. and Schiwietz G. (1991): Impact parameter dependence of electronic energy loss and straggling of incident bare ions on H and He atoms by using the coupled-channel method. Phys Rev A **44**, 2984–2992
Grande P.L. and Schiwietz G. (1993): Non-perturbative stopping power calculation for bare and neutral hydrogen incident on He. Phys Rev A **47**, 1119–1122
Grande P.L. and Schiwietz G. (2002): The unitary convolution approximation for heavy ions. Nucl Instr Meth B **195**, 55–63
Guinea F., Flores F. and Echenique P.M. (1981): Charge states for protons moving in an electron gas. Phys Rev Lett **47**, 604–607
Guinea F., Flores F. and Echenique P.M. (1982): Charge states for H and He moving in an electron gas. Phys Rev B **25**, 6109–6125.
Hohenberg P. and Kohn W. (1964): Inhomogeneous electron gas. Phys Rev B **136**, 864–871
Hubert F., Bimbot R. and Gauvin H. (1990): Range and stopping-power tables for 2.5–500 MeV/nucleon heavy ions in solids. At Data Nucl Data Tables **46**, 1–213
Hulthén L. (1942): Über die Eigenlösungen der Schrödinger-Gleichung des Deuterons. Arkiv för Matematik, Astronomi och Fysik **28A**, 1–12
ICRU (2005): Stopping of Ions Heavier Than Helium, ICRU Report 73. J ICRU **5, no. 1** Press.
Juaristi J.I. and Arnau A. (1996): Interaction of multiply charged ions with metals. Nucl Instr Meth B **115**, 173–176
Juaristi J.I., Arnau A., Echenique P.M., Auth C. and Winter H. (1999): Charge state dependence of the energy loss of slow ions in metals. Phys Rev Lett **82**, 1048–1051
Kohn W. and Sham L.J. (1965): Self-consistent equations including exchange and correlations. Phys Rev A **140**, 1133–1138
Konac G., Klatt C. and Kalbitzer S. (1998): Universal fit formula for electronic stopping of all ions in carbon and solicon. Nucl Instr Meth B **146**, 106–113
Kumakhov M.A. and Komarov F.F. (1981): Energy Loss and Ion Ranges in Solids. Gordon and Breach, New York
Lakits G., Arnau A. and Winter H. (1990): Slow-particle-induced kinetic electron emission from a clean metal surface. Phys Rev B **42**, 15–24
Langer J.S. and Vosko S.H. (1959): The shielding of a fixed charge in a high-density electron gas. J Phys Chem Solids **12**, 196–205
Lifschitz A.F. and Arista N.R. (1998): Velocity-dependent screening in metals. Phys Rev A **57**, 200–207
Lifschitz A.F. and Arista N.R. (2004): Effective charge and mean charge of swift ions in solids. Phys Rev A **69**, 012902/1–5.
Lindhard J. (1954): On the properties of a gas of charged particles. K Dan Vidensk Selsk Mat Fys Medd **28, no. 8**, 1–57
Lindhard J. and Scharff M. (1953): Energy loss in matter by fast particles of slow charge. K Dan Vidensk Selsk Mat Fys Medd **27, no. 15**, 1–31
Lindhard J. and Scharff M. (1961): Energy dissipation by ions in the keV region. Phys Rev **124**, 128–130

Lindhard J. and Winther A. (1964): Stopping power of electron gas and equipartition rule. K Dan Vidensk Selsk Mat Fys Medd **34, no. 4**, 1–22

Major J., Seeger A. and Stammler Th. (1992): Muons and pions as probes in condensed matter. Z Phys C **56**, S269–S279

Mann A. and Brandt W. (1981): Material dependence of low-velocity stopping powers. Phys Rev B **24**, 4999–5003

Martínez-Tamayo G., Eckardt J.C., Lantschner G.H. and Arista N.R. (1996): Energy loss of H and He in Al, Zn and Au, in the very low to intermediate energy range. Phys Rev A **54**, 3131

Maynard G., Chabot M. and Gardés D. (2000): Density effects and charge dependent stopping theories for heavy ions in the intermediate velocity regime. Nucl Instr Meth B **164–165**, 139–146

Maynard G., Deutsch C., Dimitriou K., Katsonis K. and Sarrazin M. (2002): Evaluation of the energy deposition profile for swift heavy ions in dense plasmas. Nucl Instr Meth B **195**, 188–215

Morenzoni E. (1992): Very slow positive muons. Z Phys C **56**, S243–S249

Morenzoni E. et al (2002): Implantation studies of keV positive muons in thin metallic layers. Nucl Instr Meth B **192**, 254–266

Nikolaev V.S. and Dmitriev I.S. (1968): On the equilibrium charge distribution in heavy element ion beams. Phys Lett A **28**, 277–278

Ormrod J.H. and Duckworth H.E. (1963): Stopping cross sections in carbon for low-energy atoms with $Z \leq 12$. Can J Phys **41**, 1424

Ormrod J.H., Macdonald J.R. and Duckworth H.E. (1965): Some low-energy atomic stopping cross sections. Can J Phys **43**, 275–284

Patterson B.D. (1988): Muonium states in semiconductors. Rev Mod Phys **60**, 69–159

Paul H. (2006): Compilation of stopping power data. Available from www2.uni-linz.ac.at/fak/TNF/atomphys/stopping/

Payne H. (1970): Screening of a foreign charge by an electron gas. Phys Rev B **1**, 3645–3648

Peñalba M., Arnau A., Echenique P.M., Flores F. and Ritchie R.H. (1992): Stopping power for protons in aluminum. Europhys Lett **19**, 45–50

Puska M.J. and Nieminen R.M. (1983): Atoms embedded in an electron gas: Phase shifts and cross sections. Phys Rev B **27**, 6121–6128

Rogers F.J., Graboske H.C. and Harwodd D.J. (1970): Bound eigenstates in the static Coulomb potential. Phys Rev A **1**, 1577–1586

Salin A., Arnau A., Echenique P.M. and Zaremba E. (1999): Dynamical nonlinear screening of slow ions in an electron gas. Phys Rev B **59**, 2537–2547

Schiwietz G. and Grande P.L. (2001): Improved charge-state formulas. Nucl Instr Meth B **175–177**, 125–131

Sham L.J. and Kohn W. (1966): One-particle properties of an inhomogeneous interacting electron gas. Phys Rev **145**, 561–567

Shima K., Mikuno T. and Tawara H. (1986): Equilibrium charge state distributions of ions ($Z1 \geq 4$) after passage through foils: Compilation of data after 1972. At Data and Nucl Data Tables **34**, 357–391

Shima K., Kuno N., Yamanouchi M. and Tawara H. (1992): Equilibrium charge fractions of ions of Z=4-92 emerging from a carbon foil. At Data and Nucl Data Tables **51**, 173–241

Sigmund P. (2004): Stopping of Heavy Ions: A Theoretical Approach, Springer Tracts in Modern Physics, Vol. 204. Springer, Berlin

Sigmund P. (2006): Particle Penetration and Radiation Effects. General Aspects and Stopping of Swift Point Charges. Springer, Berlin

Sigmund P. and Schinner A. (2000): Binary stopping theory for swift heavy ions. Eur Phys J D **12**, 425–434

Sigmund P. and Schinner A. (2002): Binary theory of electronic stopping. Nucl Instr Meth B **195**, 64–90

Stewart A.T., Shand J.B., Donaghy J.J. and Kusmiss J.H. (1962): Fermi surface of beryllium by positron annihilation. Phys Rev **128**, 118–119

Vargas P. and Christensen N.E. (1987): Bend-structure calculations for Ni_4H, Ni_4H_2, Ni_4H_3 and NiH. Phys Rev B **35**, 1993–2004

Vargas P., Kronmüller H. and Böhm M.C. (1986): Charge distributions in Ni-H clusters. J Phys F: Met Phys **16**, L275–L281

Verbeek H., Eckstein W. and Bhattacharya R.S. (1980): Negative hydrogen ion formation by backscattering from solid surfaces. Surface Sci **95**, 380–390

West R.W. (1973): Positron studies of condensed matter. Adv Phys **22**, 263–369

West R.W. (1974): Positron Studies of Condensed Matter. Taylor and Francis, New York

Yarlagadda B.S., Robinson J.E. and Brandt W. (1978): Effective-charge theory and the electronic stopping power of solids. Phys Rev B **17**, 3473–3483

Ziegler J., Biersack J.P. and Littmark U. (1985): The Stopping and Range of Ions in Solids. Pergamon, New York

Charge Transfer in Atom-Surface Interactions

J.P. Gauyacq*

Laboratoire des Collisions Atomiques et Moléculaires
Unité mixte de recherches CNRS-Université Paris-Sud, UMR 8625
Bât. 351, Université Paris-Sud, 91405 Orsay Cedex, France

Abstract

The link between the electronic structure of the solid target and the electron transfer processes in ion-surface collisions is reviewed, together with a discussion of the theoretical approaches required to treat the different cases. The different behaviors of the electron transfer process for metal or ionic crystal surfaces are presented. The main emphasis of this paper is about finite time effects on the electron transfer process, due to the finite duration of a collision event. It is shown how this can deeply modify the characteristics of the electron transfer process in the case of a metal surface with a projected band gap. A review is then presented of different open problems where finite time effects can be expected and qualitatively influence the electron transfer processes.

Contents

1 Introduction **626**

2 Resonant Charge Transfer (RCT) on a Free-Electron Metal Surface **627**

3 Electron Capture from an Ionic Crystal **631**

4 Dynamical Effects in the RCT between a Projectile and a Metal Surface **633**
4.1 Wave-Packet Propagation Approach of the RCT Process 633
4.2 Effect of the Metal Electronic Structure on the RCT – Static Case 635
4.3 Effect of the Metal Electronic Structure on the RCT – Dynamical Case . . 638

5 Open Questions **642**

* E-mail: gauyacq@lcam.u-psud.fr

5.1 Bulk Electronic Structure Effects 643
5.2 Correlation Effects 643
5.3 Surfaces with Adsorbates 645
5.4 Finite Size Effects 647

6 Conclusions **648**

References **649**

1. Introduction

When an atom approaches the surface of a solid, couplings between the electronic levels of the atom and those of the solid can result in electron jumps between the atom and the surface. This process is quite important in the context of ion(atom)-surface collisional interactions since it determines the charge state of reflected as well as of sputtered particles; it also determines the charge state of a projectile as it hits a surface or penetrates the solid, thus influencing other phenomena such as energy transfer. Collisional charge transfer has thus been the subject of quite a few experimental and theoretical detailed studies in the past years (Los and Geerlings, 1990; Rabalais, 1994; Winter, 2002; Monreal and Flores, 2004). However, there is another domain where charge transfer processes play a significant role. Quite a few excited electronic states localized on an atomic or molecular adsorbate on a surface correspond to the transient capture (or loss) of an electron by the adsorbate; electron transfer is then one of the decay channels of these transient states. Excited states and in particular charge transfer states are often invoked as intermediates in reaction processes at surfaces; indeed excitation of an adsorbate often triggers an internal evolution, involving energy transfer between electrons and heavy particle motions that can lead to the breaking of chemical bonds or the creation of new ones. In this context, electron capture or loss appears both as an important step in reaction mechanisms and as a decay channel limiting the efficiency of excited state-mediated reaction processes (Palmer, 1992).

The present article is not intended to be a comprehensive review of the field of charge transfer at surfaces. It rather concentrates on a theorist view of the process and aims at illustrating what are the physical features that influence the nature of the charge transfer process. More precisely, it will first discuss how the electronic properties of the surface, i.e. its electronic band structure, influence the charge transfer and the choice of the theoretical approach to be used to quantitatively describe the process. It then shows how finite time effects modify this simple first view, leading to the discussion of a few open problems where the qualitative nature of the active charge transfer process can still be discussed.

Different charge transfer processes are possible at surfaces. They are usually classified according to the number of electrons involved in the process (Los and Geerlings, 1990). If only one electron is involved, the electron transfer process is called resonant or quasi-resonant charge transfer. Several electrons can also be involved. If the projectile has a vacancy in one of its inner orbitals, an electron from the solid can be transferred to this inner orbital and the corresponding energy gain is used to excite another electron from the solid, in a process called Auger-electron transfer (Hagstrum, 1954; Lorente and Monreal, 1996; Cazalilla et al., 1998). The energy gain can also be used to excite the electrons in the solid collectively, leading to a plasmon-assisted electron transfer (Lorente and Monreal, 1996; Baragiola and Dukes, 1996). Finally, one can also mention that the direct two-electron transfer from the solid to the projectile has also been evidenced and described (Roncin et al., 2002). In addition to the number of electrons involved, the characteristics of the electronic levels involved in the charge transfer directly influence the qualitative nature of the charge transfer. The electronic levels on the projectile are discrete states localized on the projectile. In contrast the solid can exhibit qualitatively different types of electronic levels: the levels can be delocalized over the crystal and form a continuum of states or they can be discrete states localized on one of the sites of the crystal; more generally, the band structure of the solid target can exhibit very different properties. In addition, when adsorbates are present on the surface, electronic states can possibly be localized on the adsorbates. The present review begins with the description of two examples of one-electron transfer processes on two surfaces with very different electronic band structures: a free-electron metal (Section 2) and an ionic crystal (Section 3). This illustrates how different electronic structures of the solid lead to different qualitative pictures of the electron transfer so that the theoretical description of the charge transfer at surfaces has to involve different approaches. Then it is shown how this simple view has to be modified on metal surfaces due to finite time effects (Section 4) leading to the discussion of several open questions (Section 5).

2. Resonant Charge Transfer (RCT) on a Free-Electron Metal Surface

In a free-electron metal, the electrons interact with the metal via a local potential, constant inside the metal and exhibiting a surface barrier at the metal edge. One-electron transfer from a projectile to a free-electron metal can then be described as the evolution of a single electron in a potential describing its interaction with the projectile-target compound system. Figure 1 presents such a potential for a given projectile-surface distance. The potential is plotted along the z-axis normal to the surface and going through the atom center. One recognizes the potential well inside the metal (negative z) and the atomic potential well localized around the

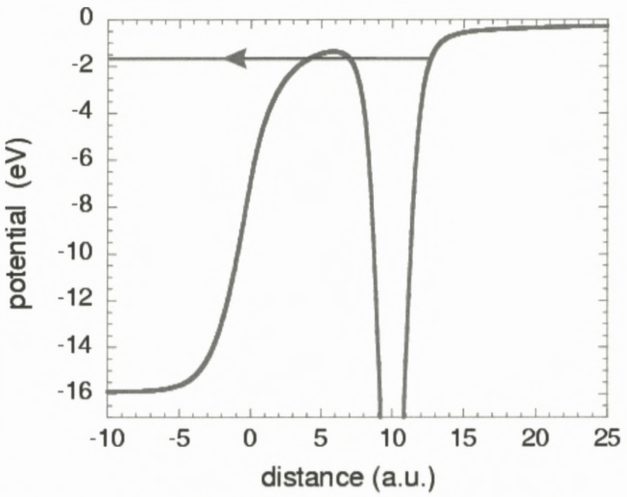

Figure 1. Schematic picture of the potential involved in the electron transfer between an atom and a free-electron metal surface. The potential is shown along an axis perpendicular to the surface and going through the atom center (negative coordinates inside the metal). An atomic level localized inside the atomic potential well is schematized by an horizontal line, together with an arrow representing the electron transfer into the metal.

projectile. An atomic level on the projectile is then degenerate with the continuum of metal states and thus, according to the Fermi golden rule, it becomes quasi-stationary. The atomic level decays by transfer of an electron into the metal states that have the same energy, so that this process is often referred to as Resonant Charge Transfer (RCT). The finite width of the level, inverse of its lifetime, gives the electron transfer rate. Another picture of the same process is to say that the electron can tunnel through the barrier separating the projectile and the surface. The direction of the charge transfer depends on the energy position of the atomic level. Indeed, if the atomic level is above the Fermi level, it is degenerate with an empty continuum (at least at 0 K) and it can decay by transfer of the electron into the metal. In contrast, if the atomic level is below the Fermi level, it is degenerate with a fully occupied continuum and no electron can be transferred into the metal. However, one can repeat the argument with electrons replaced by holes and conclude that, in that case, electron transfer occurs from the metal to the projectile. For a finite temperature, the metal states are neither fully occupied nor fully empty and RCT can occur in both directions, proportionally to the relative weight of empty and occupied states.

To describe the evolution of an atom colliding with a metal surface, one can use a semi-classical approximation, treating the heavy particle motion classically while the electron evolution is treated quantally. Such an approach is valid for not

too slow projectiles. From the above discussion, one can conclude that the energy and the width of the atomic level are the key parameters to describe the RCT process for a fixed ion-surface distance. Relying on the adiabatic approximation, one can assume that this also holds in the case of an atom colliding with a metal surface (Los and Geerlings, 1990; Geerlings et al., 1986). One can then describe the evolution of the charge state of the projectile in front of a free-electron metal via a rate equation, such as for example:

$$\frac{\mathrm{d}P}{\mathrm{d}t} = -\Gamma_{\mathrm{loss}} P + \Gamma_{\mathrm{capt}}(1 - P), \tag{1}$$

for the case of two charge states (positive ion and neutral). P is the population of the neutral state of the projectile, Γ_{loss} and Γ_{capt} are the electron loss and capture rates, as determined in a fixed projectile situation. This rate equation makes the implicit assumption that the electron transfer rates are the same in a static situation (fixed projectile-surface distance) and in the course of a collision. As for the energy and width of atomic levels in front of a free-electron metal surface, there exist nowadays a few different parameter-free approaches to compute them. They consist in looking for quasi-stationary states in a 3D-potential using complex scaling (Nordlander and Tully, 1988), coupled angular modes (Teillet-Billy and Gauyacq, 1990), stabilization (Martin and Politis, 1996; Deutscher et al., 1997), close-coupling (Merino et al., 1986; Kürpick et al., 1997; Bahrim and Thumm, 2002), wave-packet propagation (Ermoshin and Kazansky, 1996; Borisov et al., 1999a; Chakraborty et al., 2004). When applied to the same problem, these methods yield the same results. It has also been shown recently that charge transfer rates can be extracted from DFT studies on the projectile-metal system (Niedfeldt et al., 2004). Used with the adiabatic rate equation approach (Equation 1), this yields a quite satisfying account of the charge state of atoms scattered from a free-electron metal surface (Borisov et al., 1992, 1996a; Maazouz et al., 1997; Hill et al., 2000). In particular, a quite satisfying account of experimental results is obtained in the grazing angle scattering geometry, which selects atoms reflected from a defect-free area of the surface. As an example, Figure 2 shows the results for Na^+ ion neutralization in grazing angle collisions with an Al(111) surface (experimental and theoretical results from Borisov et al., 1996a). It presents the ion neutralization probability as a function of the collision velocity parallel to the surface for three different perpendicular velocities. The strong dependence of the charge state as a function of the parallel velocity is due to the so-called "parallel velocity effect" (Van Wunnick et al., 1983): the projectile level and the metal states are defined in two different Galilean reference frames, in fast motion one with respect to the other; the transformation from the metal frame to the projectile frame modifies the energy distribution of the metal electrons, strongly

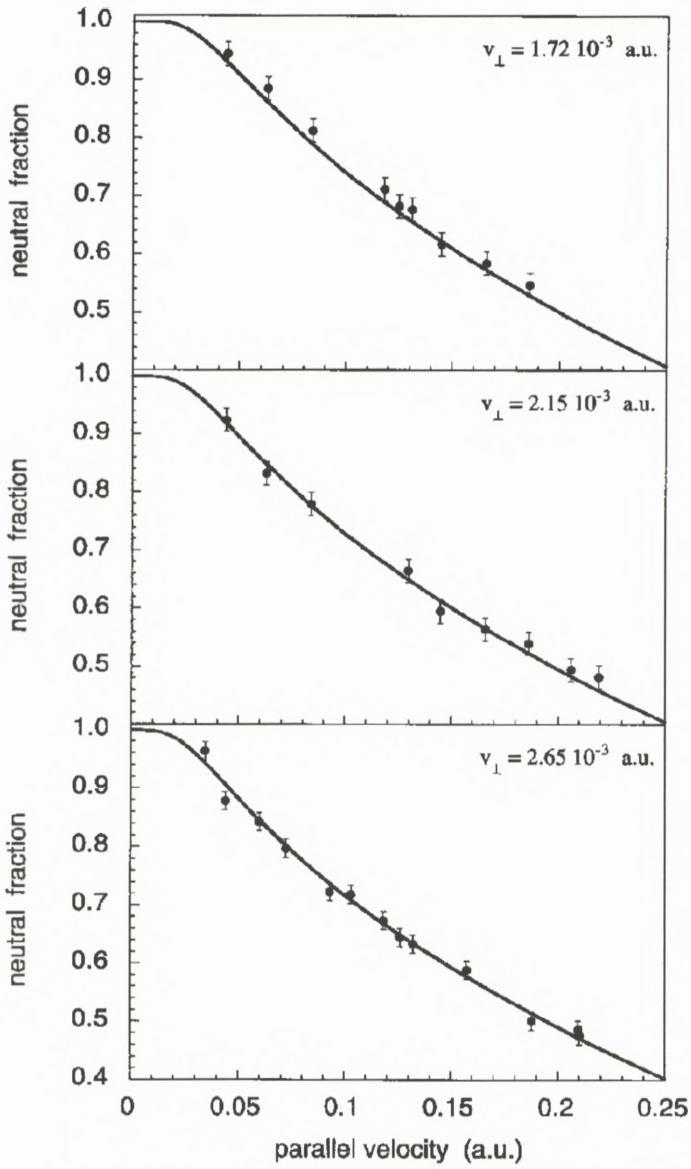

Figure 2. Neutralization probability of Na^+ ions scattering at grazing angle from an Al(111) surface. The probability is shown as a function of the collision velocity parallel to the surface for three different perpendicular velocities. Collision velocities are given in atomic units. Symbols: experimental results and lines: theoretical results (from Borisov et al., 1996a).

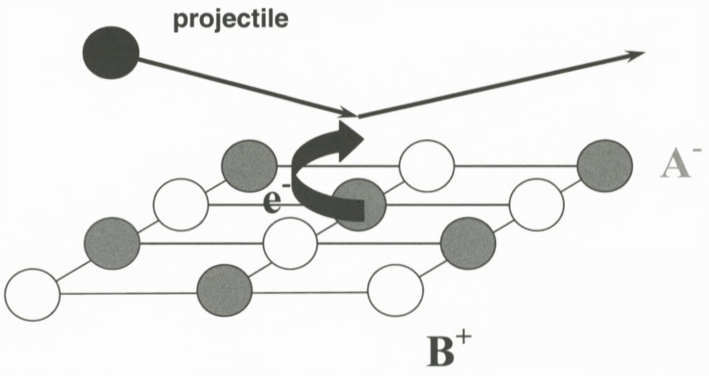

Figure 3. Schematic picture of the electron capture process during a collision on an ionic crystal surface. White spheres: B^+ cation sites; gray spheres: A^- anion sites of the crystal (only the surface plane of the crystal is represented). The projectile (dark sphere) is moving along a classical trajectory (symbolized by the two straight arrows) that hits the crystal on an anion site. Electron capture results from the binary collision between the projectile and the anion site.

influencing the direction of the charge transfer (see a detailed discussion in Van Wunnick et al., 1983; Winter, 2002). So, qualitatively and quantitatively, RCT on a free-electron metal appears to be well understood, it corresponds to irreversible transitions between discrete states of the projectile and the continuum of metal states and the time dependence of the RCT along the collision can be efficiently described via an adiabatic rate equation.

3. Electron Capture from an Ionic Crystal

Experimental studies of electron capture in grazing angle scattering of a projectile from an ionic crystal surface revealed extremely large negative ion formation probabilities, much larger than those observed on a metal surface (Auth et al., 1995; Winter, 2000). The theoretical description of the electron transfer process in this system (Borisov et al., 1996b; Borisov and Sidis, 1997) is completely different from the one discussed in the previous section. It involves binary collisions between the projectile and the anion sites of the crystal, where the valence band electrons are localized and can be captured from. The geometry of the collision when the projectile hits an anion site, A^-, of an A^-B^+ ionic crystal is sketched in Figure 3. The binding energy of the electron in the valence band in e.g. a LiF crystal is very large (around 14 eV) and much larger than the electron affinity of a typical projectile. This feature could *a priori* hinder an electron transfer between the valence band and the projectile. However, analysis of the energies of the initial state (neutral projectile and complete crystal) and of the final state (ionic projectile

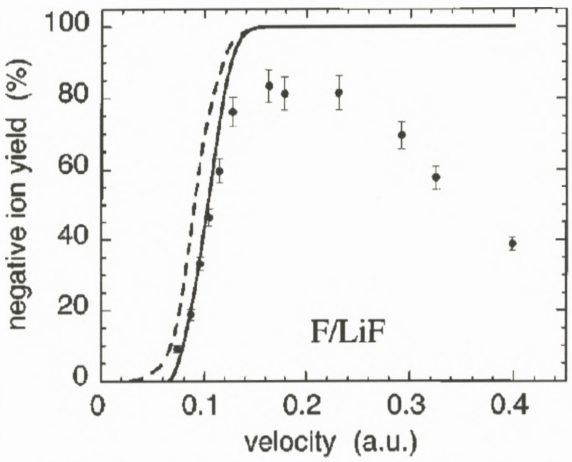

Figure 4. Negative ion yield for grazing angle scattering of F atoms on a LiF(100) surface as a function of the collision velocity parallel to the surface (in atomic units). Symbols: experimental points from Auth et al. (1995) for an incidence angle of 1° with respect to the surface plane. Theoretical results from Borisov et al. (1997) for two incidence angles: 1° and 2.5°: full and dashed lines, respectively. Figure reprinted with permission from Borisov and Sidis, Phys Rev B **56**, 10628. Copyright 1977 by the American Institute of Physics.

and one hole in an anion site of the crystal) shows that the energy defect of the electron transfer is greatly reduced by a Coulomb term arising from the interaction between the localized hole in the crystal and the ionic projectile (Borisov et al., 1996b). This "energy confluence" of the initial and final states can lead to an efficient transfer during the binary collision between the projectile and a crystal anion. After the negative ion is formed, its destruction by electron loss has to occur via electron transfer into the conduction band of the crystal or into vacuum, which are not in energetic resonance with the projectile affinity level. Hence, electron loss has to involve a dynamical process. For this reason, the electron loss process can be expected to be weak for low collision velocities. These two features, efficient capture and inefficient loss, make the negative ion formation highly probable on an ionic crystal. In addition, in the case of grazing angle collisions, since the electron transfer process is well localized around an anion site, the projectile can interact successively with different anion sites, leading to a cumulative electron capture process and to a very large negative ion probability in the scattered beam. Figure 4 (from Borisov and Sidis, 1997) presents the negative ion formation probability for F atoms incident on a LiF(100) surface at grazing incidence. The experimental negative ion yield (Auth et al., 1995) is very high, reaching 80% at maximum. The theoretical study (Borisov and Sidis, 1997) involved the determination of the energies and couplings of the states active in the charge transfer by a quantum

chemistry approach of the projectile-crystal system, one can say that it describes an atom-atom binary collision in presence of the field created by the ionic crystal. The quantum chemistry approach yields adiabatic states, eigen-functions of the electronic Hamiltonian, from which diabatic states, better suited for the dynamics treatment, are extracted. The theoretical negative ion yield (Borisov and Sidis, 1997) is seen to rise very rapidly above threshold, quickly reaching 100%. This fast increase above threshold is due to both the collision energy dependence of the electron capture in the binary collision and to the increase of the number of active sites in this grazing angle collision. The theoretical study only included the effect of capture in the binary collision and did not introduce any process for electron loss in the subsequent binary collisions; this explains the saturation of the theoretical negative ion yield at large velocities, different from the decrease of the experimental yield. Though, the threshold region, where electron loss can be thought to be weak, is well reproduced by the theoretical results.

4. Dynamical Effects in the RCT between a Projectile and a Metal Surface

The two situations depicted in the previous sections are qualitatively well understood and nowadays efficient quantitative treatments are available. The electronic structures of the two surfaces are quite different, leading to quite different descriptions of the electron transfer. Besides the existence of a continuum of states in the metal case, a key difference appears to be the reaction of the surface to electron capture: after an electron capture from a metal, the surface is still the same, i.e. one assumes a perfect instantaneous relaxation of the metal, whereas after an electron capture from an ionic crystal, a hole is present at the surface for a while. This leads to a different qualitative nature of the electron transfer and consequently, to the need to resort to different theoretical approaches for treating the charge transfer process. It is shown below on the example of RCT on a metal surface that the situation is not always that simple and that the connection between the surface electronic band structure and the characteristics of the charge transfer is not always straightforward. Non-adiabatic effects associated with the finite time duration of a collision event can appear that deeply affect the charge transfer process. These will be illustrated in the case of the RCT process on a metal surface, treated in a wave-packet propagation (WPP) approach (see Borisov et al., 1999a, for a detailed presentation of the WPP method).

4.1. Wave-Packet Propagation Approach of the RCT Process

The RCT process on a metal surface is a one-electron process and thus, one can treat it as the evolution of a single electron inside a potential representing the

electron interaction with the projectile and the metal surface (see Figure 1). The wave-packet propagation approach of this problem consists of solving the time-dependent Schrödinger equation for the active electron:

$$i\,\frac{\mathrm{d}\Psi(\vec{r},t)}{\mathrm{d}t} = H\Psi(\vec{r},t) = (T+V)\Psi(\vec{r},t), \tag{2}$$

where $\Psi(\vec{r},t)$ is the active electron wave function defined on a 3-dimensional grid of spatial points. T is the electron kinetic energy operator and V is the interaction potential of the electron with the atom+surface system. V is usually modeled as the sum of three terms: $V_{\text{e-atom}}$, the electron interaction with the core of the projectile, $V_{\text{e-metal}}$ the electron-metal surface interaction and $\Delta V_{\text{e-metal}}$, the modification of $V_{\text{e-metal}}$ due to the presence of the projectile. Various kinds of model and pseudo-potentials are available for $V_{\text{e-atom}}$, coming from earlier atomic physics studies. For $V_{\text{e-metal}}$, different modelings of the electron-surface interaction are available. A first description, taken from Jennings et al. (1988), corresponds to a free-electron metal: the electron is free i.e. the $V_{\text{e-metal}}$ potential is constant inside the metal and $V_{\text{e-metal}}$ smoothly joins an image potential outside the metal. This is typically the representation that was used in the theoretical studies on free-electron metal surfaces mentioned in Section 2. Below, results obtained with the model potential introduced by Chulkov et al. (1999) are also presented. Inside the metal, this potential is oscillating with the crystal periodicity perpendicular to the surface and it is constant in the direction parallel to the surface; it smoothly joins an image potential outside the surface. This potential is very efficient in representing the characteristics of the surface electronic band structure for electron motion perpendicular to the surface. Indeed, the modulation of the potential perpendicular to the surface opens a band gap for the electron motion in this direction, i.e. a surface-projected band gap. Surface states and/or image states can then exist on such a surface (Desjonquères and Spanjaard, 1993). $\Delta V_{\text{e-metal}}$ is introduced only in the case of a charged projectile core, it is then simply taken as the interaction between the active electron and the image of the ion core.

The wave function of the active electron $\Psi(\vec{r},t)$ is obtained from the time-dependent Schrödinger equation by time propagation, starting with an initial wave function Φ_0. Two different calculations can be performed: (i) a static calculation, in which the projectile is kept at a fixed distance from the surface and (ii) a dynamical one where the projectile is moving with respect to the surface along a classical trajectory. In both cases, the propagation is started with Φ_0 equal to the wave function of a bound state of the free projectile. In case (i), one can obtain from the survival amplitude of the system the energy and width of the projectile states interacting with the metal surface, one can also get the wave function of the quasi-stationary states. Energies and widths of the states can be

used afterwards in an adiabatic rate equation approach (Equation 1) to treat the collision dynamics. In case (ii), one directly follows the collision dynamics and obtains the final charge state after the collision. The time propagation is performed over successive infinitesimal time steps, using a split operator approximation that allows using an appropriate propagator for each term in the Hamiltonian (see Borisov et al., 1999a, for details). In the case of an atom interacting with a metal surface with translational invariance parallel to the surface, the system is invariant by rotation around the z-axis perpendicular to the surface and going through the atom center. Using cylindrical coordinates (z, ρ, ϕ) around the symmetry axis, the full 3D-problem can then be reduced to a 2D-problem, with the ϕ-part of the wave function being factored out (see Borisov et al., 1999a, for details on the propagation scheme in this case).

4.2. Effect of the Metal Electronic Structure on the RCT – Static Case

The presence of a surface-projected band gap can be expected to deeply affect the RCT in certain cases. This is illustrated in Figure 5, which presents the surface projected band structure of a free-electron metal and that of the Cu(111) surface. Figure 5 presents the energy of the metal states as a function of $k_{//}$, the electron momentum parallel to the surface. On a free-electron metal, the energy of the states varies quadratically with $k_{//}$. All energies are possible above the bottom of the conduction band. As seen in Section 2, the RCT process corresponds to the transfer of an electron between a projectile state and metal states of the same energy. On a free-electron metal, a projectile state with an energy as indicated in Figure 5 is degenerate with a whole set of $k_{//}$ states, starting at $k_{//} = 0$. In contrast, for Cu(111), a projectile state with the same energy is only degenerate with a surface state of a given finite $k_{//}$ and with a series of states of the conduction band corresponding to finite values of $k_{//}$. The metal states that can actively contribute to the RCT process are then different in the two situations and as shown below, this deeply influences the efficiency of the electron transfer in the two cases.

Figure 6 presents the wave function of the lowest lying quasi-stationary state localized on the Cs adsorbate in the Cs/Cu system. Figure 6 shows the squared modulus of the state wave function, i.e. the electron density in a plane perpendicular to the surface and containing the symmetry z-axis that goes through the atom center. The right panel of Figure 6 presents the results obtained in the free electron case and the left panel the case of the Cu(111) surface. In the case of the free-electron metal, one recognizes the Cs resonance localized around the Cs-center and a flux of electron leaving the Cs atom and going into the metal around the surface normal. This flux corresponds to the RCT process in which the electron is transferred from the Cs into the metal. As illustrated in Figure 1, the RCT can

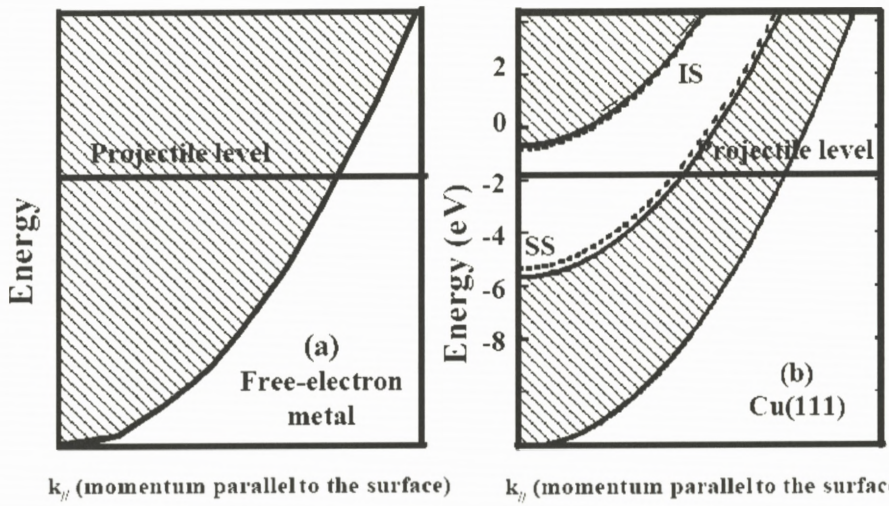

Figure 5. Schematic projected band structure of a metal. (a) Free-electron metal and (b) Cu(111) surface. The energy of the levels are presented as a function of $k_{//}$ the component of the electron momentum parallel to the surface. The shaded areas represent the valence and conduction bands of the system. In addition, in the Cu(111) case, the surface state (SS) and first image state (IS) that appear in the surface projected band gap are represented by dashed lines. The horizontal line is used for the discussion of the electron transfer process between a projectile and the metal surface: it represents the energy of the projectile level and thus allows to determine which are the metal states degenerate with the projectile level.

be viewed as the electron tunneling through the potential barrier that separates the atom and the metal. The thickness of this barrier is minimal along the surface normal and thus tunneling occurs preferentially along this direction, as seen in the right panel of Figure 6. Tunneling along the surface normal populates metal states around $k_{//} = 0$ in the band structure shown in Figure 5a. In the case of a Cu(111) surface, the situation is quite different. One can see in Figure 5b that there is not any metal state degenerate with the adsorbate state around $k_{//} = 0$; i.e. the states that are the most efficient for RCT on a free electron metal are missing in the Cu(111) case. In the left panel of Figure 6, there is only an evanescent wave in the area around the symmetry axis. The electron flux associated to RCT into Cu bulk states appears at a finite angle from the surface normal, this angle corresponds to the metal states that are degenerate with the adsorbate state which have the smallest $k_{//}$ value, i.e. it corresponds to tunneling along a direction that is the closest possible to the surface normal that is compatible with the electronic band structure. Tunneling at a finite angle is associated with a broader barrier to travel through and as a consequence the RCT rate is much smaller in the Cu(111) case (notice in the right panel how fast the electron flux is decreasing as it moves

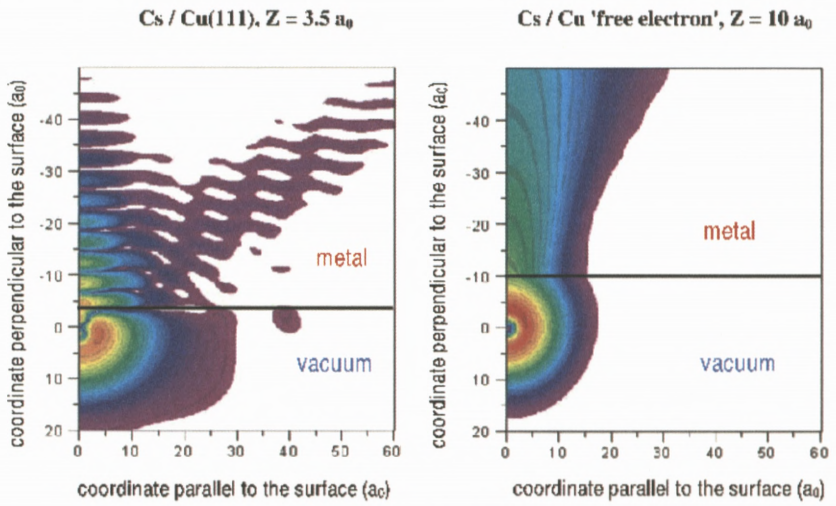

Figure 6. Logarithm of the squared modulus of the electron wave function (electron density) for the quasi-stationnary state located on the Cs adsorbate on a Cu surface. Only a cut of the density in a plane perpendicular to the surface and going through the surface is presented. The system symmetry axis is along the vertical coordinate and the metal is on the negative coordinate side. The atom is at the origin of coordinates. Right panel: free-electron metal surface with a Cs atom located at 10 a_0 from the surface. Left panel: Cu(111) surface, with a Cs adsorbate at 3.5 a_0 from the surface.

away from the surface normal). RCT into the Cu(111) surface state continuum is also possible though in this case it appears to be very weak and not visible with Figure 6 scale. Quantitative studies (Borisov et al., 1999b) show that the RCT rate amounts to 900 meV on a free-electron metal and to 7 meV on Cu(111), revealing a two orders of magnitude decrease due to the effect of the electronic band structure. Note that the RCT rates are often given in units of energy, so that the rate is directly equal to the level width, a width of 1 eV corresponds to a lifetime of 0.66 fs. Usually, the RCT process is thought to be more efficient than the other charge transfer processes since it implies one-electron transition terms. In the Cs/Cu(111) case, since RCT is much weakened, one should also consider multi-electron transition terms. A theoretical study of the contribution of electron-electron interactions to electron loss by the Cs adsorbate (the excited electron interacts with the metal electrons, leading to its transfer into the metal and to the excitation of the metal electrons) yields a multi-electron transfer rate of 14.5 meV. This is larger than the RCT rate on Cu(111), but, as expected, much smaller than the RCT rate on a free-electron metal (Borisov et al., 2001). In total, this leads to a very long lifetime, 28 fs, for the excited Cs adsorbate state on Cu(111). The Cs localized state has been studied in detail using time-

resolved 2-photon-photoemission experiments. These experiments also revealed a very long-lived transient state (Bauer et al., 1997, 1999; Ogawa et al., 1999). The long lifetime allows the Cs-localized state to be involved as an intermediate in a photo-desorption process (Petek et al., 2000). Theoretical results and experimental data are found to agree quantitatively, in particular once the Cs desorption motion is taken into account (Gauyacq and Kazansky, 2005).

Thus, in this static case (adsorbate on a metal), the electronic band structure of the metal surface is found to deeply affect the charge transfer, leading to a quasi-blocking of the RCT process in the case of a surface-projected band gap. Similar results have been found in other static systems exhibiting the same situation (excited state inside a surface-projected band gap) like other alkali/noble metal systems (Borisov et al., 2002) or core-excited Ar on a Cu surface (Gauyacq and Borisov, 2004). In all these systems, the states that can *a priori* be thought to be the most efficient ones for electron tunneling between the metal and the adsorbate are missing, leading to a severe drop of the RCT rate as compared to what happens on a free-electron metal surface.

4.3. Effect of the Metal Electronic Structure on the RCT – Dynamical Case

If instead of considering an adsorbate/metal system, one considers an atom colliding on a surface, one could, *a priori*, expect similar effects of the surface band structure to appear, i.e. one could expect very different results for collisions on a free-electron metal and on a metal surface exhibiting a surface-projected band gap. This idea is based on the supposed validity of the adiabatic rate equation (Equation 1), i.e. on the assumption that the charge transfer rate during a collision is the same as the charge transfer rate for a static atom-surface system. Below, it is shown how non-adiabatic effects can modify the dynamical case and make it look different from the static case.

Recently a joint experimental-theoretical study has been devoted to the Li^+ ion neutralization by collision with an Ag(100) surface (Canario et al., 2005). Figure 7 presents the energy and width of the Li(2s) atomic level interacting with an Ag surface, either Ag(100) or a free-electron metal model. On a free-electron metal, the energy of the 2s level is seen to increase as the atom approaches the surface and to cross the Fermi energy at a distance, Z_X. The RCT process then leads to electron capture for $Z > Z_X$ and to electron loss by the projectile for $Z < Z_X$. The level width (the RCT rate) increases quasi-exponentially as the projectile approaches the surface. The situation appears different in the case of an Ag(100) surface. Though the level width appears only slightly affected by the surface band structure, the energy of the Li(2s) is much different. The Ag(100) surface exhibits a surface-projected band gap between -2.89 eV and $+2.21$ eV (with respect to

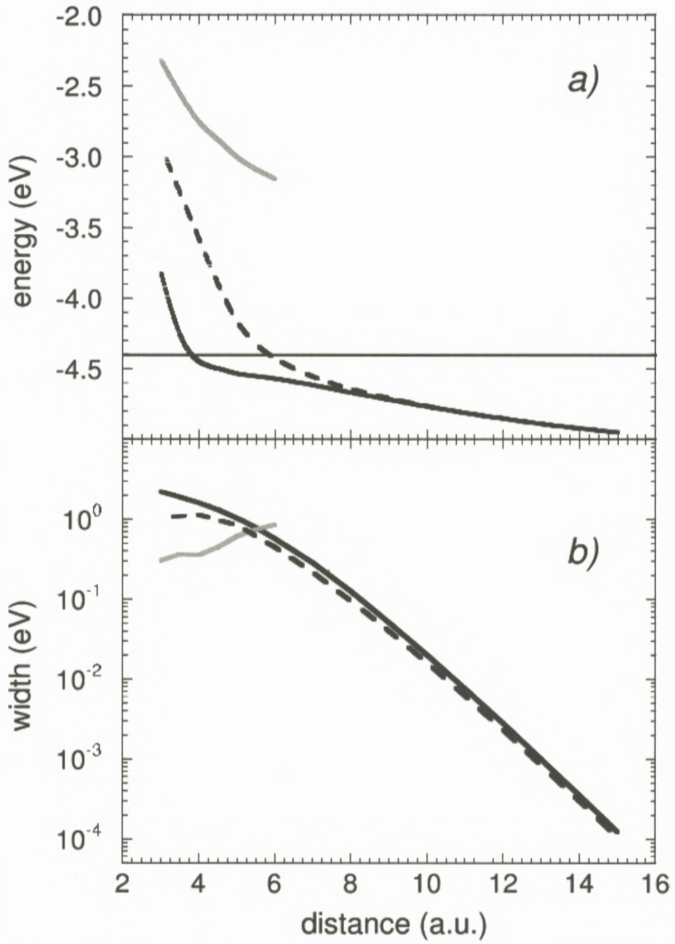

Figure 7. Energy (a) and width (b) of the adiabatic quasi-stationnary states involved in the neutralization of Li^+ ions on a Ag surface as a function of the Li-surface distance. Dashed line: state correlated to Li(2s) at infinite separation in front of a free-electron metal surface. Full black line: state correlated to Li(2s) at infinite separation in front of Ag(100). Full gray line: state correlated to the surface state resonance (from Canario et al., 2005).

vacuum), leading to a surface state resonance located at −3.19 eV. The interaction between the Li(2s) state and the 2D-surface state resonance continuum results in a state splitting off the bottom of the 2D-continuum, with which the Li(2s) level exhibits an avoided crossing as a function of Z, the Li-surface distance. As a consequence, on Ag(100), at small Z, the energy of the Li(2s) state appears much different from the free-electron case. The range of Z distances where Li^+ neutralization can occur is much broader on Ag(100) and, in an adiabatic view,

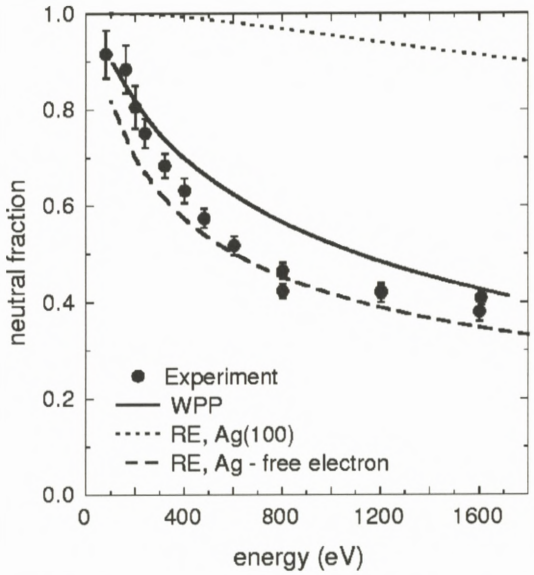

Figure 8. Neutralization probability of Li^+ ions colliding on a Ag(100) surface. Symbols: experimental results as a function of the collision energy. Dotted line: theoretical results using a rate equation approach with the adiabatic Ag(100) description. Dashed line: theoretical results using a rate equation approach with a free-electron metal description. Full line: dynamical WPP results (from Canario et al., 2005).

one would then expect a much more efficient Li^+ neutralization on Ag(100) than on a free electron metal surface.

Figure 8 presents the neutralization probability as a function of the ion collision energy. It shows the experimental results together with three different theoretical results. First, two theoretical results are obtained using the adiabatic rate equation (Equation 1) together with the energy and width obtained in the static study, for the Ag(100) or free-electron case. As discussed above, in this adiabatic approximation, the neutralization is much more efficient in the Ag(100) case. A third theoretical result is obtained using the dynamical WPP approach, i.e. with all the non-adiabatic aspects of the electron transfer taken into account. The dynamical WPP result appears rather far away from the adiabatic rate equation result for Ag(100) revealing strong non-adiabatic effects in this system. It also appears that the dynamical WPP result is in quite good agreement with the experimental results, confirming the validity of the present approach. The first conclusion is then that non-adiabatic effects are important and that one cannot deduce the collisional behavior of the system from the knowledge of the static system. One can link this with the existence of an avoided crossing between two quasi-stationary states in

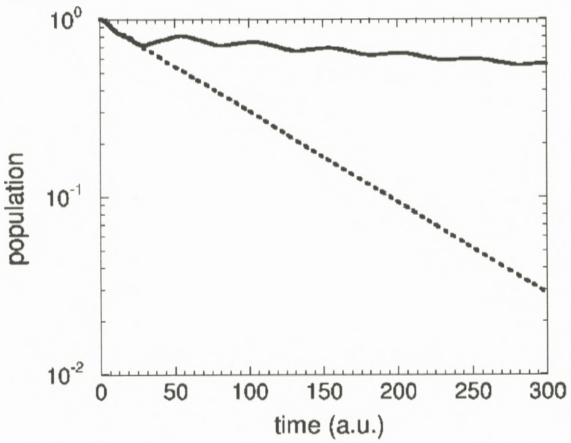

Figure 9. Survival probability as a function of time (in atomic units) for an H^- ion located at 10 a_0 from a metal surface. Dashed line: free-electron metal surface. Full line: Cu(111) surface (from Borisov et al., 1999a).

this system (see Figure 7), which should play a role at large enough velocities. However, one can also notice that the non-adiabatic effects tend to bring the Ag(100) results very close to those of a free-electron metal, i.e. that non-adiabatic effects seem to erase the effect of the Ag(100) electronic band structure.

Qualitatively, this disappearance of the band structure effect can appear surprising, though it can be understood by looking at earlier results on H^- ions interacting with a Cu(111) surface (Borisov et al., 1999a). The H^- ion level is inside the Cu(111) surface-projected band gap and similarly to the Cs/Cu(111) case, the H^- ion RCT rate is much smaller on a Cu(111) surface than on a free-electron metal surface. Figure 9 presents the survival probability of the H^- ion level at a fixed ion-surface distance from two different surfaces: a free-electron metal and Cu(111). The ion survival probability is computed with the WPP approach as outlined in Section 4.1. On the free-electron metal surface, the ion survival probability is seen to decrease exponentially with time; this further confirms the discussion in Section 2: the ion level is degenerate with a continuum and following the Fermi Golden Rule, its population decreases exponentially with time, the lifetime being the inverse of the RCT rate. On Cu(111) at late times, the population is also seen to decrease exponentially, though with a smaller slope; the slope difference between the two cases is the signature of the projected band gap effect that partially blocks the RCT on Cu(111). However, on Cu(111), the very early decay of the ion level is identical to that on a free-electron metal. This can be understood in the following way: at the beginning of the propagation, the electron wave packet is around the projectile. The electron wave packet starts to

tunnel through the barrier separating the projectile and the metal, this step is the same on the two surfaces and favors the area around the surface normal. On the free-electron metal surface, the electron wave packet spreads into the bulk. On Cu(111), as the electron wave packet penetrates into the metal, it feels the periodicity of the potential that is responsible for the band structure; more precisely, the electron wave packet is partly reflected at each atomic plane inside the metal and the interference created by these multiple reflections generates the projected band gap, i.e. prevents the electron from propagating into the metal along the surface normal. These interferences are visible in Figure 9 as the small undulations in the ion survival probability, in the Cu(111) case. After many reflections, the electron wave packet "fully knows" about the band structure and the RCT process stabilizes at a very slow rate, signature of the projected band gap effect. This discussion leads to the understanding of the Li/Ag case: if the collision is fast, i.e. if the collision time is short, the effect of the band structure does not have enough time to set in during the collision and the surface behaves as a free-electron metal surface.

This result has a few direct consequences for charge transfer studies. It illustrates that electron transfer at low and high collision velocities can be qualitatively different. The change of behavior of the RCT process as a function of the collision velocity formed the basis of the interpretation of experimental charge transfer studies on Ag(111) as a function of collision energy (Guillemot and Esaulov, 1999). For grazing angle scattering on Cu(111) surfaces (Hecht et al., 2000), the collision energy for the motion perpendicular to the surface is in the eV range and experimental and theoretical studies showed that the RCT process is deeply influenced by the Cu(111) band structure, in particular a clear signature of the role played by the surface state is present. At higher velocities, like those discussed above on the Li/Ag system, the effect of the band structure is basically absent (note that the energy scale in Figure 8 is in the keV range, showing that, in this system, the critical velocity where non-adiabatic effects appear is low).

5. Open Questions

Sections 2 and 3 have presented results on two different kinds of collisional systems where the electronic structure of the solid target is directly influencing the characteristics of the electron transfer process. Though, the last section detailed an example where the effect of the electronic structure of the solid on the charge transfer disappears when the collision time is short enough. This feature can look surprising at first sight, however, it is rather easily understood in terms of the minimum time required for the active electron to probe the structure of the solid. In addition, it brings in quite a few questions on various systems, in which it

is not obvious at first sight which are the solid characteristics that are actually influencing the charge transfer. Some of these systems are reviewed below.

5.1. Bulk Electronic Structure Effects

Theoretical studies of the RCT using a free-electron description of the metal surface have been used successfully for non-free-electron metals; possibly, the finite collision velocity was the reason for their success. We can then wonder about other solids like semi-conductors or semi-metals (graphite). Can a finite time effect remove the effect of a semi-conductor band gap? Though a few theoretical studies have been reported for collisions on Si surfaces (García et al., 2006; Lorente et al., 1997), the author is not aware of a work specifically addressing this point. Similarly, graphite is expected to present some specific features for charge transfer linked with the very small density of states around the Fermi level. This feature has been invoked (Tsumori et al., 1997) to interpret the large negative ion yields on graphite or diamond: the low density of states around the Fermi level should reduce the efficiency of re-neutralization of the negative ions formed close to the surface. Here again, one can wonder how such an effect would survive in fast enough collisions and what would be the critical velocity for the switch between the two behaviors.

5.2. Correlation Effects

The approaches to electron transfer discussed above rely on a one-electron description of the process. However, there are a large number of electrons in a solid and they can possibly lead to many body effects in the charge transfer process. Various theoretical approaches have been developed to include many body effects (Brako and Newns, 1985; Nakanishi et al., 1987; Langreth and Nordlander, 1991; Marston et al., 1993; Shao et al., 1994; García et al., 1995; Merino and Marston, 1998). The effect due to correlation on the projectile (existence of equivalent electrons or of different levels on the projectile) is significant and in the rate equation approach, it can be handled simply by introducing several charge states and/or electronic levels in the rate equations. In the case of degenerate atomic levels, this leads to extra statistical factors, bringing an unbalance between capture and loss processes (see e.g. a discussion in Zimny, 1990; Langreth and Nordlander, 1991; Gauyacq et al., 2000). Correlation inside the metal is more delicate to handle. In many cases, it does not seem to play an important role (Ustaze et al., 1998). However, in the case of a degenerate impurity interacting with a metal surface, many-body effects have been shown to lead to the appearance of a peak in the density of states close to the Fermi energy, the so-called Kondo peak. Such a peak has been observed by scanning tunneling spectroscopy (Madhavan et al., 1998).

It has been proposed to play a role in the case of collisional charge transfer (Shao et al., 1995, 1996). Indeed, an atom approaching a metal would generate a Kondo peak in the density of states; the transient population of the Kondo peak during the collision time would then influence the final outcome of the electron transfer process. However, the Kondo peak is a narrow structure which needs time to appear and the question arises whether in a finite time collision, such a peak could be generated and influence the collision. Theoretical discussions of the conditions for its appearance in a collision have been presented (Shao et al., 1996; Merino and Marston, 1998), but it has not been observed experimentally yet.

A projectile can have different electronic levels that could participate at the same time in the charge transfer process. This brings some correlation effects. For example, a positive ion can capture electrons in different levels, but once it has captured an electron on a given level, this blocks the capture on the other levels. This effect is automatically introduced in a rate equation approach by adding a population term for each level. There has been a few experimental and theoretical studies of neutralization of alkali projectiles on metal surface partially covered by alkali adsorbates, which showed that neutralization could occur both toward the ground state and toward the lowest lying excited states (Behringer et al., 1996a, 1996b; Brenten et al., 1991; Goryunov, 1998). In this case, the electron was transferred between the projectile and the target and no transition between projectile states was invoked. However, when several states are close in energy, one can expect transitions between these states to be induced by the motion of the projectile. Such transitions are linked to a non- adiabatic behavior of the collisional system. This happens for example in the case of Rydberg atoms approaching a metal surface. Rydberg states are very close in energy one from the other and can be easily mixed by the interaction with the surface. Recently, a new method has been proposed to measure the ionization distance of a Rydberg atom approaching a metal surface (Hill et al., 2000; Dunning et al., 2003). It makes use of an external electric field that can repel the ions from the surface once they are formed by ionization. Because of the presence of an external electric field, the Rydberg atoms incident on the surface are in fact in Stark states and can thus be polarized in two directions: toward the surface or away from it. A striking result of these experiments was that Stark hybrid states polarized toward the surface appear to ionize at the same distance as Stark hybrids polarized away from it (Dunning et al., 2003). This is at variance with what can be expected from static theoretical studies of the Rydberg-metal system (Nordlander, 1996), which showed drastic variations of the RCT rate as a function of polarization. In addition, these static calculations revealed the existence of many avoided crossings between Rydberg states that could induce inter-Rydberg transitions. A dynamical theoretical study of this system revealed important inter-Rydberg transitions and

allowed to account for the apparent absence of polarization effect: it is simply due to the inter-Rydberg mixing induced by the interaction with the surface and the field (Sjakste et al., 2006). In the Rydberg state case, non-adiabatic transitions between projectile states are then able to qualitatively change the outcome of a given ionization experiment. This result points at the possible importance of intra-projectile transitions induced by the collision motion; these can deeply modify the electron transfer process from the usual picture in which transitions only occur between the projectile and the target.

5.3. Surfaces with Adsorbates

The case of adsorbates present on the surface also brings some interesting questions. The effect of adsorbates on the charge transfer has often been split into two (Gauyacq and Borisov, 1998): a non-local effect associated with the change of surface work-function due to the adsorbate and local effects due to the local modifications of the potentials and couplings in the vicinity of the adsorbate. Several theoretical studies of the local perturbations on the RCT have been reported (Nordlander and Lang, 1991; Borisov et al., 1996c) that confirmed their importance, an adsorbate being able to perturb the charge transfer in a large area surrounding it (Borisov and Gauyacq, 2000). Studies including both local and non-local effects on the RCT brought detailed accounts (Goryunov et al., 1998) of experimental studies in back scattering geometry (Weare and Yarmoff, 1996) that allows selecting the impact atom, adsorbate or substrate, on the surface. Similar studies of other charge transfer processes also brought experimental evidence of charge transfer probabilities depending on the impact point on the surface (Brongersma et al., 1994). Scattering from a surface partly covered with adsorbates leads to another interesting effect if the electron active in the transfer can be temporarily captured by the adsorbate. One then has a three-body problem, the active electron making transitions between the projectile, the adsorbate and the substrate. Different time scales for the different transfer processes between the three bodies lead to quite different electron transfer behaviors. In the case of a long-lived state localized on the adsorbate, as for example for Cs adsorbates on Cu(111), a theoretical study has shown that multiple jumps of the electron between the projectile and the adsorbate are possible, leading to interferences (Sjakste et al., 2004). The charge transfer between the projectile and the surface then has the properties of charge transfer between atoms slightly perturbed by the surface environment; in particular, the irreversibility of the charge transfer with a metal surface has partly disappeared. In contrast, if the adsorbate localized state is very short-lived, like in the case of alkali adsorbates on a free-electron metal, the adsorbate-localized state appears more like a sub-structure of the metal continuum than as a meaningful intermediate in the charge transfer. As an extreme

situation, theoretical calculations in the case of H^- ions approaching an Al surface with Li adsorbates on it (Sjakste et al., 2003), revealed a very striking situation. In the static picture (fixed hydrogen projectile) there exists an avoided crossing between the H^- state and a state localized on the Li adsorbate. However, when the H^- ion approaches the surface, the active electron is not transferred to the adsorbate; the electron dynamics is always non-adiabatic in the avoided crossing region even at very low collision energy and it is as if the system was ignoring the existence of a state localized on the adsorbate. This feature should have important consequences. It means that, in general, one cannot rely on static calculations, like e.g. those performed in quantum chemistry, to predict what will happen in a collision process: the presence of an avoided crossing points at the possibility of an electron transfer process which finally turns out not to exist. Said in other words, a feature in the electronic structure of the surface (in the present case, a state localized on the adsorbate) is not playing a role in a collision. This makes it analogous to the point discussed in Section 4.3 and had to be linked with the very short lifetime of the adsorbate-localized state.

More generally defects at surfaces should influence the charge transfer process characteristics. Besides the case of adatoms or adsorbates outlined above, this effect has not been much investigated. Indeed this is not an easy problem to study in a controlled way. It could play a significant role in the case of sputtering events where one expects the surface target to be locally perturbed by the impacting particle (see articles by Wucher and Urbassek in this volume). Recently, this problem has been investigated experimentally at the individual collision level and a significant effect of the collision-induced deformation of the lattice on the charge transfer has been reported (Maazouz et al., 2003). Steps at surfaces could also influence the charge transfer process at surfaces. Very few studies have been performed on the effect of steps on the surface. Experimental evidence was reported for the enhancement of the H^- ion formation in collisions on Al surfaces in the presence of steps (Wyputta et al., 1991) and this was interpreted in Makhmetov et al. (1996) as a consequence of the asymmetry of the perturbations induced by the steps up and steps down in the so-called "parallel-velocity effect" (see Section 2). More recently, a theoretical study of charge transfer on vicinal metal surfaces also concluded on the different effect of the steps up and steps down on the charge transfer (Obreshkov and Thumm, 2006). Though, the case of a vicinal surface might be different from the case of individual steps on a surface, because of the extra periodicity brought by the vicinal surface that influences the surface located electronic states and can thus influence the charge transfer.

5.4. Finite Size Effects

A finite size (nano-structured) target can also be thought to lead to a specific behavior of the electron transfer processes. For example, in a thin film, the metal states are quantised for the motion perpendicular to the surface and the 3D-continuum of metal states becomes a set of 2D-continua. Theoretical studies of the static situation (a fixed atom in front of a thin metal film) revealed strong differences with the corresponding situation with a semi-infinite metal (Borisov and Winter, 1996; Thumm et al., 2000; Usman et al., 2001). The width of an atomic level was found to exhibit sharp variations as a function of the atom-surface distance, when the atomic level crosses one of the metal quantised levels, i.e. at the opening/closing of a 2D-continuum as a channel for electron transfer. The existence of sharp steps is connected with the 2-dimensional nature of the metal continua. This situation bears some resemblance with the case of a metal with a surface-projected band gap and 2D-surface and image states. The 2D-nature of the metal continua is also expected to lead to some specificities for the so-called "parallel velocity effect" (Yan et al., 1977), similarly to what has been observed for Cu(111) surfaces (Hecht et al., 2000). No detailed experimental studies have been reported on these systems. However, one can expect finite time effects to play a role in such systems (Usman et al., 2001). An electron will need some time to fully "know about" the quantisation in the thin film. Typically, the electron has to perform at least a back and forth trip across the film to know about its finite size. If the collision is fast, then quantisation inside the film does not play a role and the electron transfer occurs as on a semi-infinite metal. The conditions for the observation of finite size effects on charge transfer during a collision on a thin film have been discussed (Usman et al., 2001), based on a theoretical study using a dynamical wave packet propagation approach (Section 4.1). A detailed experimental study on such a system is still missing but would certainly bring a lot of information on finite size and finite time effects and their interplay.

A more extreme situation for finite size effects is provided by metal clusters adsorbed on a surface. Electron transfer between a projectile and a supported cluster is an appealing system to study, both for its expected peculiarities and for its links with catalysis. Recently two experimental studies (Liu et al., 2004; Canario and Esaulov, 2006) were devoted to such a system: alkali ion neutralization by collision on Au and Ag clusters adsorbed on TiO_2. A strong enhancement of the neutralization probability was observed when going from the semi-infinite metal to clusters and as the size of the clusters decreases. This has been interpreted as an effect of the presence of quantised states inside the cluster or equivalently to the transition of the target electronic states from a metal continuum to quantised discrete states (Liu et al., 2004; Canario and Esaulov, 2006). Similarly to the case

of thin films discussed above, this effect should be dependent on the collision velocity. Another interesting question arises in the case of supported clusters (actually it also arises in the case of atomic or molecular adsorbates). Upon adsorption, the Ag and Au clusters reach charge equilibrium with the substrate and may become negatively charged due to an electron capture from the substrate. What happens when an electron from the cluster is captured by the projectile: is the cluster/substrate charge equilibrium immediately restored, i.e. are electrons flowing between the cluster and the substrate extremely rapidly? Or does the cluster charge remain unbalanced for a while? These two behaviors remind of the difference between the two systems discussed in Sections 2 and 3, metal and ionic crystal targets. Depending on the rate of electron transfer between the cluster and the substrate, different descriptions of the projectile-cluster charge transfer should be chosen. This choice is again *a priori* dependent on the collision velocity. A detailed theoretical study of electron transfer during a collision with a supported cluster with all its finite size and finite time effects is still to be developed.

6. Conclusions

The collisional electron transfer process links discrete atomic levels of the projectile to the electronic states of the solid. Since electron transfer is very sensitive to the characteristics of the electronic structure of the solid, it can be seen as a probe of the various electronic structures that can can exist in solids. Indeed, the nature of the electron transfer process is quite different if one considers delocalized continuum states like in a metal or electronic states localized on certain sites of the solid like in an ionic crystal. For one-electron transition for example, one can expect irreversible bound state-continuum transitions in one case and reversible transitions like in atom-atom collisions in the other. These different behaviors are clearly evidenced in a series of electron transfer problems, for which efficient theoretical schemes could be developed. The present review focuses on an effect that modifies the simple view seen above and that can even eliminate the effect of some characteristics in the solid electronic structure: a collision event only lasts for a finite amount of time and this introduces finite time effects on the electron transfer. This can be related to the time-energy uncertainty relation. When viewed on a short time scale, a system cannot exhibit all the characteristics of its electronic structure and this can deeply influence the electron transfer process. There is a series of collisional systems where one can expect finite time effects to play a role and where they have not yet been observed or fully discussed. These involve for example surfaces with narrow band gaps or quasi-band gaps, with adsorbates, with thin films or with nano-structures adsorbed on them.

References

Auth C., Borisov A.G. and Winter H. (1995): High fractions of negative ions in grazing scattering of fast oxygen atoms from a LiF(100) surface. Phys Rev Lett **75**, 2292–2295

Bahrim B. and Thumm U. (2000): Charge-transfer dynamics in slow atom–surface collisions: A new close-coupling approach including continuum discretization. Surf Sci **451**, 1–6

Baragiola R.A. and Dukes C.A. (1996): Plasmon-assisted electron emission from Al and Mg surfaces by slow ions. Phys Rev Lett **76**, 2547–2550

Bauer M., Pawlik S. and Aeschlimann M. (1997): Resonance lifetime and energy of an excited Cs state on Cu(111). Phys Rev B **55**, 10040–10043

Bauer M., Pawlik S. and Aeschlimann M. (1999): Decay dynamics of photoexcited alkali chemisorbates. Real time investigation in the femtosecond regime. Phys Rev B **60**, 5016–5028

Behringer E.R., Anderson D.R., Cooper B.H. and Marston J.B. (1996a): Charge transfer in hyperthermal energy collisions of Li^+ with alkali-metal-covered Cu(001). I. Dynamics of charge state formation. Phys Rev B **54**, 14765–14779

Behringer E.R., Anderson D.R., Cooper B.H. and Marston J.B. (1996b): Charge transfer in hyperthermal energy collisions of Li^+ with alkali-metal-covered Cu(001). II. Dynamics of excited-state formation. Phys Rev B **54**, 14780–14790

Borisov A.G. and Gauyacq J.P. (2000): Resonant charge transfer in Li^+ collisions on a metal surface: Geometrical size of the perturbation introduced by an alkali impurity. Surf Sci **445**, 430–447

Borisov A.G. and Sidis V. (1997): Theory of negative ion conversion of neutral atoms in grazing scattering from alkali halide surfaces. Phys Rev B **56**, 10628–10643

Borisov A.G. and Winter H. (1996): Neutralization of Na^+-ions in grazing scattering from the surface of thin Al-films. Z Phys D **37**, 263–268

Borisov A.G., Teillet-Billy D. and Gauyacq J.P. (1992): Dynamical resonant electron capture in atom surface collisions: H^- formation in H-Al(111) collisions. Phys Rev Lett **68**, 257–261

Borisov A.G., Teillet-Billy D., Gauyacq J.P., Winter H. and Dierkes G. (1996a): Resonant charge transfer in grazing scattering of alkali-metal ions from an Al(111) surface. Phys Rev B **54**, 17166–17174

Borisov A.G., Sidis V. and Winter H. (1996b): Diabatic energy level confluence: The mechanism for negative ion conversion of neutral atoms in grazing scattering from insulator surfaces. Phys Rev Lett **77**, 1893–1896

Borisov A.G., Makhmetov G.E., Teillet-Billy D. and Gauyacq J.P. (1996c): Atoms interacting with a metal surface with adsorbates: local and non-local effects on the charge transfer. Surf Sci **350**, L205–210

Borisov A.G., Kazansky A.K. and Gauyacq J.P. (1999a): Resonant charge transfer in ion–metal surface collisions: Effect of a projected band gap in the H^--Cu(111) system. Phys Rev B **59**, 10935–10949

Borisov A.G., Kazansky A.K. and Gauyacq J.P. (1999b): Stabilisation of alkali-adsorbate-induced states on Cu(111) surfaces. Surf Sci **430**, 165–175

Borisov A.G., Gauyacq J.P., Kazansky A.K., Chulkov E.V., Silkin V.M. and Echnique P.M. (2001): Long-lived excited states at surfaces: Cs/Cu(111) and Cs/Cu(100) systems. Phys Rev Lett **86**, 488–491

Borisov A.G., Gauyacq J.P., Chulkov E.V., Silkin V.M. and Echenique P.M. (2002): Lifetime of excited electronic states at surfaces. Comparison between the alkali/Cu(111) systems. Phys Rev B **65**, 235434-1-10

Brako R. and Newns D.M. (1985): The intra-atomic Coulomb repulsion and the distribution of charge states of atoms leaving metal surfaces. Solid State Com **55**, 633–638

Brenten H., Müller H., Knorr K.H., Kruse D., Schall H. and Kempter V. (1991): The role of Auger processes in slow collisions of Li^+ ions with cesiated W(110) surfaces. Surf Sci **243**, 309–316

Brongersma H.H., Groenen P.A.C. and Jacobs J.P. (1994) Science of Ceramic Interfaces II, Nowotny J. (Ed.). Elsevier, Amsterdam

Canario A.R. and Esaulov V.A. (2006): Electron transfer processes on Ag and Au clusters supported on TiO_2(110) and cluster size effects. J Chem Phys **124**, 224710-1-10

Canario A.R., Borisov A.G., Gauyacq J.P. and Esaulov V.A. (2005): Nonadiabatic effects in atom-surface charge transfer. Phys Rev B **71**, 0121401-1-4 (R)

Cazalilla M.A., Lorente N., Diez-Muino R., Gauyacq J.P., Teillet-Billy D. and Echenique P.M. (1998): Theory of Auger neutralization and deexcitation of slow ions at metal surfaces. Phys Rev B **58**, 13991–14006

Chakraborty H., Niederhausen T. and Thumm U. (2004): Resonant neutralization of H^- near Cu surfaces: Effects of the surface symmetry and ion trajectory. Phys Rev A **70**, 052903-1-13

Chulkov E.V., Silkin V.M. and Echenique P.M. (1999): Image potential states on metal surfaces: Binding energies and wave functions. Surf Sci **437**, 330–352

Desjonquères M.C. and Spanjaard D. (1993): Concepts in Surface Science, Springer Verlag Series in Surface Science, Vol. 40

Deutscher S.A., Yiang X. and Burgdörfer J. (1997): Atomic resonances of hydrogen near aluminum surfaces: Adiabatic evolution of the ground state. Phys Rev A **55**, 466–478

Dunning F.B., Dunham H.R., Oubre C. and Nordlander P. (2003): Behavior of Rydberg atoms at surfaces: Energy level shifts and ionization. Nucl Inst Meth B **203**, 69–75

Ermoshin V.A. and Kazansky A.K. (1996): Wave packet study of H^- decay in front of a metal surface. Phys Lett A **218**, 99–104

García E.A., Goldberg E.C. and Passeggi M.C.G. (1995): Charge-transfer processes in atom-surface collisions at low energies: A Green's function approach. Surf Sci **325**, 311–322

García E.A., González Pascual C., Bolcatto P.G., Passeggi M.C.G. and Goldberg E.C. (2006): Ion fractions in the scattering of hydrogen on different reconstructed silicon surfaces. Surf Sci **600**, 2195–2206

Gauyacq J.P. and Borisov A.G. (1998): Charge transfer in atom-surface collisions: Effect of the presence of adsorbates on the surface. J Phys C **10**, 6585–6619

Gauyacq J.P. and Borisov A.G. (2004): Excited electron transfer between a core-excited $Ar^*(2p_{3/2}^{-1}\ 4s)$ atom and the metal substrate in the Ar/Cu(111) system. Phys Rev B **69**, 235408-1–14

Gauyacq J.P. and Kazansky A.K. (2005): Effect of the adsorbate motion on the femtosecond time dependence of the two-photon photoemission signal in the Cs/Cu(111) system. Phys Rev B **72**, 045418-1–12

Gauyacq J.P., Borisov A.G. and Winter H. (2000): Negative ion formation in collisions on metal surfaces: Equivalent electron description versus non-equivalent description of the negative ions. Comments on Atom Molec Phys **2**, D29

Geerlings J.J.C., Los J., Gauyacq J.P. and Temme N.M. (1986): Charge transfer in atom-surface scattering – On the validity of the semi-classical rate equation. Surf Sci **172**, 257–268

Goryunov D.G., Borisov A.G., Makhmetov G.E., Teillet-Billy D. and Gauyacq J.P. (1998): Li^+ neutralisation in back-scattering from alkali/Al(100) surfaces: Comparison between the various alkalis. Surf Sci **401**, 206–219

Guillemot L. and Esaulov V.A. (1999): Interaction time dependence of electron tunneling processes between an atom and a surface. Phys Rev Lett **82**, 4552–4555

Hagstrum H.D. (1954): Auger ejection of electrons from tungsten by noble gas ions. Phys Rev **96**, 325–335

Hecht T., Winter H., Borisov A.G., Gauyacq J.P. and Kazansky A.K. (2000): Role of the 2D surface state continuum and projected band gap in charge transfer in front of a Cu(111) surface. Phys Rev Lett **84**, 2517–2520

Hill S.B., Haich C.B., Zhou Z., Nordlander P. and Dunning F.B. (2000): Ionization of xenon Rydberg atoms at a metal surface. Phys Rev Lett **85**, 5444–5448

Jennings P.J., Jones R.O. and Weinert M. (1988): Surface barrier for electrons in metals. Phys Rev B **37**, 6113–6120

Kürpick P., Thumm U. and Wille U. (1997): Close-coupling calculations for ion-surface interactions. Nucl Inst Meth B **125**, 273–276

Langreth D. and Nordlander P. (1991): Derivation of a master equation for charge-transfer processes in atom-surface collisions. Phys Rev B **43**, 2541–2557

Liu G.F., Sroubek Z. and Yarmoff J.A. (2004): Detection of quantum confined states in Au nanoclusters by alkali ion scattering. Phys Rev Lett **92**, 216801-1–4

Lorente N. and Monreal R. (1996): Multielectron neutralization channels in ion-surface scattering. Phys Rev B **53**, 9622–9625

Lorente N., Merino J., Flores F. and Gusev M.Yu. (1997): Negative ion formation on Al, Si and LiF. Nucl Inst Meth B **125**, 277–282

Los J. and Geerlings J.J.C. (1990): Charge exchange in atom-surface collisions. Phys Rep **190**, 133–190

Maazouz M., Borisov A.G., Esaulov V.A., Gauyacq J.P., Guillemot L., Lacombe S. and Teillet-Billy D. (1997): Effect of metal band characteristics on resonant electron capture: H^- formation in the scattering of hydrogen ions on Mg, Al, and Ag surfaces. Phys Rev B **55**, 13869–13877

Maazouz P.L., Maazouz M. and Jacobs D.C. (2003): Trajectory-dependent energy- and charge-transfer in collisions of Br^+ ($P_{3/2}$) with Pt(111). Nucl Inst Meth B **203**, 225–230

Madhavan V., Chen W., Jamneala T., Crommie M.F. and Wingreen N.S. (1998): Tunneling into a single magnetic atom: Spectroscopic evidence of the Kondo resonance. Science **280**, 567–569

Makhmetov G.E., Borisov A.G., TeilletBilly D. and Gauyacq J.P. (1996): Resonant charge transfer in grazing atom-metal surface collisions: Effect of the presence of steps on the surface. Surf Sci **366**, L769–774

Marston J.B., Andersson D.R., Behringer E.R., Cooper B.H., DiRubio C.A., Kimmel G.A., and Richardson C. (1993): Many-body theory of charge transfer in hyperthermal atomic scattering. Phys Rev B **48**, 7809–7824

Martin F. and Politis M.F. (1996): Multicenter-Gaussian representation of resonant charge transfer in atom-surface interaction. Surf Sci **356**, 247–256

Merino J. and Marston J.B. (1998): Room-temperature Kondo effect in atom-surface scattering: Dynamical $1/N$ approach. Phys Rev B **58**, 6982–6991

Merino J., Lorente N., Pou P. and Flores F. (1986): Charge transfer for slow H atoms interacting with Al: Atomic levels and linewidths. Phys Rev B **54**, 10959–10969

Monreal R.C. and Flores F. (2004): Charge exchange processes in low energy ion-metal collisions. Adv Quant Chem **45**, 175–199

Nakanishi H., Kasai H. and Okiji A. (1987) Charge exchange scattering of particles from metal surfaces. Surf Sci **197**, 515–527

Niedfeldt K., Carter E.A. and Nordlander P. (2004): First principles resonance widths for Li near an Al(001) surface: Predictions of scattered ion neutralization probabilities. J Chem Phys **121**, 3751–3755

Nordlander P. (1996): Energies and lifetimes of atomic Rydberg states near metal surfaces. Phys Rev B **53**, 4125–4132

Nordlander P. and Lang N.D. (1991): Energy shifts and broadening of atomic electron levels near impurity-covered metal surfaces. Phys Rev B **44**, 13681–13688

Nordlander P. and Tully J.C. (1988): Energy shifts and broadening of excited hydrogen-atom levels in the vicinity of a metal surface. Phys Rev Lett **61**, 990–993

Obreshkov B. and Thumm U. (2006): Neutralization of H^- near vicinal metal surfaces. Phys Rev A **74**, 012901

Ogawa S., Nagano H. and Petek H. (1999): Phase and energy relaxation in an antibonding surface state: Cs/Cu(111). Phys Rev Lett **82**, 1931–1934

Palmer R.E. (1992): Electron-molecule dynamics at surfaces. Prog Surf Sci **41**, 51–108

Petek H., Weida M.J., Nagano H. and Ogawa S. (2000): Real-time observation of adsorbate atom motion above a metal surface. Science **288**, 1402–1404

Rabalais J.W. (Ed.) (1994): Low Energy Ion-Surface Interactions. Wiley, New York

Roncin P., Borisov A.G., Khemliche H., Momeni A., Mertens A. and Winter H. (2002): Evidence for F^- formation by simultaneous double-electron capture during scattering of F^+ from a LiF(001) surface. Phys Rev Lett **89**, 043201-1-4

Shao H., Nordlander P. and Langreth D.C. (1994): Many-body theory for charge transfer in atom-surface collisions. Phys Rev B **49**, 13929–13947

Shao H., Nordlander P. and Langreth D.C. (1995): Nonadiabatic effects in charge transfer in atom-surface scattering. Phys Rev B **52**, 2988–2994

Shao H., Nordlander P. and Langreth D.C. (1996): Probing the highly correlated mixed-valent state via charge transfer with atoms moving out from a surface. Phys Rev Lett **77**, 948–951

Sjakste J., Borisov A.G. and Gauyacq J.P. (2003): Wave packet propagation study of the electron transfer in back-scattering of H^- ions from alkali adsorbates on an Al surface. Nucl Inst Meth B **203**, 49–56

Sjakste J., Borisov A.G. and Gauyacq J.P. (2004): Probing adsorbate state lifetime with low energy ions. Phys Rev Lett **92**, 156101-1–4

Sjakste J., Borisov A.G. and Gauyacq J.P. (2006): Ionization of Rydberg atoms colliding with a metal surface. Phys Rev A **73**, 42903-1–11

Teillet-Billy D. and Gauyacq J.P. (1990): Position and width of a negative ion state in front of a surface: formation of $C^-(^4S)$ ions by electron capture. Surf Sci **239**, 343–352

Thumm U., Kürpick P. and Wille U. (2000): Size quantization effects in atomic level broadening near thin metallic films. Phys Rev B **61**, 3067

Tsumori K., Koppers W.R., Heeren R.M.A., Kadodwala M.F., Beijersbergen J.M. and Kleyn A.W. (1997): Large ion yields in hydrogen scattering from a graphite surface. J Appl Phys **81**, 6390–6396

Usman E.Yu., Urazgil'din I.F., Borisov A.G. and Gauyacq J.P. (2001) Quantum size effect in the resonant electron transfer between an ion and a thin metal film. Phys Rev B **64**, 205405-1–12

Ustaze S., Guillemot L., Esaulov V.A., Nordlander P. and Langreth D.C. (1998): Multi-electron effects in the interaction of F^- ions with Ag(110). Surf Sci **415**, L1027–1031

Van Wunnick J.N.M., Brako R., Makoshi K. and Newns D.M. (1983): Effect of parallel velocity on charge fraction in ion-surface scattering. Surf Sci **126**, 618–623

Weare C.B. and Yarmoff J.A. (1996): Resonant neutralization of $^7Li^+$ scattered from alkali/Al(100) as a probe of the local electrostatic potential. Surf Sci **348**, 359–369

Winter H. (2000): Scattering of atoms and ions from insulator surfaces. Prog Surf Sci **63**, 177–247

Winter H. (2002): Collisions of atoms and ions with surfaces under grazing incidence. Phys Rep **367**, 387–582

Wyputta F., Zimny R. and Winter H. (1991): H^- formation in grazing collisions of fast protons with an Al(111) surface. Nucl Inst Meth B **58**, 379–383

Yan Q., Burgdörfer J. and Meyer F.W. (1997): Grazing-ion-surface interaction as a probe of surface states. Phys Rev B **56**, 1589–1592

Zimny R. (1990): Resonant surface neutralization of alkali ions. Surf Sci **233**, 333–340

Channeling and Blocking of Energetic Charged Particles in Crystals

Jens Ulrik Andersen*

Department of Physics and Astronomy, University of Aarhus
8000 Aarhus C, Denmark

Abstract

The development of channeling and blocking since the foundation of the field was laid by Jens Lindhard in his classical paper in 1965 is discussed, and the question is asked whether this theory has passed the test of time. Have important aspects of the theory been challenged? Where has the theory needed modification or extension? Are there still open questions to be solved? A basic theoretical issue is the applicability of classical mechanics in the description. Lindhard showed that for particles heavy compared with the electron classical orbital pictures may always be applied. However, for electrons and positrons there are strong quantal features like Bragg interference. The quantal description introduced by Lindhard and co-workers has been used as the basis for a comprehensive treatment of the channeling of MeV electrons and positrons and of channeling radiation. At very high energies, GeV and TeV, the motion becomes classical, due to the relativistic increase of the field seen by the particles in the reference frame following their longitudinal motion. Channeling radiation in this regime is still an active field of research. For channeling and blocking of ions, the concept of statistical equilibrium plays a central part in Lindhard's theory. The application of this concept has been confronted with two important challenges, the first based on computer simulations and the second on experiments on the transmission of heavy ions through thin crystals. In both cases the challenges have been met and new insight has been gained but there are still problems to be solved. The channeling and blocking of ions have found very many applications, and a few problems and opportunities worth pursuing are suggested.

* E-mail: jua@phys.au.dk

Contents

1	Introduction	657
2	Collision with String of Atoms	658
3	Continuum Model	660
4	Screened Potential	661
5	Lindhard's Critical Angle	662
6	Thermal Vibrations	663
7	Dip in Yield	663
8	Planar Channeling	665
9	Channeling of Electrons and Positrons	665
10	Channeling Radiation	667
11	Dechanneling	672
12	Dechanneling by Crystal Defects	673
13	Localisation of Impurities by Channeling and Blocking	675
14	Crystal Blocking for Determination of Nuclear Lifetimes	678
15	Restricted Equilibrium in Axial Channeling	681
16	Cooling and Heating in Ion Transmission Through Crystals	684
17	Energy Loss for Channeled Particles	688
18	Crystal as Special Target for Atomic Processes	692
19	Concluding Remarks	694
References		695

Figure 1. Jens Lindhard gesturing with his pipe; with Larry Howe and the author. ICACS, Hamilton 1979.

1. Introduction

Channeling was discovered a few years before I began my graduate studies at the University of Aarhus in 1964, and I was lucky to be supervised by one of the pioneers in the field, John Davies, who brought the field to Aarhus. The local interest was stimulated by many lively "Saturday meetings" where new experimental developments were analysed and discussed. Most important was the strong involvement of Jens Lindhard, who with an impressive intellectual effort provided a theoretical foundation of the field in his famous paper from 1965 (Lindhard 1965). Before publication the theory was presented in a series of lectures, and I still remember these as a thrilling experience. There had been earlier theoretical work on channeling, including both computer simulations and analytical theory, but Lindhard's theory far surpassed this earlier work in depth of analysis, in generality of concepts, and in breadth of coverage of the phenomena. Lindhard presented his theory at the first of a series of International Conferences on Atomic Collisions in Solids (ICACS) and later developments in channeling were usually reported at these meetings. Figure 1 shows Lindhard at ICACS in Hamilton, 1979, in a characteristic pose using his pipe to make a point.

This is a brief review of the development of channeling during the following about forty years, based very much on my personal experience. I shall emphasize developments which I have found of particular interest and mainly refer to work that I have been involved in and therefore know best. I shall try to give credit

where needed to pioneering efforts by other groups but many more would have deserved to be mentioned. A main theme will be the further development of the theory of channeling on the basis of Lindhard's original paper. Have some of the basic concepts been challenged? Where has the theory been extended and where are new developments needed?

After the introduction of the basic concepts of channeling, the continuum potential and the continuum model, the question of quantum *versus* classical mechanics is considered. The quantum world of electron channeling and channeling radiation was for many years at the centre of my own interest. This is an aspect of channeling which was hardly touched upon in Lindhard's paper from 1965. However, shortly afterwards he published a paper on the quantum theory of channeling (Lervig et al., 1967), and I shall briefly discuss how this paper has provided a basis for a comprehensive, quantitative description of channeling radiation from MeV electrons and positrons. The physics of electron channeling at very high energies (GeV or TeV) is an active area of its own.

For ion channeling the focus will be on a key concept in Lindhard's theory. As a student I was especially impressed by the powerful applications of the concept of statistical equilibrium. Lindhard admired Gibbs' work on statistical mechanics and liked to quote Niels Bohr saying something like "this is how theory should be, at first very general and mathematical but then with great predictive power". Two attacks on the application of the hypothesis of statistical equilibrium in channeling will be discussed. They were based on computer simulations and on experiments, respectively. Because so fundamental concepts were challenged, the resolution of the problems has given important new insights.

The field of channeling covers an enormous area of experience and in this brief review it has been necessary to be selective. I have listed a few references to reviews covering in much more detail various aspects of channeling (Andersen et al., 1983a; Cohen and Dauvergne, 2004; Davies, 1983; Feldman et al., 1982; Gemmell, 1974; Gibson, 1975; Hofsäss, 1996; Krause and Datz, 1996; Sørensen and Uggerhøj, 1987, 1989; Uggerhøj, 2005). They may also be consulted for a more complete bibliography.

2. Collision with String of Atoms

When Lindhard first saw the picture in Figure 2 of an artist's perception of the passage of an ion through an open channel in a crystal lattice, his comment was: "this is not channeling!"

It is important to distinguish channeling from transparency. For channeling along a crystal axis, the motion is governed by correlated collisions with atoms

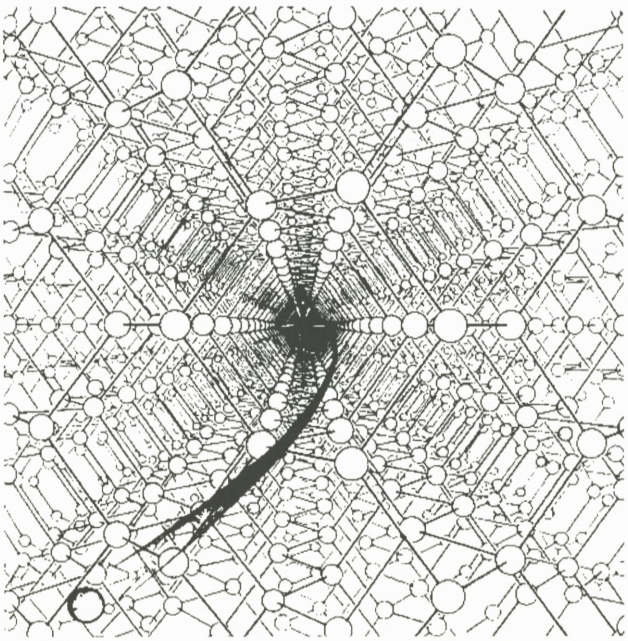

Figure 2. From "Channeling in Crystals" by W. Brandt, Sci. Am. 218, 91 (1968).

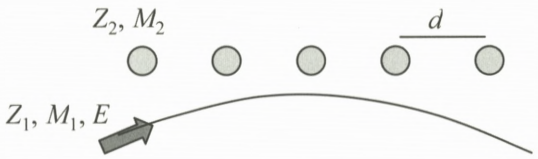

Figure 3. Deflection of ion by string of atoms.

aligned as pearls on a string, as illustrated in Figure 3. If many atoms contribute, the discrete deflections may be replaced by motion in the continuum string potential obtained by integration of the atomic interaction potential,

$$U(\vec{r}) = \frac{1}{d} \int dz V_{\text{at}}(\vec{r}, z). \tag{1}$$

Here z is the coordinate parallel to the string of atoms and $\vec{r} = (x, y)$ is the transverse coordinate vector. At large distances r, contributions from atoms on several strings must be included in the continuum potential.

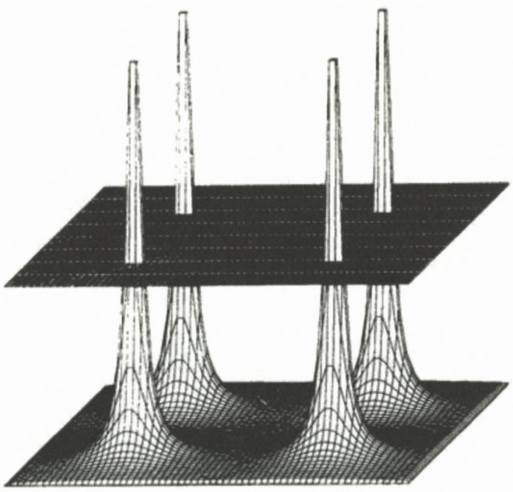

Figure 4. Axial continuum potential.

3. Continuum Model

In this continuum model there is a separation between the motion along the axis and the transverse motion, which is governed by a transverse Hamiltonian,

$$H(\vec{p}_\perp, \vec{r}) = \frac{p_\perp^2}{2M_1} + U(\vec{r}), \tag{2}$$

with conservation of transverse energy $E_\perp$. (For relativistic particles, $M_1 \to \gamma M_1$; Lervig et al., 1967.)

The string potential is repulsive and channeled ions are kept away from the atomic strings. The allowed area ($U(\vec{r}) < E_\perp$) within one unit cell in the transverse lattice of strings is denoted $A(E_\perp)$, and the total area per string is $A_0 = (Nd)^{-1}$ where N is the number density of the crystal. As illustrated in Figure 4, the motion is only for very low transverse energy confined to a single unit cell in the transverse lattice. In a classical *statistical equilibrium* at fixed $E_\perp$, with constant density on an energy shell in transverse phase space, the spatial density is constant in the allowed area for motion in two dimensions.

When the particle motion is restricted the particle is said to be channeled. Channeled particles do not have hard collisions with atoms and move through a gas of loosely bound atomic electrons. For particle incidence parallel to an axis there is therefore a very strong reduction in the yield of processes requiring a hard collision with an atom, like nuclear reactions or backscattering. Also energy loss and capture and loss of electrons are strongly modified.

4. Screened Potential

The Coulomb force between projectile and target nuclei is screened by electrons. A great simplification is obtained with Thomas–Fermi scaling:

$$U(r) = \frac{Z_1 Z_2 e^2}{d} \phi\left(\frac{r}{a}\right), \tag{3}$$

where $Z_1 e$ and $Z_2 e$ are the nuclear charges of projectile and atoms. The distance r is scaled with the Thomas–Fermi screening radius a, which for $Z_1 \ll Z_2$ is given in terms of the Bohr radius $a_0 = 0.53$ Å by

$$a = 0.8853 a_0 \, Z_2^{-1/3}. \tag{4}$$

A convenient approximation for analytical estimates is Lindhard's standard potential (Lindhard, 1965),

$$U(r) = \frac{Z_1 Z_2 e^2}{d} \ln\left(\frac{(Ca)^2}{r^2} + 1\right), \tag{5}$$

where $C \cong \sqrt{3}$. For distances r of order a, the potential is proportional to $1/r$, changing to $1/r^2$ at larger distances. Another commonly used and more accurate analytical approximation is the Molière potential. If the projectile charge is small and the screening is due only to the target electrons, a very accurate potential can be obtained from analytical approximations to the screened potential obtained from Hartree–Fock calculations (for example, the Doyle–Turner potential used often in calculations of electron diffraction and electron channeling; see Andersen et al., 1983a).

The question of the screening of the ion-atom potential is complex. It depends both on the atomic numbers of projectile and target and on the velocity of the projectile. According to the simple Bohr criterion, electrons bound to the ion with orbital velocities smaller than the ion velocity are stripped off. A characteristic velocity, separating between low velocities with nearly neutral projectiles and high velocities with only few electrons remaining on the ion, is therefore the Thomas–Fermi-scaled Bohr velocity, $Z_1^{2/3} v_0$.

The simplest case is for particles with $Z_1 \ll Z_2$ the limit of high velocities, where the screening radius, a, is determined by target electrons alone. If a few inner electrons with $\langle r \rangle \ll a$ remain on the projectile, giving it a net number of charges, Q, we may write the continuum potential $U^{(Q)}$ in terms of the potential $U^{(1)}$ for a proton as

$$U^{(Q)}(r) \cong Q U^{(1)}(r). \tag{6}$$

The number of charges, Q, can change by capture and loss but for well-channeled ions the cross sections are small and we may speak of "frozen charge states" for not too thick crystals (see Figure 28 below).

In the opposite limit of high Z_1 and low velocities the ion carries many electrons, is nearly neutral, and the screening is due to electrons on both target and projectile atoms. The screening is described fairly well by introduction of an effective atomic number, $Z^{-1/3} = (Z_1^{2/3} + Z_2^{2/3})^{-1/2}$, in the formula for the Thomas–Fermi screening radius (Equation 4) (Lindhard, 1965).

In the intermediate range, heavy ions at high velocity but carrying many electrons, the situation is not clear and further studies would be desirable. As discussed below, there is empirical evidence from blocking of fission fragments that in a high-Z material there is only a small contribution from projectile electrons to the screening. On the other hand, observations of "cooling" and "heating" of heavy-ion beams transmitted through thin crystals give clear evidence of an influence of the ion charge state on the interaction potential.

5. Lindhard's Critical Angle

Axial channeling requires incidence nearly parallel to a crystal axis. A limit to the incidence angle ψ is obtained from the expression for the string potential. The transverse momentum of a particle with angle ψ is $p_\perp = p \sin \psi \cong p\psi$ and hence the kinetic energy in the transverse motion is $E\psi^2$. The barrier for penetration into a string is of order $2Z_1 Z_2 e^2/d$ (Equation 5) and hence the critical angle is of order of the Lindhard angle,

$$\psi_1 = \left(\frac{2Z_1 Z_2 e^2}{Ed} \right)^{1/2} . \tag{7}$$

For relativistic particles with total energy $\gamma M_1 c^2$, the kinetic energy in the transverse motion turns out to be $p_\perp^2/2M_1\gamma$ and the formula (7) holds with the replacement $E \to 1/2pv = 1/2\gamma M_1 v^2$ (Lervig et al., 1967).

Lindhard introduced the rough distinction between "aligned beam" ($\psi < \psi_1$) and "random beam" ($\psi > \psi_1$). Transition from aligned to random is denoted "dechanneling" and the reverse transition "feeding-in". For random beam many aspects of the motion are like in an amorphous medium because there is no restriction of the transverse motion. However, at very high energies the correlated scattering with string atoms extends to angles much larger than the critical angle and this has important consequences, for example for the multiple scattering and for radiation from electrons and positrons.

6. Thermal Vibrations

Thermal vibrations play an important role. On the time scale of the ion motion the displacements of atoms can be considered static. The atomic recoil can be ignored in the evaluation of the scattering angle and, except for questions of coherence in electron channeling, we need not be concerned about the quantisation of atomic motion into phonons. The rms vibrational amplitude in two dimensions, ρ, is typically of order 0.1 Å. When a particle can penetrate to a distance of order ρ from strings it is able to hit atoms. With a Gaussian distribution of the thermal displacements r, $\mathrm{d}P(r) = \exp(-r^2/\rho^2)\ \mathrm{d}r^2/\rho^2$, an ion with minimum distance of approach to strings equal to $\rho\sqrt{\ln 2}$ will have the probability for a head-on collision with an atom reduced by a factor of two compared with an amorphous target. A more precise estimate of the critical angle is therefore

$$\psi_c = \left(\frac{U(\rho\sqrt{\ln 2})}{E}\right)^{1/2}. \tag{8}$$

With the standard potential in Equation (5) we obtain

$$\psi_c = \psi_1\left[\frac{1}{2}\ln\left(\frac{(Ca)^2}{\rho^2 \ln 2} + 1\right)\right]^{1/2}. \tag{9}$$

The factor on ψ_1 is close to unity.

The vibrational displacements also modify the continuum potential. Instead of the logarithmic divergence at small r the thermally averaged potential U_T has a finite maximum at $r = 0$, close to $U(\rho/\sqrt{2})$, but replacement of U by U_T leads to only a very small change in Equation (9) (Andersen and Feldman, 1970).

7. Dip in Yield

The most dramatic consequence of channeling is the nearly complete extinction of processes requiring a small impact parameter with a crystal atom. As illustrated in Figure 5, the yield of such a process, normalised to the yield in an amorphous medium, is strongly reduced for angles of incidence smaller than the critical angle. Particles incident at zero angle and at distance r from a string acquire a transverse energy $U(r)$ and can later hit a fraction $\exp(-r^2/\rho^2)$ of the vibrating atoms. With the assumption of a rapid trend towards statistical equilibrium in the allowed area (a uniform distribution), we therefore obtain

$$\chi_{\min} = \frac{1}{A_0}\int_{A_0} 2\pi r\ \mathrm{d}r \exp(-r^2/\rho^2) = \pi\rho^2/A_0. \tag{10}$$

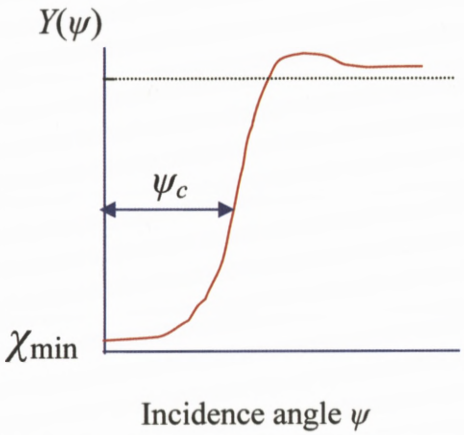

Figure 5. Axial dip in close-encounter yield.

The minimum yield χ_{min} is of order $\leq 1\%$, only. Roughly, the result may be interpreted as immediate dechanneling of the ions which hit the surface inside a distance ρ from a string. As discussed below, there are corrections, mainly due to effects of crystal planes containing the axis, which increase the minimum yield by a factor of order 3, the so-called Barrett factor first established in computer simulations (Barrett, 1973a).

Since recoils can be ignored the particle trajectories can be calculated as motion in a fixed potential. They are reversible in time if energy loss can be ignored, and this has several important consequences. One is the equivalence between channeling and blocking. Blocking occurs when charged particles are emitted from a lattice site in an axial direction, as illustrated in Figure 6. The emitted particles are blocked by the string and prevented from exiting the crystal in the axial direction. Reversibility implies that the width and minimum yield of the blocking dip are identical to those for the channeling dip. Pioneering work on blocking was carried out especially by Tulinov and his group in Moscow (Tulinov et al., 1965).

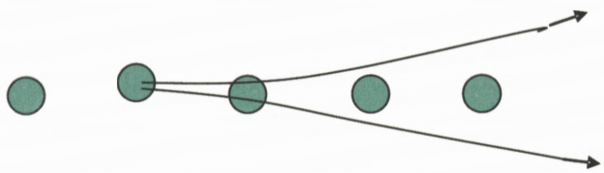

Figure 6. Blocking in the direction of a string of particles emitted from a lattice site.

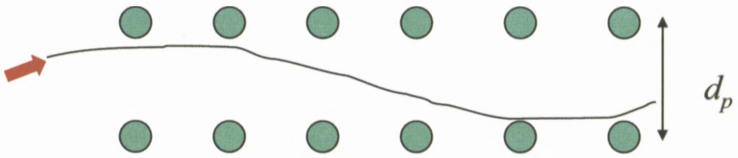

Figure 7. Planar channeling.

8. Planar Channeling

Also for particles incident on a crystal nearly parallel to a major crystallographic plane the motion can be guided by a continuum potential, given by

$$V(x) = Nd_p \int \mathrm{d}y\, \mathrm{d}z\, V_{\mathrm{at}}(x, y, z) \tag{11}$$

for a plane with spacing d_p. The density of atoms in a plane is Nd_p.

The critical angle for planar channeling is smaller by a factor of order 3 than for axial channeling. The motion is one-dimensional oscillation, as illustrated in Figure 7. Planar channeling gives rise to a dip in yield, with a narrower width and a higher minimum yield than for axial channeling. Planar effects are therefore normally less useful for applications. At very high energies, planar channeling in a bent crystal can be used to bend beams of charged particles, as first suggested by Tsyganov.

A special situation is the motion of particles nearly parallel to a set of close-packed strings in the plane. The planar channeling in this region, which Lindhard called channeling by a string of strings, is weakened because the particles can penetrate the planes between the strings. As we shall discuss below, channeling by planes is still important for the behaviour of axially channeled particles and it is a major cause of the Barrett factor on minimum yields mentioned above.

9. Channeling of Electrons and Positrons

An important issue is the question whether classical mechanics can be applied to describe ion channeling. Lindhard carried out an elegant analysis analogous to Bohr's famous argument concerning the use of classical orbital pictures in binary Coulomb scattering, which leads to the condition

$$\kappa = \frac{2Z_1 Z_2 e^2}{\hbar v} > 1, \tag{12}$$

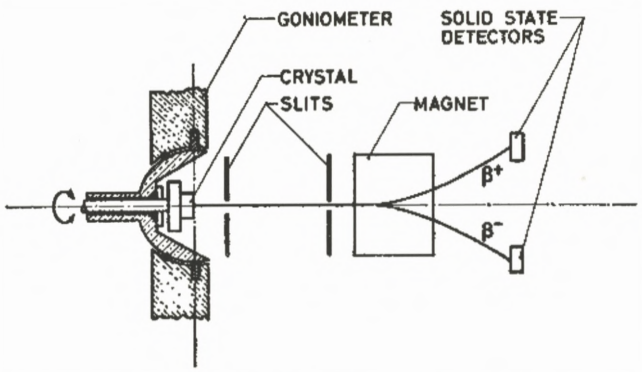

Figure 8. Set-up for observation of the emission of electrons and positrons from ^{64}Cu implanted into a copper crystal (Uggerhøj and Andersen, 1968).

where v is the projectile velocity. For correlated scattering on string atoms it was shown that for particles heavy compared with the electron the transverse motion is always classical. A particle scattering off a string can be described by a wave packet with extension small enough to give a well defined scattering angle and still large enough for the spread in direction of the motion, deriving from the uncertainty principle, to be insignificant. Qualitatively, the reason is that the parameter Z_2 in the above formula, giving the strength of the scattering potential, is in effect increased by the concerted participation of many string atoms.

Channeling of electrons and positrons was hotly debated in the late sixties and early seventies. The essentially classical features of blocking of electrons and positrons were demonstrated by Uggerhøj by observation of the emission of both particles from radioactive ^{64}Cu implanted into a copper crystal (Uggerhøj, 1966; Uggerhøj and Andersen, 1968). The beautifully simple experiment is illustrated in Figures 8 and 9. The crystal is mounted in a goniometer and two collimators determine the emission direction for both electrons and positrons. As shown in Figure 9, there is a strong decrease in yield along the axis for positrons, similar to observations for heavier particles like alpha particles. In contrast, there is a strong increase in the yield of electrons, as would be expected classically from the reversed sign of the interaction with string atoms.

The classical interpretation of these experiments was criticised and it was argued that, as known from electron microscopy, the transmission of electrons through thin crystals is dominated by coherent Bragg reflection. However, it was soon realised that this quantisation of transverse momentum does not in itself imply the absence of strong classical features. The decisive question is again whether the localisation of an electron to move close to a string or plane gives too much

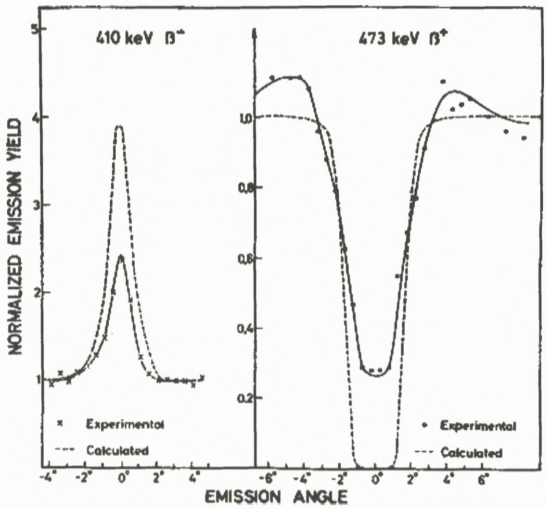

Figure 9. Observed yields along an axis, compared with continuum model calculations (Uggerhøj and Andersen, 1968).

spread in direction of motion via the uncertainty principle to allow a classical description by orbital pictures. This is determined by the number of bound states in the transverse motion, which becomes large for relativistic electrons (Gemmell, 1974; Andersen et al., 1977).

The phase space for bound states in a planar potential is larger for positrons, which oscillate in the open space between planes, and hence channeling is more classical for positrons than for electrons. Figure 10 shows a comparison between a measured planar dip in yield of wide-angle scattering for 1.2 MeV positrons and a so-called many-beam quantum calculation (Pedersen et al., 1972). The dip has an essentially classical envelope with fine structure from Bragg interference.

10. Channeling Radiation

The discovery of channeling radiation should be accredited mainly to Kumakhov, who was the first to derive the correct relativistic transformation (Kumakhov, 1976). The simplest way is to consider first the emission of radiation in the so-called rest system following the electron motion along a string or plane, and then make a Doppler transformation to the laboratory system. The outcome is that the Bohr relation between the photon frequency and the electron energy jump is modified by approximately a factor $2\gamma^2$ for emission in the forward direction. A line spectrum of planar channeling radiation was first presented by the Livermore

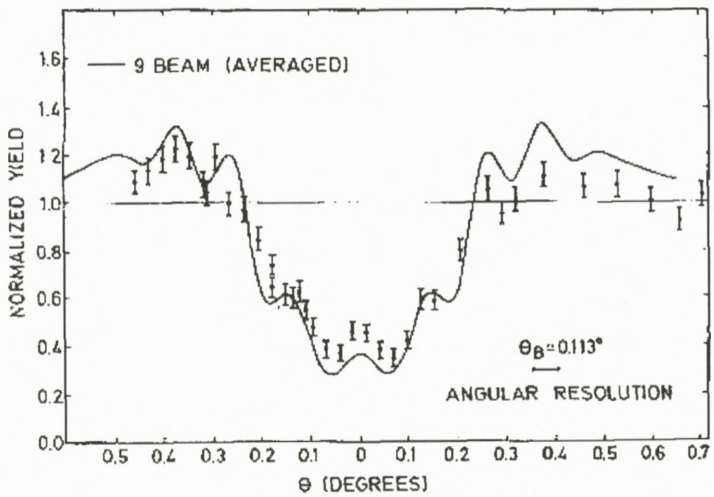

Figure 10. Wide-angle scattering near a (110) plane for 1.2 MeV positrons in Si, compared with a many-beam calculation (Pedersen et al., 1972).

group at the ICACS conference in Hamilton, 1979 (Alguard et al., 1980), and shortly afterwards we observed in Aarhus the first line spectra for axially channeled electrons (Andersen and Lægsgaard, 1980). As illustrated by the spectrum in Figure 11, the lines of channeling radiation are particularly sharp in diamond because of low Z and small thermal vibrations in this material (Guanere et al., 1982).

For not too high energies (MeV) a quantum treatment must be applied, and a systematic description can be based on the formalism developed by Lindhard and co-workers (Lervig et al., 1967; Andersen et al., 1983a). Spin effects are not important and the Klein–Gordon equation for a spinless particle with charge e and rest mass m may be used as a starting point,

$$\left\{\left[-i\hbar\nabla - \frac{e}{c}\vec{A}(\vec{R})\right]^2 c^2 + m^2c^4\right\}\psi(\vec{R},\ldots)$$
$$= [E - H_{\text{rad}} - H_{\text{latt}} - V(\vec{R},\ldots)]^2\psi(\vec{R},\ldots)\,. \tag{13}$$

Here E is the total energy of the system, and the terms H_{rad} and H_{latt} are the independent Hamiltonians of the radiation field and the crystal lattice, while $\vec{A}$ represents the vector potential of the radiation field. The trick is now to separate off a phase factor,

$$\psi(\vec{R},\ldots) = e^{iKz}\,w(\vec{r},z,\ldots), \quad \text{with} \quad \hbar^2K^2c^2 + m^2c^4 = E^2. \tag{14}$$

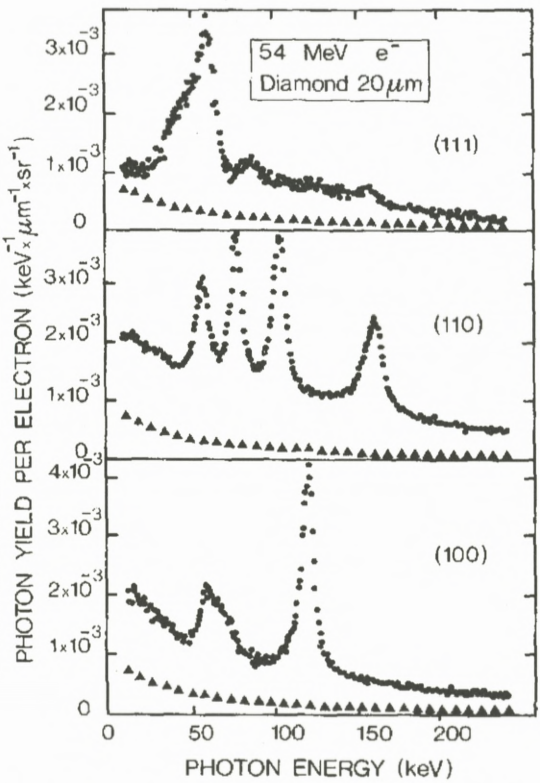

Figure 11. Photon spectra in the beam direction for 54 MeV electrons along different planes in diamond. Triangles show spectrum for incidence in a random direction (Guanere et al., 1982).

This gives an approximate equation of first order in a time parameter $t = z/v$, where v is the velocity corresponding to momentum $\hbar K$. Neglecting terms of second order, like $\partial^2/\partial z^2$ and V^2, we obtain

$$i\hbar \frac{\partial}{\partial t} w = \left[-\frac{\hbar^2}{2\gamma m} \Delta_r + V(\vec{r}, t, \ldots) + H_{\text{rad}} + H_{\text{latt}} + H_{e,r} \right] w(\vec{r}, t, \ldots)$$

$$H_{e,r} = -e \left(\beta A_z + \frac{1}{\gamma mc} \vec{A} \cdot \vec{p} \right). \tag{15}$$

The equation has the form of a non-relativistic Schrödinger equation in two dimensions, and the wave function describes the transverse channeling state. The radiation operator $H_{e,r}$ can be treated as a perturbation, and also the interaction potential can be simplified by a series of perturbation approximations. For example, the electronic excitations are treated by a replacement of V by its expectation

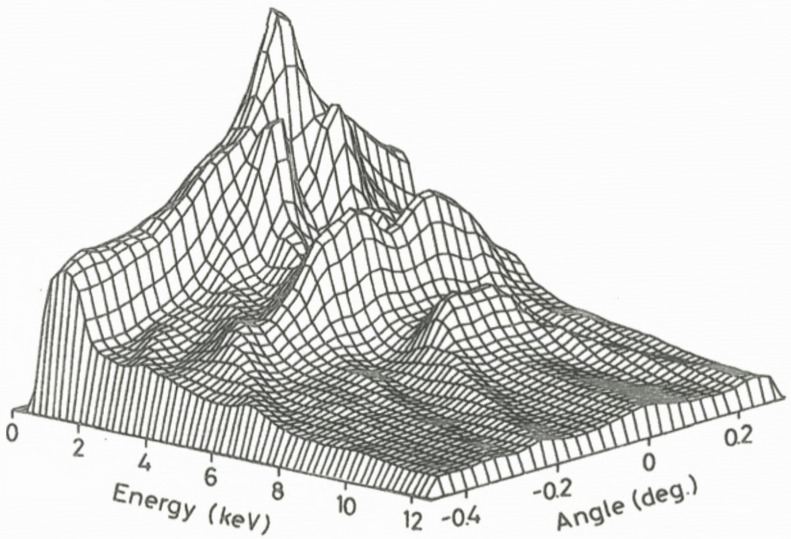

Figure 12. Photon spectra *versus* angle of incidence to a ⟨111⟩ axis for 4 MeV electrons in a 0.5 μm thick Si crystal (Andersen et al., 1982).

value $\langle V \rangle$ in the electronic ground state and a perturbation calculation of the inelastic transitions induced by the difference $V - \langle V \rangle$. Similarly, vibrational excitations of the lattice are treated by the introduction of a thermally averaged potential, with Fourier components reduced by a Debye–Waller factor. In the final step, the potential is approximated by the thermally averaged axial or planar continuum potential.

Measurements of axial channeling radiation for 4 MeV electrons along a Si⟨111⟩ direction are shown in Figure 12 (Andersen et al., 1982). In analogy to atomic states, the bound states may be labelled as s, p, d, ... with angular momentum 0, 1, 2, ... Four lines are clearly distinguished, from 2s–2p, 3d–2p, 2p–1s, and 3p–1s transitions. The angular dependence of the intensities reflects the overlap of the incoming plane wave with the initial states of the transitions, i.e., the intensity is proportional to the square of a Fourier component of the transverse wave function. The ridges at larger angles are from free-to-bound transitions.

Radiative transitions between the bound levels give photon energies in the direction of the axis equal to $h\nu = 2\gamma \Delta E_R$, where E_R is the energy level in the reference system moving with the particle in the z direction, the so-called rest system. Here the mass is non-relativistic and the potential is multiplied by a factor of γ due to the Lorentz contraction of the spacing, d, of atoms on a string. Hence the Hamiltonian is just multiplied by the factor γ. The measurements are in

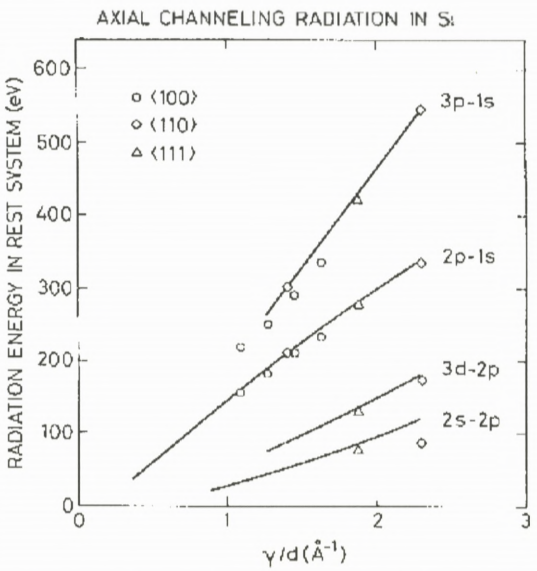

Figure 13. Comparison between calculated transition energies in the rest frame and measurements, at varying electron energy, $E = \gamma mc^2$, and for axes with different atomic spacing, d (Andersen et al., 1982).

Figure 13 seen to be reproduced quite well by calculations. Transitions along three different axes are included. The potential scales with γ/d (Equation 3) and hence measurements for channeling along three different axes can be included in one graph with scaled units. The agreement is quite good when an accurate potential (Doyle–Turner, for example) is used.

The line spectrum of channeling radiation reveals the energy spectrum of bound states, just like the Rydberg series revealed to Niels Bohr the discrete states of the hydrogen atom. Observation of the energies combined with the perturbation calculations can give quite accurate information about crystal properties like the crystal potential and the thermal vibrations (Datz et al., 1986; Hau et al., 1990). It is also possible to calculate the coherence properties from up to third order perturbation theory and reproduce the observed line widths (Andersen et al., 1983b; Hau and Andersen, 1993a, 1993b).

After a hectic period in the 1980s with many active groups, both in theory and in experiments, the activity in low-energy channeling radiation has subsided, and today it is rare to see a paper in this field. Perhaps the field is too well established. Also, the early promises of application of MeV electron beams in crystals as a radiation source seem not to have materialised. In contrast, there has been a

continued interest in radiation phenomena in crystals for high-energy electrons (GeV). The physics in this region is very different, with essentially classical motion of the electrons, and other processes like creation of particle-antiparticle pairs have been studied. The photon yield can be very strongly enhanced and, like the Bethe–Heitler bremsstrahlung spectrum for an amorphous medium, the radiation spectrum extends up to the kinetic energy of the particle. The production of hard photons for particle physics is therefore an interesting application. The effective electrical field generating the radiation corresponds to the continuum potential in the "rest system", and since it is proportional to the relativistic factor γ it becomes huge at extreme relativistic energies. This opens up for fundamental studies in strong-field electrodynamics (Uggerhøj, 2005).

11. Dechanneling

Multiple scattering is strongly reduced for channeled particles. There remain force fluctuations due to thermal vibrations and electronic scattering. One can derive a differential equation for the distribution in transverse energy, $g(E_\perp, z)$, as a function of the depth z (Beloshitsky et al., 1972; Bonderup et al., 1972),

$$\frac{\partial}{\partial z} g(E_\perp, z) = \frac{\partial}{\partial E_\perp} A(E_\perp) D(E_\perp) \frac{\partial}{\partial E_\perp} \frac{g(E_\perp, z)}{A(E_\perp)} . \tag{16}$$

This is a diffusion equation with diffusion function $D(E_\perp)$. The equation reproduces the stability of a uniform distribution in phase space, corresponding to a distribution in transverse energy which is proportional to the allowed area, $g_0(E_\perp) \propto A(E_\perp)$. Since the available area is constant at large $E_\perp$, also g_0 becomes constant. This is special for two dimensions. For planar channeling an analogous equation can be derived, with $A(E_\perp)$ replaced by the half-period of oscillation, $T(E_\perp)$. At large angles, $T(E_\perp)$ is the time interval between the crossings of planes and the equilibrium distribution is proportional to $E_\perp^{-1/2}$.

In a perfect crystal, the diffusion is due to scattering by individual electrons and to fluctuations in atomic scattering associated with thermal displacements. In an amorphous target, nuclear multiple scattering dominates. The mean square multiple scattering angle increases linearly with depth (apart from a logarithmic factor) and, as a scaling length, Lindhard introduced the depth corresponding to an rms scattering angle equal to ψ_1,

$$l_{n,\psi_1} = \frac{2}{\pi N d^2 L_n \psi_1^2} , \tag{17}$$

where the logarithmic factor, L_n, is of order 5–10. This length is roughly proportional to the energy of the particle and hence channeling can be stable over very

large thicknesses at high energies. At GeV energies, the dechanneling lengths are macroscopic (centimetres) and planar channeling in bent crystals can be used for beam bending without too much loss (Baurichter et al., 2000).

Lindhard introduced a diffusion equation already in the 1965 paper, but with the transverse momentum vector as variable. Since it is the transverse energy and not the transverse momentum which is conserved in the continuum model (without diffusion), the magnitude of the variable was in reality the square root of the transverse energy (apart from a constant), and the direction of the vector had no physical significance. The two descriptions are then equivalent but, to avoid confusion, it is better to use the transverse energy as variable.

The diffusion equation may be derived from a more general master equation by a second-order expansion in the small jumps in transverse energy. However, this expansion is not unique! By straight-forward expansion, one obtains a differential equation with an additional drift term (Oshiyama and Mannami, 1981). When Bonderup and I first carried out this expansion, we found exactly the same result and thought that we had discovered a rare error in our master's work. Wisely, we decided to celebrate with a beer in the canteen before confronting Jens Lindhard with our result. Sure enough, he had much deeper insight (Lindhard and Nielsen, 1971) and suggested the method of expansion described in our paper (Bonderup et al., 1972). The point was to conserve the detailed balance of scattering in the master equation and thereby keep the correct statistical equilibrium.

An example illustrating the accuracy of the description by diffusion is shown in Figure 14 (Kennedy et al., 1992). In the calculations, an accurate potential was applied and dechanneling by electronic and thermal scattering was included in the diffusion approximation. The two scattering mechanisms complement each other. The thermal fluctuations dominate at large transverse energies and, for example, cause the planar shoulder to be smeared out rapidly. On the other hand, thermal scattering is very weak for well channeled ions, and electronic scattering is therefore important for the increase of the minimum yield with depth of penetration.

12. Dechanneling by Crystal Defects

When dechanneling by defects is included, the diffusion equation may not be suitable. Alternative approaches are solution of a master equation, which can include large jumps in transverse energy (Gärtner et al., 1984), or brute force computer simulation.

The detection of crystal defects after ion implantation has probably been the most important application of channeling. For example, it has been of decisive

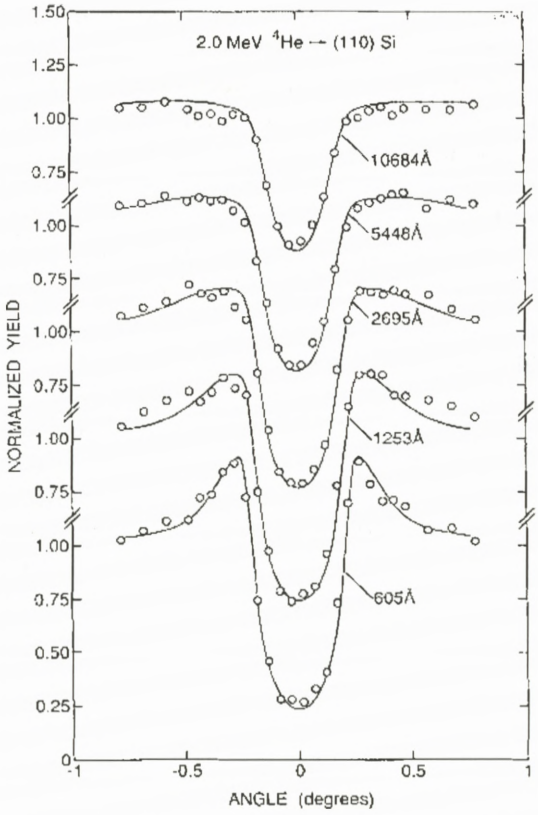

Figure 14. Depth dependence of backscattering for 2 MeV He near a (110) plane in Si, compared with dechanneling calculation (Kennedy et al., 1992).

importance in the development of ion implantation for doping of semiconductors (Mayer et al., 1970). With backscattering of MeV beams of protons or helium ions, the crystal perfection as a function of depth can be measured, as illustrated in Figure 15 (Feldman et al., 1982). The energy scale for the backscattered particles can be converted into a depth scale, as shown at the bottom. The spectrum for a beam aligned with an axis is shown for a virgin crystal as well as for an implanted crystal, and the difference in the yield can be ascribed to a combination of direct backscattering from defects and increased backscattering from atoms in perfect parts of the crystal due to dechanneling. This latter part is indicated by the dashed line and when it is subtracted the depth distribution of the damage is obtained. Methods for analysis of such spectra are today readily available and, all

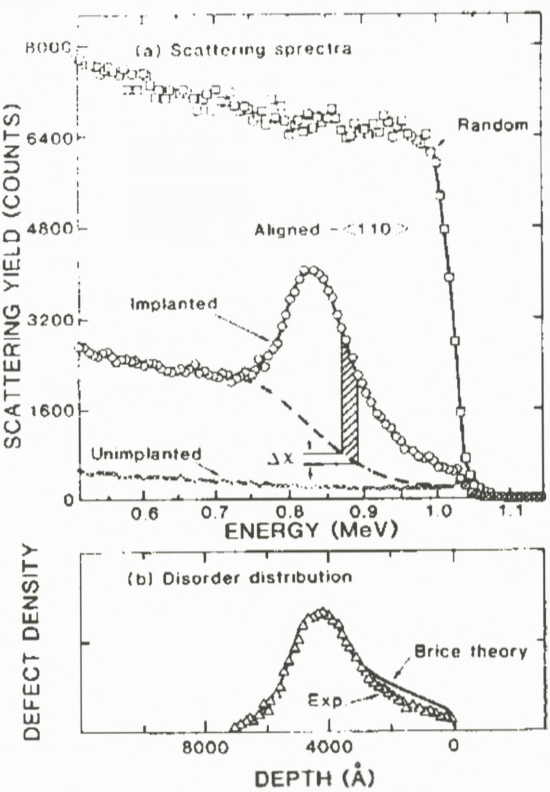

Figure 15. Illustration of the extraction of a damage profile from backscattering in aligned and random directions (Feldman et al., 1982).

in all, dechanneling is a very well developed field, except for the integration of the influence of electron capture and loss by heavy ions to be discussed later.

13. Localisation of Impurities by Channeling and Blocking

Another important application of channeling has been the use of the strong dip in yield of a close-encounter reaction to determine the location of impurity atoms in a crystal lattice. An example is the determination of the lattice configuration of nitrogen implanted into silicon (Berg Rasmussen and Bech Nielsen, 1994). Nitrogen impurities can be detected at low concentrations by a (p, α) reaction. The observed yield of this reaction together with the backscattering yield from the Si lattice is shown in Figure 16 for angular scans through the three major axes.

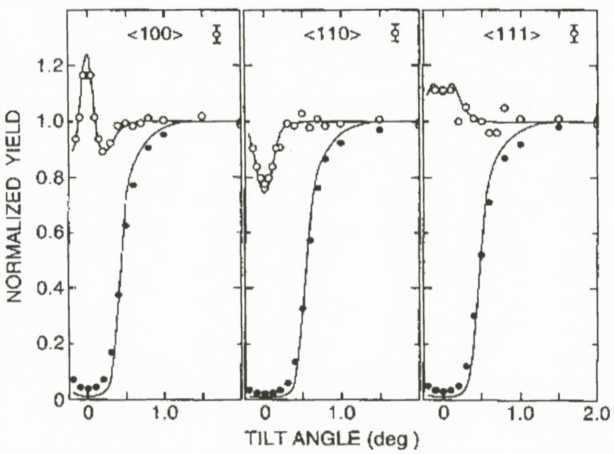

Figure 16. Angular distributions in yield of (p, α) reaction and of backscattering from Si crystal implanted with nitrogen. The lines are from calculations including dechanneling (Berg Rasmussen and Bech Nielsen, 1994).

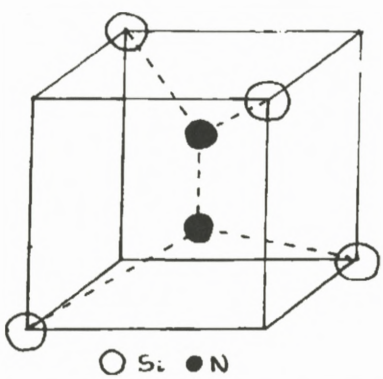

Figure 17. Nitrogen dumb-bell replacing substitutional atom in Si lattice (Berg Ramussen and Bech Nielsen, 1994).

The scans are averaged over the azimuthal angle whereby perturbations by planar effects are largely eliminated.

The data are consistent with the dumb-bell configuration illustrated in Figure 17. Two nitrogen atoms replace one silicon atom. The lines through the data points are from calculations for such a configuration. The dumb-bells are oriented randomly along the three equivalent ⟨100⟩ axes (edges of cube). Nitrogen is substitutional along one axis and interstitial along the other two. This gives a superposition of 1/3 dip and 2/3 narrow peak. An accurate potential (Doyle–

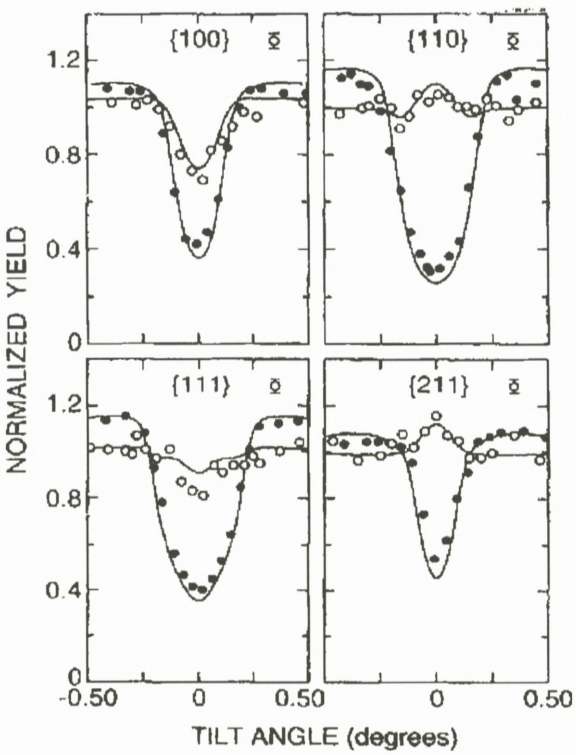

Figure 18. Planar angular scans of (p, α) and backscattering yields for nitrogen implanted Si crystal, compared with calculations including dechanneling (Berg Rasmussen and Bech Nielsen, 1994).

Turner) has been used and dechanneling for a perfect lattice has been included. This is seen to give excellent agreement with the data, both for the impurity and for the host lattice. As seen in Figure 18, also the observed structures for channeling along three different planes were found to be in good agreement with the simulation (planar scans sometimes give crucial information!; Bech Nielsen et al., 1988).

The equivalence of channeling and blocking implies that impurities can just as well be localised by observation of blocking dips for charged particles emitted from the impurity atoms. A very early example is Domeij's observation of a strong blocking dip for α-particles from ^{222}Rn implanted into a tungsten crystal (Domeij and Björkqvist, 1965). The measurements on electrons and positrons discussed above showed that information on lattice location can also be obtained from observation of the blocking effects for these light particles. This is very useful since

beta emitting isotopes are ubiquitous in the periodic table. A pioneering effort on quantitative application of this method has been made by Hofsäss (1996).

14. Crystal Blocking for Determination of Nuclear Lifetimes

In analogy to the lattice localisation of impurities the blocking effect can be used to determine how far from a lattice site the emission of charged particles takes place. For a nuclear reaction proceeding by formation of a compound nucleus, one may thereby determine the average recoil distance $v_\perp \tau$, where $v_\perp$ is the component of the compound nucleus velocity perpendicular to the axis and τ is the compound nucleus lifetime (Gibson, 1975).

Several groups have studied fission lifetimes with this technique. Since the early seventies I have been working with a group mainly from Aarhus and from the Chalk River Nuclear Laboratories on the development of this technique to study heavy ion induced fission of heavy nuclei. Because the recoil is large in these reactions, very short times can be measured, down to about one attosecond. This is still very long on the nuclear time scale and times of order 10^{-21} s are expected from statistical models at the very high excitation energies just after formation of a compound nucleus. In a series of experiments with C, O, and F projectiles on W and Ta crystals, we found results consistent with this expectation. No narrowing of the dips was found but there was an increase in the minimum yield compared with dips in elastic scattering. As illustrated in Figure 19, the results could be fitted with a superposition of mostly fast fission without lifetime effects and a contribution from slow fission after cooling down of the nucleus by emission of several neutrons (Andersen et al., 1976). The measurements for different crystal temperatures and thicknesses are examples of the experimental tests carried out to ensure that the increase in minimum yield was not due to an artefact as, for example, stronger dechanneling for fission fragments than for scattered ions. Additional confirmation was obtained from a variation of the bombarding energy: at higher energies the dips become nearly identical to the blocking dips for scattered ions, scaled in angle with $(Z_1/E)^{1/2}$ according to Equation (7).

Recently we have continued the experiments with heavier projectiles. The idea is to investigate the influence of viscosity on the nuclear mass flow at high internal temperatures. Results from other types of measurements, e.g., on the number of neutrons emitted prior to fission and on emission of giant-dipole gamma rays from the compound nucleus, have indicated that the lifetime can be rather long. The first measurements with 170–180 MeV ^{32}S projectiles gave fission blocking dips which were virtually identical to scaled dips in elastic backscattering (Karamian

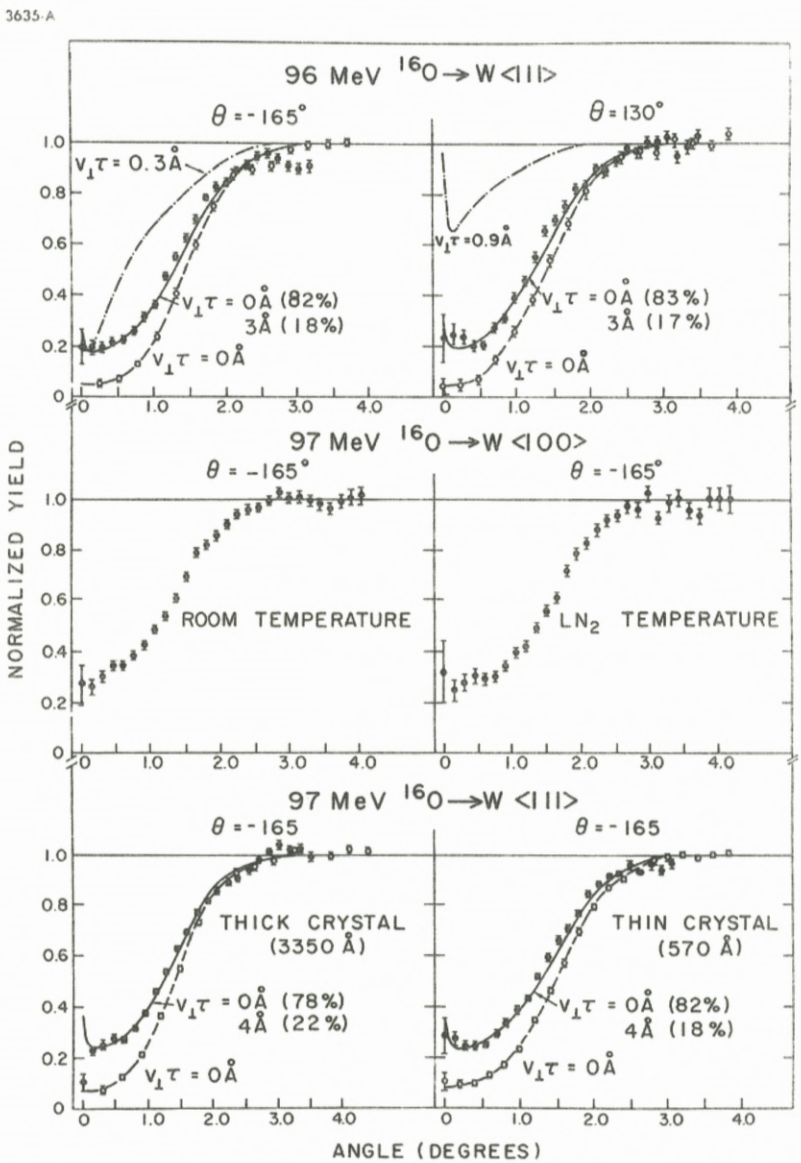

Figure 19. Blocking dips for fission fragments (filled squares) and scaled dips in elastic scattering for ^{16}O bombardment of thin tungsten crystals. The fission dips have been fitted with two components, one for very short recoil represented by the elastic dip and the other a calculated dip for a very large average recoil distance. The top left figure includes a calculation for a single lifetime with intermediate recoil distance (0.3 Å). It reproduces the minimum yield but not the width (Andersen et al., 1980).

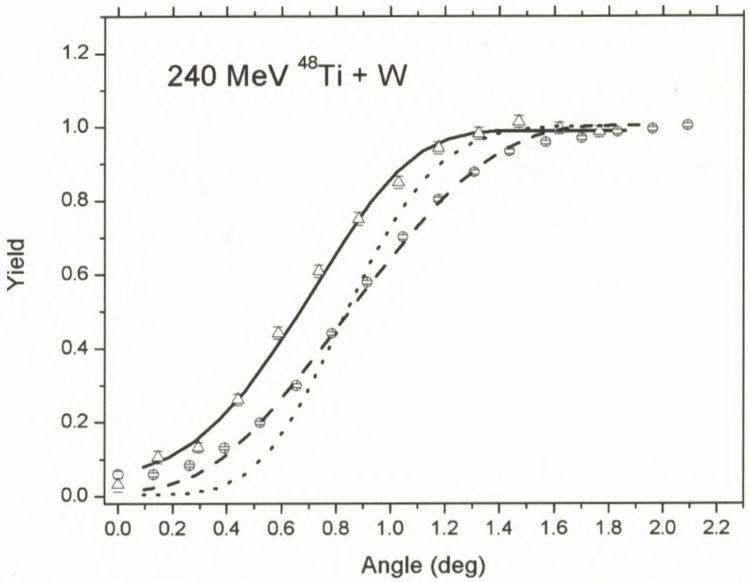

Figure 20. Blocking dip for fission fragments (triangles) and a scaled dip in elastic scattering (circles), compared with continuum-model calculations, including a correction for angular resolution, which is largest for the elastic dip. The dotted curve is for fission fragments with zero recoil while the full-drawn curve includes an exponential distribution of recoils with average displacement 0.14 Å (Forster et al., 2006).

et al., 2003). This indicates that the lifetime of the fission is below about 1 as and there is no component larger than about 1% with much longer lifetime.

A comparison with elastic backscattering is a very useful zero-lifetime normalisation. However, it is actually somewhat surprising that the agreement is so close since the fission fragments carry many electrons which should contribute to the screening of the Coulomb interaction with tungsten nuclei. Also in earlier experiments with oxygen projectiles the scaling was found to be quite accurate, as seen in Figure 19.

Very recently we have continued these experiments at Oak Ridge National Labs with even heavier projectiles, ^{44}Ti at about 240 MeV (Forster et al., 2006). The analysis indicates a clear narrowing of the fission dip compared with the scaled dip in elastic scattering. This is quite exciting because the time delay must be very long, of order 10^{-18} s, and a large fraction of the fission events must experience this delay. In Figure 20 the results for one bombarding energy are compared with a calculation for an exponential decay with an average displacement of 0.14 Å. The scaled elastic dip is seen to be in excellent agreement with the calcula-

tion for zero displacement, except for a small difference in the minimum yield that can be ascribed to crystal defects. Because the critical angle is smaller by nearly a factor of two for the scattered projectiles compared with fission fragments, the angular resolution is poorer. Hence the fission dip should be compared with the dotted curve calculated with the same resolution as for the fission fragments. The lifetime effect is very clear and the displacement corresponds to a lifetime of about 3 as. This signals a very high viscosity of the nuclear mass flow in the fission process. The physical picture of the united nucleus must correspond to a drop of syrup rather than of water. These results may also be important for the interpretation of recent, very surprising observations of long fission lifetimes for superheavy compound nuclei created in heavy-ion reactions (Drouart et al., 2005).

The observations shown in Figures 19 and 20 are also interesting from a methodological point of view. They give a clear demonstration of the power of the technique to determine not only average displacements but also the distribution of displacements. The observation in Figure 20 shows that small displacements from a lattice site are most easily detected by the narrowing of the width of the blocking (or channeling) dip, rather than by the increase of the minimum yield. The surprising accuracy of the scaling of the elastic dips is a problem which deserves theoretical and perhaps also further experimental study.

15. Restricted Equilibrium in Axial Channeling

All through the history of channeling, computer simulation has played a prominent role. The earliest ideas were inspired by simulation of the penetration of low-energy ions through crystals, and simulation is still a very valuable tool for interpretation of experiments. Probably the most advanced code was developed by John Barrett at Oak Ridge and he made important contributions to the theory of channeling on the basis of simulations. An example is the observation that the minimum yield in the axial channeling dip is underestimated by a factor of two to three, the so-called Barrett factor (Barrett, 1973a). His search for an explanation of this factor led him to publish a paper with the title: "Breakdown of the Statistical-Equilibrium Hypothesis in Channeling" (Barrett, 1973b).

The basic observation is illustrated in Figure 21. The lines indicate simulated (transverse) trajectories of ions incident on a crystal parallel to an axis and hitting the surface close to a string. In the transverse motion, the ions are accelerated away from this string and their transverse energy, $\varepsilon \equiv E_\perp$, is given for each picture. The strings are indicated by dots, and the figure shows that the flux of ions tends to be focussed onto other strings. This focussing clearly violates the assumption of

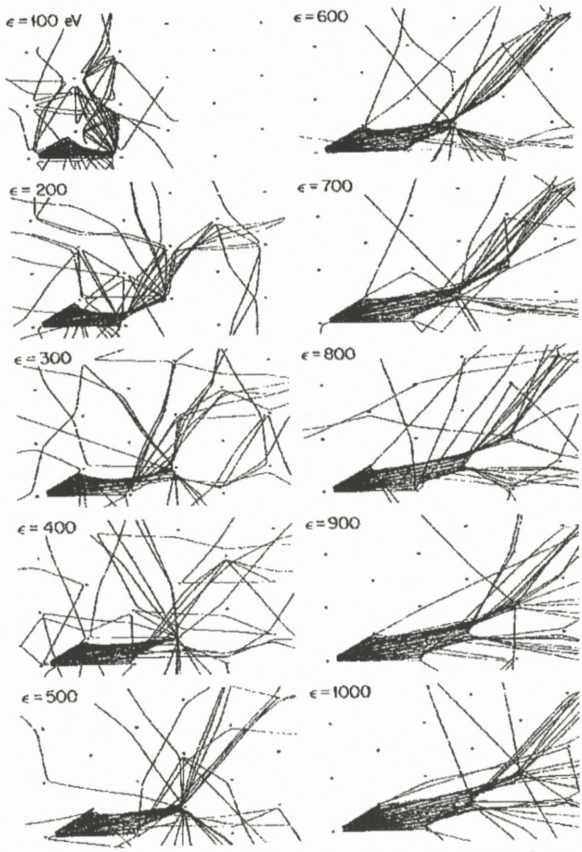

Figure 21. Projection onto (111) plane of trajectories of 3-MeV protons moving nearly parallel to [111] direction in tungsten at 1200 K (Barrett, 1973b).

a rapid trend towards statistical equilibrium on an energy shell in the transverse phase space.

This paper appeared to be a heavy blow to Lindhard's theory of channeling, in which, as noted above, arguments based on statistical equilibrium play a key role. The problem must be rooted in a restriction in phase space hindering the establishment of a full equilibrium. Typically, such a hindrance is associated with a symmetry and a corresponding conservation law, like for instance conservation of angular momentum for a system with rotational symmetry. For axial channeling, the symmetry is the regular arrangement of the strings in a two-dimensional lattice, and the conservation law is the conservation of transverse energy with respect to planes for ions moving nearly parallel to the planes.

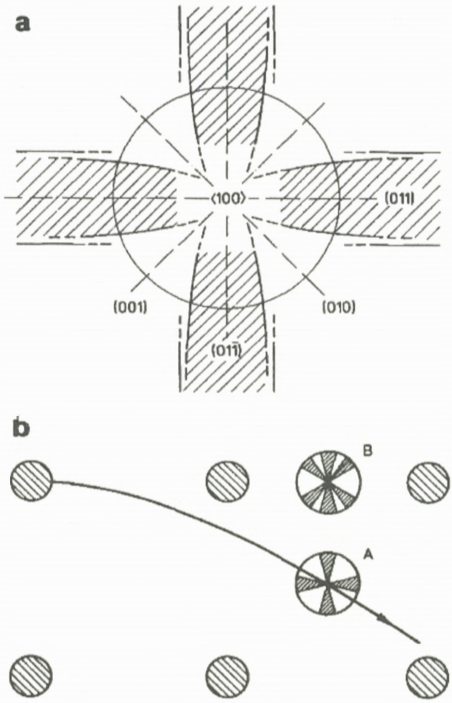

Figure 22. (a) Stereogram indicating regions of planar channeling near a ⟨100⟩ axis in Si, for a particle at position A below. (b) Transverse plane for Si ⟨100⟩. The blocked angular regions are indicated for two positions A and B, and a trajectory for a particle moving out radially from a string is shown (Andersen and Uguzzoni, 1990).

This is illustrated in Figure 22a, showing a stereogram of a small angular region around a ⟨100⟩ direction in a cubic lattice. The major planes containing the axis are indicated, and the circle shows the boundary for axial channeling at the angle ψ_1. Well outside the circle, planar channeling takes place inside the full drawn lines parallel to the plane, but close to the axis planar channeling is replaced by the so-called string-of-strings channeling with a critical angle decreasing with decreasing angle to the axis (Lindhard, 1965). The regions of channeling with respect to the strongest planes are hatched. Very close to the axis, the concept of planar channeling loses its meaning entirely.

Planar channeling divides the transverse phase space into regions with poor communication. An ion in the hatched region remains there on a depth scale determined by planar dechanneling and, *vice versa*, an ion outside the hatched area is prevented from entering this area by scattering on strings. Figure 22b illustrates how we can understand Barrett's results from this division. An ion starting

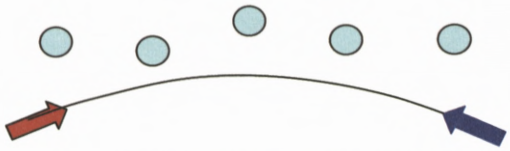

Figure 23. Reversibility of string collision.

its trajectory very close to a string is blocked from the regions of phase space corresponding to planar channeling. As indicated by the two small stereograms embedded in the figure, the blocked angular region depends on the position in the transverse plane. In the accessible, restricted phase space, we may assume a rapid trend towards equilibrium. Compared with a full equilibrium, the probability for getting very close to a string again is then higher by the ratio of the four dimensional volume of the full phase space to the volume of the restricted phase space.

These ideas were supported by simulations (Andersen and Uguzzoni, 1990) and appear to account quite well for a major part of the Barrett factor (Uguzzoni et al., 2000). There is an additional contribution from strong thermal fluctuations in the first collision with a string at the crystal surface, which determines the transverse energy of the ions giving the minimum yield. Thus the first attack on the concept of statistical equilibrium in channeling was repelled and in the process new insight was gained.

16. Cooling and Heating in Ion Transmission Through Crystals

The second attack on statistical equilibrium in channeling was of an even more fundamental nature. As noted above, it is an important constraint in the derivation of the diffusion equation for dechanneling that a constant density in phase space should be an equilibrium. The phase space is now not limited to a transverse-energy shell but extends out to angles much larger than the critical angle. The requirement follows from basic symmetries of the multiple scattering.

Consider for example the thermal scattering of an ion colliding with a string, as illustrated in Figure 23. If the energy loss in the collision is ignored, the trajectory is reversible, and this implies that thermal scattering leading from $E_\perp$ to $E'_\perp$ has the same probability as scattering from $E'_\perp$ to $E_\perp$. It is easy to see that the same symmetry must hold for changes in transverse energy due to electronic collisions. Until recently, it was believed that the only deviations from this general rule were due to energy loss of the projectile and that they must be small. The observations to be described in the following therefore came as a great surprise.

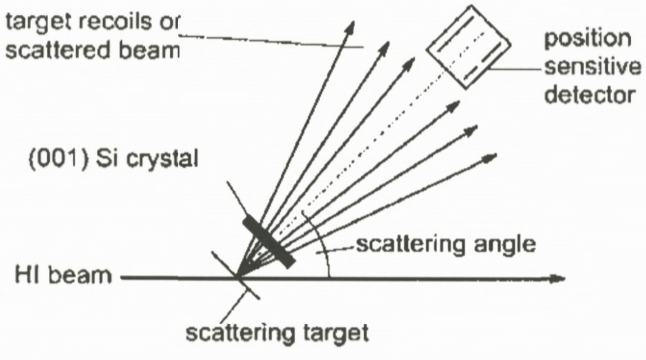

Figure 24. Geometry for transmission experiment (Assmann et al., 1999).

The set up shown in Figure 24 was designed by Assmann et al. to give a sensitive test of the equilibrium hypothesis for heavy ions transmitted through a thin crystal (Assmann et al., 1999). By scattering of a heavy-ion beam in a thin foil, a thin Si crystal was illuminated with a beam with large angular divergence, and behind the crystal the angular distribution of the ions was measured with a position sensitive detector. An isotropic beam with uniform intensity gives a constant distribution in transverse phase space inside the crystal, and if this distribution is stable, the beam will remain isotropic after the passage of the crystal.

The results shown in Figure 25 are dramatically different. To the left are the two-dimensional intensity distributions and to the right the azimuthally averaged intensity as a function of the angle to the axis. For carbon ions there is a strong accumulation of flux near the axis and the planes, denoted cooling. The transmission of Cu ions is an intermediate case, with cooling along the axis and the strongest planes but a depletion of the flux ("heating") along the weaker planes. For transmission of the heavier iodine ions, there is almost exclusively heating, and for the heaviest Au ions there is strong heating along all channeling directions.

Assmann first told me about his strange results at a conference on ion beam analysis (IBA 1995) in Phoenix, Arizona. It was clear that the underlying mechanism must violate the detailed balance of multiple scattering which secures stability of a uniform distribution in phase space. I later discussed this problem with Jens Lindhard, and we agreed that irreversible energy-loss processes must be responsible. However, after our discussion in Phoenix, Assmann modified his setup to the one illustrated in Figure 24 and obtained the striking results shown in Figure 25. It was easy to estimate the magnitude of effects due to energy loss processes, and the observed effects were clearly much larger.

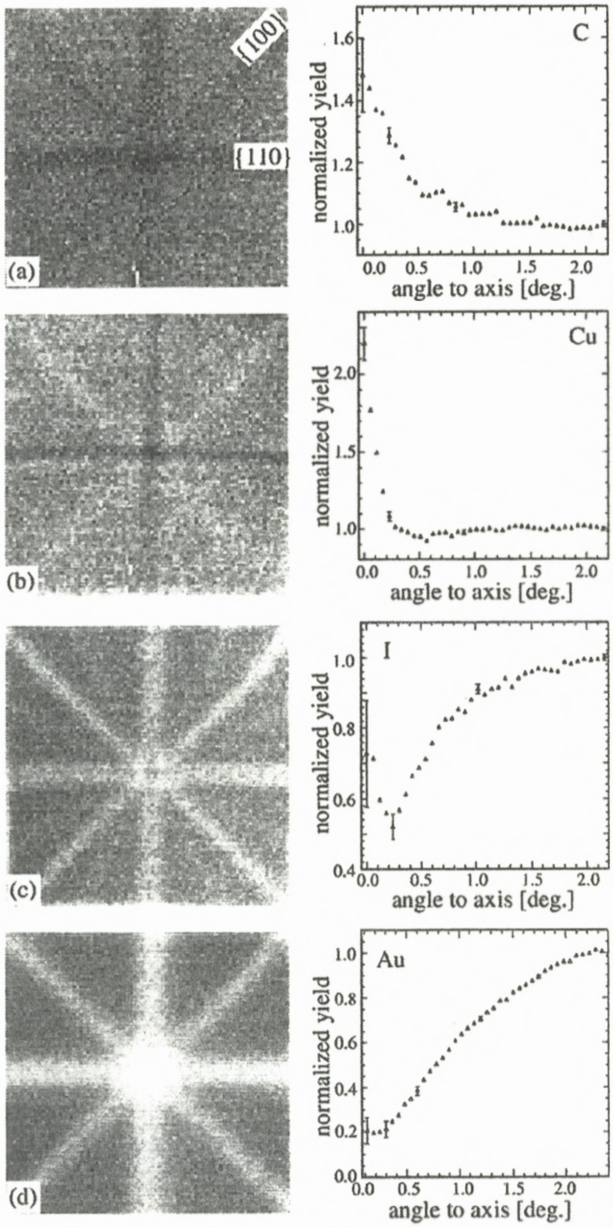

Figure 25. Flux distributions of heavy ions after transmission through (001) Si crystal. To the right azimuthally averaged intensities; (a) C recoils at 18 MeV after 8.7 μm; (b) Cu recoils at 46 MeV after 8.7 μm; (c) scattered I ions at 121 MeV after 2.9 μm; and (d) scattered Au ions at 92 MeV after 2.9 μm. The angular range is $\pm 2.2°$ (Assmann et al., 1999).

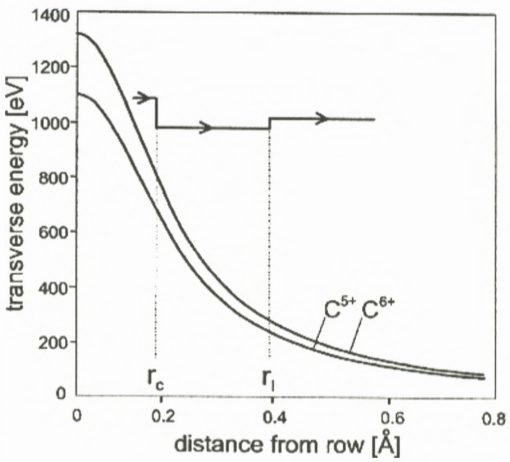

Figure 26. ⟨100⟩ Si string potentials for C^{5+} and C^{6+} ions, in the point-charge approximation (Equation 6). The horizontal line indicates the transverse energy of an ion capturing an electron at r_c and losing it at r_l (Assmann et al., 1999).

In the search for an explanation the requirement of microscopic irreversibility was the decisive clue. In addition to energy loss, also changes of the ion charge due to capture or loss of electrons are irreversible processes. Electrons bound to crystal atoms are captured and ion electrons are lost into empty states of free motion through the crystal. Furthermore, electron capture or loss can change the transverse energy of an ion. For highly stripped ions the effective continuum potential is proportional to the net charge of the ion (Equation 6). Electron capture then leads to a reduction of the transverse potential energy and electron loss to an increase. If, on the average, electron capture takes place at smaller distances from strings than electron loss there will be a net cooling effect, and this is indeed predicted to be the case at very high velocities, from the known impact-parameter dependencies of capture and loss in this limit.

The mechanism is illustrated in Figure 26. A C^{6+} ion is moving away from a string with transverse energy close to 1100 eV. At the distance r_c it captures an electron and loses the transverse energy $U^{(1)}(r_c)$. Later at a distance r_l the electron is lost again and the transverse energy $U^{(1)}(r_l)$ is gained. The cycle has led to a net loss of transverse energy, i.e., to cooling. This mechanism was shown to account qualitatively for the phenomena illustrated in Figure 25. However, it remains a challenge to explain in detail the quite complicated results of later experiments, in particular the observed transition with decreasing velocity from a flux enhance-

ment along channeling directions (cooling) to a flux depletion (heating) (Grüner et al., 2003).

These phenomena clearly offer an opportunity to study the impact parameter dependence of capture and loss processes. The information obtained with the experimental conditions illustrated in Figure 24 is complementary to that gathered from experiments with well defined incidence angle of the ion beam, which yield more detailed data on cross sections (Datz et al., 1972). In order to derive information on charge exchange processes it is necessary to establish a theoretical framework for data analysis. For example, the dependence of the channeling potential on ion charge must be investigated. Only for ions carrying few tightly bound electrons can this dependence be described in the simple manner indicated in Equation (6).

Another problem is to incorporate the capture and loss processes into the dechanneling formalism. The angular distribution of transmitted ions results from a competition between cooling/heating from capture and loss and multiple scattering, which drives the distribution towards isotropy. A first attempt has been made recently (Malyshevsky, 2005). However, it does not include properly the mechanism discussed above. I believe that this is partly because the transverse momentum is used as variable in the description. As discussed in Section 11, this can lead to confusion.

17. Energy Loss for Channeled Particles

We shall now turn to aspects of channeling which Lindhard denoted secondary phenomena, i.e., phenomena which are influenced by channeling but do not in turn affect the steering of the ions very much. The most prominent example is stopping. Studies of ion ranges, both computer simulations and range measurements, played a very important part in the discovery of channeling (see, for example, the introduction to Eriksson et al., 1967). The energy loss to atomic recoils, the so-called nuclear energy loss, is reduced most by channeling, and very long ranges of low-energy heavy ions were observed for incidence parallel to an axis in a crystal.

The selection by channeling of large impact parameters with atoms makes it possible to study the electronic energy loss at low velocities where nuclear energy loss dominates. A nice example is illustrated in Figure 27 (Eriksson et al., 1967). The oscillatory dependence of the electronic stopping cross section, S_e, on Z_1 stems from the so-called Ramsauer–Townsend effect. The cross section for electron scattering on the penetrating ion may be written as a sum over angular momenta and at low velocity the s-wave cross section dominates. With increasing strength of the scattering potential, the s-wave phase shift increases, and the cross

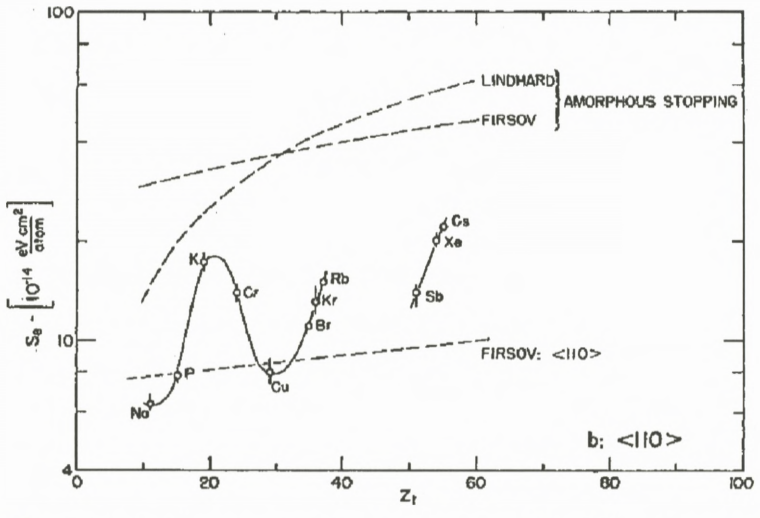

Figure 27. Electronic-stopping cross section at velocity $v = 1.5 \times 10^8$ cm/s *versus* the atomic number of the projectile, derived from the range of a perfectly channeled ion along a ⟨110⟩ direction in tungsten (Eriksson et al., 1967).

section has strong minima when the phase shift passes through multiples of π (Finnemann, 1968; Briggs and Pathak, 1973). The oscillations were first seen in the stopping in amorphous foils but the elimination of atomic recoils and the confinement of electronic scattering to the thin electron gas far from atoms make the oscillations much more prominent.

At high velocities the slowing down is mainly due to electronic energy loss. For small Z_1 it may be obtained by a quantum perturbation calculation. The resulting Bethe–Bloch formula may be written as an integral over impact parameters, leading to a logarithm of the ratio of an adiabatic radius divided by half the reduced wavelength of the electrons in the ion rest frame,

$$-\frac{\mathrm{d}E}{\mathrm{d}x} = NS_e = \frac{4\pi Z_1^2 e^4}{mv^2} NZ_2 \ln \frac{v/\omega}{\lambda/2}. \tag{18}$$

The observations of a reduced electronic energy loss for a substantial fraction of MeV protons penetrating several micron thick crystals demonstrated convincingly that channeling is not a simple transparency effect for low energy ions.

Asymptotically for large v the expression in Equation (18) has equal contributions from large and small impact parameters (equipartition). Therefore the energy loss is at high velocities reduced by about a factor of two for the best channeled particles (Lindhard, 1965). As demonstrated by Esbensen and Golovchenko

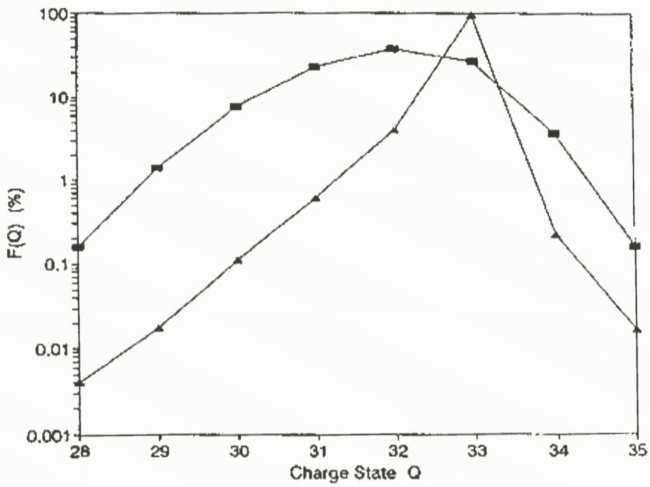

Figure 28. Charge-state distributions for a random (□) and a ⟨110⟩ aligned (Δ) beam of 15.3 MeV/u Br^{33+} ions after passage of a 1 μm Si crystal (Andersen et al., 1996).

(1976), the theory simplifies in the high-velocity limit, and excellent agreement with measurements of the energy loss for relativistic channeled particles in thin Si and Ge crystals was obtained (Esbensen et al., 1978). Also the shape of the energy distribution for channeled particles could be accounted for when fluctuations of large energy transfers in single collisions with electrons were taken into account (Landau distribution).

Many other experiments and calculations on the stopping of channeled ions have been published (Cohen and Dauvergne, 2004) but still the full potential of such studies for testing the stopping power theory has in my view not been realised. An attempt at a detailed comparison with standard stopping theory for swift heavy ions is discussed in the following.

In the experiment 15.3 MeV/u Br^{33+} ions were passed through a very thin Si crystal and both the emergent charge state and the energy-loss spectrum were measured with a magnetic spectrometer (Andersen et al., 1996). As illustrated in Figure 28, the 33+ ions with only the K-shell electrons remaining undergo very little capture or loss of electrons when the ions are incident along a ⟨110⟩ axis. This phenomenon of "frozen charge state" was especially investigated and applied by Datz and co-workers in Oak Ridge in their pioneering experiments on channeling of high-energy, heavy ions (Gemmell, 1974; Krause and Datz, 1996). It is important for the analysis of the energy loss because the complication of a fluctuating charge state is removed.

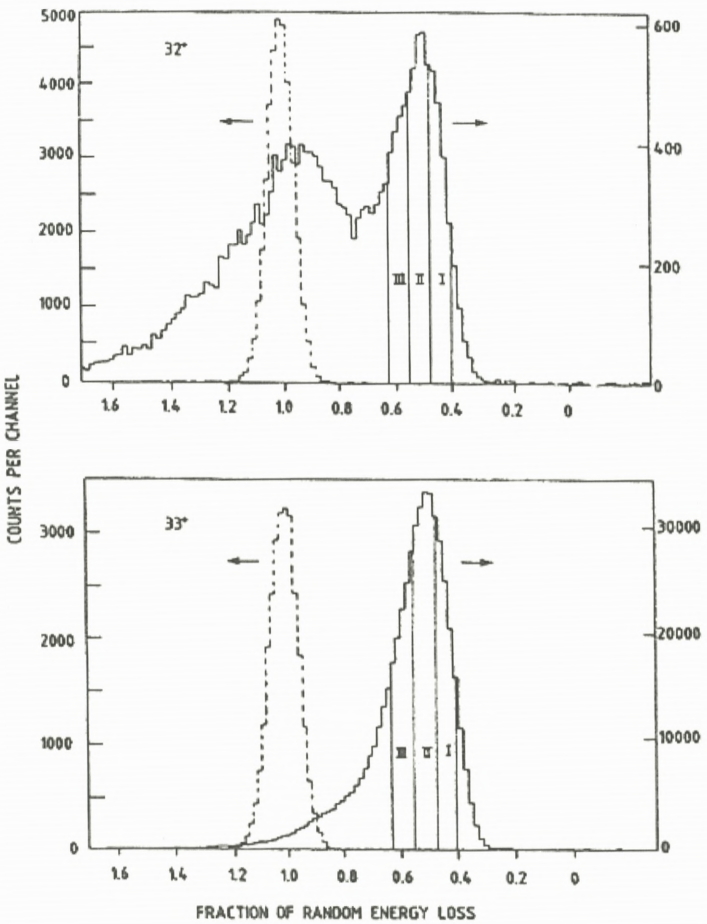

Figure 29. Energy-loss of transmitted 32+ and 33+ ions for a beam of 15.6 MeV/u $^{79}Br^{33+}$ ions. Spectra for random (- - - -) and ⟨110⟩ (—) alignment are shown as functions of the energy loss relative to the average random loss of $\Delta E = 4.9$ MeV for the 1 μm thick Si target (Andersen et al., 1996).

The energy spectra for exiting 33+ and 32+ ions are shown in Figure 29. For reference, also the energy spectrum for ions incident in a random (i.e., non-channeling) direction is shown, and the energy loss is given as a fraction of the random energy loss (4.9 MeV for 1μm Si). Nearly all the 33+ ions have an energy loss much smaller than for random incidence, reflecting that nearly all the ions are channeled. The spectrum for the much fewer 32+ ions contains two parts, well channeled ions which have captured a valence electron, with an energy spectrum

similar to that for 33+ ions, and poorly channeled ions which have entered the crystal close to a string and scattered to angles of order ψ_1, with energy loss similar to or even larger than random. There is also a small component of such ions in the 33+ spectrum but it is strongly enhanced for 32+ ions because the capture probability is much higher for random than for channeled ions (Figure 28).

For the analysis of the energy loss, the well channeled ions have been divided into three groups. For fixed trajectory, the straggling in energy loss is small. This can be seen from the width of the random energy loss peak which has about equal contributions from charge-exchange straggling and Bohr straggling (fluctuations in hard collisions). For channeled particles there is only the Bohr straggling and it is reduced due to the lower electron density. In contrast to the situation for relativistic particles discussed above, the width of the energy loss distribution therefore comes mainly from the distribution in transverse energy and the associated variation of the allowed area in the transverse plane. If the spatial variation of the energy loss rate is known, the energy distribution can be calculated and compared with the measurement.

The analysis was based on a simple description of the energy loss as consisting of three parts, the energy transfers to K-, L-, and M-shell electrons. The corresponding oscillator strengths and excitation frequencies could be estimated rather accurately, and the dependence of the energy loss on transverse energy was then calculated. Compared with the Bethe–Bloch formula given above there are two important corrections for heavy ions. First Bohr's kappa (Equation (12) with $Z_2 = 1$) is larger than unity and the classical counterpart, the Bohr formula, should be applied instead, with the reduced electron wavelength replaced by the classical collision diameter. Second, there may be a significant so-called Barkas correction which is of third order in Z_1. It is about 5%, only, for the present case. Good agreement with the measurement was obtained. The dependence of the stopping on transverse energy turns out to come partly from the spatial variation of the density of valence (M-shell) electrons, partly from the adiabatic cut-off of energy loss to the L-shell at large impact parameters with atoms.

18. Crystal as Special Target for Atomic Processes

Studies of energy loss are just one example of the use of crystals as special targets for measurements on atomic processes (Krause and Datz, 1996). For channeled ions, the target is essentially a gas of the valence electrons. This has been utilised to study capture processes like radiative electron capture and dielectronic electron capture.

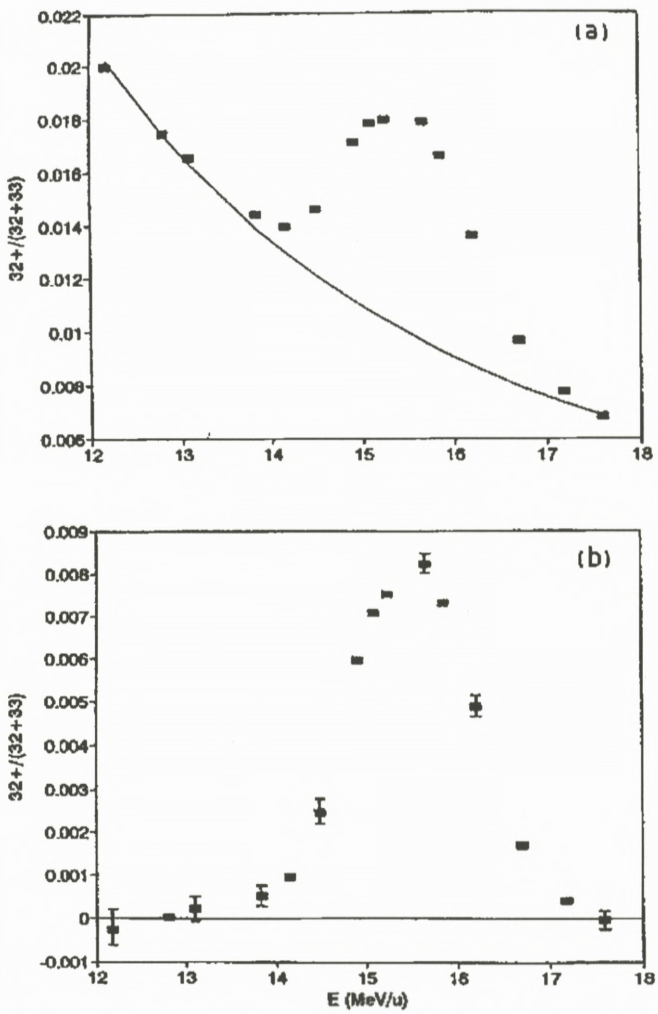

Figure 30. (a) The charge state fraction $32^+/(32^+ + 33^+)$ for channeled ions with energy loss in the windows I, II, and III in Figure 29, as a function of the ion energy. (b) Data in (a) after subtraction of a smooth background (Andersen et al., 1996).

An example, from the experiment with Br^{33+} ions discussed above, is illustrated in Figure 30. The ratio between the numbers of 32+ and 33+ ions within the energy window I+II+III in Figure 29 is here plotted as a function of the bombarding energy. The peak in Figure 30b, obtained after subtraction of a smooth background from other capture processes, occurs at a velocity where the energy

of a valence electron in the ion frame of reference matches the K-shell binding energy minus twice the L-shell binding. An electron can then be captured with simultaneous excitation of a K-shell electron. The width of the resonance comes from the spread of electron velocities in the electron gas.

Another process which should be mentioned in this connection is resonant coherent excitation, sometimes called the Okorokov effect (Okorokov, 1965). Here a Fourier component of the periodic field from a string of atoms is used to excite a bound electron. Channeling is again used to avoid close collisions and thereby to maintain a well defined atomic state during the interaction. The excitation can be observed either by detection of radiative de-excitation outside the crystal or by observation of the emergent charge state distribution as a function of bombarding energy. At velocities where a multiple of the frequency of collisions with atoms on a string matches a transition frequency in the ion, the atomic excitation gives rise to an increase in the rate of electron loss and hence to an increase in the charge state. The effect was first observed unambiguously at Oak Ridge (Moak et al., 1979). Recently, mainly a Japanese group working at the high-energy accelerator laboratory RIKEN has been active in this area, extending the observations to heavier ions carrying a few electrons (Nakai et al., 2005).

19. Concluding Remarks

The physics of channeling is rich in interesting, sometimes quite surprising phenomena, and channeling and blocking have very many applications. I have reviewed some of the aspects of channeling which I have found it most exciting to work on and hope that the reader will experience some of this excitement. With the rapid development of computers, simulation has become increasingly important in the interpretation of experiments, but the analytical theory founded by Jens Lindhard remains the basis for our understanding of the phenomena.

Channeling is a mature field but there are still challenging problems. The basic binary scattering is described by a screened Coulomb potential and, except for simple, limiting cases, there is considerable uncertainty in the representation of the combined screening by target and projectile electrons. I have mentioned two cases where this uncertainty is a problem. One is the application of blocking to measure nuclear lifetimes. It is important to be able to compare blocking dips for reaction products and for elastically scattered projectile ions, and this requires an accurate scaling of the critical angle for blocking with the atomic number of the blocked ions. Another example is the analysis of "heating" and "cooling" phenomena in the penetration of energetic heavy ions through thin crystals where

a precise description of the dependence of the interaction potential on the ion charge state is needed.

Channeling of ions in crystals makes it possible to study the impact parameter dependence of atomic processes. The simplest example is energy loss, and studies of the modified stopping under channeling conditions played an important role in the discovery of channeling. Usually the question has been what we can learn about ion channeling from the energy loss spectrum. One may turn the question around and ask what we have learned about energy loss processes from channeling observations and what we can still learn. I have argued that if experiments and calculations are planned with this question in mind there may be scope for new investigations of the energy loss of channeled ions. New opportunities are also offered by the recently discovered "cooling" and "heating" phenomena which are very sensitive to the impact parameter dependence of the capture and loss of electrons.

References

Alguard M.J., Swent R.L., Pantell R.H., Datz S., Barrett J.H., Berman B.L. and Bloom S.D. (1980): Radiation from channeled leptons. Nucl Instrum Methods **170**, 7–13

Andersen J.U. and Feldman L.C. (1970): Comparison of average-potential models and binary-collision models of axial channeling and blocking. Phys Rev B **1**, 2063–2069

Andersen J.U. and Lægsgaard E. (1980): Characteristic radiation from channeled electrons. Phys Rev Lett **44**, 1979–1982

Andersen J.U. and Uguzzoni A. (1990): A restricted equilibrium in phase space for axial channeling. Nucl Instrum Methods Phys Res B **48**, 181–186

Andersen J.U., Lægsgaard E., Nielsen K.O., Gibson W.M., Forster J.S., Mitchell I.V. and Ward D. (1976): Time evolution of heavy-ion-induced fission studied by crystal blocking. Phys Rev Lett **36**, 1539–1542

Andersen J.U., Andersen S.K. and Augustyniak W.M. (1977): Channeling of electrons and positrons. Kgl Dan Vid Selsk Mat Fys Medd **39, no. 10**, 1–58

Andersen J.U., Jensen A.S., Jørgensen K., Lægsgaard E., Nielsen K.O., Forster J.S., Mitchell I.V., Ward D., Gibson W.M. and Cuomo J.J. (1980): Lifetime measurements for heavy-ion-induced fission by the crystal-blocking technique. Kgl Dan Vid Selsk Mat Fys Medd **40, no. 7**, 1–56

Andersen J.U., Bonderup E., Lægsgaard E., Marsh B.B. and Sørensen A.H. (1982): Axial channeling radiation from MeV electrons. Nucl Instrum Methods **194**, 209–224

Andersen J.U., Bonderup E. and Pantell R.H. (1983a): Channeling radiation. Ann Rev Nucl Part Sci **33**, 453–504

Andersen J.U., Bonderup E., Lægsgaard E. and Sørensen A.H. (1983b): Incoherent scattering of electrons and linewidth of planar-channeling radiation. Physica Scripta **28**, 308–330

Andersen J.U., Chevallier J., Ball G.C., Davies W.G., Forster J.S., Geiger J.S., Davies J.A., Geissel H. and Kanter E.P. (1996): Dielectronic recombination and energy loss for He-like ^{79}Br ions channeled in a thin single crystal of Si. Phys Rev A **54**, 624–635

Assmann W., Huber H., Karamian S.A., Grüner F., Mieskes H.D., Andersen J.U., Posselt M. and Schmidt B. (1999): Transverse cooling or heating of channeled ions by electron capture and loss. Phys Rev Lett **83**, 1759–1762

Barrett J.H. (1973a): Monte Carlo channeling calculations. Phys Rev B **3**, 1527–1547

Barrett J.H. (1973b): Breakdown of the statistical-equilibrium hypothesis in channeling. Phys Rev Lett **31**, 1542–1545

Baurichter A., Biino C., Clément M., Doble N., Elsener K., Fidecaro G., Freund A., Gatignon L., Grafström P., Gyr M., Hage-Ali M., Herr W., Keppler P., Kirsebom K., Klem J., Major J., Medenwaldt R., Mikkelsen U., Møller S.P., Siffert P., Uggerhøj E., Vilakazi Z.Z. and Weisse E. (2000): Channeling of high-energy particles in bent crystals – Experiments at the CERN SPS. Nucl Instrum Methods in Phys Res B **164–165**, 27–43

Bech Nielsen B., Andersen J.U. and Pearton S.J. (1988): Lattice location of deuterium interacting with the boron acceptor in silicon. Phys Rev Lett **60**, 321–324

Beloshitsky V.V., Kumakhov M.A. and Muralev V.A. (1972): Multiple scattering of channeled ions in crystals. Rad Effects **13**, 9–22

Berg Rasmussen F. and Bech Nielsen B. (1994): Microstructure of the nitrogen pair in crystalline silicon studied by ion channeling. Phys Rev B **49**, 16353–16360

Bonderup E., Esbensen H., Andersen J.U. and Schiøtt H.E. (1972): Calculations on axial dechanneling. Rad Effects **12**, 261–266

Briggs J.C. and Pathak A.P. (1973): Momentum transfer cross sections and the Z1 oscillations in stopping power. J Phys C **6**, L153–L157

Cohen C. and Dauvergne D. (2004): High energy ion channeling; Principles and typical applications. Nucl Instrum Methods Phys Res B **225**, 40–71

Datz S., Martin F.W., Moak C.D., Appleton B.R. and Bridwell L.B. (1972): Charge changing collisions of channeled oxygen ions in gold. Rad Effects **12**, 163–169

Datz S., Berman B.L., Dahling B.A., Hynes M.V., Park H., Kephart J.O., Klein R.K. and Pantell R.H. (1986): On the dependence of electron planar channeling radiation upon lattice vibration amplitude. Nucl Instrum Methods Phys Res B **13**, 19–22

Davies J.D. (1983): The channeling phenomenon – And some of its applications. Physica Scripta **28**, 294–302

Domeij B. and Björkqvist K. (1965): Anisotropic emission of α-particles from a monocrystalline source. Phys Lett **14**, 127–128

Drouart A., Charvet J.L., Dayras R., Nalpas L., Volant C., Chbihi A., Escano Rodriguez C., Frankland J.D., Morjean M., Chevallier M., Dauvergne D., Kirsch R., Lautesse P., Ray C., Testa E., Cohen C., L'Hoir A., Jacquet D. and Laget M. (2005): Evidence of $Z = 120$ compound nucleus formation from lifetime measurements in the ^{238}U+Ni reaction at 6.62 MeV/nucleon. In: Proceedings of International Symposium on Exotic Nuclei, Peterhof 2004. World Scientific, Singapore, pp 192–197

Eriksson L., Davies J.A. and Jespersgaard P. (1967): Range measurements in oriented tungsten single crystals (0.1–1.0 MeV). I. Electronic and nuclear stopping powers. Phys Rev **161**, 219–234

Esbensen H. and Golovchenko J.A. (1976): Energy loss of fast channeled particles. Nucl Phys A **298**, 382–396

Esbensen H., Fich O., Golovchenko J.A., Madsen S., Nielsen H., Schiøtt H.E., Uggerhøj E., Vraast-Thomsen C., Charpak G., Majewski S., Odyniec G., Petersen G., Sauli F., Ponpon J.P. and

Siffert P. (1978): Random and channeled energy loss in thin germanium and silicon crystals for positive and negative 2–15-GeV/c pions, kaons, and protons. Phys Rev B **18**, 1039–1054

Feldman L.C., Mayer J.W. and Picraux S.T. (1982): Materials Analysis by Ion Channeling. Academic Press, New York

Finnemann J. (1968): En redegørelse for resultaterne af beregninger over spredning af elektroner med lav energi på afskærmede Coulombfelter. Thesis under supervision of J. Lindhard, Physics Institute, University of Aarhus

Forster J.S., Andersen J.U., Beene J.R., Broude C., Chevallier J., Galindo-Uribarri A., Gomez del Campo J., Karamian S.A., Krause H.F., Radford D., Uguzzoni A. and Vane C.R. (2006): to be published

Gärtner K., Hehl K. and Schlotzhauer G. (1984): Axial dechanneling: II. Point defects. Nucl Instrum Methods B **4**, 55–62

Gemmell D.S. (1974): Channeling and related effects in the motion of charged particles through crystals. Rev Mod Phys **46**, 129–227

Gibson W.M. (1975): Blocking measurements of nuclear decay times. Ann Rev Nucl Sci **25**, 465–508

Grüner F., Assmann W., Bell F., Schubert M., Andersen J.U., Karamian S., Bergmaier A., Dollinger G., Görgens L., Günther W. and Toulemonde M. (2003): Transverse cooling and heating in ion channeling. Phys Rev B **68**, 174104-1 to 12

Guanere M., Sillou D., Spighel M., Cue N., Gaillard M.J., Kirsch R.G., Poizat J.-C., Remmillieux J., Berman B.L., Cattillon P., Roussel L. and Temmer G.M. (1982): Sharp-line and broad-continuum radiation from electrons channeled in diamond. Nucl Instrum Methods **194**, 225–228

Hau L.V. and Andersen J.U. (1993a): Channeling radiation beyond the continuum model: The phonon "Lamb shift" and higher-order corrections. Phys Rev A **47**, 4007–4032

Hau L.V. and Andersen J.U. (1993b): Line shifts of channeling radiation from MeV electrons. Rad Eff Def Sol **25**, 75–80

Hau L.V., Lægsgaard E. and Andersen J.U. (1990): Thermal vibrations in Si studied by channeling-radiation spectroscopy. Nucl Instrum Methods Phys Res B **48**, 244–247

Hofsäss H. (1996): Emission channeling. Hyperfine Interactions **97-8**, 247–283

Karamian S.A., Forster J.S., Andersen J.U., Assmann W., Broude C., Chevallier J., Geiger J.S., Grüner F., Khodyrev V.A., Malaguti F. and Uguzzoni A. (2003): Fission lifetimes of Th nuclei measured by crystal blocking. Eur Phys J A **17**, 49–56

Kennedy E.F., Bech Nielsen B. and Andersen J.U. (1992): Planar channeling dips in backscattering yield. Nucl Instrum Methods in Phys Res B **67**, 236–240

Krause H.F. and Datz S. (1996): Channeling heavy ions through crystalline lattices. Adv At Mol Opt Phys **37**, 139–180

Kumakhov M.A. (1976): On the theory of electromagnetic radiation of charged particles in a crystal. Phys Lett A **57**, 17–18

Lervig Ph., Lindhard J. and Nielsen V. (1967): Quantal treatment of directional effects for energetic charged particles in crystal lattices. Nucl Phys A **96**, 481–504

Lindhard J. (1965): Influence of crystal lattice on motion of energetic charged particles. Kgl Dan Vid Selsk Mat Fys Medd **34, no. 14**, 1–64

Lindhard J. and Nielsen V. (1971): Studies in statistical dynamics. Kgl Dan Vid Selsk Mat Fys Medd **38, no. 9**, 1–42

Malyshevsky V.S. (2005): Statistical theory of charge state distributions of channeled heavy ions. Phys Rev B **72**, 094109-1 to 10

Mayer J.W., Eriksson L. and Davies J.A. (1970): Ion Implantation in Semiconductors. Academic Press, New York

Moak C.D., Datz S., Crawford O.H., Krause H.F., Dittner P.F., Gomez del Campo J., Biggerstaff J.A., Miller P.D., Hvelplund P. and Knudsen H. (1979): Resonant coherent excitation of channeled ions. Phys Rev A **19**, 977–993

Nakai Y., Ikeda T., Kanai Y., Kambara T., Fukinishi N., Komaki K., Kondo C., Azuma T. and Yamazaki Y. (2005): Resonant coherent excitation of 2s electron of Li-like Fe ions to the $n = 3$ states. Nucl Instrum Methods Phys Res B **230**, 90–95

Okorokov V.V. (1965): The coherent excitation of nuclei moving through a crystal. Yad Fiz **2**, 1009 [Sov J Nucl Phys **2**, 719 (1966)]

Oshiyama T. and Mannami M. (1981): Diffusion models of dechanneling of energetic H^+-ions in single crystals. Phys Lett **81A**, 43–46

Pedersen M.J., Andersen J.U. and Augustyniak W.M. (1972): Channeling of positrons. Rad Effects **12**, 47–52

Sørensen A.H. and Uggerhøj E. (1987): Channeling and channeling radiation. Nature **325**, 311–318

Sørensen A.H. and Uggerhøj E. (1989): Channeling, radiation and applications. Nucl Sci Appl **3**, 147–205

Tulinov A.F., Kulikauskas V.S. and Malov M.M. (1965): Proton scattering from a tungsten single crystal. Phys Lett **18**, 304–307

Uggerhøj E. (1966): Orientation dependence of the emission of positrons and electrons from ^{64}Cu embedded in single crystals. Phys Lett **22**, 382–383

Uggerhøj E. and Andersen J.U. (1968): Influence of lattice structure on motion of positrons and electrons through single crystals. Can J Phys **46**, 543–550

Uggerhøj U.I. (2005): The interaction of relativistic particles with strong crystalline fields. Rev Mod Phys **77**, 1131–1171

Uguzzoni A., Gärtner K., Lulli G. and Andersen J.U. (2000): The minimum yield in channeling. Nucl Instrum Methods B **164–165**, 53–60

Penetration Phenomena at Relativistic Energies

U.I. Uggerhøj*

Department of Physics and Astronomy, University of Aarhus
DK-8000 Aarhus C, Denmark

Abstract

A number of different penetration phenomena for relativistic particles are presented. Included in the discussion are subjects like the Chudakov effect, nuclear size effect, heavy ion pair production and bremsstrahlung, fragmentation, nuclear-charge pickup, penetration in bent and straight crystals and formation zone effects such as the Landau–Pomeranchuk–Migdal effect and the Ternovskii–Shul'ga–Fomin effect.

Contents

1 Introduction **700**

2 Ionization Energy Loss **701**
2.1 Restricted Energy Loss 701
2.2 Density Effect – Fermi Plateau 702
2.3 Chudakov Effect 702
2.4 Ionization Energy Loss for Ions 704
2.4.1 Nuclear Size Effect 704
2.4.2 Free-Free Pair Production and Bremsstrahlung 705
2.4.3 Bound-Free Pair Production 705
2.5 Ionization Energy Loss for Channeled Ions 705

3 Fragmentation **707**
3.1 Nuclear-Charge Pickup 708
3.2 Some Remaining Puzzles and Problems 709

* E-mail: ulrik@phys.au.dk

4 Bent Crystals **710**
4.1 Critical Curvature 710
4.2 Bending of Particle Beams 710
4.3 Dechanneling 711
4.4 Model for Deflection Efficiency 711
4.5 Extraction of Particles 712
4.6 Some Remaining Puzzles and Problems 713

5 Radiative Energy Loss and Pair Production – Leptons and Photons **713**
5.1 Interactions in Electromagnetic Fields 713
5.2 Strong Field Effects 714
5.3 Formation Lengths 714
5.3.1 Classical Formation Length 714
5.3.2 Quantum Formation Length 715
5.4 Amorphous Targets 715
5.4.1 The Bethe–Heitler Yields 715
5.5 Radiation Emission and the LPM Effect in Amorphous Matter 717
5.6 Pair Production and the LPM Effect in Amorphous Matter 719
5.7 LPM Effects in Crystalline Matter 720
5.7.1 Radiation Emission and the LPM Effect in Crystalline Matter . . 722
5.7.2 Pair Production and the LPM Effect in Crystalline Matter 723
5.8 Thin Targets – Ternovskii–Shul'ga–Fomin Effect 724
5.9 Dielectric Suppression – Ter-Mikaelian Effect 725
5.10 Some Remaining Puzzles and Problems 725

6 Conclusion **726**

Acknowledgement **726**

References **726**

1. Introduction

A thorough understanding of penetration phenomena is essential to a wide range of applications, ranging from detector construction to semiconductor fabrication. In the present review, the attention is restricted to penetration phenomena for relativistic particles, i.e. particles for which the kinetic energy E exceeds the rest mass m. In this case, the Lorentz factor $\gamma = E/mc^2$ becomes significantly larger than unity, and stopping phenomena not observed at lower energies become relatively important. Two examples are nuclear charge pick-up mediated by a $\gamma n \to p\pi^-$ reaction through virtual photons and radiative energy loss or its "symmetric" counterpart, pair production.

The emphasis in this review will be on presenting in a short form the relevant modifications to standard formulae, with references given to sources where such effects were first derived or observed as well as to sources with more rigour, rather than full derivations of the formulae or detailed surveys of the experiments. In this connection, it is attempted to discuss the physics contents of the presented effects and an estimate of their relavance to other areas. The presentation is by no means exhaustive, but reflects the personal interests of the author.

2. Ionization Energy Loss

It is shown in a number of treatments (Sigmund, 2006; Yao et al., 2006; Jackson, 1975) that the energy loss owing to the ionization during penetration of a medium at high energies is given by the Bethe formula

$$-\frac{\mathrm{d}E}{\mathrm{d}x} = \frac{4\pi N Z_1^2 Z_2 e^4}{m\beta^2 c^2}\left(\frac{1}{2}\ln\frac{2mc^2\beta^2\gamma^2 T_{\max}}{I^2} - \beta^2 - \frac{\delta(\beta\gamma)}{2}\right), \tag{1}$$

where $Z_1 e$ is the charge of the projectile, $Z_2 e$ is the charge of the lattice nuclei, N the atomic density, I the ionization potential and $T_{\max} = 2mc^2\beta^2\gamma^2/(1 + 2\gamma m/M + (m/M)^2)$ is the maximum kinetic energy which can be transferred to a free electron of rest mass m in a single collision with a projectile of mass M and Lorentz factor $\gamma = 1/\sqrt{1-\beta^2}$ (Yao et al., 2006). The last term in Equation (1) is the density effect correction, to be discussed below.

2.1. Restricted Energy Loss

In a number of different experiments, it is not the energy loss of the penetrating particle that is of main interest, it is rather the energy *deposited* in the substance that is measured. Part of the energy loss suffered by the projectile may e.g. appear in the form of energetic knock-on electrons (electrons escaping the medium with high energy as a result of a binary collision with the projectile). This happens for instance when this – so-called restricted – energy loss is measured in a silicon surface-barrier detector. In this case, an equation similar to Equation (1) applies, but with $T_{\max}$ replaced by the smaller value T_{cut} (corresponding to the smallest energy sufficient for an electron to have a range of half the target thickness) and the second term in the square bracket, β^2, modified by a multiplier $(T_{\mathrm{cut}} + T_{\max})/2$. At relativistic energies, the restricted energy loss in e.g. silicon is $\simeq 330$ keV/mm for not too thick targets.

2.2. Density Effect – Fermi Plateau

As is also discussed in a number of excellent textbooks (Sigmund, 2006; Yao et al., 2006; Jackson, 1975), the Lorentz contraction of the electric field as seen from the target frame makes distant collisions more important at increasing energies. However, at sufficiently large distances, the medium acts as a dielectric, changing the electromagnetic field of the penetrating particle from its value in vacuum thus reducing the contribution from the distant collisions. At very high energies the replacement

$$\frac{\delta(\beta\gamma)}{2} \to \ln\frac{\hbar\omega_p}{I} + \ln(\beta\gamma) - \frac{1}{2} \tag{2}$$

in Equation (1) must be made (Yao et al., 2006), where ω_p is the plasma frequency. This replacement corresponds to a much slower rise of the stopping power with increasing energy than in the case without density effect.

2.3. Chudakov Effect

A considerable contribution to the ionization energy loss originates from large transverse distances, $b_q \simeq v/\omega_p$. If a penetrating assembly of separate charges are internally spaced less than this distance, the ionization is influenced by interference terms from the charges. This can be the case e.g. for an energetic hydrogen molecule that is stripped upon entry to the substance, but it can also be an effect present for a electron-positron pair where each participating charge screens the charge of the other as seen from the relevant distance b_q in the medium. The energy loss thus diminishes close to the creation point if the created pair is sufficiently energetic and therefore forward directed. This is the so-called Chudakov effect. Under the assumption that the created pair moves in a straight line after creation, the only angle that contributes to the separation is the emission angle $1/\gamma_p$. Thus, after having traversed a distance given by

$$l_s = \frac{\beta\hbar\omega}{mc\omega_p}, \tag{3}$$

the pair from a photon of energy $\hbar\omega$ would be separated by $b_q = v/\omega_p$.

This would result in a reduced restricted energy loss at distances smaller than about l_s from the creation vertex, due to internal screening. The result from the destructive interference term is a (restrictive) energy loss of the pair (Berestetskii and Geshkenbain, 1956; Akhiezer and Shul'ga, 1996)

$$\frac{\mathrm{d}E_\pm}{\mathrm{d}t} = 2\frac{\alpha\hbar\omega_p^2}{\beta}\left[\ln\frac{\sqrt{2mc^2T_{(\mathrm{cut})\,\max}}}{\hbar\omega_p} - K_0\left(\frac{s\omega_p}{\beta c}\right)\right], \tag{4}$$

where $K_0(x)$ is the modified Bessel function of the second kind with order zero and s is the transverse separation of the pair which exceeds the longitudinal separation by a factor γ. As usual, the plasma frequency is given from $\omega_p^2 = 4\pi N Z_2 e^2/m$ where NZ_2 is the number density of electrons.

For small separations s the modified Bessel function can be approximated by $K_0(x) \simeq \ln(1/x)$ which results in

$$\frac{\mathrm{d}E_\pm}{\mathrm{d}t} \simeq 2\,\frac{\alpha\hbar\omega_p^2}{\beta}\ln\left(s\sqrt{2mc^2T_{\mathrm{cut}}}\right) \tag{5}$$

at small distances from the vertex. For large separations the modified Bessel function tends exponentially to zero, corresponding to loss of effective internal screening, and twice the standard expression for the stopping power at high speed in a Fermi gas, see e.g. Sigmund (2006, equation (5.165)), is retrieved from Equation (4).

In principle, in order to convert from internal separation s to traversed distance x, the emission angle $y_e = x/\gamma_p$ and multiple Coulomb scattering (Yao et al., 2006) contributions

$$y_m = \sqrt{\frac{2}{3}}x\theta_0 = \sqrt{\frac{2}{3}}x\,\frac{13.6\ \mathrm{MeV}}{\beta cp}\sqrt{\frac{x}{X_0}}\left(1 + 0.038\ln\frac{x}{X_0}\right) \tag{6}$$

must be added. However, since the multiple scattering is affected by the internal screening as well, this contribution is usually neglected.

Figure 1 shows a calculation of the relative reduction in (restricted) energy loss during the penetration of a gold foil. Clearly, according to Equation (3), foils with smaller plasma frequencies would be preferable, but since pair creation is roughly proportional to Z_2^2 it is advantageous to use high-Z materials, of which gold is a good choice because of its structural properties. There have been a few measurements of the Chudakov effect from cosmic ray tracks in emulsions (Perkins, 1955; Jain, 1962) – about a dozen in total – and at least one proposal for a measurement in an accelerator environment (Zielinski, 1985). However, most of such proposals seem to forget the inherent noise contribution from thin solid-state detectors, originating from the capacitance.

A closely related effect has recently been calculated for Cherenkov radiation emission from e^+e^- pairs in the vicinity of the creation point (Mandal et al., 2005). This internal screening effect may affect decisively the behaviour of the Cherenkov emission in neutrino-induced electromagnetic showers.

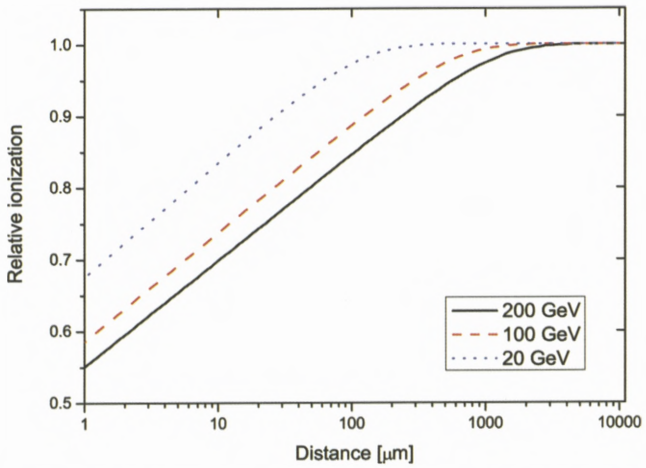

Figure 1. The relative reduction in (restricted) energy loss during the penetration of a gold foil as a function of penetration length for 200, 100 and 20 GeV electron-positron pairs.

2.4. Ionization Energy Loss for Ions

2.4.1. *Nuclear Size Effect*

Once the de Broglie wavelength of the electron impinging on the projectile nucleus – as seen from the frame of the penetrating particle – becomes of the order of the nuclear size or smaller, the stopping force diminishes. Alternatively, expressed as in the original paper by Lindhard and Sørensen (1996), once the angular momentum corresponding to an encounter with the nucleus γmcR exceeds $\hbar/2$ where $R = 1.2 \text{ fm} \cdot A^{1/3}$ is the nuclear radius, A being the projectile mass number, the phase shift compared to the point nucleus case becomes modified. These conditions translate into a Lorentz factor

$$\gamma = \frac{\lambda\!\!\!^{-}}{2R} \simeq \frac{160}{A^{1/3}}, \tag{7}$$

beyond which the nuclear size becomes important for the stopping. Thus for $\gamma \gtrsim 27$, one can expect the nuclear size for lead to be significant, and an accurate evaluation shows that in the case of uranium, the influence of the finite nuclear size on the stopping becomes 1% already at $\gamma = 10$ (Lindhard and Sørensen, 1996). Even stronger effects from the finite nuclear size is expected in straggling, since it originates from close collisions. However, straggling measurements performed on relativistic ion beams have so far been completely dominated by multiple Coulomb scattering, such that firm conclusions were excluded (Datz et al., 1996).

2.4.2. *Free-Free Pair Production and Bremsstrahlung*
Apart from the nuclear size effect in stopping, there remains the possibilities of the penetrating ion producing bremsstrahlung and/or pair creation. Both of these processes may contribute to the slowing down of the projectile and have been treated theoretically by Sørensen (2003, 2005). In Sørensen (2003) it is shown that the discrepancy between measured values (Datz et al., 1996) and theoretical values including the nuclear size effect (Lindhard and Sørensen, 1996) is likely to be due to energy loss originating from pair production in the screened nuclear field. In Sørensen (2005) it is shown that the condition that the projectile stays intact during the slowing down process, is in fact a very restrictive one. It limits the bremsstrahlung emission which in this treatment amounts to a few permille of the stopping power related to pair production. Thus, for bare lead on a lead target, Sørensen found that the stopping force related to pair production becomes dominant compared to the ionization contribution for γ exceeding a few 10^3, with the bremsstrahlung channel constantly being much smaller.

2.4.3. *Bound-Free Pair Production*
A closely related effect appears in electron capture by relativistic heavy ions where one of the contributing channels is bound-free pair production instead of free-free as above. This effect is of particular interest to the heavy ion collider community since it may limit the lifetime of stored heavy ion beams – an ion capturing an electron no longer has the correct charge per momentum to stay within the machine acceptance.

There are three mechanisms for the ion to capture an electron: Radiative electron capture (REC), non-radiative electron capture (NRC) and electron capture from pair production (ECPP). In ECPP, the pair is created in the strong electromagnetic field of the interaction with the target nucleus, the electron is captured, while the positron is lost. The REC and NRC processes become of less importance than ECPP for projectiles with $\gamma \gtrsim 100$. Measurements have been performed of the cross section for ECPP summed over all final nl states (Krause et al., 2001). Surprisingly, these measurements agree very well with theoretical values for capture to the $1s$ state only, although capture to higher states are expected to yield a $\simeq 30\%$ increase. This discrepancy is not understood.

2.5. Ionization Energy Loss for Channeled Ions

For channeled particles (the channeling phenomenon is introduced in more detail below), a path-dependent average energy loss for relativistic particles was calculated by Esbensen and Golovchenko (1978)

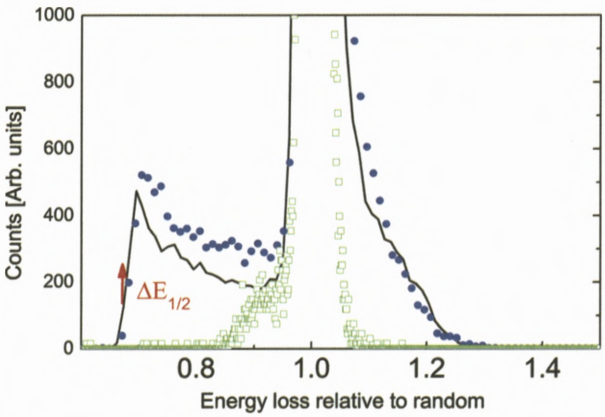

Figure 2. Energy-loss distribution for 33 TeV fully stripped lead nuclei penetrating a silicon single crystal along the (110) plane. The full-drawn curve represents the simulated values for energy loss in this orientation, the filled dots the results for the oriented crystal and the open squares the results for the randomly oriented crystal (Møller et al., 2001). The minimum energy loss for channeled particles $\Delta E_{1/2}$ is indicated by the arrow.

$$\frac{\mathrm{d}E}{\mathrm{d}x}(\mathbf{b}) = \frac{2\pi e^4 N}{mv^2} Z_1^2 \left[\big(Z_2 + Z_2(\mathbf{b})\big) \ln \frac{2mv^2\gamma^2}{I} + C(\mathbf{b}) \right], \tag{8}$$

where $NZ_2(\mathbf{b})$ is the local electron density at position $\mathbf{b}$ in the transverse plane and $C(\mathbf{b})$ is a velocity-independent term dependent on the local electron density at position b. The terms $(Z_2 + Z_2(b))\beta^2$ and $Z_2\delta$ were added in the square parenthesis to include relativistic effects (Esbensen et al., 1978). Also the reduction in the well-defined leading edge $\Delta E_{1/2}$ of the energy-loss distribution for channeled particles was calculated to be (Esbensen et al., 1978)

$$\left(\frac{\mathrm{d}E}{\mathrm{d}x}(\mathbf{b})\right)_{1/2} = \left(\frac{\mathrm{d}E}{\mathrm{d}x}(\mathbf{b})\right) + \frac{2\pi e^4 N}{mv^2} Z_1^2 Z_2(\mathbf{b}) \big[-1.18 + \beta^2 + \ln \kappa(\mathbf{b}) \big], \tag{9}$$

where

$$\kappa(\mathbf{b})) = \frac{2\pi e^4 N}{mv^2} Z_1^2 Z_2(\mathbf{b}) \frac{t}{T_{\max}}. \tag{10}$$

In Figure 2 the energy-loss distribution is shown for 33 TeV fully stripped lead nuclei penetrating a silicon single crystal along the (110) plane. The single crystal is acting as an active target, measuring the restricted energy loss for the channeled and above-barrier (random) particles. The full-drawn curve represents the simulated values for energy loss in this orientation, the filled dots the results

for the oriented crystal and the open squares the results for the randomly oriented crystal (Møller et al., 2001). From the results of the simulation, split into transverse energy components, it is shown that the right-hand edge corresponding to energy loss above that of the random orientation, originates from transverse energies close to the barrier height, 20–25 eV. Conversely, the left-hand edge, corresponding to energy losses approaching 60% of that of the random orientation, stems from ions channeled deep in the potential well, 0–5 eV transverse energy, as expected (Møller et al., 2001). The minimum energy loss for channeled particles $\Delta E_{1/2}$ is well described by the theory developed by Esbensen and coworkers (Esbensen et al., 1978; Esbensen and Golovchenko, 1978), as indicated by the arrow in Figure 2.

For the channeled ions, close encounter processes are heavily suppressed and the nuclear size effect as well as pair production are not expected to play a significant role.

3. Fragmentation

In order to facilitate an efficient design of a collimation system for the CERN Large Hadron Collider (LHC) operating as an ion-collider, it is necessary to test nuclear fragmentation models in a wide range of masses and energies of colliding nuclei. This must be done to make the foundation for an extrapolation to higher beam energies as solid as possible and thus reduce the likelihood of e.g. superconducting magnet quench as a result of interception of fragments. In comparison to the LHC operating with protons, collimation of heavy ions in the LHC is a complex task (Jowett et al., 2003). The reason for this is the traditional division into primary and secondary collimators where the primary in the case of protons almost exclusively acts as a scatterer and the secondary intercepts the scattered particles (Jeanneret, 1998). In the case of ions, the primary collimator to a large extent generates fragments, the motion and distribution of which are much less well known than multiple scattering distributions. Thus, systematic experimental tests of fragmentation models over a wide range of beam energies, targets and/or projectiles are needed to determine the accuracy of such models. Fragmentation and nuclear-charge pick-up reactions for ultrarelativistic Pb in a variety of targets have been investigated. Predictions of several fragmentation models (Scheidenberger et al., 2002, 2004) compared quite well to the experimental data.

The data and calculations for indium shown in Figure 3 show a nice agreement in shape as well as for the absolute value. The cross sections for nuclear-charge pickup channel forming $_{50}$Sn nuclei were also measured and calculated. This

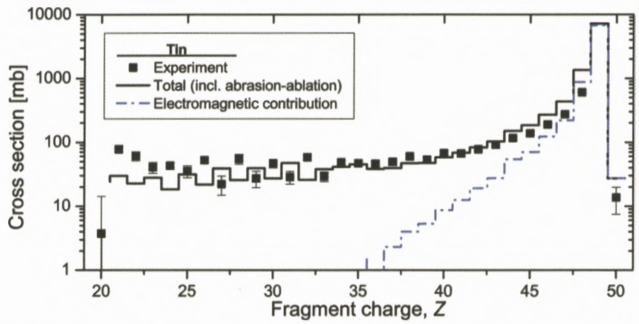

Figure 3. Fragmentation cross sections for ultrarelativistic In on Sn. The filled squares represent the measured values, the full line is the total expected cross section based on the abrasion-ablation model including the electromagnetic contribution and the dash-dotted line is the electromagnetic contribution alone (Uggerhøj et al., 2005b).

process is attributed to the electromagnetic production of a negative pion by an equivalent photon as will be discussed in the next section.

3.1. Nuclear-Charge Pickup

Many experiments have found evidence for electromagnetic processes in reaction channels, where either the fragment mass A and/or the fragment atomic number Z were lower than those of the incoming projectile. Those channels are by far the dominating ones due to the large number of conceivable (hadronic and electromagnetic) processes, which all lead to a reduction in Z and/or A (such as knockout, sequential breakup, evaporation, etc.). This has been discussed in the section on fragmentation. In rare cases, however, the nuclear charge Z of the projectile is increased, a process which in the following will be called nuclear charge pickup, $\Delta Z = +1$. Such reactions can be explained at low energies, below the Fermi energy in nuclei, by proton transfer through the nuclear overlap zone. At relativistic energies, however, the Fermi spheres of projectile and target are never overlapping, which prevents transfer of, e.g., a target proton to the projectile. Instead, one process that may lead to nuclear charge pickup is Δ-resonance formation and decay in nucleon-nucleon collisions. For intermediate energies, $\gamma \lesssim 10$, this is the most likely elementary process in which a projectile neutron can be converted into a proton, e.g., by $n \to \Delta^0 \to p + \pi^-$ with subsequent absorption of the proton in the projectile and emission of the π^-. At ultrarelativistic energies, $\gamma \gtrsim 100$, a different mechanism of nuclear-charge-changing interactions between heavy ions becomes significant. This channel opens, because the maximum equivalent photon energy, $E_{\max} = \gamma\hbar c/b_c$, exceeds the pion production

threshold of 140 MeV, b_c being the minimum impact parameter in electromagnetic interactions. In collisions using 158 GeV per nucleon Pb projectiles, the maximum equivalent photon energy exceeds the pion production threshold by factors of 20 to 40, depending on the target. A π^- produced in such a reaction, $\gamma n \rightarrow \pi^- p$, may be emitted while the associated proton may be captured to form a residual nucleus with $\Delta Z = +1$ compared to the projectile. In general, this resulting nucleus is highly excited and is likely to deexcite by neutron evaporation. Measurements with 158 GeV per nucleon Pb (Scheidenberger et al., 2002, 2004) and 158 GeV per nucleon In projectiles (Uggerhøj et al., 2005b) were performed, yielding results in good agreement with elaborate calculations for the nuclear charge pick-up, based on the Weizsäcker–Williams method of virtual quanta.

3.2. Some Remaining Puzzles and Problems

For the subject of ionization energy loss, an experimental proof of the Chudakov effect in an accelerator based beam is still lacking. With cosmic ray investigations, the total number of observed suppressed events is less than about a dozen. Another interesting question is if the straggling is affected by the nuclear size. However, as discussed above, the competing mechanism of beam broadening – multiple Coulomb scattering – has so far prohibited trustworthy conclusions to be drawn from data. On the other hand, there is nothing fundamental prohibiting such a measurement which may also shed light on the explanation of the remaining small discrepancy between energy loss data and theory including the nuclear size. Concerning the theory of the nuclear size effect, a more accurate potential than the square well potential for the nuclear term (like a Woods–Saxon potential) is not expected to lead to any significant alteration of the calculated values for the nuclear size effect. The important distance in this effect is the (reduced) Compton wavelength, and small changes on the scale of nuclear distances, about two orders of magnitude smaller, will be almost completely insignificant.

For the subject of fragmentation of heavy ions, the bremsstrahlung spectrum from a heavy ion has not yet been observed nor have positrons with energies above 10 MeV. Is the pair production the origin of the discrepancy between experimental values for the energy loss of heavy ions and theory including the nuclear size effect as Sørensens calculations indicate?

For ECPP the experiment includes capture to all states, whereas theoretical values are calculated for capture to the 1s state only. The convincing agreement between theory and experiment may therefore be fortuitous.

4. Bent Crystals

The guidance of channeled particles in a crystal persists even if the crystal is slightly bent, such that the particle may be deviated from its original direction of motion as in a magnetic dipole. Since the fields that are responsible for this deviation are the extremely strong fields present near the lattice nuclei, the corresponding bending strength can reach a magnitude of the equivalent of several thousand Tesla. It is therefore possible to design a crystalline "kicker" with an equivalent deflection power of 10 Tm by use of a device that is of the order 0.1 m long.

In Baurichter et al. (2000) a concise introduction to the field is given along with a summary of the results obtained at the CERN SPS. In these texts extensive reference lists are included. For a short introduction to the field, see Møller (1995).

4.1. Critical Curvature

There is a certain curvature at which the particles will dechannel in a bent crystal due to the centrifugal force that tends to increase the interactions with the lattice nuclei. Estimating this curvature, it was found in the late seventies that as long as the curvature fulfills the condition:

$$\kappa \leq \kappa_c = \frac{\pi Z_1 Z_2 e^2 N d_p}{pv} \tag{11}$$

the charged particle can channel in a bent crystal. The minimum radius of curvature, $R_c = 1/\kappa_c$, at 7 TeV is 11.5 and 5.48 m for the (110) planes in Si and Ge, respectively. As κ_c is approached a rising fraction F, the so-called dechanneling fraction, is lost from the channeled states and is therefore unable to follow the curvature through the whole crystal.

4.2. Bending of Particle Beams

In consideration of the strong fields in a crystal it is understandable that a crystal has a superb bending power. One can calculate the equivalent magnetic field, $B = \kappa p/(Z_1 e)$, corresponding to the critical curvature κ_c as:

$$B_c[\mathrm{T}] = 1.5 \cdot 10^3 Z_2 \cdot n d_p \, [\text{Å}^{-2}]. \tag{12}$$

This critical field is $B_c \simeq 2500$ Tesla for a silicon crystal. Clearly, Equation (12) shows that a high-Z material is preferable for deflection.

4.3. Dechanneling

The length, L_D, over which a planar channeled beam of protons in a straight crystal has been reduced to the fraction 1/e of the initial intensity by transfer to non-channeled states by multiple scattering is given for $\gamma \gg 1$ by:

$$L_D = \frac{256}{9\pi^2} \frac{pv}{\ln(2\gamma mc^2/I_Z) - 1} \frac{a_s d_p}{Z_1 e^2}, \tag{13}$$

where I_Z is the ionisation potential. Equation (13) has been shown to be in good agreement with measured values of L_D at room temperature over a fairly wide range of energies. At 7 TeV, the values of L_D for Si and Ge are 2.9 m and 2.5 m which by far exceeds the dimensions of the crystals proposed for use. It appears from Equations (11) and (13) that heavy ions of the same momentum per charge pv/Z_2 to a first approximation (i.e. disregarding reactions that may probe the internal structure such as fragmentation) should behave like protons in bent crystals. Since heavy, fully stripped ions are composite particles of high charge a number of additional effects may appear, such as electromagnetic dissociation and/or nuclear interactions. In the restframe of the incident ion with the Lorentz factor $\gamma \simeq 160$ the extremely strong, crystal electric fields $\mathcal{E} \lesssim 10^{11}$ V/cm are boosted to very high values. It is thus not *a priori* excluded that electromagnetic dissociation for example through a giant dipole resonance is significant (Fusina and Kimball, 1987; Pivovarov et al., 1990). The fundamental frequency in the ion restframe for interaction with the lattice is $\omega_0 = 2\pi\gamma\beta c/d$ which is of the order 1 MeV for a characteristic lattice spacing $d \simeq 2$ Å.

4.4. Model for Deflection Efficiency

Since the straight crystal dechanneling favours small crystal lengths and the curvature favours long crystal lengths (for fixed angle), there is an optimum crystal length which depends on the angle and which is only weakly dependent on energy when the length is expressed in units of the dechanneling length. Given $\eta_F = F_D\kappa_c/\kappa \simeq 3$, where F_D is the dechanneling fraction, the approximate deflection efficiency is (Baurichter et al., 2000)

$$\varepsilon_{\text{appr.}} = \varepsilon_S \cdot e^{-L/L_D} \cdot \left(1 - \eta_F \frac{\theta}{(L/L_D)L_D\kappa_c}\left(1 + 2\frac{L}{L_D}\right)\right), \tag{14}$$

where

$$L_D\kappa_c = \frac{256}{9\pi} \frac{Z_2 N d_p^2 a_s}{\ln(2\gamma mc^2/I)} \tag{15}$$

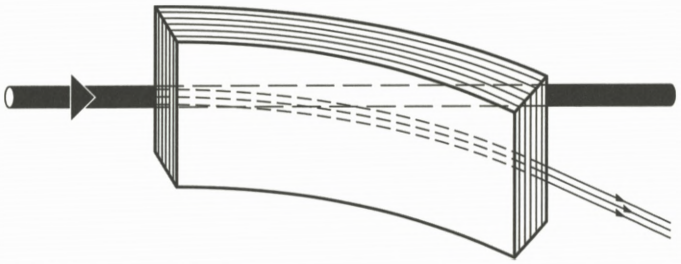

Figure 4. A schematical drawing of extraction of particles from the halo of a circulating beam by means of a bent crystal. From Møller (1995).

is only logarithmically dependent on energy and is 0.251 and 0.451 for Si and Ge along (110) at 7 TeV. Here L denotes the crystal length and the crystal is assumed to have a uniform curvature.

Equation (14) has a maximum at the optimum length

$$\frac{L}{L_{\mathrm{D}}} = -\frac{1+\sqrt{1-4\big(2-(L_{\mathrm{D}}\kappa_c/\eta_F\cdot\theta)\big)}}{2\big(2-(L_{\mathrm{D}}\kappa_c/\eta_F\cdot\theta)\big)} \tag{16}$$

with an efficiency value at this maximum of

$$\varepsilon_{\mathrm{max}}^{\mathrm{appr.}} \simeq \varepsilon_{\mathrm{S}}\left[\left(1-\sqrt{\frac{\eta_F\cdot\theta}{L_{\mathrm{D}}\kappa_c}}\right)^2 - 2\frac{\eta_F\cdot\theta}{L_{\mathrm{D}}\kappa_c}\left(1-\sqrt{\frac{\eta_F\cdot\theta}{L_{\mathrm{D}}\kappa_c}}\right)\right]. \tag{17}$$

As expected, heavy ions are deflected with equal efficiencies for the same momentum per charge – nuclear and electromagnetic interactions play a very minor role only (Uggerhøj et al., 2005a).

4.5. Extraction of Particles

Multi-pass extraction schemes yield extraction efficiencies that are higher than the single-pass extraction for beam divergencies larger than the planar critical angle. The reason is that particles that encounter the crystal and are not channeled will not necessarily be lost and may be extracted on a later turn in the machine. Furthermore, parameters of the accelerator lattice such as e.g. the betatron amplitude function that determines the beam size and divergence, become important for the extraction efficiency.

An actual implementation of a crystalline extraction device – in principle as shown in Figure 4 – at the coming LHC at CERN has recently been proposed

(Uggerhøj and Uggerhøj, 2005). This would enable a nearly continuous beam of 7 TeV protons extracted towards the LHC beam dump with an intensity of $\simeq 5{\cdot}10^8$ per second and a horizontal emittance as low as 20 μm·μrad.

4.6. Some Remaining Puzzles and Problems

The field of relativistic particle deflection in bent crystals is by now rather mature, with – in the opinion of the author – few big puzzles or questions left. For an application, though, the radiation sensitivity of the deflection process for heavy ions has never been investigated, while it is known that deterioration does not happen in high energy proton beams until a fluence of $10^{20}/\text{cm}^2$. Most of the other aspects of the phenomenon are well described by the model calculations mentioned or by more elaborate simulations.

5. Radiative Energy Loss and Pair Production – Leptons and Photons

5.1. Interactions in Electromagnetic Fields

When passing matter, a photon can convert into an electron-positron pair in the electromagnetic field of a nucleus or a target electron. The presence of the external field is required to conserve energy and momentum in the creation process. Likewise, radiation emission can take place when a charged particle interacts with the external field.

By crossing symmetry pair production and radiation emission are two connected examples of the same physical process. One may for instance consider turning the Feynman diagram for bremsstrahlung a quarter of a turn to obtain the (simplified) diagram for pair production. Therefore the descriptions of the two processes are closely connected and e.g. their total cross sections differ only by a factor 7/9 due to different kinematic properties in the final state.

The radiation from relativistic particles is mainly propagating within a narrow cone of width $1/\gamma$ along the forward direction of the emitting particle. Based on the same mechanism, a pair created by a high energy photon is typically moving inside an angle $1/\gamma_p$ to the direction of the initial photon where γ_p is understood as $\hbar\omega/mc^2$. This typical value is of interest in connection with formation lengths to be discussed later.

In 1955, Dyson and Überall suggested the increase of bremsstrahlung emission for electrons penetrating e.g. a lead crystal close to a crystalline direction, compared to incidence along a random direction. This is in some sense a precursor to the strong field theory discussed below, since contrary to the following coherence theories, the enhancement along crystallographic directions was predicted to be

significantly larger than one. Shortly after their initial discovery, the theory of coherent bremsstrahlung and coherent pair production, was developed, see e.g. Palazzi (1968).

5.2. Strong Field Effects

At sufficiently high energies, however, a new phenomenon arises: strong field effects. The reason for this new behaviour at high energies can be seen as the possibility of achieving an enormously high field in the restframe of the emitting or produced particle. Emission and conversion probabilities can be calculated in this frame where the strong crystalline fields are Lorentz-boosted by γ and therefore become comparable to or even stronger than the critical field $\mathcal{E}_0 = m^2c^3/e\hbar = 1.32 \cdot 10^{16}$ V/cm. As Lindhard has phrased it: "[The electric forces on a channeled, relativistic electron in a single crystal has] an effect simulating that of an exceedingly large magnetic field of slowly varying magnitude" (Lindhard, 1991). Under small angles of incidence to a crystal, the strong electric fields of the nuclear constituents add coherently in the continuum approximation. Thus, a macroscopic, continuous field with a peak value of the order $\mathcal{E} \simeq 10^{11}$ V/cm is obtained. Therefore, in the restframe of an ultrarelativistic electron with a Lorentz factor of $\gamma \simeq 10^5$, the field encountered becomes comparable to the critical (or Schwinger-) field, $\mathcal{E}_0 = m^2c^3/e\hbar = 1.32 \cdot 10^{16}$ V/cm, corresponding to a magnetic field $B_0 = 4.41 \cdot 10^9$ T. The incident particle moves in these immensely strong fields over distances up to that of the crystal thickness, i.e. up to several mm. Since the quantity $\gamma\mathcal{E}/\mathcal{E}_0$ is a relativistic invariant, the behaviour of charged particles in strong fields as $\mathcal{E}_0$ can be investigated by use of ultrarelativistic electrons in strong crystalline fields. An introduction to these "strong field effects" can be found in Sørensen (1991) and Uggerhøj (2005).

5.3. Formation Lengths

As first discovered by Ter-Mikaelian, it takes relatively long time and therefore long distance for an energetic electron to create a photon. The interactions of the electron over this "formation zone" may affect the radiation spectrum destructively or constructively.

5.3.1. *Classical Formation Length*

One approach to derive the formation length, is to consider the photon "formed" by the time it takes for a photon to advance with respect to the electron by one

reduced wavelength, $\lambda/2\pi$ and by the corresponding distance of travel of the electron, l_f:

$$\frac{l_f}{v} = \left(l_f + \frac{\lambda}{2\pi}\right)\frac{1}{c}, \tag{18}$$

which for $v = \sqrt{(1 - 1/\gamma^2)}c \simeq c$ yields

$$l_f = \frac{2\gamma^2 c}{\omega}, \tag{19}$$

where v is the speed of the electron, c the speed of light and $\gamma = E/mc^2$ the Lorentz factor related to the energy of the electron, E, and its rest mass, m. Alternative methods – leading to the same result – can be found in Uggerhøj (2005).

5.3.2. *Quantum Formation Length*

In quantum theory, taking the recoil imposed on the electron by the emitted photon into account, the formation length can be calculated by use of the minimum longitudinal momentum transfer to the nucleus, $q_\parallel = p - p_f - \hbar\omega/c$. The photon propagates in a medium with velocity c/n_r and momentum $\hbar k_r = \hbar n_r k$ where $n_r = \sqrt{\varepsilon(\omega)} = \sqrt{1 - \omega_p^2/\omega^2}$ is the index of refraction, $\varepsilon(\omega)$ the dielectric function and $\omega_p = \sqrt{4\pi n Z e^2/m}$ the plasma frequency. By the uncertainty relation $l_f = \hbar/q_\parallel$ where p and p_f denote the momentum of the electron before and after the radiation event, respectively (Ter-Mikaelian, 1972) the formation length can be obtained.

The formation length under these conditions becomes:

$$l_f = \frac{2\gamma^2 c}{\omega^*} \quad \text{with} \quad \omega^* = \omega \cdot \frac{E}{E - \hbar\omega} \simeq \omega, \tag{20}$$

where $\hbar\omega$ is the energy of the photon.

5.4. Amorphous Targets

5.4.1. *The Bethe–Heitler Yields*

The cross section for radiation emission in an amorphous foil can be found from the Bethe–Heitler formula (Bethe and Heitler, 1934; Heitler, 1954) which is derived in perturbative QED and is approximately given by:

$$\frac{\mathrm{d}\sigma}{\mathrm{d}\hbar\omega} = \frac{16}{3} Z_2^2 \alpha r_e^2 \frac{1}{\hbar\omega}\left(1 - \frac{\hbar\omega}{E} + \frac{3}{4}\left(\frac{\hbar\omega}{E}\right)^2\right)\ln(183 Z_2^{-1/3}), \tag{21}$$

where $r_e = e^2/mc^2 = \alpha\lambda\!\!\!^{-} = \alpha^2 a_0$ is the classical electron radius, $\alpha = e^2/\hbar c$ the fine-structure constant, a_0 the Bohr radius and the logarithmic factor indicates complete screening, $\gamma \gg 1$. From this and the number density of atoms, n, the radiation length, X_0, can be found

$$\frac{1}{X_0} = N \int_0^E \frac{\hbar\omega}{E} \frac{\mathrm{d}\sigma}{\mathrm{d}\hbar\omega} \mathrm{d}\hbar\omega = 4Z_2^2 \alpha N r_e^2 \ln(183 Z_2^{-1/3}). \tag{22}$$

An incident particle statistically loses all but 1/e of its energy by emission of bremsstrahlung in passing a foil of thickness X_0. The radiation probability for emission with an energy between E and E_0 is found as

$$W = 1 - \exp(-\Delta t \cdot W_0) \tag{23}$$

with

$$W_0 = \int_{E_0}^E N \cdot \mathrm{d}\sigma \simeq \frac{4}{3}\frac{1}{X_0}\left(\ln\frac{E}{E_0} - \frac{5}{8}\right), \tag{24}$$

where Δt is the thickness of the foil where the radiation takes place and the approximation for W_0 is valid when the incident energy is much larger than the cut-off due to acceptance, $E \gg E_0$.

From W the probability of emitting two photons or more is calculated for $E \gg E_0$ according to a Poisson-distribution

$$f(N_\gamma) = \frac{p^{N_\gamma} e^{-p}}{N_\gamma!}, \tag{25}$$

where $p = \Delta t W_0(E, E_0)$ and N_γ is the number of photons.

In the above approach, the radiation produced by scattering off the target electrons has been neglected since this term is proportional to Z_2 and is small compared to Equation (21). A more accurate expression is thus obtained by replacing Z_2^2 by $Z_2(Z_2 + 1)$, in good agreement with data (Tsai, 1974).

For pair production, the Bethe–Heitler theory (Heitler, 1954) gives the number of pairs created per unit length, $N_p = N\sigma$, per relative energy of the electron/positron, $\xi_\pm = E_{e^\pm}/\hbar\omega$ as approximately:

$$\frac{\mathrm{d}N_p}{\mathrm{d}\xi_\pm} = \frac{16}{3} Z_2^2 \alpha r_e^2 N \left(\frac{3}{4} - \xi_\pm + \xi_\pm^2\right) \ln(183 Z_2^{-1/3}) \tag{26}$$

or by use of Equation (22) simply

$$\frac{\mathrm{d}N_p}{\mathrm{d}\xi_\pm} = \frac{1}{X_0}\left(\xi_+^2 + \xi_-^2 + \frac{2}{3}\xi_+\xi_-\right) \tag{27}$$

with the total yield

$$N_p = \int_0^1 \frac{\mathrm{d}N_p}{\mathrm{d}\xi_\pm}\,\mathrm{d}\xi_\pm = \frac{7}{9}\frac{1}{X_0}\,. \tag{28}$$

Note here the similarity between the cross sections for radiation emission and pair production, Equations (21) and (26), originating from the crossing symmetry of the processes.

The length over which a particle statistically scatters an RMS angle $1/\gamma$ in an amorphous material due to multiple Coulomb scattering is given approximately by

$$l_\gamma = \frac{\alpha}{2\pi} X_0, \tag{29}$$

where α is the fine-structure constant and X_0 the radiation length.

5.5. Radiation Emission and the LPM Effect in Amorphous Matter

The study of the Landau–Pomeranchuk–Migdal (LPM) effect was spurred by the finding of Ter-Mikaelian, that photon emission by an energetic electron and pair production by an energetic photon happen over a relatively large distance known as the formation length. The formation length extends over distances many orders of magnitude larger than interatomic spacings. The LPM effect is a suppression of the bremsstrahlung or pair production yield originating from multiple Coulomb scattering within the formation length (Migdal, 1956; Landau and Pomeranchuk, 1953b).

Several experiments have presented evidence for the LPM effect in amorphous targets (Hansen et al., 2004). Even at electron energies corresponding to $\gamma = 5 \cdot 10^4$ only a small fraction of photon energies are affected. Since the "threshold" below which the photon yield is suppressed increases approximately with the energy of the electron squared (see below), to get a substantial fraction of the full spectrum of photons affected by LPM suppression requires energies of 250 GeV ($\gamma = 5 \cdot 10^5$) and above (Hansen et al., 2003, 2004).

In crystals, the LPM effect was investigated experimentally in the late eighties (Bak et al., 1988) in the 10 GeV region and later for 150 GeV electrons (Baurichter et al., 1997).

The majority of radiation emission takes place within a cone of opening angle $1/\gamma$ to the direction of the electron. So destructive interference may result if the electron scatters outside this zone. Therefore, if the formation length exceeds the

length l_γ, the emission probability decreases or, put differently, the effective formation length shortens. Equation (20) combined with Equation (29) leads to the threshold of the LPM effect at energies:

$$\hbar\omega^{\mathrm{q}}_{\mathrm{LPM}} = \frac{E^2}{E + E_{\mathrm{LPM}}}\,; \quad \hbar\omega^{\mathrm{c}}_{\mathrm{LPM}} \simeq \frac{E^2}{E_{\mathrm{LPM}}}\,, \tag{30}$$

where

$$E_{\mathrm{LPM}} = \frac{mc^2 X_0}{4\pi a_0} = 7.684 \cdot X_0\ \mathrm{TeV/cm} \tag{31}$$

and a_0 is the Bohr radius. The value in parenthesis denotes the classical (recoilless) limit.

The LPM cross section for bremsstrahlung is given by Migdal as (Migdal, 1956; Landau and Pomeranchuk, 1953b; Klein, 1999):

$$\frac{\mathrm{d}\sigma_{\mathrm{LPM}}}{\mathrm{d}\hbar\omega} = \frac{4\alpha r_e^2 \xi(s)}{3\hbar\omega}\big(y^2 G(s) + 2[1 + (1-y)^2]\phi(s)\big) \times Z^2 \ln(184 Z^{-1/3}), \tag{32}$$

where $G(s)$, $\phi(s)$ and $\xi(s)$ are functions of $s = \sqrt{E_{\mathrm{LPM}}\hbar\omega/8E(E-\hbar\omega)\xi(s)}$, i.e. $\xi(s)$ is defined recursively, but can be well approximated, see e.g. Klein (1999). Here y denotes the fractional photon energy, $\hbar\omega/E$, Z the nuclear charge of the target and $r_e = \alpha^2 a_0$ the classical electron radius. In the limit $G(s) = \phi(s) = 1$ the Bethe–Heitler cross section is obtained. The Migdal expression, Equation (32), is relatively straightforward to implement in a Monte-Carlo simulation and compares well with experimental values.

Figure 5 shows an example of the measurements performed with 287 GeV electrons at CERN (Hansen et al., 2004). The aim of extending the accelerator based investigations by a factor 10 in energy compared to earlier experiments was twofold: To investigate a possible "compensation effect" proposed by Bell (1958) that would leave the effective radiation length unchanged (Hansen et al., 2003) and to explore the regime where the quantum recoil starts to become significant (Hansen et al., 2004). The experiment also provided a measurement of E_{LPM} for Cu, Ta and Ir by a comparison between data and simulated values where E_{LPM} was used as a free parameter. Subsequently, both Zakharov (2003) and Baier and Katkov (2004) calculated theoretical expectations which in both cases compared favourably to the experiment.

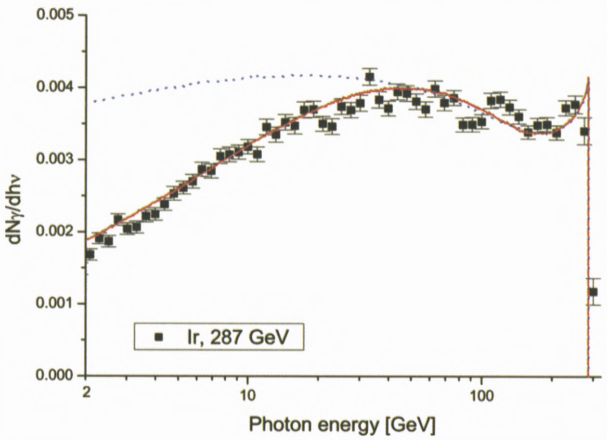

Figure 5. Photon energy spectra for 287 GeV e^- incident on a 4.4% X_0 Ir target. The filled squares with error bars are logarithmically binned measured values, the solid line is the simulated value including the LPM effect and the dotted line is the simulated value excluding the LPM effect, i.e. the Bethe–Heitler value. For details, see Hansen et al. (2003, 2004).

5.6. Pair Production and the LPM Effect in Amorphous Matter

Since pair-production can be considered the crossing-symmetry equivalent of photon emission, this process can be expected to be suppressed by the LPM mechanism as well. This has, however, not been verified experimentally.

For pair production, a classical version of the formation length is the length it takes to separate a created pair transversely by two Compton wavelengths, λ_c, when the pair is emitted with an opening angle $1/\gamma_p$:

$$l_{\mathrm{f}}^{\mathrm{pair}} = 2\gamma_p \lambda_c = \frac{2\gamma_p^2 c}{\omega}\,. \tag{33}$$

Therefore, the formation length increases with the energy of the pair (where $\gamma_p \equiv \hbar\omega/mc^2$).

When calculated properly by means of longitudinal momentum transfer, the formation length for pair production becomes:

$$l_{\mathrm{f}}^{rmpair} = \frac{2\gamma_p^2 c}{\omega^{\#}} \quad \text{with} \quad \omega^{\#} = \frac{\omega}{\eta_+ \eta_-}\,, \tag{34}$$

where $\eta_\pm$ is defined as $E_{\mathrm{e}^\pm}/\hbar\omega$ with $E_{\mathrm{e}^\pm}$ being the energy of the created electron or positron. It is an important distinction relevant to the Landau–Pomeranchuk–Migdal effect that l_{f} increases with increasing energy of the pair, whereas the

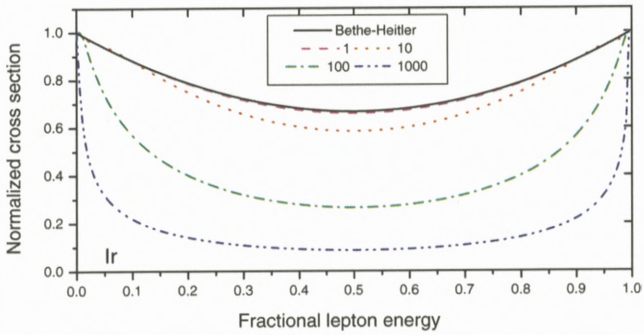

Figure 6. Calculated values for the normalized LPM pair production cross section $X_0 n\, \mathrm{d}\sigma/\mathrm{d}\eta$ where $\eta = E_{e^\pm}/\hbar\omega$ is the fractional energy of one lepton. The solid line is the Bethe–Heitler cross section, while (from the top) the dashed, dotted, dot-dashed and dot-dot-dashed correspond to photon energies $\hbar\omega$ =1, 10, 100 and 1000 TeV, respectively.

formation length for radiation emission decreases with increasing energy of the emitted photon for fixed energy of the radiating particle. On the other hand, the similarity between the two formation lengths when expressed as functions of γ, γ_p, ω^* and $\omega^\#$ reflect the crossing symmetry of the processes.

In the Migdal theory, the LPM cross section for pair production is given as (Migdal, 1956; Landau and Pomeranchuk, 1953b; Klein, 1999):

$$\frac{\mathrm{d}\sigma_{\mathrm{LPM}}}{\mathrm{d}\eta} = \frac{4\alpha r_e^2 \xi(\overline{s})}{3} \cdot \big(G(\overline{s}) + 2[\eta^2 + (1-\eta)^2]\phi(\overline{s})\big), \tag{35}$$

where $G(\overline{s})$, $\phi(\overline{s})$ and $\xi(\overline{s})$ are as given above, but functions of $\overline{s} = \sqrt{E_{\mathrm{LPM}}/8\eta\hbar\omega(1-\eta))\xi(\overline{s})}$. Again, in the limit $G(\overline{s}) = \phi(\overline{s}) = 1$ the Bethe–Heitler cross section is obtained.

As expected from Equation (34) symmetric pairs ($\eta_+ \simeq \eta_- \simeq 0.5$) are suppressed the most and to obtain a noticeable effect the photon energy must at least be of the order E_{LPM}.

From Figure 6 it is clear that even with a secondary beam of 4–5 TeV electrons derived from the 7 TeV proton beam of the LHC under construction at CERN, a measurement of the LPM effect in pair production is exceedingly demanding as the suppression amounts to a few percent only, even for symmetric pairs.

5.7. LPM Effects in Crystalline Matter

In the so-called continuum approximation (Lindhard, 1965), charged particles incident on a single crystal with small angles to crystallographic directions, experience the collective, screened nuclear fields as if smeared along the string or

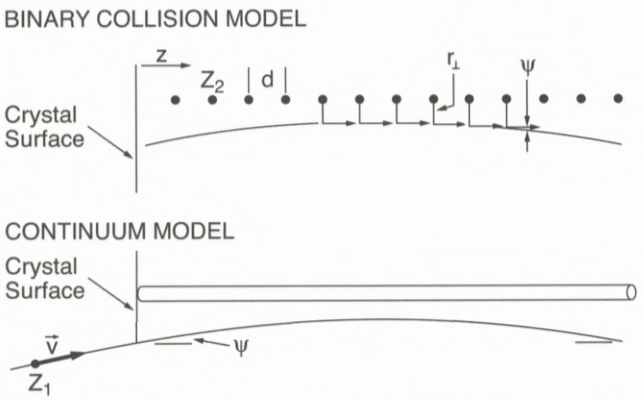

Figure 7. A schematical drawing of the discrete nature of the scattering centers in a crystal and the resulting continuum approximation.

plane, see Figure 7. For incidence with angles smaller than the so-called critical angle ψ_c, the particle has a low transverse momentum with respect to the axis or plane of the crystal. Thus it can be restricted to areas away from the nuclei (positively charged particles) or close to the nuclei (negatively charged particles). In this case the particle is channeled and is guided by the lattice such that a separation of the longitudinal and transverse motions is present. The result is a conserved "transverse energy" and therefore a transverse potential in which the particle moves. For an introduction to channeling at high energies, see e.g. Sørensen (1991) and Sørensen and Uggerhøj (1989).

The condition for the particle to be channeled is expressed by Lindhard's critical angle, ψ_c:

$$\frac{1}{2}pv\psi^2 \leq \frac{1}{2}pv\psi_c^2 = U_0 \;\Leftrightarrow\; \psi \leq \psi_c = \sqrt{\frac{2U_0}{pv}}\,, \tag{36}$$

where ψ is the angle to the crystallographic direction. Equation (36) states that the transverse energy must be smaller than the height of the transverse potential, U_0. The axial and planar critical angles are given by Lindhard as $\psi_1 = \sqrt{4Z_1Z_2e^2/pvd}$ and $\psi_p = \sqrt{4Z_1Z_2e^2Nd_pCa_s/pv}$ respectively, where Nd_p is the planar density of atoms, d the interaxial spacing, d_p the planar spacing, $C \simeq \sqrt{3}$ is Lindhard's constant and a_s is the (Thomas–Fermi) screening distance.

For incidence along an axial direction with somewhat larger angles $\psi_1 < \psi \lesssim 50\psi$, but still in the continuum approximation, the penetrating particle scatters off many strings of atoms, preserving the polar angle in each collision while changing the azimuthal angle in a stochastic fashion (Akhiezer et al., 1991).

The beam will reach an equilibrium state in azimuthal angles giving a uniform doughnut in angle space once the ensemble of particles has traversed a length given for $\psi \leq \psi_1$ by (Lindhard, 1965):

$$\lambda_{\perp}^{<} \simeq \frac{4\psi}{\pi^2 N \, \mathrm{d}a_s \psi_1^2} \tag{37}$$

and for $\psi \geq \psi_1$ roughly as (Bak et al., 1984; Andersen et al., 1980):

$$\lambda_{\perp}^{>} \approx 4\lambda_{\perp}^{<} \frac{\psi^2 u_1}{\psi_1^2 a_s}, \tag{38}$$

where u_1 is the one-dimensional thermal vibration amplitude of the lattice atoms. Doughnuts exist for angles much larger than ψ_1, implying that the continuum approximation is valid also for non-channeled, above-barrier particles. For a recent measurement of doughnuts, see Kirsebom et al. (2001b).

5.7.1. *Radiation Emission and the LPM Effect in Crystalline Matter*
The suppression due to doughnut scattering can be even more severe than due to multiple Coulomb scattering: If the particle is incident with a fixed angle ψ to the axis and deflects through an azimuthal angle ϕ, the change in angle becomes $\theta \simeq 2\psi \sin(\phi/2) \simeq \phi\psi$ and equating this with $2/\gamma$ an estimate for the length over which the particle scatters outside the radiation cone is obtained (Bak et al., 1988):

$$l_{\gamma\,\mathrm{d}} = \left(\frac{\phi}{2\pi}\right)^2 \lambda_{\perp} = \frac{\lambda_{\perp}}{\gamma^2 \psi^2 \pi^2}, \tag{39}$$

with $\lambda_{\perp}$ given by Equations (37) and (38) which denote the length required for the doughnut to develop fully. The length $l_{\gamma\,\mathrm{d}}$ can become smaller than l_{γ}, even along an axis where multiple Coulomb scattering is enhanced for negatively charged particles. Therefore suppression of radiation as well as for pair production can occur if the incident or produced particles doughnut scatter enough over one formation length to end outside the radiation cone.

The energy below which the radiation emission is suppressed by doughnut scattering can be estimated by use of Equations (20), (37), (38) and (39) as:

$$\hbar\omega \leq \hbar c \gamma^4 \pi^4 \psi_1^2 a_s \, \mathrm{d}N/2 \cdot \psi \tag{40}$$

for electrons inside the critical angle and:

$$\hbar\omega \leq \hbar c \gamma^4 \pi^4 \psi_1^4 a_s^2 \, \mathrm{d}N/8u_1 \cdot \psi^{-1} \tag{41}$$

outside the critical angle. Since $\psi_1^2 \propto 1/\gamma$ the doughnut scattering suppressions show a γ^3 and γ^2 dependence, respectively.

5.7.2. *Pair Production and the LPM Effect in Crystalline Matter*

The energy beyond which the pair production LPM suppression happens can be estimated by use of Equations (34), (37), (38) and (39) as:

$$\hbar\omega \geq \hbar\omega_{c\mathrm{d}}^{<} \simeq \frac{2mc^2}{\xi_+\xi_-\lambda_c\pi^4 N\,\mathrm{d}a_s\psi_1^2\gamma_p^2}\cdot\psi^{-1} \tag{42}$$

for pair production with the produced particles inside the critical angle and:

$$\hbar\omega \geq \hbar\omega_{c\mathrm{d}}^{>} \simeq \frac{8mc^2u_1}{\xi_+\xi_-\lambda_c\pi^4 N\,\mathrm{d}a_s^2\psi_1^4\gamma_p^2}\cdot\psi \tag{43}$$

for pair production with the produced particles outside the critical angle. Note that $\hbar\omega_{c\mathrm{d}}^{>}$ does not depend on γ_p since $\psi_1^2 \propto 1/\gamma$, but that $\psi_{\min} \simeq \psi_1$. As an example, consider the production of symmetric pairs along the $\langle 100\rangle$ axis in a diamond at room temperature – in this case $\hbar\omega_{c\mathrm{d}}^{>} \simeq \psi mc^2 \cdot 4 \cdot 10^9 \simeq 2$ GeV$\cdot\psi[\mu\mathrm{rad}]$ such that the effect should be observable down to ≈50 GeV. Likewise, for Ge $\langle 110\rangle$ the effect should extend down to ≈180 GeV for incidence outside ψ_1 and down to ≈80 GeV for incidence of a 150 GeV photon inside ψ_1 where the critical angle is calculated for a positron of the same energy. The effect of the reduced formation length in a strong field has not been taken into account, i.e. the formulas have been found for $\chi \leq 1$. More details can be found in Uggerhøj (2004).

Another effect of the LPM type is the reduction of the incoherent contribution due to coherent effects (Kononets, 1999; Tikhomirov, 1987a; Baier and Katkov, 2006). It is analogous to the self-suppression effect as a result of the diminishing formation length in a strong crystalline field, only in this case the suppression is of the incoherent contribution.

It is clear from Figure 6 that the LPM suppression in pair production for presently available accelerator energies is negligible. Even for a near future few-TeV electron beam generating bremsstrahlung photons, an experimental assessment would be extremely demanding. However, crystals may in fact present a possibility for measuring LPM suppression in pair production with beams in the few-hundred GeV region available today. The main reason is that the photon conversion into pairs in an aligned crystal predominantly takes place where the field is strongest, i.e. at small transverse distances from the string of nuclei, $r_\perp \simeq u_1$. At this transverse location, also the multiple Coulomb scattering is drastically increased - by up to three orders of magnitude! For this reason, one may expect the threshold for LPM suppression to decrease by approximately the same three orders of magnitude corresponding to a replacement of TeV by GeV. However, it is only the incoherent contribution that becomes suppressed and since the coherent contribution quickly dominates the pair production cross section, the

strong incoherent suppression becomes a small correction to the total yield *except* near the threshold for strong field effects where the incoherent contribution plays a significant role (Baier and Katkov, 2005).

5.8. Thin Targets – Ternovskii–Shul'ga–Fomin Effect

The formation length for radiation emission increases as shown with decreasing photon frequency. Thus, at a certain point the formation zone extends beyond the thickness of the foil. In this case, the radiation yield also becomes suppressed. Studies of this effect were first performed by Ternovskii and later extended by Shul'ga and Fomin and others. The first confirmation was obtained in experiments performed at SLAC (for references, see Uggerhøj et al., 2005c).

As to the extent of the effect, the analysis is applicable for target thicknesses $l_\gamma < \Delta x < l_\mathrm{f}$, see e.g. Shul'ga and Fomin (1998). Therefore, by use of Equation (20) and setting $\Delta x = l_\mathrm{f}/k_\mathrm{f}$ the effect appears for photon energies

$$\hbar\omega_\mathrm{TSF} = \frac{E}{1 + k_\mathrm{f}\Delta x/2\gamma\lambda_c}, \tag{44}$$

where $k_\mathrm{f} > 1$. The threshold of the effect is located at $k_\mathrm{f} = 1$, i.e. for $E/(1 + \Delta x/2\gamma\lambda_c)$.

The magnitude of the effect is evaluated from the averaged radiation spectrum (Shul'ga and Fomin, 1998)

$$\left\langle \frac{\mathrm{d}E}{\mathrm{d}\hbar\omega} \right\rangle \simeq \frac{2\alpha}{\pi}\left(\ln\frac{\Delta x}{l_\gamma} - 1\right) \tag{45}$$

and since for the Bethe–Heitler case

$$\left\langle \frac{\mathrm{d}E}{\mathrm{d}\hbar\omega} \right\rangle = \frac{4\Delta x}{3X_0},$$

the suppression factor, κ, can conveniently be expressed as

$$\kappa \simeq \frac{k_\gamma}{6(\ln k_\gamma - 1)}, \tag{46}$$

where $\Delta x = k_\gamma l_\gamma$ and $k_\gamma > 1$. As an example, for $\Delta x = 4.4\% X_0$ and $E = 287$ GeV, $k_\gamma = 0.044 \cdot 4\pi/\alpha \simeq 76$ yielding a suppression $\kappa = 3.8$, but for photon energies lower than $\hbar\omega_\mathrm{TSF} = 0.9$ GeV in Ir and 0.2 GeV in Cu.

5.9. Dielectric Suppression – Ter-Mikaelian Effect

In a medium with index of refraction, n, the velocity c/n replaces the photon velocity c. By use of this replacement in Equation (18) and the index of refraction expressed as $n = 1 - \omega_p^2/2\omega^2$, a modified formation length is obtained

$$\frac{1}{l_{f\varepsilon}} \simeq \frac{\omega}{2\gamma^2 c} + \frac{\omega_p^2}{2\omega c} = \frac{1}{l_f} + \frac{1}{l_{df}}, \tag{47}$$

where $\omega_p = \sqrt{4\pi NZe^2/m}$ is the plasma frequency, NZ being the electron density. The inverse of the dielectric formation length, $l_{df} = 2\omega c/\omega_p^2$, becomes dominating in Equation (47) for photon energies below the value

$$\hbar\omega_d = \gamma\hbar\omega_p. \tag{48}$$

Therefore – in close analogy with the density effect in ionization energy loss – formation lengths beyond l_{df} are effectively cut off. Thus, for photon energies in the regime below $\hbar\omega_d$ the photon yield is suppressed by the Ter-Mikaelian effect, also known as dielectric suppression or the longitudinal density effect, see e.g. Ter-Mikaelian (1972). However, as plasma frequencies are of the order 50 eV/$\hbar$, even electron energies as high as 287 GeV in iridium leads to a suppression only below $\hbar\omega_d = 86$ MeV.

5.10. Some Remaining Puzzles and Problems

For the subject of radiative energy loss and pair production, the inhibiting effects have almost all been studied experimentally for the radiation emission case only. For the LPM suppression, as mentioned, an experimental test in amorphous materials for pair production would require extreme attention to detail, even for a 1 TeV photon beam. However, use of the fact that multiple scattering is strongly increased in crystals may be utilized to reduce this energy scale by about three orders of magnitude.

New initiatives include the investigations of structured or sandwich-targets, where many thin foils are spaced small distances – corresponding to the formation length for a particular photon energy – apart. The spacers are typically chosen with as long a radiation length as possible, e.g. low density polyethylene. From such arrangements of targets, resonances should appear as predicted by theory (Blankenbecler, 1997a, 1997b; Baier and Katkov, 1999).

Contemporary research in the field of relativistic beams in crystals, is pursuing the first detection of so-called crystalline undulator radiation. This type of radiation is achieved by passing positrons of e.g. 10 GeV through a crystal

that has been manipulated to a sinusoidal shape in the direction transverse to the beam propagation, see e.g. Mikkelsen and Uggerhøj (2000). It is hoped that even self-amplified stimulated emission may someday be a possibility, leading to MeV photon beams of unprecedented brillance (Korol et al., 2004).

6. Conclusion

As shown in this review, there are still many intriguing questions and puzzles to be pursued within the subject of penetration phenomena for relativistic beams. Although at first sight many of the mentioned effects may seem of secondary importance, some of them are actually necessary ingredients to understand e.g. the efficiency of calorimeters at the next generation of particle physics experiments or the behaviour connected with detection of giant air showers as e.g. in the Pierre Auger Observatory, presently under commissioning in Argentina.

Acknowledgement

It is a pleasure to thank P. Sigmund for the invitation to Ion06, held in an extraordinarily beautiful setting, as well as for his kind encouragement to write this review.

References

Akhiezer A.I. and Shul'ga N.F. (1996): High Energy Electrodynamics in Matter, Gordon and Breach

Akhiezer A.I., Truten V.I. and Shul'ga N.F. (1991): Dynamic chaos in the motion of charged particles through a crystal. Phys Rep **203**, 289–343

Andersen S.K. et al. (1980): Influence of channeling on scattering of 2–15 GeV/c protons, π^+, and π^- incident on Si and Ge crystals. Nucl Phys B **167**, 1–40

Baier V.N. and Katkov V.M. (1999): Landau–Pomeranchuk–Migdal effect and transition radiation in structured targets. Phys Rev D **60**, 076001

Baier V.N. and Katkov V.M. (2004): Variation of radiation length due to LPM effect. Phys Lett A **327**, 202–209

Baier V.N. and Katkov V.M. (2005): Coherent and incoherent pair creation by a photon in oriented single crystal. Phys Lett A **346**, 359–366

Baier V.N. and Katkov V.M. (2006): Coherent and incoherent radiation from high-energy electron and the LPM effect in oriented single crystal. Phys Lett A **353**, 91–97

Bak J.F. et al. (1984): Detailed investigation of the channeling phenomena involved in bending of high-energy beams by means of crystals. Nucl Phys B **242**, 1–30

Bak J.F. et al. (1988): Channeling radiation from 2 to 20 GeV/c electrons and positrons, (II) axial case. Nucl Phys B **302**, 525–558

Baurichter A. et al. (1997): Radiation emission and its influence on the motion of multi-GeV electrons and positrons in strong crystalline fields. Phys Rev Lett **79**, 3415–3418

Baurichter A. et al. (2000): Channeling of high-energy particles in bent crystals – Experiments at the CERN SPS. Nucl Instr Meth B **164–165**, 27–43

Bell J.S. (1958): Bremsstrahlung from multiple scattering. Nucl Phys **8**, 613–620

Berestetskii V.B. and Geshkenbain B.V. (1957): Ionizational slowing down of high-energy electron positron pairs. Sov Phys JETP **4**, 609–610

Bethe H. and Heitler W. (1934): On the stopping of fast particles and on the creation of positive electrons. Proc Roy Soc A **146**, 83–112

Blankenbecler R. (1997a): Structured targets and the Landau–Pomeranchuk–Migdal effect. Phys Rev D **55**, 190–195

Blankenbecler R. (1997b): Multiple scattering and functional integrals. Phys Rev D **55**, 2441–2448

Datz S. et al. (1996): Effect of nuclear size on the stopping power of ultrarelativistic heavy ions. Phys Rev Lett **77**, 2925–2928

Dyson F.J. and Überall H. (1955): Anisotropy of bremsstrahlung and pair production in single crystals. Phys Rev **99**, 604–605

Esbensen H. and Golovchenko J.A. (1978): Energy loss of fast channeled particles. Nucl Phys A **298**, 382–396

Esbensen H. et al. (1978): Random and channeled energy loss in thin germanium and silicon crystals for positive and negative 2 – 15-GeV/c pions, kaons, and protons. Phys Rev B **18**, 1039–1054

Fusina R. and Kimball J.C. (1987): Resonant excitation of fast nuclei in crystals. Nucl Instr Meth B **27**, 368–373

Hansen H.D., et al. (2003): Is the electron radiation length constant at high energies? Phys Rev Lett **91**, 014801

Hansen H.D., et al. (2004): The LPM effect for multi-hundred GeV electrons. Phys Rev D **69**, 032001

Heitler, W. (1954): The Quantum Theory of Radiation. Dover, New York

Jackson J.D. (1975): Classical Electrodynamics. John Wiley, New York

Jain P.L. (1962): Nucleon-nucleon interactions at energies greater than 10^{12} eV. Phys Rev **125**, 679–687

Jeanneret J.B. (1998): Optics of a two-stage collimation system. Phys Rev ST Accel Beams **1**, 081001

Jowett J.M., Jeanneret J.-B. and Schindl K. (2003): Heavy ion beams in the LHC. In: Proceedings Particle Accelerator Conference, Vol. 3, pp 1682–1684

Klein S. (1999): Suppression of bremsstrahlung and pair production due to environmental factors. Rev Mod Phys **71**, 1501–1538

Kirsebom K., et al. (2001b): Radiation emission and its influence on the motion of multi-GeV electrons and positrons incident on a single diamond crystal. Nucl Instr Meth B **174**, 274–296

Kononets Yu.V. (1999): The basic QED processes in strong crystalline fields – Selected topics of recent developments. In: Pisin Chen (Ed.), Quantum Aspects of Beam Physics, Monterey 1998. World Scientific

Korol A.V., Solov'yov A.V. and Greiner W. (2004): Channeling of positrons through periodically bent crystals: On the feasibility of crystalline undulator and gamma-laser. Int J Mod Phys E **13**, 867–916

Krause H. et al. (2001): Electron capture and ionization of 33-TeV Pb ions in gas targets. Phys Rev A **63**, 032711

Landau L.D. and Pomeranchuk I.J. (1953b): Electron-cascade processes at ultra-high energies. Dokl Akad Nauk SSSR **92**, 735 [English translation available in Landau, L.D. (1965): The Collected Papers of L.D. Landau. Pergamon, New York, pp 589–593]

Lindhard J. (1965): Influence of crystal lattice on motion of energetic charged particles. K Dan Vidensk Selsk Mat Fys Medd **34, no. 14**, 1–64

Lindhard J. (1991): Quantum-radiation spectra of relativistic particles derived by the correspondence principle. Phys Rev A **43**, 6032–6037

Lindhard J. and Sørensen A.H. (1996): Relativistic theory of stopping for heavy ions. Phys Rev A **53**, 2443–2456

Mandal S.K., Klein S.R. and Jackson J.D. (2005): Cherenkov radiation from e^+e^- pairs and its effect on ν_e induced showers. Phys Rev D **72**, 093003

Migdal A.B. (1956): Bremsstrahlung and pair production in condensed media at high energies. Phys Rev **103**, 1811–1820

Mikkelsen U. and Uggerhøj E. (2000): A crystalline undulator based on graded composition strained layers in a superlattice. Nucl Instr Meth B **160**, 435–439

Møller S.P. (1995): High-energy channeling – Applications in beam bending and extraction. Nucl Instr Meth A **361**, 403–420

Møller S.P. et al. (2001): Random and channeled energy loss of 33.2 TeV Pb nuclei in silicon single crystals. Phys Rev A **64**, 032902

Palazzi G.D. (1968): High-energy bremsstrahlung and electron pair production in thin crystals. Rev Mod Phys **40**, 611

Perkins D.H. (1955): Ionization at the origin of electron pairs, and the lifetime of the neutral pion. Phil Mag **46**, 1146–1148

Pivovarov Yu.L., Shirokov A.A. and Vorobiev S.A. (1990): Coherent electromagnetic excitation and disintegration of relativistic nuclei passing through crystals. Nucl Phys A **509**, 800–822

Scheidenberger C. et al. (2002): Electromagnetically induced nuclear-charge pickup observed in ultrarelativistic Pb collisions. Phys Rev Lett **88**, 042301

Scheidenberger C. et al. (2004): Charge-changing interactions of ultrarelativistic nuclei. Phys Rev C **70**, 014902

Shul'ga N.F. and Fomin S.P. (1998): Effect of multiple scattering on the emission of ultrarelativistic electrons in a thin layer of matter. Sov Phys JETP **86**, 32–38

Sigmund P. (2006): Particle Penetration and Radiation Effects. Springer

Sørensen A.H. (1991): Channeling, bremsstrahlung and pair creation in single crystals. In: Fried H.M. and Müller B. (Eds), Vacuum Structure in Intense Fields, NATO ASI, Vol. 255, Plenum Press, New York, pp 91–118 [Reprinted in: Channeling, bremsstrahlung and pair creation in single crystals. Nucl Instrum Meth B **119**, 2–29 (1996)]

Sørensen A.H. (2003): Stopping of relativistic heavy ions; the pair production and bremsstrahlung channels. AIP Conf Proc **680**, 102–105

Sørensen, A.H. (2005): Pair production and bremsstrahlung contributions to the stopping of relativistic heavy ions. Nucl Instr Meth B **230**, 12–16

Sørensen A.H. and Uggerhøj E. (1989): Channeling, radiation and applications. Nucl Sci Appl **3**, 147

Ter-Mikaelian M.L. (1972): High-Energy Electromagnetic Processes in Condensed Media. Wiley Interscience, New York

Ter-Mikaelian M.L. (2001): Electromagnetic radiative processes in periodic media at high energies. Map Fiz Nauk **171**, 597–624 [Sov Phys Usp **44**, 571–596 (2001)]

Tikhomirov V.V. (1987a): The position of the peak in the spectrum of 150 GeV electron energy losses in a thin germanium crystal is proposed to be determined by radiation cooling. Phys Lett A **125**, 411–415

Tsai Y. (1974): Pair production and bremsstrahlung of charged leptons. Rev Mod Phys **46**, 815–851; Erratum (1977): Rev Mod Phys **49**, 421–423

Uggerhøj U.I. (2004): The Landau–Pomeranchuk–Migdal effect for amorphous and crystalline matter. Mod Phys Lett B **18**, 309–325

Uggerhøj U.I. (2005): The interaction of relativistic particles with strong crystalline fields. Rev Mod Phys **77**, 1131–1171

Uggerhøj U.I. and Uggerhøj, E. (2005): Strong crystalline fields – A possibility for extraction from the LHC. Nucl Instr Meth B **234**, 31–39

Uggerhøj U.I. et al. (2005a): Strong suppression of nuclear-charge changing interactions for 18 TeV/c In ions channeled in a bent Si crystal. Phys Lett B **619**, 240–246

Uggerhøj U.I. et al. (2005b): Charge-changing interactions of ultrarelativistic in nuclei. Phys Rev C **72**, 057901

Uggerhøj U.I. et al. (2005c): Formation length effects in very thin targets. Phys Rev D **72**, 112001

Yao W.-M. et al. (2006): Review of particle physics. J Phys G **33**, 1+

Zakharov B.G. (2003): Description of the CERN SPS data on the Landau–Pomeranchuk–Migdal effect for photon bremsstrahlung in the quantum regime. Sov Phys JETP Lett **78**, 759–762

Zielinski I.P. (1985): On the possibility of the electronic measurement of the King–Perkins–Chudakov effect for electron pairs using a multilayer silicon detector. Nucl Instr Meth A **238**, 562–563

Early History of Ion Beam Physics

John A. Davies*

7 Wolfe Ave., Deep River, Ontario
Canada KOJ 1PO

Abstract

In order to understand better the physics of radiation damage due to fast-neutron recoil atoms in nuclear reactors, Dr. W.B. Lewis (the research director at Chalk River Nuclear Laboratories) suggested to me in 1956 that we should investigate the range of 0–100 keV ions in solids. Soon afterwards, a Harwell report on Ar and Kr trapping and release during implantation (later published by Carter et al., 1962) caught Dr. Lewis's attantion and re-enforced his belief in the need for 0–100 keV ion ranges in solids. Hence, for almost 50 years, I have wandered through the field of atomic collisions in solids and have collaborated with many of the Ion06 participants – especially with Ingmar Bergström, Peter Sigmund (our host), Hans Henrik Andersen, Len Feldman, Jens Ulrik Andersen, Preben Hvelplund, Jim Williams, Bruce Winterbon. Over the years, we have established strong bonds of friendship and have had a lot of fun together. Tonight, I shall enjoy sharing with you some personal reminiscences on this early history. Since time permits, I shall also outline two of the many unsolved problems we have encountered.

Contents

1 Introduction **732**

2 Pre-1962 History **733**

3 1962–1965: Channeling **739**

4 Unsolved Problems **744**

References **747**

* E-mail: davies@magma.ca

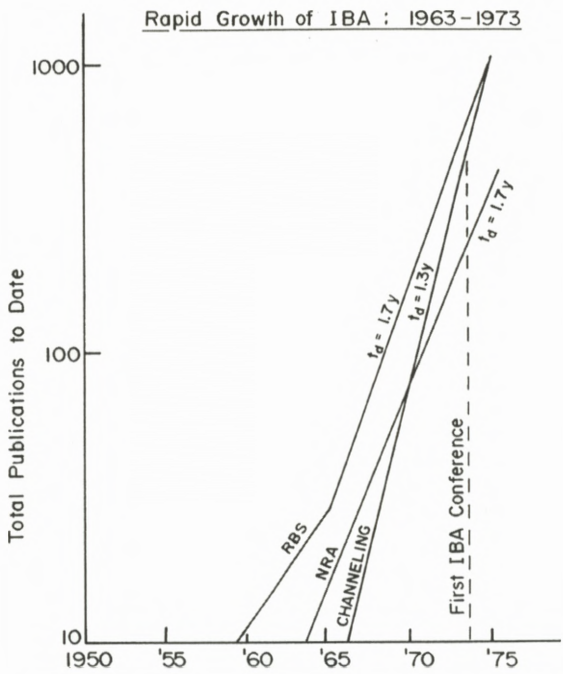

Figure 1. Publications growth rate in nuclear reaction analysis (NRA), Rutherford backscattering (RBS) and channeling. Adapted from Bujdoso et al. (1982).

1. Introduction

Figure 1 (Bujdoso et al., 1982) depicts the extremely rapid growth that occurred during the 1960s in three important sections of the field: namely, in Rutherford scattering, channeling, and nuclear reaction techniques. In each section, the total number of publications in the literature grew from less than 10 papers in the early 60s to more than 1000 by 1970: i.e., with doubling times under two years! By the end of the 60s, ion implantation of Si had become the major driving force in the field. However, prior to 1965 there was very little interest from the semiconductor field, apart from a couple of unsuccessful doping attempts by Ohl (1952) and by Kingsbury and Ohl (1952) at Bell Laboratories.

Indeed, the major interest in ion-beam physics came initially from two quite different sources: (i) Nuclear reactor sites such as Chalk River (F. Brown, J.A. Davies, G. Sims, J. Whitton), Oak Ridge (M. Robinson, O.S. Oen, S. Datz), Brookhaven (C. Erginsoy), Harwell (M.W. Thompson, R.S. Nelson), Aachen (G. Leibfried, C. Lehmann, P. Sigmund), ISPRA (Hj. Matzke) and Garching (R.

Behrisch, R. Sizmann, H. Lutz), where the primary motive was to study the physics of fast-neutron recoils; and (ii) European nuclear spectroscopy groups such as the Bohr Institute (N. Bohr, G. Sidenius, Skilbreid), and Oersted Institute (J. Koch) in Copenhagen, Aarhus University (J. Lindhard, K.O. Nielsen), the Nobel Institute of Physics in Stockholm (I. Bergström, B. Domeij, L. Eriksson), Chalmers Institute in Goteborg, (O. Almen, G. Bruce), the FOM Institute in Amsterdam (J. Kistemaker, P. Rol, J. Fluit) and Orsay in Paris (R. Bernas), who collaborated (after World War II) in developing low-energy (~50 keV) heavy-ion accelerators with high mass resolution, known as electromagnetic isotope separators. Their main objective was to prepare radioactive targets for nuclear spectroscopy. This latter group also had a keen interest in many related problems of ion-beam physics, such as sputtering, target stability, ion ranges and ion-source development. They even initiated their own conference series, with meetings in Harwell (1955), Amsterdam (1957), Vienna (1960), Orsay (1962) and Aarhus (1965).

Until the mid 1960s, there was almost no overlap between these two scientific communities.

2. Pre-1962 History

Theoretical work in ion-beam physics goes back to Bohr's (1948) comprehensive monograph on atomic particle penetration through matter, and to Lindhard's "Notes on Atomic Collisions" series (Lindhard and Scharf, 1961; Lindhard et al., 1963a, 1963b). In the nuclear reactor community, theoretical work was carried out mainly at Aachen and Jülich by Leibfried and his students, Lehmann and Sigmund, and at Oak Ridge by Robinson and Oen. Peter Sigmund moved from Aachen to Denmark at an early stage of his career, firstly in 1962 at the Danish Nuclear Reactor centre Riso where (in collaboration with H.H. Andersen) he initiated his lifelong interest in radiation effects, and then in 1964 at the Institute of Physics in Aarhus. His subsequent theoretical contributions to sputtering, scattering and energy-loss processes are well known to all of us.

Experimental work on ion ranges goes back to the 1957 publications[1] of Baulch and Duncan (1957) who studied the range of ~100-keV α-recoil atoms in gases, and of Bredov and Okuneva (1957) who used chemical etching to obtain range profiles of radioactive ^{137}Cs atoms in Ge (Figure 2). Bredov compared his experimental distribution with that predicted using Bohr's exponentially screened potential – and obtained rough agreement. However, at such low energies (4 keV),

[1] The 1956 Rutherford Backscattering study by K.O. Nielsen was never published – except in his doctoral thesis – and did not come to our attention until my first visit to Scandinavia in 1962.

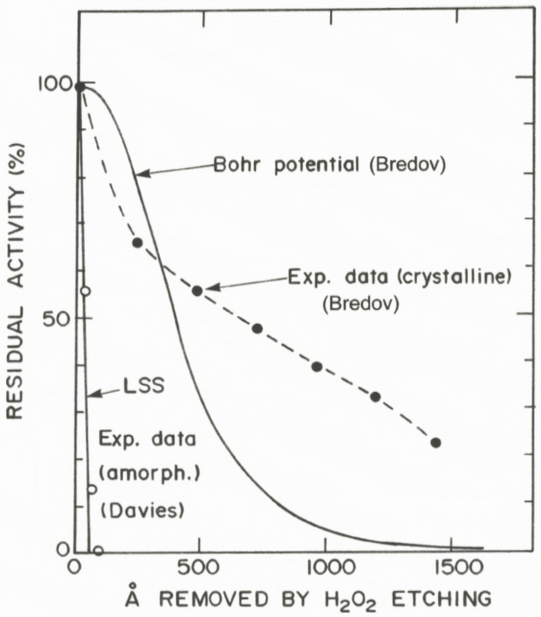

Figure 2. Depth profile of 4-keV ^{137}Cs in Ge. Adapted from Davies et al. (1962). Experimental data: • Bredov; ○ Davies. Theoretical curves based on the Bohr potential and on Lindhard et al.'s (1963b) Thomas–Fermi treatment.

Lindhard et al. (1963b) had shown[2] that Thomas–Fermi screening was more appropriate – and would predict much shorter ranges. At that time, we suspected that Bredov's chemical etching technique might be at fault. Hence, one of my early range measurements (Davies et al., 1962) was to repeat his ^{137}Cs in Ge experiment using our own special two-step transmission technique: namely, (i) deposit thin Ge films of various thicknesses on thick Al targets and implant 4-keV ^{137}Cs ions into each film; (ii) dissolve the Ge film completely in aqueous H_2O_2 (which does not attack the underlying Al) and measure the residual radioactivity.

Our data agreed well with Lindhard et al. (1963b) and hence we blamed Bredov's deep penetration on poor experimental technique. However, Bredov had used single-crystal Ge, whereas our evaporated films were probably amorphous. In hindsight, Bredov's (1957) result may even have been evidence of channeling, which he had failed to recognize because his theoretical estimate used a much too strongly screened potential.

[2] Although Lindhard did not publish this work until 1963, some of my nuclear spectroscopy colleagues at Chalk River were already familiar with his work as early as 1958.

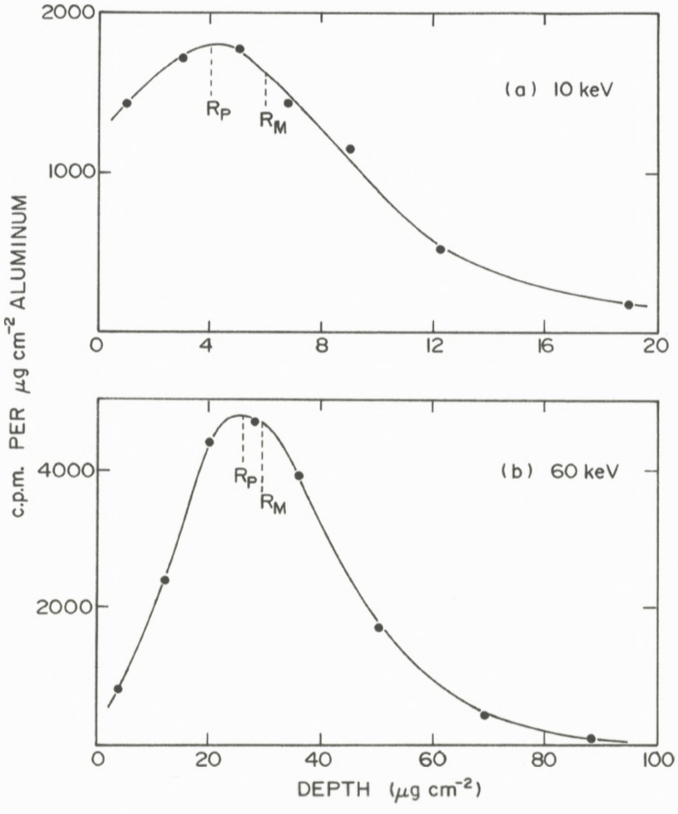

Figure 3. Depth profiles of ^{24}Na in polycrystalline Al (Davies and Sims, 1961). The peak position R_P represents the "most probable" value of the range, whereas R_M is the "median" value at which 50% of the implanted beam has been stopped. The prominent "tail", especially in the 10-keV case, encouraged Robinson and Oen (1963) to make Monte Carlo simulations of channeling.

Our early range studies (Davies and Sims, 1961; Brown and Davies, 1961; Davies et al., 1963; McCargo et al., 1963) consisted in developing a two-step anodic oxidation/stripping technique for obtaining detailed depth profiles in Al, W and (later) Si. In each of these targets, very uniform oxide films are prepared by anodic oxidation, with thicknesses varying linearly with applied voltage from a few atomic layers up to several hundred. In each case, a suitable solvent exists which rapidly dissolves the oxide layer, without attacking the underlying metal. Hence, by repeating this two-step process, a detailed depth profile is obtained. Two typical range profiles are shown in Figure 3.

In each case, the mean range agreed well with LSS theory, but a small fraction ($\sim$10%) penetrated much deeper than predicted. These small "tails" eventually led Robinson and Oen (1963) to postulate a channeling mechanism in the occasionally aligned polycrystalline grains. But at Chalk River, our thinking was influenced strongly by the neutron-diffraction concepts of Brockhouse and Iyengar (1958). Since the wavelength of a 60-keV Na beam is only $\sim 10^{-6}$ nm, the corresponding Bragg angle (θ_{Bragg}) is very small ($\sim 10^{-6}$ radians) and *diffraction* effects are therefore negligible.

In 1960, a mini-conference on keV ion ranges was held at Chalk River, in which the Powers and Schmitt groups both participated. Powers and Whaling (1962) reported on the use of proton backscattering to measure range profiles in high-dose implants of $\sim$100-keV nitrogen and oxygen ions. Schmitt and Sharp (1958) and VanLint et al. (1961) presented mean-range estimates derived by measuring the escape fraction of radioactive keV and sub-keV recoils produced in thin foils by (γ, n) nuclear reactions.

Sputtering is another field that was investigated extensively in these early years, especially in Amsterdam and Goteborg. In the early 1960s, Rol et al. (1960) and Fluit and Rol (1964) reported that sputtering yields in monocrystalline copper exhibited a strong orientation dependence. Initially, this was attributed to a geometrical "transparency" effect, because sputtering is largely a near-surface phenomenon. Almen and Bruce (1961a, 1961b) published two papers, documenting an exceptionally detailed study of sputtering behaviour of some 25 different metals bombarded by 45-keV Kr ions (Figure 4). Particularly noteworthy was their observation of a periodic dependence of sputtering yield on the atomic number Z_2 of the target. Large peaks in sputtering yield occur around Z_2 values of 30 (Zn), 48 (Cd) and 80 (Hg) which correspond nicely with minima in their binding energy U_s. Two metals, Mg and Al, exhibit anomalously low sputtering yields. However, years later, the Amsterdam group found that this could be attributed to the presence of protective surface oxides with much higher binding energies; under ultra-high vacuum conditions, the sputtering yield increased suddenly by almost a factor of ten when the surface oxide was sputtered away.

The year 1961 was a memorable one for two reasons: (i) the Chalk River nuclear spectroscopy group purchased a 70-keV isotope separator with excellent mass resolution (1:4000) from a Swedish company (this instrument was an ideal accelerator for our radioactive implantations); and (ii) Ingmar Bergström arranged to visit us for 2 months, since the new accelerator was an exact copy of his own isotope separator in Stockholm. His visit established the first major bridge between the two scientific communities – our nuclear reactor group and the European nuclear spectroscopists – and a remarkably fruitful interaction was

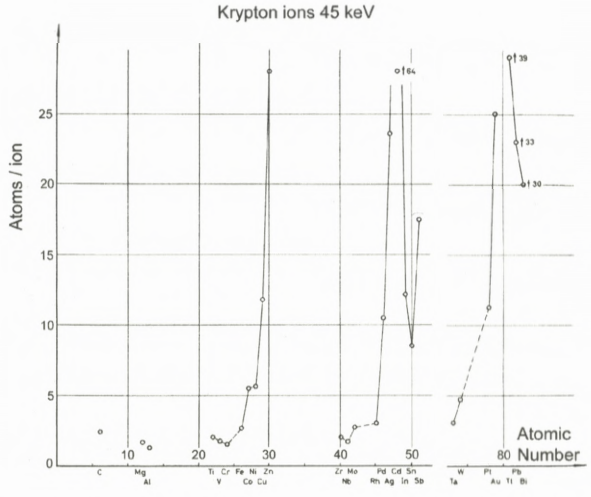

Figure 4. Sputtering yield Y_S as a function of target atomic number Z_2 for 45-keV Kr bombardment (Almen and Bruce, 1961a).

the result. Ingmar helped us to broaden the Chalk River program to include other aspects of ion-beam physics such as dose effects, sputtering and thermal stability of implanted targets (Bergström et al., 1963). He also invited me to Stockholm for 3 months to collaborate with his student Bo Domeij, en route to the 1962 isotope separator meeting in Orsay – he even persuaded my research director to finance my whole trip! During this Stockholm visit, he introduced me to many of his Scandinavian colleagues: O. Almen in Goteborg, G. Sidenius at the Bohr Institute, and especially K.O. Nielsen and J. Lindhard in Aarhus. Karl Ove Nielsen had only just arrived in Aarhus in 1962 as the newly appointed professor of experimental physics; Jens Lindhard on the other hand had been there already for 5–6 years. This resulted in my spending the year 1964–1965 in Aarhus, collaborating closely with several Danish graduate students, two of whom (J.U. Andersen and P. Hvelplund) are participants at Ion06 (J.U. Andersen and P. Hvelplund), and also with another well known "foreign guest" Peter Sigmund. But, by 1964 channeling had already been "discovered" – so let us first go back and complete our history of the pre-channeling era.

Other early studies of ion-beam physics include Sidenius' nuclear stopping cross-section data in gas targets (Bohr Institute) and Loftager's later work in Aarhus in which large peaks in the nuclear stopping cross-section were observed whenever the collision distance corresponded to an inner-shell overlap.

Electronic stopping of heavy ions was investigated by several experimental groups. Ormrod and Duckworth (1963) measured energy loss in transmission through thin carbon foils and observed an unexpected periodic dependence on the atomic number Z_1 of the ion beam. This Z_1 oscillation effect was later extended to higher energies and heavier ion beams by Fastrup et al. (1965) and by Hvelplund and Fastrup (1968). Using gas targets and single-collision coincidence techniques, Afrosimov et al. (1963) in Leningrad and Kessel et al. (1965) at the University of Connecticut reported sharp steps in the inelastic energy-loss Q, as successive inner shells overlap during the collision – i.e., firstly, L-L overlap, then K-L, and finally K-K. Eventually, this work led to the discovery of high-energy molecular X-ray bands (Saris et al., 1972).

A particularly memorable milestone in the field of electronic stopping was the discovery of the surface-barrier detector by Mayer and Gossick (Mayer and Gossick, 1956; Mayer, 1959). With this new energy-dispersive spectrometer, an entire energy spectrum could be obtained simultaneously in a single measurement (i.e., within minutes), whereas the old cumbersome magnetic spectrometers had required hours or even days of step-by-step data collection. Initially, the physics community failed to show much interest in this new detector. However, in September 1960, this was rectified when the Asveville workshop on Semiconductor Detectors brought together almost all the future pioneers of ion-beam analysis – Georges Amsel, Walter Brown, Geoff. Dearnaley, Walt Gibson, Jim Mayer, Laurie Miller.

For many of us, one puzzling aspect of the Si solid-state detector was the unexpectedly large value of 3.67 eV per electron/hole pair, i.e., more than three times the Si band gap energy E_i of 1.1 eV. In Ge, this discrepancy between ε and E_i was even larger, i.e., $\varepsilon_{\mathrm{Ge}} = 3.7$ eV whereas E_i is only 0.66 eV. However, a few years ago, Len Feldman came across a 1961 paper by Shockley (1961) which contains a surprisingly simple and accurate explanation for these large ε values, namely:

$$\varepsilon = E_i + 2E_{\mathrm{f}} + rE_{\mathrm{R}}, \tag{1}$$

where E_{f} ($\sim 0.6E_i$) is the mean final energy of an electron or hole when it can no longer create additional electron/hole pairs. The Raman phonon energies E_{R} (0.063 eV in Si, and 0.037 eV in Ge) were obtained from neutron scattering data (Brockhouse and Iyengar, 1958; Palevsky et al., 1959), and the mean-free-path ratio $r = L_{\mathrm{ionization}}/L_{\mathrm{phonon}}$ was obtained from the quantum yield measurements of Vavilov (1959). Substituting $r_{\mathrm{Si}} = 17.5$ and $r_{\mathrm{Ge}} = 57$ in Equation (1), we obtain:

$$\varepsilon_{\mathrm{Si}} = 2.2E_i + 1.10 = 3.5 \text{ eV}, \tag{2a}$$

$$\varepsilon_{\mathrm{Ge}} = 2.2E_i + 2.11 = 3.6 \text{ eV}. \tag{2b}$$

Note the good agreement with the experimental ε values of 3.67 eV in Si and 3.7 eV in Ge. Note too the similarity in magnitude between the first term $2.2E_i$ in Equation (2) and the modified Kinchin–Pease relationship (Sigmund, 1969) between the energy $(-\Delta E)$ to create a Frenkel pair and the displacement energy E_{d} in a collision cascade; namely, $(-\Delta E) = 2.38E_{\mathrm{d}}$.

We shall return later to a still unresolved aspect of solid-state detectors, namely why do high-energy heavy ions exhibit almost the same ε value as protons and electrons?

3. 1962–1965: Channeling

A detailed account of the "channeling story" has already been published (Davies et al., 1992) in the proceedings of the 10th Ion Beam Analysis conference in Eindhoven. A few personal reminiscences are recalled here.

In March 1962, just before my departure for Stockholm, Robinson and Oen (whom I had not yet even met) phoned from Oak Ridge to inform us that their computer program could successfully simulate the "tails" in our polycrystalline range profiles – and attributed them to a coulombic steering process, occurring in those crystalline grains which accidentally had a low-index direction aligned with the incident beam direction. At first, they named their steering process "tunneling" but, to avoid confusion with quantum mechanical tunneling, they soon changed the name to "channeling". Hence, by the time I arrived in Stockholm in 1962, we were already growing single crystals of Al and W in order to verify the existence of channeling.

During my Stockholm visit, Bent Elbek (Bohr Institute) gave a nuclear physics seminar at the Nobel Institute of Physics. While I no longer recall even the title of his seminar, I still vividly remember our midnight discussions, while sharing the Institute's top-floor guest apartment. We discussed the possible origin of the exponential "tails" in all the Chalk River range profiles – and suddenly Elbek recalled that K.O. Nielsen (1956) at the Bohr Institute had used helium backscattering plus a magnetic spectrometer to measure *in situ* the range distribution of 40-keV Gd in polycrystalline Al (Nielsen, 1956). His resulting depth profile (Figure 5) was an excellent Gaussian peak, with absolutely *no* evidence of a deeply penetrating "tail", even down at the 10^{-3} level.

This posed quite a dilemma! Various experimental artifacts might be able to *create* a spurious tail, but it is hard to imagine an artifact that could cause a real tail to disappear. Fortunately, the next morning Bo Domeij, who was collaborating in some range-profile measurements during my Stockholm visit, proposed

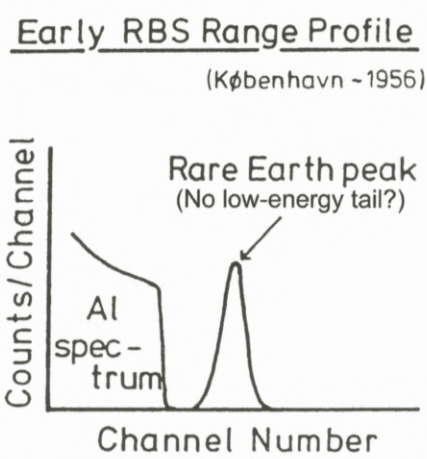

Figure 5. K.O. Nielsen's RBS spectrum of 40-keV Gd in polycrystalline Al, using a magnetic spectrometer (Nielsen, 1956).

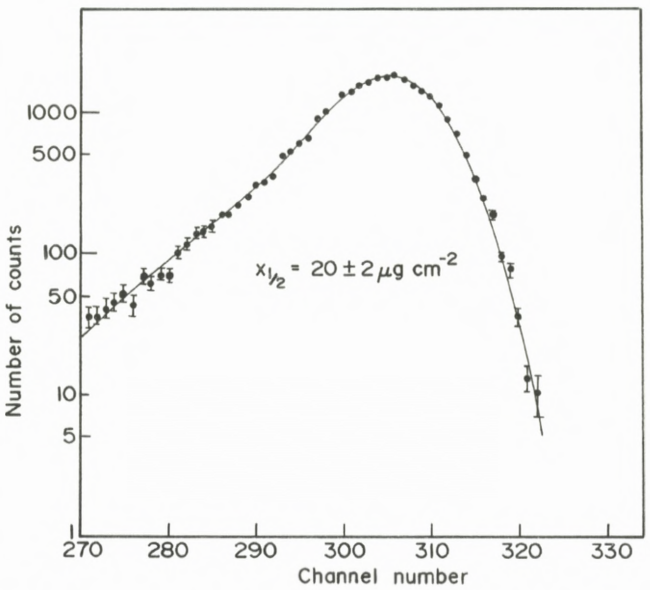

Figure 6. α-particle spectrum from 210-keV ^{222}Rn, implanted into polycrystalline Al. The resulting $x_{1/2}$ for the exponential "tail" agrees well with the value of 17 ± 2 μg/cm^{-2} obtained subsequently by the anodic oxidation/stripping technique (Domeij et al., 1963).

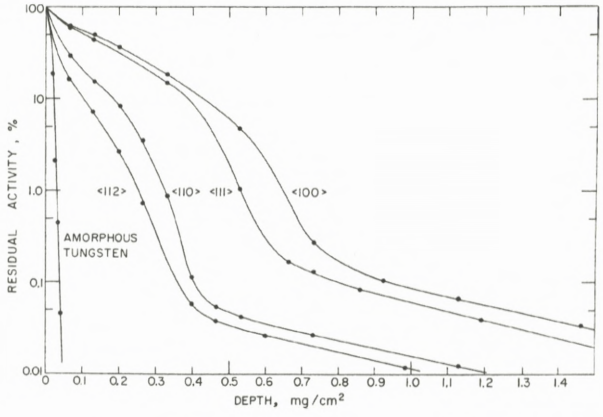

Figure 7. Integral penetration profiles of 40-keV ^{125}Xe, implanted into single-crystal W along various crystallographic directions (Domeij et al., 1964a).

an ingenious experiment to resolve the problem. We would implant ^{222}Rn into polycrystalline Al and determine the resulting depth profile by two independent methods: (i) measure the energy spectrum of the emitted α-particles, using one of the newly developed solid-state detectors; and (ii) use the anodizing/stripping technique on the same implanted target. The α-spectrum (Figure 6) verified the existence of a small penetrating "tail". Furthermore, both techniques exhibited the same magnitude and $x_{1/2}$ values for the exponential tail of the profile (Domeij et al., 1963).

A few months after my return to Canada, Robinson and Oen invited a small group of us to Oak Ridge to discuss their computer range simulations. By then, single crystals had finally become available – and range profiles in aligned monocrystalline tungsten (Figure 7), aluminum (Piercy et al., 1964), silicon (Davies et al., 1964) and copper (Lutz and Sizmann, 1963) soon confirmed the existence of channeling. Also, Domeij et al. (1964b) measured profiles in amorphous Al_2O_3 and WO_3 and, as would be expected, found no tail.

In September 1963, a small conference was held at Chalk River to discuss the significance of these single crystal results. Despite its small size (less than 25 participants), all major groups were represented, which indicates how small the ion-beam physics community was 43 years ago. By the end of 1963, channeling had been observed, not only in heavy-ion range profiles, but also in MeV proton-transmission experiments through Si crystals (Figure 8) by Dearnaley (1964) and through very thin Au crystals Nelson and Thompson (1963).

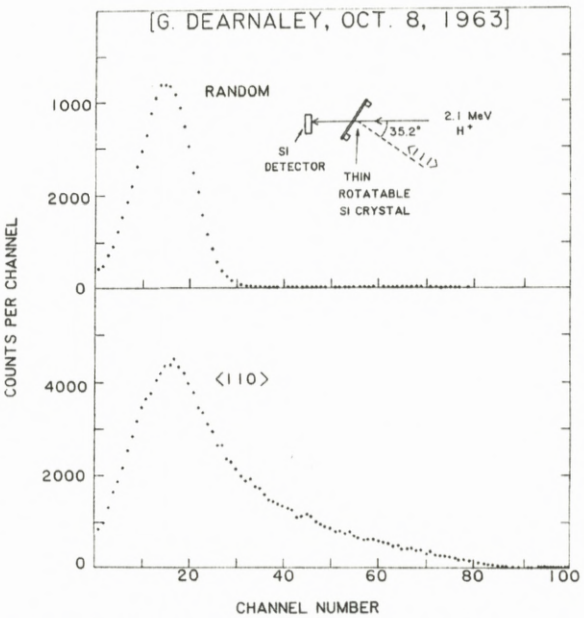

Figure 8. Energy spectrum of 2.1 MeV protons, after transmission through a 30 μm Si (111) crystal at 35.2° tilt from the ⟨111⟩ axis: (a) random incidence; (b) incidence along an ⟨110⟩ axis (Dearnaley, 1964).

In 1964–1965, I was a guest scientist with K.O. Nielsen's accelerator group in Aarhus. During my visit, Lindhard (1965) developed and published his definitive theoretical treatise on channeling, indicating the unique role of "close-impact" processes in measuring quantitatively the non-channeled component of the beam. Experimental verification of Lindhard's concepts soon followed, using nuclear reactions (Andersen et al., 1965), Rutherford scattering (Bogh and Uggerhoj, 1965) and inner-shell X-rays (Khan et al., 1966, 1967), Lindhard's theoretical paper contained also an elegant proof of reversibility between channeling of an external beam and "blocking" of energetic positive particles emitted (or backscattered) from lattice sites within the crystal. Since Stockholm at that time lacked a suitable MeV accelerator, Domeij (1965) again devised an ingenious ^{222}Rn implantation experiment. He injected ^{222}Rn into tungsten single crystals and used the blocking pattern of the emitted α-particles (Figure 9) to verify the concept of reversibility. His measurements also established that ~80% of the Rn atoms must reside on lattice sites. This was the first use of channeling to study lattice location of embedded foreign atoms (Domeij, 1965).

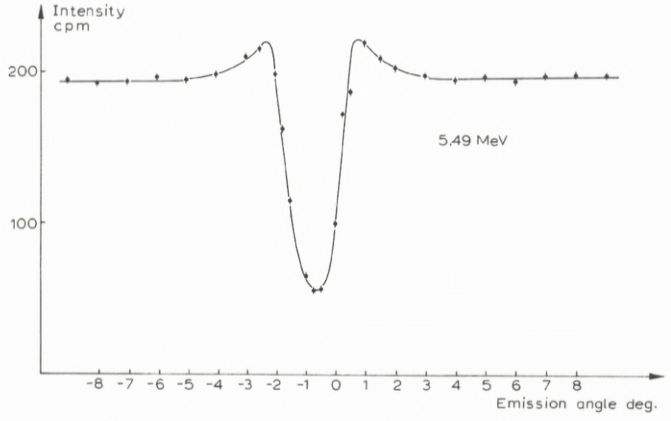

Figure 9. Angular dependence of the 5.49 MeV α-particles emitted from ^{222}Rn, implanted at 60-keV into (111) tungsten (Domeij, 1965).

Other pioneering studiers of MeV ion channeling include early blocking measurements by Tulinov et al. (1965) in the Soviet Union and by Gemmell and Holland (1965) at the Argonne, and also the single-crystal transmission studies of Gibson et al. (1965).

Many of these channeling studies were presented at the Electromagnetic Isotope Separators conference in Aarhus in mid-June 1965 and published in Nucl. Instr. Meth. Vol. 38. More than 50% of the papers at this meeting involved solid-state applications and hence a new biannual conference series (ICACS) was split off (Table 1), with the initial one being held in Chalk River in 1967. At the 1965 Aarhus meeting, less than 10% of the papers involved semiconductor applications. Yet, within two years, a fully dedicated Implantation of Semiconductors conference was held in Grenoble (1967) – and by 1970 this had expanded into another regular conference series. In 1968, the first Gordon conference on Particle-Solid Interactions was held in New Hampshire and this too became a biannual event. In 1973, another ion-beam conference series – Ion Beam Analysis – was initiated at IBM (Yorktown Heights) and the following year the inaugural conference of the Ion Implantation of Metals series was held at Sandia (Albuquerque). With the exception of the Gordon conference, all the biannual conference series in Table 1 are still flourishing.

Table 1. Ion Beam Physics Conferences

1965	ICACS – split off from the Electromagnetic Isotope Separators conference series – biennial.
1967	Grenoble – Ion Implantation of Semiconductors.
1968	Gordon Conference – Particle-Solid Interactions – biennial series, terminated in 1996.
1970	Implantation of Semiconductors – biennial.
1973	Ion Beam Analysis (IBA) – biennial.
1974	Implantation of Metals – biennial.
1978	Ion Beam Modification of Materials (IBMM) – formed by combining the above Implantation conference series (Semiconductors and Metals) – biennial.
1979	Radiation Effects in Insulators – biennial.
1980	Surface Modification of Metals by Ion Beams (SM^2IB) - biennial.

4. Unsolved Problems

This concludes my account of the early history of ion-beam physics. However, since "Unsolved Problems" is one of the main themes of Ion06, let me close by briefly recalling two unsolved problems from these early years: (i) the so-called "supertail" in well-channeled range profiles in tungsten; and (ii) the response of solid-state detectors to high-E heavy ions.

(i) Tungsten "supertails"

In almost all channeled range profiles in W, a small fraction (typically ~0.1%) of the radioactive ions penetrate to extremely large depths (Figure 7), independent of the incident energy (Domeij et al., 1964a, figure 3). Cavid Erginsoy (1964) postulated that perhaps some sort of quantum restriction was preventing the best-channeled ions from undergoing any energy loss. However, Carl Wandel (Aarhus, 1964) made an alternative suggestion that avoided having to invoke any exotic new physics. He pointed out that best-channeled ions probably create *no* displacements near the end of their tracks and hence could diffuse as free interstitial atoms. Perhaps, such interstitial diffusion in tungsten is rapid at room temperature and, if so, then the enhanced motion should occur equally in all three dimensions. Erginsoy's "super-channeling" model on the other hand would enhance the penetration only along the incident beam direction. One of the Aarhus graduate students (P. Jespersgaard) therefore injected ^{133}Xe into a W (111) crystal firstly

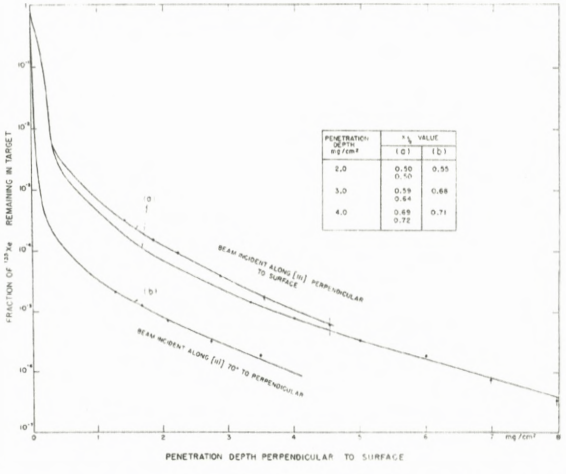

Figure 10. Integral penetration profiles for 20-keV ^{133}Xe in (111) W: (a) beam injected along [111] direction perpendicular to the surface; (b) beam injected along [11$\bar{1}$] direction at 70.7° from the perpendicular (Davies and Jespersgaard, 1966).

along the ⟨111⟩ axis perpendicular to the surface, and secondly along the ⟨111⟩ at 70.7° from the perpendicular (Davies and Jespersgaard, 1966). Note that the channeled depth profile (Figure 10) is reduced ~3-fold for the 70.7° axis, whereas the "supertail" depth scale is unaffected. Hence, a 3-dimensional diffusion-type process, as proposed by Wandel, must be involved.

At 30 K, the supertail is almost two orders of magnitude larger (i.e., about 10% of the beam), indicating that the fraction ending up as interstitial atoms is strongly temperature dependent (see figure 3 in Davies et al., 1968). Furthermore, the supertail can be completely suppressed by using a high-dose Ne bombardment to introduce trapping centres into the crystal before allowing it to warm up from 30 K. This shows that the interstitial diffusion process must be negligible at 30 K, but extremely rapid at room temperature. A similar experiment at 78 K, by Hermann et al. (1966) shows that the interstitial process is still negligible at liq. nitrogen temperature.

One other point: Andersen and Sigmund (1965) predicted that, when $Z_{ion} > Z_{target}$, even the best-channeled ions create displacements near the end of their track – and therefore, would not exhibit a "supertail". Unfortunately, for a high-Z target such as tungsten, there are not many heavier radiotracers available. Nevertheless, Domeij and Eriksson (1965) were able to implant ^{222}Rn and, as predicted, they found no "supertail".

So far, tungsten is the only crystal exhibiting such clear evidence of an interstitial diffusion process. Thus, one unsolved problem is whether channeling can be used to induce similar interstitial diffusion effects in other crystal lattices. The most likely candidate is the chemically similar bcc crystal, Mo, but perhaps other bcc crystals such as Ta and Nb should also be considered. Furthermore, in Si and other elementary semiconductors, group-III dopants (B, Al, etc.) and also Au exhibit a fast-diffusion behaviour that is probably interstitial.

(ii) ε (eV per electron/hole pair) for high-E heavy ions

Contrary to widespread belief, the so-called "pulse-height defect" (PHD) for heavy ions is surprisingly small, or even *negative*, provided the ion energy is higher than the Bragg peak. During the 1960s, electrons, protons, and even He ions were found to exhibit approximately the same ε value, namely 3.67 eV. Furthermore, ε seemed to be independent of ion energy and unaffected by channeling. Heavier ions at MeV energies exhibited somewhat larger ε values, but this was attributed to significant E-loss contributions from nuclear stopping and from the finite window thickness of the detector.

However, by the 1980s, the picture had changed considerably. Careful measurements in several laboratories (Kemper and Fox, 1972; Langley, 1973; Mitchell et al., 1975) showed that, at $E > 2$ MeV, helium ions produce a slightly *larger* pulse height than protons, i.e., the PHD for helium is actually *negative*. After applying small corrections for nuclear stopping and window loss, Lennard and Winterbon (1987) observed a linear dependence of ε on the stopping power, $\mathrm{d}E/\mathrm{d}x$ (MeV/micron), namely,

$$\varepsilon = 3.67 - 0.2\frac{\mathrm{d}E}{\mathrm{d}x}. \tag{3}$$

However, the cause of this $\mathrm{d}E/\mathrm{d}x$ dependence has not yet been established.

Note that Equation (3) would predict a very large negative PHD for very heavy ions. Recently, ε has been measured by Comedi and Davies (1992) and by Weijers et al. (2002), using heavy ions at energies above the Bragg peak value, so that nuclear stopping and window corrections become extremely small (<0.5%). Their observed ε values for a wide range of heavy ions (Table 2) are within a few % of the proton value of 3.67 eV, despite the much denser plasma along the heavy-ion track. A satisfactory explanation for this almost constant ε value has not yet been found. Also, why does the linear $\mathrm{d}E/\mathrm{d}x$ dependence of Equation (3) break down for ions heavier than helium?

Table 2. ε (eV per electron/hole pair) at $E > E_{\text{Bragg}}$.

Ion	E (MeV)	$\mathrm{d}E/\mathrm{d}x$ (MeV/μm)	$\varepsilon_{\text{predicted}}$	$\varepsilon_{\text{observed}}$	Reference
e, γ			3.67	3.67	Lennard and Winterbon (1987)
H	1.0	0.09	3.67	3.67	Lennard and Winterbon (1987)
He	5.0	0.30	3.63	3.64	Lennard and Winterbon (1987)
^{12}C	25	1.20	3.47	3.58	Comedi and Davies (1992)
^{35}Cl	30	4.50	2.80	3.55	Comedi and Davies (1992)
^{32}S	60	3.70	2.90	3.52	Weijers et al. (2002)
^{81}Br	140	9.30	1.80	3.71	Weijers et al. (2002)
^{107}Ag	2000	8.00	2.10	3.70	Weijers et al. (2002)

This seems an appropriate place to end our historical review, having reminded the reader that some unsolved (and hopefully interesting) ion-beam problems still exist.

References

Afrosimov V.V., Gordeev Yu.S. and Panov M.N. (1963): Characteristic inelastic energy losses in single collisions. Private communication

Almen O. and Bruce G. (1961a): Collection and sputtering experiments with noble gas ions. Nucl Instr Meth **11**, 257–278

Almen O. and Bruce G. (1961b): Sputtering experiments in the high-energy region. Nucl Instr Meth **11**, 279–289

Andersen H.H. and Sigmund P. (1965): Defect distributions in channeling experiments. Nucl Instr Meth **38**, 238–240

Andersen J.U., Davies J.A., Nielsen K.O. and Andersen S.L. (1965): An experimental study of the orientation dependence of p, γ yields in monocrystalline aluminum. Nucl Instr Meth **38**, 210–215

Baulch D.L. and Duncan J.F. (1957): The range-energy relation for α-recoil atoms. Austr J Chem **10**, 112–127

Bergström I., Brown F., Davies J.A., Graham R.L. and Kelly R. (1963): On the electromagnetic separation method of preparing sources for precision β-spectroscopy. Nucl Instr Meth **21**, 249–274

Bogh E. and Uggerhoj E. (1965): Experimental investigation of the orientation dependence of Rutherford scattering yield in single crystals. Nucl Instr Meth **38**, 216–220

Bohr N. (1948): The penetration of energetic atomic particles through matter. Kgl Dan Vid Selsk Mat Fys Medd **18, no. 8**, 1–144

Bredov M.M. and Okuneva I.M. (1957): Deep penetration of ions of moderate energy in materials. Sov Phys Dokl **113**, 795–798

Brockhouse B.N. and Iyengar P.K. (1958): Normal modes of germanium by neutron spectrometry. Phys Rev **111**, 747–754

Brown F. and Davies J.A. (1961): The effect of energy and integrated flux on the retention and range of inert gas ions injected at keV energies in metals. Can J Phys **41**, 844–857

Bujdoso E., Lyon W.S. and Noszlopi I. (1982): Prompt nuclear analysis: Growth and trends – A scientometric study. J Radioanal Chem **74**, 197–238

Carter G., Colligon J.S. and Leck J.H. (1962): Ion sorption in the presence of sputtering. Proc Phys Soc **79**, 299–309

Comedi D. and Davies J.A. (1992): Pulse-height response of Si surface-barrier detectors to 5–70 MeV heavy ions. Nucl Instr Meth B **67**, 93–97

Dabbs, J.W.T. and Walter F.J. (Eds) (1960): Proceedings of the Conference on Semiconductor Nuclear Particle Detectors, Ashville, N.C. Published in Nucl Science Series Report 32, Publ. 871 (Natl Acad of Sciences, Washington 1961)

Davies J.A. and Jespersgaard P. (1966): Anomalous penetration of xenon in tungsten crystals – A diffusion effect. Can J Phys **44**, 1631–1638

Davies J.A. and Sims G.A. (1961): The range of ^{24}Na ions of keV energies in aluminum. Can J Chem **39**, 601–610

Davies J.A., McIntyre J.D. and Sims G.A. (1962): The range of ^{137}Cs ions of keV energies in germanium. Can J Chem **40**, 1605–1610

Davies J.A., Brown F. and McCargo M. (1963): Range of ^{133}Xe and ^{41}Ar ions with keV energies in aluminum. Can J Phys **41**, 829–843

Davies J.A., Ball G.C. and Domeij B. (1964): Range of energetic ^{125}Xe in monocrystalline silicon. Can J Phys **42**, 1070–1080

Davies J.A., Eriksson L. and Whitton J.L. (1968): Range measurements in oriented tungsten single crystals: III. Influence of temperature on the maximum range. Can J Phys **46**, 573–579

Davies J.A., Amsel G. and Mayer J.W. (1992): Reflections and reminiscences from the early history of RBS, NRA and channeling. Nucl Instr Meth B **64**, 12–28

Dearnaley G. (1964): The channeling of Mev ions through silicon detectors. IEEE Trans Nucl Sci **NS-11**, 243–253

Domeij B. (1965): Crystal lattice effects in the emission of charged particles from monocrystalline sources. Nucl Instr Meth **38**, 207–209

Domeij B. and Eriksson L. (1965): Private communication

Domeij B., Bergström I., Davies J.A. and Uhler J. (1963): A method of determining heavy-ion ranges by analysis of α-line shapes. Arkiv Phys **24**, 399–411

Domeij B., Brown F., Davies J.A., Piercy G.R. and Kornelsen E.V. (1964a): Anomalous penetration of keV ions in monocrystalline tungsten. Phys Rev Lett **12**, 363–366

Domeij B., Brown F., Davies J.A. and McCargo M. (1964b): Ranges of heavy ions in amorphous oxides. Can J Phys **42**, 1624–1634

Erginsoy C. (1964): Anomolous penetration of rare gas atoms in lattice channels. Phys Rev Lett **12**, 366–367

Fastrup B., Hvelplund P. and Sautter C.A. (1965): Stopping cross-sections in carbon of 0.1–1.0 MeV atoms with $Z_1 < 20$. Nucl Instr Meth **38**, 260–260

Fluit J.M. and Rol P.K. (1964): Angular dependent sputtering of Cu single crystals by 20-keV noble gas ions. Physica **30**, 857–869

Gemmell D.S. and Holland R.E. (1965): Blocking effects in the emergence of charged particles from single crystals. Phys Rev Lett **14**, 945–948

Gibson W.M., Erginsoy C., Wegner H.E. and Appleton B.R. (1965): Direction and energy distribution of charged particles transmitted through single crystals. Phys Rev Lett **15**, 357–360.

Hermann H., Lutz H. and Sizmann R. (1966): Zur Eindringtiefe von 70 keV-Kryptonionen in Wolfram-einkristallen. Z Naturforsch **219**, 365–366

Hvelplund P. and Fastrup B. (1968): Stopping cross-sections in carbon of 0.2–1.5 MeV atoms with $21 < Z_1 < 39$. Phys Rev **165**, 408–414

Kemper K.W. and Fox J.D. (1972): Comparative pulse-height anomaly for protons and α-particles in silicon surface-barrier detectors. Nucl Instr Meth **105**, 333–334

Kessel Q.C., Russek A. and Everhart E. (1965): Three discrete Q values in Ar^+/Ar° collisions. Phys Rev Lett **14**, 484–486

Khan J.M., Potter D.L., Worley R.D. and Smith H.P., Jr. (1966): Characteristic X-Ray production in single crystals (Al, Cu, W) by proton bombardment. Part I. Phys Rev **148**, 413–419

Khan J.M., Potter D.L., Worley R.D. and Smith H.P., Jr. (1967): Characteristic X-Ray production in single crystals (Al, Cu, W) by proton bombardment. Part II. Phys Rev **163**, 81–85

Kingsbury E.F. and Ohl R.S. (1952): Photoelectric properties of ionically bombarded silicon. Bell Syst Tech J **31**, 804–815

Langley R.A. (1973): Study of the response of silicon surface-barrier detectors to protons and alpha particles. Nucl Instr Meth **113**, 109–112

Lennard W.N. and Winterbon K.B. (1987): Response of silicon detectors to protons and helium ions. Nucl Instr Meth B **24–25**, 1035–1038

Lindhard J. (1965): Influence of the crystal lattice on the motion of energetic charged particles. Kgl Dan Vid Selsk Mat Fys Medd **34, no. 14**, 1–64

Lindhard J. and Scharff M. (1961): Energy dissipation of ions in the keV region. Phys Rev **124**, 128–130

Lindhard J., Nielsen V, Scharff M. and Thomsen P.V. (1963a): Notes on Atomic Collisions: Integral equations governing radiation effects. Kgl Dan Vid Selsk Mat Fys Medd **33, no. 10**, 1–42

Lindhard J., Scharff M. and Schiott H.E. (1963b): Notes on Atomic Collisions: Range concepts and heavy ion ranges. Kgl Dan Vid Selsk Mat Fys Medd **33, no. 14**, 1–42

Lutz H. and Sizmann R. (1963): Super ranges of fast ions in copper single crystals. Phys Lett **5**, 113–114

Mayer, J.W. (1959): Performance of germanium and silicon surface barrier diodes as alpha particle spectrometers. J Appl Phys **30**, 1937

Mayer, J. and Gossick, B. (1956): Use of Au-Ge broad area barrier as alpha particle spectrometer. Rev Sci Instr **27**, 407–408

McCargo M., Davies J.A. and Brown F. (1963): Range of ^{133}Xe and ^{41}Ar ions of keV energies in tungsten. Can J Phys **41**, 1231–1244

Mitchell J.B., Agami S. and Davies J.A. (1975): The use of surface-barrier detectors for energy calibration of MeV ion accelerators. Rad Effects **28**, 133–139

Nelson R.S. and Thompson M.W. (1963): The penetration of energetic ions through open channels in a crystal lattice. Phil Mag **8**, 1677–1689

Nielsen K.O. (1956): The range of atomic particles with energy around 50 keV. Private communication (doctoral thesis)

Ohl R.S. (1952): Properties of ion-bombarded silicon. Bell Syst Tech J **31**, 104–121

Ormrod J.H. and Duckworth H.E. (1963): Stopping cross-sections in carbon for low-energy atoms with Z less than 12. Can J Phys **41**, 1424–1442

Palevsky H., Hughes D.J., Kley W. and Tunkelo E. (1959): Lattice vibrations in silicon by scattering of cold neutrons. Phys Rev Lett **2**, 258–259

Piercy G.R., McCargo M., Brown F. and Davies J.A. (1964): Experimental evidence for the channeling of heavy ions in monocrystalline aluminum. Can J Phys **42**, 1116–1134

Powers D. and Whaling W. (1962): Range of heavy ions in solids. Phys Rev **126**, 61–69

Robinson M.T. and Oen O.S. (1963): Computer studies of the slowing down of energetic atoms in crystals. Phys Rev **132**, 2385–2398

Rol P.K., Fluit J.M. and Kistemaker J. (1960): Sputtering of Cu by bombardment with ions of 5–25 keV. Physica **26**, 1000–1008

Saris F.W., Van der Weg W.F., Tawara and Laubert R. (1972): Radiative transitions between quasi-molecular levels during energetic atom-atom collisions. Phys Rev Lett **28**, 717–720

Schmitt R.A. and Sharp R.A. (1958): Measurement of the range of recoil atoms. Phys Rev Lett **1**, 445–447

Shockley W. (1961): Problems related to p-n junctions in silicon. Czech J Phys B **11**, 81–121

Sigmund P. (1969): On the number of atoms displaced by implanted ions or energetic recoil atoms. Appl Phys Lett **14**, 114–117

Tulinov A.F., Kulikauskas V.S. and Malov M.M. (1965): Proton scattering from a tungsten single crystal. Phys Lett **18**, 304–307

VanLint V.A.J., Schmitt R.A. and Suffredini C.S. (1961): Range of 2–60 keV recoil atoms in Cu, Ag and Au. Phys Rev **121**, 1457–1463

Vavilov V.S. (1959): On photo-ionization by fast electrons in germanium and silicon. J Phys Chem Solids **8**, 223–226

Wandell C. (1964): Private (unpublished) communication on the origin of the tungsten 'supertail'

Weijers T.D.M., Davies J.A., Elliman R.G., Ophel T.R. and Timmers H. (2002): Silicon detector response to heavy ions at energies of 1–2 MeV per a.m.u. Nucl Instr Meth B **190**, 387–390

Index

This index has been compiled on the basis of keywords provided by the authors of individual contributions. Each entry refers to the start page(s) of the respective contribution(s).

adatoms 357
affinity level 465
affinity, electron 465
alkali layer 465
amorphisation 13, 227
amorphous materials 383
amorphous zones 329
amorphous-crystalline interfaces 227
amorphous-crystalline multilayers 227
analysis, ion beam 133
angular distribution 405
annealing, dynamic 227
approximation, Gaussian 151
athermal melting 293
atmospheres, generation of 13
atomic displacements 227
Auger electron spectroscopy 497
Auger electron spectroscopy, electronic temperatures 497
Auger electron spectroscopy, inner shell ionisation 497
Auger electron spectroscopy, track potential 497
band gaps, surface projected 625
Barkas correction 557
beam diagnostics 37
Bethe stopping theory 557
Betz–Grodzins models 595
binary encounter collisions 497
biological effectiveness 37
Bloch stopping theory 557
blocking 655
Bohr stopping theory 557
Bohr–Lindhard models 595
Bradley–Harper theory 207
bubbles 329
buried interfaces 133
carbon ions 357
carbon nanotubes 357
cells, ion tracks in 59
channeled particles, radiation from 655
channeling 731
channeling, energy loss in 655
charge exchange 557
charge state 109
charge transfer 625
charge transfer, multi-electron 625
charge transfer, resonant 625
chemical effects 357
Chudakov effect 699
classical *versus* quantal description 655
cluster emission 405, 433
cluster emission, fragmentation 405
cluster formation 405
cluster impact 433
collective excitations 497
configurational energy states 383
correction, Barkas 557
correction, shell 557
correlated emission 497
cosmic rays 13
Coulomb explosion 293
coupling, surface 497
craters 329, 433
crystal-glass transition 383

crystal-glass transition, amorphization 383
crystal-glass transition, ergodicity 383
crystal-glass transition, percolution transition 383
crystallisation, epitaxial 227
damage, electron irradiation 357
damage, ion 227
damage, lower-energy electron 357
damage, nuclear collision 357
damage, radiation 357, 731
dechanneling 655
defects, extended 329
defects, ion-induced 207
defects, point 357
density correction in stopping 557
deposition 87
deposition, radial energy 59
depth resolution, ultimate 133
detector, solid state 731
diagnostics, beam 37
diffusion, radiation enhanced 13
diffusion, surface 207
displacements, atomic 227
distribution, angular 405
distribution, energy 405
divertor 87
dosimetry 37
double strand breaks 59
dynamic annealing 227
dynamic screening 151
effects, chemical 357
effects, finite size 625
effects, relativistic 655
effects, single ion 329
effects, strong field 699
electron affinity 465
electron emission 525
electron emission, kinetic electron emission 525
electron emission, potential electron emission 525
electron irradiation damage 357
electron number statistics, coincident measurement 525
electron number statistics, surface-scattered projectiles 525
electron spectra 557
electron sputtering 357
electron yield, total 525
electronic desorption 13
electronic excitations 13
electron-photon coupling 263
emission, cluster 433
encounter collisions, binary 497
energy distribution 405
energy loss in channeling 655
energy states, configurational 383
energy, fusion 87
energy-loss profile, width of 151
energy-loss spectra 557
enhanced FIBs, need for 133
epitaxial crystallisation 227
epitaxy, solid phase 227
equilibrium charge states of ions in solids 595
erosion 87
evolution, morphology 187
evolution, nanophore 187
excitations, collective 497
excitations, electronic 13
experimental distinction between kinetic and potential electron emission 525
extended defects 329
FAIR project 109
fast melting 109
fast neutron recoil atoms 731
Fermi shuttle 497
finite size effects 625
formation length 699
fragmentation 699
free-electron metals *versus* band structure 625
fullerenes 357
fusion energy 87
fusion, inertial 109
gas release 731
gas trapping 731
Gaussian approximation 151
generation of atmospheres 13
grain sputtering 13
graphene 357
graphite 357
grazing incidence 525
guided self-organization, nanoscale morphology control 187

heating and cooling 655
heavy ions 595
high charges, primary ionisation 497
high-resolution 329
history 731
image potential 465
impact parameter dependence 151
impact, cluster 433
impurities and defects 655
inertial fusion 109
infinite velocity 465
instability 207
instability, morphological 187
insulator surfaces 525
insulators 595
insulators, amorphisable 263
insulators, non-amorphisable 263
interaction, plasma-surface 87
interfaces, amorphous-crystalline 227
interfaces, buried 133
internal and exit charge states 595
interstellar medium 13
interstitials 357
ion beam analysis 133
ion channeling 227
ion damage 227
ion emission, secondary 465
ion range in tissue 37
ion ranges 731
ion scattering limits 133
ion tracks 13
ion tracks, in cells 59
ionic crystals 263
ion-induced defects 207
ionisation potential 465
ionisation probability 465
ionization and excitation probability 405
ionization energy loss 699
ionization, multiple 151
ions carbon 357
ions, w-values for 37
irradiation, single cell 59
isotope separator 731
kinetic Monte Carlo 207
kinetics, relaxation 187
layer, alkali 465
level width 465
light ions 595
Lindhard theory 655
linear cascade sputtering 405
localised *versus* delocalised capture 625
low-energy electron damage 357
LPM effect 699
magnetospheric ions 13
materials, amorphous 11
measurements, stopping 557
melting, athermal 293
metal *versus* insulator surfaces 625
metal surfaces 525
metals 329, 595
micro beam 59
micrometeorite impact 13
microscopy, transmission electron 329
minimum yields and widths 655
monolayer resolution 151
morphological instability 187
morphology evolution 187
morphology, surface 207
multi-electron charge transfer 625
multilayers, amorphous-crystalline 227
multiple ionization 151
nanophore evolution 187
nano-structures 133
nanotubes, carbon, 357
need for enhanced FIBs 133
non-adiabatic transitions 625
non-proportionality effects, slow molecular projectiles 525
nuclear collision damage 357
nuclear lifetimes 655
nuclear spectroscopy 731
organic and molecular solids, desorption mechanism 405
organic and molecular solids, secondary ion formation 405
organic and molecular solids, sputter depth profile 405
parallel velocity effect 625
pattern formation 207
perturbation, strong 497
phase transition 109, 357
planetary regolith 13

planning, treatment 37
plasma-surface interaction 87
point defects 357
polyatomic projectile impact, emission mechanism 405
polyatomic projectile impact, excitation and ionization phenomena 405
polyatomic projectile impact, linear cascade and spike regime 405
probability, ionisation 465
proton pick-up 699
quantum dots 133
radial energy deposition 59
radiation chemistry 13
radiation damage 357, 731
radiation enhanced diffusion 13
radiation from channeled particles 655
radiation synthesis 13
radiological weight factor 59
radiolysis 13
radiotherapy 37
rate equation 625
recoil atoms, fast neutron 731
relativistic effects 655
relativistic effects, in stopping 557
relaxation kinetics 187
release, gas 731
resolution, monolayer 151
resonant charge transfer 625
ripples, 207
saturation effects 595
scattering 557
scattering limits, ion 133
screening 557
screening, dynamic 151
secondary ion emission 465
segregation 13
semiconductors 329, 595
sensitivity, ultimate 133
shell correction 557
shock wave 293
single cell irradiation 59
single collision 151
single ion effects 329
single strand breaks 59
slow hydrogen in solids, bound states 595
slow hydrogen in solids, pions 595
slow hydrogen in solids, positive muons 595
slow hydrogen in solids, positrons 595
solid phase epitaxy 227
solid state detector 731
spatial resolution, ultimate 133
spectra, electron 557
spectra, energy-loss 557
spectroscopy, Auger electron 497
spectroscopy, nuclear 731
spikes 433
sputter yield 207
sputtering 13, 207, 433
sputtering, angular distribution 433
sputtering, depth of origin 433
sputtering, electron 357
sputtering, energy distribution 433
sputtering, grain
sputtering, linear cascade 405
sputtering, molecular and organic solids 433
sputtering, preferential sputtering 433
sputtering, yield 433
stellar shocks 13
stellar winds 13
stoichiometry determination, ultimate 133
stopping 557
stopping, density correlation in 557
stopping, relativistic effects in 557
stopping measurements 557
stopping power 109
stopping power, ratios 37
stopping power, threshold 293
stopping theory, Bethe 557
stopping theory, Bloch 557
stopping theory, Bohr 557
straggling 557
strand breaks, double 59
strand breaks, single 59
strong field effects 699
strong perturbation 497
structure, track 59
supertail 731
surface coupling 497
surface diffusion 207
surface morphology 207
surface perturbation 465

surface projected band gaps 625
surface ripples 207
surface structure triangulation 525
surface topography 433
surfaces, insulator 525
surfaces, metal 525
swift-ion tracks 433
thermal spike 293
thermal vibrations 655
thermodynamics 293
thermodynamics, supercooling 293
thermodynamics, superheating 293
threshold behaviour 525
threshold, stopping power 293
tissue, ion range in 37
total electron yield 525
track description 263
track description, Poisson law 263
track description, threshold of track formation 263
track description, track morphology 263
track description, velocity effect 263
track mechanics 293
track mechanics, hillock formation 293
track mechanics, ion hammering 293
track model 263
track model, electron-photon coupling 263
track model, energy deposition 263
track model, linear energy loss 263
track model, radial energy distribution 263
track model, sputtering 263
track model, transient thermal process 263
track structure 59
tracks, swift-ion 433
transitions, non-adiabatic 625
transitions, phase 109
transmission electron microscopy 329
transport theory 433, 497
trapping, gas 731
treatment planning 37
triangulation, surface structure 525
tunnelling 625
tunnelling model 465
ultimate depth resolution 133
ultimate sensitivity 133
ultimate spatial resolution 133
ultimate stoichiometry determination 133
vacancies 357
velocity effect 557
velocity effect, parallel 625
viscoleastic properties 383
voids 329
warm dense matter 109
weight factor, radiological 59
width of energy-loss profile 151
work function 465
w-values for ions 37
yields and widths, minimum 655
zones, amorphous 329

Manuscript

General. – Manuscripts and illustrations must comply with the details given below. The original manuscript and illustrations plus one clear copy of both should be sent to the editor of the series. Manuscripts on digital media are accepted; contact the editor in advance, giving technical specifications.

A manuscript should contain no less than 48 printed pages. This also applies to the Mat.fys. Medd. where contributions to the history of science are welcome.

Language. – Manuscripts in Danish, English, German and French are accepted; in special cases other languages too. Linguistic revision may be made a condition of final acceptance.

Title. – Titles should be kept as short as possible, preferring words useful for indexing and information retrieval.

Abstract, Summary. – An abstract in English is required. It should be of 10-15 lines, outline main features, stress novel information and conclusions, and end with the author's name, title, and institutional and/or private postal address. – Papers in Danish must be provided with a summary in another language as agreed between author and editor.

Manuscript. – Page 1 should contain title, author's name and the name of the Academy. Page 2: Abstract, author's name and address. Page 3: Table of contents if necessary. Consult a *recent* issue of the series for general layout. Indicate the position of illustrations and tables. A printout must accompany manuscripts submitted electronically.

Figures. – All illustrations submitted must be marked with the author's name. It is important that the illustrations are of the highest possible quality. Foldout figures and tables should be avoided.

References. – In general, the editor expects all references to be formally consistent and in accordance with accepted practice within the particular field of research. Bibliographical references should be given in a way that avoids ambiguity.

Correspondence

Manuscripts are to be sent to

The Editor
Det Kongelige Danske Videnskabernes Selskab
H.C. Andersens Boulevard 35
DK-1553 Copenhagen V, Denmark.
Tel: +45 33 43 53 00
Fax: +45 33 43 53 01.
E-mail: e-mail@royalacademy.dk.
www.royalacademy.dk

Questions concerning subscription to the series should be directed to the Academy

Editor Flemming Lundgreen-Nielsen

Det Kongelige Danske Videnskabernes Selskab
The Royal Danish Academy of Sciences and Letters

Matematisk-fysiske Meddelelser

Priser ekskl. moms / Prices excl. VAT

45	*Magnetism in Metals.* A symposium in Memory of Allan Mackintosh, Copenhagen, 26-29 August 1996. Invited Review Papers. 1997. Edited by *D.F. McMorrow, J. Jensen* and *H.M. Rønnow.*	500, -
46:1	Caspar Wessel: *On the Analytical Representation of Direction. An Attempt Applied Chiefly to Solving Plane and Spherical Polygons.* Translated by *Flemming Damhus.* With introductory chapters by *Bodil Branner, Nils Voje Johansen, Kirsti Andersen.* Edited by *Bodil Branner* and *Jesper Lützen.* 1999. 150 pp. Fig.	500, -
46:2	*Around Caspar Wessel and the Geometric Representation of Complex Numbers.* Invited papers. Edited by *Jesper Lützen.* 2001. 304 pp.	300, -
47	Aksel Wiin-Nielsen: *On Limited Predictability.* 1999. 40 pp.	50, -
48	Aksel Wiin-Nielsen: *On Atmospheric Waves.* 2000. 53 pp.	80, -
49	Anders Hald: *On the History of Series Expansions.* 2002. 88 pp.	140, -
50	U. Bernth, R. Brousse, R. Frei & H. Sørensen: *The Origin of Phonolites and Thachytes from the Col de Guéry Area.* Le Mont-Dore, Massif Central, France. 2002. 61 pp.	100, -
51	Anders Hald: *Nogle danske statistikeres liv og deres værker.* 2005. 36 pp.	40, -
52:1	*Ion Beam Science: Solved and Unsolved Problems.* Invited lectures presented at a symposium arranged by the Royal Danish Academy of Sciences and Letters, Copenhagen, 1-5 May 2006. Part I. Edited by *Peter Sigmund.* 2006. 376 pp.	350, -
52:2	*Ion Beam Science: Solved and Unsolved Problems.* Invited lectures presented at a symposium arranged by the Royal Danish Academy of Sciences and Letters, Copenhagen, 1-5 May 2006. Part II. Edited by *Peter Sigmund.* 2006. 384 pp.	350, -

Printed in Denmark by Special-Trykkeriet Viborg a-s.
ISSN 0023-3323. ISBN10 87-7304-330-3; ISBN13 978-7304-330-1